

DAVID DAVIES

COMPUTATIONS OF TOMORROW'S RAIN

DEPARTMENT OF METEOROLOGY

MCGILL UNIVERSITY

Ph.D. Thesis

ABSTRACT

A numerical scheme to predict precipitation amount on a computer has been developed and put into routine use. It operates in sequence with a baroclinic model based on the potential vorticity equation. Large scale and small scale precipitation amounts are predicted every hour for each of three layers of the atmosphere. The large scale amounts are computed from "wet" vertical motions, which are based on "dry" vertical motions made available by the baroclinic model, and explicit forecasts of temperature and dew point depression. The small scale amounts are computed from three empirical formulae.

In some recent experiments the precipitation scheme and the baroclinic model were integrated in parallel. The main innovations were in the baroclinic model. They included a coefficient of eddy diffusion of potential vorticity which depends on the baroclinicity, seasonal variations in the linkages between the levels, and the incorporation of latent heat, radiation, and ocean heating effects.

COMPUTATIONS OF TOMORROW'S RAIN

DAVID DAVIES

COMPUTATIONS OF TOMORROW'S RAIN

by

David Davies

A thesis submitted to the Faculty of Graduate Studies
and Research in partial fulfilment of the requirements
for the degree of Doctor of Philosophy

Department of Meteorology,
McGill University,
Montreal, Canada

July, 1970

ACKNOWLEDGEMENTS

I am deeply indebted to Dr. Michael Krizak, Head of the Dynamic Prediction Research Unit, for arousing a long dormant ambition to register for doctorate studies, and for assigning the precipitation scheme project which provided me with the material for this thesis. I appreciate the encouragement Mr. J.M. Leaver, O.I.C. of the Central Analysis Office, has given me while I have been working on the Precipitation scheme project.

Marvin P. Olson and W.S. Creswick have been responsible for the 1968 and 1970 versions of the baroclinic model which made a successful precipitation scheme possible. Dr. A.J. Robert, Dr. M. Krizak, R.A. Strachan, and Dr. W.L. Godson have also made major contributions to the development of the baroclinic model at one time or another.

Joseph Simla collaborated with me in the early planning stages of the precipitation project. Dr. Maurice B. Danard contributed several specific ideas which are acknowledged in the text.

Mr. J. Simla, Head of the Computer Services Unit, and his staff have always been fully co-operative in making computer facilities available, and took over the responsibility of optimising the running times of the precipitation programs when they became operational. Mr. R. Anderson, Head of the Analysis and Prognosis Unit, and his staff have monitored the operational precipitation forecasts with enthusiasm, and have been very helpful in drawing unusual features to my attention.

Special thanks go to Yvon R.G. Bourassa and Mrs Claudette Thibeault. Mr. Bourassa was responsible for most of the systems aspects, both for the original sequential precipitation scheme and the parallel model

experiments, including in particular the control programs which move data to and from the disk and drum. He wrote the skill factor verification program, including the objective analysis of precipitation reports, and processed the skill factor data from the operational run and the parallel model experiments. He also wrote the characteristic areas verification program for monitoring the height, temperature, and dew point depression forecasts produced in the operational run. Mr. Bourassa drew up the charts from the parallel model experiments and arranged for their reduction to thesis page size. Mrs. Thibeault wrote the input and output programs for the parallel model experiments, and prepared the climatological charts of 850, 700 and 500 mb temperatures, ocean temperatures, and snow cover. She also wrote the threat score evaluation programs, and processed the threat score data and the characteristic areas program data from the operational run. She efficiently organised the production of the manuscript, drafted the Figures other than the charts, prepared many of the Tables, and did about two-thirds of the typing. I thank Miss Therese Savoie for doing the remainder of the typing.

Prof. B.W. Boville provided valuable editorial assistance in the preparation of the manuscript.

I thank all colleagues in the Dynamic Prediction Research Unit, both past and present, for their many helpful discussions, and for providing a stimulating intellectual environment in which to work.

Finally, I wish to acknowledge with gratitude the support of Canadian Meteorological Service in allowing me the privilege of pursuing this research.

TABLE OF CONTENTS

Acknowledgments	ii
List of Tables	xii
List of Figures	xxii
List of Symbols	xxxii
Abstract	xxxvi
Résumé	xxxvii
Part I : Introduction	1
1. General Aims	1
2. Historical Highlights	1
3. Current Problems	5
3.1 The problem of predictability	5
3.2 Primitive equations models vis-a-vis filtered equations models	8
3.3 Potential vorticity equation models vis-a-vis omega equation models	9
4. General Review of Precipitation Forecasting by Computer	10
Part II : The Sequential Version of the Baroclinic Model	12
5. The History of the CAO Baroclinic Model	12
5.1 Introductory remarks	12
5.2 Godson's proposed model	13
5.3 The prototype model	14

5.4	The octagon model	18
5.5	The 1968 operational model	21
5.6	The 1970 operational model	24
6.	The Baroclinic Model Equations and the Primary and Secondary Constraints	28
7.	Derivation of the Baroclinic Model Equations without Constraints	34
8.	Numerical Values of the Control Coefficients	37
9.	The Change-over from Smoothing to Eddy Diffusion Constraints	42
10.	The Derived 700 mb Stream Function Forecasts	48
11.	Verification Scores for the Forecast Height Charts	53
11.1	Standard areas	53
11.2	Characteristic areas	54
Part III : The Sequential Version of the Precipitation Scheme		64
12.	Origins of the Sequential Approach	64
13.	Tables of Unit Condensation Rate	66
14.	Choice of Moisture Parameter: Dew Point Depression	70
15.	The Large Scale Precipitation Amount	72
16.	The "Dry" Vertical Motion	82

17. The "Wet" Vertical Motion	91
18. The Temperature Forecasts	109
19. The Dew Point Depression Forecasts	129
20. The Small Scale Precipitation Amount	149
20.1 The empirical approach	149
20.2 Frontal showers	151
20.3 Air mass showers	152
20.4 Induced instability showers	156
21. The Total Precipitation	156
22. The Evaluation of the Operational Precipitation Forecasts	164
Part IV : The Pilot Project on Parallel Operation	200
23. The Pilot Model	200
Part V : The Main Parallel Model Experiments	208
24. Outline	208
25. The Control Coefficients	212
26. The Eddy Diffusion Terms	218
27. Mountain and Friction Effects	228
28. The Diabatic Effects: I & II Latent Heat Release and Absorption	232

29.	The Diabatic Effects: III Ocean Heating	239
30.	The Diabatic Effects: IV Radiation	243
31.	The Parallel Baroclinic Model	249
	31.1 The final version	249
	31.2 The unsuccessful experiments	250
32.	The Parallel Precipitation Scheme	255
	32.1 The large scale precipitation amount	255
	32.2 The "dry" vertical motion	255
	32.3 The "wet" vertical motion	258
	32.4 The temperature forecasts	258
	32.5 The dew point depression forecasts	261
	32.6 The small scale precipitation amount	263
	32.7 The total precipitation	263
33.	Other Features	264
	33.1 Cloud forecasts	264
	33.2 Terminal forecasts	265
	33.3 Derived 1000 mb height forecasts	265
34.	Results	266
35.	Discussion	356
	35.1 The case of 12Z Jan 29th 1969	356
	35.2 The case of 00Z Jul 26th 1969	359
	35.3 The case of 12Z Sep 9th 1969	360
	35.4 The case of 00Z Nov 18th 1969	360

35.5	The case of 00Z Dec 21st 1969	362
35.6	The case of 12Z Dec 25th 1969	365
35.7	The case of 00Z Jan 25th 1970	368
35.8	The case of 00Z Jan 27th 1970	370
35.9	The case of 00Z Jan 28th 1970	372
35.10	The case of 00Z Mar 3rd 1970	374
35.11	The case of 00Z Mar 26th 1970	376
35.12	Summary	377
Part VI : Conclusions		380
36.	Conclusions	380
References		387
Appendix A : A Review of Some Basic Equations		393
A1.	Equations Governing a Dry Atmosphere	393
A2.	Equations Governing a Moist Unsaturated Atmosphere	397
A3.	Equations Governing a Moist Saturated Atmosphere	400
Appendix B : A Catalogue of Numerical Procedures		405
B1.	Introduction	405

B2. The Definition of a Stencil Operator	405
B3. The Standard Smoother	406
B4. The Five-point Smoother	406
B5. The Standard Unsmoother	407
B6. The Special Unsmoother	408
B7. Horizontal First Derivatives: I Standard Finite Difference Formulae	408
B8. Horizontal First Derivatives: II Special finite Difference Formulae	409
B9. Horizontal Second Derivatives: Standard Finite Difference Formulae	411
B10. The Laplacian Finite Difference Operator	412
B11. The Standard First Order Jacobian Operator	413
B12. The Shuman Jacobian	414
B13. First Derivatives of Pressure: Finite Difference Formulae	414
B14. Second Derivatives of Pressures: Finite Difference Formulae	416
B15. Special Non-centred First Derivative of Pressure at 200 mb	416
B16. First Derivatives of Time: Finite Difference Formulae	418
B17. Formulae For Computing RESE Verification Scores	419

B18. Second Derivatives Parallel and Normal to the Flow	420
Appendix C : The Main Integration Cycle of the Sequential Baroclinic Model	421
C1. Details of the Main Integration Cycle	421
C2. Limitations on the Main Integration Cycle	425
Appendix D : Terrain Effects	427
D1. Primary Constraints Due to Terrain	427
Appendix E : Skill Factor Verifications of Precipitation Amount Forecasts	434
E1. The Grid-point Approach to Objective Verification	434
E2. The Objective Analysis of Observed Precipitation	434
E3. The Penalty Table Verification Score	437
E4. The Penalty Table Skill Factors	438
Appendix F : The Three-dimensional Relaxations	440
F1. Petterssen's Equation	440
F2. The Baroclinic Model	441
Appendix G : The Low Tropopause Marker	442

G1. The Definition of N_E	442
Appendix H : Formulae for Secondary Latent Heat Effects	443
H1. Liquefaction or Freezing of Falling Precipitation	443
H2. Evaporation of Falling Precipitation	444
Appendix I : The Effective Ocean Equilibrium Temperatures	445
I1. At the 1000 mb Level	445
I2. At the Levels Aloft	447

LIST OF TABLES

Table	Page
1. Numerical values of miscellaneous constants	41
2. Values of the static stability, σ_s , for the "dry" standard atmosphere.	41
3. Values of the eddy diffusion coefficients used in the 1970 baroclinic model.	45
4. Values of the eddy diffusion coefficients used in the derived 700 mb stream function forecasts and also in the vertical motion computations of the 1970 model.	50
5. Tables of unit condensation rate, $U_p(T)$ in 10^{-6} inches rain/hour, for layers 150 mb thick (except the layer centred at 500 mb which is 250 mb thick) ascending at 1 mb/hour,	69
6. Values of the latent heat factor H^* at -10 C deg and 0 C deg, the static stability of the standard atmosphere, and the static stability of an "arbitrary rainy atmosphere".	93
7. Values of the constants used in the maximum amplification restrictions imposed on the "wet" vertical motions.	97
8. Typical first-hour values for the 700 mb vertical motion fields.	103
9. Values of the constants used in the adjustments to the 850 mb temperature fields when spurious air mass instability develops.	110

Table	Page
10. Values of the constants used in the vertical motion damping formula.	110
11. Moist adiabatic lapse rate tables, $\frac{dT}{dp} _{\theta w}$	111
12. Values of the constant used in the computation of $\frac{dT}{dp} _{\theta}$	112
13. Maximum and minimum restrictions on the temperature fields.	113
14. Values of T_{50}^L , the 500 mb temperature of a parcel of air lifted adiabatically from 850 mb, used in the computation of the Showalter Index.	114
15. Initial time values of the eddy diffusion coefficients used in the forecast equations for temperature and dew point depression; these are augmented by 1% per hour.	118
16. Values of the constants used in computing $\frac{dS}{dp} _{\theta}$	132
17. Values of the constants used in the term representing upward diffusion of moisture from the Earth's surface.	133
18. Values of the constants in the term representing net evaporation from falling precipitation.	133
19. The constants used in the dew point depression prediction scheme that were reset at the time of the change-over from the octagon model to the 1968 model.	135

Table	Page
20. Typical winter and summer values of the mean errors of the 36-hour dew point depression forecasts over the 504-point grid.	146
21. Values of the constants used in the empirical formula for frontal showers, air mass showers, and induced instability showers.	155
22. Values of the eddy diffusion coefficients used at all levels in the pilot model.	202
23. Mean 48-hour CRFSE verification scores for five cases.	205
24. Mean magnitudes of the displacement and depth errors of the five major low centres in the 48-hour forecasts of 850 mb height.	206
25. Values of the constants used in the eddy diffusion constraints of the parallel model.	222
26. Values of the constants used in the computation of the effective latent heat.	233
27. Values of the constants used in the ocean heating term.	240
28. Values in hours of the e_m , e_{mn} , and e_{mnn} used in the computation of $(\tau_y)_m$ when $P_0 = 1000, 925, 775$ and 625 mb.	245
29. Values of the constants, other than the e-factors, which are used in the computation of the radiation term.	245

Table	Page
30. Values of the constants used in the vertical motion damping formula in the parallel model experiments.	260
31. CRMSE Verification Scores for the 238-point grid for the 850 mb height forecasts for the series of test cases integrated in the parallel model experiments.	313
32. CRMSE Verification Scores for the 238-point grid for the 700 mb height forecasts for the series of test cases integrated in the parallel model experiments.	314
33. CRMSE Verification Scores for the 238-point grid for the 500 mb height forecasts for the series of test cases integrated in the parallel model experiments.	315
34. CRMSE Verification Scores for the 238-point grid for the 200 mb height forecasts for the series of test cases integrated in the parallel model experiments.	316
35. CRMSE Verification Scores for the 504-point grid for the 850 mb height forecasts for the series of test cases integrated in the parallel model experiments.	317
36. CRMSE Verification Scores for the 504-point grid for the 700 mb height forecasts for the series of test cases integrated in the parallel model experiments.	318
37. CRMSE Verification Scores for the 504-point grid for the 500 mb height forecasts for the series of test cases integrated in the parallel model experiments.	319

Table	Page
38. CRMSE Verification Scores for the 504-point grid for the 200 mb height forecasts for the series of test cases integrated in the parallel model experiments.	320
39. CRMSE Verification Scores for the interior of the 1221-point grid for the 850 mb height forecasts for the series of test cases integrated in the parallel model experiments.	321
40. CRMSE Verification Scores for the interior of the 1221-point grid for the 700 mb height forecasts for the series of test cases integrated in the parallel model experiments.	322
41. CRMSE Verification Scores for the interior of the 1221-point grid for the 500 mb height forecasts for the series of test cases integrated in the parallel model experiments.	323
42. CRMSE Verification Scores for the interior of the 1221-point grid for the 200 mb height forecasts for the series of test cases integrated in the parallel model experiments.	324
43. RMSE Verification Scores for the 238-point grid for the 850 mb temperature forecasts for the series of test cases integrated in the parallel model experiments.	325
44. RMSE Verification Scores for the 238-point grid for the 700 mb temperature forecasts for the series of test cases integrated in the parallel model experiments.	326

Table	Page
45. RMSE Verification Scores for the 238-point grid for the 500 mb temperature forecasts for the series of test cases integrated in the parallel model experiments.	327
46. RMSE Verification Scores for the 504-point grid for the 850 mb temperature forecasts for the series of test cases integrated in the parallel model experiments.	328
47. RMSE Verification Scores for the 504-point grid for the 700 mb temperature forecasts for the series of test cases integrated in the parallel model experiments.	329
48. RMSE Verification Scores for the 504-point grid for the 500 mb temperature forecasts for the series of test cases integrated in the parallel model experiments.	330
49. RMSE Verification Scores for the interior of the 1015-point grid for the 850 mb temperature forecasts for the series of test cases integrated in the parallel model experiments.	331
50. RMSE Verification Scores for the interior of the 1015-point grid for the 700 mb temperature forecasts for the series of test cases integrated in the parallel model experiments.	332
51. RMSE Verification Scores for the interior of the 1015-point grid for the 500 mb temperature forecasts for the series of test cases integrated in the parallel model experiments.	333

Table	Page
52. RMSE Verification Scores for the 238-point grid for the 850 mb dew point depression forecasts for the series of test cases integrated in the parallel model experiments.	334
53. RMSE Verification Scores for the 238-point grid for the 700 mb dew point depression forecasts for the series of test cases integrated in the parallel model experiments.	335
54. RMSE Verification Scores for the 238-point grid for the 500 mb dew point depression forecasts for the series of test cases integrated in the parallel model experiments.	336
55. RMSE Verification Scores for the 504-point grid for the 850 mb dew point depression forecasts for the series of test cases integrated in the parallel model experiments.	337
56. RMSE Verification Scores for the 504-point grid for the 700 mb dew point depression forecasts for the series of test cases integrated in the parallel model experiments.	338
57. RMSE Verification Scores for the 504-point grid for the 500 mb dew point depression forecasts for the series of test cases integrated in the parallel model experiments.	339
58. RMSE Verification Scores for the interior of the 1015-point grid for the 850 mb dew point depression forecasts for the series of test cases integrated in the parallel model experiments.	340

59. RMSE Verification Scores for the interior of the 1015-point grid for the 700 mb dew point depression forecasts for the series of test cases integrated in the parallel model experiments. 341
60. RMSE Verification Scores for the interior of the 1015-point grid for the 500 mb dew point depression forecasts for the series of test cases integrated in the parallel model experiments. 342
61. Threat Scores for 00-24 hours for a threshold of 0.01 inches for the series of test cases integrated in the parallel model experiments. 343
62. Threat Scores for 12-36 hours for a threshold of 0.01 inches for the series of test cases integrated in the parallel model experiments, 344
63. Threat Scores for 24-48 hours for a threshold of 0.01 inches for the series of test cases integrated in the parallel model experiments. 345
64. Threat Scores for 00-24 hours for thresholds of 0.25 inches, 0.50 inches, and 1.00 inch for the series of test cases integrated in the parallel model experiments. 346
65. Threat Scores for 12-36 hours for thresholds of 0.25 inches, 0.50 inches, and 1.00 inch for the series of test cases integrated in the parallel model experiments. 347

Table	Page
66. Threat Scores for 24-48 hours for thresholds of 0.25 inches, 0.50 inches, and 1.0 inch for the series of test cases integrated in the parallel model experiments.	348
67. Table I and Table II Skill Factors for 06-12 hours for the series of test cases integrated in the parallel model experiments.	349
68. Table I and Table II Skill Factors for 18-24 hours for the series of test cases integrated in the parallel model experiments.	350
69. Table I and Table II Skill Factors for 30-36 hours for the series of test cases integrated in the parallel model experiments.	351
70. Table I and Table II Skill Factors for 42-48 hours for the series of test cases integrated in the parallel model experiments.	352
71. Table I and Table II Skill Factors for 00-24 hours for the series of test cases integrated in the parallel model experiments.	353
72. Table I and Table II Skill Factors for 12-36 hours for the series of test cases integrated in the parallel model experiments.	354

Table	Page
73. Table I and Table II Skill Factors for 24-48 hours for the series of test cases integrated in the parallel model experiments.	355
74. Numerical values of the constants in the formula for a first derivative of pressure (B13.2)	415
75. Numerical values of the constants in Haltiner's parabolic fit formula for a second derivative of pressure (B14.2)	416
76. Definitions of the precipitation amount categories	439
77. Penalty tables reflecting the interests of prospective users mainly concerned about whether precipitation will or will not occur.	439
78. Values of the constants used in the iteration to determine the effective ocean equilibrium temperature at 1000 mb, $(T_{\alpha})_{1000}$	446
79. Values of the constants used in the determination of the effective ocean equilibrium temperatures aloft.	448

LIST OF FIGURES

Figure	Page
1. The various finite difference grid networks.	22
2. The standard field of mountain pressure height (P_g) which is used in the operational run.	31
3. The special field of mountain pressure height (P_g) which is used in the parallel model experiments.	32
4. Monthly mean corrected root-mean-square error (CRMSE) scores in dkm for the 12, 24 and 36-hour forecasts of 1000 mb height, together with the corresponding persistence scores.	56
5. Monthly mean corrected root-mean-square error (CRMSE) scores in dkm for the 12, 24 and 36-hour forecasts of 850 mb height, together with the corresponding persistence scores.	57
6. Monthly mean corrected root-mean-square error (CRMSE) scores in dkm for the 12, 24 and 36-hour forecasts of 700 mb height, together with the corresponding persistence scores.	58
7. Monthly mean corrected root-mean-square error (CRMSE) scores in dkm for the 12, 24 and 36-hour forecasts of 500 mb height, together with the corresponding persistence scores.	59

8. Monthly mean corrected root-mean-square error (CRMSE) scores in dkm for the 12, 24 and 36-hour forecasts of 200 mb height, together with the corresponding persistence scores. 60
9. The three layers of the atmosphere for which precipitation computations are carried out. 67
10. Monthly mean values of the percentages of grid-points at which the 13, 25 and 35-hour forecasts of the "wet" vertical motion fields have the correct sign. 107
11. Monthly mean root-mean-square error (RMSE) scores in deg C for the 12, 24 and 36-hour forecasts of 850 mb temperature, together with the corresponding persistence scores. 123
12. Monthly mean root-mean-square error (RMSE) scores in deg C for the 12, 24 and 36-hour forecasts of 700 mb temperature, together with the corresponding persistence scores. 124
13. Monthly mean root-mean-square error (RMSE) scores in deg C for the 12, 24 and 36-hour forecasts of 500 mb temperature, together with the corresponding persistence scores. 125

14. Monthly mean root-mean-square error (RMSE) scores in deg C for the 12, 24 and 36-hour forecasts of 850 mb dew point depression, together with the corresponding persistence scores. 142
15. Monthly mean root-mean-square error (RMSE) scores in deg C for the 12, 24 and 36-hour forecasts of 700 mb dew point depression, together with the corresponding persistence scores. 143
16. Monthly mean root-mean-square error (RMSE) scores in deg C for the 12, 24 and 36-hour forecasts of 500 mb dew point depression, together with the corresponding persistence scores. 144
17. A schematic representation of the main features of the precipitation scheme. 163
18. Monthly mean threat scores for the sequential forecasts of 24-hour total precipitation amount which were issued operationally in the period December 1967 to March 1970. 168
19. Monthly mean threat scores for the sequential forecasts of 24-hour precipitation amount which were issued operationally from June 1969 to March 1970. 170

Figure

Page

20. Histograms showing the frequency distributions of the (total-large) threat score (%) differences, for 57 selected Canadian stations, for the precipitation forecasts issued operationally in the period June 1969 to March 1970. 171
21. A diagram showing the frequency distribution of threat score with precipitation occurrence for forecasts of precipitation amount for 00-24 hours. 172
22. A diagram showing the frequency distribution of threat score with precipitation occurrence for forecasts of precipitation amount for 12-36 hours. 173
23. Monthly mean threat scores for the sequential forecasts of 24-hour precipitation amount which were issued operationally from August to December 1969. 175
24. Monthly mean threat scores for the sequential forecasts of 24-hour precipitation amount which were issued operationally from August to December 1969. 178
25. Monthly mean Table I skill factors for the sequential forecasts of precipitation amount for 00-24 hours which were issued operationally in the period August 1968 to April 1970. 180

Figure	Page
26. Monthly mean Table II skill factors for the sequential forecasts of precipitation amount for 00-24 hours which were issued operationally in the period August 1968 to April 1970.	181
27. Monthly mean Table I skill factors for the sequential forecasts of precipitation amount for 12-36 hours which were issued operationally in the period August 1968 to April 1970.	182
28. Monthly mean Table II skill factors for the sequential forecasts of precipitation amount for 12-36 hours which were issued operationally in the period August 1968 to April 1970.	183
29. Monthly mean Table I skill factors for the sequential forecasts of precipitation amount which were issued operationally for class A grid points in the period August 1968 to April 1970.	184
30. Monthly mean Table II skill factors for the sequential forecasts of precipitation amount which were issued operationally for class A grid points in the period August 1968 to April 1970.	185
31. Monthly mean values of the average 24-hour precipitation amount/grid point for the sequential forecasts which were issued operationally for class A grid points in the period August 1968 to April 1970.	186

32. Monthly mean values of the average 6-hour precipitation amount/grid point for the sequential forecasts which were issued operationally for class A grid points in the period August 1968 to April 1970. 187
33. The set of 850 mb height charts for the case of 12Z Jan 29th 1969. 269
34. The set of 700 mb height charts for the case of 12Z Jan 29th 1969. 270
35. The set of 500 mb height charts for the case of 12Z Jan 29th 1969. 271
36. The set of 200 mb height charts for the case of 12Z Jan 29th 1969. 272
37. The set of 00-24 hour precipitation charts for the case of 12Z Jan 29th 1969. 273
38. The set of 24-48 hour precipitation charts for the case of 12Z Jan 29th 1969. 274
39. The set of 850 mb height charts for the case of 00Z Nov 18th 1969. 275
40. The set of 500 mb height charts for the case of 00Z Nov 18th 1969. 276

Figure	Page
41. The set of 00-24 hour precipitation charts for the case of 00Z Nov 18th 1969.	277
42. The set of 24-48 hour precipitation charts for the case of 00Z Nov 18th 1969.	278
43. The set of 850 mb height charts for the case of 00Z Dec 21st 1969.	279
44. The set of 700 mb height charts for the case of 00Z Dec 21st 1969.	280
45. The set of 500 mb height charts for the case of 00Z Dec 21st 1969.	281
46. The set of 200 mb height charts for the case of 00Z Dec 21st 1969.	282
47. The set of 00-24 hour precipitation charts for the case of 00Z Dec 21st 1969.	283
48. The set of 24-48 hour precipitation charts for the case of 00Z Dec 21st 1969.	284
49. The set of 850 mb height charts for the case of 12Z Dec 25th 1969.	285
50. The set of 700 mb height charts for the case of 12Z Dec 25th 1969.	286

Figure	Page
51. The set of 500 mb height charts for the case of 12Z Dec 25th 1969.	287.
52. The set of 200 mb height charts for the case of 12Z Dec 25th 1969.	288
53. The set of 00-24 hour precipitation charts for the case of 12Z Dec 25th 1969.	289
54. The set of 24-48 hour precipitation charts for the case of 12Z Dec 25th 1969.	290
55. The set of 850 mb height charts for the case of 00Z Jan 25th 1970.	291
56. The set of 500 mb height charts for the case of 00Z Jan 25th 1970.	292
57. The set of 00-24 hour precipitation charts for the case of 00Z Jan 25th 1970.	293
58. The set of 24-48 hour precipitation charts for the case of 00Z Jan 25th 1970.	294
59. The set of 850 mb height charts for the case of 00Z Jan 27th 1970.	295
60. The set of 700 mb height charts for the case of 00Z Jan 27th 1970.	296

Figure	Page
61. The set of 500 mb height charts for the case of 00Z Jan 27th 1970.	297
62. The set of 200 mb height charts for the case of 00Z Jan 27th 1970.	298
63. The set of 00-24 hour precipitation charts for the case of 00Z Jan 27th 1970.	299
64. The set of 24-48 hour precipitation charts for the case of 00Z Jan 27th 1970.	300
65. The set of 850 mb height charts for the case of 00Z Jan 28th 1970.	301
66. The set of 500 mb height charts for the case of 00Z Jan 28th 1970.	302
67. The set of 00-24 hour precipitation charts for the case of 00Z Jan 28th 1970.	303
68. The set of 24-48 hour precipitation charts for the case of 00Z Jan 28th 1970.	304
69. The set of 850 mb height charts for the case of 00Z Mar 3rd 1970.	305
70. The set of 500 mb height charts for the case of 00Z Mar 3rd 1970.	306

Figure

Page

- | | | |
|-----|---|-----|
| 71. | The set of 00-24 hour precipitation charts for the case of 00Z Mar 3rd 1970. | 307 |
| 72. | The set of 24-48 hour precipitation charts for the case of 00Z Mar 3rd 1970. | 308 |
| 73. | The set of 850 mb height charts for the case of 00Z Mar 26th 1970. | 309 |
| 74. | The set of 500 mb height charts for the case of 00Z Mar 26th 1970 | 310 |
| 75. | The set of 00-24 hour precipitation charts for the case of 00Z Mar 26th 1970. | 311 |
| 76. | The set of 24-48 hour precipitation charts for the case of 00Z Mar 26th 1970. | 312 |
| 77. | Weight curve for objective analysis of observed reports of 6-hour & 24-hour precipitation amount. | 435 |

LIST OF SYMBOLS

This list contains the definitions of symbols which are standard or appear frequently in the text.

S ($= T - T_d$) is the dew point depression

$\langle F \rangle$ is the finite difference approximation to F . Note that this is a general symbol used with some ambiguity that has to be resolved by the context. For instance, the symbol itself does not specify whether a first order or a second order finite difference approximation is to be used. This information is provided by the context. Note also that Appendix B contains definitions of particular finite difference approximations and other numerical operators.

(x, y, p, t) is the co-ordinate system, attached to the Earth and rotating with it.

$(\hat{i}, \hat{j}, \hat{k})$ is the set of unit vectors parallel to the x , y , and z directions respectively.

z is the height of a constant pressure surface. Note that (x, y, z) constitutes a right-handed system.

$\underline{V} = \frac{dx}{dt} \hat{i} + \frac{dy}{dt} \hat{j} = u \hat{i} + v \hat{j} = \underline{V}^r + \underline{V}^d$ is the horizontal wind.

$\underline{V}^r = \hat{k} \times \frac{g}{f_0} \nabla \psi$ is the rotational part of the horizontal wind and

ψ is the corresponding stream function.

$\underline{V}^d = \frac{g}{f_0} \nabla \chi$ is the divergent part of the horizontal wind and

χ is the corresponding velocity potential function.

$\omega = \frac{dp}{dt}$ is the vertical motion.

$$\frac{d}{dt} = \frac{\partial}{\partial t} + \underline{V} \cdot \nabla + \omega \frac{\partial}{\partial p}$$

$$\frac{D}{Dt} = \frac{\partial}{\partial t} + \underline{V}^r \cdot \nabla$$

$$\frac{D^*}{Dt} = \frac{\partial}{\partial t} + \underline{V} \cdot \nabla$$

$$\nabla = \hat{i} \frac{\partial}{\partial x} + \hat{j} \frac{\partial}{\partial y}$$

$$\nabla^2 = \frac{\partial^2}{\partial x^2} + \frac{\partial^2}{\partial y^2} \quad , \quad \text{the Laplacian operator}$$

F is an arbitrary variable.

$$J (F_1 , F_2) = \frac{\partial F_1}{\partial x} \frac{\partial F_2}{\partial y} - \frac{\partial F_1}{\partial y} \frac{\partial F_2}{\partial x} \quad , \quad \text{the Jacobian operator.}$$

g is the acceleration due to gravity.

$$f = 2 \Omega \sin \phi$$

Ω is the angular velocity of the Earth.

ϕ is the latitude.

f_0 is the value of f at latitude 45 N.

T is the temperature.

T_d is the dew point.

ρ is the density of air (including moisture where appropriate).

R is the gas constant for unit mass of dry air.

C_v is the specific heat of dry air at constant volume.

C_p is the specific heat of dry air at constant pressure.

$$k = R/C_p$$

p_0 is 1000 mb.

$\theta = T(p_0/p)^k$, the potential temperature (see also (A1.7))

$\sigma = - \frac{1}{\rho \theta} \frac{\partial \theta}{\partial p}$, the static stability (see also (A1.15))

I is the Showalter Index.

L is the amount of latent heat released when one gram of water vapour condenses into liquid water.

L_i is the amount of latent heat released when one gram of water vapour sublimates into ice.

L_{iw} is the amount of latent heat released when one gram of liquid water freezes into ice.

$U_p(T)$ is the unit condensation rate, i.e. the condensation rate per unit ascending vertical motion, for a saturated layer of air of central temperature T and defined so as to have a central pressure p , which may be 850, 700 or 500 mb. The layers centred at 850 and 700 mb are taken to be 150 mb thick, and the one centred at 500 mb is taken to be 250 mb thick.

$U_p^i(T, S, S^*)$ is the unit precipitation rate, i.e. the precipitation rate per unit ascending vertical motion, for a layer of air of central temperature T , central dew point depression S , and defined so as to have a central pressure p , which may be 850, 700 or 500 mb. The thicknesses of the layers are the same as for $U_p(T)$.

S^* is the threshold dew point depression at which the onset of large scale precipitation occurs.

τ_l is the large scale precipitation.

τ_f is the frontal precipitation.

τ_a is the air mass shower precipitation.

τ_i is the induced instability shower precipitation.

m is the map scale factor.

d is the horizontal grid spacing on a map based on a polar stereographic projection.

ΔF is an increment of F .

C_d is the surface drag coefficient.

$Q = \hat{k} \cdot \nabla \times \underline{v} + f = \frac{g}{f_0} \nabla^2 \psi + f$ is the absolute vorticity.

dq is a non-integrable increment of heat added to unit mass of air.

$H = - \frac{R}{C_p p} \frac{dq}{dt}$ is a special heat function defined for mathematical convenience.

H_1 is the special heat function associated with the change of water vapour either into liquid water or into ice.

H_2 is the special heat function associated with the thawing or sublimation of ice particles falling into a particular layer of air from the layers above, or the freezing or evaporation of liquid water droplets falling into a particular layer from the layers above.

- H_3 is the special heat function associated with ocean heating.
 H_4 is the special heat function associated with radiation effects.
 r is the water vapour mixing ratio.
 r_w is the saturated water vapour mixing ratio.
 R_V is the gas constant for water vapour.
 C_{VW} is the specific heat at constant volume for water vapour.
 C_{pV} is the specific heat at constant pressure for water vapour.
 C_{pW} is the specific heat at constant pressure for saturated water vapour.
 R' is the gas constant for moist unsaturated air.
 C'_V is the specific heat at constant volume for moist unsaturated air.
 C'_p is the specific heat at constant pressure for moist unsaturated air.
 $\epsilon = M_w/M \quad (\approx 0.62)$
 M_w is the molecular weight of water vapour.
 M is the effective molecular weight of dry air.
 $\kappa' = R'/C'_p$
 e is the partial pressure of water vapour.
 e_w is the partial pressure of saturated water vapour.
 ρ_w is the density of saturated water vapour.
 ρ_L is the density of liquid water.
 r_L is the liquid water mixing ratio.
 r_i is the ice mixing ratio.
 Θ_w is the potential wet bulb temperature, i.e. the wet bulb temperature the air would have if moved dry or moist adiabatically to 1000 mb.
 C_L is the specific heat for liquid water.
 C_i is the specific heat for ice.

DAVID DAVIES

COMPUTATIONS OF TOMORROW'S RAIN

DEPARTMENT OF METEOROLOGY
MCGILL UNIVERSITY

Ph.D. Thesis

ABSTRACT

A numerical scheme to predict precipitation amount on a computer has been developed and put into routine use. It operates in sequence with a baroclinic model based on the potential vorticity equation. Large scale and small scale precipitation amounts are predicted every hour for each of three layers of the atmosphere. The large scale amounts are computed from "wet" vertical motions, which are based on "dry" vertical motions made available by the baroclinic model, and explicit forecasts of temperature and dew point depression. The small scale amounts are computed from three empirical formulae.

In some recent experiments the precipitation scheme and the baroclinic model were integrated in parallel. The main innovations were in the baroclinic model. They included a coefficient of eddy diffusion of potential vorticity which depends on the baroclinicity, seasonal variations in the linkages between the levels, and the incorporation of latent heat, radiation, and ocean heating effects.

RESUME.

Un procédé numérique destiné à prédire la quantité de précipitation à l'aide d'un ordinateur a été développé et utilisé de façon régulière. Il fonctionne à la suite d'un modèle barocline se servant de l'équation du tourbillon potentiel. Une prévision des quantités de précipitation et à la grande et à la petite échelle est faite pour chaque heure et pour trois couches de l'atmosphère. Les quantités à la grande échelle sont calculées à l'aide de mouvements verticaux tenant compte de l'humidité. Ces derniers sont dérivés des mouvements verticaux du modèle barocline traitant l'air comme étant sec et de prévisions explicites de la température et du décalage entre la température et le point de rosée. Les quantités de précipitation à la petite échelle sont calculées selon trois formules empiriques.

Lors d'expériences récentes la méthode de prévision pour la précipitation et le modèle barocline furent utilisés parallèlement. Les innovations principales se trouvèrent dans le modèle baroclinité, des variations saisonnières dans le couplage des couches, de la chaleur latente, de la radiation et des sources ou puits océaniques de chaleur.

PART I : INTRODUCTION

1. General Aims

Numerical Weather Prediction is a relatively young science which has grown up since 1945. Nevertheless much progress has already been made and there are many numerical models of the atmosphere in routine use. So far the main emphasis has been on the prediction of the heights of constant pressure surfaces for the next one or two days. The amount of effort that has gone into predicting the clouds and weather associated with these flow patterns is small by comparison. The present thesis describes a modest attempt to correct this imbalance; it presents an atmospheric model in which those physical processes involving moisture are given something of the prominence accorded to them by Nature. In other words, this doctoral dissertation is concerned with the problem of putting the weather into numerical weather prediction.

Three things are needed to set the present work in perspective. First, a brief review of the historical highlights of the development of numerical weather prediction. Second, a summary and some discussion of the basic problems now facing researchers in the field. Third, a technical account of all closely related previous work including a fairly detailed treatment of those aspects of direct relevance.

2. Historical Highlights

Meteorological text books state that the physical laws which govern the motion of the atmosphere are well known. They are the classical principles expressing the conservation of momentum, of mass, and of energy, supplemented by the equation of state for a gas. Of course, even a cursory reflection reveals that this is not quite

the whole story. Changes of physical state and changes of chemical composition have also to be taken into account when such processes occur to a significant extent. In the troposphere the moisture budget is an important additional factor because it is the one most directly involved with the weather. Nevertheless, if one chooses to omit the complications arising from the presence of moisture, the existence of these classical principles means that the motion of the atmosphere may be described by five differential equations and the gas law. L.F. Richardson attempted to manually integrate these equations by numerical methods during World War I. He failed because sound and gravity waves violated the criterion for computational stability enunciated by Courant, Friedrichs, and Lewy (1928). Charney (1948) showed that in theory this problem could be overcome by using the vorticity equation to filter out non-meteorological waves. The practicality of this approach was then demonstrated by Charney, Fjortoft, and Von Neumann (1950), who successfully integrated a geostrophic barotropic model on an electronic computer using one-hour time-steps. By 1955 a stream function barotropic model, developed by Cressman (1958) (1960), was in routine use at the Joint Numerical Weather Prediction Unit in Washington; it included an empirical Helmholtz term to control long-wave retrogression. Seven years later, in 1962, a three-level baroclinic model came into routine use at Washington; it was also developed by Cressman (1963). Meanwhile, with the appearance of faster computers, it had become feasible to integrate the six basic equations directly, in their undifferentiated or primitive form, using time-steps of ten minutes. Consequently, in 1966 the National Meteorological Center (NMC), Washington, was able to put a six-layer primitive equations model, developed by Shuman and

Hovermale (1968), into routine operational use. Each time a more sophisticated model became operational, or even when a major innovation was introduced into an existing model, there was a marked improvement in the verification scores of the predicted charts issued by Washington.

The trend of events in other countries has followed the pattern set by Washington. In Canada, Kwizak et al (1960) carried out preliminary research in the Operational Development and Evaluation (ODE) Unit of the Central Analysis Office (CAO) in the years 1955-62. This was done using the computer facilities of McGill University. The CAO obtained the first computer of its own, a CDC G-20, in 1962. Soon afterwards a Canadian version of the barotropic model made its operational debut. A three-level baroclinic model was also developed at the CAO, but in practice it was not feasible to fully incorporate this into the operational run until a faster computer, an IBM 360-65, was installed in 1967. In 1968 the CAO baroclinic model finally did go fully operational. At the same time a three-layer precipitation scheme also went operational. This scheme was the one developed by the author and reported on in some depth in this thesis.

One important feature of the 1968 CAO baroclinic-precipitation package anticipates the plans of the World Meteorological Organization (WMO) for establishing the World Weather Watch (WWW) in the 1970s; see _____ (1967a). All integrations are carried out for a limited area on the basis of the early radio-sonde transmissions of mandatory level data up to 500 mb, known as RADAT, from stations in North America and adjacent ocean areas. Precipitation forecasts can thus be transmitted over the operational facsimile circuits 3 hours and 5 minutes after observation time. This is more than three hours earlier than transmission could occur if computations were to await all the

Northern Hemisphere traffic. The plans for WWV call for the establishment of a three-tier hierarchy of Weather Centres. At the apex of this system will be three World Weather Centres which will be located in Washington, Moscow, and Canberra. Below the World Weather Centres will come the Regional Weather Centres, and below them will come the National Weather Centres. Each World Weather Centre will be responsible for providing the Regional Weather Centres, in its area of jurisdiction, with hemispheric or global forecasts. Similarly, each Regional Weather Centre will provide National Weather Centres with regional forecasts which will have a more detailed fine structure. And in all probability, at least for a decade or two, the regional forecasts will be issued before the hemispheric forecasts because they can be based on RADAT data. It appears, therefore, that the main function of the hemispheric forecasts issued by the World Weather Centres, i.e. hemispheric forecasts prepared from data mainly collected at some particular observation time, will be to provide boundary conditions for more detailed regional forecasts prepared from data mainly collected at the next observation time. This state of affairs will likely exist for as long as radio-sonde ascents continue to be the main and the most reliable method for observing meteorological conditions aloft.

The CAO in Montreal will undoubtedly become one of the Regional Weather Centres under the jurisdiction of the World Weather Centre in Washington. As has already been pointed out, the existing CAO baroclinic-precipitation package contains a strong element of the World Weather Watch philosophy. This means that it only needs a satisfactory communication link between Washington and Montreal

>

to make the technological dream that is the World Weather Watch come true. For then the six-layer primitive equations model in Washington could provide boundary conditions for the baroclinic model in Montreal. In fact this is already happening to a limited extent, and the two offices are becoming joined together in a de facto symbiosis of the type envisaged for a World Weather Centre and an associated Regional Weather Centre.

3. Current Problems

3.1 The problem of predictability

The WMO has set up a Global Atmospheric Research Program (GARP) to investigate the scientific problems underlying the implementation of the World Weather Watch; see _____ (1969). A planning committee was established in 1966. In the following year, 1967, this committee published a statement enunciating three main problems; _____ (1967b). The first was predictability. The second was ocean-atmosphere interaction. The third was lack of knowledge concerning tropical meteorology. While there is no doubt that the last two problems are of great importance, they will not be discussed further here because they are not of direct relevance to this thesis. Predictability, on the other hand, is of such fundamental importance to all work in numerical weather prediction that some remarks on the subject are appropriate.

Errors in forecasting may arise from various sources. Some of these are:

- (1) Errors in initial analysis (also errors in verifying analysis).
- (2) Numerical errors such as truncation and round-off errors.

- (3) Errors due to approximations in the applications of known physical laws.
- (4) Lack of knowledge concerning physical laws such as those underlying the precise mechanisms of condensation.
- (5) Errors arising due to interactions with very small scale phenomena which occur in the atmosphere but are not resolvable by a finite difference grid network.
- (6) Real uncertainties in the future of the atmosphere.

It is conceivable that real uncertainties in the future of the atmosphere could arise as a consequence of the amplification of quantum events. The existence of macroscopic systems having this type of non-unique future is well-recognised by the scientific community. The author — Davies (1966),(1968) — has attempted to outline a mathematical argument that such uncertainties might also arise in situations governed by classical physics. Briefly, the case that the atmosphere has a unique future in situations governed by classical physics depends on the assumption that all meteorological variables, such as temperature, and their spatial derivatives are continuous in a strict mathematical sense. It can be argued that the continuity assumption may break down in a turbulent regime, and hence that there is no particular reason why the classical — but molecular — atmosphere should have a non-unique future. Essentially this argument rests on the idea that the concept of continuity and the concept of scale are not independent of one another for a physical variable such as temperature which is really a statistical property of the air molecules. Since in a turbulent flow the motions on any scale can be affected by non-linear interactions with smaller scale phenomena, it can be argued with full mathematical rigour that this is equivalent

to the breakdown of continuity. Real uncertainties of this type are not yet recognised by the scientific community. However, it is interesting to note that among meteorologists in recent years a new school of thought has arisen which recognises a source of error half-way between (5) and (6), viz:

(5 $\frac{1}{2}$) Errors arising due to interactions with unknown and unknowable small scale phenomena which occur in the atmosphere.

The recognition of (5 $\frac{1}{2}$) has come about mainly on pragmatic grounds due to the realisation that no matter how small a grid length is adopted for a numerical model there will still be smaller scale phenomena in the real atmosphere which will interact with the motions on a scale resolvable by the grid. Recognition of error source (5 $\frac{1}{2}$) implies a certain ambivalence with regard to the question of whether a classical atmosphere may have more than one future. This ambivalence arises because in discussing the problem it has become customary to use words and statements carefully chosen so as to avoid the issue of whether or not a classical atmosphere can have more than one future.

Several workers, e.g. Lorenz (1969), Smagorinsky (1969), have taken up the study of the problem of predictability and their main conclusion to date appears to be that in principle the atmosphere should be predictable for about three weeks in advance. In concerning themselves with the problem of predictability the scientists of the GARP committee have generally viewed the topic in a pessimistic light. They have regarded predictability limitations as being the ultimate barrier to weather forecasting. What does not seem to have been realised heretofore is that a pessimistic outlook for forecasting the occurrence of natural weather has a very important corollary. The

corollary is an optimistic outlook for weather control that is economically feasible. In other words, pessimism for forecasting natural weather means optimism for forecasting man-made weather. This follows because an atmosphere without a predictability problem must be relatively insensitive to all small man-made disturbances. On the other hand, an atmosphere with a predictability limitation must be relatively sensitive to small man-made disturbances and in principle it should be possible to judiciously choose the location of artificial disturbances so as to induce desired large-scale characteristics at some time in the future.

3.2 Primitive equations models vis-a-vis filtered equations models

Historically, of course, filtered equations models came into use to permit numerical integrations using one-hour time-steps. Primitive equations models came back into favour for three reasons. First, computer technology advanced sufficiently to permit ten-minute time-steps. Second, in practice nobody has had much success with using the complete form of the vorticity equation in a filtered model. Even when inserted, such terms as the twisting-tilting term do not seem to benefit filtered models. Third, many physical effects can be handled in a straightforward manner by a primitive equations model, but can only be incorporated into filtered equations models with some difficulty.

In view of the tremendous success of NMC's six-layer primitive equations model, and the fact that no filtered equations model has yet managed to perform nearly so well, it has come to be generally believed that filtered models have had their day. This attitude has been reinforced by the successful experiments of Kvizak (1970) with

the semi-implicit method of integration, which permits time-steps of one hour even with primitive equations models, though at the cost of introducing an iterative relaxation procedure into the integration cycle of multi-level models.

However, two assumptions underlie this faith in primitive equations models. The first is that filtered models and primitive equations models are equally well adapted for fine-grid integrations over small areas for which time-dependent boundary conditions are supplied by a hemispheric or global model working on the standard grid. The second is that there are no important physical effects which can be handled more naturally by a filtered model. The second assumption will be discussed in this thesis.

3.3 Potential vorticity equation models vis-a-vis omega equation models

There are two alternative ways of integrating filtered equation models based on simplified forms of the vorticity equation and the thermodynamic equation. This situation arises because at any time-step these two equations have two unknowns, the stream function tendency and the vertical motion (ω). Thus one may first eliminate the vertical motion by deriving the potential vorticity equation. Or one may first eliminate the stream function tendency by deriving the omega equation. In the former case the potential vorticity equation is a three-dimensional Helmholtz equation which can be solved for the stream function tendency directly. In the latter case the omega equation is a three-dimensional Poisson equation which can be solved for the vertical motion. Once the vertical motion is known, its vertical derivatives can be computed, and hence one can solve the vorticity equation for the stream function tendency.

The three-level model in operational use at NMC from 1962-66 utilised the omega equation approach. It had the advantage that, once a relatively simple form of the omega equation had been solved at some particular time-step, some attempt could be made to take the more complicated terms of the vorticity equation into account at the same time-step, instead of simply dropping them. For instance, inclusion of the term representing advection by the divergent part of the wind improved the forecasts. A disadvantage was that essentially three sets of three-dimensional Poisson equation relaxations had to be carried out, although two of these were conveniently separated out into two-dimensional relaxations.

The three-level model in operational use at the CAO utilises the potential vorticity equation approach. In its adiabatic form it has the advantage that it only requires one three-dimensional Helmholtz relaxation, though apparently, as will be seen, this no longer holds true when diabatic effects are included in the model.

4. General Review of Precipitation Forecasting by Computer

There are two main numerical techniques for predicting precipitation amount in operational use. One of these is the technique developed by Shuman and Hovermale (1968) in conjunction with the NMC six-layer primitive equations model. It is an adaptation of a graphical technique developed earlier by Younkin, Larue and Saunders (1965). Subjective amendments have to be made to the computer produced forecasts before they can be transmitted to users. The other technique is in use at the CAO. This is the one developed by the author -- Davies (1967a), Davies and Olson (1968), Kwizak and Davies (1969),

and Davies (1970) — and reported upon in this thesis. The computer produced forecasts are transmitted to the users without any subjective amendments being made. Another technique that should be mentioned here is one developed by Glahn and Lowry (1967), (1969) at the Techniques Development Laboratory of the Systems Development Office, US Weather Bureau. It is essentially the same as the NMC technique except for three things. First, all moisture computations are carried out over a fine grid mesh one quarter the standard size. Second, the initial moisture analysis is based on multiple regression equations which specify saturation thickness as a function of surface dew point, sky condition, weather and station elevation. Third, the actual observed precipitation amount is used as the predicted amount for the first six-hour period of a 24-hour forecast.

There have also been several limited studies on predicting precipitation amount reported in the literature. These include studies by Collins and Kuhn (1954), Danard (1963), (1964), (1966a), (1966b), Estoque (1956), Harley (1963), (1965), Kuhn (1953), Pedersen (1963), Smagorinsky and Collins (1955), Smebye (1958), Spar (1963), Swayne (1956), Thompson and Collins (1953), and Vederman (1961). Of these, as will be seen later, the work of Danard bears the closest resemblance to that of the author.

More recently, Bushby and Timpson (1967) have developed a ten-layer primitive equations model which runs over a fine mesh grid and includes a technique for predicting precipitation. While the published results of this work appear to be very impressive, it is not yet feasible to run the model on an operational basis.

PART II : THE SEQUENTIAL VERSION OF THE BAROCLINIC MODEL

5. The History of the CAO Baroclinic Model

5.1 Introductory remarks

The objective of this Section is to provide a general account of the history of the sequential version of the baroclinic model now in operational use at the Central Analysis Office. The Sections that follow will contain detailed discussions of a more technical nature.

The operational baroclinic model is referred to as the sequential version because it runs in sequence with the operational precipitation scheme. And this is the principal feature which distinguishes the operational baroclinic model from the experimental baroclinic model reported upon later in this dissertation. The experimental baroclinic model, by contrast, runs in parallel with the precipitation scheme. It will be referred to, naturally enough, as the parallel version. Briefly, in a sequential operation the baroclinic model is integrated right out to the end of the forecast period before any precipitation computations commence. This means that the sequential version of the baroclinic model has to be completely independent of the precipitation scheme. In a parallel operation, on the other hand, the baroclinic model and the precipitation scheme are integrated simultaneously. This permits the precipitation scheme to interact back with the baroclinic model. For instance, the effects of release of latent heat can be fed back in this manner. The origins of the sequential approach are discussed more fully in Section 12. This is because they are tied in more closely to the precipitation scheme than to the baroclinic model.

The historical highlights in the development of numerical models of the atmosphere were reviewed in Section 2. Briefly, by the early 1950s it had been established that useful barotropic forecasts of the 500 mb flow pattern could be obtained by doing numerical integrations of a simple form of the vorticity equation using time steps of one hour. By the late 1950s, with barotropic models already in routine use, development work was underway on baroclinic models based on simplified forms of the vorticity equation and the thermodynamic equation. As mentioned in Section 3.3, two approaches were open to investigators. One of these, the omega equation approach, was adopted by the NMC in Washington. It ultimately led to the development of the moderately successful Gressman model (1963) which saw operational service from 1962 to 1966. The other approach is the one which uses the potential vorticity equation. This is the approach adopted in the CAO baroclinic model.

5.2 Godson's proposed model

The CAO baroclinic model was conceived at the Stanstead Seminar in 1957. For it was on this occasion that Godson (1958b) proposed a new kind of four-level baroclinic model. This model was to be based on a finite difference form of the potential vorticity equation in which the vertical derivatives were to be evaluated by a semi-statistical method. It appears that, at the time, the semi-statistical technique for handling vertical derivatives was regarded as the chief novel feature of the proposed model. There were two reasons for this. First Charney (1948) had earlier suggested that a numerical model could be based on the potential vorticity equation. Second, the proposed semi-statistical

technique appeared to be such a promising way of evaluating vertical derivatives that it could be applied at 1000 mb as well as at upper levels; this implied that the 1000 mb surface could be incorporated into the baroclinic model as a full working level. In retrospect, however, it is clear that the real significance of Godson's paper lay in the fact that it gave a considerable impetus to Charney's idea that the potential vorticity equation could be used as the basis for a numerical model of the atmosphere. The semi-statistical technique for evaluating vertical derivatives, which had originally seemed so promising, turned out to be of secondary importance because it did not lead to much in the way of practical benefits. In particular, it never became possible to incorporate the 1000 mb into the model as a full working level. And it was not found advantageous to use anything more complicated than a simple first order formula for the vertical finite difference approximations. However, the static stabilities at the various levels are to some extent arbitrary quantities in a potential vorticity equation model, and appropriate optimum values for them can best be obtained by applying a procedure rather similar to that used in Godson's semi-statistical technique.

5.3 The prototype model

In 1959 the Operational Development and Evaluation Unit obtained access to the McGill IBM 650 computer. This enabled four experimental projects to be undertaken with a view to establishing an operational numerical weather prediction program at the Central Analysis Office. In one of these projects, Eddy et al (1961) carried out some preliminary research on objective analysis. In a second project, Kwizak and Robert (1963) successfully integrated a barotropic model based on a stream

function wind. The other two projects, which began in 1960, both involved baroclinic models. Strachan (1962) investigated a three-level omega equation model. And, finally, the CAO baroclinic model was born. Robert (1963) did some experiments with a potential vorticity equation model. He prepared five 48-hour forecasts and carried stream function information at 1000, 850, 500 and 200 mb. The objective of carrying out two prototype baroclinic model experiments simultaneously was to enable a comparative evaluation of the two approaches to be made. On the average both models performed about the same and produced slightly better forecasts than the barotropic model at 500 mb. The results of the two projects were therefore sufficiently conclusive to suggest that both types of baroclinic model had some merit, but not to indicate which of the two was superior to the other. This was all the information one could really expect to acquire from these preliminary experiments as they were necessarily very limited in scope. Consequently, no clearcut guidance about which approach was the better one emerged from comparative evaluations of the forecasts produced by the prototype integrations. Nevertheless the value of this early work should not be underrated. For the first time the feasibility of a baroclinic model based on the potential vorticity equation approach was fully demonstrated. The feasibility of a baroclinic model based on the omega equation was successfully confirmed. And a considerable amount of technical expertise was acquired in the process.

What did emerge from the prototype integrations was that each model appeared to have one inherent advantage over the other. This was not very helpful information. The two apparent advantages balanced each other out when discussions were held on the relative merits of the two models. In

retrospect this was perhaps just as well. Neither apparent advantage turned out to be real. The first apparent advantage arose in connection with the vertical motion. Long range plans called for the CAO to issue numerical forecasts of precipitation amount, and it was realised that this could not be done without vertical motion fields. Vertical motions are computed explicitly in the omega equation model, but not in the potential vorticity equation model. This was not thought to be greatly to the advantage of the omega equation model. In principle, at least, it was easy to see that vertical motions were implicitly available from the potential vorticity equation model. For once the stream function tendencies are known it should be possible to solve the thermodynamic equation for the vertical motion. In practice, as it subsequently turned out, this procedure runs into certain complications when one tries to allow for latent heat effects. These complications were eventually overcome, with some loss of elegance but, apparently, with no loss of accuracy. So they proved to be only a temporary handicap. This aspect will be discussed more fully in Section 16. The second advantage concerned predicted charts of 1000 mb height. Historically, operational meteorologists have always attached considerable importance to their prognostic surface charts. This meant that there would be a strong demand for machine-produced forecast 1000 mb charts. The prototype model based on the potential vorticity equation undeniably produced something that was easily recognisable as a forecast chart of 1000 mb height. The prototype omega equation model had not done so. This difference in performance was magnified by the suspicion that the omega equation could never produce prognostic charts of 1000 mb height in a

straightforward manner. Whereas, of course, by virtue of Godson's (1958b) proposed semi-statistical method for evaluating vertical finite differences, there appeared to be no reason why the 1000 mb should not be incorporated as a full working level of a model based on the potential vorticity equation. In practice this supposed advantage turned out to be entirely an illusion. The prototype integration of the model based on the potential vorticity equation foreshadowed what was to come. Robert (1963) was not able to incorporate the 1000 mb into the model as a full working level. He did not allow the 1000 mb stream function to affect the stream functions at the other levels in any way. Nor did he take into account the 1000 mb vorticity. So, in effect, the prognostic 1000 mb charts of the prototype model were obtained by a derived field technique which amounted to nothing more than using a weighted mean of the advectations of stream function thickness for the layers 1000 to 850 mb and 1000 to 500 mb. Superficially, Robert's (1963) published 1000 mb charts of forecast height seemed to indicate that even this derived field technique led to acceptable results. It was therefore thought that further investigation, either by trial and error, or along the lines suggested by Godson (1958b), would lead to improvements. Unfortunately, this view turned out to be over-optimistic. It has not been possible to improve on the prototype derived field technique for obtaining prognostic 1000 mb charts. This derived field technique is, at least in principle, completely independent of the main integration cycle of the model. And it will work just as well, or just as poorly, with an omega equation model as it does with a potential vorticity equation model. Consequently, a potential vorticity equation model does not

have any natural advantage over an omega equation model when it comes to doing 1000 mb predictions. In retrospect, therefore, it can be seen that both apparent advantages were unreal. It is fortunate that neither supposed advantage played a very great role in determining the approach to be used in the CAO baroclinic model.

The ultimate decision to base the CAO baroclinic model on the potential vorticity equation was taken in 1962. It was justified as follows. The results of the prototype baroclinic model experiments had not indicated a great deal beyond the fact that the omega equation approach and the potential vorticity equation approach were both equally feasible. But it was known that the NMC in Washington had already carried out a great deal of research on an omega equation model. Whereas nobody else was known to be working on a model based on the potential vorticity equation. The choice was therefore between duplicating NMC's work and breaking new ground. Generally speaking, scientific research is more valuable when it is original than when it is a repeat of earlier efforts. Consequently, a CAO model based on the potential vorticity equation was likely to lead to greater returns than one based on the omega equation.

5.4 The octagon model

A CDC G-20 computer was installed at the CAO in 1962. For the next couple of years much effort was devoted to the task of establishing and improving a rudimentary operational run. This consisted of four main features: automatic data extraction designed by Strachan (1965), objective analysis developed by Kruger (1965), (1969), (1970) and Kruger and Asselin (1968), the solution of the balance equation developed by Asselin (1967),

and a barotropic model checked out by Simla (1964). All work was done using a 1709-point octagonal grid. Following the lead of NMC, the stream function barotropic model was subjected to three successive improvements. First, terrain effects were simulated by the inclusion of a mountain and friction term of the type proposed by Cressman (1960). Second, the 12-hourly smoothing operation was expanded to include an unsmoother as well as a smoother as suggested by Shuman (1957). This reduced the damping of short wavelength features of synoptic importance whilst retaining control over two-gridlength noise. Third, the standard first order finite difference Jacobian operator was replaced by the second order finite difference Jacobian designed by Shuman and Vanderman (1965). This speeded up the short wave advection rates and made them more realistic. Meanwhile a 1709-point grid version of the baroclinic model was being programmed and tested. As in the prototype, the 1000, 850, 500 and 200 mb pressure surfaces were chosen as the working levels at which to carry stream function information. Because the barotropic model had so clearly benefited from the inclusion of a terrain term, unsmoothing, and the Shuman Jacobian, the same three features were carried over into the baroclinic model. In 1964 a series of test cases was run with control coefficients corresponding to standard atmosphere values for the static stabilities. The results were very disappointing. Overdevelopment was rampant everywhere. Systems moved too slowly at 850 mb and too rapidly at 200 mb. In 1965 the control coefficients were reset at values prescribed by an optimisation procedure which minimised the RMSE verification scores for a number of selected cases. The net effect was to reduce the linkage between the levels and make the baroclinic model much more

barotropic in nature. The overdevelopment problem was cured, but at the cost of almost prohibiting any baroclinic development at all from taking place. Unfortunately, phasing problems at 850 mb and 200 mb were worse than ever. The weak linkage between the levels meant that 850 mb systems tended to move along barotropically with the 850 mb flow. Similarly, 200 mb systems tended to move along barotropically with the 200 mb flow. At this stage Robert and Olson (1966) undertook a careful reappraisal of each step of the integration procedure. The main conclusion of their investigation was that the unsmoother should not have been carried over from the barotropic model. Sure enough, once the unsmoother was dropped it became possible to restore some of the linkage between the levels and increase the baroclinicity of the model. The optimization procedure used earlier was then repeated. It yielded an entirely new set of control coefficients which minimized the RMSE verification scores for some selected cases. This time the outcome was more satisfactory. The static stability values corresponding to the final control coefficients were more realistic. Some degree of baroclinic deepening was permitted by the model. And although the phasing problems between the levels were still plainly evident, they tended to be less pronounced than they had been earlier. While this optimization process was going on several other aspects of the model were also examined in some detail. For instance, the empirical constants used to control long-wave retrogression were reset at new values which gave slightly better verification scores. And several minor variants of the terrain term were tested. In addition, every effort was made to incorporate the 1000 mb stream function into the model as a full working level. But this particular venture did not meet with any success. In 1966 this period of intensive development finally bore fruit. A moderately successful baroclinic model became available for routine use. Unfortunately, another

year was to elapse before it could be incorporated into the operational run. The CAO baroclinic model took too long to integrate on the CDC machine.

5.5 The 1968 operational model

An IBM 360-65 computer was installed at the CAO in August 1967. Plans called for the sequential baroclinic-precipitation package to be introduced into the operational run as soon as possible thereafter. Certain operational requirements had to be laid down in some detail. Accordingly, the baroclinic model and the precipitation scheme had to be specially tailored to meet these requirements. This is where the baroclinic model ran into three new problems.

The first problem related to grid size. The 1709-point octagonal grid was dropped when the switch-over was made to the IBM machine. Instead a 2805-point rectangular grid (55 x 51) was made the working area for objective analysis. However, the baroclinic model was only integrated over a 1221-point rectangular sub-area (37 x 33) of the main grid. Both the full 2805-point grid and the 1221-point grid are shown in Fig. 1, together with some other grids which are used in the precipitation scheme and will be referred to in PART III. Some experiments were therefore carried out by Kwizak and Olson - see Davies and Olson (1968) and Kwizak and Davies (1969) - to discover which grids should be used for the balance equation conversions from height to stream function and back again. What appeared to be the most satisfactory procedure was then adopted into routine use. The initial time stream function fields were obtained by balancing the height fields over the 2805-point grid and then extracting the required 1221-point sub-areas. In addition, the initial time 2805-point stream function fields were converted back into 2805-point height fields by the reverse balance procedure. The height fields so obtained were not quite the same as the original height fields. The slight differences

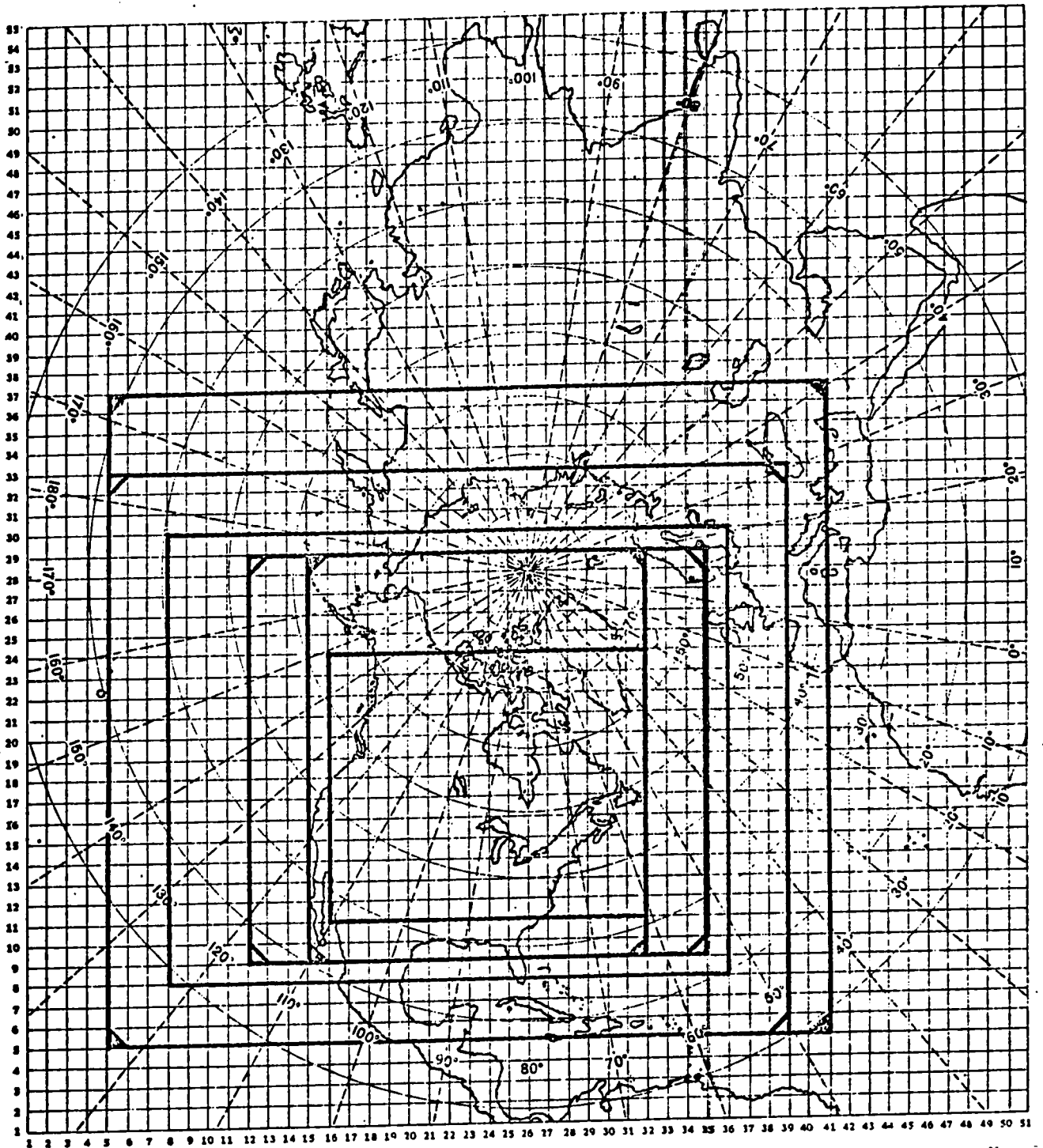


Fig. 1 : The various finite difference grid networks. The large 2805-point grid is used for the objective analysis. The 1221-point grid is used by the baroclinic model. The 1015-point grid, which has the bottom left-hand corner in common with the 1221-point grid, is used for the temperature and dew point depression forecasts. The 667-point grid is used for the diabatic effects in the parallel model. The 504-point grid is used for the precipitation forecasts. The 378-point grid is used for the objective analysis of precipitation amount. The 238-point grid is a special verification area.

were due mainly to the changes introduced when the height fields were ellipticised to ensure that the solution of the balance equation would be convergent, but there was also a small contribution from an inherent numerical bias which arises in the use of the balance equation. See Asselin (1967) for a discussion of these two problems. There was, of course, a reason for routinely reconstituting the initial time 2805-point height fields in this manner. The boundaries of the predicted height fields had to be specified when the reverse balance procedure was applied to prognostic stream function fields at output times. The best assumption that could be made in the 1968 model was that the height fields remained constant on the boundary during the forecast period, but constant at their reconstituted initial time values, not at those which were originally analysed.

The second problem arose from the fact that the sequential baroclinic-precipitation package was to be based on the early transmissions of the North American radiosonde reports, the RADAT reports. These only provide information up to 500 mb and so there is no data made available for the 200 mb height analysis. The trial field for the 200 mb objective analysis has therefore to be used for the initial time chart instead of the objective analysis itself. This trial field was obtained by the thickness advection technique developed by McClellan, Page, Robinson and Yacowar (1966) which used the current 500 mb height chart - the one which had just been analysed from the new RADAT information - and the 12-hour old 500 and 200 mb height charts.

The third problem was the most unexpected one. Soon after the first successful precipitation forecasts had been produced on the IBM computer, disaster struck. The baroclinic model began to exhibit computational instability at 200 mb. This was completely contrary to previous experience

as there had not been a single instance of computational instability in the many hundreds of cases run on the CDC machine. It turned out that the cause was the critical position of one of the new boundaries which cut across the main westerly jet stream over Japan. Fortunately, Kwizak and Olson - see Davies and Olson (1968) and Kwizak and Davies (1969) - were able to devise a simple method to protect computational stability. The wind was tested at each point of the 200 mb stream function chart at every time step. If it was becoming supercritical at some particular point, then a local smoothing operator was applied just at that point to cut the wind down to a sub-critical value. In applying this procedure the critical wind speed had to be taken slightly less than the value normally given for the Courant, Friedrichs, and Levy (1928) criterion for computational stability. This was because the Jacobian term was evaluated by Shuman and Vanderman's (1965) second order scheme instead of a simple first order formula.

Once these three problems had been solved there were no more obstacles to be overcome. In February 1968 sequential versions of the baroclinic model and the precipitation scheme were introduced into the operational run. Highly successful height and precipitation forecasts were routinely produced twice-a-day by essentially the same computer programs for the next two years.

5.6 The 1970 operational model

Further development work was carried out in 1968 and 1969. During this period the sequential version of the baroclinic model evolved slowly over the course of many experiments. The end result was something which was indisputedly an improved baroclinic model. This replaced its predecessor in the operational run in February 1970.

The 1970 operational model contains four principal new features. The first of these is the incorporation of time-dependent boundary conditions using a technique developed by Creswick and Olson (1970). Variable lateral boundary values of stream function tendency and vorticity for the 1221-point grid are generated in a straightforward manner by doing an integration of the same basic form of the baroclinic model (except, of course, for the variable boundaries) over the full 2805-point grid, but starting from an initial time twelve hours earlier than the production run. This hemispheric integration is carried out in the "MOP UP RUN", about nine hours after observation time, when there is little operational demand for computing time. Production run integrations over the 1221-point grid are then carried out quickly, as before, as soon as the early transmissions of the North American radio-sonde reports, the RADAT reports, have been received. But the use of time-dependent boundary conditions means that maximum benefits are now obtained from the twelve hours old hemispheric data. The main advantage gained is that there is a tremendous improvement in the quality of the forecast height patterns in those areas of the Pacific ocean which are downstream from the inflow boundaries. By 36 hours these improvements are sometimes noticeable over the West Coast of North America.

The second major innovation in the 1970 model is the inclusion of eddy diffusion terms in the model equations, thereby eliminating the need for twelve-hourly smoothing procedures. Creswick and Olson (1970) adopted this feature from the author's work - see Kwizak and Davies (1969) - on eddy diffusion in the parallel version of the baroclinic model. Accordingly, a fuller discussion will be postponed until later in the thesis. The eddy diffusion terms yield predicted height patterns with more detail than could be obtained with the 1968 model. For instance, the 500 mb low centres at 36 hours generally have an extra contour around them which would have been lost with the old smoothing procedures. And, most important, this extra

detail is obtained without any deterioration in verification scores. From the viewpoint of the precipitation scheme, one of the major advantages of using eddy diffusion is that the computed vertical motions, and hence the computed precipitation amounts, change gradually from hour to hour. In the 1968 model the computed vertical motions would steadily build up and grow more noisy for twelve hours, and then be drastically cut down and flattened out in the first time step after smoothing. In addition, the eddy diffusion terms help to keep the moving features at different levels in phase with one another. This is more evident between 500 and 850 mb than between 500 and 200 mb because the lower levels are linked together more strongly in the model. The net result is that in the 1970 model there is a slight speeding up in the advection of 850 mb low centres, as compared to the 1968 model, and a somewhat less perceptible - at least due to this cause, see next paragraph - slowing down in the advection of the 200 mb troughs and ridges. Nevertheless, the control coefficients - which were optimised for the 1968 model - allow so little interaction between 500 and 200 mb that eddy diffusion alone is not enough to enforce realistic 500-200 mb relationships.

Consequently, the third change in the 1970 model is that the 200 mb advection speeds are slowed down by wholly artificial means. The computed winds at 200 mb are merely multiplied by 0.75 when computing the potential vorticity advection at this level. Incidentally, the across-the-board scaling down of the 200 mb winds, in conjunction with the eddy diffusion terms, makes the 1970 model less prone to computational instability than its predecessor. This probably eliminates the need for the special local smoother mentioned in (5.5), although it has actually been retained in the 1970 model as an extra safeguard against blow-ups.

The last of the principal new features of the 1970 model is that, by

special request, the 12-hour 200 mb height forecasts produced by the six-level primitive equations model in Washington are transmitted up to the CAO in digital form over the teletype circuits. These are used unamended as the initial time 200 mb height fields for the production run integrations. They replace the initial time 200 mb heights used in the 1968 model which were derived by the thickness advection technique of McClellan et al (1966). In fact, the 1970 model actually went operational before it was possible to finalize arrangements for the teletype transmissions of the 200 mb height forecasts from Washington. There was therefore a short interim period during which the 12-hour 200 mb height forecasts produced by the hemispheric baroclinic model were used as initial time charts for the production run. A comparison of the 12-hour 200 mb height forecasts from the two different models indicated that the main differences were usually over the Pacific, due presumably to the Washington objective analysis taking into account military weather reports not generally available. In addition, with the baroclinic model some kind of bias problem was encountered which tended to perpetuate itself in no-data areas through the objective analysis cycle.

The 1970 model, by virtue of the inclusion of eddy diffusion terms, may be regarded as intermediate between the 1968 model and the parallel model reported on later in this thesis. However, the 1970 model differs from the parallel model in two important respects. First, it has no diabatic effects. Second, it does not include the 700 mb surface as a full working level at which stream function information is carried. Furthermore, the 1970 model uses control coefficients which were optimized for the 1968 model.

6. The Baroclinic Model Equations and the Primary and Secondary Constraints

This Section presents a unified view of the baroclinic model as a whole and introduces the formal definitions of primary and secondary constraints. The next Section indicates how the baroclinic model equations are derived. Section 8 examines the problem of assigning numerical values to the control coefficients. Appendix C documents the numerical procedures employed in the main integration cycle, and also summarises the limitations on these procedures. Appendix D deals with the primary constraints due to terrain. Section 9 discusses the smoothing procedures of the earlier models, and explains how these have been replaced by primary and secondary constraints due to eddy diffusion in the 1970 model. Section 10 is devoted to the derived 700 mb stream function forecasts. Finally, Section 11 provides some statistics on verification scores.

The equations of the baroclinic model are:

$$\left\langle \frac{D_m}{Dt} \left\{ \frac{g}{f_0} \nabla^2 \psi'_m + f + k \sum_{n=1}^k C_{mn} \psi'_n \right\} \right\rangle = \langle G_m \rangle + \langle E_m \rangle + \langle B_m \rangle \quad (6.1)$$

$m = 1, 2, 3, k$

In the sequential models the levels $m = 1, 2, 3, 4$ correspond to 1000, 850, 500 and 200 mb respectively. The notation $\frac{D_m}{Dt}$ implies that $\frac{D}{Dt}$, i.e. the total horizontal time derivative in which the advection due to the divergent part of the wind is taken to be zero, is to be evaluated at the m 'th level. The characteristics of the model are to a large degree determined by the numerical values assigned to the C_{mn} . The C_{mn} are therefore known as the control coefficients. Any term which appears on the R.H.S. of (6.1) is defined to be a primary constraint on the baroclinic model. Thus the terms G_m , E_m , and B_m , whose physical

significance will be revealed in a later paragraph, will all be referred to as primary constraints. The main integration cycle of the baroclinic model is devoted to the task of solving (6.1) for the unknown stream function tendencies, $\left\langle \frac{\partial \psi_m}{\partial t} \right\rangle$, given the values of the stream function fields and the primary constraints. This is a topic which is taken up in Appendix C.

Once the $\left\langle \frac{\partial \psi_m}{\partial t} \right\rangle$ are known, the actual integration in time is carried out by applying the time step equation:

$$\psi_m^{t+\Delta t} = \psi_m^{t-\Delta t} + 2\Delta t \left\{ \left\langle \frac{\partial \psi_m}{\partial t} \right\rangle^t + \langle \epsilon_m \rangle \right\} \quad (6.2)$$

$m=1,2,3,4$

Equation (6.2) is easily recognisable as a slightly modified version of the standard centred time difference formula (B16.1). For the first time step, instead of (6.2), a correspondingly modified form of the forward time difference formula (B16.2) is used:

$$\psi_m^{t+\Delta t} = \psi_m^t + \Delta t \left\{ \left\langle \frac{\partial \psi_m}{\partial t} \right\rangle^t + \langle \epsilon_m \rangle \right\} \quad (6.3)$$

$m=1,2,3,4$

The terms ϵ_m which appear in (6.2) and (6.3) are defined to be the secondary constraints on the baroclinic model. As will be noted in Section 9, secondary constraints have to be applied when eddy diffusion effects are introduced into the model. In all work reported in this thesis, with the exception of the recent fine grid investigations of Paulin (1969), the time step, Δt , was taken to be fixed at one hour. This has generally been sufficient to satisfy the Courant, Freidrichs and

Lewy (1928) criterion for computational stability. However, some difficulties were encountered at 200 mb in the 1968 model due to one of the lateral boundaries cutting across the main jet stream over Japan. These difficulties, and the simple technique which was developed to cope with them, were discussed in (5.5).

The primary and secondary constraints represent certain physical effects. The first primary constraints, G_m , represent terrain effects. Adaptations of Cressman's (1960) mountains and friction term have been included in the sequential models by Davies and Olson (1966), Robert and Olson (1967), and Creswick and Olson (1970). As already mentioned, these are described in some detail in Appendix D. Fig. 2 shows the relatively smooth field of mountain pressure-height, P_g , which is used in the sequential model; this was originally due to Berkofsky and Bertoni (1955). For convenience of comparison, Fig. 3 shows the more detailed P_g field used in the parallel model. The second primary constraints, E_m are eddy diffusion of potential vorticity terms. These are applied in conjunction with secondary constraints which are terms representing eddy diffusion of stream function. The whole eddy diffusion procedure involving primary and secondary constraints was originally developed by the author - see Kwizak and Davies (1969) - for use in the parallel model. However, it has also been incorporated into the most recent sequential model, the 1970 operational model, by Creswick and Olson (1970). Consequently, the formulation of the eddy diffusion terms is presented without discussion in Section 9. A fuller treatment is deferred until later in the thesis. The third primary constraints, B_m have been taken to be zero in the sequential models. They

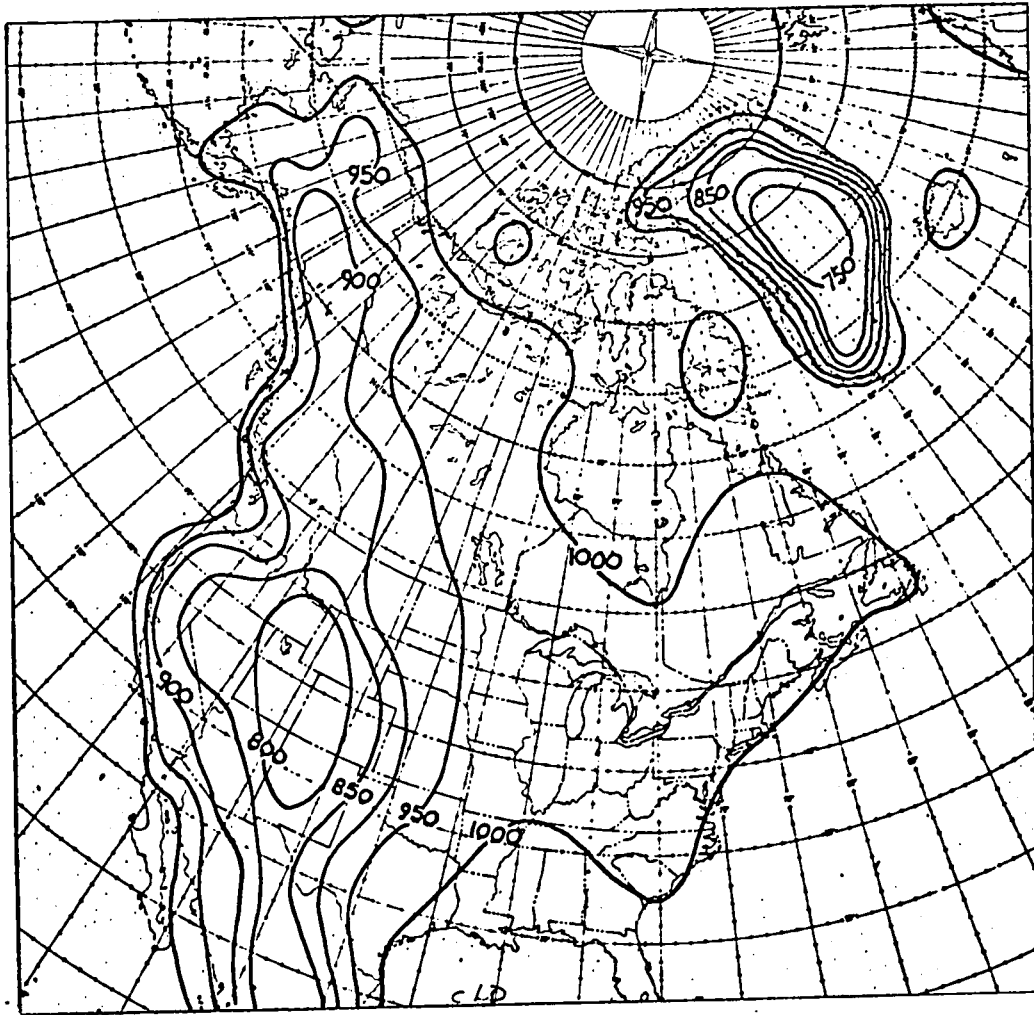


Fig. 2: The standard field of mountain pressure height (P_g) which is used in the operational run.

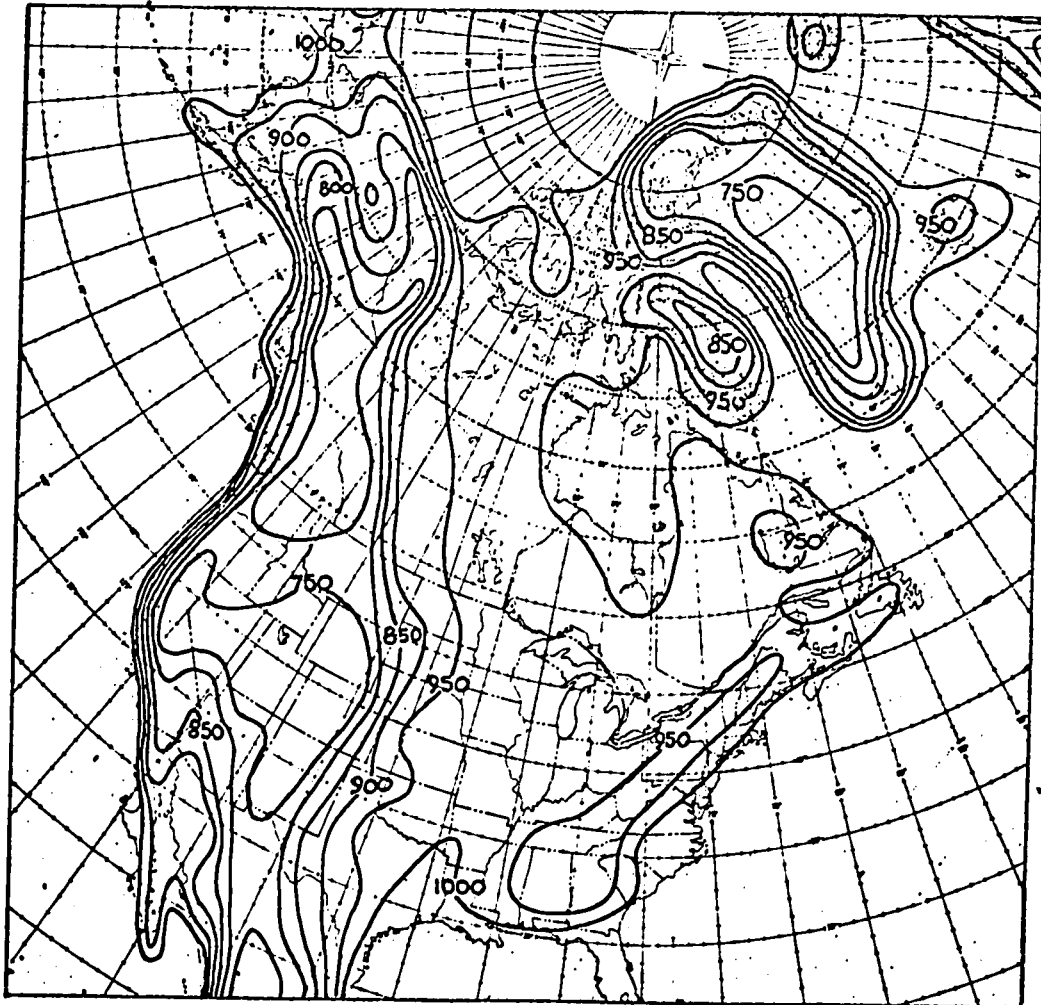


Fig. 3: The special field of mountain pressure height (P_g) which is used in the parallel model experiments.

represent the diabatic effects which are included in the parallel model.

It remains to make a few remarks on the input and output procedures. The objective analysis scheme developed by Kruger (1965) (1969) (1970) and Kruger and Asselin (1968) produces height charts of constant pressure surfaces for a hemispheric grid. The field meteorologists expect to receive predicted height charts. But the baroclinic model works with stream function information, not height information. This is because spurious anticyclogenesis, a problem discussed by Kwizak and Robert (1963), arises in any model which uses geostrophic winds for advection purposes. Consequently, at initial time the objectively analysed height fields have to be converted into stream function fields before they are fed into the model. And at output times the predicted stream function fields have to be converted back into height fields. The conversion procedure is based on the balance equation (A1.11), which is a diagnostic relationship between height and stream function. Stream function fields are obtained from height fields by solving the "forward" balance equation using the special technique developed by Asselin (1967). Height fields are obtained from stream function fields by solving the "reverse" balance equation, which in this case reduces to a Poisson equation. In the 1968 and 1970 models some special balance equation problems arose due to the use of the 1221-point grid. These were discussed in (5.5) and (5.6).

A clear overall picture of the baroclinic model in action now emerges. At initial time the objectively analysed height fields are converted into stream function fields by means of the forward balance equation. The integration then proceeds from time step to time step by the leap frog marching process which has become so familiar to NWP

specialists. At the beginning of the general time step the stream function values for the current hour and the preceding hour are known. This permits the primary and secondary constraints to be evaluated as required. The main integration cycle, which is the principal feature of the model, then solves equation (6.1) for $\left\langle \frac{\partial \psi_m}{\partial t} \right\rangle$. Finally, the newly computed values of $\left\langle \frac{\partial \psi_m}{\partial t} \right\rangle$ are inserted into the time step equation (6.2) to produce predicted stream function values for the next hour. This completes the time step for the current hour and leaves everything ready to embark on the time step for the next hour, which thus in turn becomes the current hour. Integrations may be carried out in this way for any length of time by alternating applications of (6.1) and (6.2). At the desired output hours, predicted height fields are obtained from predicted stream function fields by solving the "reverse" balance equation.

7. Derivation of the Baroclinic Model Equations without Constraints

If the primary constraints are all taken to be zero, the baroclinic model equations (6.1) reduce to:

$$\left\langle \frac{D_m}{Dt} \left\{ \frac{g}{f} \nabla^2 \psi_m + f + k \frac{\partial \psi_m}{\partial z} - C_{mn} \psi_n \right\} \right\rangle = 0 \quad (7.1)$$

$m=1, 2, 3, 4$

The purpose of this Section is to indicate how (7.1) may be derived from a simplified form of the vorticity equation (A1.9) and a convenient form of the thermodynamic equation (A1.13). This derivation is based on the papers of Charney (1948), Godson (1958b), and Robert (1963). In the next Section there will be some discussion of the problem of assigning numerical

values to the control coefficients.

The simplified form of the vorticity equation may be obtained from (A1.9) by neglecting the twisting-tilting term, the vertical advection term, and the horizontal advection term associated with the divergent part of the wind, and by replacing the absolute vorticity by f_0 in the divergence term:

$$\frac{D}{Dt} \left(\frac{g}{f_0} \nabla^2 \psi + f \right) = f_0 \frac{\partial w}{\partial p} \quad (7.2)$$

The convenient form of the thermodynamic equation is based on the assumption:

$$\frac{g}{f_0} \frac{D}{Dt} \left(\frac{\partial \psi}{\partial p} \right) \approx \frac{g}{f} \frac{D^*}{Dt} \left(\frac{\partial z}{\partial p} \right) \quad (7.3)$$

In the notation the presence or absence of the star on the D/Dt operator denotes the presence or absence of an advection term due to the divergent part of the wind. Substitution of (7.3) into (A1.13) yields:

$$\frac{g}{f_0} \frac{D}{Dt} \left(\frac{\partial \psi}{\partial p} \right) + \frac{w\sigma}{f} = \frac{H}{f} \quad (7.4)$$

Under adiabatic conditions equation (7.4) reduces further to:

$$\frac{g}{f_0} \frac{D}{Dt} \left(\frac{\partial \psi}{\partial p} \right) + \frac{w\sigma}{f} = 0 \quad (7.5)$$

The potential vorticity equation is derived by eliminating w between equations (7.2) and (7.5):

$$\frac{D}{Dt} \left(\frac{g}{f_0} \nabla^2 \psi + f \right) + \frac{\partial}{\partial p} \left\{ \frac{gf}{\sigma} \frac{D}{Dt} \left(\frac{\partial \psi}{\partial p} \right) \right\} = 0 \quad (7.6)$$

The next step is to assume that:

$$\frac{\partial}{\partial p} \left\{ \frac{gf}{\sigma} \frac{D}{Dt} \left(\frac{\partial \psi}{\partial p} \right) \right\} \approx \frac{D}{Dt} \left\{ \frac{\partial}{\partial p} \left(\frac{gf}{\sigma} \frac{\partial \psi}{\partial p} \right) \right\} \quad (7.7)$$

This assumption implies that f/σ depends only on p . In the CAO baroclinic model there are nominally four working levels. Consequently, at the m 'th level, there must exist the vertical finite difference approximations corresponding to $\frac{\partial}{\partial p} \left(\frac{gf}{\sigma} \frac{\partial \psi}{\partial p} \right)$ which can be expressed in the form of a linear combination of the ψ_n at all levels, i.e. :

$$\left\langle \frac{\partial}{\partial p} \left(\frac{gf}{\sigma} \frac{\partial \psi}{\partial p} \right) \Big|_m \right\rangle = 4 \sum_{n=1}^4 C_{mn} \psi_n \quad (7.8)$$

$m = 1, 2, 3, 4$

where the numerical values assigned to the C_{mn} depend on the actual choice of vertical finite difference formula. In practice, as will be seen later, certain difficulties are encountered in evaluating the control coefficients if a level is not a full working level, or is not adjacent to two full working levels; i.e. certain difficulties are encountered if a level is not a true interior level. Some of these difficulties may be overcome by assuming the vertical boundary conditions to be $w = 0$ at the bottom and the top of the atmosphere. Godson (1958b), when he first proposed a baroclinic model based on the potential vorticity equation, attempted to justify the use of (7.8) for both interior and outer levels without regard

to vertical boundary conditions. Briefly, he proposed that vertical interpolations to the stream function fields should be obtained by statistically deriving the polynomial curves which give the best fit to the known stream functions at the working levels. This would effectively express the stream functions' p -dependence in functional form, completely separate from their x - and y -dependence, thus enabling the control coefficients to be evaluated by analytical differentiation of the L.H.S. of (7.8). Unfortunately, as discussed at some length in Section 5, this particular approach did not fulfil its early promise.

Substitution of (7.7) and (7.8) into the finite difference version of (7.6) yields (7.1). This completes the derivation of the baroclinic model equations without constraints.

8. Numerical Values of the Control Coefficients

The most satisfactory way of assigning numerical values to the control coefficients of the model is to proceed as follows. The first step is to deduce a reasonably accurate first guess set of values by assuming realistic physical configurations and vertical boundary conditions. For instance, at this stage one usually assumes the static stabilities correspond to a standard atmosphere at latitude 45N, and that the vertical motion is zero at the top and the bottom of the atmosphere. The second step is to gradually optimise these first guess values by minimizing the RMSE verification scores for a series of selected test cases.

Robert (1963) gave the detailed calculations involved in the derivation of a typical first-guess set of control coefficients. He called the values he obtained the "dynamical-equivalent" control coefficients to emphasise the fact that they had not been derived by Godson's (1958b) semi-statistical

technique.

It is worth pointing out that there are certain arbitrary aspects to be considered in the derivation of a first-guess set of control coefficients. This will be shown here by deriving another first guess set of control coefficients using a procedure slightly different to that of Robert (1963). Consider a model with working levels at 850 ($m = 2$), 500 ($m = 3$), and 200 mb ($m = 4$). The 1000 mb level will be ignored for the moment as it involves special difficulties. The computation of the control coefficients by a direct application of (7.8) is straightforward at 500 mb because it is the interior level. A simple expansion gives:

$$\left\langle \frac{\partial}{\partial p} \left(\frac{gf}{\sigma} \frac{\partial \psi}{\partial p} \right) \Big|_3 \right\rangle = \left\langle \frac{gf}{\sigma_3} \frac{\partial^2 \psi}{\partial p^2} \Big|_3 \right\rangle + \left\langle g \frac{\partial(f/\sigma)}{\partial p} \Big|_3 \frac{\partial \psi}{\partial p} \Big|_3 \right\rangle \quad (8.1)$$

The parabolic fit formula for the first (B13.2) and second (B14.2) and second (B14.2) derivatives of pressure may be substituted into (8.1) from Appendix B to give:

$$\left\langle \frac{\partial}{\partial p} \left(\frac{gf}{\sigma} \frac{\partial \psi}{\partial p} \right) \Big|_3 \right\rangle = \frac{gf}{\sigma_3} \left[a_2^2 \psi_2 + a_3^2 \psi_3 + a_4^2 \psi_4 \right] \quad (8.2)$$

$$+ \left[gf \left(\frac{a_2'}{\sigma_2} + \frac{a_3'}{\sigma_3} + \frac{a_4'}{\sigma_4} \right) \left(a_2' \psi_2 + a_3' \psi_3 + a_4' \psi_4 \right) \right]$$

Thus,

$$C_{3n} = \frac{gf}{4c_3} \left[a_n^2 + \left(\frac{c_3}{c_2} a_2' + a_3' + \frac{c_3}{c_4} a_4' \right) a_n' \right] \quad n=2,3,4 \quad (8.3)$$

At the outer levels, 850 and 200 mb, one normally makes use of the boundary condition that $W=0$ at the bottom and at the top of the atmosphere. Thus, instead of using (7.8) directly to evaluate the control coefficients, one has to return to the vertical finite difference version of (7.2) and substitute for $\left\langle \frac{\partial W}{\partial p} \right\rangle$ using a boundary W and an interior value of W given by (7.4). Matters are simplified if the boundary conditions are chosen more specifically to be $W=0$ at 1025 mb, and $W=0$ at 50 mb. This gives:

$$\left. \begin{aligned} C_{22} &= -\frac{gf}{4c_{775}} \left(\frac{1}{350^2} \right) \\ C_{23} &= -C_{22} \\ C_{24} &= 0 \\ C_{42} &= 0 \\ C_{43} &= \frac{gf}{4c_{350}} \left(\frac{1}{300^2} \right) \\ C_{44} &= -C_{43} \end{aligned} \right\} \quad (8.4)$$

Numerical values can be assigned to a_n^1 and a_n^2 from Appendix B, and also to g and f_0 from Table 1. Taking the σ to have numerical values corresponding to the "dry" standard atmosphere as given in Table 2,

and also taking $f = f_c$, (8.3) and (8.4) yield the following control coefficient matrix:

$$C_{mn} = \begin{bmatrix} ? & ? & ? & ? \\ 0 & -5.23 & 5.23 & 0 \\ 0 & 4.56 & -5.68 & 1.12 \\ 0 & 0 & 1.92 & -1.92 \end{bmatrix} \quad 10^{-3} \text{ dkm}^{-1} \text{ hr}^{-1} \quad (8.5)$$

By contrast, the control coefficient matrix used by Robert (1963) in the prototype experiments was:

$$C_{mn} = \begin{bmatrix} -3.28 & 2.625 & 0.984 & 0 \\ \times 10^5 & \times 10^5 & \times 10^5 & \\ 0 & -7.066 & 6.41 & 0 \\ 0 & 6.41 & -7.69 & 0.624 \\ 0 & 0 & 0.578 & -1.234 \end{bmatrix} \quad 10^{-3} \text{ dkm}^{-1} \text{ hr}^{-1} \quad (8.6)$$

The optimised set which Olson - see Davies and Olson (1968) - derived for use in the 1968 operational model, and which is also used in the 1970 model, is different again:

$$C_{mn} = \begin{bmatrix} -5.0 & 4.5 & 0.5 & 0 \\ \times 10^4 & \times 10^4 & \times 10^4 & \\ 0 & -5.50 & 4.80 & 0 \\ 0 & 2.50 & -3.45 & 0.50 \\ 0 & 0 & 0.27 & -0.62 \end{bmatrix} \quad 10^{-3} \text{ dkm}^{-1} \text{ hr}^{-1} \quad (8.7)$$

The large magnitude values for the first row coefficients in (8.6) and (8.7), together with the associated zero off-diagonal coefficients in the first column, merely reflect the fact that the 1000 mb predictions are produced independently from the other levels by means of a derived field technique which does not take the vorticity into account. As mentioned in Section 5,

Constant	Value	Units
R	3.72×10^7	$\text{dkm}^2 \text{hr}^{-2} / \text{C deg}$
ϵ	1.2715×10^7	$\text{dkm} \text{hr}^{-2}$
f_0	0.3702	hr^{-1}

Table 1 : Numerical values of miscellaneous constants

Level (mb)	σ_S ($\text{dkm}^2 \text{mb}^{-2} \text{hr}^{-2}$)
1000	1010
850	1360
775	1830
700	1950
500	3570
350	6800
200	58000

Table 2 : Values of the static stability, σ_S , for the "dry" standard atmosphere.

this derived field technique is still retained in the operational model because there is no satisfactory way of evaluating $\frac{\partial}{\partial p} \left(\frac{\sigma^2}{\sigma} \frac{\partial \psi}{\partial p} \right)$ at 1000 mb. The RISE optimization technique merely confirms that the best one can do is to drop the 1000 mb vorticity and the linkage from 1000 mb to the other levels. Another important feature common to both (8.6) and (8.7) is that, except at 1000 mb, an empirical correction factor has been subtracted from each diagonal element to control spurious long wave retrogression. In Robert's (1963) prototype set (8.6) this empirical

correction factor was taken to be $-0.656 \times 10^{-3} \text{ dkm}^{-1} \text{ hr}^{-1}$ at all three levels. The optimised set (8.7), on the other hand, uses empirical correction factors of -0.70×10^{-3} , -0.45×10^{-3} , and $-0.35 \times 10^{-3} \text{ dkm}^{-1} \text{ hr}^{-1}$ at 850, 500 and 200 mb respectively. Cressman (1958) first used an empirical correction factor of this type to control spurious long wave retrogression in the barotropic model. Robert and Laflamme (1962) and the author - Davies (1967b) - proved that empirical correction factors were also theoretically necessary for the baroclinic model by doing a linear perturbation analysis of (7.1). That this is true in practice can easily be demonstrated by doing integrations without empirical correction factors and observing the spurious behaviour of the long waves.

The control coefficient sets (8.5) and (8.6) are both supposed to be based on the straightforward application of finite difference techniques using "dry" standard atmosphere static stabilities. Yet there are other differences between them besides the presence or absence of the empirical correction factors. These differences serve to underline the fact that there is no such thing as a uniquely defined set of dynamical coefficients. An unavoidable element of arbitrariness arises in the finite difference approximations. Consequently, the best one can hope to do in a model such as this is to come up with order-of-magnitude estimates of the individual control coefficients and then subsequently adjust them by optimisation over a series of test cases.

9. The Change-over from Smoothing to Eddy Diffusion Constraints

The 1970 operational model contains primary and secondary eddy diffusion constraints. These eliminate the need for the smoothing

operators which were applied every twelve hours in the earlier sequential models.

Except at initial time, the primary constraints, E_m , which appear in the baroclinic model equations (6.1) are given in analytical form by:

$$E_m = K_D^* \nabla^2 \left(\frac{g}{f_0} \nabla^2 \psi_m + f + 4 \sum_{n=1}^4 C_{mn} \psi_n \right) \quad (9.1)$$

$m = 1, 2, 3, 4$

where K_D^* is the coefficient of eddy diffusion of potential vorticity.

The finite difference form of (9.1) is:

$$\frac{1}{4K} \langle E_m \rangle^k = K_D \nabla^2 \left(K \nabla^2 \psi_m^{k-1} + \frac{f}{4} + \sum_{n=1}^4 C_{mn} \psi_n^{k-1} \right) \quad (9.2)$$

$m = 1, 2, 3, 4$

where K is defined by (C1.3) and

$$K_D = \frac{L f_0}{g} K_D^* \quad (9.3)$$

Equation (9.2) has been divided throughout by $4K$ to make it suitable for direct substitution into (C1.4). The secondary constraints, ϵ_m , which appear in the time step equation (6.2) are given in analytical form by:

$$\epsilon_m = K_d^* \nabla^2 \psi_m \quad m = 1, 2, 3, 4 \quad (9.4)$$

where K_d^* is the coefficient of eddy diffusion of stream function.

The finite difference form of (9.4) is:

$$\langle \varepsilon_m \rangle \Big|_t^t = K K_d \nabla^2 \psi_m^{t-1} \quad (9.5)$$

$$m = 1, 2, 3, 4$$

were again K is defined by (C1.3) and

$$K_d = \frac{1}{9} \frac{f_0}{K} K_d^* \quad (9.6)$$

At initial time, as no previous hour stream functions are available, both primary and secondary constraints are taken to be zero:

$$\left. \begin{array}{l} \frac{1}{4K} \langle \varepsilon_m \rangle \Big|_{t=0}^{t=0} = 0 \\ \langle \varepsilon_m \rangle \Big|_{t=0} = 0 \end{array} \right\} m = 1, 2, 3, 4 \quad (9.7)$$

The important thing to note about both (9.2) and (9.5) is that the finite difference evaluations have to be carried out using the previous hour values of the stream functions, not the current ones. This is because, as pointed out by Danard (1966a), the eddy diffusion constraints are dissipation terms of the type which have to be integrated by a forward time step in order to preserve computational stability. See Richtmeyer (1957) for a full discussion of this aspect of finite difference techniques.

The foregoing procedure was originally developed by the author - see Kwizak and Davies (1969) - for use in the parallel model. The actual values assigned to the eddy diffusion coefficients in the 1970 model are given in Table 3. These were determined by Creswick and Olson (1970) by optimising the verification scores for a series of test cases. The optimisation integrations were done using the control coefficients (8.7) which were retained by the 1970 model although originally derived for the

level(mb)	K_D^* ($10^7 \text{dkm}^2 \text{hr}^{-1}$)	K_d^* ($10^7 \text{dkm}^2 \text{hr}^{-1}$)	K_D (dkm)	K_d (dkm)
1000	0.429	2.147	0.5	2.5
850	0.515	0.601	0.6	0.7
500	0.429	0.429	0.5	0.5
200	0.859	0.859	1.0	1.0

Table 3 : Values of the eddy diffusion coefficients used in the 1970 baroclinic model

1968 model. Creswick and Olson (1970) found it simpler to specify zero eddy diffusion constraints at initial time, i.e. (9.7), instead of using slightly different applications of (9.1) and (9.4) for the forward time step. Briefly, the main advantages of replacing smoothing with eddy diffusion constraints are threefold. First, the predicted height patterns contain more detail with the eddy diffusion constraints. This additional detail does not lead to any deterioration of the RMSE verification scores. Second, there is an improvement in the vertical phasing of the predicted height patterns. Third, the derived vertical motion fields computed by the precipitation scheme change smoothly from hour to hour. In earlier models the vertical motion fields changed abruptly every twelfth hour when the smoothing operator was applied. A fuller discussion of the eddy diffusion terms will be deferred until later in the thesis.

In the 1968 model, which of course had no eddy diffusion constraints, the following smoothing procedure was applied after completion of the 12 th, 24 th and 36 th time steps. The newly predicted stream function fields for

the next hour and the current stream function fields of the time step just completed - which would have served respectively as the current and one hour old stream function fields in the time step about to begin - were all smoothed by an application of the standard smoothing operator (B3.1). For instance, after completion of the 24 th time step all the 24-hour and 23-hour stream function fields were subjected to the standard smoother (B3.1). In addition, after the completion of the 12 th time step the smoothed 12-hour and 11-hour stream function fields at 500 mb were unsmoothed by an application of the standard unsmoothing operator (B5.1). This was the only time step and the only level at which the standard unsmoother was applied. Finally, to provide more accurate first guess fields for use in the relaxation process (C1.10) in the next time step, and thereby speed up the convergence slightly, the stream function tendency fields just computed were also subjected to the standard smoother (B3.1). As mentioned in Section 5, in the earlier work on the octagon model the standard unsmoother was applied at all levels every twelve hours. Unfortunately, attempts to optimise the control coefficients with the unsmoother led to a pseudo-barotropic set that did not permit very much linkage between the levels. This paradoxical situation arose because several successful features of the barotropic model checked out by Simla (1964), including the smoother-unsmoother combination, had been carried over to the baroclinic model under the assumption that what was good for the barotropic must also be good for the baroclinic. That this supposition was an erroneous one was eventually demonstrated by Robert and Olson (1966). They took the unsmoother out of the model and repeated the optimisation procedure. They ended up with a truly baroclinic set of control

coefficients which gave physically realistic interactions between the levels. Experimentation along the way indicated that it paid to retain the unsmoother at 500 mb at 12 hours. The smoothing procedures established by this work remained a feature of the baroclinic model until they were replaced by eddy diffusion constraints.

The characteristics of the response curves of smoothing operators are well known. They have been discussed by Shuman (1957) and Asselin (1966). Briefly, the standard smoother (B3.1) eliminates two-gridlength waves entirely and severely damps other short waves. The standard unsmoother (B5.1), on the other hand, amplifies short waves. In combination, the two operators still eliminate two-gridlength waves, and still damp other short waves, but the degree of damping is much reduced especially for the longer short waves. The thing to remember, of course, is that these remarks describe what happens to the actual field which is subjected to the smoothing and unsmoothing operators, and only to this actual field. Thus, when the smoother-unsmoother combination is applied to four individual stream function fields, the short waves in these stream function fields themselves are damped in the manner one would expect from the response curves. But the snag is that the response curves offer no guarantee about what will happen to the short waves in the associated stream function thickness fields. In fact the thickness short waves can and do amplify. So much so, as the early work on the octagon model so clearly demonstrates, that with physically realistic control coefficients there is a net generation of potential vorticity.

10. The Derived 700 mb Stream Function Forecasts

The sequential version of the precipitation scheme requires hourly values of the 700 mb stream function field for the 1015-point grid shown in Fig. 1. These cannot be provided directly by the sequential baroclinic model because the 700 mb surface is not one of its working levels. Consequently, the best that can be done is to carry the 700 mb stream function along in the RADAT RUN integrations with derived field status. The actual derived field computations are discussed here in PART II because they constitute a natural adjunct to the baroclinic model. In practice, however, they have always been included in the precipitation scheme.

In the 1970 model the derived 700 mb charts are obtained by means of the following procedure. The initial time stream function field at 700 mb is obtained from the initial time height field in the same way as at the other levels. The first step is to solve the "forward" balance equation over the full 2805-point grid. This results in a hemispheric stream function field from which the 1015-point grid values can be extracted. The actual forecast equation is:

$$\frac{D_{70}}{Dt} \left\{ a_p (\psi_{85} - \psi_{70}) + (1 - a_p) (\psi_{50} - \psi_{70}) \right\} + a_p K_{D85}^* \nabla^2 \psi_{85} + (1 - a_p) K_{D50}^* \nabla^2 \psi_{50} - K_{D70}^* \nabla^2 \psi_{70} = 0 \quad (10.1)$$

where a_p is a constant and the K_D^* are eddy diffusion coefficients. Note that, except for minor differences in the eddy diffusion terms, equation (10.1) is formally equivalent to the $m=1$ component of (6.1) for the operational set of control coefficients (8.7). For a regular centred time step the finite difference form of (10.1) may be written:

$$\begin{aligned} \psi_{70}^{t+1} = & \psi_{70}^{t-1} + a_p (\psi_{85}^{t+1} - \psi_{85}^{t-1}) + (1-a_p)(\psi_{50}^{t+1} - \psi_{50}^{t-1}) \\ & + K(2\Delta t) \left[\mathcal{J}_g(\psi_{70}^t, \{a_p \psi_{85}^t + (1-a_p)\psi_{50}^t\}) \right. \\ & \left. - \left\{ a_p K_{D85} \nabla^2 \psi_{85}^{t-1} + (1-a_p) K_{D50} \nabla^2 \psi_{50}^{t-1} - K_{D70} \nabla^2 \psi_{70}^{t-1} \right\} \right] \quad (10.2) \end{aligned}$$

where K is defined by (C1.3), the K_D are related to K_D^* as in (9.4), and as usual Δt is one hour. Along the boundaries of the 1015-point grid the values of the 700 mb stream function are made time-dependent by applying:

$$\psi_{70}^{t+1} = \psi_{70}^{t-1} + a_p (\psi_{85}^{t+1} - \psi_{85}^{t-1}) + (1-a_p)(\psi_{50}^{t+1} - \psi_{50}^{t-1}) \quad (10.3)$$

For the corresponding forward time step which must be done at initial time the same formulae (10.2) and (10.3) apply except that the $(t-1)$ superscripts become t , the $(2\Delta t)$ becomes (Δt) , and the eddy diffusion terms are taken to be zero to conform to (9.7). The constant a_p is taken to 0.615, a value originally obtained by subjective optimisation for the octagon model in which smoothing took the place of eddy diffusion. Table 4 lists the values of the eddy diffusion coefficients. These might seem a little high in view of the fact that $(\psi_{85}^{t+1} - \psi_{85}^{t-1})$ and $(\psi_{50}^{t+1} - \psi_{50}^{t-1})$ already reflect the primary and secondary eddy diffusion constraints on the baroclinic model itself. However, the resultant 700 mb height forecasts do not appear to be relatively too smooth, or distorted in any way, in comparison with the height forecasts for the other levels.

Level (mb)	K_D^* (10^7 dkm 2 hr $^{-1}$)	K_D (dkm)
850	0.859	1.000
700	0.752	0.875
500	0.644	0.750
200	1.288	1.500

Table 4: Values of the eddy diffusion coefficients used in the derived 700 mb stream function forecasts and also in the vertical motion computations of the 1970 model.

Consequently, it was felt wiser to retain the Table 4 values rather than risk producing derived 700 mb stream function forecasts with too little effective smoothing. There is currently no operational demand for predicted 700 mb height fields, and so none have been produced since March 1970. During February and March 1970 700 mb height forecasts were produced for the characteristic areas verification program which will be described in the next Section. The conversion from predicted stream function fields to predicted height fields was carried out in the usual manner by applying the "reverse" balance equation over the 1015-point grid. This required the specification of predicted 700 mb heights along the boundaries of the 1015-point grid. As in the 1968 model, these were simply extracted from the 2805-point initial time height field obtained by applying the "reverse" balance equation to the 2805-point grid initial time stream function field. No attempt was made to generate time-dependent boundary values for the predicted 700 mb height fields. Obviously, there was an inconsistency here

as (17.3) does allow the boundaries of the 700 mb stream function fields to be time-dependent. However, this is a small difficulty which could easily be overcome if a demand arises for predicted 700 mb height fields.

The derived 700 mb procedure used earlier in both the 1968 model and the octagon model was almost the same as that just described for the 1970 model. As in the models themselves, however, twelve hourly smoothing operators were employed instead of eddy diffusion terms. This meant, of course, that all the K_D^* in (10.1) were taken to be zero. The smoothing operators were slightly trickier to handle than in the models. In applying (10.2) the golden rule was that all stream function fields for the same level must have been subjected to identical smoothing procedures. For instance, at the 23 rd time step the $(t+1)$ values of the 850 and 500 mb stream functions made available by the baroclinic model would be 23-hour values which would have been subjected to the standard smoothing operator (B3.1). The t and $(t-1)$ values of the same fields, however, would not have been smoothed by the baroclinic model. Accordingly, before commencing the 23 rd time step computations with (10.2) it was necessary to apply the standard smoothing operator (B3.1) to the 21-hour and 22-hour stream function fields for all three levels, 850, 700 and 500 mb. The 11 th and 35 th time steps had to be handled in the same way, except that at the 11 th time step the 9-hour and 10-hour 500 mb stream function fields had also to be subjected to the standard unsmoother (B5.1). Of course, this problem of matching up the smoothing of the stream function fields at different time steps only arose because the derived field program was included in the sequential precipitation scheme. If the baroclinic model and the derived field program were integrated simultaneously, the

smoothing operators could all be applied at the same time step.

In the early development work on the octagon model it was not possible to objectively verify any derived 700 mb height forecasts. This was because these forecasts were produced for a half-octagon grid for which there was no "reverse" balance equation program available. Consequently, the 700 mb stream function forecasts had to be assessed subjectively. In particular, they were carefully checked for horizontal and vertical consistency. As individual charts the 700 mb stream function forecasts appeared to be intermediate in quality between their 850 and 500 mb counterparts. They were therefore considered to be reasonably satisfactory in the horizontal. In all cases the phasing of the 700 mb features was intermediate between the corresponding features at 850 and 500 mb. The vertical consistency was therefore rated as highly satisfactory as the baroclinic model itself would permit. This was in marked contrast to the lack of vertical consistency of the 1000 mb charts produced by essentially the same derived field technique. The crucial difference, of course, is that the 700 mb charts are derived by interpolation, whereas the 1000 mb ones involve an extrapolation. Interpolation ensures vertical consistency, but extrapolation does not. The same kind of subjective assessments of the 700 mb stream function forecasts were made when the 1968 model was introduced into the operational run. The conclusions were similar to those drawn earlier for the octagon model.

The first objective assessments of the 700 mb height forecasts were made in March 1969. At that time a comprehensive verification program came into routine use. This computed the RMSE verification scores for the characteristic areas of the combination of baroclinic model and precipitation

scheme. The results confirmed the subjective assessments of the relative worth of the individual 700 mb charts. A fuller discussion of the RMSE verification scores is contained in the next Section.

11. Verification Scores for the Forecast Height Charts

11.1 Standard Areas

The root-mean-square errors (RMSE) of the height forecasts produced operationally by the baroclinic model in the RADAT RUN have been monitored by two different verification programs. The first of these was designed to function on a long term basis. It computes RMSE scores for the whole 1221-point grid and also for the standard verification areas in use by the National Meteorological Center in Washington, or at least for those of them which happen to fall inside the 1221-point grid integration area.

These standard verification areas, five in number, have come to be internationally recognised. Their positions are given by Holyoke (1965) who adds a sixth area more appropriate for Canadian interests. Essentially the same verification program, with some extensions to handle the extra standard areas, is also used to monitor the height forecasts produced by the hemispheric model in the MOP UP RUN.

The purpose of having a standard areas verification program is to permit direct comparisons between the performances of the CAO baroclinic model and the models used by other countries. To this end monthly summaries of the statistics generated by the standard areas verification program are reported elsewhere by Creswick and Olson (1970), and Davies and Olson (1971). They are not given here because they present an overall picture which is qualitatively very similar to that portrayed by the

characteristic areas verification program which will be described next.

11.2 Characteristic Areas

Unfortunately, the standard areas do not match the CAO operational grids too well. For instance, the eastern boundary of standard area 2 coincides with a characteristic boundary of the 1970 model, namely the eastern boundary of the 1221-point grid, whereas the western boundary of the same standard area falls well within the 1221-point grid. It is unaesthetic, and probably slightly unscientific, to base internal value judgements at the CAO on verification scores for areas which do not have a reasonably symmetrical relationship to the characteristic areas of the main production run. Partly because of this consideration, and partly because of the need to verify other quantities such as the temperature fields, the author designed a second verification program to operate for a limited time. It computes RMSE scores for characteristic areas instead of for standard ones. And it does this not only for the height forecasts produced by the baroclinic model itself, but also for some of the predicted variables related to the precipitation scheme. More specifically, it verifies the RADAT RUN forecasts of height, including the derived 700 mb height, and the three levels of temperature and dew point depression for the interior of the 1015-point grid and the full 504-point grid shown in Fig.1. The exclusion of the boundaries of the larger grid means that the figures quoted for the 1015-point grid are actually for the 891 interior points; this is a matter of convenience to avoid introducing yet another grid-size into the dissertation. Unfortunately, because of the growth in the demand for computer time, no indefinite

operational commitment could be made to this more comprehensive verification program. Consequently, it was run on a routine basis for just over a year, from March 1969 to March 1970, and then withdrawn. The principal verification statistics which have been gathered in these 13 months are summarised in this thesis. They will serve as a rough guide to the general effectiveness of the forecasts produced by the sequential model, and thereby provide some kind of background against which the forecasts of the parallel model may be judged. It should be noted that the monthly mean scores for March 1969 to January 1970 are for the 1968 model, and those for March 1970 are for the 1970 model. The change-over between the two operational models occurred about one third the way through February 1970, and so the mean scores for this month are hybrid ones weighted 2 to 1 in favour of the 1970 model.

Fig.4 is a diagram showing the monthly mean corrected root-mean-square error (CRMSE) verification scores for the 12, 24 and 36-hour 1000 mb height forecasts, both for the 1015-point and the 504-point grids, together with the corresponding persistence scores. As is customary for height charts, the individual scores which go to make up the monthly averages have been corrected to take into account the difference between the mean of the forecast chart and the mean of the verifying chart; i.e. the CRMSE verification scores are computed from the formula (B17.2) which is given in Appendix B. Figs. 5, 6, 7 and 8 give the same information for 850, 700, 500 and 200 mb respectively. It is clear from Fig. 7 that the baroclinic height forecasts at 500 mb beat the corresponding persistence forecasts by quite a handsome margin. This is true even at 36 hours. Also, comparing the last two months with the rest, it is obvious that at 500 mb the monthly mean

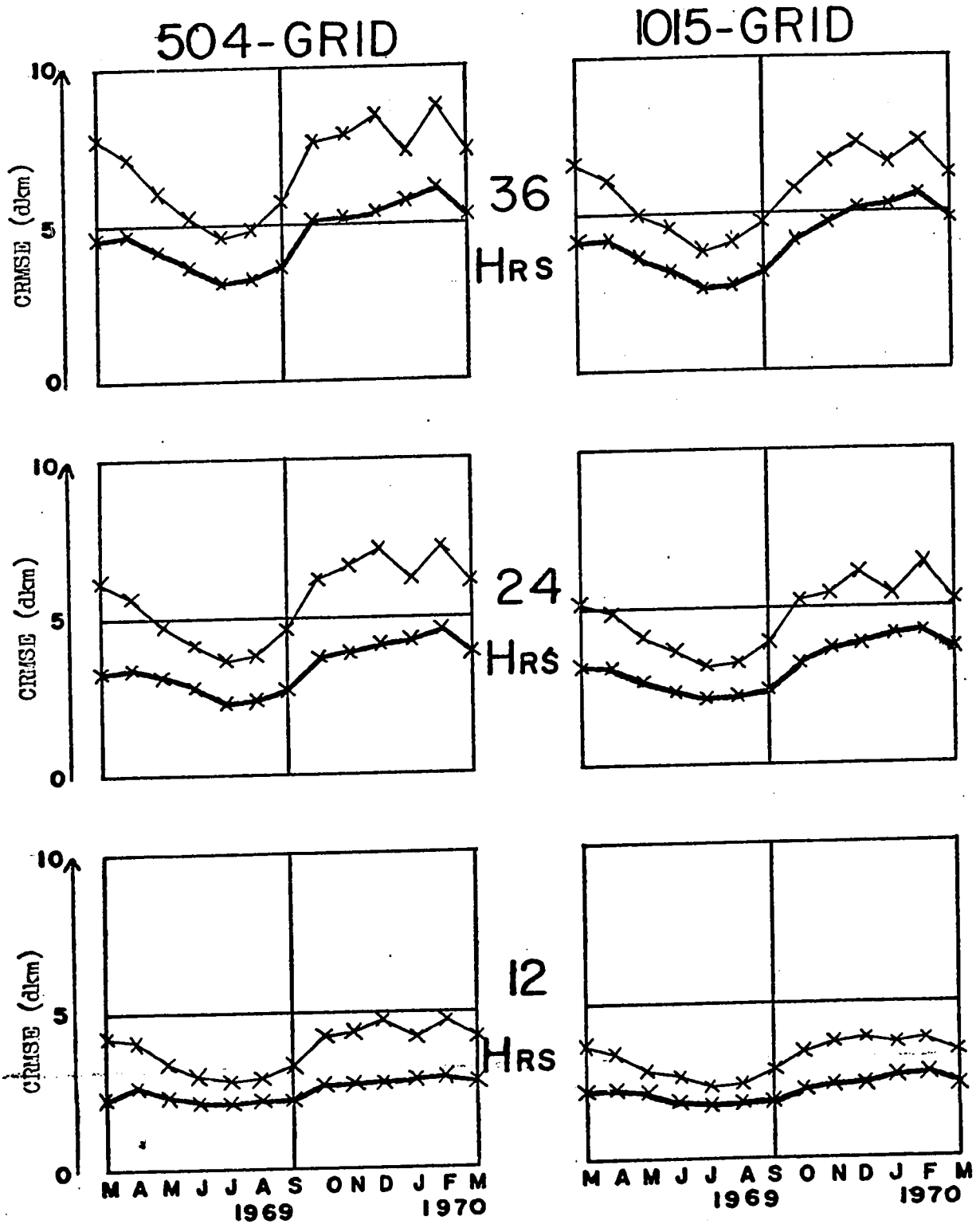


FIG 4 : Monthly mean corrected root-mean-square error (CRMSE) scores in dlcm for the 12, 24 and 36-hour forecasts of 1000mb height, together with the corresponding persistence scores. The diagrams on the left are for the 504-point grid, and those on the right are for the 1015-point grid. The thick curves are the forecast scores, and the thin curves are the persistence scores.

Z850MB

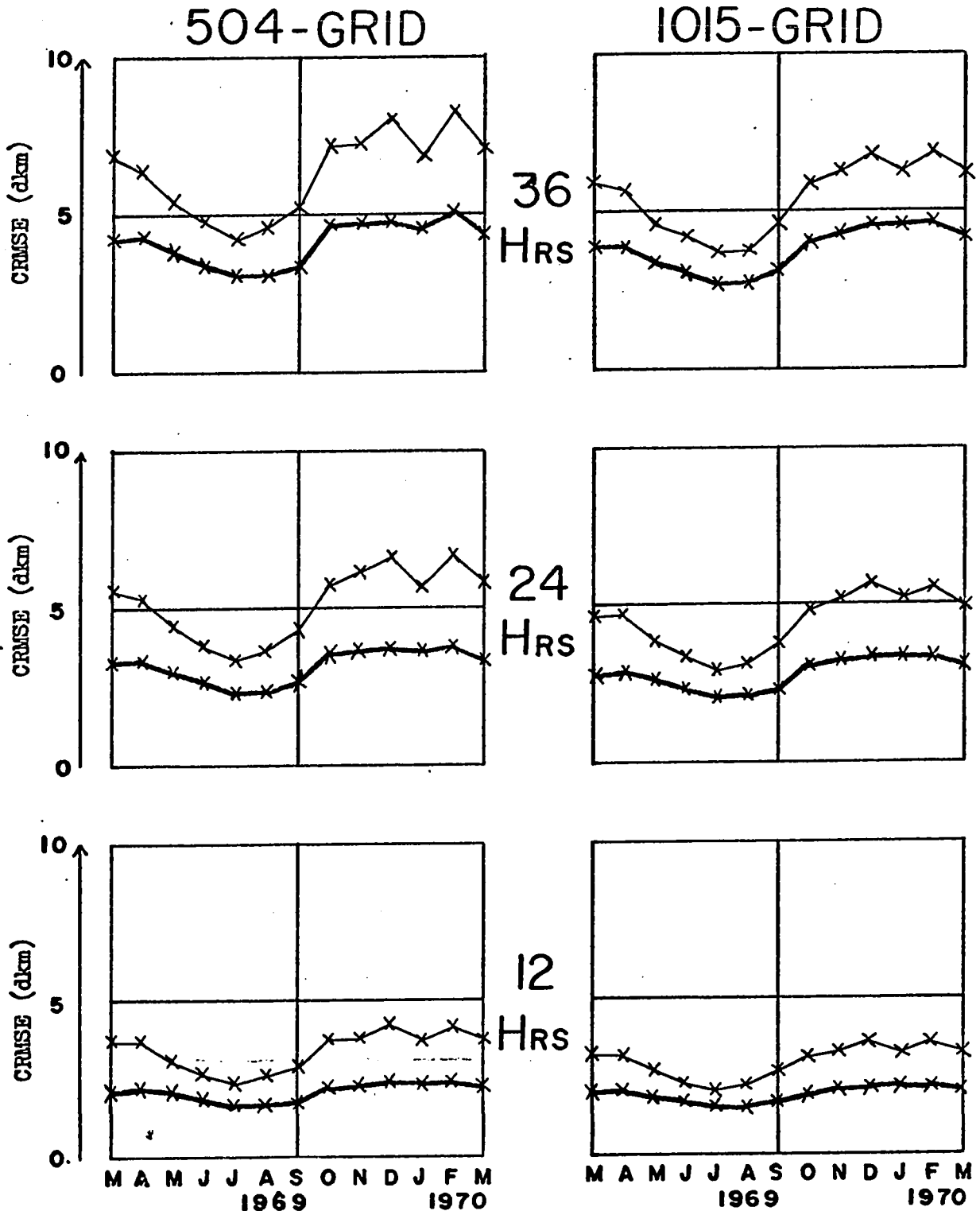


FIG 5: Monthly mean corrected root-mean-square error (CRMSE) scores in dkm for the 12, 24 and 36-hour forecasts of 850mb height, together with the corresponding persistence scores. The diagrams on the left are for the 504-point grid, and those on the right are for the 1015-point grid. The thick curves are the forecast scores, and the thin curves are the persistence scores.

Z 700 MB

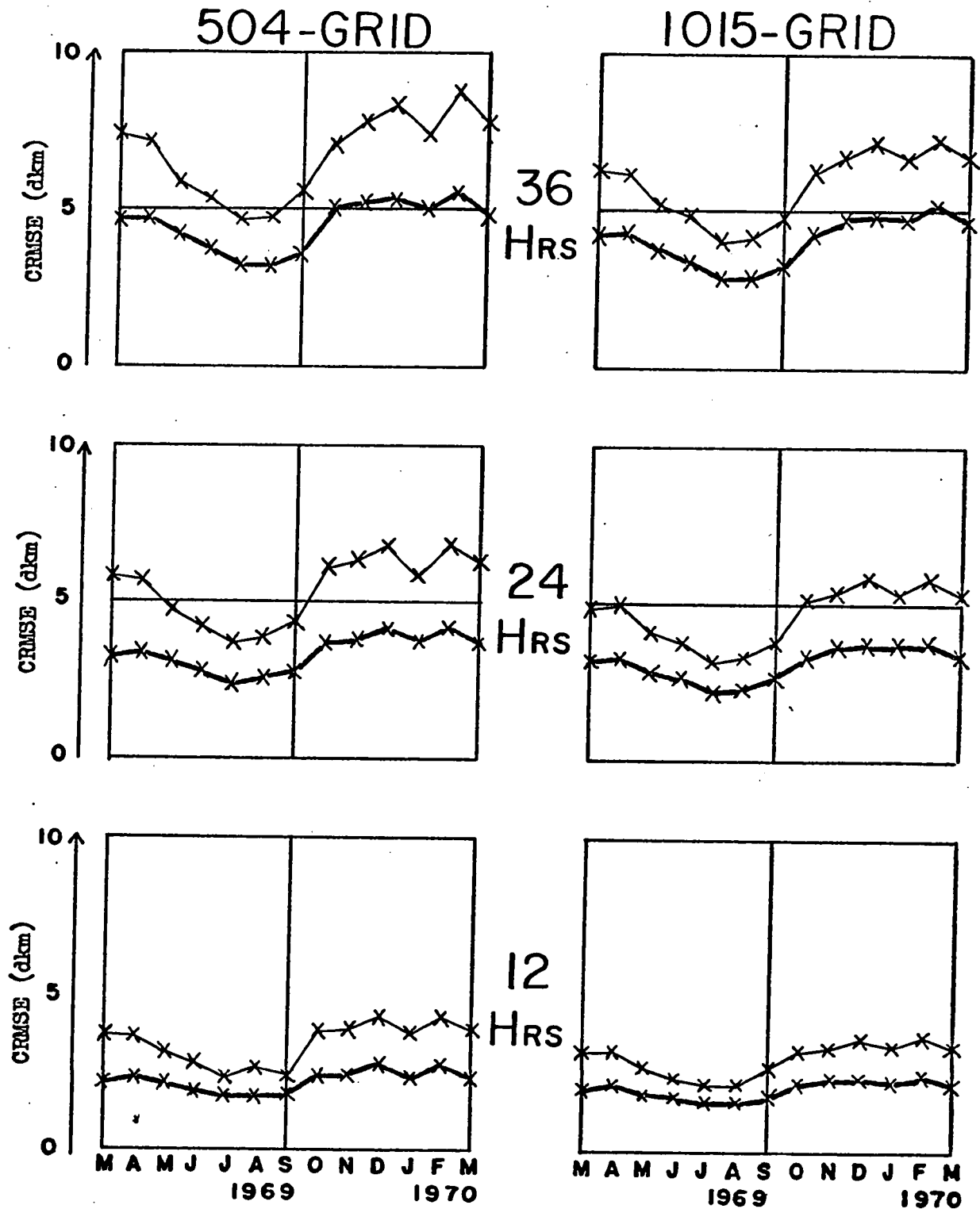


FIG6: Monthly mean corrected root-mean-square error (CRMSE) scores in dkm for the 12, 24 and 36-hour forecasts of 700mb height, together with the corresponding persistence scores. The diagrams on the left are for the 504-point grid, and those on the right are for the 1015-point grid. The thick curves are the forecast scores, and the thin curves are the persistence scores.

Z500MB

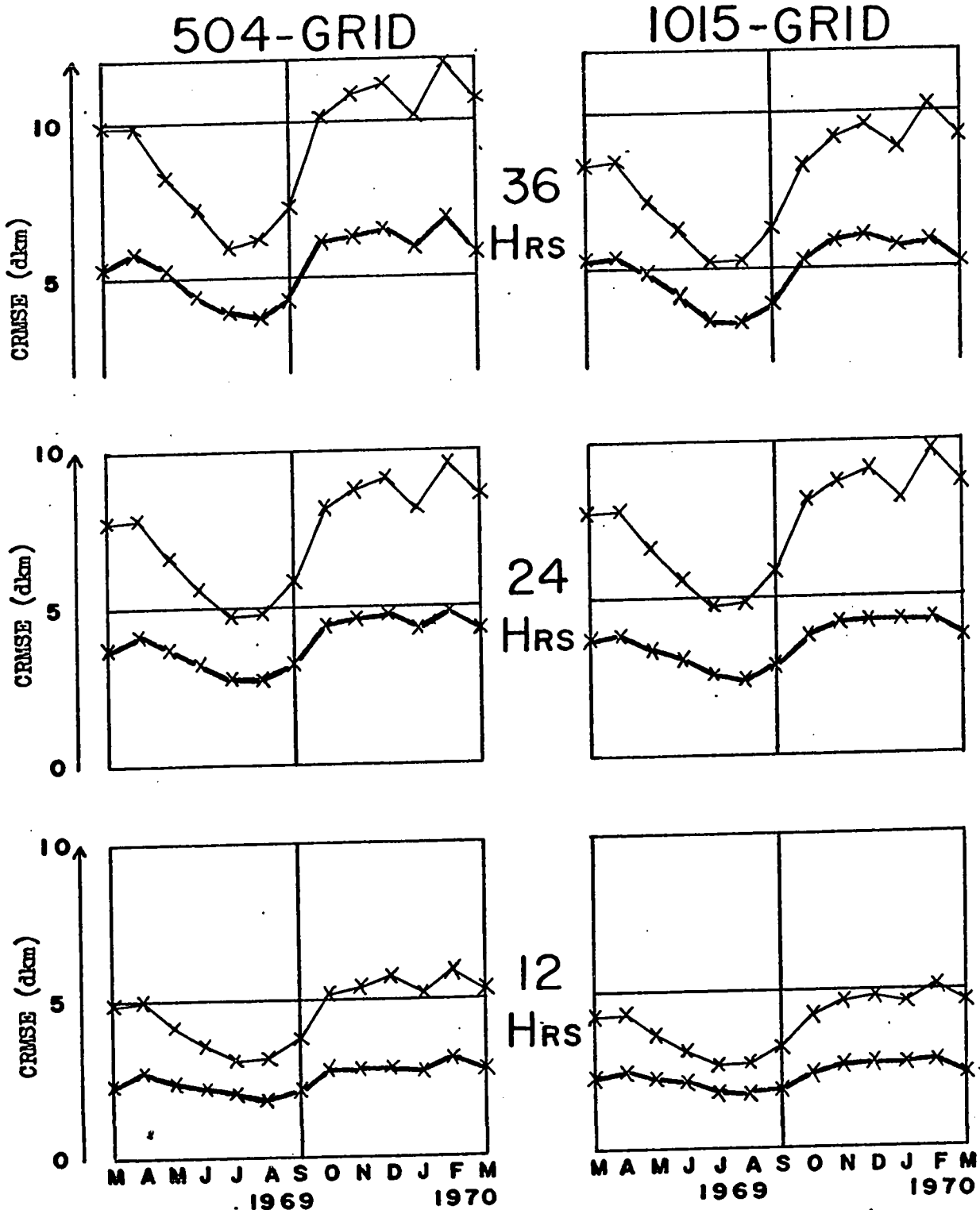


FIG 7: Monthly mean corrected root-mean-square error (CRMSE) scores in dkm for the 12, 24 and 36-hour forecasts of 500mb height, together with the corresponding persistence scores. The diagrams on the left are for the 504-point grid, and those on the right are for the 1015-point grid. The thick curves are the forecast scores, and the thin curves are the persistence scores.

Z200 MB

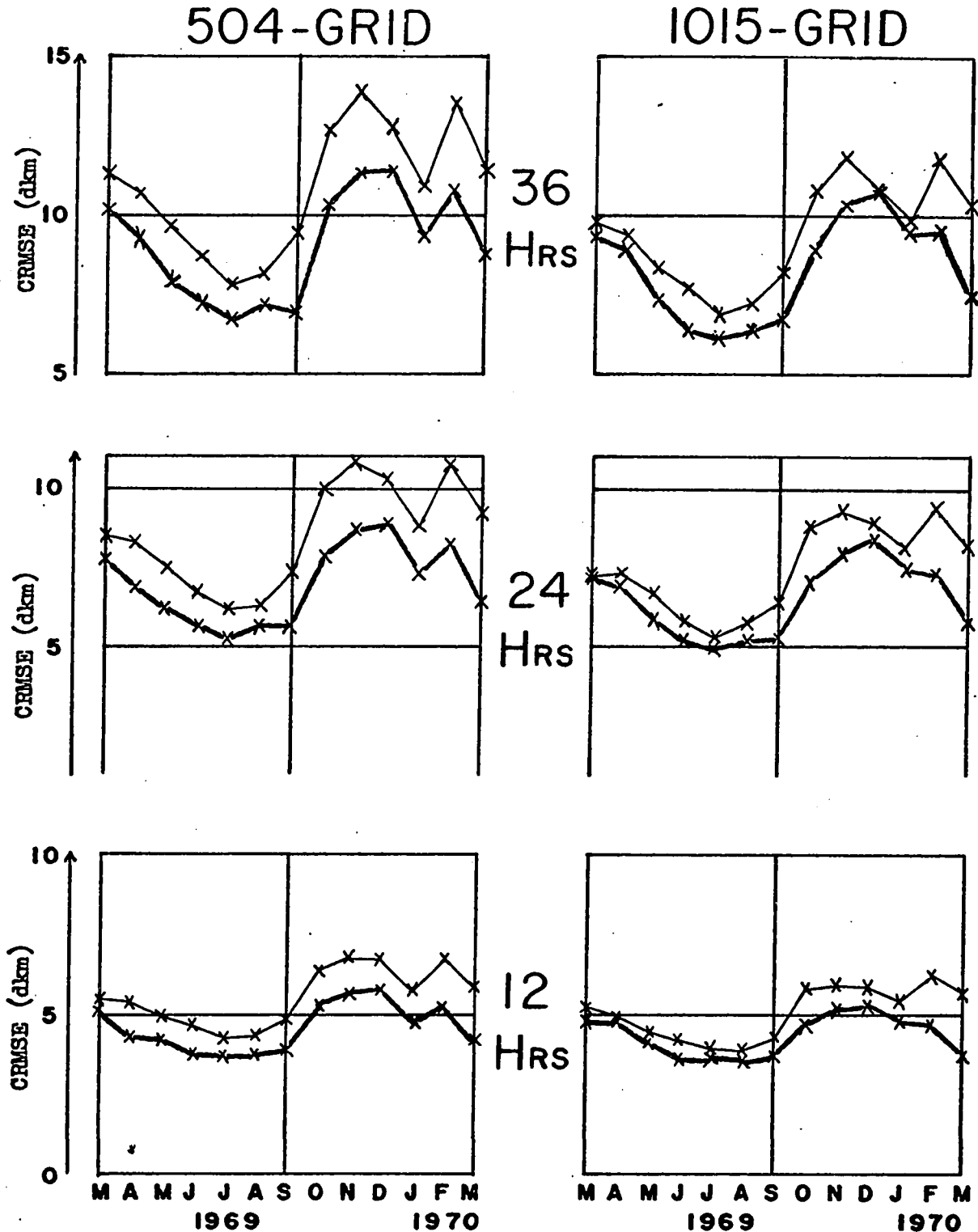


FIG 8: Monthly mean corrected root-mean-square error (CRMSE) scores in dkm for the 12, 24 and 36-hour forecasts of 200mb height, together with the corresponding persistence scores. The diagrams on the left are for the 504-point grid, and those on the right are for the 1015-point grid. The thick curves are the forecast scores, and the thin curves are the persistence scores.

verification scores for the 1970 model are about the same as for the 1968 model. This is in spite of the fact that the height forecasts produced by the 1970 model exhibit somewhat more detail than those produced by the 1968 model. Turning now to Figs. 4, 5 and 6, it can be seen that the comments just made about the height forecasts at 500 mb also apply to the height forecasts at 1000, 850, and 700 mb. Further, Figs. 5, 6 and 7 show that the monthly mean verification scores at 700 mb exhibit patterns which are in every sense intermediate between the ones at 500 mb and the ones at 850 mb. This is evidence to suggest that the height forecasts at 700 mb do not suffer unduly in comparison to those at the other levels because they are produced by a derived field technique. Although, of course, this does not mean that the promotion of the 700 mb field to the status of a full working level of the baroclinic model would not lead to improvements at all levels. Fig. 8 shows that there was a striking improvement in the CRMSE scores for the 200 mb height forecasts when the 1968 model was replaced by the 1970 model. For the first eleven months the scores at 200 mb are not nearly so impressive as they are at the other levels, but at least they do consistently beat persistence. For the last two months, however, the scores at 200 mb beat persistence by a much more respectable margin, although still not to the same degree as at the other levels.

The characteristic areas verification program also computed CRMSE scores for what might be called zero-hour forecasts. These were obtained by verifying the initial time "reverse" balance height field against the original initial time height fields. As explained in (5.5), the initial time "reverse" balance height fields were used in the 1968 model to provide

boundary conditions for the predicted height fields. They are obtained by applying the "reverse" balance equation to the initial time 2805-point grid stream function fields, which in turn are obtained by applying the "forward" balance equation to the original initial time height fields. At 850 and 700 mb the zero-hour height forecasts had CRMSE scores which varied from about 0.15 dkm in summer to about 0.25 dkm in winter. At 1000 and 500 mb the corresponding range was from 0.20 dkm in summer to 0.35 dkm in winter. At 200 mb the range was from 1.0 dkm to 1.5 dkm in the 1968 model, but these values appeared to be cut down by more than half by the introduction of the 1970 model. There is a subtle inference to be drawn from the figures just quoted. It is that even an idealised baroclinic model could not produce 12, 24, and 36-hour height forecasts with zero verification scores. The best one could hope to do with the baroclinic model, at least without changing the balance equation program, is to match the zero-hour scores. There are two reasons for this. First, the height forecasts obtained from the stream function forecasts, by solving the "reverse" balance equation, must be fully ellipticised. The verifying height analyses, on the other hand, are objective analyses which have not been ellipticised. Second, there is a small bias problem which arises in the solution of the balance equation. See Asselin (1967) for a discussion of these two problems. In any case, the net result is that the zero-hour scores represent irreducible minima beyond which the 12, 24 and 36-hour verification scores may not go. The reduction of the zero-hour 200 mb scores by the 1970 model is not too difficult to explain. Neither model starts from an objectively analysed 200 mb height field as no new 200 mb data is available for the RADAT RUN. As mentioned in (5.6),

February and March 1970 were part of the interim period during which the new model was unable to use the 12-hour 200 mb height forecasts from the Washington primitive equations model. So for these two months the initial time 200 mb height charts that went into the 1970 model were simply the 12-hour forecasts from the hemispheric baroclinic model. These would automatically have been fully ellipticised because they were produced from predicted stream function fields via the "reverse" balance equation. During this period, therefore, the entire zero hour 200 mb score of the 1970 model must have been due to the bias problem. In the 1968 model, on the other hand, the initial time 200 mb height charts were generated by the thickness advection technique of McClellan et al (1966). No special precautions were taken to ensure that these were ellipticised. Consequently, before computing the stream function fields, the "forward" balance equation program would have had to make adjustments to eliminate any hyperbolic points. It seems reasonable to assume that the bias contribution is about the same for both 1970 and 1968 models. If this is the case, then the difference in the zero-hour 200 mb scores is attributable solely to the ellipticisation adjustments in the 1968 model. That, of course, raises the question of what kind of zero-hour 200 mb scores are associated with the final version of the 1970 model. The 200 mb height forecasts from the primitive equations model may not be completely free of hyperbolic points. But they are produced by a highly sophisticated model, so they should require much less ellipticisation than the 200 mb height fields generated by the thickness advection technique. So, presumably, one should expect the final 1970 model to have zero-hour 200 mb scores with a summer to winter range of something like 0.6 dkm to 0.9 dkm. This estimate has not yet been checked.

PART III : THE SEQUENTIAL VERSION OF THE PRECIPITATION SCHEME

12. Origins of the Sequential Approach

The author has developed a fully automatic scheme to produce three-layer numerical forecasts of precipitation amount on a computer. From the beginning the scheme was specially designed to work in conjunction with the CAO baroclinic model. Nevertheless, many of its features are sufficiently general in nature to be readily adaptable to a primitive equations model when the time comes for such a change-over to be made.

As mentioned in Section 5.1, the development work has been carried out in two stages. In the first stage the baroclinic model and the precipitation scheme are integrated in sequence to one another; in the second stage they are integrated in parallel so that the precipitation scheme can and does interact back with the baroclinic model. The sequential scheme was developed before the parallel scheme for the following three reasons:

- (i) Nobody at the CAO had had any previous experience whatsoever with the problem of how to predict precipitation amount on a computer. Nor was there much in the way of guidance on the subject to be found in the literature. Under such circumstances it was felt that it would be prudent to separate out the problem of predicting precipitation from the problem of predicting interactions such as the feedback of effects due to the release of latent heat.
- (ii) During the time the original development work was being carried out the computer facilities were comparatively limited. Those were the days before the installation of the IBM 360/65 machine when the CAO had only a CDC G-20 computer. The lack of drum and disk storage

devices was in itself a powerful inducement to confine all research on the precipitation project to the sequential mode of operation.

- (iii.) There was a strong demand for computer-produced forecasts of precipitation amount from the Forecast Services Division of the Meteorological Branch. This meant that every attempt had to be made to develop an operational program as soon as possible.

Subtle though the point may be, note that the decision to proceed with research into a precipitation scheme operating in sequence with the baroclinic model did not imply a decision to concentrate on the development of a purely diagnostic precipitation scheme. In fact a purely diagnostic stage of the development was carefully avoided for three reasons. These were:

- (a) A six-hour time period is the shortest one for which precipitation amounts are observed. So meaningful evaluations of a precipitation scheme cannot be carried out unless it contains a predictive element.
- (b) One of the major weaknesses common to many of the earlier graphical precipitation schemes was that they tended to ignore the prediction aspects of the problem. For instance, in any diagnostic scheme it is soon recognised that a knowledge of the temperature is essential in order to compute precipitation amount. This means that, before such a diagnostic scheme can be applied to obtain precipitation forecasts, it is necessary to devise a method for obtaining predicted temperatures. So, in this respect, the sequential precipitation

scheme must be more sophisticated than a purely diagnostic scheme, because it must predict temperatures and other quantities as well as precipitation.

- (c) The assumptions made in the baroclinic model may affect the computations in the precipitation scheme. For instance, in the baroclinic model the assumption is made that the static stability divided by the Coriolis parameter is a function of pressure only. This has dire consequences if carried over too literally into the precipitation scheme, for if no special precautions are taken it results in the appearance of singularities in the "wet" vertical motion fields. This type of problem is not encountered in a purely diagnostic scheme. It only becomes apparent when one actually tries to use the baroclinic model as a basic tool for predicting precipitation amount.

In essence, then, the foregoing remarks testify to the fact that the decision to develop a sequential precipitation scheme was a sound one. It was the outcome of a middle of the road policy between, on the one hand, a purely diagnostic scheme which might tend to overlook the prediction aspects, and, on the other, a parallel scheme in which the problems of handling interactions might obscure the more mundane problems of predicting precipitation amount itself.

13. Tables of Unit Condensation Rate

A unit mass of ascending saturated air has a most important physical property. If supersaturation does not occur, and if the moist adiabatic

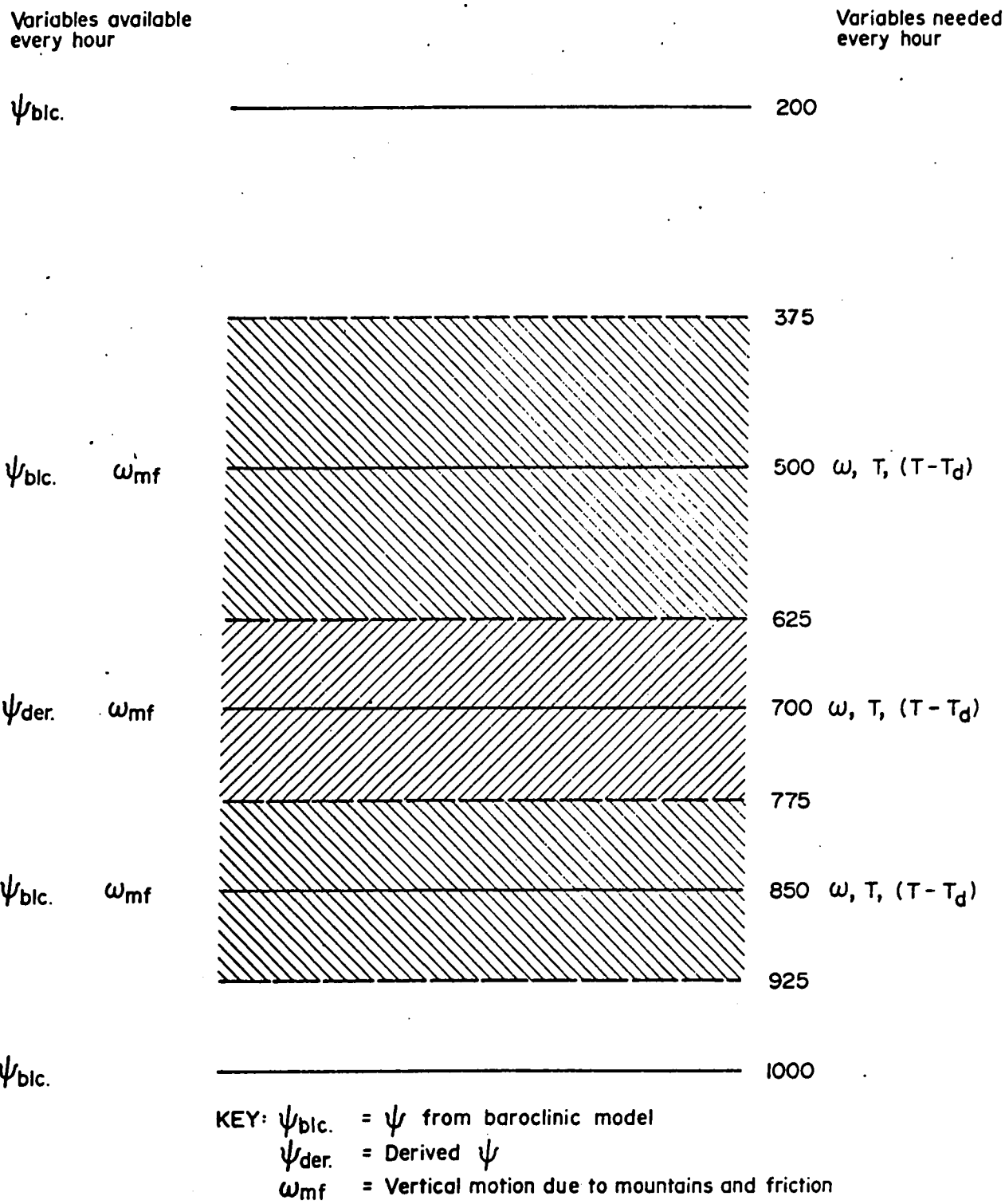


Figure 9

The Three Layers of the Atmosphere for Which Precipitation Computations are Carried Out; and the Variables Which are (a) Available and (b) Needed, Each Hour

assumption holds true, then the rate of condensation of water vapour is uniquely determined by the vertical velocity, the temperature and the pressure. Because the dependence on vertical velocity is a linear one, Fulks (1935) was able to prepare tables of condensation rate for varying temperature and pressure for a unit mass of air ascending with unit vertical velocity; see also the Smithsonian Tables (1958). The important basic theory underlying Fulks' tables is reviewed in Appendix A. By making appropriate changes of units, it is possible to construct tabular values of hourly condensation amount for the particular saturated layers of the atmosphere under consideration. These will be referred to as tables of unit condensation rate, $U_p(T)$. For the vertical finite difference scheme of Fig. 9, which is the one used in the precipitation scheme, these values are given in Table 5 at intervals of 10 C deg. All actual computations are based on a more complete version of Table 5 giving values at intervals of 1 C deg.

Three things have to be known before the tables of unit condensation rate can be used to compute the large scale condensation amount. They are the large scale vertical motion, the temperature, and some measure of the moisture content of the air. For the first two of these quantities there is no ambiguity about what is actually wanted. But there are several methods of specifying the moisture content of the air. So one of the first problems facing someone about to embark on the design of a precipitation scheme is the choice of moisture parameter.

C deg	850 mb (150 mb layer)	700 mb (150 mb layer)	500 mb (250 mb layer)
- 70			20
- 60	22	38	30
- 50	33	56	40
- 40	44	75	123
- 30	126	169	497
- 20	270	366	1137
- 10	511	714	2009
0	812	1088	2875
10	1098	1445	3830
20	1373	1769	
30	1660		
\hat{U}_p	1500	1500	2500

Table 5: Tables of unit condensation rate, $U_p(T)$ in 10^{-6} inches rain/hour, for layers 150 mb thick (except the layer centred at 500 mb which is 250 mb thick) ascending at 1mb/hour, Values of \hat{U}_p are also given.

14. Choice of Moisture Parameter: Dew Point Depression

The moisture content of the air may be specified in many alternative ways. The most common ones are the dew point depression, the dew point, the mixing ratio, the specific humidity, the relative humidity, the wet bulb temperature, the wet bulb potential temperature, and the vapour pressure. Provided that the temperature and pressure are given, a knowledge of any one of these quantities allows all the others to be computed. As far as precipitation computations are concerned, the important thing one wishes to know is how close the air is to saturation. The choice of moisture parameter should therefore take into account the accuracy with which predictions of closeness to saturation can be made. Convenience should also be taken into consideration.

Moisture reports from the radio-sonde ascents are transmitted in the form of dew point depression. Consequently, dew point depression is the moisture parameter that is objectively analysed in the CAO operational program. This is done partly as a matter of convenience. But, also, it is done because in principle one should analyse directly reported quantities in preference to derived quantities, at least in cases where no good reason exists to do otherwise, simply to avoid any errors which might arise due to approximations made in the derivation process. As objectively analysed fields of dew point depression are made available on a routine basis at the CAO, the natural thing to do is to carry over the dew point depression into the precipitation scheme and make it the moisture parameter to be used for prediction purposes -- i.e. at the CAO the dew point depression is without a doubt the most convenient moisture parameter to use in a precipitation scheme.

All techniques to predict a moisture parameter must be based on the conservation of mass of water vapour in the atmosphere. However, a prediction of a moisture parameter does not generally constitute a prediction of closeness to saturation. In fact only two of the nine moisture parameters listed at the beginning of this Section provide a direct measure of closeness to saturation without a knowledge of the temperature field. These are the dew point depression and the relative humidity. All the others, including the mixing ratio and the potential wet bulb temperature, require a specification of the temperature field before any estimate of closeness to saturation can be made. For instance, a predicted value of the mixing ratio does not in itself provide any information about closeness to saturation. One must also have a predicted value of the temperature in order to compute a predicted value of saturation mixing ratio. The difference between the predicted saturation mixing ratio and the predicted mixing ratio then constitutes a measure of closeness to saturation. So in such cases the accuracy of prediction of closeness to saturation will depend on the accuracy of prediction of both the moisture parameter and the temperature. In other words the accuracy of the precipitation forecasts will be very sensitive to errors in the predicted moisture parameter and will also be very sensitive to errors in the predicted temperature field. With the dew point depression, on the other hand, the accuracy of the precipitation forecasts will still be very sensitive to errors in the predicted moisture parameter, but relatively insensitive to errors in the predicted temperature field. This is because the temperature is only used to compute the absolute moisture content of saturated air. With the dew point depression one does not use the temperature explicitly to test

for closeness to saturation, as one does, for example, with the mixing ratio. Now it is true that a knowledge of the temperature is needed when one actually predicts dew point depression, but the dependence is again one of low sensitivity. Furthermore, for any scheme based on the vorticity equation, this dependence is not as critical as the dependence of the vertical motion computations on the static stability, which must implicitly or explicitly involve the temperature in some way or other. Even with a primitive equations approach the thermodynamic equation, and hence the static stability, must enter into the integration procedure in some way which will ultimately affect the prediction of the moisture parameter.

To summarise, there are two reasons why the dew point depression should be selected as the moisture parameter in the CAO precipitation scheme. First, predictions of closeness to saturation are given directly by predictions of dew point depression, but not by any of the other commonly used moisture parameters except the relative humidity. Second, the dew point depression is the most convenient moisture parameter to use for prediction purposes. This is because observations of the moisture content of the air are both reported and objectively analysed in the form of dew point depression.

15. The Large Scale Precipitation Amount

In the sequential precipitation scheme the hourly amount of large scale precipitation, \mathcal{P}_L , which is predicted to fall from a layer of central pressure, p , central temperature, T , and central dew point depression, S , is given by:

$$\mathcal{P}_L = \begin{cases} - \left(\frac{S^{**} - S}{S^{**}} \right) U_p(T) w & \text{if } w < 0 \text{ and } S < S^{**} \\ 0 & \text{if } w \geq 0 \text{ or } S \geq S^{**} \end{cases} \quad (15.1)$$

where W is the "wet" vertical motion and $U_p(T)$ is the unit condensation rate given by the tables described in Section 13. The quantity S^* is the threshold dew point depression at which the onset of precipitation occurs. The concept of a threshold dew point depression and the associated introduction of the factor $(S^* - S)/S^*$ into formula (15.1) is probably the most important single item contributing to the success of the precipitation scheme. Some remarks on its origins are therefore in order.

Consider a volume of air with a vertical dimension corresponding to one of the three layers of Fig. 9, and with both horizontal dimensions equal to one gridlength. Assume that the vertical motion, W and the dew point depression, S , of this volume of air are completely homogeneous in the sense that each constituent parcel has the same vertical motion and the same dew point depression as all other parcels. Assume also that a uniform and well-behaved lapse rate exists throughout. Then, providing supersaturation does not occur, and providing the moist adiabatic assumption holds true, the large scale condensation amount, τ'_p , is given by:

$$\tau'_p = \begin{cases} -U_p(T) W & \text{if } W < 0 \text{ and } S = 0 \\ 0 & \text{if } W \geq 0 \text{ or } S > 0 \end{cases} \quad (15.2)$$

In the first tests at the CAO the condensation amount was assumed to be equal to the precipitation amount and formula (15.2) was used to predict precipitation amount directly. The results were totally unsatisfactory. This was particularly true near initial time because reported values of dew point depression are rarely zero. Even in clouds and precipitation reported values of dew point depression usually run at 2 or 3 deg C.

Naturally, the initial time objective analyses of the dew point depression fields are unable to portray features not present in the reported observations, so they rarely possess grid point values that are saturated. If vertical and horizontal advection were the only processes going on in the precipitation scheme, some areas of the chart would become saturated early on in the integration. This is evident from the fact that $\frac{dS}{dt}$ is of the order of 0.1 deg C/mb (see Table 14) so that ascending vertical motions of 10 mb/hour would take about three hours to saturate air originally possessing a dew point depression of three degrees. However, these first tests showed that even on the predicted charts the saturated areas are still far too small to account for the observed regions of precipitation. Furthermore, vertical and horizontal advection are not the only processes going on in the operational version of the sequential precipitation scheme. As will be seen later, a term representing the eddy diffusion of dew point depression has to be included in the moisture prediction equation to ensure computational stability. This term has the effect of reducing the size of any saturated area to even smaller proportions than it would otherwise be. So it seems that no precipitation scheme based on dew point depression can predict realistic amounts of precipitation with formula (15.2). This conclusion was drawn independently by the author - see Davies (1967a) - and Danard (1966a).

It has already been mentioned that, according to radio-sonde reports, dew point depressions of about 2 or 3 degrees C are usually observed when precipitation is actually occurring. This consideration led both the author - again see Davies (1967a) - and Danard (1966a) to independently propose the following revised formula for the prediction of precipitation amount:

$$T_p = \begin{cases} -U_p'(T, S, S^*)w & \text{if } w < 0 \text{ and } S < S^* \\ 0 & \text{if } w \geq 0 \text{ or } S \geq S^* \end{cases} \quad (15.3)$$

where the concept of a threshold dew point depression, S^* , is now introduced, and $U_p'(T, S, S^*)$ is not a unit condensation amount but a unit precipitation amount having a dependence on S and S^* as well as on T . The author originally chose

$$U_p'(T, S, S^*) = U_p(T) \quad \text{for } S < S^* \quad (15.4)$$

and this gave fairly successful forecasts. Meanwhile, however, Danard (1966a) had decided that it was not physically realistic to allow a sudden onset of precipitation equal to the full saturated condensation amount at the instant the dew point depression becomes less than the threshold value. So he chose his unit precipitation rate to be of the form:

$$U_p'(T, S, S^*) = \left(\frac{S^* - S}{S^*} \right) U_p(T) \quad \text{for } S < S^* \quad (15.5)$$

This allows the large scale precipitation amount to increase gradually from zero at the threshold dew point depression to the full value at true saturation. The advantages of a gradual onset were immediately obvious to the author when he became aware of Danard's work. Consequently, a switch-over was made from form (15.4) to form (15.5). This is how formula (15.1) came to be an important feature of the CAO precipitation scheme at a fairly early stage of the development work. It is, of course possible

that a non-linear expression for $U_p'(T, S, S^*)$ might give better results than Danard's linear form (15.5). However, even a non-linear expression would have to satisfy the two conditions:

$$U_p'(T, S, S^*) = U_p(T) \quad \text{when } S=0 \quad (15.6)$$

$$\text{and } U_p'(T, S, S^*) = 0 \quad \text{when } S=S^* \quad (15.7)$$

These restrictions, and the considerations that led up to them, make it unlikely that the optimum form of $U_p'(T, S, S^*)$ deviates much from a straight line.

When the concept of a threshold dew point depression is applied in practice one has, of course, to assign a numerical value to S^* . Danard (1966a) used a value of $S^* = 7.5$ deg C in his work. In the limited series of tests which were run early on at the CAO with form (15.4), i.e. the "sudden onset" threshold, the optimum value for S^* appeared to be about 3 deg C. After the switch-over to form (15.5) a more extensive series of tests was carried out to determine the appropriate value for S^* . The author found that the value reported by Danard, i.e. $S^* = 7.5$ deg C, gave best results near initial time, but that $S^* = 5$ deg C gave best results near the end of a 48-hour forecast period. Consequently, the final version of the sequential scheme incorporated a time-dependent S^* given by

$$S^* = S_0^* - \frac{\Delta S^*}{t_0} t \quad (15.8)$$

where t is the number of hours which have elapsed since initial time, $S_0^* = 7.5$ deg C, $\Delta S^* = 2.5$ deg C, and $t_{48} = 48$ hours. One further sophistication was introduced into the 1970 version of the sequential precipitation scheme. For the first time, S^* was made dependent on the mountain field, P_g , but only at those grid points in the middle of mountainous areas. This is accomplished by testing the values of P_g at the top, bottom, left and right grid points. If any one of these four values is greater than 925 mb, then no adjustment is made to the S^* given by (15.8). However, if P_g has a value less than 925 mb at all four surrounding grid points, then S^* is determined not from (15.8) but from the following formula instead

$$S^* = \left(S_0^* - \frac{\Delta S^* t}{t_{48}} \right) \left(\frac{P_g - P_n^*}{P_0^* - P_n^*} \right) \quad (15.9)$$

where $P_0^* = 1013.3$ mb and

$$P_n^* = \begin{cases} 700 \text{ mb} & \text{when } n = 850 \text{ mb} \\ 500 \text{ mb} & \text{when } n = 700 \text{ mb} \\ 300 \text{ mb} & \text{when } n = 500 \text{ mb} \end{cases} \quad (15.10)$$

The objective of this small modification was to reduce the systematic over-forecasting of precipitation on high mountain plateaus. Note that coastal grid points are not affected by this change.

It remains to discuss the physical implications of using formula (15.1) to predict precipitation amount instead of using formula (15.2) to predict condensation amount and then equating this to the precipitation amount. If the amount of precipitation predicted at a grid point is to be representative of the surrounding area, then it must be some kind of areal average of the precipitation predicted for the region of roughly one square grid-length in dimension which is centred at that grid point. Formula (15.2) can only be applied to predict such an areal average when the following three conditions are true:

- (i) If uniform, or at least pseudo-uniform, conditions of vertical motion, dew point depression, and temperature lapse rate prevail throughout this region.
- (ii) If it is legitimate to equate condensation rate to precipitation rate, i.e. if the moist adiabatic assumption holds true.
- (iii) If supersaturation does not occur.

In the real atmosphere, of course, these three conditions are simply not valid in the meteorologically active areas in which precipitation occurs. The first condition breaks down because of scale considerations. Even in large scale disturbances most precipitation mechanisms depend, at least in part, on dynamic phenomena of a scale smaller in dimension than the spacing of the standard finite difference grid. In other words the lateral dimensions of the largest quasi-homogeneous precipitation cell associated with a cyclone are generally no larger than some distance between one and two orders of magnitude smaller than the lateral dimensions of the cyclone itself. This can be seen quite clearly by studying the structure of cloud

patterns in satellite photographs. The second condition is impossible to meet. Cloud formation is a necessary intermediate step in the precipitation process. The third condition does not hold either. Supersaturation does occur in nature, and the degree to which it does so depends on the supply of condensation nuclei available.

Suppose it were possible to devise a numerical scheme which accurately portrayed the details of all the physical processes leading up to the production of precipitation. What would such an idealised scheme be like? How would it account for the breakdown of the three conditions necessary for the application of formula (15.2)? To begin with, it would probably have to use a horizontal grid with a much greater resolution than the one in standard use. It would also have to carry a new "cloudiness" variable along in the integration scheme. This "cloudiness" variable would have to be a fairly accurate estimate of the amount of liquid water present in the form of cloud droplets. And it would have to allow supersaturation to occur. Given a scheme with these three sophistications, would it be possible to know at what level of supersaturation condensation occurs? No precise specification is possible, even in cases where there are ample condensation nuclei available, because there are no exact physical laws governing supersaturation and condensation. At least no such laws are known. So the best that could be attained is some kind of empirical relationship between supersaturation and condensation. In such a sophisticated scheme would it be possible to use formula (15.2) to compute the condensation amount when there is sufficient supersaturation for condensation to occur? It might be possible if the horizontal resolution were sufficiently great to describe all the scales of motion that are significant to the large scale accumulation of condensation amount. But from the very nature of the

condensation process this seems highly unlikely. At best one might hope to achieve results that were less and less unrealistic as one increased the resolution. So some approximate or empirical technique would probably still have to be employed to estimate the amount of condensation occurring due to motions on a scale not resolvable by the grid. And all this presupposes that either one would have no difficulty computing amended unit condensation rates to take into account the breakdown of the moist adiabatic assumption, or that this breakdown could be taken care of by an empirical formula. Finally, would such a sophisticated scheme allow the precipitation rate to be computed from the other known variables? This would have to be done by computing the rate of conversion of cloud droplets or ice particles into precipitation. Once again there are no known physical laws which say precisely when precipitation starts to gush forth from a cloud of non-precipitating droplets or ice particles. So, again, the best that could be done would be to resort to some empirical formula.

From the preceding discussion it can be seen that any numerical scheme that attempted to account directly for all the physical processes leading to precipitation would have to be an extremely complicated one. It would have to employ a different empirical formula at each of three or more intermediate stages of the computations. This procedure would be inelegant. It could also be wrong. It could be wrong because the whole idea of using an empirical formula is to express some effect of great interest in terms of primary quantities that are known. By definition, such an empirical relationship must be open to direct verification, i.e. the effect itself and the primary quantities must be in some sense measurable. For instance, formula (15.1) was incorporated into the sequential precipitation scheme because with the specified value of S^* it gave a better correspondence between observed

and predicted precipitation amount than did other formulae, or for that matter than did the same formula with different values of S^* . In principle there is no intermediate empirical quantity in formula (15.1) because S is a primary quantity and, in principle at least, W is directly computable from primary quantities. Suppose the degree of supersaturation at which condensation occurs, sub-grid scale condensation processes, and the rate of conversion of cloud droplets or ice particles to precipitation were able to be represented by "empirical" formulae. The final product, the precipitation amount, would then be related by an "empirical" formula to an intermediate quantity, the amount of water substance present in cloud form. This quantitative measure of cloudiness would in turn be related by an "empirical" formula to at least one other intermediate quantity, the degree of supersaturation at which condensation occurs, which would itself be related by an "empirical" formula to the primary quantities. None of the intermediate quantities could be verified by information obtained in routine meteorological observations. And so there would be no satisfactory way of individually investigating the effectiveness of the "empirical" formula used at each intermediate stage. Only the final product, the precipitation amount, could be verified and so it would only be possible to assess the collective effectiveness of all intermediate "empirical" formulae. The empiricism of such a chain of intermediate "empirical" formulae must always be open to doubt in cases where intermediate verifications of accuracy cannot be carried out. And the propriety of a chain procedure is also questionable on the grounds of redundancy. For there will always remain the suspicion that the final product could be directly related to the primary quantities by a single empirical formula.

In view of all these grave difficulties it seems unlikely that an accurate detailed representation of all the physical processes leading to the production of precipitation will be established on a computer in the near future. So it looks as if formula (15.1), or something rather similar to it, will be an important feature of precipitation schemes for some time to come. This is because simplicity is not its only attraction. Formula (15.1) also gives excellent precipitation forecasts. And any errors that do arise are in almost all cases clearly attributable to some other source.

This Section has explained how the sequential precipitation scheme converts large scale condensation amounts into large scale precipitation amounts. Section 14 gave the reasons for selecting the dew point depression as the moisture parameter. In Section 13 it was pointed out that three basic meteorological variables need to be known before the unit condensation rates given in Table 5 can be used to compute the large scale condensation amount. These are the large scale vertical motion, the temperature, and a measure of the moisture content of the air — the dew point depression. The next four Sections describe how these three variables are obtained.

16. The "Dry" Vertical Motion

In baroclinic models based on the omega equation, such as those of Cressman (1963) or Danard (1966a), (1966b), the vertical motions are computed explicitly as part of the main integration cycle. The CAO model, however, is based on the potential vorticity equation, not the omega equation. Consequently, as mentioned in Section (5.3), the vertical motions are only implicit and a separate calculation has to be carried out to recover them explicitly. This Section describes how "dry" vertical motion fields are actually computed from the hourly stream function fields by an application

of the thermodynamic equation. They are referred to as "dry" because adiabatic conditions are assumed throughout. The next Section will explain how the "dry" vertical motions are converted into "wet" vertical motions by taking into account the release of latent heat. In order to satisfy operational requirements the "dry" and "wet" vertical motions are only computed for the 504-point grid of Fig. 1.

In the 1970 version of the sequential precipitation scheme the 700 and 500 mb "dry" vertical motions, W_d , are based on the following analytical equation:

$$W_d = - \frac{gf}{\sigma_{f_0}} \left\{ \frac{D}{Dt} \left(\frac{\partial \psi}{\partial p} \right) - \frac{\partial}{\partial p} \left(K_D^* \nabla^2 \psi \right) \right\} + N_g W_g^* \quad (16.1)$$

where K_D^* is an eddy diffusion coefficient and $N_g W_g^*$ is an explicit terrain vertical motion component which will be explained in a moment. Or, more accurately, (16.1) is the analytical counterpart of the finite difference equations which are actually used to compute W_d at 700 and 500 mb. The first term on the R.H.S. of (16.5) arises simply enough by solving (7.5) for omega. Equation (7.5), it will be remembered, is the convenient form of the thermodynamic equation (A1.13) which was derived by assuming adiabatic conditions and the approximation (7.3). The second term on the R.H.S. of (16.1) had to be introduced to accommodate the eddy diffusion terms in the 1970 baroclinic model. The third term on the R.H.S. of (16.1) is an explicit terrain component, $N_g W_g^*$. Theoretically, one would expect the terrain vertical motion to be contained implicitly in the first term on the R.H.S. of (16.1), since the terrain constraints (D1.1) are included in the baroclinic model. In practice, however, it turns out that the implicit terrain vertical motion seriously underestimates the

actual terrain vertical motion. This is particularly true for the shorter wave-length components which, for reasons to be discussed later, are unduly suppressed by the chain of finite difference computations linking (Dl.2) to (16.1). Consequently, something had to be done to ensure that, for instance, the amounts of precipitation predicted on the West Coast are consistent with the W_g values computed from (Dl.2). The simplest solution was to augment the "dry" vertical motions at each level with an explicit terrain vertical motion, $N_g W_g^*$. The symbol W_g^* , which was first used in (Dl.13), represents the terrain-induced vertical motion through the troposphere. As in (Dl.13), it is assumed to be given by:

$$W_g^* = \frac{(P-200)}{(P_g-200)} W_g \quad (16.2)$$

The symbol N_g merely denotes that fraction of W_g^* which is to be reinserted into (16.1). Originally, in early experiments on the octagon model, a value of 0.33 was assigned to N_g . This still seemed to lead to underestimates of the upslope rainfall on the West Coast, compared to what would be expected from the W_g values computed from (Dl.2), so N_g was boosted upwards until it became apparent that $N_g = 1$ gave best results. Consequently, a value of unity was used for N_g in later work on the octagon model and also in the 1968 model, and this was carried over into the 1970 model. The discussion of the explicit terrain vertical motion will be taken up again later on in the Section.

At 700 and 500 mb the finite difference equation corresponding to (16.1) at the general time step is:

$$\begin{aligned}
 \omega_d|_n^t = & -\frac{gf}{\sigma-f_0} \left\{ \left[\left\langle \frac{\partial \psi}{\partial p} \right\rangle \Big|_n^{t+1} - \left\langle \frac{\partial \psi}{\partial p} \right\rangle \Big|_n^{t-1} \right] \frac{1}{2\Delta t} \right. \\
 & + K \mathcal{J} \left(\psi_n^t, \left\langle \frac{\partial(N_j \psi)}{\partial p} \right\rangle \Big|_n^t \right) \\
 & \left. - K \left\langle \frac{\partial(K_D \nabla^2 \psi)}{\partial p} \right\rangle \Big|_n^{t-1} \right\} + N_g \omega_g^*|_n^t \quad (16.3)
 \end{aligned}$$

$$n = 700, 500$$

where K is defined by (C1.3); K_D is related to K_D^* as in (9.3); Δt is as usual the time step of one hour; the superscripts $(t+1)$, t , and $(t-1)$ denote values for the next, current, and preceding time steps; the vertical derivative finite difference operators $\left\langle \frac{\partial}{\partial p} \right\rangle \Big|_n$ are evaluated by means of the parabolic fit formula (B13.2); and N_j is equal to unity except when it premultiplies the 200 mb stream functions in the finite difference evaluation of $\left\langle \frac{\partial(N_j \psi)}{\partial p} \right\rangle \Big|_{50}^t$, when it is taken to be 0.75 to compensate for the arbitrary across-the-board scaling down of the 200 mb winds by 75% in the 1970 model, an improvisation which was mentioned in Section (5.6). In particular, note that the standard first order finite difference operator (B11.1) is used to evaluate the Jacobian term, and not Shuman's second order form (B12.1). The implications of this will be discussed later on in the Section. The factor (f/σ) is assumed to depend on pressure only, and is evaluated at latitude 45 N by taking the static stabilities to have the "dry" standard atmosphere values given in Table 2. This is the same as what is purportedly done in the baroclinic model. The actual values used for the eddy diffusion coefficients are given in Table 4. They are the same as those used in (10.2) for the derived 700 mb

forecasts. At initial time, when a forward time step has to be used, ω_d is computed from a modified form of (16.3). All the $(t-1)$ superscripts are changed to t , and the $2\Delta t$ is replaced by Δt . Further, to match the baroclinic model, the eddy diffusion term is dropped completely.

Unfortunately, (16.3) cannot be used at 850 mb. Briefly, as mentioned in Section 5, this is because the vertical phasing between the predicted stream functions at 1000 mb and those at the other levels is not sufficiently reliable. As will be explained in more detail in the next Section, the phasing inadequacies of the 1000 mb charts were originally discovered when (16.3) was used to compute the 850 mb vertical motions and the results at initial time were compared to the 850 mb vertical motions produced by the diagnostic scheme of Haltiner et al (1963). Instead of computing the 850 mb vertical motions by means of (16.3), the following improvised formula is used:

$$\omega_d|_{85}^t = \tau_a \frac{(\sigma_s)_{70}}{(\sigma_s)_{85}} \left[\omega_d|_{70}^t - N_g \omega_g^*|_{70}^t \right] + N_g \omega_g^*|_{85}^t \quad (16.4)$$

where $\tau_a = 0.6$ and the static stabilities are those of the standard atmosphere given in Table 2. As in (16.3), ω_g^* is given by (16.2) and N_g is unity.

The preceding paragraphs have just described how ω_d is computed from the hourly stream functions produced by the 1970 model. In the 1968 and octagon models there was no need to introduce the factor N_j , as there was no artificial scaling down of the 200 mb winds, and so in effect N_j was invariably taken to be equal to 1. The only other difference was that 12-hourly smoothing was used instead of the eddy diffusion terms.

Effectively, this meant that the values of K_D were taken to be zero in (16.3). And the golden rule about matching up the smoothing of the stream function fields for (10.2) also applied here. Thus at the 22 nd time step, which produced the "dry" vertical motion charts for 21 hours, equation (16.3) was applied in a straight-forward manner because the stream function fields provided by the baroclinic model for 20, 21 and 22 hours were homogeneous insofar as none of them had been smoothed. But at the 23 rd time step the stream functions which were provided for 23 hours had been smoothed. Consequently, it was necessary to subject the stream functions for 21 and 22 hours to the same smoothing operator before applying (16.3) to compute the "dry" vertical motion for 22 hours. As in the case of the derived 700 mb, this technical problem of matching the smoothing only arose because the vertical motions were computed in the precipitation portion of a sequential operation, and not in the baroclinic model part. However, it was an important problem because totally unrealistic vertical motion fields would have been computed if (16.3) had been applied to unmatched fields.

So far the discussion has concentrated mostly on the actual mechanics of the "dry" vertical motion computations. It is now appropriate to say a few words about each of the following topics:

- (i) The implications of the use of the standard Jacobian in (16.3).
- (ii) The reasons why an explicit vertical motion component has to be inserted in (16.3) and (16.4).
- (iii) The role of the eddy diffusion term in (16.3).
- (iv) The evaluation of the factor γ_a in (16.4).
- (v) The quandary presented by N_j in (16.3).

Each item will be dealt with independently of the others. Admittedly, this is an oversimplification, but it is the only way one can hope to draw meaningful conclusions.

The standard Jacobian was a feature of the "dry" vertical motion computations in the octagon model and has been retained in the 1968 and 1970 models. There appeared to be no compelling reasons to change to the Shuman Jacobian, and in fact there was some evidence that such a change might yield adverse results until better baroclinic models become available.

The mere fact that (16.4) has to be used instead of (16.3) at 850 mb means that there is no hope of recapturing the full terrain vertical motion at this most important level. The use of the standard Jacobian and the terrain constraint in the particular form (D1.1) may also contribute to the failure to recover the terrain vertical motions from the stream function fields. All these considerations serve to justify the use of the explicit terrain vertical motion term.

The "dry" vertical motions implicit in the 1970 model do include eddy diffusion effects. Physically, the derivation of the baroclinic model equations (6.1) complete with primary eddy diffusion constraints (9.1) can be done in only one way. Namely, by starting out from a more sophisticated form of the thermodynamic equation (7.5) which itself includes an eddy diffusion term. In other words by starting out from a thermodynamic equation which looks very much like (16.1) without the explicit terrain vertical motion component. So there is no doubt that the "dry" vertical motion from the 1970 model should contain an eddy diffusion term. There remains to decide what values to assign to K_D^* , and whether K_D^* should appear

inside or outside the pressure derivative operator. In practice, the eddy diffusion coefficients of Table 4 were obtained by adding the eddy diffusion coefficients associated with the secondary constraints to half those associated with the primary constraints, and simply interpolating between 850 and 500 mb to obtain the 700 mb values. Earlier numerical experience with smoothing operators in the baroclinic model suggested it would be wiser to stick to the golden rule, enunciated in Section 10, that all derived field computations should employ smoothing or eddy diffusion operators which are matched as closely as possible to those used in the baroclinic model at each individual level. Consequently, the K_D^* was kept inside the pressure derivative operator and this led to perfectly satisfactory results. It is clear that the eddy diffusion term may serve as a fine scale adjustment to the vertical motions near active centres; increasing K_D^* reduces such motions and vice versa.

The numerical factor, γ_a , which appears in equation (16.4), is a somewhat arbitrary number representing, if anything, the hypothetical ratio of the "dry" vertical motion at 850 mb to that at 700 mb, in the absence of terrain effects, when there is no vertical variation in the static stability. Trial and error experiments with the octagon model led to the best precipitation forecasts when γ_a was set equal to 0.6, so this value has been incorporated into the operational run. The whole factor $\gamma_a \frac{(\sigma_s)_{70}}{(\sigma_s)_{85}}$ therefore works out to 0.85, perhaps a trifle higher than might be expected on purely physical grounds. The major disadvantage that arises from the use of (16.4) is that the 850 mb "dry" vertical motions will always tend to be in phase with those at 700 mb. The use of (16.4) is justified here because it permits the atmosphere to be broken up into

three layers for the moisture computations, and the author - Davies (1967a) - has demonstrated that this increase in vertical resolution does lead to better precipitation forecasts than a similar single-layer scheme. Nevertheless, this is recognised as nothing more than an interim procedure which will be replaced when a better method for computing the 850 mb "dry" vertical motions has been developed.

One of the least satisfactory aspects of the "dry" vertical motion computations is the need to make $N_j = 0.75$ when it premultiplies the 200 mb stream function in (16.3). However, this is the only consistent way of compensating for the 75% across-the-board reduction of the 200 mb winds in the 1970 model, and one is reluctant to make compromise adjustments when faced with these wholly artificial manipulations of the baroclinic model equations.

The foregoing discussions have examined a maze of detail about the "dry" vertical motion computations. Three important questions will serve to bring the overall picture back into perspective. First, how good are the final W_d fields? In view of all the little idiosyncracies just cited, and in view of the fact that these presumably interfere with each other in an unknown fashion, it may come as a surprise to the reader to discover that the final W_d fields do in fact bear a remarkable resemblance to those found in nature. Yet such is the case. As will be revealed in the next Section, there is ample evidence to show that the "wet" vertical motion fields, despite their imperfections, are worthy simulators of the atmosphere. This would be impossible if the "dry" vertical motion fields were not equally satisfactory. The explanation for this success is as follows. The many approximations and arbitrary procedures which enter

into the computations are broadly limited on physical grounds. But physics alone is insufficient to specify the exact details of what should be done in a numerical simulation scheme of this type. The exact details therefore become enmeshed in ambiguities of one sort or another. If properly handled, these ambiguities do not lead to chaos. Instead they offer opportunities to impose fine scale tuning controls on the simulated characteristics. Adjustments can then be made by trial and error, using synoptic experience as a guide, to find the best match with the atmosphere. The second question is a more subtle one. Many of the techniques, such as the use of the standard Jacobian in (16.3), were originally developed for the octagon and 1968 models. These were simply amended for the 1970 model, they were not fully redesigned. Is it not possible that better results would be obtained with current more advanced models if the Shuman Jacobian were used in (16.3), and if a few of the other techniques were similarly redesigned? As will be seen later in this thesis, this question has been answered at least partly in the affirmative for the parallel model. While it is possible that some design changes would also prove beneficial for the 1970 model, any improvements are likely to be of a more marginal nature. Consequently, it seems wiser to deploy available resources on the parallel model at this time. The third question is this. Why has the discussion on the "dry" vertical motions been separated so completely from the discussion on the incorporation of latent heat effects? The next Section supplies the answer.

17. The "Wet" Vertical Motion

The "dry" vertical motions of the last Section are converted into "wet" vertical motions by taking the release of latent heat into account. In the

1970 version of the sequential precipitation scheme this is done in the following manner:

$$\omega = \begin{cases} \hat{\omega}_w & \text{if } S < S^* \text{ and } \omega_d < 0 \text{ and } \omega_w \leq \hat{\omega}_w \\ \omega_w & \text{if } S < S^* \text{ and } \omega_d < 0 \text{ and } \omega_w > \hat{\omega}_w \\ \omega_d & \text{if } S \geq S^* \text{ or } \omega_d \geq 0 \end{cases} \quad (17.1)$$

where

$$\hat{\omega}_w = n(\omega^*) \omega^* \quad (17.2)$$

$$\omega_w = \frac{\sigma_s}{(\sigma' - H^* f_0/f)} \omega_d \quad (17.3)$$

$$\omega^* = \frac{\sigma_s}{\sigma'} \omega_d \quad (17.4)$$

$$H^* = \frac{R g L}{C_p P \Delta P} \left(\frac{S^* - S}{S^*} \right) U_p(T) \quad (17.5)$$

$$\sigma' = \sigma_s + \left(\frac{S^* - S}{S^*} \right) \left(\frac{f_0 \sigma_w}{f} - \sigma_s \right) \frac{U_p(T)}{\hat{O}_p} \quad (17.6)$$

and

$$n(\omega^*) = \begin{cases} n_1 & \text{if } \omega^* \geq \omega_1 \\ \frac{a_w(\omega_1 - \omega^*) + b_w(\omega_2 - \omega^*)^2 + c_w}{\omega^*} & \text{if } \omega_1 > \omega^* > \omega_2 \\ n_2 & \text{if } \omega^* \leq \omega_2 \end{cases} \quad (17.7)$$

The formulae (17.1) - (17.7) are valid for all three levels, 850, 700 and 500 mb. The quantity (H_w^*) is the heat function, H , defined by (A1.14). Or, more precisely, it is the special case of this heat function which arises when the diabatic effects are due to the release of latent heat. On the R.H.S. of (17.5) the quantity Δp is the thickness of the layer surrounding the pressure level p . $U_p(T)$ is the unit condensation rate defined in Section 13. S^* is the threshold dew point depression introduced in Section 15, and the remaining symbols are standard ones which are included in the list of symbols which appears at the beginning of the thesis. The quantity σ' is the moist static stability which (17.6) defines to be a linear interpolation between the static stabilities of the "dry" standard atmosphere, σ_s , and an arbitrary rainy atmosphere, σ_w , to which temperature and latitude corrections have been applied. Values of σ_s and σ_w are given in Table 6, together with the values of H^* for fully saturated air at 0 C deg and -10 C deg which are listed for comparison purposes. The values of \hat{U}_p are given in Table 5.

Level	H^*		Static Stability	
	-10 C deg	0 C deg	Standard Atmosphere	Arbitrary Rainy Atmosphere
	850 mb	920	1470	1360
700 mb	1570	2390	1950	3100
500 mb	3710	5300	3570	5200

Table 6: Values of the latent heat factor H^* at -10 C deg and 0 C deg, the static stability of the standard atmosphere, and the static stability of an "arbitrary rainy atmosphere". The units are $\text{dkm}^2 \text{mb}^{-2} \text{hr}^{-2}$.

They correspond to about the maximum values of $U_p(\tau)$ which will be encountered in the North American region, exclusive of such abnormalities as hurricanes. Or at least they do at 850 and 500 mb. The 700 mb value has been deliberately overestimated by about 15% to favour the latent heat amplification of vertical motion at this level. Superficially, formula (17.3) bears the same relationship to the diabatic version of the convenient form of the thermodynamic equation (7.4) as the "dry" vertical motion (16.1) bears to the adiabatic version of the convenient form of the thermodynamic equation (7.5). However, the baroclinic model is based on the assumption that (σ'/f) is equal to (σ'_s/f_0) . This assumption can still be applied in the "dry" vertical motion equation (16.1), but it cannot be carried over unambiguously to (17.3). The reason is that, as Table 6 shows, when the air is saturated the magnitude of H^* can easily exceed the magnitude of σ'_s . This means that if σ' were taken to be equal to σ'_s , then (17.3) could and would develop singularities when $\sigma'_s = H^* f_0 / f$. Such singularities never occur in the real atmosphere, of course, because $\left[-\frac{D}{Dt} \left(\frac{\partial \psi}{\partial p} \right) \right]$, i.e. $\frac{D^* T}{Dt}$ (see (7.3) and (A1.2)), will pass through a zero and change sign at the same time as $(\sigma' - H^* f_0 / f)$; and, if necessary, there will be convective adjustments to ensure this. Under fully saturated conditions in the real atmosphere $\frac{D^* T}{Dt}$ will be of the opposite sign to that of ascending vertical motion when the actual lapse rate is intermediate between the dry adiabatic and moist adiabatic. In the model, because dry conditions are assumed, $\left[-\frac{D}{Dt} \left(\frac{\partial \psi}{\partial p} \right) \right]$ must always have the same sign as the vertical motion. So to ensure the correct sign for the vertical motion in the model, $(\sigma' - H^* f_0 / f)$ must not be allowed to become negative. Nor must it be

allowed to approach too closely to zero. For the sake of simplicity the foregoing remarks have ignored the complications arising from eddy diffusion and terrain effects. This difficulty is avoided by introducing the concept of the static stability of an arbitrary rainy atmosphere, σ_w . The values of this quantity which are given in Table 6 are well inside the physically realistic range, but they were actually chosen as much for their numerical convenience as for their physical properties. Since H^* has to include a $(s^* - s)/s^*$ factor to be consistent with large scale precipitation formula (15.1), a moist static stability factor σ' with a similar dependence on the $(s^* - s)/s^*$ factor has to be defined for use in (17.3). The H^* term in (17.3) includes the f_0/f factor because the static stability assumptions, both in the baroclinic model and in the "wet" vertical motion computations, relate to the ratio (σ/f) and not to σ alone. This is indicated more clearly by rewriting (17.3) as:

$$\omega_w = \frac{\sigma_s f / f_0}{(\sigma_s f / f_0 - H^*)} \omega_d \quad (17.8)$$

The factor $U_p(T)/\hat{U}_p$ builds a temperature dependence into the definition of σ' , (17.6), to take cognizance of the fact that the threat of singularities is considerably reduced in cold air. Without this temperature factor the value of σ' would be suitable for warm air, but excessively large for cold air. Similarly, the factor f_0/f builds a latitudinal dependence into the definition of σ' , (17.6), so as to best accommodate the latitudinal variation of $(f_0 H / f)$ in (17.3). Although (17.3) works quite well when the "dry" vertical motions are small, it can sometimes lead to excessive amplifications when the "dry" vertical motions are already large. One way of getting round this difficulty would have been to insert

a "dry" vertical motion dependence into the definition of σ^1 . However, it was simpler to prescribe maximum allowed amplifications by means of (17.2) and (17.7). Note that the amplification limits are imposed not on the "dry" vertical motion, ω_d , but on the quantity ω^* which is defined by (17.4). This has the effect of making the restrictions depend on temperature, since σ^1 is itself temperature-dependent. In fact this means that the maximum amplifications allowed for the "dry" vertical motions are greater for cold air than they are for warm air. The quantities a_w , b_w and c_w in (17.7) are chosen to make $\eta(\omega^*)$ a quadratic function of ω^* in the region $\omega_1 \geq \omega^* \geq \omega_2$, such that:

$$\eta(\omega^*) = \begin{cases} \eta_1 & \text{when } \omega^* = \omega_1 \\ \eta_2 & \text{when } \omega^* = \omega_2 \\ \eta_3 & \text{when } \omega^* = \omega_3 \end{cases} \quad (17.9)$$

The actual values of η_1 , η_2 , η_3 , ω_1 , ω_2 , ω_3 , a_w , b_w and c_w are given in Table 7. The complete formulae relating a_w , b_w and c_w to η_1 , η_2 , η_3 , ω_1 , ω_2 and ω_3 are given elsewhere by the author; see Davies (1967a).

The octagon version of the "wet" vertical motion computations was almost the same as the 1970 one just described. It differed, however, in that three factors were omitted. These were the factor (f_0/f) which multiplies H^* in (17.3), the factor (f_0/f) which multiplies c_w in the definition of σ^1 , (17.6), and the factor $[U_p(\tau)/\sigma_p]$ which also appears in (17.6). This meant that all three factors were set equal to one everywhere. In the original development work it was realised that to be consistent with the baroclinic model the H^* term should include

the factor (f_0/f) , but that this would introduce an equatorial singularity into the equations.

Constant	850 mb	700 mb	500 mb	Units
η_1	5	5	5	-
η_2	1.33	1.50	1.33	-
η_3	2.5	3.0	2.5	-
W_1	-4	-4	-4	mb hr ⁻¹
W_2	-36	-40	-36	mb hr ⁻¹
W_3	-16	-16	-16	mb hr ⁻¹
a_w	0.390	0.722	0.390	-
b_w	0.0395	0.0509	0.0395	mb ⁻¹ hr
c_w	-60.5	-86	-60.5	mb hr ⁻¹

Table 7: Values of the constants used in the maximum amplification restrictions imposed on the "wet" vertical motions.

It was also realised that σ' should have some kind of temperature dependence, but it was not evident what form this temperature dependence should take. Needless to say, singularities were an anathema to be avoided at all costs, and the prospects of coming up with a sensible temperature variation for σ' were bleak at a time when there were many other more urgent problems to solve. Accordingly, as an interim measure, the "wet" vertical motions were computed without allowing for any variation in f , and without introducing any temperature dependence into σ' . Unfortunately, with a σ' independent of temperature there was not enough latent heat amplification over Canada, the very area which is of central importance for the precipitation forecasts. Consequently, when the

precipitation scheme was reprogrammed for the 1968 model the (f_0/f) factor was included in the H^* term, and σ' was made temperature dependent by introducing the $[U_p(T)/\hat{U}_p]$ factor. The particular factor $[U_p(T)/\hat{U}_p]$ was decided upon after studies of individual charts had indicated that the most consistent latent heat effects were obtained when the temperature dependence of σ' matched that of H^* . These two changes led to improved precipitation forecasts for Canada, but the (f_0/f) factor led to excessive "wet" vertical motions in the south-west and south-east corners of the 504-point grid, which are ocean areas south of latitude 30 N. These were controlled by the maximum amplification restrictions (17.2), but were still an undesirable feature of the precipitation scheme. Consequently, it was decided that σ' and H^* should also have matching latitudinal variations, and this led to the introduction of the (f_0/f) factor in the σ_w term of (17.6) with the 1970 model.

An interesting corollary to the 1970 method is obtained by substituting (17.5) and (17.6) into (17.3):

$$W_w = \frac{\sigma_s W_d}{\sigma_s + \left(\frac{S^* - S}{S^*}\right) \frac{U_p(T)}{\hat{U}_p} \left\{ \frac{f_0}{f} \left[\sigma_w - \frac{R_g L \hat{U}_p}{C_p P \Delta P} \right] - \sigma_s \right\}} \quad (17.10)$$

A special case of (17.10) occurs when $\sigma_w = (R_g L \hat{U}_p) / (C_p P \Delta P)$:

$$W_w = \frac{W_d}{\left[1 - \left(\frac{S^* - S}{S^*}\right) \frac{U_p(T)}{\hat{U}_p} \right]} \quad (17.11)$$

It is slightly disturbing to note that (17.11) contains the essential ingredients of (17.10), for the $\frac{f_0}{f} \left[\sigma_w - \frac{R_g L \hat{U}_p}{C_p P \Delta P} \right]$ term can only play a marginal role in determining the "wet" vertical motion. It actually works out to be slightly positive at 850 and 500 mb, and slightly negative at 700 mb, as can be seen by substituting numerical values for \hat{U}_p and σ_w

from Tables 5 and 7. This suggests that the precipitation scheme would probably work just as well with (17.11) replacing (17.3).

The arbitrary assumptions regarding σ_w are not the only scientific ambiguities arising in the "wet" vertical motion computations. There is also approximation (7.3), of which more will be said later in the thesis. And the latent heat calculation for H^* is for precipitation, as given by empirical formula (15.1), and not for condensation. Furthermore, as has already been remarked upon in the last Section, it is not strictly correct to use (7.4) to compute ω , as (17.3) essentially does, unless the ω_d , or more precisely the $\frac{D}{Dt} \left(\frac{\partial \psi}{\partial p} \right)$, have been computed from a baroclinic model which also takes H^* into account. This is because the stream function tendencies would have been different if latent heat effects had been fed back into the baroclinic model. Generally speaking, if latent heat effects were somehow included in the baroclinic model, one would expect the magnitude of $\frac{\partial}{\partial t} \left(\frac{\partial \psi}{\partial p} \right)$ in baroclinic short waves to increase where there is precipitation. In particular, if the actual lapse rate were intermediate between the moist adiabatic and dry adiabatic, and conditions were fully saturated, then in (16.1) the magnitude of the stream function tendency term would be greater than the magnitude of the advection term, and ω_d would work out to be positive in spite of the precipitation. Of course, in such a case, the conversion to "wet" vertical motion would include a change of sign, and so reveal ω_d to be more a quantity of numerical convenience than a meaningful physical variable.

In spite of all the little inconsistencies, approximations, and rather arbitrary procedures which characterise both the "wet" and "dry" phases of the computations, the final vertical motion fields are of a

very high quality. Unfortunately, it is not possible to support this assertion by directly verifying the computed vertical motion fields. Direct measurements of the large scale vertical motions in the atmosphere are not made in the routine meteorological observation program. Instead it is necessary to rely on indirect evidence. Such indirect evidence is of three types. The first is elementary. The vertical motion fields do not exhibit any obvious deficiencies. Or, at least, they do not exhibit any obvious deficiencies other than the fact that those at 850 mb are exactly in phase with the ones at 700 mb. This was established by inspecting a large number of individual cases. The 700 mb vertical motion charts have been subjected to a particularly close scrutiny by field forecasters because they have been transmitted over the facsimile circuits for $2\frac{1}{2}$ years. Freedom from obvious flaws is much stronger evidence than it sounds. Most of the development work on the vertical motion computations was actually concerned with the detection and eradication of obvious flaws. This type of research activity is by no means uncommon in numerical weather prediction. The second type of evidence involves comparisons with vertical motion fields computed by other techniques. In particular, at one stage of the work on the octagon model some fairly detailed comparisons were made between the first hour "dry" vertical motions computed from the baroclinic model and the diagnostic "dry" vertical motions produced by the technique of Haltiner et al (1963). First hour values were used to avoid the complications arising from the use of a forward timestep at initial time. At that time the correlation between the two sets of vertical motion charts was very good at 700 and 500 mb. The patterns of the two sets of charts at these levels were recognisably the same when viewed from a short distance

away, although differences of detail were discernible in a close-up inspection. However, the corresponding correlations at 850 mb were initially very poor. The cause turned out to be the 1000 mb stream function fields from the baroclinic model, as discussed in Section 5. Since those early days the vertical motion fields from the baroclinic model have been improved considerably, for instance, by taking latent heat effects into account. More recent comparisons with the diagnostic vertical motions produced by the technique of Haltiner et al (1963) show much greater differences. The vertical motion fields from the baroclinic model now not only have stronger maxima and minima than their Haltiner counterparts, but they also contain more detailed patterns which appear to be meteorologically real. Comparisons with vertical motion fields from other sources have been made from time to time. The conclusions drawn on such occasions have varied in degree, but usually they have been similar in kind to those made for the recent Haltiner comparisons. The vertical motion fields from the baroclinic model tend to display both greater magnitudes and more detail than vertical motion fields from other sources. However, there is a limit to the usefulness of carrying out comparisons of vertical motion fields. It does not take long for a discussion of the pros and cons of small differences to enter the realm of speculation. The third type of evidence comes from the direct verification of the precipitation forecasts against the reported precipitation amounts. This is tantamount to an indirect verification of the vertical motion fields because precipitation amount is linearly dependent on vertical motion. As will be reported in Section 22, the predicted precipitation patterns almost always bear a reasonably close

resemblance to those which are observed. Consequently, one can justifiably infer that the vertical motion fields are equally satisfactory. The three types of evidence, taken together, lead to the conclusion that the "wet" vertical motion fields are high quality simulations of the large scale vertical motions in the atmosphere.

Some of the general properties of the "wet" vertical motion fields were monitored by the characteristic areas verification program described in Section 11. Most of the accumulated information, which covers just more than a year, is for the 1968 model. In digest form it provides a fairly comprehensive picture of the type of "wet" vertical motion field one might expect to encounter. For instance, on an average kind of day during the winter months the 700 mb "wet" vertical motion charts behaved as follows. At the first hour the root-mean-square magnitude was about 6 mb/hour, the maximum ascent was in the range -30 to -40 mb/hour, and the maximum subsidence was about 20 to 30 mb/hour. Results are quoted for the first hour rather than at initial time because this is when the first centred time step is taken. The magnitudes of these values then increased by about 0.5% to 1% per hour until the first application of the standard smoothers at 10 hours. As mentioned in Section 16, the necessity of maintaining matched stream function fields meant that the vertical motion computations effectively passed through the smoothing operation two hours ahead of the baroclinic model itself. The values immediately after smoothing were about 12% smaller than the corresponding first hour values, so this meant that the values just prior to smoothing were actually cut down by about 20%. The same thing happened as the forecasts progressed from 10 hours to 22 hours, the next smoothing time, and once again as they

progressed to the last smoothing time at 34 hours. Consequently, at 35 hours the first-hour values had been reduced by about $1/3$, so that the root-mean-square magnitude was about 4 mb/hour, the maximum ascent was in the range -20 to -30 mb/hour and the maximum subsidence 12 to 20 mb/hour. Naturally, the general trends indicated by the foregoing remarks may be masked by synoptic developments in individual cases. One unsatisfactory feature that showed up moderately frequently, usually in the last twelve hours, was that uncoupling between odd and even time steps became evident. Sometimes the uncoupling variations would be a barely discernible 2 or 3%; occasionally they would grow to a vast 15 or 20%. The corresponding first-hour values at 700 mb for winter days that are meteorologically active, and also for winter days that are meteorologically quiet, are given in Table 8.

Type of day	RMS	WINTER		SUMMER		
		Maximum ascent	Maximum subsidence	RMS	Maximum ascent	Maximum subsidence
Active	8/10	- 50/ - 62	25/35	4/5	- 25/ - 35	20/25
Average	6	- 30/ - 40	20/30	3	- 15/ - 20	13/18
Quiet	4	- 15/ - 25	15/25	1/2	- 5/ - 10	5/10

Table 8: Typical first-hour values for the root-mean-square, maximum ascent and maximum subsidence of the 700 mb "wet" vertical motion charts. The units are mb/hour. Winter and summer ranges are given for active, average, and quiet days. These values were obtained by monitoring the output from the 1968 model, but they should also be valid for the 1970 model.

There were about a dozen winter cases for which the maximum ascent just surpassed -50 mb/hour, but in no instance did it get as low as -63 mb/hour. Table 8 also lists similar sets of first-hour values at 700 mb for summer days. A word of caution here. The numerical values appearing in the vertical motion charts transmitted over the facsimile circuits cannot be compared directly to those in Table 8. This is because the facsimile charts are contoured using the incredible unit of minus microbars/sec. The numbers appearing on the facsimile charts have therefore to be multiplied by a conversion factor of -3.6 to make them meaningful in terms of Table 8. In all cases, winter and summer, the variation in time after the first hour was rather similar to that for average winter days; i.e. values increased by about 8% in between smoothing times, only to be cut down by about 20% at each hour the smoothing operators were applied. Uncoupling problems were most common and most severe in active winter cases. As is to be expected from (16.4), the properties of the 850 mb "wet" vertical motion charts were very similar to those at 700 mb. In general, the root-mean-square, maximum ascent and maximum subsidence values at 850 mb were about 0.9 times their counterparts at 700 mb. This ratio is slightly higher than the $\tau_a(\alpha_s)_{70}/(\alpha_s)_{85}$ factor of (16.4), which is about 0.85, because of the greater terrain contribution at 850 mb. At 500 mb the correlation with 700 mb was not nearly so great. At the first hour the root-mean-square, maximum ascent and maximum subsidence values at 500 mb were usually about 0.7 to 0.8 of the corresponding values at 700 mb. This ratio tended to be higher on quiet summer days and lower on active winter days. However, the net drop off with time was not so great as at the other levels. By 35-hours the

500 mb "wet" vertical motions tended to retain about $3/4$ of their first-hour amplitudes. So either the noise build-up between smoothing times was slightly greater at 500 mb, or else the smoothers themselves were slightly less effective at this level. In summer the mean "wet" vertical motions at all levels were in the range 0 to -0.5 mb/hour; in winter they were in the range -0.2 to -1.2 mb/hour. However, the mean at 700 mb was usually, but by no means invariably, about 1.5 to 2 times larger than the mean at 500 mb, whereas the mean at 850 mb usually lay somewhere in between.

After the 1968 model was replaced by the 1970 model, the following changes in properties were inferred from monitoring the "wet" vertical motion charts in February and March 1970. The most important change, of course, was the elimination of the adverse effects of smoothing. The tremendous discontinuities in the time sequence of vertical motion charts every twelve hours completely disappeared. There was also an unexpected side effect. The uncoupling problem has also been completely cured. Getting down to the details, the first-hour values of the "wet" vertical motion fields are about the same as they were before at 850 and 700 mb. Thereafter, as the forecasts progress, there is generally a steady decrease in all values of about 0.5% per hour, so that by 35 hours they are down to about $5/6$ of their first-hour values. At 500 mb the first-hour values seem to be down by about 15% . Then there appears to be a more rapid fall off than at the other levels for the first twelve hours, perhaps as much as 1% per hour, until the rate slows down to about the same 0.5% figure as at the other levels. This makes the 35-hour 500 mb "wet" vertical motions just under 80% of their first-hour values, which works out to be just under $2/3$ of the first-hour values they would have had in the 1968 model. The

precipitation grand totals for the 1970 model were about as for the 1968 model at 850 and 700 mb, but about 25% lower at 500 mb. From the preceding remarks it appears that at least part of this difference in behaviour arises from changes in the relative net decay characteristics at the three levels.

Besides monitoring general properties, the characteristic areas verification program also compared predicted "wet" vertical motion charts against first-hour "wet" vertical motion charts which were produced in later runs, but which were valid for the same real time. Specifically, the 13-hour "wet" vertical motion forecasts were compared to the 1-hour "wet" vertical motion charts produced in the next run, the 25-hour forecasts were compared to the 1-hour charts produced in the next run but one, and the 35-hour forecasts were compared to the 1-hour charts produced in the next run but two. No 37-hour "wet" vertical motion forecasts are produced in the operational run, so the last one available was used instead. Once again comparisons were based on the first-hour "wet" vertical motions because these correspond to the first centred time step. These comparisons only constitute a kind of pseudo-verification procedure, not a true one. This is because the verifying charts are not based directly on observations; they are themselves computed quantities. Unfortunately, too, RMSE verification scores are practically meaningless for vertical motion charts because neither the grid-point values themselves, nor their errors, have a normal distribution. So the best that could be done was to compute the percentage of grid points at which the predicted "wet" vertical motion fields had the same sign as the corresponding first-hour fields. The results are shown in Fig. 10. The sign

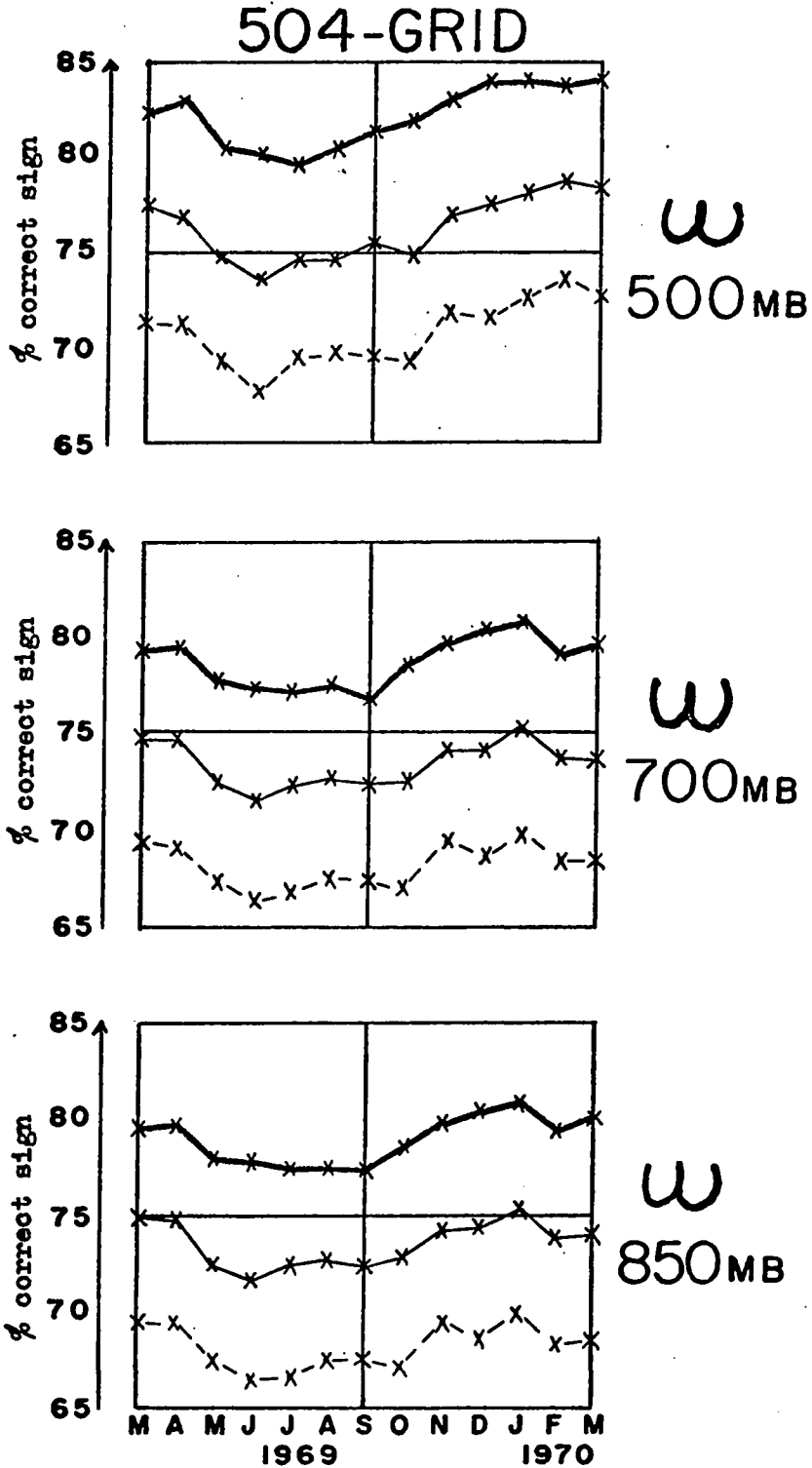


FIG 10: Monthly mean values of the percentages of grid-points at which the 13, 25 and 35-hour forecasts of the "wet" vertical motion fields have the correct sign. The thick curves are the 13-hour forecasts, the thin curves are the 25-hour forecasts, and the dashed curves are the 35-hour forecasts. The lower, middle and upper diagrams are for 850, 700 and 500mb respectively. The verifying "wet" vertical motion fields are 1-hour forecasts from subsequent runs. All values are for the 504-point grid.

correlations are a bit higher in winter than in summer, and a bit higher at 500 mb than at the other levels. No doubt this is because the weather systems are better organised in winter, and because the advection speeds are more realistically simulated at 500 mb than at the lower levels. The information in Fig. 10 may be quickly summarised by quoting averages for the whole year. At 500 mb the sign correlation with the first-hour "wet" vertical motion charts is about 82% at 13 hours, 76% at 25 hours, and 71% at 35 hours. The corresponding figures at both 700 and 850 mb are 79% at 13 hours, 73% at 25 hours, and 68% at 35 hours.

Over the whole year, for the 1968 model, the average number of maximum amplification restrictions (17.2) imposed on the "wet" vertical motions at each time step over the 504-point grid were as follows: at 850 mb, 12 grid points; at 700 mb, 9 grid points; and at 500 mb, 3 grid points. These figures are about 1/3 the maximum numbers of restricted grid points as the distribution is skew. The variations from month to month reflect changes in the objective analysis procedures more than the season. Further, the results are based on diagnostic totals for the entire run, so there is no information available about how they varied during the forecast period. Neither is there any information about geographic distribution. Presumably, though, most of the restricted grid points were either in the south-west and south-east corners of the 504-point grid, where the f_0/f factor of (17.3) was a problem, or else in other ocean no-data areas where there was a lack of vertical consistency in the initial time objective analyses. There has been some reduction in the numbers of restricted grid points in the 1970 model, but there is not yet enough information to decide how the overall figures have changed.

This concludes a fairly comprehensive account of how forecasts of vertical motion are obtained in the operational run, and what their general properties are. As was seen in Section 13, vertical motion is the first basic meteorological variable needed to compute the large scale precipitation amount. The second is temperature.

18. The Temperature Forecasts

The temperature forecasts in the 1970 version of the sequential precipitation scheme are based on the following analytical equation:

$$\frac{\partial T}{\partial t} = -\underline{V}^r \cdot \nabla T + w \left(\frac{dT}{dp} - \frac{\partial T}{\partial p} \right) + K_D^* \nabla^2 T - \frac{P}{R} H_4 \quad (18.1)$$

where K_D^* is an eddy diffusion coefficient, and H_4 is the special heat function (A1.14) for net radiation effects. Essentially, (18.1) is a version of the thermodynamic equation which serves as a prognostic equation for temperature. Under dry conditions it corresponds to (A1.17) so that

$$\frac{dT}{dp} = \frac{dT}{dp|_e} \quad ; \quad \text{under saturated condition it corresponds to (A3.9) so that}$$

$$\frac{dT}{dp} = \frac{dT}{dp|_{e_w}} .$$

The finite difference form of (18.1) is:

$$T_n^{t+1} = T_n^{t-1} + 2\Delta t \left\{ -K \mathcal{J}(\psi_n^t, T_n^t) + (w')^t \left[\frac{dT}{dp} \Big|_n^t - \left\langle \frac{\partial T}{\partial p} \right\rangle \Big|_n^t \right] + K K_D \nabla^2 T_n^{t-1} - \frac{P}{R} H_4 \Big|_n^{t-1} + h_s \Big|_n^t \right\} \quad (18.2)$$

$$n = 850, 700, 500$$

where K is given by (C1.3) and K_D is related to K_D^* as in (9.3). The time step, Δt , is the same as that used in the baroclinic model, namely one hour. The term h_s which appears in (18.2), but not in (18.1), is an empirical correction factor which is applied only at 850 mb, and only when

the Showalter Index, I , is less than some critical value. More specifically:

$$h_s = \begin{cases} 0 & \text{if } n=700 \quad \text{or } n=500 \quad \text{or } I \geq I_h \\ -[a_s + b_s(t-t_0)] & \text{if } n=850 \quad \text{and } I < I_h \end{cases} \quad (18.3)$$

where $(t-t_0)$ is the time in hours which has elapsed since initial time. Values of a_s , b_s and I_h are given in Table 9. The quantity w' is a damped version of the "wet" vertical motion given by:

$$w' = \frac{w}{1 + \left| \frac{w}{w_c} \right| + b_c \left(\frac{w}{w_c} \right)^2} \quad (18.4)$$

where w_c and b_c are constants given in Table 10.

Constant	Value	Units
I_h	-3	C deg
a_s	0.26	C deg
b_s	0.005	C deg hour ⁻¹

Table 9: Values of the constants used in the adjustments to the 850 mb temperature fields when spurious air mass instability develops.

Level	Predicted Quantity	w (mb hr ⁻¹)	w_c (mb hr ⁻¹)	b_c
850	T	all	3	0.2
700	T	all	9	0.2
500	T	all	3	0.2
all	S	$w > 0$	35	0.2
all	S	$w < 0$	40	0.2

Table 10: Values of the constants used in the vertical motion damping formula; b_c is dimensionless. The values given for w_c are for initial time; these are reduced by 1% per hour.

The total pressure derivative is obtained from:

$$\frac{dT}{dP} = \begin{cases} \left(\frac{dT}{dP}\right)_\theta & \text{if } S \geq S^* \\ \left(\frac{dT}{dP}\right)_\theta \frac{S}{S^*} + \left(\frac{dT}{dP}\right)_{\theta_w} \left(\frac{S^* - S}{S^*}\right) & \text{if } S < S^* \end{cases} \quad (18.5)$$

As noted in Appendix A3, $\left.\frac{dT}{dP}\right|_{\theta_w}$ at a given level depends only on the temperature and is obtained from tables giving values at intervals of 1 deg C. Table 11 lists a shortened form of these tables in which the interval is 10 deg C.

Temperature (C deg)	$\left.\frac{dT}{dP}\right _{\theta_w}$ (10^{-4} C deg mb ⁻¹)		
	850 mb	700 mb	500 mb
-70			640
-60	374	455	960
-50	561	683	1280
-40	747	910	1287
-30	750	913	1290
-20	727	877	1190
-10	643	790	1037
0	570	660	840
10	500	540	667
20	413	467	
30	363		

Table 11: Moist adiabatic lapse rate tables, $\left.\frac{dT}{dP}\right|_{\theta_w}$.

By differentiating (A1.7), and converting from degrees Kelvin to degrees

Celsius, it follows that:

$$\left. \frac{dT}{dP} \right|_{\theta} = \frac{R}{C_p P} (T + 273.2) \quad (18.6)$$

For convenience of application, this is rewritten in the form:

$$\left. \frac{dT}{dP} \right|_{\theta} = b_{\theta} (T + 273.2) \quad (18.7)$$

Constant	850 mb	700 mb	500 mb	Units
b_{θ}	3.36	4.08	5.71	10^{-4} mb^{-1}

Table 12: Values of the constant used in the computation of $\left. \frac{dT}{dP} \right|_{\theta}$.

where values of b_{θ} are given in Table 12. The partial derivative with respect to pressure, $\left(\frac{\partial T}{\partial P} \right)$, is evaluated by means of the parabolic fit formula (B13.1) at 700 mb. But simple non-centred formulae have to be applied at 850 and at 500 mb because no temperature information is available either at 1000 mb or at 200 mb. In practice, formula (B13.2) is applied at all three levels with appropriate sets of coefficients. Note that the standard Jacobian operator (B11.1) is used to evaluate the advection term. And, as usual, (hour - 1) values have to be used in the eddy diffusion term. The radiation effect, $\left(-\frac{P}{R} H_4 \right)$, was adapted from the recent work on parallel operation. For this reason, and also because of some computer hardware complications involving storage limitations in the operational run, the discussion of this term will be deferred until later in the thesis. As usual, a forward time step has to be employed at initial time to start off the leapfrog marching

process which characterises the integration procedure. This is done by applying a slightly amended form of (18.1) in which the $(t-1)$ superscripts are replaced by t , and the $2\Delta t$ is replaced by Δt . The T_n^{t+1} given by (18.2), and also the initial time temperature fields, are not allowed to exceed the maxima and minima limits of Table 13.

Level (mb)	Minimum Temperature Allowed (C deg)	Maximum Temperature Allowed (C deg)
850	-60	30
700	-60	20
500	-70	10

Table 13: Maximum and minimum restrictions on the temperature fields.

This restriction is imposed by testing each grid point in turn. If the temperature is greater than the allowed maximum it is reset to that maximum, and similarly if it is lower than the allowed minimum it is reset to that minimum.

As will be explained in Section 20, the Showalter Index, I , is used in the computation of small scale precipitation amount because it is a reliable indicator of air mass instability. It is a quantity which can be obtained quite easily on a computer by a table look-up procedure. First, a parcel of air is lifted adiabatically from 850 mb to 500 mb, taking saturation into account if it occurs. The 500 mb temperature it

ends up with, T_{50}^L , depends only on the temperature and dew point depression at 850 mb, and so its value can be interpolated from Table 14.

The Showalter Index is then simply defined by:

$$I = T_{50} - T_{50}^L \quad (18.8)$$

		S_{85} (C deg)						
		0	5	10	15	20	25	30
T_{85} (C deg)	30	13.8	8.7	4.3	0.1	-3.9	-7.4	-10.4
	25	7.3	2.4	-2.3	-6.8	-10.0	-12.8	-14.9
	20	0.5	-4.5	-9.5	-13.5	-16.2	-18.2	-20.2
	15	-7.0	-11.8	-15.3	-18.2	-20.6	-23.7	-25.0
	10	-14.0	-18.2	-21.8	-24.6	-27.0	-28.2	-29.8
	5	-21.5	-25.2	-27.9	-30.2	-31.8	-32.5	-33.4
	0	-30.0	-32.0	-33.7	-35.6	-36.4	-37.2	-37.8
	-5	-36.2	-38.3	-39.8	-40.5	-41.3	-41.8	-42.2
	-10	-42.5	-44.2	-44.9	-45.5	-46.0	-46.4	-46.8

Table 14: Values of T_{50}^L , the 500 mb temperature of a parcel of air lifted adiabatically from 850 mb, used in the computation of the Showalter Index. The units are C deg. The Showalter Index is not computed if $T_{85} < -10$ C deg.

The precipitation scheme carries temperature fields at 850, 700 and 500 mb for the 1015-point grid of Fig. 1. However, the full form of equation (18.2) can only be applied inside the 504-point grid of Fig. 1. This is because the "wet" vertical motions, the Showalter Index, and the

radiation term are only available over the smaller grid. In the remainder of the 1015-point grid, which constitutes a wide border around the 504-point grid, a truncated form of (18.2) has to be used. This contains only the advection and eddy diffusion terms. A comparatively inactive border zone of this type is in any case necessary, and it has to be at least two or three grid points wide. Otherwise there is some incompatibility between the vertical motion term and the assumption of zero temperature tendencies along the boundary of the 1015-point grid, and this results in the development of unrealistic distortions near the boundary.

The temperature forecast scheme has another minor feature which was originally designed as a safety device, but in practice has turned out to be a valuable diagnostic indicator of trouble with the input charts which are fed into the precipitation scheme at initial time. This feature is based on the following approximate relationship between the stream function thickness and temperature:

$$\frac{\partial T}{\partial x} \approx - \left(\frac{p g f}{R f_0} \right) \frac{\partial}{\partial x} \left(\frac{\partial \psi}{\partial p} \right) \quad (18.9)$$

Equation (18.9) is derived by operating on the hydrostatic equation (A1.2) with $\frac{\partial}{\partial x}$, and then substituting the rotational part of the wind for the geostrophic wind. Its finite difference counterpart is:

$$\left[T \right]_{x(1d)} = - \left(\frac{p g f}{R f_0} \right) \left[\left\langle \frac{\partial \psi}{\partial p} \right\rangle \Big|_n \right]_{x(1d)} \quad n=700, 500 \quad (18.10)$$

where the (1d) indicates the standard x-derivatives are to be taken over one gridlength instead of the usual two. The parabolic fit formula (B13.1) is used to evaluate the pressure derivatives. At 9, 21 and 33 hours the finite difference relationship (18.10) is enforced in the square nine-point

region centred on "significant" maxima and minima. This is done by proceeding from left to right along each of the three lines in turn. Of course, starting from a point to the left of, but not included in, the nine-point area, one eventually computes a temperature for a point to the right of, but not included in, the patched area. This new temperature will not generally be the same as the existing temperature at that point. To overcome this problem, the new temperature at this right-hand point is restored to its original value by computing the correction factor and distributing it equally among the amended grid points in that line. Equation (18.10) cannot be applied at 850 mb because of the phasing problems of the 1000 mb stream function field. Consequently, the best one can do is to apply the R.H.S. of (18.10) evaluated for $n = 700$ mb to compute the L.H.S. of the same equation evaluated for $n = 850$ mb. A maximum is deemed significant if the temperature at a grid point is more than 1.5 deg C warmer than each of the eight surrounding grid points. And a minimum is deemed significant if the temperature at a grid point is more than 1.5 deg C cooler than each of the eight surrounding points. The boundaries are never amended by this procedure and so the points adjoining the boundaries are not tested for significant maxima or minima.

It will now be shown that (18.1), or at least its finite difference counterpart (18.2), does indeed allow for latent heat effects in a reasonably realistic manner. Two things have been accomplished by taking the moist adiabatic lapse rate into account. The vertical motion has been amplified. And $\left[\frac{dT}{dp} - \frac{\partial T}{\partial p} \right]$ has been reduced. Superficially, remembering (A1.16) and (A1.7), it may seem as if the complex manoeuvres of Sections 16 and 17 had accomplished nothing more than producing the

quantity

$$\omega_d \frac{\left(\frac{dT}{dp} \Big|_{\theta} - \frac{\partial T}{\partial p} \right)}{\left(\frac{dT}{dp} - \frac{\partial T}{\partial p} \right)} \quad (18.11)$$

and calling it the "wet" vertical motion. If this were the case, the capacity of (18.2) to handle latent heat effects would be entirely illusory. Fortunately, it is easy to demonstrate that this is not so. Under fully saturated conditions $\left(\frac{dT}{dp} \Big|_{\theta_w} - \frac{\partial T}{\partial p} \right)$ will be negative when the lapse rate lies between the moist adiabatic and the dry adiabatic. Thus when the vertical motion is negative the whole term $\omega \left[\frac{dT}{dp} \Big|_{\theta_w} - \frac{\partial T}{\partial p} \right]$ will be positive. This represents a true simulation of the effects of the release of latent heat and something which could not be attained by the dry adiabatic equation. So Sections 16 and 17 did after all accomplish something and the final "wet" vertical motions are sufficiently realistic to have a useful application in (18.2) as well as in the actual prediction of large scale precipitation. This point may be pursued further by re-reading the discussion on the vertical motion computations.

The advantages of using (18.1) as a prognostic equation for temperature can only be realised in practice if its finite difference counterpart, (18.2), is computationally stable. As has already been mentioned, the eddy diffusion term is sufficient to prevent horizontal instability due to the amplification of two-gridlength waves. The actual values of the eddy diffusion coefficients at initial time are given in Table 15. It is advantageous to have a larger coefficient at 850 mb than at 500 mb, and also to augment all values by 1% per hour as the forecasts progress in time. Vertical instability was encountered in the first experiments with the octagon model when moderately strong inflow conditions occurred

at the outside levels. And it made no difference if "dry" vertical motions were used instead of "wet" ones. It soon became evident that the cause of the trouble was the non-centred finite difference approximations for $\frac{\partial T}{\partial p}$ at 850 and 500 mb.

Level (mb)	K_D^* (10^7 dkm ² hr ⁻¹)	K_D (dkm)
850	6.44	7.5
700	5.15	6.0
500	3.86	4.5

Table 15: Initial time values of the eddy diffusion coefficients used in the forecast equations for temperature and dew point depression; these are augmented by 1% per hour.

The cure turned out to be a simple one. The magnitudes of the "wet" vertical motion are damped by formula (18.4) before being applied in (18.2). The best verification scores were obtained when heavy damping factors were applied at 850 and 500 mb, and a moderately heavy one even at 700 mb where there was no vertical stability problem. The actual values of W_c and b_c which are used in formula (18.4) are given in Table 10. The severity of the damping can be judged from the fact that at 850 and 500 mb a "wet" vertical motion of 10 mb/hour is cut down to about 1.5 mb/hour, one of 20 mb/hour to about 1.25 mb/hour, and that nowhere does the magnitude of the damped vertical motion exceed about 2 mb/hour. At 700 mb the figures are roughly three times these. Yet vertical stability is achieved with the W_c values at 850 and 500 mb an order of magnitude larger than those cited in Table 10, and no damping at all of the "wet" vertical motion at

700 mb. Two other features of the temperature forecast scheme play minor roles in ensuring computational stability. The thickness-temperature amendments (18.10) of nine-point areas surrounding significant maxima and minima are only applied at 9, 21 and 33 hours. They are a hold-over from an early attempt to control vertical instability in the octagon model. It was an unsuccessful attempt because the patched areas tended to link together in chains when there was no damping of the vertical motion. But in some cases the technique did slow down the development of computational instability. Consequently, it was decided to retain it as an extra safety feature in the operational precipitation scheme. Quite unexpectedly, it turned out to be a valuable diagnostic indicator of trouble with the input charts. At initial time the maximum and minimum values of all the charts which enter the precipitation scheme have to satisfy identification checks. This is a precautionary measure to provide protection against a hardware malfunction. For instance, if by some mischance the precipitation scheme picks up a height field at 500 mb instead of one at 700 mb, it will immediately come out of an error exit. But the most common kind of error arising from a hardware malfunction is that yesterday's objective analyses, say of the temperature fields, are passed into the precipitation scheme instead of the current ones. Naturally, these satisfy the identification checks and so when the precipitation forecasts come out looking a bit odd there is no direct clue as to what has happened. However, in a normal run the total number of maximum and minimum amendments is usually zero, although it is occasionally one, two or even three. In an abnormal run, when there is something wrong with one or more of the input charts, such as an incorrect initial time or an accidental displacement of the grid network from its true

position, the total amendment count jumps to at least five and may rise to more than twenty altogether. An intermediate figure, say a total count of four or five, may be an indicator of some lack of vertical consistency in the objective analysis. The absolute maximum and minimum restrictions of Table 13 were first incorporated into the 1968 model. They were inserted to provide a rigid guarantee that the various table look-ups based on temperature would not pick up numbers from outside the prescribed table areas. They were not primarily intended to serve as a hamhanded kind of protection against computational instability. Nevertheless, they would in fact massively suppress any strongly amplifying numerical phenomenon which could not be controlled by eddy diffusion and damped vertical motion. So, in this sense, they do serve as a second line of defence against computational instability. In practice, however, these restrictions are not called into play to provide stability control. Diagnostic print-outs of the numbers of restricted points are made after each run as part of the operational routine. These show that no restrictions whatsoever were imposed on the 700 and 500 mb temperature fields from January 1968 to May 1970. Nor were any minimum restrictions imposed on the 850 mb temperature field for the same period. However, there were some maximum restrictions on the 850 mb temperatures. These start to occur towards the end of May, increase to about 20 or 30 corrections a run in July, and then gradually die down again until they disappear in September. Or at least this happens for forecasts originating from 00Z initial times. Even in July there are usually no maximum temperature restrictions at 850 mb for forecasts originating from 12Z, although one or two cases do crop up. These results are not difficult to explain.

In summer the reported 850 mb temperature do regularly exceed 30 deg C in the mountain areas of the southern U.S. at 00Z. So the maximum restrictions that are imposed at 850 mb are physical and not numerical in nature. The sets of 850 mb tables could, of course, be extended out to 40 deg C to accomodate these very warm temperatures. But, on the other hand, as 850 mb temperatures of over 30 deg C only occur when the ground level is close to the 850 mb surface, it may actually be preferable to leave the present restrictions in force. The empirical correction factor h_s , which is defined by (18.3), was not introduced into (18.2) to control computational instability. Instead it serves to compensate for the systematic underadvection of cold air by the baroclinic model in certain critical areas of the 850 mb chart. Without h_s , spurious regions of highly unstable air would sometimes develop along cold fronts. These would have large negative values of the Showalter Index associated with them, and so cause some difficulties for the small scale precipitation computations of Section 20. There is one further item which should be commented upon. Instead of (18.5), it would make more physical sense to use:

$$\frac{dT}{dp} = \begin{cases} \left(\frac{dT}{dp}\right)_\theta & \text{if } S \geq S^* \text{ or } w \geq 0 \\ \left(\frac{dT}{dp}\right)_\theta \frac{S}{S^*} + \left(\frac{dT}{dp}\right)_{\theta_w} \left(\frac{S^* - S}{S^*}\right) & \text{if } S < S^* \text{ and } w < 0 \end{cases} \quad (18.12)$$

However, (18.5) gave better verification scores than (18.12). Or at least it did before the radiation term was introduced. The reason might have been that the mean values of the forecast temperature fields were usually too warm, especially in winter, without the radiation term. Using (18.5) instead of (18.12) tends to cool down the mean temperatures slightly, and

so provide some small compensation for the lack of radiation. Further tests will have to be carried out to see if (18.12) works better than (18.5) now that a radiation term has been incorporated into (18.2).

The temperature forecasts produced in the operational run from March 1969 to March 1970 were monitored by the characteristic areas verification program described in Section 11. The RMSE scores were the principal quantities actually computed. These provide a meaningful measure of the accuracy of the temperature forecasts because, as in the case of height forecasts, the errors have an approximately normal distribution. Fig. 11 consists of six diagrams showing the monthly means of the RMSE verification scores for the 12, 24 and 36-hour forecasts of 850 mb temperature, together with the corresponding monthly mean persistence scores. The left-hand diagrams are for the 504-point grid, and those on the right are for the 1015-point grid. The thick curves are the forecast scores and the thin curves are the persistence scores. Figs. 12 and 13 consist of similar sets of six diagrams for the 700 and 500 mb temperature forecasts. From these three Figs. it can be seen that all the temperature forecast scores beat their persistence counterparts by a fairly wide margin. And this margin increases with time as the forecasts progress from 12 hours to 36 hours. It is gratifying to note, too, that the differences between the forecast scores and the persistence scores are more marked for the 504-point grid than they are for the 1015-point grid. This is to be expected since (18.2) is used as the forecast equation inside the 504-point grid, and only a truncated form of the same equation is used in the remainder of the 1015-point grid. In assessing the results one should note that the persistence scores for the 1015-point grid are lowered over

T850

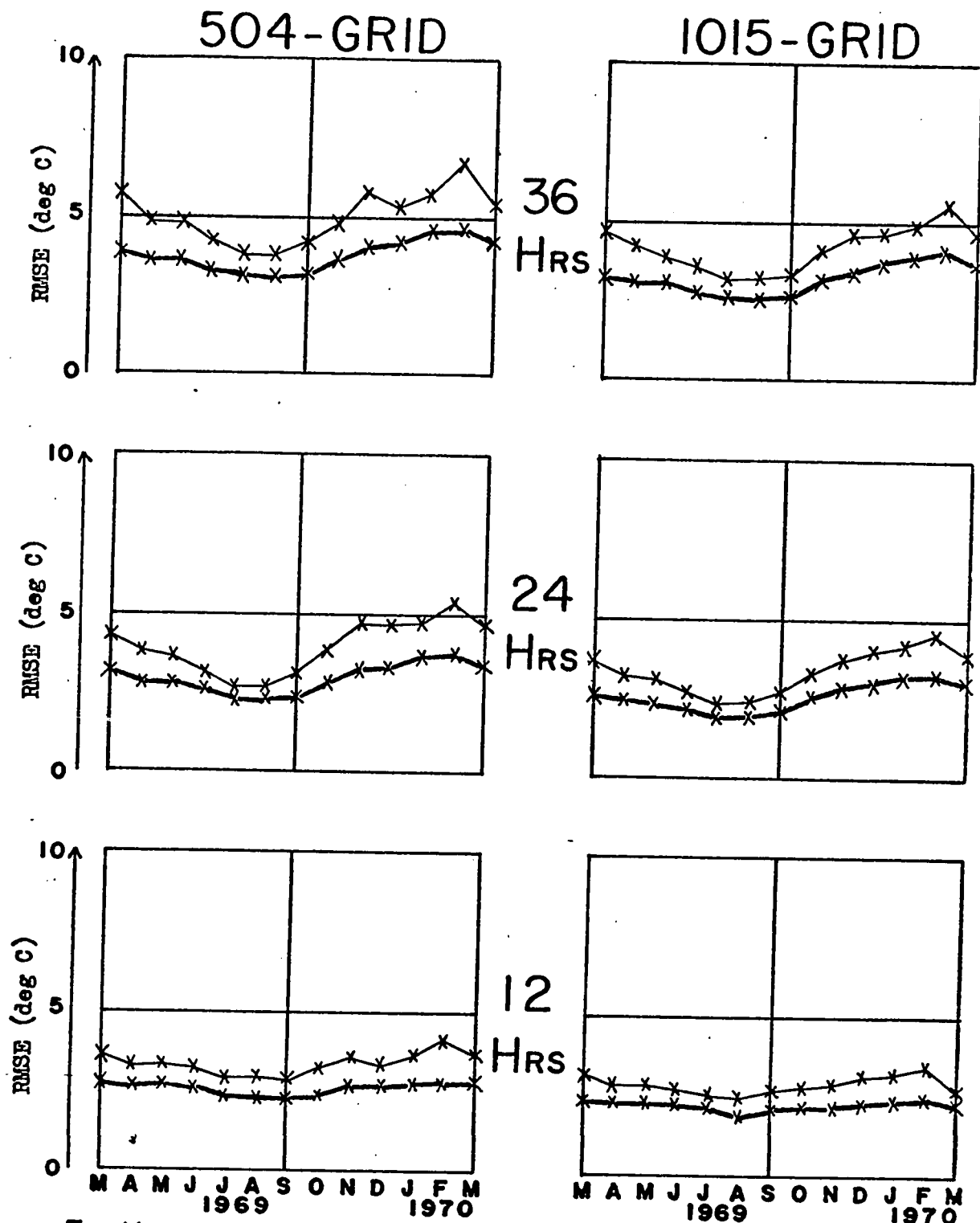


FIG 11: Monthly mean root-mean-square error (RMSE) scores in deg C for the 12, 24 and 36-hour forecasts of 850mb temperature, together with the corresponding persistence scores. The diagrams on the left are for the 504-point grid, and those on the right are for the 1015-point grid. The thick curves are the forecast scores, and the thin curves are the persistence scores.

T 700

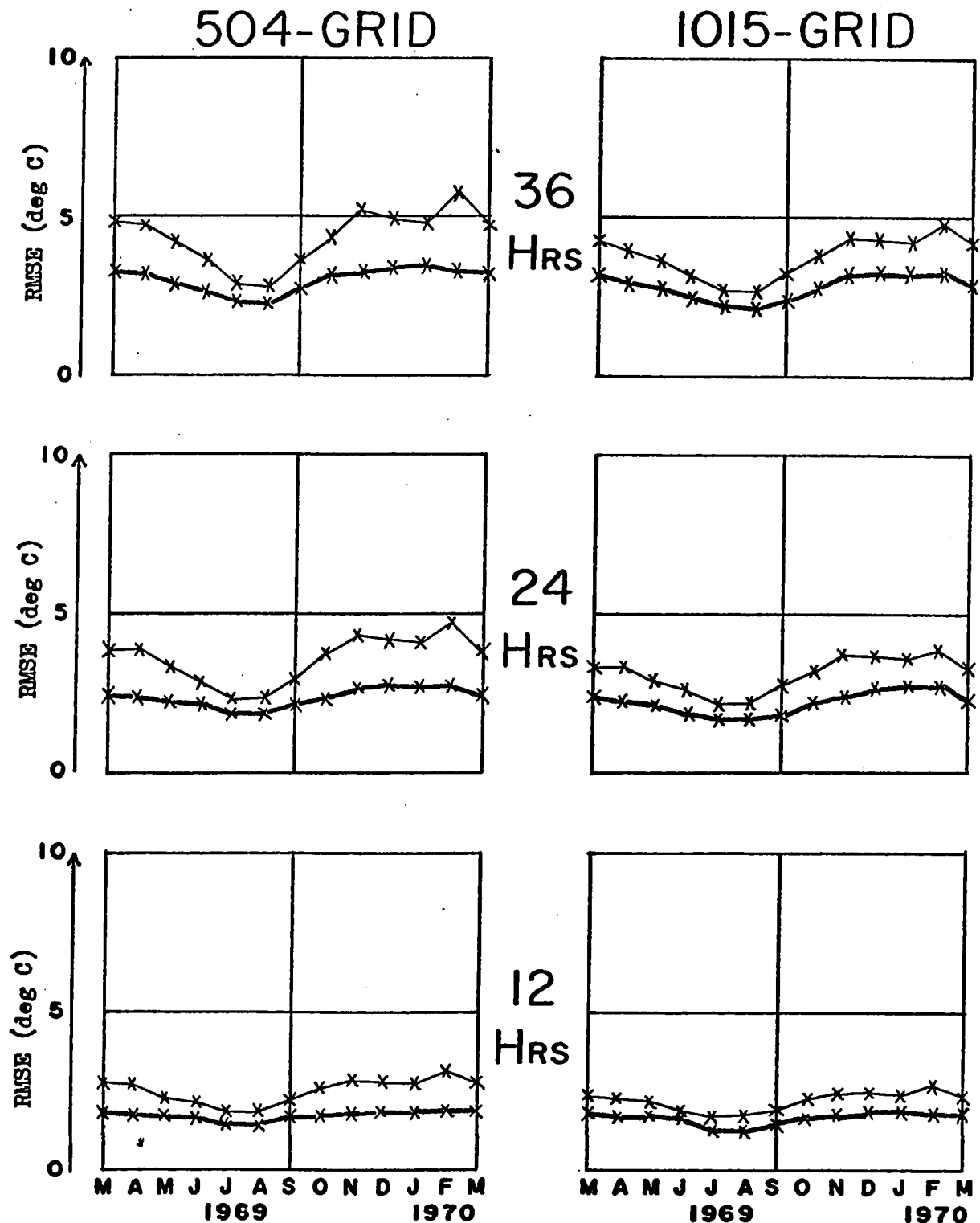


FIG 12: Monthly mean root-mean-square error (RMSE) scores in deg C for the 12, 24 and 36-hour forecasts of 700mb temperature, together with the corresponding persistence scores. The diagrams on the left are for the 504-point grid, and those on the right are for the 1015-point grid. The thick curves are the forecast scores, and the thin curves are the persistence scores.

T500

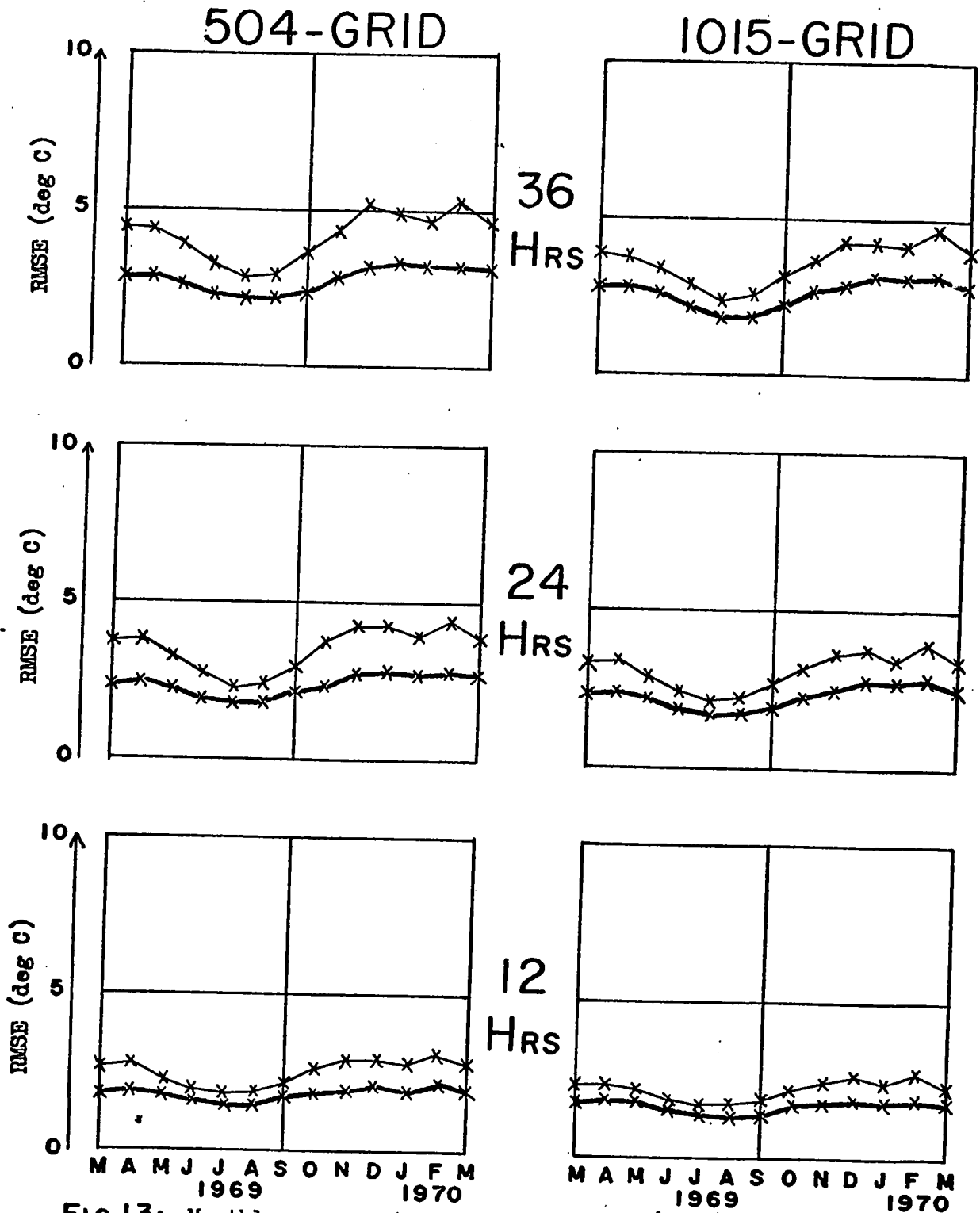


FIG 13: Monthly mean root-mean-square error (RMSE) scores in deg C for the 12, 24 and 36-hour forecasts of 500mb temperature, together with the corresponding persistence scores. The diagrams on the left are for the 504-point grid, and those on the right are for the 1015-point grid. The thick curves are the forecast scores, and the thin curves are the persistence scores.

the Pacific Ocean because only a small amount of data enters the objective analysis cycle. Figs. 11-13 have two other qualitative features which are worth noting. The seasonal variation in the forecast scores is invariably less than the seasonal variation in the corresponding persistence scores, and the temperature forecasts at 850 mb show less skill than those at 700 and 500 mb. This latter trait is undoubtedly explained by the fact that the net effects of the heat exchange processes between the atmosphere and the underlying surface are of much greater magnitude at 850 mb than they are at higher levels.

The characteristic areas verification program also revealed systematic seasonal errors in the means of the forecast temperature fields produced by the 1968 model. In winter, over the 504-point grid, the means of the 36-hour forecast fields were usually 1 to 2 deg C too warm. The corresponding figures in summer depended on whether the initial time was 00Z or 12Z. The 36-hour forecasts from 00Z were usually 0 to 1 deg C too warm, and those from 12Z were usually 0 to 1 deg C too cool. These mean errors can largely be attributed to the neglect of radiation effects, both in the form of long wave cooling and solar heating, and to a lesser extent to the neglect of ocean heating effects. If the monthly mean errors at individual grid points had been monitored, instead of the mean errors of individual forecasts, these would have shown errors of larger magnitude than the figures just quoted. This is because heating and cooling effects are usually taking place simultaneously over different parts of the grid, and so tend to cancel each other out when the mean errors are computed for the 504-point grid. In the 1970 model an attempt was made to reduce these systematic seasonal errors by introducing the radiation term into (18.1). Unfortunately,

because of hardware complications in February and March 1970, it has not yet been possible to judge how effective the new term is.

Quantitatively, at 500 mb the RMSE scores for 36-hour temperature forecasts over the 504-point grid range from about 3.5 deg C in winter to about 2 deg C in summer. At 700 mb the corresponding range is from 3.5 deg C in winter to about 2.25 deg C in summer, and at 850 mb it is from 4.5 deg C in winter to about 3 deg C in summer. In considering the acceptability of these verification figures, it should be remembered that the temperature forecasts are not produced for their own sake, but as an intermediate step in the prediction of precipitation amount. More specifically, the forecast temperatures enter into the computation of large scale precipitation amount in three different ways. They are used to compute:

- (i) The unit condensation amount, $U_p(T)$, from Table 5.
- (ii) $\frac{dT}{dP}$; i.e. $\left(\frac{dT}{dP}\right)_e$ from equation (18.7), and $\left(\frac{dT}{dP}\right)_{ev}$ from Table 11.
- (iii) $\frac{dS}{dP}$; i.e., as will be seen from the next Section, $\left(\frac{dS}{dP}\right)_e$ from (19.5)

In all these instances, the accuracy of the temperature forecast is not very critical. Errors of 2 or 3 deg C can be tolerated without any major repercussions, and even errors of 5 deg C are by no means disastrous. So the magnitudes quoted for the RMSE scores are themselves very acceptable. But, of course, if the errors have an approximately normal distribution, one has to be prepared to encounter errors 2 or 3 times greater than the RMSE values. So, from a purely statistical point of view, one may expect unacceptable errors, say of the order of 10 deg C, at something like 5% of the grid points in the forecast charts at 36 hours, and marginally acceptable errors, say of 5 to 8 deg C, at another 5% of the grid points.

It is easy to confirm these statistical expectations by examining sample 36-hour forecasts of the temperature fields and comparing them with the corresponding verifying fields. Further, as so often happens, the charts themselves are more revealing than any statistics about their RMSE scores. From inspection, one notices immediately that the major errors occur when the displacements of warm tongues of air associated with baroclinic waves are incorrectly predicted. Unfortunately, these are the very areas where one expects to find precipitation. However, one also notices that the predicted positions of these tongues of warm air are broadly consistent with the predicted height fields, and that the temperatures inside a forecast tongue match up very well with those inside the corresponding verifying tongue when due allowance is made for the displacement error. So it seems that the major errors are attributable to the baroclinic model, and not to the temperature prediction scheme based on (18.2). This is not to say that the temperature prediction scheme is perfect. But it does mean that the major errors can only be reduced by improving the baroclinic model. As will be explained in Section 20, forecast temperatures also enter into the prediction of small scale precipitation amount. The unit condensation rates, $U_p(\tau)$, of Table 5 are needed once again. In addition, the Showalter Index and the horizontal temperature gradients are also used. As these quantities both involve taking derivatives of the temperature fields, either in the vertical or the horizontal, the accuracy with which they are predicted drops off quite rapidly with time. The errors in the Showalter Index predictions tend to be more serious near cold fronts than they are elsewhere. This happens because of the systematic under-advection of cold air by the baroclinic

model at 850 mb in these regions. The phenomenon is controlled to some extent by the introduction of the h_s term into (18.2). The situation is not quite so bad as it seems for the horizontal temperature gradients. The predicted temperature charts are always much smoother than the corresponding verifying charts because of the relatively high values which are used for the eddy diffusion coefficients and the vertical motion damping factors. But these high values were adopted because they led to better verification scores. So, in general, the suppressed detail, even if physically real, would have been off position if it had been retained in the forecast charts. Consequently, only temperature gradients which are associated in some way with large scale patterns will persist in the forecast charts for any length of time, and even these will steadily weaken. The net result is that those detailed features of the temperature gradient configurations which are most difficult to forecast are subjected to the most severe attrition with time. And no new features are predicted to develop.

This Section has explained the procedures for obtaining the hourly temperature forecasts and discussed the quality of the predicted temperature fields. The temperature and the "wet" vertical motion are two of the three basic variables required for the prediction of large scale precipitation amount. The third is the dew point depression.

19. The Dew Point Depression Forecasts

The dew point depression forecasts in the 1970 version of the sequential precipitation scheme are based on the following analytical equation:

$$\left. \begin{aligned} \frac{\partial S}{\partial t} = -\underline{V}^r \cdot \nabla S + w \left[\frac{dS}{dp} - \frac{\partial S}{\partial p} \right] + K_D^* \nabla^2 S - \frac{P}{R} H_4 - \Gamma_S \\ S \neq 0 \end{aligned} \right\} (19.1)$$

where K_D^* is an eddy diffusion coefficient, H_4 is the same special heat function (A1.14) for net radiation effects as that which appears in (18.1), and Γ_S represents effects due to moisture sources. The condition stipulates that supersaturation does not occur. Under dry conditions $\frac{dS}{dp} = \left(\frac{dS}{dp} \right)_e$; under appropriate saturated conditions $\frac{dS}{dp} = \left(\frac{dS}{dp} \right)_{\theta_w} \equiv 0$. Essentially, of course, (19.1) is an equation expressing the conservation of moisture substance, and it is directly comprehensible from this point of view. Alternatively, though, one can think of the moisture conservation equation as being:

$$\frac{\partial T_d}{\partial t} = -\underline{V}^r \cdot \nabla T_d + w \left[\frac{dT_d}{dp} - \frac{\partial T_d}{\partial p} \right] + K_D^* \nabla^2 T_d + \Gamma_S \quad (19.2)$$

Then one can go on to "derive" (19.1) by subtracting (19.2) from (18.1). However, there is a physical reason for regarding (19.1) as a more primary expression of conservation of moisture than (19.2). It is simply that when and where saturation occurs is taken care of automatically by (19.1), but no information whatsoever about saturation is contained explicitly in (19.2). In fact, it was for this very same reason that the dew point depression was chosen as the moisture parameter in Section 14. In a sense, of course, it is the standard symbolism which is a little misleading here. One gets so used to writing the dew point depression as a difference of two quantities, $(T - T_d)$, that there are mental barriers to thinking about it as a single entity of some significance in its own right. This is why the

present dissertation has abandoned the standard symbolism for the dew point depression in favour of the single symbol, S .

The finite difference form of (19.1) is:

$$S_n^{t+1} = S_n^{t-1} + 2\Delta t \left\{ -K \mathcal{J}(\psi_n^t, S_n^t) + (\omega^t)^t \left[\left. \frac{dS}{dp} \right|_n^t - \left\langle \frac{\partial S}{\partial p} \right\rangle \Big|_n^t \right] \right. \\ \left. + K K_D \nabla^2 S_n^{t-1} - \gamma_s \frac{p}{R} H_4 \Big|_n^{t-1} - \left[S \right]_n^t \right\} \quad (19.3)$$

$n=850, 700, 500$

where K is given by (C1.3) and K_D is related to K_D^* as in (9.3). The quantity ω^t is still the damped version of the "wet" vertical motion given by (18.4), but now the magnitude of ω_c is set an order of magnitude higher than it was earlier for the temperature forecasts. See Table 10 for the actual values. Since $\left(\frac{dS}{dp} \right)_{\theta_w} \equiv 0$, the total pressure derivative is obtained from:

$$\frac{dS}{dp} = \begin{cases} \left(\frac{dS}{dp} \right)_{\theta} & \text{if } S \geq S^* \\ \left(\frac{dS}{dp} \right) \frac{S}{S^*} & \text{if } S < S^* \end{cases} \quad (19.4)$$

With sufficient accuracy,

$$\left(\frac{dS}{dp} \right)_{\theta} = a_d + b_d T \quad (19.5)$$

where the temperature is in degrees Celsius and a_d and b_d are constants given in Table 16. The partial derivative with respect to pressure, $\left\langle \frac{\partial S}{\partial p} \right\rangle$, is evaluated at 700 mb by means of the parabolic fit formula (B13.1). At each of the 850 and 500 mb levels, however, one tenth of the 700 mb value is used instead of resorting to a non-centred finite difference

formula. The factor γ_s , which appears in (19.3) but not in (19.1), is an empirical reduction in magnitude of the radiation effect.

Constant	Level			Units
	850 mb	700 mb	500 mb	
a_d	8.71	9.56	13.4	10^{-2} C deg mb $^{-1}$
b_d	2.42	2.83	4.10	10^{-4} mb $^{-1}$

Table 16: Values of the constants used in computing $\frac{dS}{dP}|_0$

Currently, γ_s is set equal to 0.3, but it may later be adjusted upwards. As mentioned in the last Section, it is convenient to defer the discussion of the radiation term until later in the thesis. This is because it is a new feature which has just recently been adopted from the parallel model.

The moisture source term, Γ_s , is broken down into two parts:

$$\Gamma_s = \Gamma_s' + \Gamma_s'' \quad (19.6)$$

The first part, Γ_s' , represents the net upward eddy diffusion of moisture from the Earth's surface, and is given by:

$$\Gamma_s' = \begin{cases} c_d(S - S_d) & \text{if } S > S_d \\ 0 & \text{if } S \leq S_d \end{cases} \quad (19.7)$$

where the values of c_d and S_d are given in Table 17. The second part, Γ_s'' , represents the net evaporation from precipitation falling into a dry layer from the layers above, and is given by:

$$\Gamma_s'' = \begin{cases} 0 & \text{if } S_n \leq S^* \text{ (or } n=500) \\ (S_n - S^*) (B_n^{70} S_{70}' + B_n^{50} S_{50}') & \text{if } S_n > S^* \end{cases} \quad (19.8)$$

Constant	Level			Units
	850 mb	700 mb	500 mb	
S_d	15	20	25	C deg
C_d	0.1	0.1	0.1	hr ⁻¹

Table 17: Values of the constants used in the term representing upward diffusion of moisture from the Earth's surface.

where

$$S_m' = \begin{cases} 0 & \text{if } S_m \geq S^* \text{ or } W_m \geq 0 \\ \left(\frac{S^* - S_m}{S^*} \right) & \text{if } S_m < S^* \text{ and } W_m < 0 \end{cases} \quad m=700, 500 \quad (19.9)$$

and the values of B_n^{70} and B_n^{50} are given in Table 18.

	m (Level)			Units
	850 mb	700 mb	500 mb	
B_m^{70}	0.1	0	0	hr ⁻¹
B_m^{50}	0.1	0.1	0	hr ⁻¹

Table 18: Values of the constants in the term representing net evaporation from falling precipitation.

Note that, as in the case of (18.2), the standard Jacobian operator (B11.1), is used to evaluate the advection term, and (hour - 1) values have to

be used in the diffusion term. The forward time step that has to be taken at initial time is handled in exactly the same way for dew point depression as it is for temperature. This involves making slight amendments to equation (19.3) so that the $(t-1)$ superscripts are replaced by t , and the $(2\Delta t)$ factor by (Δt) . The S_n^{t+1} given by (19.3), and also the initial time dew point depression fields, are never allowed to become negative. This restriction is imposed by testing each grid point in turn, and resetting any negative values to zero.

As in the case of the temperature, the precipitation scheme carries dew point depression fields at 850, 700 and 500 mb for the 1015-point grid of Fig. 1. Once again the full form of equation (19.3) can only be applied inside the 504-point grid of Fig. 1. This is because the "wet" vertical motions and the radiation term are only available over the smaller grid. In the remainder of the 1015-point grid, the part which lies outside the 504-point grid, a truncated form of (19.3) has to be used. This contains the advection and eddy diffusion terms; it also contains Γ_S' , but not Γ_S'' . Again, a comparatively inactive border zone is in any case necessary. This guarantees that the assumption of $\frac{\partial S}{\partial x} = 0$ along the horizontal boundaries will not cause any distortion problems.

The 1970 scheme for predicting dew point depression differed in only one respect from the 1968 version. The radiation term was added. However, there were several small improvements made at the time of the change-over from the octagon model to the 1968 model. First, the following relationship was used instead of (19.4) in the octagon model:

$$\frac{dS}{dp} = \begin{cases} \left(\frac{dS}{dp}\right)_\theta & \text{if } S > 0 \text{ or } w > 0 \\ 0 & \text{if } S = 0 \text{ and } w \leq 0 \end{cases} \quad (19.10)$$

although, of course, $\left(\frac{dS}{dp}\right)_\theta$ was still obtained from (19.5). This was because no thought had been given to the possibility of using (19.4), and (19.10) seemed to give better results than:

$$\frac{dS}{dp} = \begin{cases} \left(\frac{dS}{dp}\right)_\theta & \text{if } S \geq S^* \quad \text{or } w \geq 0 \\ \left(\frac{dS}{dp}\right)_\theta \frac{S}{S^*} & \text{if } S < S^* \quad \text{and } w < 0 \end{cases} \quad (19.11)$$

Second, in the octagon model it was assumed that $\left\langle \frac{\partial S}{\partial p} \right\rangle$ was zero at all levels. Third, in the octagon model there was no attempt made to allow for evaporation from falling precipitation. Effectively, this meant that Γ_s'' was taken to be zero. Fourth, several of the constants used in the dew point depression prediction scheme were reset. These are listed in Table 19, together with their old and new values.

quantity	condition	level	octagon	1968&70	units
w_c	$w \geq 0$	all	20	35	mb/hour
w_c	$w < 0$	all	40	40	mb/hour
S_d	-	850	15	15	deg C
S_d	-	700	15	20	deg C
S_d	-	500	15	25	deg C

Table 19: Some of the constants used in the dew point depression prediction scheme were reset at the time of the change-over from the octagon model to the 1968 model. These are listed here together with their old and new values.

Successful forecasts of dew point depression can only be obtained if (19.3) is computationally stable. Horizontal instability due to the

amplification of two-gridlength waves is controlled by the eddy diffusion term in exactly the same way as in (18.2). In fact, as indicated in Table 15, the eddy diffusion coefficients have the same initial time values for both temperature and dew point depression, and they are augmented hourly by 1% in exactly the same manner. No problems were encountered with vertical stability in the development work with the octagon model. But this was because non-centred finite difference approximations were avoided by taking $\langle \frac{\partial S}{\partial p} \rangle$ to be zero everywhere. Nevertheless, some experiments were carried out with damped vertical motions, and it was found that better forecasts of both dew point depression and precipitation amount were obtained by applying a very light damping factor. Further, best results were obtained when subsiding vertical motions were damped more heavily than ascending ones. By contrast, the optimum procedure for temperature forecasts involved damping to a much heavier degree, but made no distinction between up and down vertical motions. As can be seen from Table 16, $\left(\frac{dS}{dp}\right)_\theta$ is of the order of 0.1 deg C/mb. Over most of the map $\langle \frac{\partial S}{\partial p} \rangle$ will usually be an order of magnitude smaller, so under dry conditions cannot be expected to contribute much to (19.3). Nevertheless, in the 1968 model it was decided to add the $\langle \frac{\partial S}{\partial p} \rangle$ term at 700 mb, not because appreciable improvements in the forecasts were expected, but because this particular term could be computed quite easily. This small but natural innovation had a slightly perplexing ramification. It was not clear what, if anything, should be done to evaluate $\langle \frac{\partial S}{\partial p} \rangle$ at the other levels. Obviously, after the earlier difficulties with vertical instability in the temperature forecasts, it would have been an unsound move to suddenly start using non-centred finite difference approximations

at 850 and 500 mb. Eventually, an interim procedure was adopted as it was found to be safe to use one tenth the 700 mb value of $\left(\frac{\partial S}{\partial p}\right)$ at the other levels. Meanwhile, of course, (19.4) had been substituted for (19.10), and the term representing evaporation from falling precipitation had been added to (19.3). At this juncture, studies of individual cases suggested that some of the constants should be reset at new values. The two actual changes that were made are indicated in Table 19. First, a variation with level was incorporated into the term representing the net upward eddy diffusion of moisture. This made it most effective at 850 mb and least effective at 500 mb. Second, the damping of downward vertical motion was reduced to make it almost the same as that for upward vertical motion. Presumably, this was made possible by the adoption of (19.4) in place of (19.10). All these changes, taken together, led to improvements in the dew point depression forecasts. But the preservation of vertical stability was a necessary prerequisite to the achievement of this objective. It was accomplished with only a comparatively mild damping of the vertical motions. For instance, an ascending vertical motion of 10 mb/hour is reduced to 8 mb/hour, one of 20 mb/hour is reduced to 13 mb/hour, and one of 40 mb/hour is cut down to 18 mb/hour. And even this degree of damping is probably not essential for vertical stability. After all, it was originally imposed to obtain better verification scores, not to remedy vertical instability. Two other features of the scheme for producing dew point depression forecasts play significant roles in ensuring computational stability. In both cases the restrictions that are imposed are primarily physical in nature. The numerical benefits they happen to bestow are side effects. One of these features, of course, is that

supersaturation is strictly prohibited. Under no circumstances whatsoever is the S_n^{t+1} of (19.3) allowed to become negative. In theory this sounds like a massive restriction. But in practice it is not. Diagnostic counts of the number of times this restriction is enforced are printed out after every operational run. At each of the 850 and 500 mb levels, on the average, there are only about 5 grid points at which the restriction is enforced. And this figure is for the whole run, not just a single time step. At 700 mb, on the average, the corresponding count is about 9. So far, the maximum number of restrictions enforced at any one level in a single 36-hour run is 145. There are only a few counts at a single level, perhaps a dozen a year, over 100. The precipitation forecasts would not be very successful if they required full saturation! There are two reasons why so few grid points need to have negative dew point depressions corrected to zero. In the absence of other effects, the eddy diffusion term makes it impossible to maintain a single fully saturated grid point from one hour to the next. Again in the absence of other effects, the term $w \frac{dS}{dp}$ is generally insufficient to generate full saturation on its own when $\frac{dS}{dp}$ is evaluated by means of formula (19.4). So, usually, full saturation can only be attained with some assistance from the vertical and horizontal advection terms, which would have to more than compensate for the eddy diffusion drying as supersaturation is approached. Nevertheless, as examination of the predicted dew point depression charts shows, there is no trouble at all in getting down to within half a degree of true saturation, and this is more than is needed for the precipitation scheme to work very well. The remaining feature which contributes to computational stability is the term \sqrt{S} , given

by (19.7), which simulates the net upward eddy diffusion of moisture from the Earth's surface. The octagon model forecasts were perfectly stable without this term, but very dry areas would develop in regions of strong subsidence. The numerical properties of these dry areas were unremarkable, but from a climatological point of view the degree of dryness did not make sense. And so it was to overcome a physical weakness, not a numerical one, that the Γ_s' term was introduced. However, as the $\left\langle \frac{\partial S}{\partial p} \right\rangle$ term was included in the 1968 model, but not in the earlier work, it is conceivable that Γ_s' now serves a numerical purpose as well as a physical one. This is unlikely, because of the precautions that were taken with the introduction of $\left\langle \frac{\partial S}{\partial p} \right\rangle$, but it is not impossible. The only way to check would be to do some runs without the Γ_s' term and see what happened. To sum up, the situation regarding computational stability seems to be rather similar to that for the temperature forecasts. The primary stability controls are the eddy diffusion terms, the vertical motion damping factors, and the deliberately undervalued $\left\langle \frac{\partial S}{\partial p} \right\rangle$ terms at the outside levels. However, if by some mischance these happen to fail, then there is a second line of defence against computational instability. This is provided by the prohibition of supersaturation and the presence of the Γ_s' term, although the primary role of both these features is a physical one. One last aspect of the scheme for predicting dew point depressions should be noted. Physically, it is a little puzzling that better results appear to be obtained when $\frac{dS}{dp}$ is evaluated by (19.4) rather than by (19.11). In Section 18 it was seen that a similar small mystery exists in the temperature forecast scheme. In the case of the temperatures, the lack of a radiation term at the time the tests were carried out was suggested

as a possible explanation. Weak though this explanation is, no better one can be offered for the dew point depressions. So, once again, it seems that the earlier tests should be repeated, this time with the radiation term in, to see if the former conclusion about the superiority of (19.4) still stands up.

The dew point depression forecasts produced in the operational run from March 1969 to March 1970 were also monitored by the characteristic areas verification program described in Section 11. Once again, the RMSE scores were the principal quantities actually computed. Unfortunately, these do not necessarily provide a reliable guide to either the accuracy or the value of the dew point depression forecasts. For one thing, to say that the errors have a normal distribution is not a very good approximation. The fact that supersaturation is prohibited is bound to distort the error distribution curve in some way. Also, the objectively analysed dew point depression charts contain much more elaborate detail than the corresponding height and temperature analyses. But this initial time detail rapidly disappears in the prediction scheme. The forecast dew point depression charts, even at twelve hours, look comparatively smooth. Consequently, the RMSE scores must reflect this great difference in smoothness between predicted and verifying charts. In particular, they will be somewhat larger than the corresponding RMSE scores for the forecast temperatures. For although the forecast temperature fields are also smoother than the objectively analysed temperature fields, the difference is not nearly to the same degree as it is for the dew point depression fields. The value of the dew point depression forecasts depends on the use to which they are put. So the only thing that really matters

for the large scale precipitation computations is the accuracy of the dew point depression forecasts in those areas which are relatively close to saturation. An error of 2 or 3 deg C is of some consequence when $S < S^*$. But an error of 10 deg C matters not a whit when $S \gg S^*$. Qualitatively, the same remarks apply to the small scale precipitation computations. Unfortunately, the displacements and intensities of the dry areas of the dew point depression fields turn out to be the most difficult features to predict. So the RMSE scores, which do not discriminate between errors in dry areas and errors in moist areas, may be a poor indicator of the value of the dew point depression forecasts. Nevertheless, in spite of all these misgivings, the RMSE scores are not devoid of interest and so the results of monitoring the operational run are presented here. Fig. 14 consists of six diagrams showing the monthly means of the RMSE verification scores for the 12, 24, and 36-hour forecasts of 850 mb dew point depression, together with the corresponding monthly mean persistence scores. The left-hand diagrams are for the 504-point grid, and those on the right are for the 1015-point grid. The thick curves are the forecast scores and the thin curves are the persistence scores. Figs. 15 and 16 consist of similar sets of six diagrams for the 700 and 500 mb dew point depression forecasts. The first thing that strikes one about these three Figs. is that the monthly mean forecast scores are invariably better than the corresponding persistence scores. This is a feat which the original development work on the octagon model did not manage to accomplish; see Davies (1967) p. 58. So, presumably, the changes made in the 1968 model were indeed improvements. The second thing that Figs. 14-16 show is that the seasonal variations are quite small. In fact in some cases

(T-TD)850

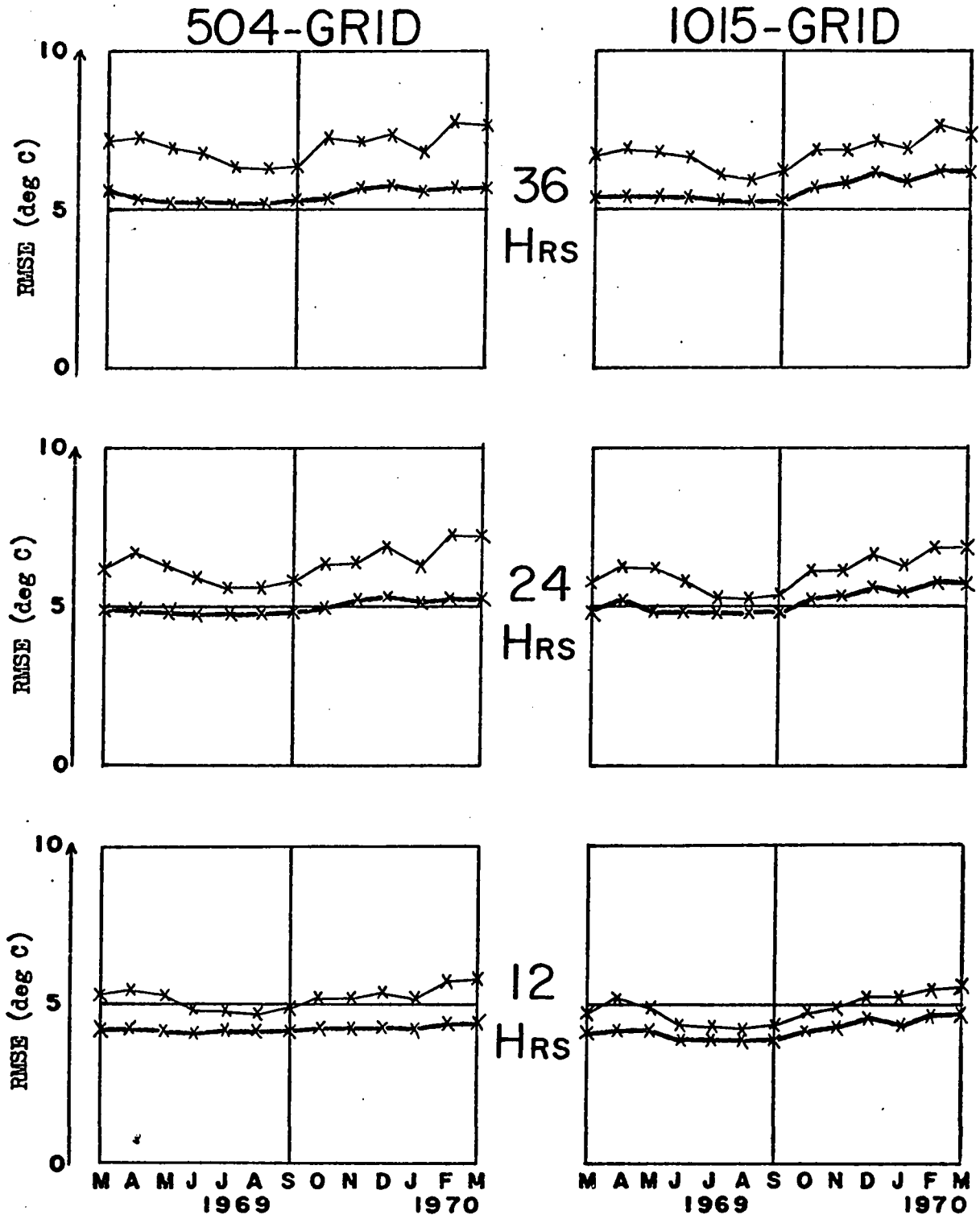


FIG 14: Monthly mean root-mean-square error (RMSE) scores in deg C for the 12, 24 and 36-hour forecasts of 850mb dew point depression, together with the corresponding persistence scores. The diagrams on the left are for the 504-point grid, and those on the right are for the 1015-point grid. The thick curves are the forecast scores, and the thin curves are the persistence scores.

(T-TD)700

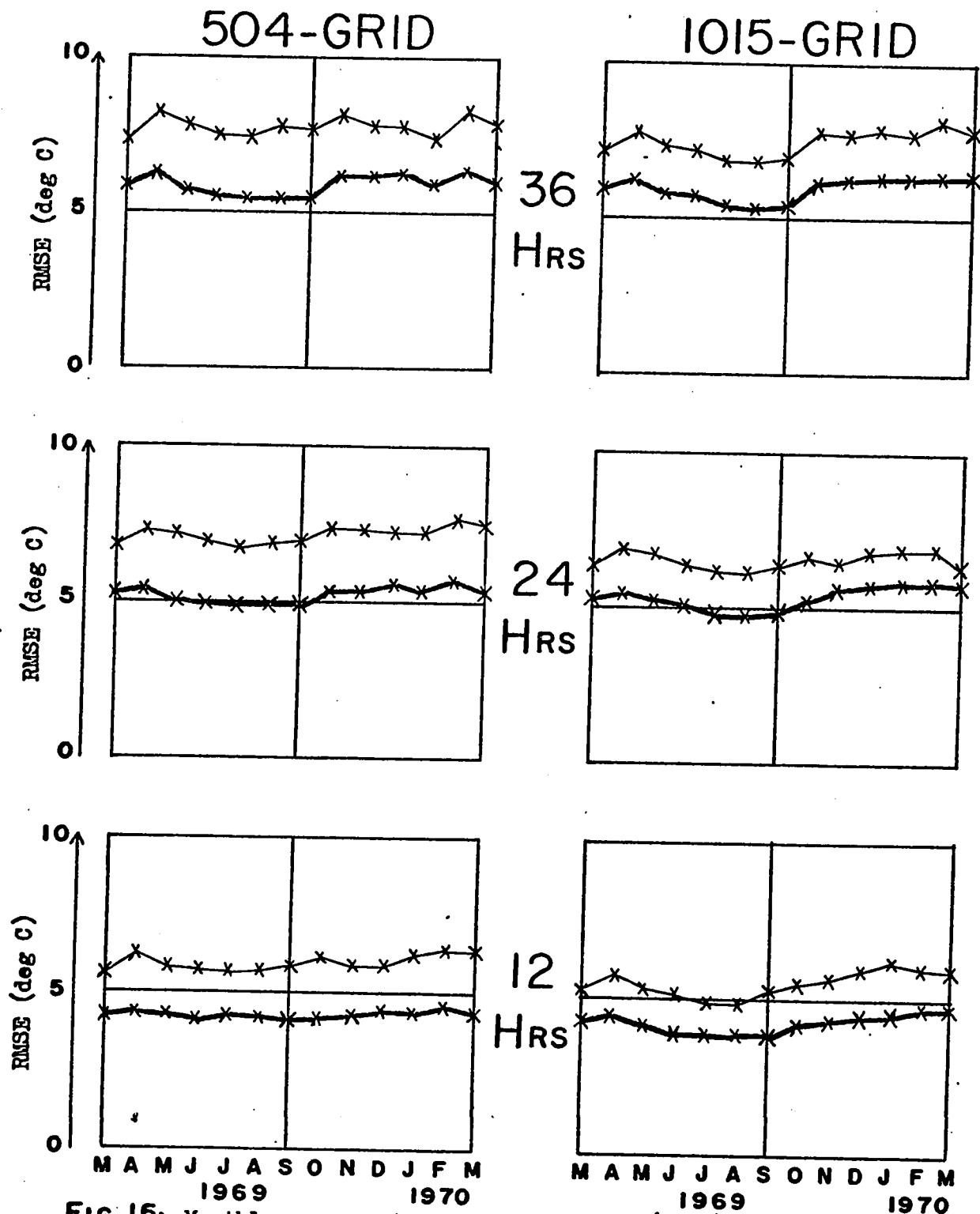


FIG 15: Monthly mean root-mean-square error (RMSE) scores in deg C for the 12, 24 and 36-hour forecasts of 700mb dew point depression, together with the corresponding persistence scores. The diagrams on the left are for the 504-point grid, and those on the right are for the 1015-point grid. The thick curves are the forecast scores, and the thin curves are the persistence scores.

(T-TD)500

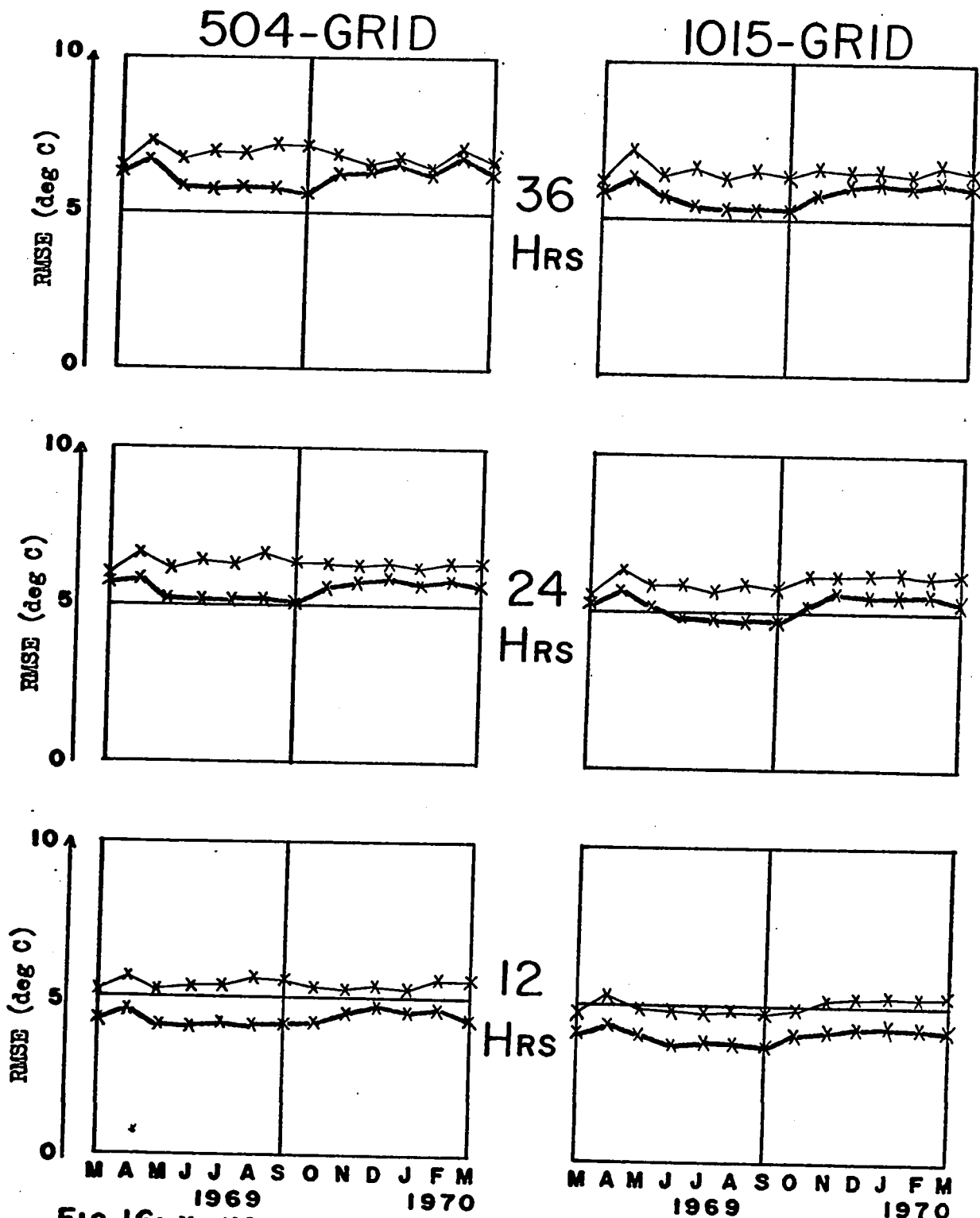


Fig 16: Monthly mean root-mean-square error (RMSE) scores in deg C for the 12, 24 and 36-hour forecasts of 500mb dew point depression, together with the corresponding persistence scores. The diagrams on the left are for the 504-point grid, and those on the right are for the 1015-point grid. The thick curves are the forecast scores, and the thin curves are the persistence scores.

the seasonal variations are so small that they are barely discernible. For example, the curve showing the 12-hour scores for the 850 mb forecasts over the 504-point grid is practically a straight line. Third, it is interesting to note that the worst dew point depression forecasts are at 500 mb. This was the level that had the best temperature forecasts. Fourth, a rather discouraging result, the forecast scores are quite poor at 12 hours. The best monthly mean 12-hour RMSE score for the dew point depression forecasts is 4 deg C. This is only slightly better than the worst monthly mean 36-hour RMSE score for the temperature forecasts. On the other hand, the dew point depression forecasts do not seem to deteriorate very rapidly after 12 hours. This behaviour, as anticipated, reflects the fact that all the forecast charts are much smoother than the verifying charts. The RMSE scores will not be discussed further here because they are an inadequate tool for evaluating dew point depression forecasts.

The characteristic areas verification program also monitored the mean errors of the forecast dew point depression charts. Typical winter and summer values for 36-hour forecasts originating at 00Z and 12Z are listed in Table 20. These results, which are for the 504-point grid, clearly reflect the failure to account for radiation effects in the 1968 model.

Subjective assessments of individual dew point depression forecasts lead to two main conclusions. First, the moist regions associated with active weather systems are handled quite well in a broad sense. However, the detailed fine structure which is associated with a single cyclone at initial time is soon reduced to a homogeneous blob of moisture. Second, as in the case of the temperature forecasts, the major errors in displacement

of the main moist regions seem to be associated with errors in the predicted height patterns rather than with errors in the moisture prediction scheme.

Level	Summer		Winter	
	00Z	12Z	00Z	12Z
850 mb	- 0.3	1.8	- 0.8	- 0.3
700 mb	- 0.3	1.0	- 1.4	- 0.9
500 mb	0.0	1.0	- 1.7	- 1.2

Table 20: Typical winter and summer values of the mean errors of the 36-hour dew point depression forecasts over the 504-point grid. The units are deg C.

The foregoing discussion has not been a wholly satisfactory one. This is because the problem of scale has obtruded much more forcefully than it did earlier with the other predicted quantities. Although the problem of scale was present with the forecasts of height, temperature, and vertical motion, it always seemed to be a secondary consideration. In the case of temperature, for instance, there was certainly more detail in the objectively analysed charts than any of the forecasts. But the loss of detail with time was a more gradual one, in the sense that the 12-hour temperature forecasts had a degree of smoothness which appeared to be roughly mid-way between that of the initial time charts and that of the 24-hour forecasts. One reason for this is that the objectively analysed temperature fields are themselves reasonably smooth to begin with. Another is that obvious fronts are among the more important details

appearing in the initial time temperature charts, and it is possible to follow the progression of these quite unambiguously in a series of forecast charts and also in the corresponding series of verifying analyses. In fact, it is precisely this continuity in time which provides strong evidence that the objective temperature analyses are of high quality. For it means that much of the detail which is present in the initial time temperature fields is both realistic and appropriate to the spacing of the standard grid. The same cannot be said of the dew point depression fields. Much of the detailed fine structure present in the objective analyses cannot be followed along from one synoptic time to the next with any degree of certainty. Only conglomerations of fine scale structures display good time continuity. In this respect the objective analyses of the dew point depression fields are more like the temperature gradient patterns associated with the objectively analysed temperature fields than they are like the actual temperature fields themselves. So it is no wonder that it is difficult to produce dew point depression forecasts with detailed fine structures which bear some resemblance to those of the verifying analyses. In any case, one can argue that detailed dew point depression forecasts are not really required for the prediction of large scale precipitation amount at the standard grid points. After all, as was explained earlier, formula (15.1) was designed to take care of large scale precipitation mechanisms associated with dynamic phenomena of dimension at least one order of magnitude smaller than cyclones. If this is true, then obviously there could be important implications for the objectively analysed dew point depression fields now being produced at the CAO. It could mean that the objective analysis procedures which work so well for height fields

and temperature fields should not in future be applied quite so freely to the dew point depression fields as they have been in the past. It could mean, perhaps, that the present objective analyses of dew point depression show details that are neither completely realistic nor fully appropriate to the spacing of the standard grid; and this could be one reason why such features show such poor time continuity. For instance, it is possible that the aliasing problem is much more acute for dew point depression fields than it is for temperatures, and that steps should be taken to compensate for this in some way. The reported dew point depression values certainly show much more vertical and horizontal variation than the reported temperature values in the vicinity of an active weather system. And it does seem unreasonable to expect these variations to be reflected faithfully in an objective analysis over the standard grid. Yet, on the other hand, Glahn and Lowry (1967), (1969) report quite convincingly that a detailed moisture analysis is of vital importance in getting more accurate precipitation forecasts, at least over short time periods. However, they do their moisture analysis and prediction over a fine scale grid, and they produce their precipitation forecasts for a fine scale grid, although their advecting winds are interpolated from the standard grid. This suggests that detailed objective analyses of moisture are only appropriate for finer grid scales than the standard one. Certainly, the aliasing problem would not be so acute for a fine grid. But the work of Glahn and Lowry also suggests that there is not much point in doing fine grid moisture analysis and prediction unless one also produces forecasts of precipitation amount for a fine grid. This is a topic which is outside the scope of the present thesis. However, as will be seen in the next Section, finer grids are not the only way of

coping with the problem of scale.

20. The Small Scale Precipitation Amount

20.1 The Empirical Approach

Computations based on (15.1) are only successful in predicting large scale precipitation amount. They completely fail to catch small scale shower activity due to heavy cumulus and cumulonimbus clouds. This inability to cope with convective showers is not a weakness which can be easily remedied by improving the resolution of the model. Even if the horizontal grid spacing were to be increased by two orders of magnitude, and even if there were enough reported observations to justify an objective analysis on this scale, there would still be little hope of simulating the internal dynamics of an individual heavy cumulus cloud. So, at least in the foreseeable future, fine grid forecasts based on (15.1) can only be expected to improve the resolution of the large scale precipitation patterns. They cannot be expected to cope with convective shower activity any more successfully than a standard grid model. Yet a professional meteorologist can predict the areas where showers are likely to occur in the next six hours. And he can do it reasonably well with the number of reporting stations that are now in existence. Essentially, then, his forecasts are based on a knowledge of what types of large scale configurations of the atmosphere lead to showers. So not only should a computer be able to predict showers too, but it should be able to do it for the standard grid. The weather forecaster's experience and practical knowledge have somehow got to be expressed in a form which can be handled by a computer. There is only one way this can be done. That is by resorting to the use

of empirical formulae. Empirical formulae are essential for predicting convective showers on a standard grid. And they are just as essential for predicting convective showers on a fine grid.

Three such empirical formulae are presented in the succeeding portions of this Section. However, these did not suddenly appear from nowhere in final form. They were developed in the following manner. First, the occurrence of convective precipitation was broken down into three categories: frontal showers, air mass showers, and induced instability showers. This was an important step because it meant that a different empirical formula would have to be developed for each category. Second, three "first guess" empirical formulae were postulated. These were fairly simple and based on practical forecasting experience. The third step was to amend the "first guess" formulae by trial and error. This was done by actually making forecasts on the computer, noting what the deficiencies were, and then attempting to correct them by changing the formulae. For instance, the "first guess" formulae would probably predict showers in some of the right places, but not in all of them. And they would also predict showers in many of the wrong places. So attempts would have to be made to introduce showers where they had been missed and eliminate them where they were not wanted. And, of course, any changes would have to be made without disturbing those areas where showers had been correctly forecast. What happened in practice was that most of the attempted changes made things worse rather than better. But some of the changes were beneficial. These eventually led to the following empirical formulae.

20.2 . Frontal Showers

The hourly precipitation amount due to frontal showers, Υ_f , is given by:

$$\Upsilon_f = \begin{cases} K_f U_p (T) (\Phi_1 - G_f) (w - w_f) (S - S_f^*) \Phi_4 & \text{if } (\Phi_1 - G_f) > 0 \text{ and } S < S_f \text{ and } w < w_f \text{ and } \Phi_2 > 0 \\ 0 & \text{if } (\Phi_1 - G_f) \leq 0 \text{ or } S \geq S_f \text{ or } w \geq w_f \text{ or } \Phi_2 < 0 \end{cases} \quad (20.2.1)$$

where

$$\Phi_1 = \frac{g}{f_0 K} \left| \langle \nabla T \rangle \right|^2 = \frac{K}{K_0} |\nabla T|^2 \quad (20.2.2)$$

$$\Phi_2 = \frac{g}{4 f_0 K} \langle \nabla^2 \psi \rangle = \frac{K}{K_0} \nabla^2 \psi \quad (20.2.3)$$

$$\begin{aligned} \Phi_3 &= \frac{1}{4} \left(\frac{g}{f_0 K_0} \right)^2 \left\langle \left(\frac{\partial T}{\partial y} \right)^2 \frac{\partial^2 T}{\partial x^2} + \left(\frac{\partial T}{\partial x} \right)^2 \frac{\partial^2 T}{\partial y^2} - \left(\frac{\partial T}{\partial x} \right) \left(\frac{\partial T}{\partial y} \right) \frac{\partial^2 T}{\partial x \partial y} \right\rangle \\ &= \left(\frac{K}{K_0} \right)^2 \left\{ \left[\frac{T}{y} \right] \left[\frac{T}{xx} \right] + \left[\frac{T}{x} \right] \left[\frac{T}{yy} \right] - \left[\frac{T}{x} \right] \left[\frac{T}{y} \right] \left[\frac{T}{xy} \right] \right\} \end{aligned} \quad (20.2.4)$$

$$\Phi_4 = (1 + a_f \Phi_2) \left(1 + b_f \frac{\Phi_3^2}{\Phi_1} \right) \quad (20.2.5)$$

and K_f , G_f , w_f , K_0 , S_f^* and S_f are constants given in Table 21. Physically, empirical formula (20.2.1) recognises the existence of small scale turbulent activity in the vicinity of significant horizontal

temperature gradients. This turbulent activity is presumed to give rise to showery precipitation provided that there is not too much large scale subsidence, provided that the air is not too dry, and provided that the relative vorticity is cyclonic. The amount of precipitation due to frontal showers is assumed to be dependent on the product of the following factors:

- (i) The unit condensation rate.
- (ii) The amount by which the square of the temperature gradient exceeds a threshold value.
- (iii) The amount by which the large scale vertical motion is less than a threshold value.
- (iv) The amount by which the dew point depression is less than some specified value.

In addition there is assumed to be a slight linear dependence on the relative vorticity; and also on the square of the second spatial derivative of the temperature taken in a direction perpendicular to that of the temperature gradient, to further enhance the precipitation amounts in the neighbourhood of troughs (troughs of warm air aloft). Formula (20.2.1) was originally developed for the octagon model, but it has been carried over to the 1970 model unchanged. In particular, the constants of Table 21 still retain their original values. The effectiveness of this approach to the prediction of frontal showers is discussed in Section 22.

20.3 Air Mass Showers

The hourly precipitation amount due to air mass showers, τ_a , is given by:

$$\gamma_a = \begin{cases} K_a U_p(T) (t_a - 12)(24 - t_a) (I_a^* - I')^2 (w - w_a)(S - S_a^*) & \text{if } I' < I_a \text{ and } w < w_a \text{ and } S < S_a \text{ and } 12 < t_a < 24 \\ 0 & \text{if } I' \geq I_a \text{ or } w \geq w_a \text{ or } S \geq S_a \text{ or } t_a \leq 12 \end{cases} \quad (20.3.1)$$

where t_a is the local time-of-day, in hours, as computed from the longitude,

$$I' = \begin{cases} I_a^{**} & \text{if } I < I_a^{**} \\ I & \text{if } I \geq I_a^{**} \end{cases} \quad (20.3.2)$$

$$w_a = \begin{cases} 1 & \text{if } w_a^* \leq 1 \\ w_a^* & \text{if } 1 < w_a^* < 10 \\ 10 & \text{if } w_a^* \geq 10 \end{cases} \quad (20.3.3)$$

$$K_a = (1 - b_a \cos \alpha_a) K_a^* \quad (20.3.4)$$

$$w_a^* = 10 \Phi_1 / (G_f)_{70} \quad (20.3.5)$$

$$\alpha_a = 2\pi n_a / 365 \quad (20.3.6)$$

n_a is the day of the solar year, counting from the winter solstice, Dec. 21 st, and b_a , K_a^* , S_a , S_a^* , I_a , I_a^* and I_a^{**} are constants given in Table 21.

Physically, empirical formula (20.3.1) recognises the existence of afternoon air mass shower activity in areas of fairly unstable Showalter Index, provided there is not too much large scale subsidence, and provided the air is not too dry. The amount of precipitation due to air mass showers is assumed to depend on the product of the following factors:

- (i) The season of the year.
- (ii) The unit condensation rate.
- (iii) A quadratic function of local time-of-day with a maximum at 1800 hours.
- (iv) The square of the amount by which the Showalter Index is less than some specified value.
- (v) The amount by which the large scale vertical motion is less than some threshold value, which itself has some dependence on the temperature gradient.
- (vi) The amount by which the dew point depression is less than some specified value.

The air mass shower formula which was originally developed for the octagon model differed slightly from (20.3.1) in two respects. First, there was no seasonal variation. Second, Eastern Standard Time was used instead of local time-of-day. Both changes were incorporated into the 1968 model. The values of K_a^* , S_a , S_a^* , I_a , I_a^* and I_a^{**} in Table 21 have not been changed since the work on the octagon model was carried out. Though, of course, the seasonal variation coefficient, b_a , was effectively set to zero for the octagon model.

Constant	Units	Level	Value	Conditions
K_o	$\text{dkm}^{-1} \text{hr}^{-1}$	all	7.063×10^{-3}	-
K_f	$\text{C deg}^{-3} (2 \times \text{grid distance})^2$	all	4.762×10^{-4}	-
W_f	mb hr^{-1}	all	10	-
G_f	$\text{C deg}^2 (2 \times \text{grid distance})^2$	850 mb	150	Initial time Values only. These are augmented by 2% per hour.
G_f	$\text{C deg}^2 (2 \times \text{grid distance})^2$	700 mb	50	
G_f	$\text{C deg}^2 (2 \times \text{grid distance})^2$	500 mb	50	
S_f	C deg	all	10	-
S_f^*	C deg	all	12	-
a_f	dkm^{-1}	all	0.1	-
b_f	C deg^{-2}	all	0.2	$\bar{\Phi}_3 > 0$
b_f	C deg^{-2}	all	0	$\bar{\Phi}_3 \leq 0$
I_a	C deg	850 mb	3	-
I_a	C deg	700 mb	3	-
I_a	C deg	500 mb	2	-
I_a^*	C deg	all	3	-
I_a^{**}	C deg	all	-3	-
S_a	C deg	all	10	-
S_a^*	C deg	all	12	-
b_a	-	all	0.3	-
K_a^*	$\text{hr}^{-2} \text{C deg}^{-3}$	850 mb	0.289×10^{-3}	-
K_a^*	$\text{hr}^{-2} \text{C deg}^{-3}$	700 mb	0.289×10^{-3}	-
K_a^*	$\text{hr}^{-2} \text{C deg}^{-3}$	500 mb	0.521×10^{-3}	-
K_i	C deg^{-2}	850 mb	0.444	-
K_i	C deg^{-2}	700 mb	0.444	-
K_i	C deg^{-2}	500 mb	1.0	-

Table 21 : Values of the constants used in the empirical formula for frontal showers, air mass showers, and induced instability showers. (Note: $\bar{\Phi}_3$ is defined by (20.2.4))

20.4 Induced Instability Showers

The hourly precipitation amount due to induced instability showers,

τ_i , is given by:

$$\tau_i = \begin{cases} K_i (I_a - I')^2 (\tau_l + \tau_f) & \text{if } I' < I_a \\ 0 & \text{if } I' \geq I_a \end{cases} \quad (20.4.1)$$

where I' is given by (20.3.2) and the values of K_i and I_a are given in Table 21. The symbols τ_l and τ_f , of course, respectively denote the amounts of large scale precipitation and frontal shower precipitation.

Physically, empirical formula (20.4.1) recognises that shower activity is induced in large scale precipitation and along fronts when the Showalter Index takes on unstable values. The values of K_i given in Table 21 were the ones used in the 1968 and 1970 models. In the octagon model the same value of K_i was used at 500 mb, but 0.556 C deg^{-2} was used at 850 and 700 mb.

21. The Total Precipitation

The total hourly precipitation amount for a layer, τ^* , is computed from the following formula:

$$\tau^* = \begin{cases} \tau' & \text{if } \tau' < \hat{\tau} \\ \hat{\tau} & \text{if } \tau' \geq \hat{\tau} \end{cases} \quad (21.1)$$

where

$$\tau' = \tau_l + \tau_f + \tau_a + \tau_i \quad (21.2)$$

and $\hat{\gamma}$ is 0.05556 inches. In other words, the total hourly precipitation for a layer is computed by simply adding the three small scale amounts to the large scale amount, except that it is not allowed to exceed $\hat{\gamma}$. The value of $\hat{\gamma}$ was chosen so that the maximum 24-hour precipitation at a single grid point would be 4 inches. In practice, the restriction is enforced in two stages. First, γ_p is not allowed to exceed $\hat{\gamma}$. And then, later, the sum of the three small scale components is not allowed to exceed $(\hat{\gamma} - \gamma_p)$. Diagnostic counts of the numbers of times these restrictions are imposed are printed out after each run. These show that the large scale precipitation amount has never been restricted at 850 mb at any time of the year, and that it has never been restricted at 700 and 500 mb during the summer months. Even in winter, the large scale precipitation amount is only occasionally restricted at 700 mb; the greatest number of restrictions ever imposed at this level in a 36-hour run was 29. At 500 mb, on the other hand, the number of large scale restrictions seems to depend on the synoptic situation. Periods of ten or twenty days with 10 to 40 restrictions per 36-hour run are interspersed with similar periods of no restrictions. The greatest number of restrictions ever imposed at 500 mb was 184, but there have only been three counts over 100. The small scale precipitation amount at each level is restricted about 50 to 250 times in most 36-hour runs. On the average, that works out to be about 4 grid points/hour, or less than 1% of the grid/hour. The maximum numbers of small scale precipitation restrictions that have been recorded so far are 939 at 850 mb, 678 at 700 mb, and 764 at 500 mb. In effect, the restrictions on the total precipitation amount reflect the fact that the three formulae (20.2.1), (20.3.1) and (20.4.1) comprise

linear relationships which cease to be valid when γ' approaches $\hat{\gamma}$. Essentially, the problem is that only a limited amount of moisture can be precipitated out of the atmosphere, and linear formulae must break down as this value is approached. The three formulae should really be non-linear, of course, but for practical purposes an artificial lid serves almost as well as an upper limit imposed by non-linearity.

The total hourly precipitation amount received at the ground is usually, but by no means invariably, the sum of the total precipitation amounts falling out of each of the three layers. The exceptions arise because two corrections may be applied to the layer totals. The first of these corrects for the presence of mountains, and the second for evaporation into a dry layer. The mountain correction is in itself quite a straightforward one. If the mountains actually project up into the 150 mb layer centred at 850 mb, then the total precipitation falling out of that layer is cut down proportionately. Obviously, precipitation cannot fall out of the inside of a mountain. Similarly, if $P_9 < 775$, reductions are made in the total precipitation amount falling out from the 150 mb layer centred at 700 mb. In formula form, the mountain reduction factors at 850, 700 and 500 mb, M_{85} , M_{70} and M_{50} , respectively, are defined by:

$$\begin{aligned}
 M_{85} &= \begin{cases} 1 & \text{if } P_9 \geq 925 \\ \left(\frac{P_9 - 775}{150} \right) & \text{if } 925 > P_9 > 775 \\ 0 & \text{if } P_9 \leq 775 \end{cases} \\
 M_{70} &= \begin{cases} 1 & \text{if } P_9 \geq 775 \\ \left(\frac{P_9 - 625}{150} \right) & \text{if } P_9 < 775 \end{cases} \\
 M_{50} &= 1
 \end{aligned} \quad (21.3)$$

There are no mountains as high as 700 mb in the 504-point grid. Consequently, M_{70} never becomes zero and the 500 mb precipitation is never reduced at all. Note that these mountain reduction factors are something quite different to the mountain dependence of S^* described in Section 15. In the absence of mountains, the total precipitation amount falling out of the 500 mb layer is multiplied by an evaporation reduction factor $(1 - E_{70}^{50})$ if $S_{70} > S^*$; and by a further reduction factor $(1 - E_{85}^{50})$ if $S_{85} > S^*$. Similarly, the total precipitation amount falling out of the 700 mb layer is multiplied by $(1 - E_{85}^{70})$ if $S_{85} > S^*$. The evaporation factors E_n^m are given by the following empirical formula:

$$E_n^m = \begin{cases} 0 & \text{if } S_n \leq S^* \text{ or } n \leq m \\ \frac{U_n(T_n)(S_n - S^*) \Psi_m}{A_n} & \text{if } S_n > S^* \text{ and } n > m \end{cases} \quad (21.4)$$

$n = 850, 700$
 $m = 850, 700, 500$

where

$$\Psi_n = \frac{\hat{T}}{100 \tau_n^*} + \frac{\tau_n^*}{\hat{T}} - 0.9 \left(\frac{\tau_n^*}{\hat{T}} \right)^2 \quad n = 700, 500 \quad (21.5)$$

S^* is given by (15.8), and not by (15.9), even when mountains are present, and where A_{85} is 0.0225 in units of (deg C) (inches of rain/hour for a layer 150 mb thick ascending at 1 mb/hour), i.e. the units of $S U_p(T)$, and A_{70} is 0.0192 in the same units. Due allowance has also to be made for the presence of mountains when the evaporation amounts are actually computed, so in practice the mountain and evaporation corrections are applied simultaneously. The total precipitation from a layer received at the ground, τ_n , is given by the following formula:

$$\tau_n = \begin{cases} \tau_n^{**} & \text{if } \tau_n^{**} \geq 0 \\ 0 & \text{otherwise} \end{cases} \quad (21.6)$$

where

$$\tau_n^{**} = M_n \tau_n^* (1 - E_{70}^n M_{70}) (1 - E_{85}^n M_{85}) \quad (21.7)$$

$n = 850, 700, 500$

The most noteworthy feature of the evaporation correction is the non-linearity of the Ψ_n given by (21.5). This innovation was first included in the 1970 model. It permits very light precipitation to be evaporated away completely, but does not greatly diminish heavy precipitation. The 1968 model had a similar evaporation correction, but Ψ was not evaluated by (21.5); instead the following linear formula was used:

$$\Psi_n = \frac{\tau_n^*}{\tau} \quad n = 700, 500 \quad (21.8)$$

This had two disadvantages. Light precipitation was not cut down enough, and heavy precipitation was reduced too much. No evaporation correction was included in the octagon model. The mountain correction has not been changed since it was first introduced in the octagon model.

It is a comparatively easy matter to classify the type of precipitation from each layer at each grid point according to the following criteria (which are expressed in Cdeg):

- (i) If $T_{85} \geq -3$, all layers rain.
- (ii) If $T_{85} < -3$ and $T_{70} \leq 0$, all layers snow.
- (iii) If $-10 \leq T_{85} < -3$ and $T_{70} > 0$, snow from 850 mb layer and freezing rain from the 700 and 500 mb layers.
- (iv) If $T_{85} < -10$ and $T_{70} > 0$, snow from the 850 mb layer and ice pellets from the 700 and 500 mb layers.

In practice, neither freezing rain nor ice pellets are ever forecast at a grid point.

Time integrated predictions of precipitation amount for 6-hour and 24-hour periods are obtained by adding the hourly totals received at the ground. In practice, it is convenient to add up the 6-hour amounts first, and then add four of these together to get the 24-hour amounts. Since the hourly amounts are assumed to be for centred time periods, the values every six hours straddle two six-hour periods and have to be divided up between them. No precipitation amounts are computed for the forward time-step which has to be taken at initial time. Nor are any computed for the 36 th hour. These small omissions are rectified by multiplying the 1-hour and 35-hour values by 1.5. For the purposes of verification it is very important to have a clear dividing line between precipitation and no precipitation. Trace amounts introduce an unwanted ambiguity and so they are eliminated in the following manner. After the 6-hour and the 24-hour totals have been computed, all grid-point values are examined for significance. If a 24-hour amount is greater than or equal to 0.01 inches, then that value is retained.

If a 24-hour amount is less than 0.01 inches but greater than or equal to 0.005 inches, and if one of the constituent 6-hour amounts is also greater than 0.005 inches, then the 24-hour value is reset to 0.01. Otherwise, if the 24-hour amount is non-zero it is reset to zero. Similarly, if a 6-hour amount is greater than or equal to 0.01 inches, it is left unchanged; if it is less than 0.01 inches but greater than or equal to 0.005 inches, it is reset to 0.01 inches; otherwise it is reset to zero if it is not already zero. Time integrated predictions of the large scale precipitation and each of the precipitation classes can be carried out in exactly the same way as for the total precipitation.

This completes the description of how the sequential precipitation forecasts are obtained. For convenience, the main steps in the process are summarised in the flow diagram of Fig. 17. So now it only remains to discuss how useful these forecasts are. This is a topic which is taken up in the next Section.

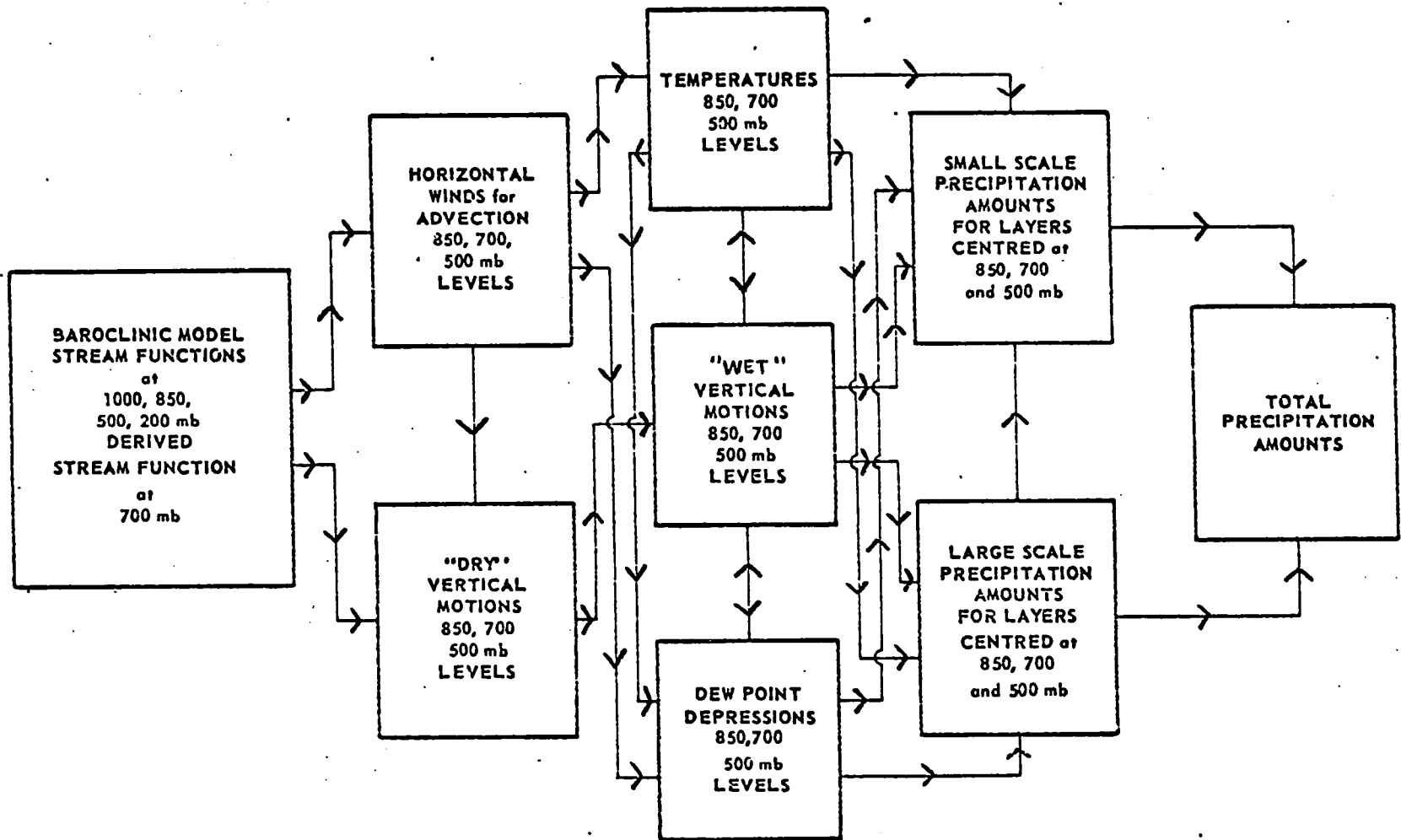


Fig. 17: A schematic representation of the main features of the precipitation scheme. The arrows indicate the direction of flow of information. All computations are performed on an hourly basis.

22. The Evaluation of the Operational Precipitation Forecasts

The precipitation forecasts issued operationally have been verified by two objective techniques. One of these involves the computation of threat scores. The other involves the computation of penalty table skill factors. When examining the results, it should be borne in mind that good forecasts lead to threat scores that are high, but to skill factors that are low. Further, whereas the level of zero skill is somewhat ambiguous for threat scores, because it depends quite strongly on the actual occurrence of precipitation, it is quite unequivocally 100% for the skill factors. In addition, the precipitation forecasts have been verified by various objective and semi-objective procedures in the Weather Centrals across Canada. And they have also been assessed subjectively on a day-to-day basis. It is perhaps worth pointing out here that RMSE scores are quite worthless for evaluating precipitation forecasts. This is partly because neither the predicted amounts nor their errors have normal distributions, and partly because they fail to take into account the crucial importance of the onset of precipitation.

The primary interest in objective verification scores, from the operation point of view, is to accumulate monthly mean figures on a long term basis. These should meet three requirements:

- (i) They should permit comparisons to be made with quantitative precipitation forecasts issued elsewhere.
- (ii) They should be sensitive enough to reflect improvements resulting from small to moderate modifications.
- (iii) They should monitor the performance of the precipitation forecasts with and without the small scale contributions.

The first requirement is fulfilled by the threat score evaluations. The second and third requirements are met to some degree by the penalty table skill factor assessments, and to a slightly lesser degree by the threat score evaluations.

The "threat score" is a simple but crude indicator of the usefulness of precipitation forecasts. In addition to simplicity, the other chief advantage of the threat score is that it is commonly quoted in the literature.

- (i) Precipitation forecasts at some particular selection of N_T stations are obtained by quadratic interpolation from the predicted grid-point values. These, of course, will be for a given time period which will almost invariably be 24 hours.
- (ii) Some particular threshold value of precipitation amount is specified; usually this will be 0.01 inches.
- (iii) A count is made of the number of stations, N_0 , at which the observed precipitation amount exceeds the threshold value. Each of these N_0 stations will be one of the original set N_T .
- (iv) A count is made of the number of stations, N_F , at which the interpolated forecast amount exceeds the threshold value. Again, each of these N_F stations will be one of the original N_T .

(v) A count is made of the number of "hits", N_H , i. e. the number of stations at which both the observed amount and the interpolated forecast amount exceed the threshold value.

(iv) The threat score is then given by:

$$\text{Threat Score} = \frac{N_H}{N_O + N_F - N_H} \times 100\% \quad (22.1)$$

And it is valid for the set of N_T stations, the given time period, and the specified threshold value.

A threat score of 100% therefore corresponds to a perfect forecast, and one of zero to a complete bust. There are two other special cases worthy of note. When zero precipitation is predicted everywhere the threat score is 0%. But when some precipitation is predicted for every grid point the threat score is $\frac{N_O}{N_T} \times 100\%$. So, probably, this is the threat score value which should be regarded as the borderline between skill and no skill. Although the threat score evaluation procedure described here is based on the use of station data, it could easily be adapted for grid-point data. However, nobody has actually computed threat scores for grid-points.

Unfortunately, the first precipitation forecasts issued operationally could not be verified on the computer. This was because the observed precipitation reports were not processed by the automatic data extraction (ADE) procedures at that time. Threat scores for a precipitation threshold of 0.01 inches were therefore computed manually for 57 selected Canadian stations. This was done once-a-day from December 1967 to September 1969 for forecasts of 00-24 hours and 12-36 hours which verified for the same time period. The ADE of observed precipitation reports began on an operational basis in August 1968. However, the handling of incorrect reports presented several small problems and it took over six months to discover these and take steps to circumvent them. Consequently, it was not until June 1969 that the threat scores for the 57 selected Canadian stations could be produced automatically by the computer on a twice-a-day basis. The automatic procedures, for the first time, also computed separate threat scores for the total precipitation forecasts and the large scale precipitation forecasts. Fig. 18 displays the resulting monthly mean threat scores for the total precipitation forecasts for the whole period from December 1967 to April 1970, including the four months overlap between the manual and automatic procedures. The thick curve is for the period 00-24 hours, and the thin curve is for 12-36 hours. The differences during the overlap period were partly due to the fact that the automatic threat scores were computed twice-a-day, at 00Z and at 12Z, whereas the manual ones were only computed at 12Z. They could also be partly attributed to certain practical difficulties in the manual procedure. When the threshold line passed through a station a subjective decision had to be taken about which side of the line it actually was. This kind of dilemma was compounded by the fact that the threshold line was traced from the original

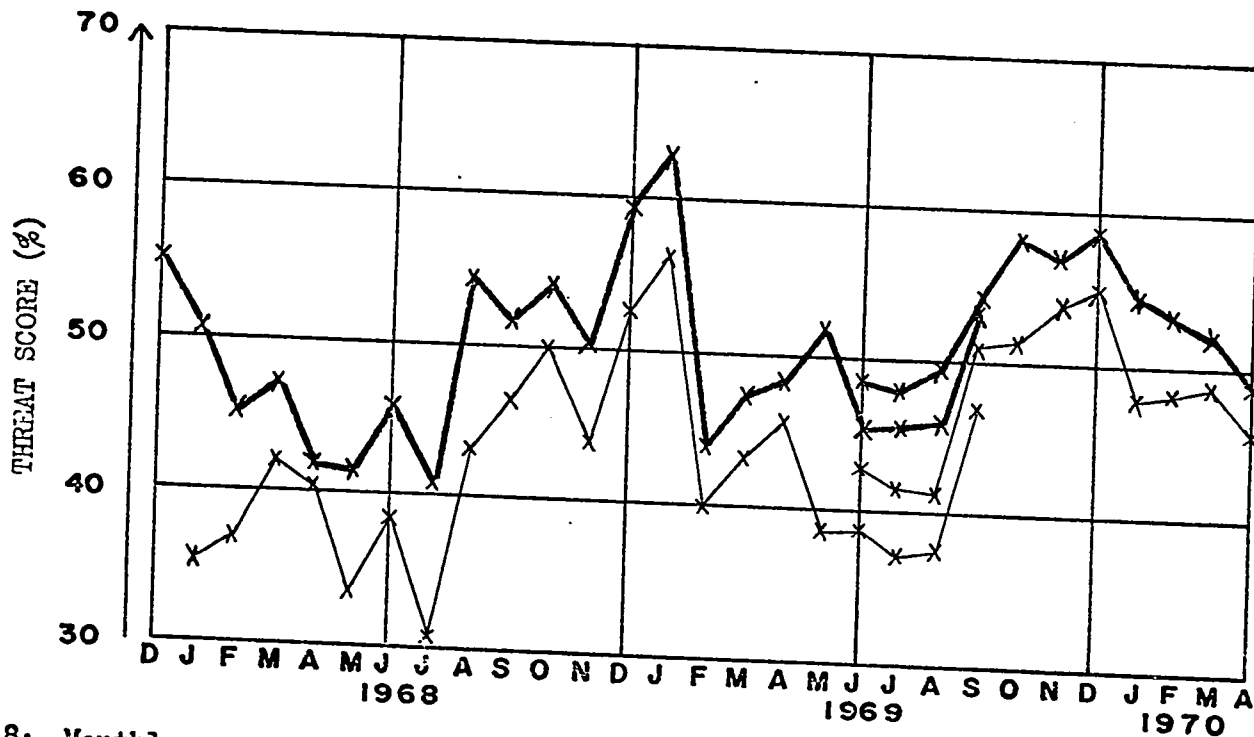


FIG 18: Monthly mean threat scores for the sequential forecasts of 24-hour total precipitation amount which were issued operationally in the period December 1967 to March 1970. These were calculated for 57 selected Canadian reporting stations. The thick curve is for the period 00-24 hours, and the thin curve is for 12-36 hours. The calculations were done manually until September 1969, and by computer from June 1969, so there was an overlap period of four months.

for the purposes of verification and so could easily be in error by a pencil thickness. Spot checks of many individual cases also revealed that the missing station lists of the manual and automatic computations did not match up very well. Sometimes the computer picked up stations missed by the manual extraction, and sometimes it was the other way round. The discrepancies usually seemed to make the automatic threat scores slightly higher than the manual ones. Monitoring the numbers of missing stations revealed some other surprises. First, about twice a month a large number of stations are missing, presumably due to communications troubles. To cope with this problem, all cases with more than 12 missing stations were excluded from the monthly means. In the remaining cases, i.e. the vast majority, the average number of missing stations was 4. So the statistics are really based on 53 stations and not on 57. Fig. 19 displays the monthly mean threat scores for total precipitation - the thick curves - and large scale precipitation - the thin curves - for June 1969 to March 1970; these results are still for the 57 selected Canadian stations. For 00-24 hours the only clearcut difference was in July when the total precipitation scored about 3% higher than the large scale. Out of the ten months the total precipitation scored higher five times, the large scale scored higher four times, and once they were the same. For 12-36 hours clearcut differences of about 2 to 3% showed up in July and August, and on both occasions they were in favour of the total precipitation. Out of the ten months, the total precipitation scored higher nine times, and lower once. Some associated frequency distributions are shown in Figs. 20, 21, and 22. Fig. 20 consists of two histograms showing the frequency distributions of the (total - large scale) threat score differences. Figs. 21 and 22 show the distribution of threat scores with precipitation occurrence for 00-24

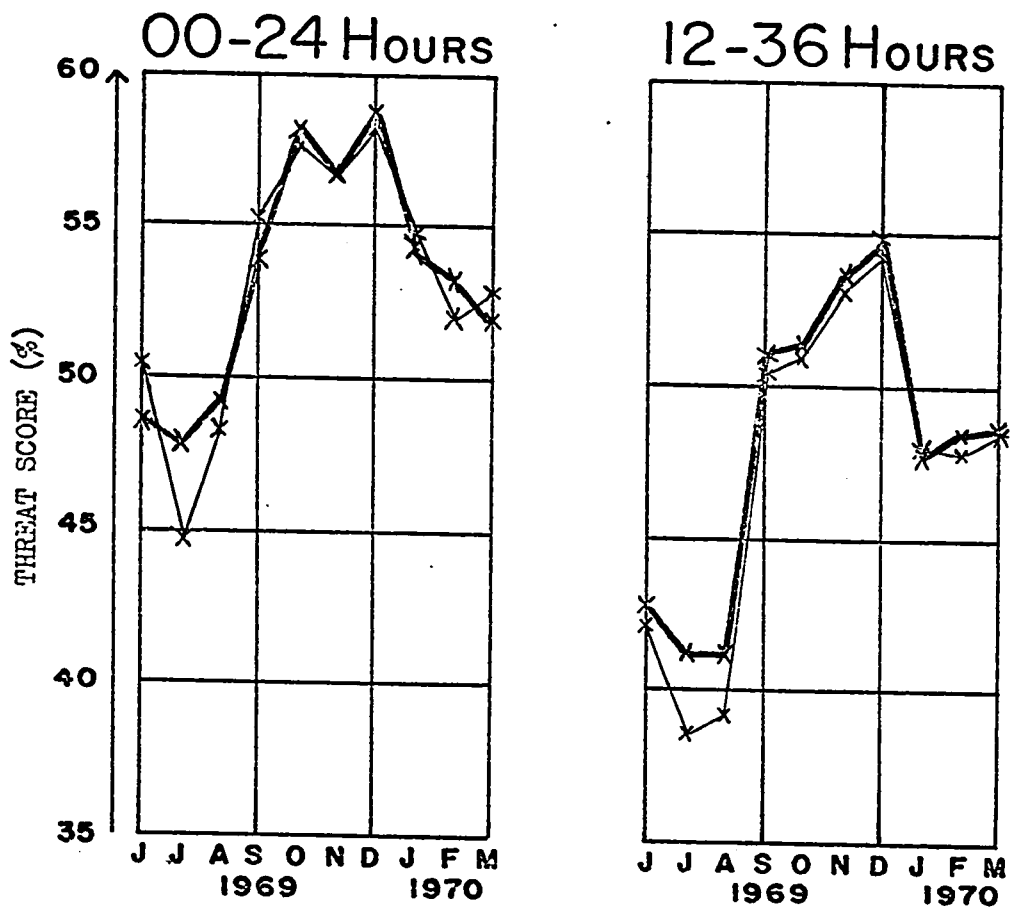


FIG 19: Monthly mean threat scores for the sequential forecasts of 24-hour precipitation amount which were issued operationally from June 1969 to March 1970. These were computed for 57 selected Canadian Stations. The thick curves are for the total precipitation forecasts, ie. the large scale precipitation plus the small scale precipitation, and the thin curves are for the large scale precipitation forecasts alone. The left hand diagram is for the period 00-24 hours, and the righthand diagram is for 12-36 hours.

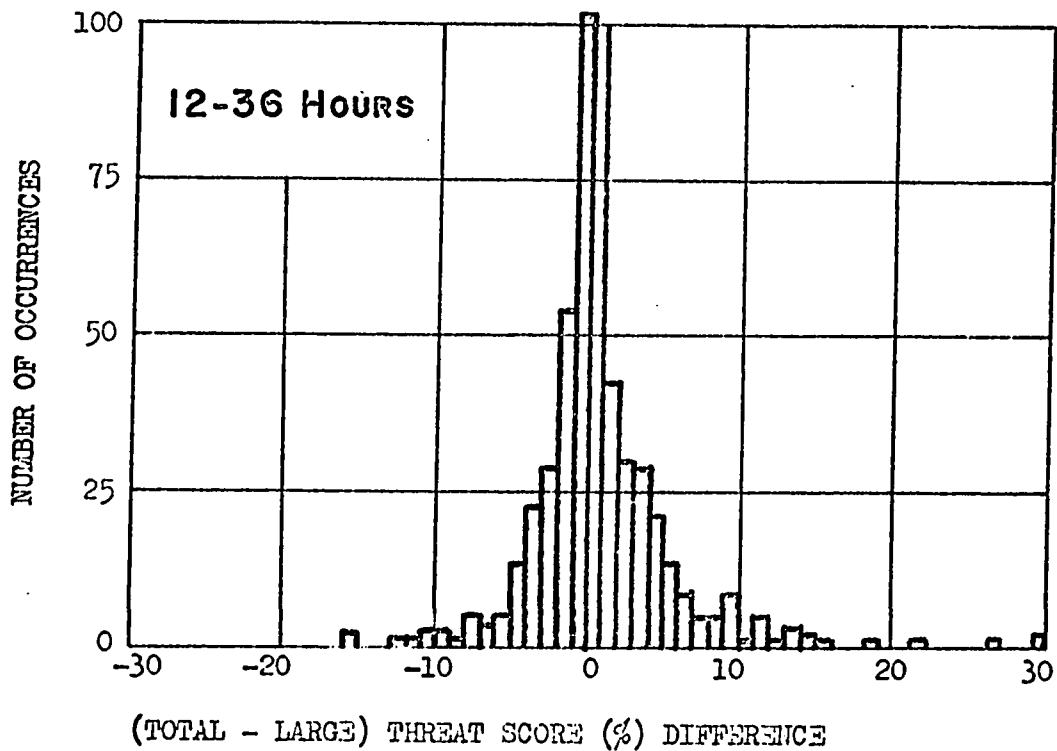
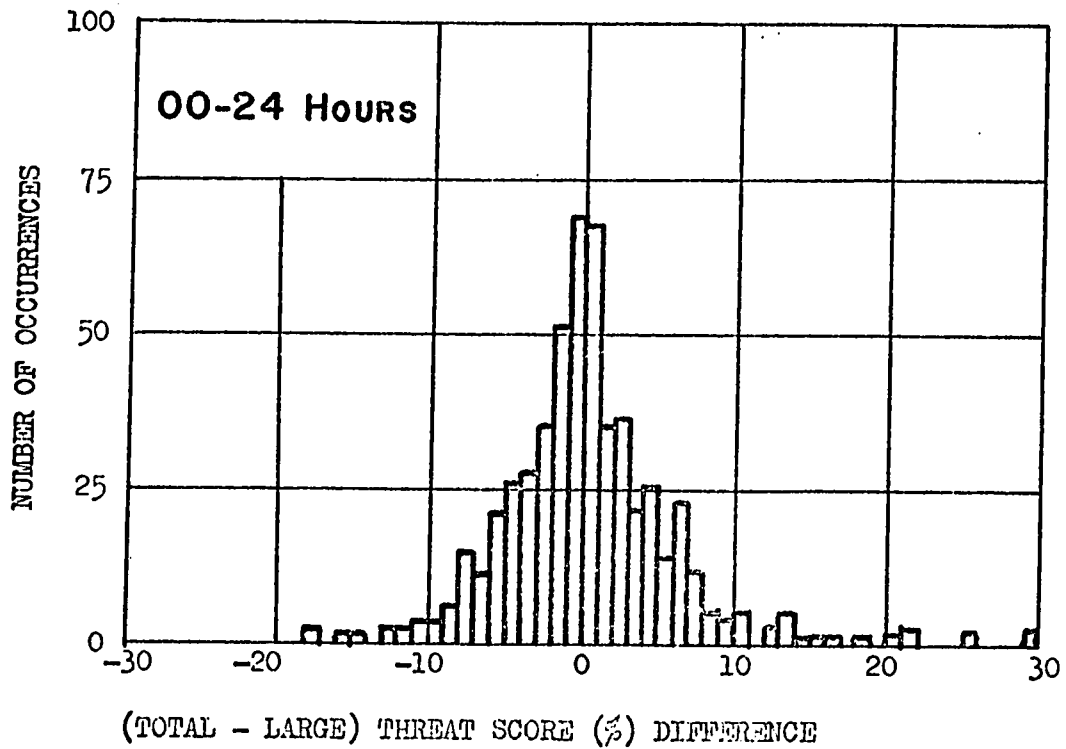


Fig 20: Histograms showing the frequency distributions of the (total-large) threat score (%) differences, for 57 selected Canadian stations, for the precipitation forecasts issued operationally in the period June 1969 to March 1970. The upper diagram is for 00-24 hours, and the lower one for 12-36 hours.

NUMBER OF STATIONS AT WHICH PRECIPITATION IS OBSERVED

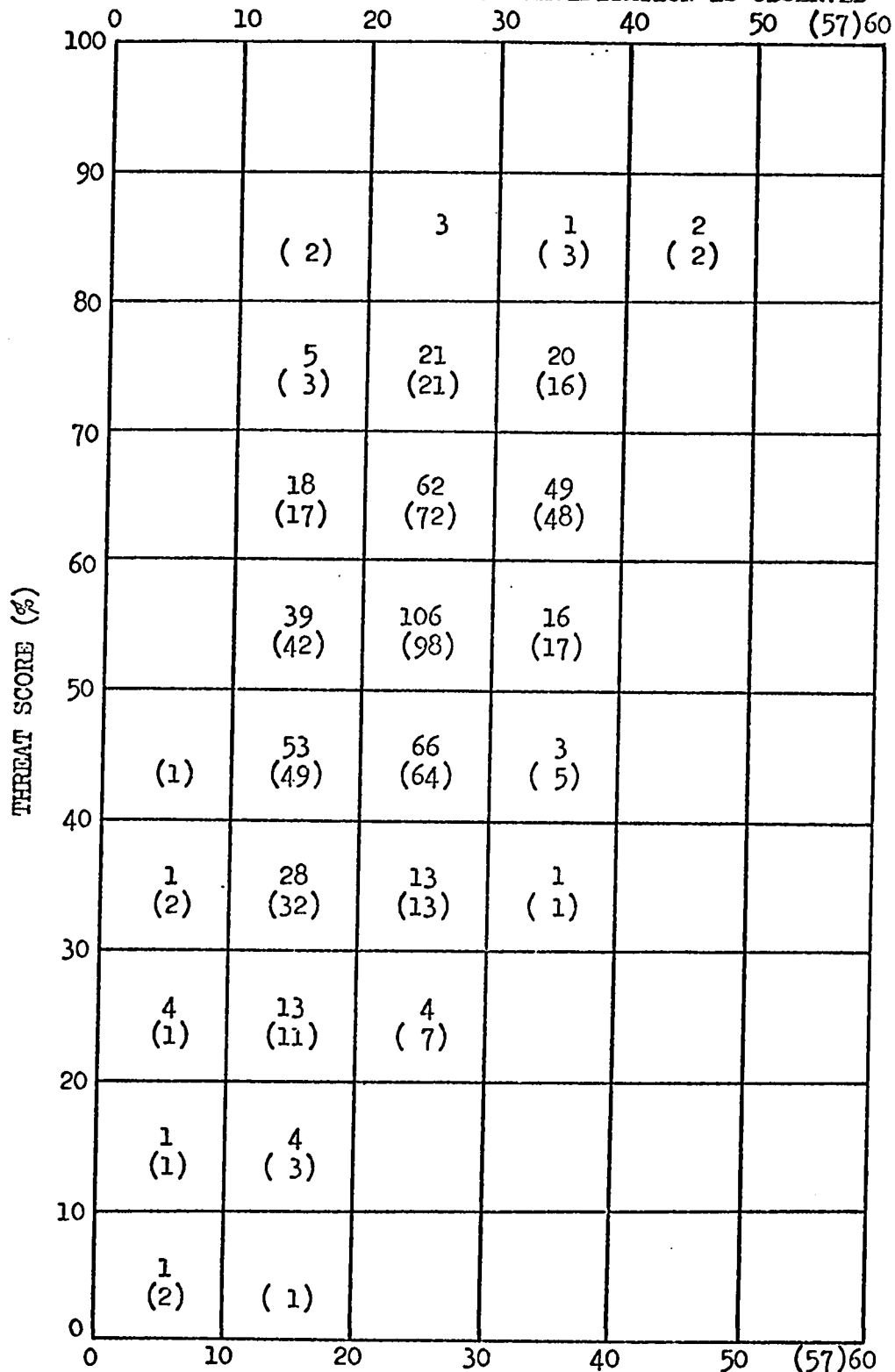


Fig 21: A diagram showing the frequency distribution of threat score with precipitation occurrence for forecasts of precipitation amount for 00-24 hours. The threat score value is given on the vertical axis, and the number of stations at which precipitation is observed is given on the horizontal axis. The unbracketed numbers in each box indicate the frequency distribution for total precipitation (large scale plus small scale), and the bracketed numbers are for large scale precipitation alone. These results are based on the threat score values which were computed for 57 selected Canadian reporting stations from June 1969 to March 1970.

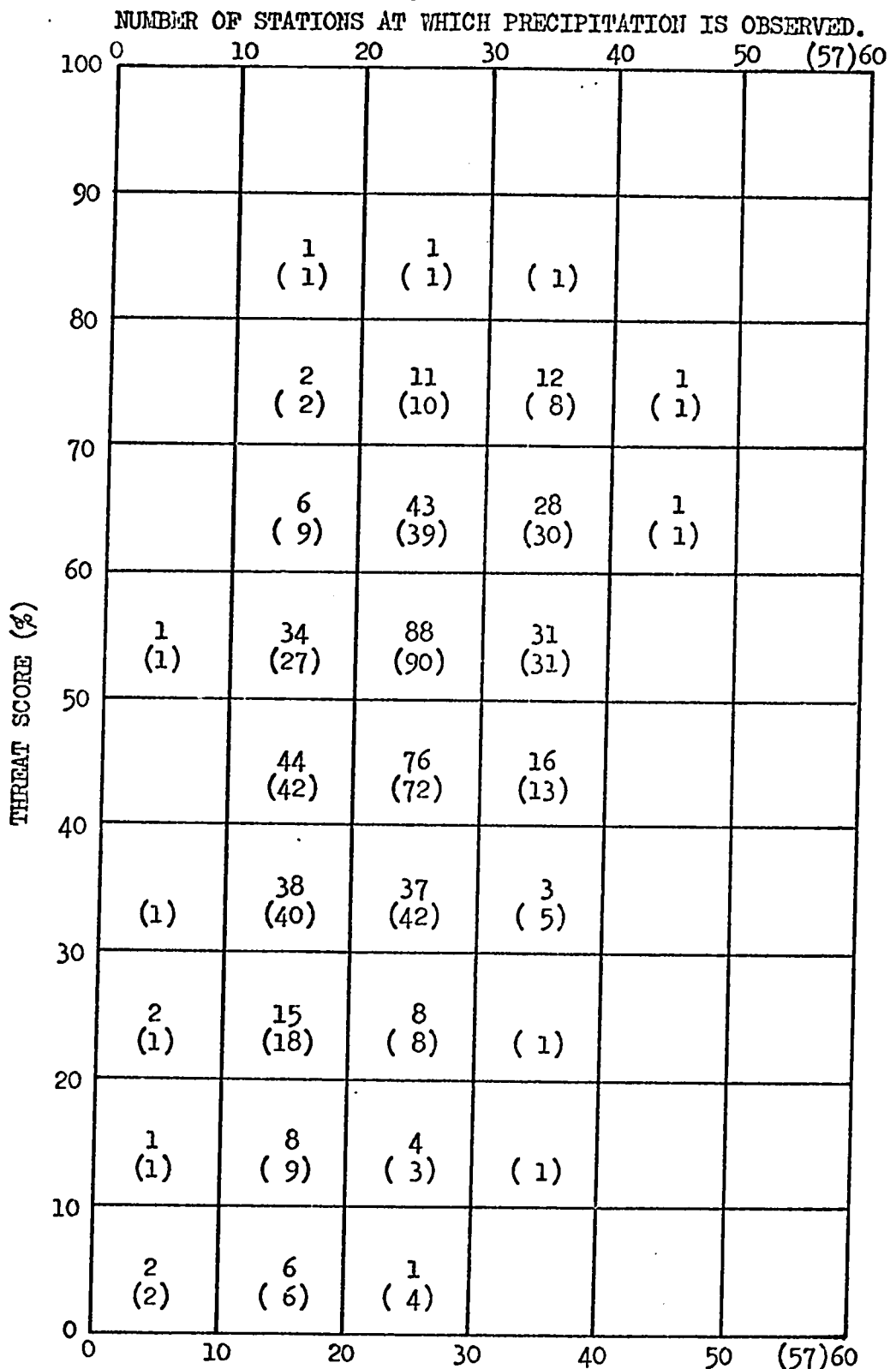


Fig 22: A diagram showing the frequency distribution of threat score with precipitation occurrence for forecasts of precipitation amount for 12-36 hours. The threat score value is given on the vertical axis, and the number of stations at which precipitation is observed is given on the horizontal axis. The unbracketed numbers in each box indicate the frequency distribution for total precipitation (large scale plus small scale), and the bracketed numbers are for large scale precipitation alone. These results are based on the threat score values which were computed for 57 selected Canadian reporting stations from June 1969 to March 1970.

and 12-36 hours respectively. The total distributions are indicated by the unbracketed numbers, and the large scale distributions by the bracketed ones. These three Figs. confirm that there are no pronounced differences between the threat score verifications of the total and large scale precipitation forecasts for 57 selected Canadian stations in the entire period June 1969 to March 1970. While this is broadly true for both 00-24 and 12-36 hours, there is some slight evidence that the small scale effects improve the forecasts for 12-36 hours. Figs. 20 and 21 do, however, demonstrate something else in a very striking fashion. They show that the computed threat score is correlated with occurrence of observed precipitation. And the correlation is such that a low threat score is just as likely to be an indicator of a dry day as it is of a poor forecast. Naturally, this does not help to increase one's confidence in threat score evaluations. The overall mean threat score for the total precipitation for 00-24 hours is about 50%, and for 12-36 hours about 44%. Both these figures are recognised as being quite high. However, it was realised that the geographical location of Canada might favour high threat scores. In summer, for instance, Canada probably tends to have more frequent occurrences of large scale precipitation than the United States, and less frequent occurrences of convective precipitation. Consequently, a more comprehensive threat score evaluation package was made available in August 1969. This was run twice-a-day for five months until hardware considerations led to its withdrawal from operational use. It computed threat scores for a precipitation threshold of 0.01 inches for all received Canadian reports, all received U. S. reports, and finally for all received North American reports. On the average, there were 182 Canadian reports and 200 U.S. ones. Fig. 23

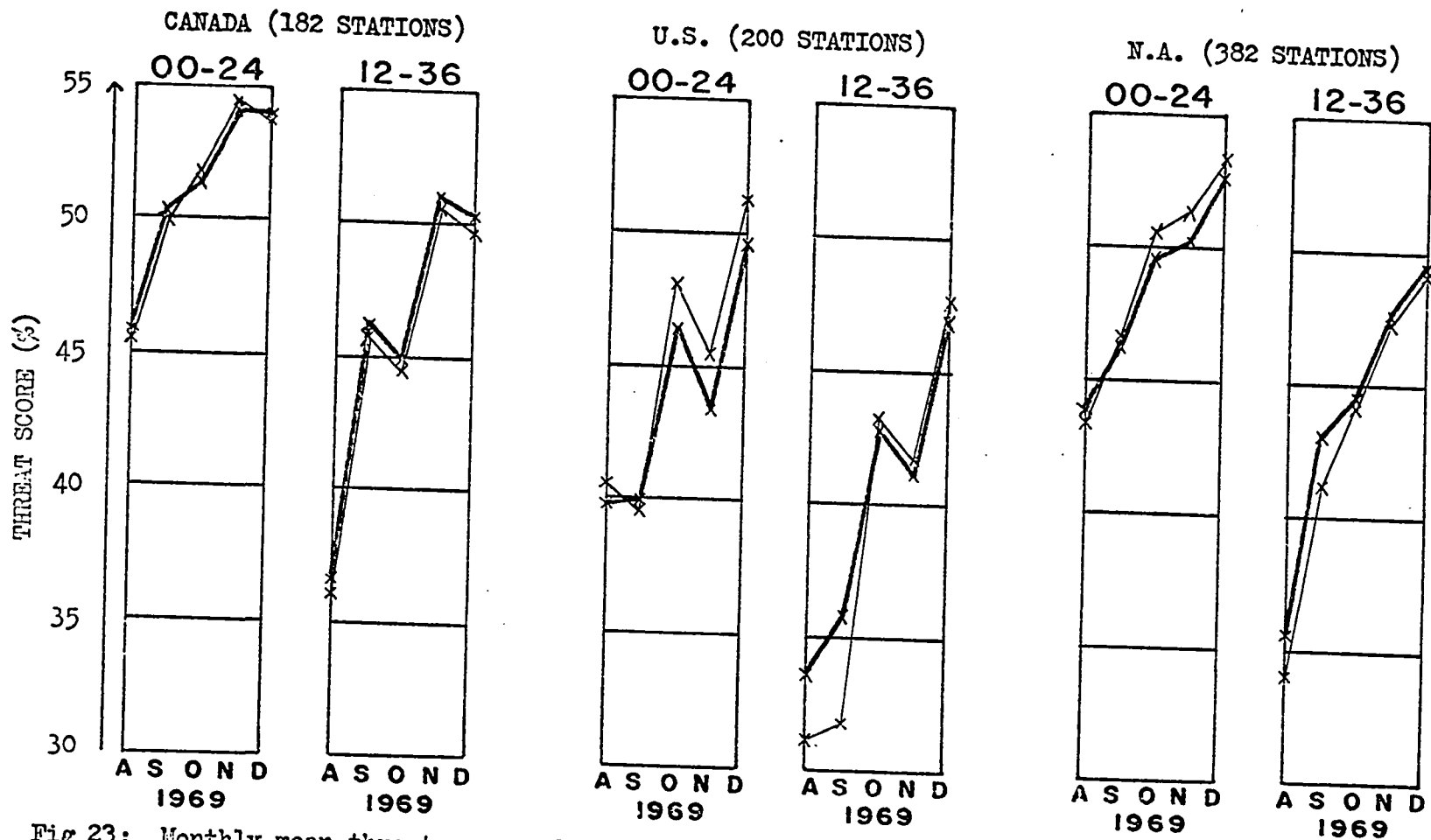


Fig 23: Monthly mean threat scores for the sequential forecasts of 24-hour precipitation amount which were issued operationally from August to December 1969. From left to right, the pairs of diagrams show results for 00-24 and 12-36 hours, first for all received Canadian reports, then for all received U.S. reports, and finally for all received North American reports. On the average there were 182 reports from Canada and 200 from the U.S. The thick curves are for the total precipitation forecasts, and the thin curves are for the large scale precipitation forecasts alone.

shows the monthly mean threat score values that resulted. Once again the thick curves are for total precipitation and the thin curves for large scale precipitation. The threat scores for all received Canadian stations were roughly 4% lower than those for the 57 selected Canadian stations. However, the general conclusions about the relative merits of the total and large scale precipitation forecasts remain unchanged. For 00-24 hours the total forecasts were slightly better than the large scale forecasts for three of the five months, and the reverse was true for the other two months. It is interesting to note that the relative results for total and large scale precipitation for September and October were interchanged in the two Canadian threat score computations; and also that the November scores were worse than October and December for the 57 selected stations, but better for all received Canadian stations. For 12-36 hours the total forecasts were slightly better than the large scale forecasts for all five months. The differences between the results for the 57 selected stations and all Canadian stations can be attributed to two sources. First, none of the 57 selected stations are north of latitude 60 N, whereas about 35 of the 182 all Canadian stations were in these northern regions. Second, the 57 stations were selected because their weather reports were judged to be among the most reliable ones in the populated areas of Canada, and at the same time not prone to precipitation from local effects. Both these factors will tend to reduce the threat scores for all Canadian stations. The inclusion of the northern stations will do so because there is less observed precipitation in the Arctic than in southern Canada. As Figs. 21 and 22 showed, the threat score is correlated to precipitation occurrence. And, of course, the inclusion of stations particularly prone to local effects will lower the threat scores because these are not taken into account in the forecasts. The threat scores

for all received U.S. stations were roughly 6% lower than those for all Canadian stations, and roughly 10% lower than those for the 57 selected Canadian stations. Further, the addition of the small scale effects reduced the threat scores for 00-24 hours by about 2% from October to December, and even slightly hurt the forecasts for 12-36 hours during these months. The threat scores for all received North American stations were intermediate between those for all Canada and all U. S. The more comprehensive evaluation package also computed threat scores for all received North American stations for thresholds of 0.25 inches, 0.5 inches and 1 inch. The corresponding monthly mean values are shown in Fig. 24. Once again the total precipitation is indicated by the thick curves, and the large scale precipitation by the thin curves. As one would expect, the threat scores drop off sharply with increasing threshold. In addition, the presence of the small scale effects becomes increasingly beneficial as one progresses to higher thresholds.

The second objective verification technique, which involves the computation of penalty table skill factors, is described fully in Appendix E. Briefly, though, the main features of the technique are as follows. Grid-point forecasts of precipitation amount are verified against objective grid-point analyses of the corresponding observed amounts. However, in order to obtain meaningful results, the analysed grid points are assigned to Class A, Class B or Class C, according as to whether the data coverage is good, fair, or poor. Skill factors are computed for two penalty tables. In the Table I verifications under-forecasting and over-forecasting are considered to be equally harmful. In the Table II verifications under-forecasting is considered to be twice

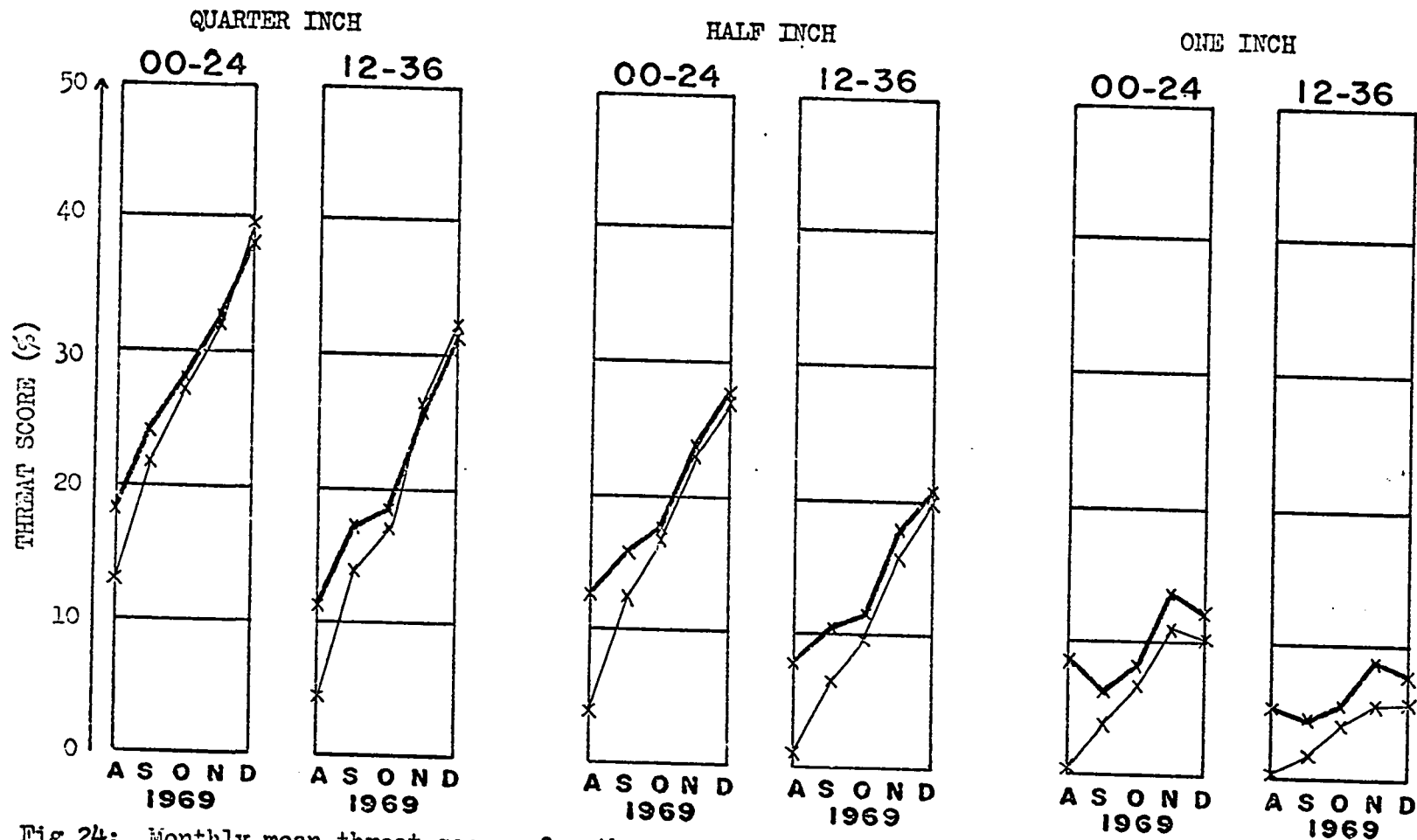


Fig 24: Monthly mean threat scores for the sequential forecasts of 24-hour precipitation amount which were issued operationally from August to December 1969. From left to right, the pairs of diagrams show results for 00-24 and 12-36 hours, first for a quarter inch threshold, then for a half inch threshold, and finally for a one inch threshold. All diagrams are based on all received North American reports, which averaged 382 during this period. The thick curves are for the total precipitation forecasts, and the thin curves are for the large scale precipitation forecast alone.

as harmful as over-forecasting. Operational skill factor verifications commenced when the precipitation reports were made available by the ADE procedures. Consequently, results are available for the 21-month period from August 1968 to April 1970. These are summarised here for the whole period, but it should be borne in mind that for the first six to nine months there were ADE problems of one sort or another. In the development work on the octagon model, as described in Davies (1967b), skill factors were computed for the 504-point and 238-point grids shown in Fig. 1. The smaller grid was introduced in the first place because comparisons had to be made with the precipitation forecasts produced by an automated version of the technique developed by Harley (1963) (1965) and Penner (1963), and these were only made available over the 238-point grid. However, some comparisons for different kinds of precipitation forecast had already been carried out for the 504-point grid, and so as a matter of interest these were repeated for the 238-point grid. Statistical significances of the differences between the various sets of forecasts were computed for both grids using applications of the Student "t" test described in Brooks and Carruthers (1953). Surprisingly, these differences were more significant for the 238-point grid than they were for the 504-point grid. At the time, the reason for this was thought to be that evaluations over the larger grid included stations in Alaska and Florida which were surrounded by no data areas, and which were also nearer to the boundaries of the stream function grid. Accordingly, arrangements were made to compute skill factors for both the 504-point grid and the 238-point grid in the operational run. Figs. 25 to 32 show results for the 238-point grid. Figs. 25, 26, 27 and 28 all show the monthly mean skill factors for

TABLE I

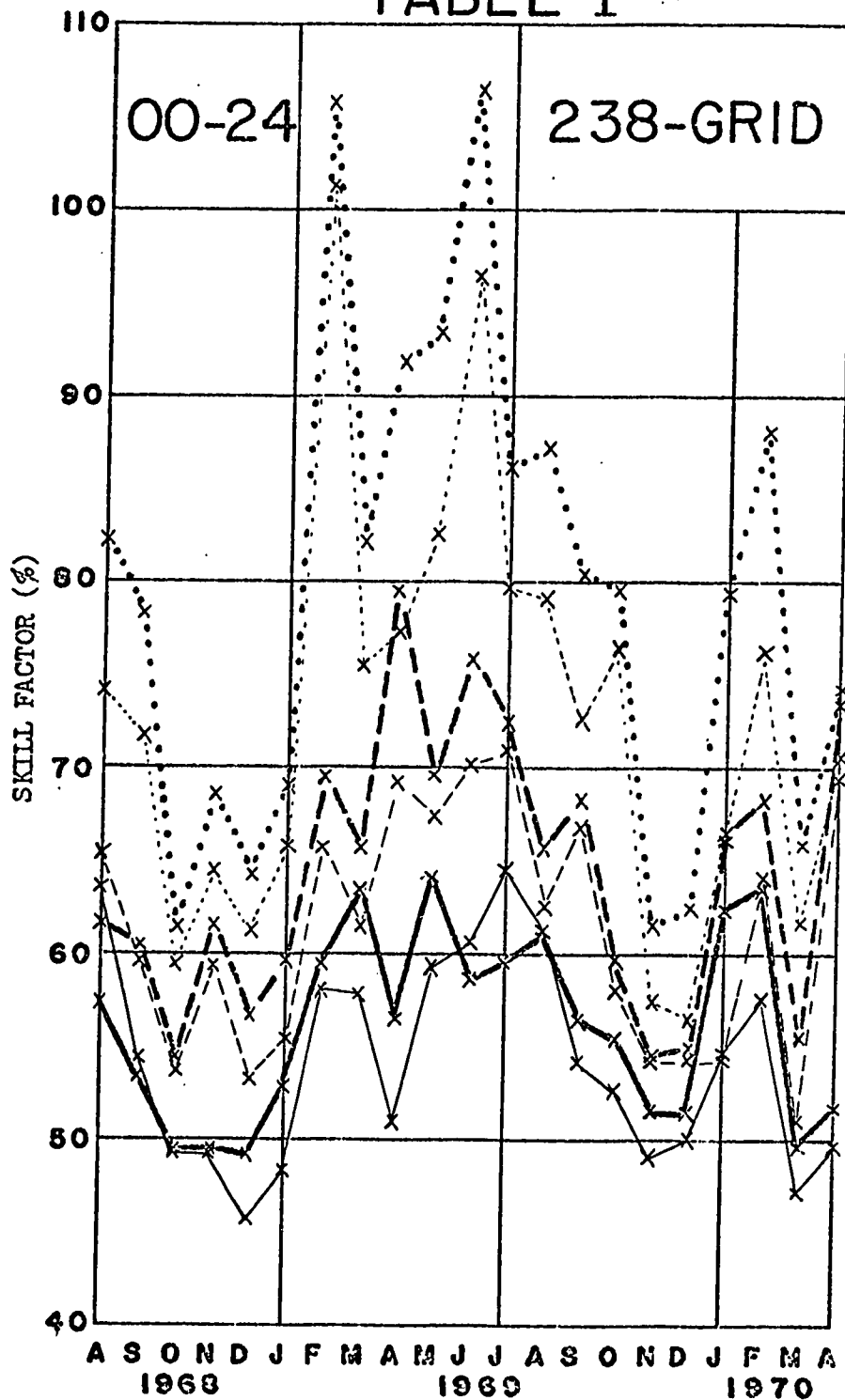


FIG 25: Monthly mean Table I skill factors for the sequential forecasts of precipitation amount for 00-24 hours which were issued operationally in the period August 1968 to April 1970. These results are for the 238-point grid. The thick curves are for total precipitation and the thin curves are for large scale precipitation. The two solid curves are for class A grid points, the two dashed curves for class B, and the two dotted curves for class C. On the average, there were 110 gridpoints in class A, 41 in class B, and 33 in class C.

TABLE II

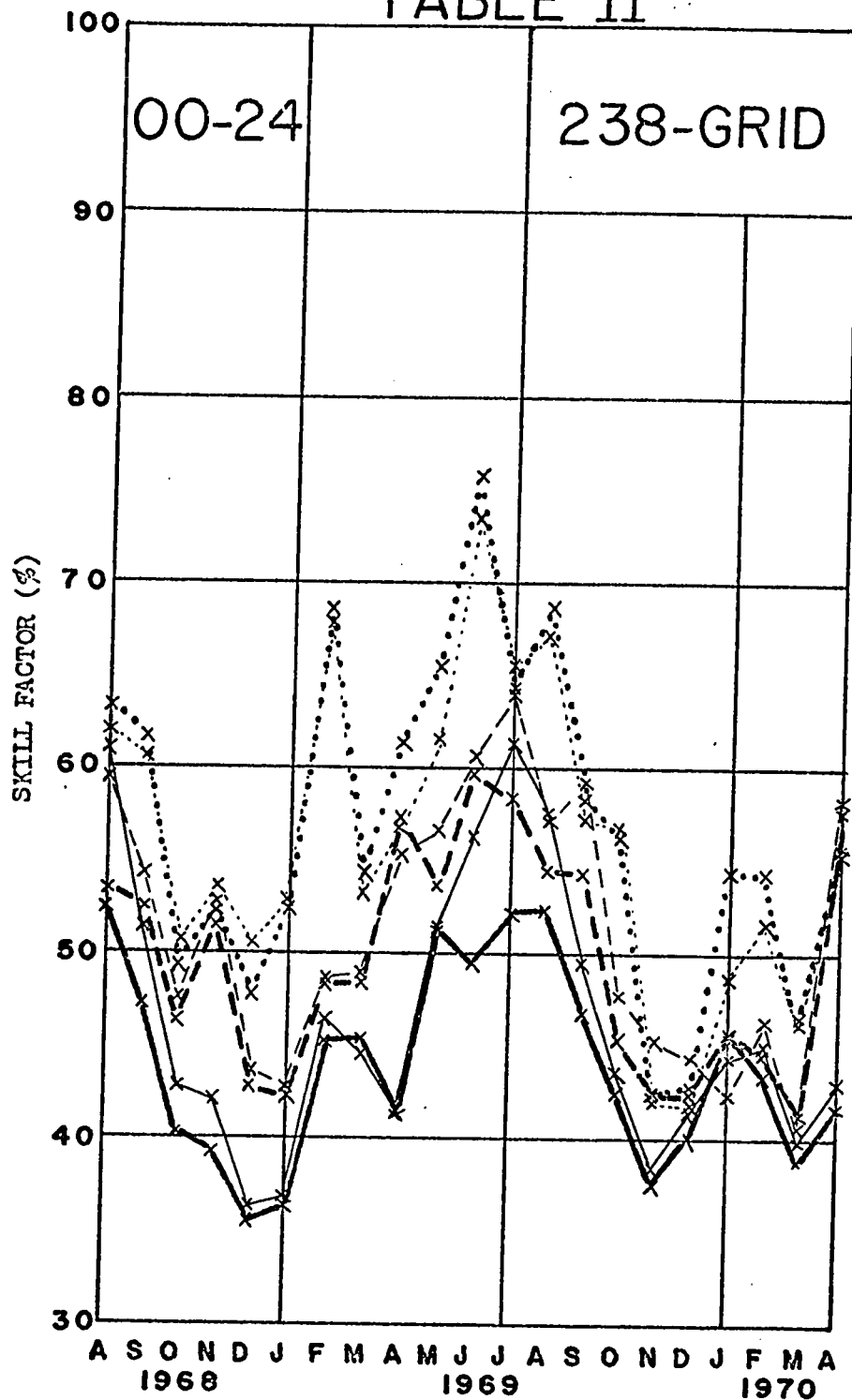


FIG 26: Monthly mean Table II skill factors for the sequential forecasts of precipitation amount for 00-24 hours which were issued operationally in the period August 1968 to April 1970. These results are for the 238-point grid. The thick curves are for total precipitation and the thin curves are for large scale precipitation. The two solid curves are for class A grid points, the two dashed curves for class B, and the two dotted curves for class C. On the average, there were 110 gridpoints in class A, 41 in class B, and 33 in class C.

TABLE I

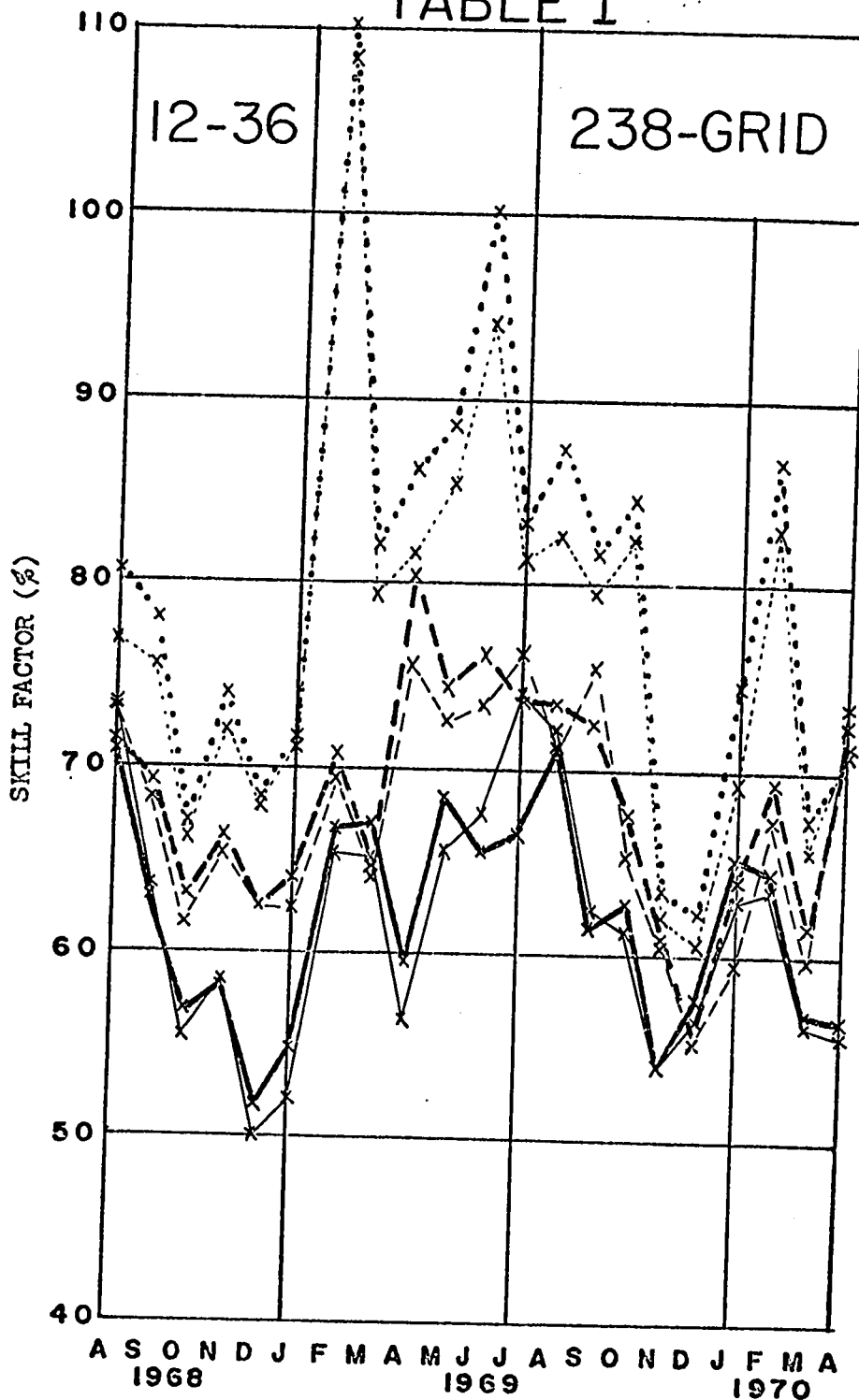


FIG 27: Monthly mean Table I skill factors for the sequential forecasts of precipitation amount for 12-36 hours which were issued operationally in the period August 1968 to April 1970. These results are for the 238-point grid. The thick curves are for total precipitation and the thin curves are for large scale precipitation. The two solid curves are for class A grid points, the two dashed curves for class B, and the two dotted curves for class C. On the average, there were 110 gridpoints in class A, 41 in class B, and 33 in class C.

TABLE II

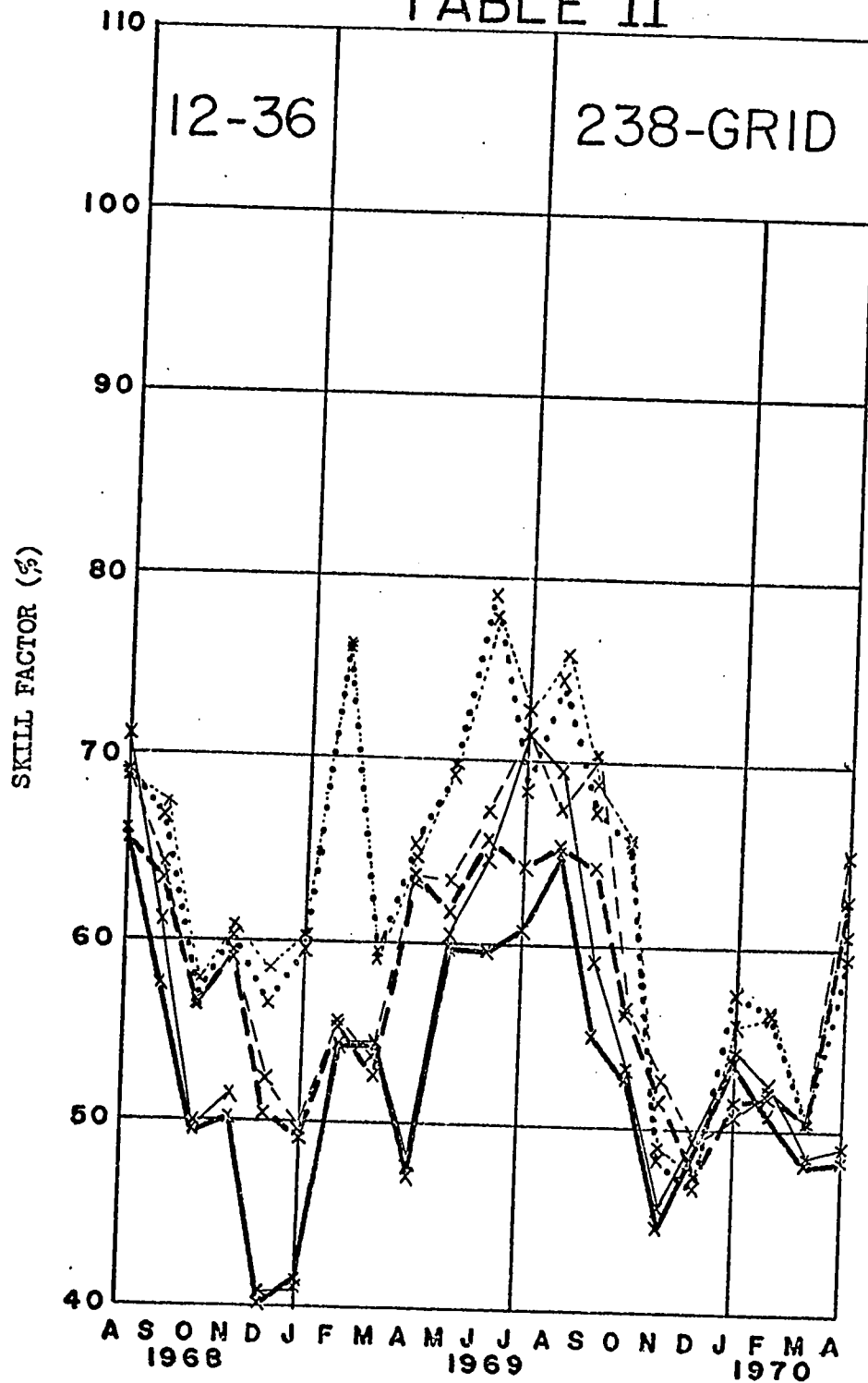


FIG 28: Monthly mean Table II skill factors for the sequential forecasts of precipitation amount for 12-36 hours which were issued operationally in the period August 1968 to April 1970. These results are for the 238-point grid. The thick curves are for total precipitation and the thin curves are for large scale precipitation. The two solid curves are for class A grid points, the two dashed curves for class B, and the two dotted curves for class C. On the average, there were 110 gridpoints in class A, 41 in class B, and 33 in class C.

TABLE I

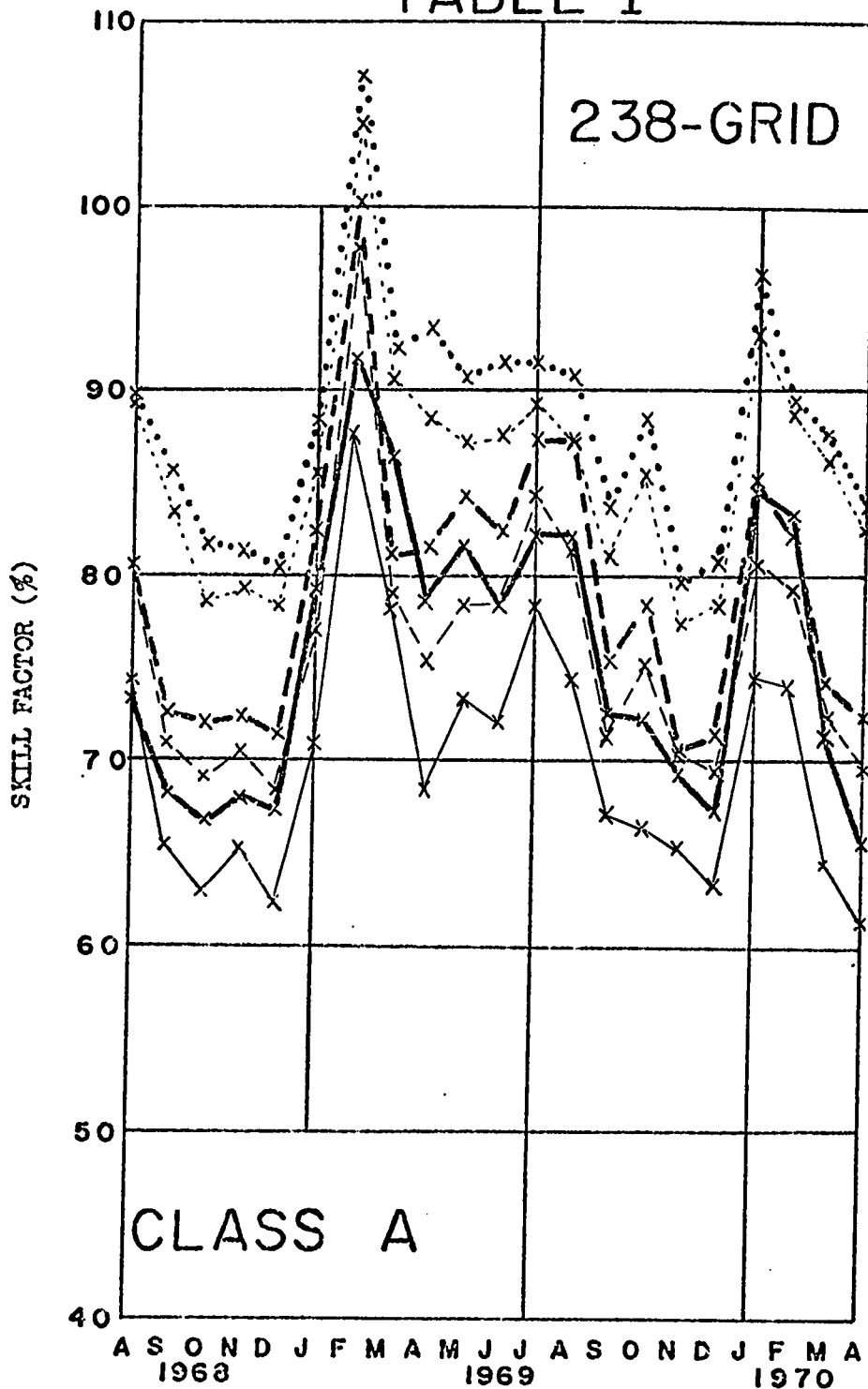


FIG 29: Monthly mean Table I skill factors for the sequential forecasts of precipitation amount which were issued operationally for class A grid points in the period August 1968 to April 1970. These results are for the 238-point grid and on the average there were 110 grid points in class A. The thick curves are for total precipitation and the thin curves are for large scale precipitation. The two solid curves are for 06-12 hours, the two dashed curves are for 13-24 hours, and the two dotted curves are for 30-36 hours.

TABLE II

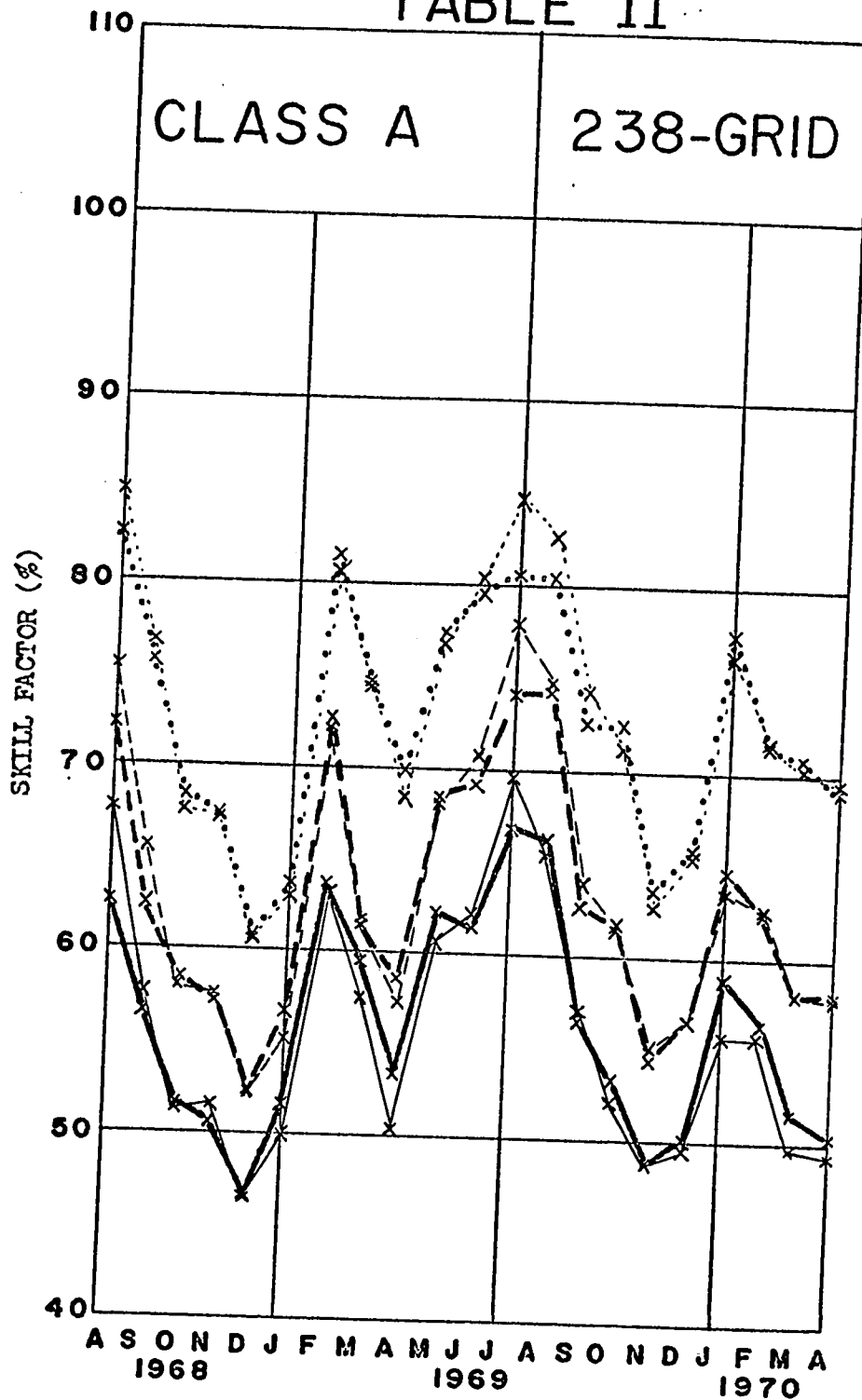


FIG 30: Monthly mean Table II skill factors for the sequential forecasts of precipitation amount which were issued operationally for class A grid points in the period August 1968 to April 1970. These results are for the 238-point grid and on the average there were 110 grid points in class A. The thick curves are for total precipitation and the thin curves are for large scale precipitation. The two solid curves are for 06-12 hours, the two dashed curves are for 18-24 hours, and the two dotted curves are for 30-36 hours.

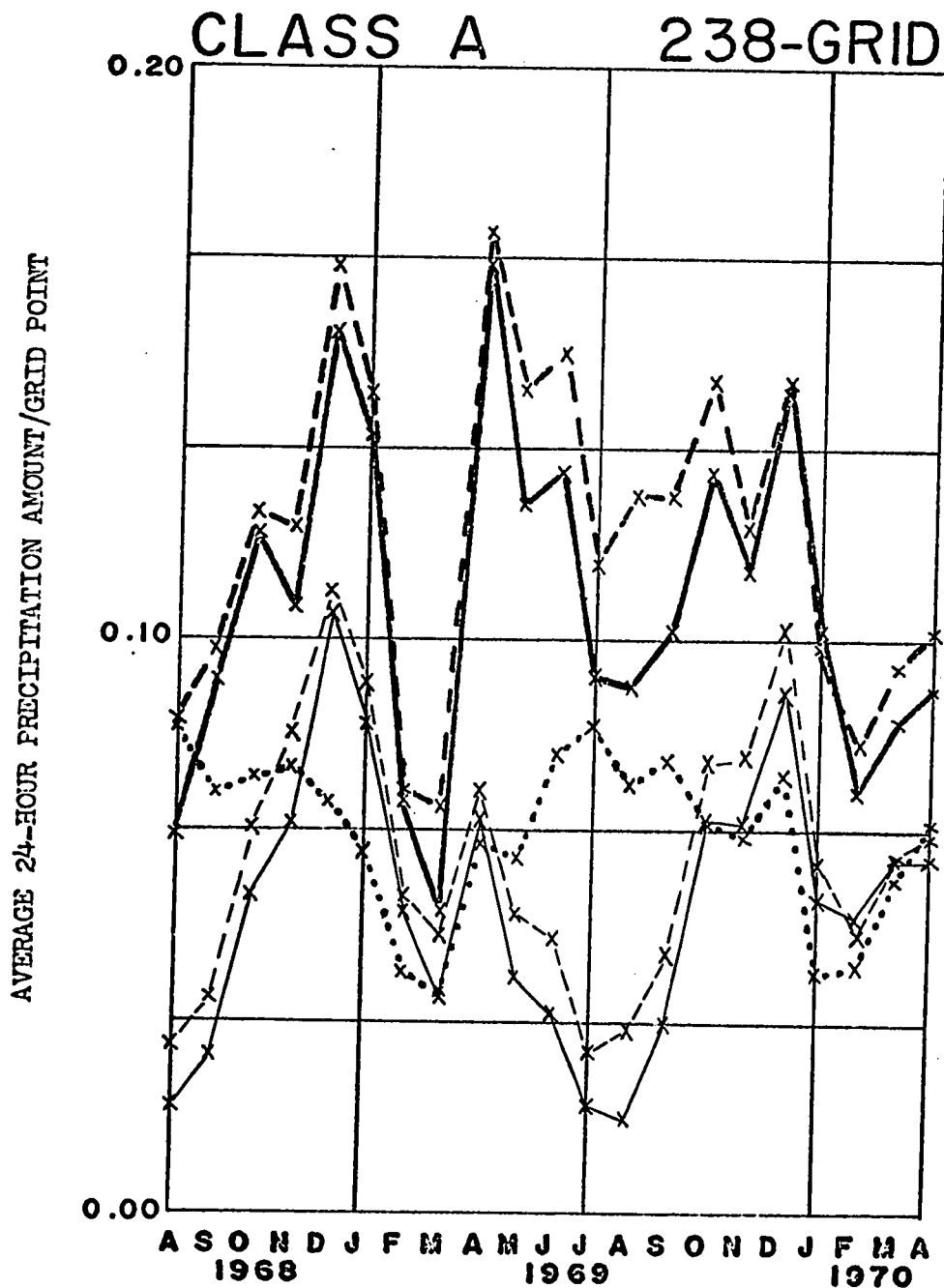


FIG 31: Monthly mean values of the average 24-hour precipitation amount/grid point for the sequential forecasts which were issued operationally for class A grid points in the period August 1968 to April 1970. These results are for the 238-point grid, and on the average there were 110 grid points in class A. The dashed thick curve is for the total precipitation for 00-24 hours and the solid thick curve is for the total precipitation for 12-36 hours. Similarly, the dashed thin curve is for the large scale precipitation for 00-24 hours, and the solid thin curve is for the large scale precipitation for 12-36 hours. The dotted thick curve indicates the corresponding objectively analysed values of the observed precipitation.

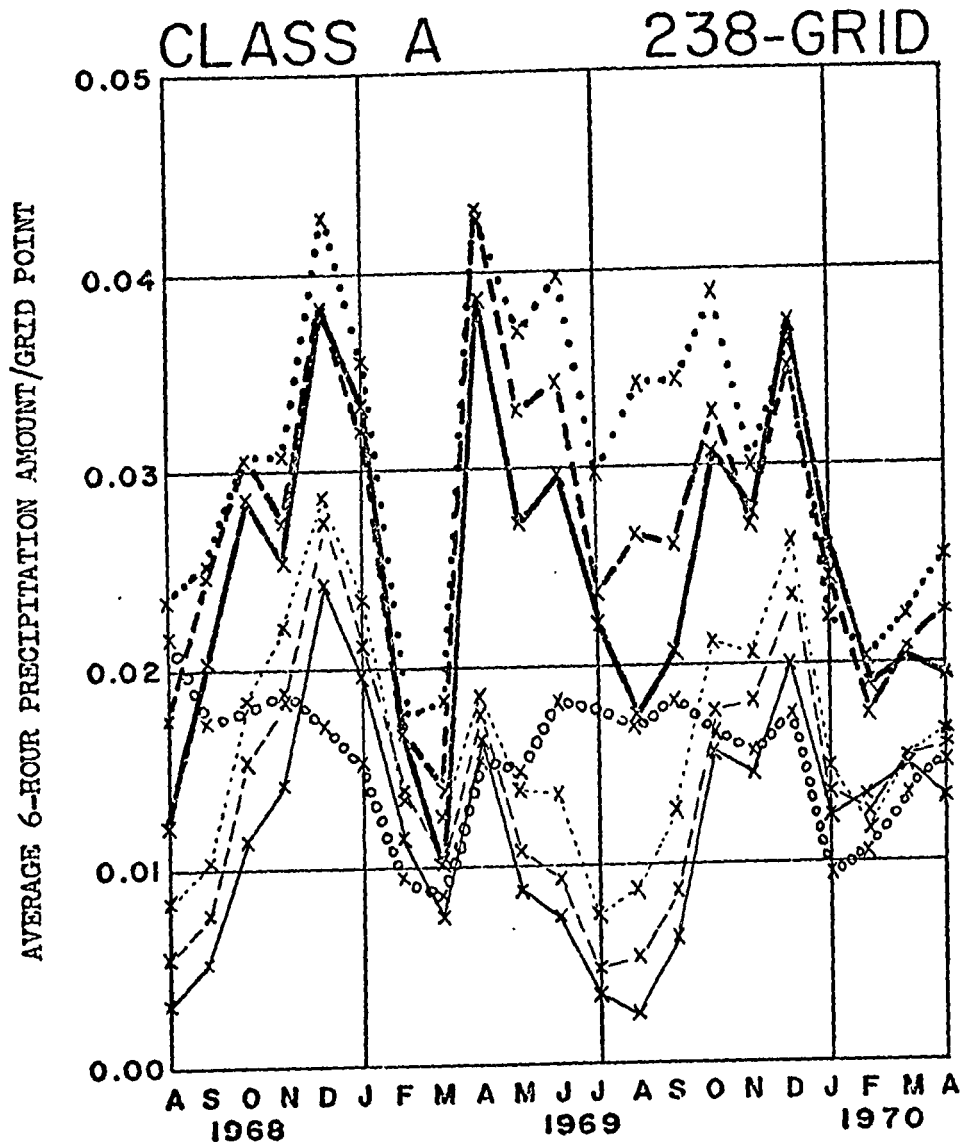


FIG 32: Monthly mean values of the average 6-hour precipitation amount/ grid point for the sequential forecasts which were issued operationally for class A grid points in the period August 1968 to April 1970. These results are for the 238-point grid, and on the average there were 110 grid points in class A. The dotted, dashed and solid curves are for 06-12 hours, 18-24 hours and 30-36 hours respectively, and in each case the thick curves are for total precipitation and the thin curves for large scale precipitation. The circled thick curve indicates the corresponding objectively analysed values of the observed precipitation.

24-hour verification periods; Figs. 25 and 26 are for 00-24 hours, and Figs. 27 and 28 are for 12-36 hours. However, Figs. 25 and 27 are computed for Penalty Table I, whereas Figs. 26 and 28 are computed for Penalty Table II. Information is displayed in a similar manner in all four diagrams. The thick curves are for total precipitation and the thin curves are for large scale precipitation. The solid curves are for Class A grid points, the dashed curves for Class B, and the dotted curves for Class C. On the average, there were 110 grid points in Class A, 41 in Class B, 33 in Class C, and 53 in no data areas. All four diagrams show quite clearly that the skill factors tend to be lower in winter and higher in summer. They also show that, on the whole, Class A grid-points verify better than Class B grid-points, and the Class B grid-points verify better than Class C grid-points. They also show that the relative worth of the total precipitation forecasts compared to the large scale precipitation forecasts deteriorates from Class A to Class B, and again from Class B to Class C. Similar conclusions may be drawn from the 6-hour results. Consequently, one should regard these inter-class comparisons primarily as being evaluations of the worth of the objective analyses, and only secondarily as evaluations of the worth of the forecasts. However, at the same time, the mere fact that Class B and Class C points lie along the coast lines will doubtless contribute to the differences between the classes, simply because the proximity of no data areas will tend to make the stream function forecasts poorer in these regions. For both these reasons the Class B and Class C results will not be discussed further. The usefulness of the forecasts will be judged entirely on the basis of the Class A results. Consider first the Class A results for 00-24 hours. The Table I results of

Fig. 25 show that the total precipitation forecasts are usually significantly better in summer, but that the large scale precipitation forecasts are usually significantly better for the rest of the year. The Table II results of Fig. 26 show that the total precipitation forecasts are much better than the large scale forecasts in summer, and slightly better for the rest of the year. Consider next the Class A results for 12-36 hours. Figs. 27 and 28 show that the comments just made about the Class A results for 00-24 hours also apply to the Class A results for 12-36 hours. Note that, in all four Figs., the first two complete months of results for the 1970 model, March and April 1970, are quite encouraging. Quantitatively, for total precipitation, the average skill factor values for Class A for the whole 21 months are approximately as follows: for Table I, 56% for 00-24 hours, and 63% for 12-36 hours; for Table II, 44% for 00-24 hours, and 53% for 12-36 hours. The corresponding values for large scale precipitation are about 1% lower for Table I and 1% higher for Table II. In all cases, the summer and winter values are, respectively, about 8% above and below the corresponding overall averages.

Figs. 29 and 30 show the monthly mean skill factors for Class A grid points for 6-hour verification periods. Fig. 29 is for Table I, and Fig. 30 is for Table II. Once again the thick curves are for total precipitation, and the thin curves are for large scale precipitation. The solid curves are for 06-12 hours, the dashed curves for 18-24 hours, and the dotted curves for 30-36 hours. The forecasts for 00-06 hours, 12-18 hours, and 24-30 hours could not be verified because no ADE is done at the intermediate synoptic times, 06Z and 18Z. This was particularly unfortunate for the 1968 model because of the smoothing of the stream

function fields. The results of the octagon model work showed quite definitely that the 6-hour time periods following the smoothing times are the most reliable ones for verification purposes. The main features of Figs. 29 and 30 are the seasonal variations of the individual curves and the steady deterioration of the skill factors with time. The Table I results of Fig. 29 show that the large scale precipitation forecasts always do better than their total counterparts, irrespective of season, but that the degree of the difference diminishes with time. The Table II results of Fig. 30 show that there is not much to choose between the total and the large scale precipitation forecasts, although the total forecasts are slightly better in summer and slightly worse in winter. Once again, the first results with the 1970 model are quite encouraging. In particular, the Table I skill factors for 06-12 hours set a record in April 1970. Quantitatively, for total precipitation, average skill factor values for Class A over the whole 21 months are approximately as follows: for Table I, 77% for 06-12 hours, 80% for 18-24 hours, 89% for 30-36 hours; for Table II, 57% for 06-12 hours, 64% for 18-24 hours, and 71% for 30-36 hours. The corresponding figures for large scale precipitation for Table I are 73%, 77% and 87% respectively; the Table II figures are the same as for the total precipitation. All these 6-hour values are, of course, much higher than the corresponding 24-hour values quoted earlier.

Fig. 31 shows the monthly mean values of the average 24-hour precipitation amount/grid point for Class A grid points. The thick curves are for total precipitation, and the thin curves are for large scale precipitation. The solid curves are for 12-36 hours, and the dashed curves are for 00-24 hours. The thick dotted curve indicates the corresponding

objectively analysed values of the observed precipitation. The first thing to notice about Fig. 31 is that the average 24-hour observed precipitation/grid point oscillates between 0.04 inches in winter and 0.08 inches in summer. The 24 hour forecasts of large scale precipitation amount/grid point, on the other hand, oscillate between about 0.10 inches in December and 0.03 inches in July. So the seasonal oscillation of the large scale precipitation has about the same amplitude as the seasonal oscillation of the observed precipitation, but unfortunately it is about 180 degrees out-of-phase. It was precisely because of this gross under-forecasting of the large scale precipitation in the summer months that the small scale effects were introduced in the first place. However, the total precipitation seems to over-compensate for this summer deficiency, and at the same time it adds some extra precipitation in winter when it is not really wanted. To put things in perspective, however, it should be pointed out that the small scale contributions comprise about 75% of the total forecast precipitations in summer, and only 25% in winter. This is the type of thing that the small scale effects were designed to do. Another aspect of Fig. 31 which is quite interesting concerns the relative behaviour of the curves for the two forecast periods. Both the total and large scale amounts drop off from 00-24 hours to 12-36 hours. But usually the reduction is only about 15-20%, a much smaller value than was commonly imagined. Once again the March and April 1970 results bode reasonably well for the 1970 model. Fig. 32 contains the same kind of information as Fig. 31, but for the 6-hour periods instead of the 24-hour ones. The comments made about Fig. 31 also apply to Fig. 32, except that the shorter time period has to be taken into account.

The skill factor results for the 504-point grid were virtually the same as for the 238-point grid. The only difference was that all the 504-point grid skill factors were uniformly worse by about 2-3%, total and large scale precipitation alike. This shows that the differences in significance obtained for the two different grids in the octagon model experiments were due to the biased sample of cases. The cases were chosen, after all, because there were interesting weather systems in mid-continent, not because of what was going on in Alaska and Florida. In the monthly mean figures there are weather systems in Alaska and Florida as well as in mid-continent, so differences of significance no longer show up. However, the across-the-board decrease in skill factor is doubtless due to the proximity of no-data areas.

In both the threat score and skill factor verifications, the differences between the total and large scale precipitation forecasts were tested for statistical significance each month by applying the Student "t" test as described by Brooks and Carruthers (1953). The results are not quoted here because they merely confirm the common sense interpretations of Figs. 18-32. Tests of statistical significance are probably more useful when applied to limited series of ten or twenty cases.

The regional studies undertaken in the Weather Centrals across Canada were, like the threatscores, based on the verification of station or "spot" forecasts interpolated from the predicted areal values at the grid-points. On the whole, they tended to confirm the results of the CAO objective verification procedures. However, there were two interesting findings. It appears that in the Maritimes, unlike the rest of Canada, the computer forecasts tend to systematically under-estimate the actual

precipitation amount. This must be because the baroclinic model systematically under-estimates East Coast deepening. In British Columbia, as might be expected, local orographic effects are much more important than elsewhere.

The subjective assessments have led to three significant conclusions. These may be summarised as follows. First, the most serious errors in the precipitation forecasts are directly attributable to errors in the predicted stream function patterns produced by the baroclinic model. In particular, the most unsatisfactory precipitation forecasts are associated with developing low centres which move rapidly in the atmosphere. Even the 1970 baroclinic model tends to under-develop such systems and move them along much too slowly. The second conclusion is a very interesting one because it concerns complex systems of two or more low centres, moving together, but spaced about two grid-lengths apart. Normally, when there is a well-defined single structure, the precipitation forecasts that are issued for the same low centre from consecutive initial times are broadly consistent with one another. The maximum amounts predicted will increase or decrease, sometimes sharply, but they will not alternate up and down. With double-centred lows, on the other hand, there are marked vacillations in maximum amount from one initial time to the next, and these may persist for three or four days as such systems track across the continent. What apparently happens in such cases is that the baroclinic model is able to resolve only one low. If it happens to pick up one of the real low centres, and loses its companion completely -- i.e. if one low is dominant at initial time -- then comparatively large maximum precipitation amounts are predicted. On the other hand, if the baroclinic model is able to

resolve neither actual low, but instead only a broad fictitious trough mid-way between them -- i.e. if both lows are of about equal prominence at initial time -- then comparatively small maximum precipitation amounts are predicted. The vacillations in the forecasts from one initial time to the next merely reflect the struggle for supremacy that is going on between the two lows in the real atmosphere. Usually, the comparatively large precipitation amounts work out to be better forecasts. However, the actual speed of motion of complex systems of this type is predicted quite accurately by the sequential baroclinic model. It seems that in the real atmosphere these complex lows move more slowly than their more simple counterparts. The normal under-advection by the baroclinic model, which only resolves one low in any case, therefore becomes advantageous. And the predicted precipitation areas verify quite well even if the amounts do jump up and down every twelve hours. The third conclusion is that there are a few systematic errors in the precipitation forecasts. One of the most obvious of these, in the 1968 model, was the tendency to forecast too much precipitation in mountain plateaus. This was corrected in the 1970 model, as indicated by (15.9), by making S^* dependent on p_g . Another pronounced error is that too much frontal precipitation is predicted for the Arctic Front. Most of the other systematic errors are similar to those revealed by the objective verification techniques. However, one concerns precipitation type. The dividing line between snow and rain is predicted too far north when there is already snow on the ground. In such circumstances, obviously, the criteria of Section 21 fail to take into account the presence of an isothermal layer or inversion near the ground.

Some general remarks on the interpretation of the precipitation forecasts are in order at this juncture. The most important thing to remember about the forecast charts is that the scheme produces values of precipitation amount at the grid-points of the standard finite difference network. These values should not really be interpreted as spot forecasts at the grid-points, they should instead be regarded as predictions of the average amount of precipitation to fall in the area surrounding the grid-point. This area can roughly be regarded as a square of side one grid-length having the grid-point itself at the centre. However, it was decided that Weather Centrals and Weather offices would find contoured charts of precipitation amount more convenient to use than a print-out of grid-point values. A special computer program was therefore designed to transform the predicted grid-point values of precipitation amount into the actual contoured charts which are transmitted over the facsimile circuits.

Unfortunately, in order to do this, it is necessary to regard the predicted grid-point values as spot values and not as areal averages. Although this procedure is, in general, a reasonably satisfactory one, it should be realised that there are two important implications. First, the contoured areal average forecasts, even if accurate, will add a collar about 50 miles wide to all the actual precipitation areas. The precise width of this collar will vary from 0 to 100 miles, depending on how the actual precipitation area is situated with respect to the grid-points. In the threat score verifications, the collar effect is evident in the relative numbers of stations predicted and observed to have precipitation. On the average, over the whole year, the number of stations predicted to have total precipitation runs about 20% more than the numbers actually observed;

the corresponding figure for large scale precipitation is about 10%. In the skill factor verification procedure, by contrast, no such areal over-forecasting shows up because it uses grid-point analyses of the reported amounts and contoured charts of these analyses will have collars of their own. In fact, because the radius of influence in the analysis scheme is set at 1.25 grid-lengths, the areas of total precipitation on the predicted charts appear to be under-forecasts of about 5%; the predicted areas of large scale precipitation are under-forecasts of about 15%. This suggests, perhaps, that the radius of influence in Fig. . should be cut down to about 1 grid-length. The second implication of contouring the areal average forecasts, of course, is that it is impossible to portray features smaller in dimension than one gridlength. In particular, contoured areal average charts have broad flat maxima, whereas contoured station reports exhibit narrow sharp peaks. Now the field meteorologist expects the contoured QPF charts to tell him two things. First, where the precipitation areas are going to be. Here the presence of the 50-mile collar is not a great inconvenience. The major areas of precipitation and no precipitation are fairly well-defined, and in between them are border zones, including the collar, which may or may not have precipitation. The second thing the field meteorologist wants to know is what the maximum amounts are going to be. Obviously, the contrast between the shapes of the actual and predicted maxima creates some difficulties. If true areal averages were predicted the contours would not show amounts anywhere near the actual maxima. Yet if the contoured forecasts show the actual maxima, they must show them spread over too large an area. W. S. Creswick has suggested that one way out of this dilemma would be to redesign the contouring program so

as to sharpen up the maxima; this is a possibility which will be explored in due course. In the operational model an attempt was made to arrive at a compromise position. However, as matters stand now, it looks as if this compromise position was not chosen as well as it might have been. The tendency to over-forecast is too pronounced over most of the map, so the broad flat forecast maxima tend to be closer to the actual maxima than they are to the areal averages.

This tendency to over-forecast the precipitation amount is evident no matter what kind of verification is carried out. Yet it was not apparent in the original series of test cases which were run on the octagon model. Perhaps the main reason for this was the fact that the original test cases were chosen because very active weather systems were present in mid-continent, and the baroclinic model grossly under-developed the main low centres in these cases. Consequently, the precipitation scheme was designed to cope with extreme under-development, rather than with average under-development, and so naturally might be expected to over-forecast in the average kind of situation. This is confirmed by the fact that the operational precipitation scheme generally predicts the correct amounts in the worst storms; the over-forecasting problem occurs in the average situation. Unfortunately, it is not possible to know in advance how much under-development there will be in the model. So it could be dangerous to tamper too much with the present scheme. After all, the worst storms are the important ones even if they do not contribute a great deal to the monthly mean verification figures. What might be done with the large scale precipitation, for instance, is to introduce a small vertical motion variation into the unit precipitation formula, and rewrite (15.5) as:

$$U_p'(T, S, S^*, \omega) = \begin{cases} \left[\left((4+2X) \left(\frac{S}{S^*} \right)^2 - (3+2X) \left(\frac{S}{S^*} \right) + 1 \right) U_p(T) \right] & \text{if } S < S^* \\ 0 & \text{if } S \geq S^* \end{cases} \quad (22.2)$$

where

$$X = \frac{\omega_x - |\omega|}{\omega_x} \quad (22.3)$$

and ω_x is some specified constant, say 50 mb/hour in winter and 25 mb/hour in summer. This would make:

$$U_p'(T, S, S^*, \omega) = \begin{cases} 0 & \text{when } S = S^* \\ 0.5(1-X) & \text{when } S = S^*/2 \\ 1 & \text{when } S = 0 \end{cases} \quad (22.4)$$

Hopefully, (22.2) would go some way towards reducing the large scale precipitation amounts associated with the weaker low centres, while not affecting the major storm centres too much; though, of course, it does not really solve the problem of how to anticipate under-development in the baroclinic model. As for the small scale precipitation, it is quite clear that the major problems are arising with the over-prediction of frontal precipitation. This means that the various frontal precipitation constants should be reset at more appropriate values, or the empirical formula

redesigned slightly, and that some special attention should be given to the problem of temperature gradients behind the Arctic Front. Also, the value of $\hat{\gamma}$ in (21.1) should be made temperature dependent. It is not clear why the frontal showers are not working out so well in the operational run as they did in the original development work. Limited experiments have shown that the frontal precipitation is much more sensitive than expected to the use of a trial field as an initial time 200 mb height chart. But this seems unlikely to be the sole cause. Presumably, the other differences between the octagon model and the 1968 model have also adversely affected the frontal shower computations. The air mass showers seem to be working out quite well, but perhaps it would be worthwhile including a latitudinal variation as well as a seasonal one. One aspect which needs more study is the role the small scale effects play in mountain areas.

Modifications to the precipitation scheme may cure some of the systematic errors which have been revealed by monitoring the forecasts over a long period of time. But the improvements which result are likely to be minor ones. Major improvements in the precipitation forecasts can only be brought about in two ways:

(i) By increasing the resolution of the grid network.

(ii) By improving the baroclinic model itself.

Harvey (1969) and Paulin (1969) have started to carry out some experiments with a fine-grid baroclinic model. Their results so far have been quite encouraging, and it look as though their work will lead to more detailed precipitation forecasts for the first day. However, only a more sophisticated baroclinic model can lead to better precipitation forecasts for the second day, to more accurate computations of tomorrow's rain.

PART IV : THE PILOT PROJECT ON PARALLEL OPERATION23. The Pilot Model

A pilot project was carried out on the CDC machine in 1967. The objective was to investigate the feasibility of improving the forecasts by operating the baroclinic model and the precipitation scheme in parallel. In view of the work reported by Danard (1963), (1964), (1966a), (1966b), the main improvements were expected to come from the incorporation of latent heat effects.

Hardware limitations made it necessary to restrict the investigations to a 342-point rectangular grid (19 x 18) centred on North America. Consequently, fields of z , ψ , T , and S were all carried for the whole grid, while ω and Υ were computed for the interior points. Besides the reduction in grid, there were three other major modifications made to the octagon model. First, the 700 mb stream function field was promoted to the status of a full working level of the baroclinic model. Second, the smoothing procedures were replaced by eddy diffusion terms. Third, latent heat feedback was incorporated.

The 700 mb level is of primary importance for the processes involving moisture. Consequently, the stream function at 700 mb was substituted for the one at 1000 mb in the relaxation cycle. This did not detract from the model in any way because the 1000 mb level only had derived field status, even though it was actually programmed into the relaxation cycle. The following set of control coefficients was computed from the standard atmosphere static stabilities of Table 2 using an approach very similar to that described in Section 8 :

$$[C_{mn}] = \begin{bmatrix} -4.452 & 4.321 & 0 & 0 \\ 5.551 & -9.846 & 4.164 & 0 \\ 0 & 2.917 & -3.210 & 0.162 \\ 0 & 0 & 0.116 & -0.247 \end{bmatrix} 10^{-2} \text{ dkm}^{-1} \text{ hr}^{-1} \quad (23.1)$$

In the notation, $m = 1$ now corresponds to 850 mb, $m = 2$ to 700 mb, $m = 3$ to 500 mb, and $m = 4$ to 200 mb. The empirical correction factor was taken to be $-0.131 \times 10^{-2} \text{ dkm}^{-1} \text{ hr}^{-1}$ at all levels.

The model was integrated exactly as described in Section 6 ; in particular, the main integration cycle was identical to that of Appendix C. The only differences from the octagon model arose in the evaluation of the primary and secondary constraints.

Smoothing every twelve hours was known to lead to the tremendous time discontinuities in the vertical motion fields described in Section 17. Equally deleterious effects were evident in the precipitation forecasts, and it was feared that these might have grave repercussions for latent heat feedback. Consequently, it was decided to abandon the smoothing procedures altogether. Instead, a switch-over was made to the eddy diffusion approach which normally guaranteed time continuity. Earlier, Danard (1966a), (1966b) had successfully used eddy diffusion terms in an omega equation model. It was soon discovered that the introduction of the eddy diffusion of potential vorticity alone led to computational instability. For when primary constraint (9.1) is applied to (6.1) without any secondary constraint (9.4) blow-ups readily occur. What happens is that at a few points Q_m grows large and positive while $\sum_{n=1}^4 C_{mn} \psi_n$ grows large and negative, thus permitting $(Q_m + \frac{1}{4} \sum_{n=1}^4 C_{mn} \psi_n)$ to remain small. This phenomenon is successfully counteracted by applying the secondary constraint (9.4) to the time step equation (6.2).

Thus in the pilot model the terms $\langle E_m \rangle$ of (6.1) and $\langle E_m \rangle$ of (6.2) were computed exactly as described in Section 9, but with the values of the eddy diffusion coefficients as given in Table 22. The one small difference was at initial time when the current hour value of an eddy diffusion term was used instead of zero. Some experimentation was done with separate eddy diffusion coefficients for Q_m and $\sum C_{mn} \psi_n$, and with different eddy diffusion coefficients at each level, but most of these variations seemed to lead to inferior results.

K_D^* (dkm ² hr ⁻¹)	K_d^* (dkm ² hr ⁻¹)	K_D (dkm)	K_d (dkm)
3.436×10^7	0.086×10^7	4.0	0.1

Table 22 : Values of the eddy diffusion coefficients used at all levels in the pilot model.

The amount of latent heat released by the large scale precipitation was easy to compute. It was given by:

$$H_1 = \begin{cases} H^* w & \text{if } w < 0 \text{ and } S < S^* \\ 0 & \text{if } w \geq 0 \text{ or } S \geq S^* \end{cases} \quad (23.2)$$

where H_1 is the special heat function defined by (A1.14), but for the latent heat alone, and H^* is defined by (17.5). As these were preliminary experiments, no attempt was made to include the latent heat released by the small scale precipitation. Note that H_1 could only be computed from (23.2) at the end of a time step, after the stream function tendencies and vertical motions had already been obtained. This was not thought to necessarily be a disadvantage, because according to Richtmeyer(1957) (hour - 1) values should in any case be used in dissipative terms.

Unfortunately, once the 850, 700 and 500 mb fields of H_1 had been computed, it was not clear what exactly should be done with them.

The primary constraints B_m of (6.1) were therefore computed in two different ways. The first approach was to take:

$$\langle B_m \rangle |^t = \left\langle f_0 \frac{\partial}{\partial p} \left(\frac{H_1}{\sigma} \right) \right\rangle |^{t-1} \quad (23.3)$$

and use (E13.1) and (E15.4) to evaluate the pressure derivatives, taking $H_1 = 0$ at 1000 and 200 mb, and standard atmosphere values of σ from Table 2. In the second approach ω is written as a sum of two components:

$$\omega = \omega^I + \omega^{II} \quad (23.4)$$

where ω^I is the vertical motion that would be a solution of the omega equation if H_1 were zero, and ω^{II} is the additional vertical motion due to the presence of H_1 . After substituting (23.4) into the complete omega equation, and then subtracting off those terms which constitute the definition of ω^I , the remaining terms are:

$$\nabla^2 \omega^{II} + \frac{f f_0}{\sigma} \frac{\partial^2 \omega^{II}}{\partial p^2} = \frac{1}{\sigma} \nabla^2 H_1 \quad (23.5)$$

an equation originally due to Petterssen et al (1962). Taking the vertical boundary conditions to be $\omega^{II} = 0$ at 1000 and 200 mb, equation (23.5), or at least its finite difference counterpart, may be solved for ω^{II} by the three-dimensional relaxation procedure described in Appendix F. The primary constraint was then taken to be:

$$\langle B_m \rangle |^t = \left\langle f_0 \frac{\partial \omega^{II}}{\partial p} \right\rangle |^{t-1} \quad (23.6)$$

where, once again, the pressure derivatives were evaluated by (E13.1) and (E15.4).

The term $\langle G_m \rangle$ was evaluated at the current hour by the terrain-induced divergence approach of (D1.14) and (D1.9). However, when $p_g \geq 850$, as no 1000 mb wind was available, the 850 mb stream function wind was taken as the wind at ground level. And, of course, as $m = 1$ now corresponded to a full working level, 850 mb, this meant that $G_1 = G_2 = G_3$.

The octagonal model version of the precipitation scheme was carried over to the pilot project virtually unchanged. Though, of course, the smoothing was dropped, and there was no longer any need to compute a derived 700 mb stream function field. No attempt was made to include eddy diffusion terms in the vertical motion computations.

The first latent heat feedback experiments were a failure. Some kind of computational instability was encountered in the integrations when $\langle B_m \rangle$ was evaluated by formula (23.3). The problem was not entirely unanticipated because in this approach, as can be seen from (23.2), $\frac{\partial H_1}{\partial p}$ varies linearly with $\frac{\partial w}{\partial p}$. The $\langle B_m \rangle$ therefore appeared to be more dynamic than dissipative in nature, and so presumably should have been evaluated at the current hour instead of at (hour - 1). Unfortunately, appropriate current hour evaluations could not be considered without abandoning the normalisation procedure inside the main relaxation cycle of Appendix C.

The second approach to the incorporation of latent heat feedback was more successful. The model could be integrated without any trouble at all. Consequently, three 48-hour forecasts were prepared for each of a series of five cases. The first two of these forecasts were produced by the pilot model with and without latent heat feedback; the third was from the octagon model. The results were quite surprising. Both sets

of pilot model forecasts displayed much more detail than the corresponding octagon model forecasts. CRMSE verification scores were computed for the interior points of the 342-point grid, i.e. for a 272-point grid (17 x 16), using formula (B17.2). Table 23 gives the 48-hour scores for 850 and 500 mb. The pilot model gave much better CRMSE scores at 850 mb, both

Level (mb)	"wet" pilot model CRMSE (dkm)	"dry" pilot model CRMSE (dkm)	octagon model CRMSE (dkm)	persistence CRMSE (dkm)
850	5.4	5.4	6.7	7.8
500	8.3	8.5	8.1	11.8

Table 23 : Mean 48-hour CRMSE verification scores for five cases. The results are for the pilot model with latent heat ("wet"), the pilot model without latent heat ("dry"), and also for the octagon model.

with and without latent heat feedback, and almost held its own at 500 mb. This was in spite of the fact that the small grid boundaries were kept constant in the pilot model, whereas they were allowed to vary in the octagon model because they were well inside the 1709-point integration area. And in spite of the fact that the pilot model forecasts displayed vastly more detail than those of the octagon model. Each of the five cases had one major low centre at 850 mb which could easily be tracked. Some of these were passing through a deepening phase and some were not. At 48 hours, for the five cases, the mean magnitudes of the displacement errors of these major low centres are given in Table 24, together with the corresponding means of the absolute errors of their depths. These dramatic low level improvements were well illustrated by the group of 850 mb height charts which were published by Kwizak and Davies (1969).

Mean magnitude	Units	Pilot Model		Octagon Model
		"wet"	"dry"	
Displacement error	grid-lengths	1.7	2.0	3.2
Depth error	dkm	5.8	7.8	14.0

Table 24 : Mean magnitudes of the displacement and depth errors of the five major low centres in the 48-hour forecasts of 850 mb height.

Some discussion is now in order to put these interesting results in perspective. The pilot project established the feasibility of getting better forecasts by parallel operation. This was the original objective. However, the startling improvements obviously came from the term representing the eddy diffusion of potential vorticity, and not from the latent heat feedback. This was a complete surprise. The eddy diffusion terms were originally introduced merely to preserve time continuity. There is no doubt they serve this purpose because they eliminate the need for smoothing. The reason that they also yielded unexpected additional dividends can be explained qualitatively as follows. The short wave features of vorticity and $\frac{\partial^2 \psi}{\partial p^2}$, i.e. $\sum_{n=1}^4 C_{mn} \psi_n$, tend to be exactly out of phase with each other, and of equal magnitude. But the potential vorticity is nothing more and nothing less than the sum of these two quantities. The medium wave potential vorticity patterns therefore have the inherent capacity of implicitly containing short wave vorticity features and their associated complementary short wave $\sum_{n=1}^4 C_{mn} \psi_n$ features. Further, as the prognostic equations of the model (6.1) are in terms of the potential vorticity, this means that the short wave vorticity and $\sum_{n=1}^4 C_{mn} \psi_n$ features are advected along with medium wave advection

speeds, i.e. without the usual finite difference attenuation associated with short wave advection. In a sense, then, it appears that the eddy diffusion term (9.1) permits the medium wave potential vorticity patterns to serve as carrier waves for the prognosis of short wave vorticity and $\sum_{n=1}^k C_{mn} \psi_n$ features, which are then reconstituted explicitly by the relaxation process which is essentially of a diagnostic nature.

The pilot project integrations were not without their unsatisfactory aspects. To begin with, none of the precipitation forecasts produced by the pilot model verified better than their counterparts from the octagon model. This was true both for the total and the large scale precipitation. It was thought that the omission of the eddy diffusion terms from the W computations might be one reason for this. Also, there were distorted precipitation patterns on the West Coast due to obvious boundary problems. The second slightly disconcerting feature was that the latent heat feedback, though clearly beneficial, did not play the important role that had been expected. Obviously, the adequacy of the approach based on (23.6) must be questioned further. The practical disadvantage of having to solve the finite difference form of (23.5) is that it involves a secondary relaxation cycle. One final unsatisfactory aspect of the pilot model experiments was not fully appreciated until work was well under way on the main parallel model. This was that the depths of the lows at 850 and 700 mb were not fully consistent with one another.

By the time the main pilot project had been completed, one thing had become apparent. The normalisation procedure of the main integration cycle, described in Appendix C, was becoming more of a handicap than an advantage. Consequently, a second pilot project was run over the same 342-point grid to check out the three-dimensional relaxation procedure described in Appendix F. This was fully successful in all respects. The stage was now set for the main parallel model experiments.

PART V : THE MAIN PARALLEL MODEL EXPERIMENTS24. Outline

The success of the pilot project led to the more comprehensive experiments on parallel operation which are reported here, in PART V of this thesis. Some preliminary planning and programming was done in the latter half of 1968. The main development work was carried out in 1969 and early 1970. This culminated in the integration of a series of eleven test cases in May 1970. For comparison purposes, the same series of test cases was also integrated using the 1968 model. The highlights of the results are presented in Section 32.

In this thesis the parallel model experiments are reported as a self-contained investigation. In actuality, of course, they constitute part of the continuing research program at the CAO which is aimed at producing better height and precipitation forecasts for operational consumption. Two aspects of the experiments serve to underline this broader context. First, some of the more successful features of the current project were actually adapted for operational use while the new work was still in progress. As mentioned in PARTS II and III, the 1970 model includes the eddy diffusion constraints, a version of the radiation term, and several other smaller items from the parallel model. Second, several features of the parallel model are still in an early experimental stage. These led to some obvious imperfections in the results of the test integrations.

The main objective of the parallel model experiments was to improve the precipitation forecasts for the second day. Evaluations of the operational precipitation forecasts were quite clear about one thing.

The main errors after 24 hours could be attributed to errors in the predicted depths and displacements of the flow patterns. Better baroclinic forecasts were therefore a necessary prerequisite for improved computations of tomorrow's rain. This meant that the emphasis had to be placed on improving the baroclinic model rather than on improving the precipitation scheme itself. The pilot project had investigated the possibility of producing better height forecasts by a parallel operation which included the feedback of the effects of latent heat. The results showed vast improvements in the predicted depths and displacements of five major low centres at 850 mb. But, somewhat surprisingly, the main source of these improvements turned out to be a new term, the eddy diffusion of potential vorticity, which had originally been put into the model merely to accommodate the latent heat experiments. The latent heat feedback itself had also improved the forecasts, but not nearly to the same degree. When the current project was undertaken, therefore, it was assumed that research on the eddy diffusion procedure had already been completed. It was assumed that further improvements would have to come from taking into account additional diabatic effects, variable static stabilities, and the neglected terms of the vorticity equation.

The baroclinic model and the precipitation scheme were completely reprogrammed in a highly flexible manner for the new experiments on parallel operation. The 1221-point grid was retained for the baroclinic model, and the 1015-point grid for the temperature and dew point depression forecasts. However, the vertical motions, all diabatic effects, and the precipitation amounts were computed for a 667-point grid. All three of

these grids are shown in Fig. 1. As in the pilot project, the 700 mb stream function field was made a full working level of the baroclinic model. But the three-dimensional relaxation of Appendix F superceded the normalised two-dimensional relaxations of Appendix C. And the special P_9 field of Fig. 3 replaced the standard one of Fig. 2. Otherwise, the baroclinic model was formulated more or less as in Section 6, with a series of primary constraints on the R.H.S. of equation (6.1) and a secondary constraint on the R.H.S. of equation (6.2). Few changes were made to the precipitation scheme. To facilitate the diabatic and other experiments a large amount of climatological data was extracted for the 667-point grid. This consisted of monthly mean temperatures at 850, 700 and 500 mb, monthly mean sea surface temperatures, monthly mean charts of effective ocean area, and monthly mean snow cover charts. Appropriate daily mean charts of these quantities could then be interpolated as required.

The first phase of the experiments centred on the diabatic effects. Reasonably adequate empirical formulae were developed for the net heating rates due to radiation effects and ocean heating. But, unfortunately, it never became fully clear what should be done with these heating rates once they had been obtained. Nor was it possible to significantly improve on the way latent heat feedback was handled in the pilot project. Consequently, all diabatic effects were ultimately fed into the baroclinic model via Petterssen's equation (23.5), a procedure which is even less satisfactory for radiation and ocean heating than it is for latent heat. Many time-consuming experiments were carried out with variable static stability and the neglected terms in the vorticity equation. They all led

nowhere. Meanwhile, what were thought to be minor changes were being made to the control coefficients, the terrain constraint, and the eddy diffusion constraints. The most successful of these involved the eddy diffusion procedure whose importance was consistently under-rated throughout the experiments. The details of the innovations which were actually included in the final series of test integrations are reported in the following Sections.

25. The Control Coefficients

The control coefficient matrix is given by the sum of two matrices, one invariant and the other seasonally dependent, viz. :

$$[C_{mn}] = [\bar{C}_{mn}] - [C'_{mn} \sin \alpha_c] + [\mu_{mn}] \quad (25.1)$$

where

$$[C_{mn}] = \begin{bmatrix} -2.625 & 2.625 & 0 & 0 \\ 3.75 & -6.75 & 3.0 & 0 \\ 0 & 3.0 & -3.8 & 0.8 \\ 0 & 0 & 0.33 & -0.33 \end{bmatrix} 10^{-2} \text{ dkm}^{-1} \text{ hr}^{-1} \quad (25.2)$$

$$[C'_{mn}] = \begin{bmatrix} -0.875 & 0.875 & 0 & 0 \\ 1.25 & -1.75 & 0.5 & 0 \\ 0 & 0.5 & -0.9 & 0.4 \\ 0 & 0 & -0.11 & 0.11 \end{bmatrix} 10^{-2} \text{ dkm}^{-1} \text{ hr}^{-1} \quad (25.3)$$

$$[\mu_{mn}] = \begin{bmatrix} -0.16 & 0 & 0 & 0 \\ 0 & -0.12 & 0 & 0 \\ 0 & 0 & -0.10 & 0 \\ 0 & 0 & 0 & -0.08 \end{bmatrix} 10^{-2} \text{ dkm}^{-1} \text{ hr}^{-1} \quad (25.4)$$

and

$$\alpha_c = \frac{2\pi N_c}{365} \quad (25.5)$$

where N_c is the day-of-year measured from April 21 st, a month after the

spring equinox, so that $\sin \alpha_c = 0$ on April 21 st and Oct. 21 st,
 $\sin \alpha_c = 1$ on July 21 st, and $\sin \alpha_c = -1$ on Jan. 21 st.

This set of control coefficients was chosen for the following reasons. From a linear perturbation analysis of the baroclinic model equations (6.1), the author - Davies (1967b) - had earlier concluded that the control coefficient matrix should be symmetric. Consequently, the first test runs with the parallel model were carried out with $C_{12} = C_{21}$. The resulting forecasts were unsatisfactory because the depths of the 850 mb lows were inconsistent with those at 700 mb. The inadequacy of the lower boundary condition, particularly with the eddy diffusion terms in the model, led to pronounced over-development of the 850 mb systems relative to those at 700 mb. Some experimentation showed that this problem disappeared if C_{21} was chosen to be about 40 to 50% greater than C_{12} . The pilot model results were then re-examined for consistency between the depths of 850 and 700 mb lows. Sure enough, there had also been relative over-development at 850 mb in the pilot model forecasts. There were three reasons why it had not been noticed earlier. First, the control coefficient matrix (23.1) used in the pilot model experiments had fortuitously had the C_{21} 25% greater than the C_{12} . Consequently, the degree of relative over-development was much less noticeable than with symmetric coefficients. Second, no forecast 700 mb charts had been produced by the octagon model, because no "reverse" balance equation program was available for the half octagon grid used by the derived 700 mb stream function routine. This meant that attention had been focused on the 850 and 500 mb levels for which complete sets of forecast charts were available. Third, of course, the over-development was not absolute and so could not be discerned from looking at the 850 mb charts alone. Special problems also arose with the

linkage between 500 and 200 mb. Some preliminary experiments led to two principal conclusions. First, the advection speeds at 500 mb are governed largely by the magnitude of C_{34} . Second, the degree of intensification of troughs and ridges at 200 mb, measured relative to their counterparts at 500 mb, depends on the ratio C_{43}/C_{34} . For January cases, best results were obtained with comparatively large values of C_{34} and comparatively small values of C_{43} . For autumn cases the reverse was true. Obviously, the position of the tropopause must be a critical factor. In January, when the 200 mb surface is usually in the stratosphere over most of North America, the level of maximum wind will on the average be at about 300 mb and the 200 mb motions will be forced ones. High values of C_{34} are therefore needed to compensate for the dynamic effects of the missing 300 mb, and low values of (C_{43}/C_{34}) are needed to simulate the fairly heavy stratospheric damping at 200 mb. In the autumn, when the tropopause is on the average much nearer 200 mb, there is no longer any need to compensate for the missing level of maximum wind. Consequently, lower values of C_{34} must be used to avoid over-advection at 500 mb, and higher values of (C_{43}/C_{34}) must be used to more properly allow for the effects of tropospheric development at 200 mb. The experiments with C_{34} and C_{43} led to the idea of seasonal variations in the control coefficients. In general, obviously, the greater the magnitudes of the control coefficients, the greater the linkage between the levels, and the greater the degree of development. Some experiments soon showed that more development was needed in January than in the autumn. Consequently, the control coefficients (25.1) were selected for use in the final series of test cases reported in this thesis.

Some further discussion is now in order. According to (7.8), the control coefficients are supposed to vary inversely with the static stability. The static stability tends to be low in summer, high in winter, and very high in the stratosphere. One would therefore expect that, except for C_{43} , the seasonal variations would be the reverse of those of (25.1). The reason this is not so is that dynamic considerations have also to be taken into account. For instance, as has already been mentioned, the level of the tropopause is important for C_{34} in a manner only indirectly related to the static stability. Similarly, the existence of fronts and jet streams means that, in the regions of dynamic importance, the levels are dynamically linked together much more strongly in winter than in the autumn. To some degree, this stronger linkage can be simulated by control coefficients of larger magnitude. Nevertheless, as will be seen from the results, control coefficient matrix (25.1) is not fully satisfactory. In the preliminary experiments summer cases were not run because they are generally not too interesting from the point of view of the model. The one summer case that was run in the final series of integrations was a disappointment. Although the sinusoidal variations seemed to work out reasonably well for the autumn, winter, and spring, they appear to lead to too little linkage between the levels in summer. So it looks as if the optimum seasonal variations should have sharp peaks in January, but scarcely no variation from April to October. This is confirmed by the fact that better results were obtained for January with even higher values of C_{34} than those given by (25.1), but it was not possible to fit these and the optimum autumn values on a sinusoidal curve.

It had been hoped that the change-over to three-dimensional relaxation, described in Appendix F, would permit some experiments in which the control coefficients varied over the grid. Unfortunately, four problems arise. First, $\frac{\partial C_{mn}}{\partial t}$ cannot be evaluated in (6.1). Before starting any integrations, therefore, one has to assume something like:

$$\sum_{n=1}^4 \left\{ \frac{\partial C_{mn}}{\partial t} + \underline{V}_m^r \cdot \nabla C_{mn} - K_D^* \nabla^2 C_{mn} \right\} \psi_n \approx 0 \quad (25.6)$$

Second, it is quite difficult to compute the upper level static stabilities without any forecast temperatures above 500 mb. One can do no better than use the 500 mb temperature and the vertical wind profile to estimate where the tropopause is. Third, there are some problems with the convergence of the relaxation scheme. Fourth, dynamic considerations and the inadequacies of the upper and lower boundary conditions entered into the choice of (25.1), so presumably they should also enter into grid-point computations of $[C_{mn}]$. Nevertheless attempts were made to overcome all these problems and some integrations were actually carried out with the $[C_{mn}]$ variable over the grid. The results were disastrous. The trouble appeared to be that the magnitudes of the C_{mn} were correlated with the sign of the stream function tendency, i. e. large C_{mn} magnitudes were associated with tendency falls and small C_{mn} magnitudes were associated with tendency rises. To compensate for this, the rising tendency areas therefore had larger magnitudes than the falling tendency areas, and the forecast charts rapidly lost their meteorological significance. Best results were obtained by making the C_{mn} depend fairly strongly on the vertical wind shear, but this was merely a way of reducing

the correlation with the stream function tendency. In any case, even these results were clearly inferior to those obtained with constant control coefficients. The possibility of taking steps to eliminate or cancel out the correlation was considered. For instance, the mean magnitude of the positive and negative tendencies computed from constant control coefficients could be enforced, and the variable $[C_{mn}]$ integrations could be used merely to provide the ratios of the values at different grid points. However, it was decided that too many dubious steps had already been taken in this particular venture, and that the time had come to abandon the idea of incorporating variable $[C_{mn}]$ until a thorough re-assessment of the parallel model had been carried out. It is difficult to believe that the real reason for the failure of these integrations was approximation (25.6), or the method of computing the 200 mb static stabilities, or the problems in relaxation. Yet in the real atmosphere the stream function tendencies are correlated with the static stabilities and this does not prevent the magnitudes of the positive and negative areas in the stream function tendency fields being, broadly speaking, in balance. So it looks as if the missing terms of the vorticity equation, or smaller scale dynamical effects, must become important with a variable static stability.

26. The Eddy Diffusion Terms

The primary eddy diffusion constraint used in (6.1) has evolved from (9.1) to the following form:

$$E_m = K^*(x, y, p_m, t) \nabla^2 \left(\frac{g}{f_0} \nabla^2 \psi_m + 4 \sum_{n=1}^4 C_{mn}^* \psi_n \right) \quad (26.1)$$

$m=1, 2, 3, 4$

where

$$[C_{mn}^*] = [\bar{C}_{mn}] - [C'_{mn} \sin \alpha_c] \quad (26.2)$$

$[C_{mn}]$ is given by (25.2), $[C'_{mn}]$ by (25.3), and α_c by (25.5).

The main innovation in (26.1) is that the eddy diffusion coefficient has become a full variable instead of being constant. In addition, however, the Coriolis term and the empirical factors to control long wave retrogression, i.e. the $[\mu_{mn}]$ of (25.4), have been dropped from the potential vorticity. For convenience, define:

$$K_D(x, y, p_m, t) = \frac{4f_0}{g} K^*(x, y, p_m, t) \quad (26.3)$$

The finite difference form of (26.1) is taken to be:

$$\frac{1}{4K} \langle E_m \rangle^t = \begin{cases} \hat{\psi}_m & \text{if } \psi_m > \hat{\psi}_m > 0 \text{ or } 0 > \hat{\psi}_m > \psi_m \\ \psi_m & \text{otherwise} \end{cases} \quad (26.4)$$

where

$$\psi_m = K_D(x, y, p_m, t) \nabla^2 \left\{ K \nabla^2 \psi_m^{t-1} + \sum_{n=1}^4 C_{mn}^* \psi_n^{t-1} \right\} \quad (26.5)$$

$$\hat{\psi}_m = - (V_m^* + \Xi_m^*) \quad (26.6)$$

$$V_m^* = -\mathcal{J}(\psi_m^{t-1}, [K\phi^2\psi_m^{t-1} + \frac{f}{4}]) \quad (26.7)$$

$$\Xi_m^* = -\mathcal{J}(\psi_m^{t-1}, [\sum_{n=1}^k C_{mn}\psi_n^{t-1}]) \quad (26.8)$$

$$\hat{\Xi} = K_0 \hat{\mathcal{J}} / K \quad (26.9)$$

$$\hat{V}_m = \begin{cases} 0 & \text{if } m = 1, 2 \\ \hat{\Xi}/4 & \text{if } m = 3 \\ \hat{\Xi} & \text{if } m = 4 \end{cases} \quad (26.10)$$

$$\Xi_m = \begin{cases} \hat{\Xi} & \text{if } |\Xi_m^*| > \hat{\Xi} \\ |\Xi_m^*| & \text{if } |\Xi_m^*| \leq \hat{\Xi} \end{cases} \quad (26.11)$$

$$V_m = \begin{cases} \hat{V}_m & \text{if } |V_m^*| > \hat{V}_m \\ |V_m^*| & \text{if } |V_m^*| \leq \hat{V}_m \end{cases} \quad (26.12)$$

$$f_m = [(\hat{\Xi})^2 - (\Xi_m)^2] / [(\hat{\Xi})^2 + (\Xi_m)^2] \quad (26.13)$$

$$\eta_m = \begin{cases} 1 & \text{if } m = 1, 2 \\ \frac{[(\hat{V}_m)^2 - (V_m)^2]}{[(\hat{V}_m)^2 + (V_m)^2]} & \text{if } m = 3, 4 \end{cases} \quad (26.14)$$

$$K_D(x, y, p_m, t) = \sum_m \eta_m K_D (1 - a_\eta \sin \alpha_c) \quad (26.15)$$

\mathcal{J} is the standard Jacobian operator (B11.1); K is defined by (C1.3); $[C_{mn}]$ is given by (25.1); α_c is given by (25.5) such that $\sin \alpha_c = -1$ on January 21 st and $\sin \alpha_c = 1$ on July 21 st; and the values of K_0, K_D, a_η and \hat{J} are given in Table 25.

The general time step equation has evolved from (6.2) to

$$\Psi_m^{t+\Delta t} = \left[\Psi_m^{t-\Delta t} + 2\Delta t \left\{ \left\langle \frac{\partial \Psi_m}{\partial t} \right\rangle^t + \langle \epsilon_m \rangle \right\} \right] - 2K_T \left[\Psi_m^{t-\Delta t} - \Psi_m^t + \Delta t \left\{ \left\langle \frac{\partial \Psi_m}{\partial t} \right\rangle + \langle \epsilon_m \rangle \right\} \right] \quad (26.16)$$

where the value of K_T , which may be regarded as a coupling constant,

is given in Table 25; and Δt is as usual the time step of one hour.

However, the time step equation which is used for the first hour remains unchanged in the form (6.3).

The finite difference form of the secondary eddy diffusion constraint used in (26.16) has evolved from (9.5) to:

$$\langle \epsilon_m \rangle^t = \begin{cases} \langle \hat{\epsilon}_m \rangle^t & \text{if } \langle \epsilon_m^{**} \rangle^t \langle \hat{\epsilon}_m \rangle^t > 0 \\ \langle \epsilon_m^{**} \rangle^t & \text{or } 0 > \langle \hat{\epsilon}_m \rangle^t \langle \epsilon_m^{**} \rangle^t \\ & \text{otherwise} \end{cases} \quad (26.17)$$

where

$$\langle \hat{\epsilon}_m \rangle^t = -\frac{1}{2} \left\langle \frac{\partial \Psi_m}{\partial t} \right\rangle^t \quad (26.18)$$

$$\langle \epsilon_m^{**} \rangle^t = \begin{cases} \langle \epsilon_m^* \rangle^t & m=1, 2, 3 \\ \langle \epsilon_m^* \rangle^t - \overline{\langle \epsilon_m^* \rangle^t} & m=4 \end{cases} \quad (26.19)$$

$$\langle \epsilon_m \rangle^t = K K_D (1 + a_\eta^* \sin \alpha_c) [1 + (t - t_0) a_t] (1 + a_\epsilon N_E) \nabla^2 \psi_m^{t-1} \\ + K K_D (1 - a_\eta \sin \alpha_c) \left\{ \mathcal{Z}_P^* [\psi]_{PP} + \mathcal{Z}_N^* [\psi]_{NN} \right\} \quad (26.20)$$

$$\mathcal{Z}_P = \begin{cases} 1 & \text{if } |V^r| \geq V_B \\ \mathcal{Z}_P^* & \text{if } V_B > |V^r| > V_C \\ 0 & \text{if } |V^r| \leq V_C \end{cases} \quad (26.21)$$

$$\mathcal{Z}_P^* = \frac{(V_B - V_C)^2 - (V_B - |V^r|)^2}{(V_B - V_C)^2 + (V_B - |V^r|)^2} \quad (26.22)$$

$$\mathcal{Z}_N = \begin{cases} 1 & \text{if } |V^r| \geq V_A \\ \mathcal{Z}_N^* & \text{if } V_A > |V^r| > V_B \\ 0 & \text{if } |V^r| \leq V_B \end{cases} \quad (26.23)$$

$$\mathcal{Z}_N^* = \frac{(V_A - V_B)^2 - (V_A - |V^r|)^2}{(V_A - V_B)^2 + (V_A - |V^r|)^2} \quad (26.24)$$

$(t - t_0)$ is the time in hours measured from initial time; the operator occurring in (26.19) is the standard smoother (B3.1); and \mathcal{Z}_{PP} and \mathcal{Z}_{NN} are the second derivative finite difference operators

(B18.1) and (B18.4) which are taken parallel and normal to the flow

respectively; K is defined by (C1.3); α_c is given by (25.5); the values of $K_d, K_D, V_A, V_B, V_C, a_\eta^*, a_\eta, a_t$ and a_ϵ are given in Table 25; and N_ϵ is the low tropopause marker of Appendix G which has a value of unity if the tropopause is very low but a value of zero otherwise.

Constant	Value	Units
K_0	7.063×10^{-3}	dkm ⁻¹ hour ⁻¹
\hat{J}	0.5	dkm hour ⁻¹
a_η	0.3333	-
a_η^*	0.5	-
a_t	0.03	hour ⁻¹
a_ϵ	3.0	-
V_A	9.852×10^3	dkm hour ⁻¹
V_B	7.389×10^3	dkm hour ⁻¹
V_C	4.926×10^3	dkm hour ⁻¹
K_T	0.025	-
K_d	0.6	dkm
K_D	3.0	dkm
K_d^*	0.516×10^7	dkm ² hour ⁻¹
K_D^*	2.577×10^7	dkm ² hour ⁻¹

Table 25: Values of the constants used in the eddy diffusion constraints of the parallel model.

The revised mathematical formulations for $\langle E_m \rangle$ and $\langle \epsilon_m \rangle$ appear somewhat formidable. However, they have evolved in a rational manner from the simpler expressions which preceded them. Certain inadequacies were found to be associated with the use of (9.2) and (9.5). The causes of these were tracked down and eliminated one by one, but in the process the formulation grew more elaborate. The K_T term was introduced into the general time step equation (26.16) at a comparatively late stage of the experimentation as a precaution against uncoupling problems of the type discussed by Robert, Shuman and Gerrity (1970). This term therefore has no direct bearing on the discussion that follows. However, mild uncoupling oscillations seem to be associated with the diabatic effects and the amplitudes of these were greatly reduced when the change-over was made from (6.2) to (26.16).

In the first experiments it became apparent that the eddy diffusion scheme used in the pilot project had one major drawback. Cold lows which are essentially barotropic in nature are smoothed out much too heavily. The reason for this was not hard to find. When $\nabla^2 \left(\sum_{n=1}^k C_{mn} \psi_n \right)$ is zero, the primary constraint (9.1) reduces to $K_D^* \nabla^2 Q$ and the eddy diffusion term merely acts as a heavy smoother. So the improvements in the prediction of baroclinic short waves had only been attained at the cost of some deterioration in the handling of barotropic situations. Once this problem had been diagnosed, the solution was qualitatively quite obvious. The coefficient of eddy diffusion of potential vorticity had to be made large in baroclinic short waves and small or even zero in barotropic situations. Physically, this makes good sense. One expects much more eddy activity to occur in baroclinic short waves than in the barotropic areas of the map.

Unfortunately, it was not such an easy matter to lay down quantitative rules for the variation of $K_D(x, y, p_m, t)$ over the grid. The final form (26.15) was only arrived at after a fair amount of trial and error experimentation. The quantity Ξ_m^* defined by (26.8) serves as the principal diagnostic of baroclinicity; the factor $f(\Xi_m)$ given by (26.13) is in effect a sophisticated on/off switch. Certain complications caused by the presence of jet streams made it necessary to introduce a similar V variation at 200 mb, and it turned out to be advantageous to carry this over to 500 mb in a milder form. As it stands, (26.15) is probably slightly deficient because it gives low values of $K_D(x, y, p_m, t)$ down the axis of a baroclinic wave where Ξ_m^* passes through a change of sign. The seasonal variation was introduced because experiments showed this to be advantageous for January and autumn cases; no experiments were done with summer cases. Once again this makes good physical sense. One expects more eddy diffusion of potential vorticity in January than in the autumn. However, it might be preferable to have the seasonal variation implicit rather than explicit. For instance, a dependence on the temperature gradient could be built into (26.15) in such a way that $K_D(x, y, p_m, t)$ would naturally be large in the winter months without having to introduce the $\sin \alpha_c$ factor. The $[M_{mn}]$ contribution to the control coefficient matrix was dropped from (26.1) because it appeared to lead to some small anomalies. Physical considerations led to the f term also being dropped from (26.1), though its presence or absence did not seem to affect the forecasts very much.

Six distinct problems arose in connection with the secondary constraint. The most disconcerting of these concerned slow moving cold

lows with anti-symmetric flow patterns around them; i.e. with a stronger flow on one side and a weaker flow on the other. In the real atmosphere these lows drift around slowly in the direction given by the stronger flow. In the model the same lows tended to become more symmetrical; i.e. the actual low centres migrated from the strong flow side to the weak flow side. Unfortunately, this meant that in the model the lows moved perpendicularly to their actual track in the real atmosphere. Though both real and model motions were slow, the discrepancies in position could become as much as two gridlengths in 48 hours. An investigation showed that in such situations an application of the standard smoother (B3.1) has the same kind of effect, but it is much harder to detect unless one is actually looking for it. The problem was overcome by not allowing the eddy diffusion term of (6.2) to change the sign of the originally-computed stream function tendency, nor to reduce its magnitude by more than half. At the same time a restriction of a similar nature was placed on the primary constraint; this is embodied in the \hat{U}_m of (26.4) and (26.6). The second problem was that strong flows sometimes became a little noisy, though without becoming computationally unstable. This was overcome by introducing the non-isotropic dynamic component which constitutes the second term on the R.H.S. of (26.20). Briefly, it acts in the following manner. Moderately strong flows are subjected to a strong additional eddy diffusion effect in a direction parallel to the flow, but not normal to the flow. Very strong flows are subjected to a strong additional eddy diffusion effect of the standard isotropic type. Flows which are not strong are not affected at all. The third problem was that the application of the secondary constraint led to a spreading and weakening of the 200 mb

jet streams, essentially because they became smeared into the cold air. Naturally, the incorporation of the dynamic component made this defect worse than ever. The solution was to adopt the special procedure indicated by (26.19). The net eddy diffusion term at 200 mb is computed by subtracting a smoothed eddy diffusion component from the original gross value. The fourth problem was that the same eddy diffusion coefficient gave predicted charts which were too smooth in January and too detailed in the autumn. This led to the introduction of the seasonal variation in K_d . The fifth problem was that fairly small eddy diffusion coefficients gave the best verification scores at 12 hours, but larger ones fared better at 48-hours. So a time-dependence was built into the formulation. The current increment rate of 3% per hour leads to the initial values being increased $5\frac{1}{2}$ times by 48 hours. The sixth problem concerned the behaviour of cold low centres in the Arctic during the autumn. These seemed to fill fairly rapidly in the atmosphere, but not in the model. On the other hand, similar cold lows in mid-latitudes tended to persist both in the atmosphere and in the model. So to re-insert the primary constraint was out of the question. It was suspected that the differences in behaviour might have something to do with the Arctic cases having very low tropopauses. Consequently, the low tropopause marker procedure of Appendix G was developed to permit the application of a heavier eddy diffusion coefficient in such recalcitrant regions. This appeared to be satisfactory for the autumn cases. Unfortunately, a major computer hardware change became imminent when the development work had progressed to this stage. Further experimentation would have meant lengthy delays in the completion of the project. Consequently, it was decided to go ahead with the running of

the final series of test cases. Regrettably, the results showed quite clearly that the special low tropopause procedure is inappropriate for January cases.

The whole eddy diffusion procedure described in this Section has one grave drawback. It concerns the treatment of two low centres when they are quite close together and are of about the same depth. In such cases the 1968 model is only able to resolve one low centre. It predicts a broad flat trough linking the two real lows. But at least the predicted trough is in approximately the correct position. As mentioned in Section 22, this is because double-low systems move more slowly than their single-centred counterparts in the real atmosphere, and the systematic under-advection of 850 mb features by the 1968 model nicely compensates for this phenomenon. The parallel model is still only able to resolve one low in the middle of the two real centres. But then the primary constraint leads to an anomalous deepening of this unreal feature, and proceeds to move it along in the flow just as if it were a real solitary vortex. Some attempt was made to devise a diagnostic procedure to detect the presence of double-lows, and then accord them special treatment in the prediction cycle. However, this particular line of investigation only led to the design of highly efficient noise amplifiers.

It is interesting to compare the eddy diffusion procedure described here with that used by Smagorinsky, Manabe and Holloway (1965). They also used variable eddy diffusion coefficients, but these depended only on a property of the total horizontal flow which they called the total horizontal deformation. They did not take the baroclinicity into account when computing the horizontal eddy diffusion coefficients.

27. Mountain and Friction Effects

The primary constraints due to terrain, G_m , are given by

$$G_m = g_1 G_m^I + (1 - g_1) G_m^{II} \quad m=1,2,3,4 \quad (27.1)$$

where

$$\left. \begin{aligned} G_1^I &= \frac{f}{\Delta p^I} \frac{(1000-200)}{(P_g-200)} \omega_g \\ G_2^I &= G_3^I = G_4^I = 0 \end{aligned} \right\} \quad (27.2)$$

$$G_m^{II} = \begin{cases} \frac{\frac{3}{2} f (P_m-200)^{1/2} \omega_g}{(P_g-200)^{3/2}} & \text{if } P_g > P_m \\ \frac{\frac{3}{2} f \omega_g}{(P_g-200)} & \text{if } P_g \leq P_m \end{cases} \quad (27.3)$$

$$g_1 = \begin{cases} 1 & \text{if } P_g \geq 925 \\ (P_g - 775)/150 & \text{if } 775 < P_g < 925 \\ 0 & \text{if } P_g \leq 775 \end{cases} \quad (27.4)$$

Δp^I is 100 mb, and ω_g is given by the analytical formula (D1.2). The finite difference version of ω_g^t is computed using (D1.12) except that U_g and V_g are evaluated at $(t-1)$ in the mountain term as well as in the friction term. When $P_g > 850$ mb, as in the pilot model, the 850 mb stream function wind is taken to be the wind at ground level. In addition, the special P_g field of Fig. 3 is used instead of the

standard P_g field of Fig. 2 The standard C_d field is retained.

Before entering into a discussion of the comparative merits of G_m^I and G_m^{II} , it is helpful to quickly review the principal effects of each component of the terrain term. The mountain term comes into play most forcibly when a westerly flow crosses a north-south mountain range. It results in a pronounced ridging over the mountains and the formation of a lee trough down wind. The friction term comes into play most forcibly in 850 mb low centres. It produces a filling tendency which therefore serves to counteract any development that might be taking place. This effect has been discussed by Danard (1969b). The G_m^I term is a form of lower boundary forcing very similar to (Dl.1). The G_m^{II} term is a slightly more sophisticated form of terrain-induced divergence forcing than that described in Appendix D; it assumes that the terrain-induced vertical motion, w_g^* falls off according to a $3/2$ power law, viz:

$$w_g^* = w_g \left(\frac{p-200}{P_g-200} \right)^{3/2} \quad (27.5)$$

Experimental integrations were carried out both with $G_m = G_m^I$ and with $G_m = G_m^{II}$. The following observations were made about the comparative effectiveness of the mountain term in the two approaches.

Ridging tendencies over the mountains were usually under-estimated with G_m^I , but handled quite well with G_m^{II} . On the other hand, the pressure level variation of the amplitudes of the lee troughs was much more realistic with G_m^I than it was with G_m^{II} . In particular, 500 mb short wave troughs moving down wind from a mountain area were slowed down quite realistically by G_m^I , whereas they usually had an excessive

tendency to stall in the lee trough position with G_m^{II} . While the important mountain effects are sometimes handled better by G_m^{I} and at other times by G_m^{II} , it seems that the important friction effects are always handled better by G_m^{I} . This is because the friction component of G_m^{I} has a very similar effect to the reduction in magnitude of C_{12} ; both tend to keep the depths of the 850 mb lows consistent with those at 700 mb. In fact, it is slightly disconcerting to find that the formulation of the terrain constraint is not entirely independent of the choice of the control coefficients. With G_m^{I} one can use a slightly larger magnitude value of C_{12} than might otherwise be possible, because any over-development tendencies at 850 mb will be strongly counteracted. As will now be evident, the final formulation of the terrain term (27.1) is a compromise which combines the advantages of G_m^{I} in lowland areas with those of G_m^{II} in the mountains.

Some of the inadequacies of the operational precipitation forecasts had been blamed on the excessive smoothness of the standard P_g field of Fig. 2. The special P_g field of Fig. 3 was therefore prepared for use in the current experiments. It portrays actual geographic features, such as the sharpness of the West Coast mountain ranges, in a much more realistic fashion than the standard P_g field. Also, the effective mountain height at a grid-point was taken between the maximum and mean heights in that neighbourhood, instead of simply the mean height. As will be evident from the results, the use of the special P_g field improves both the precipitation forecasts and the height forecasts. However, these better forecasts were not obtained when the special P_g field was first introduced. There were a few snags which had to be ironed out first. One problem which was encountered was the uncoupling of odd and even time steps. The author

attributed this at least partially to the use of current hour values of the terrain term, and so a change-over was made to (hour - 1) values for both the mountain and friction components. As mentioned in Appendix D, Creswick and Olson (1970) independently decided that the friction term should be evaluated at (hour - 1) in an eddy diffusion model. Another disadvantage arising from the special P_9 field seemed to be associated with the use of the absolute vorticity as a factor of the terrain constraints; e.g. as in in (D1.1). Two-gridlength waves appeared in some places as a result of the mountain forcing, and these could not be fully suppressed by the eddy diffusion terms. The reason for their persistence with appreciable amplitude was that the two-gridlength mountain forcing was effectively amplified quite strongly by the two-gridlength vorticity factor. This problem was cured by eliminating the relative vorticity altogether, and just leaving the f as the multiplication factor. However, this must reduce the effectiveness of the friction term. Theoretically, it should also mean that the mountain term leads to excessive ridging, and under-emphasised lee troughing. But this is not a matter to be too concerned about because in the past the mountain ridging tendencies have always been under-estimated. In retrospect, therefore, it can be seen that it would probably have been better to us \bar{Q} — i. e. the absolute vorticity subjected to the standard smoothing operator (B3.1) — instead of f in (27.2), though possibly not in (27.3).

28. The Diabatic Effects: I & II Latent Heat Release and Absorption

The latent heat released by large scale precipitation was computed in exactly the same way as in the pilot model; i.e. the special heat function H_1 is given by (23.2). The only refinements concerned differentiation between the liquid and ice phases, and some special procedures in mountainous areas. Attempts were also made to treat the latent heat released by small scale precipitation in a similar manner. However, these were soon abandoned. Latent heat feedback from small scale precipitation resulted in anomalous lows sprouting up all over the place. These immediately began to generate large scale precipitation, which in turn made more latent heat available for development, and thereby hastened the degeneration of the whole map into a non-meteorological mess. It therefore seems reasonable to conclude that in the atmosphere the latent heat released by small scale precipitation serves to amplify only the small scale circulations, and that there is no direct linear feedback of any significance to the synoptic scale motions. At least this is probably true for disorganised convective shower activity, whether air mass or frontal in nature. For organised convective shower activity, such as that simulated by the large scale precipitation contribution to the induced instability showers (20.4.1), it may be a different story.

There is a 10% difference between the latent heat of condensation of water and the latent heat of sublimation of ice. Consequently, it is worthwhile taking into account whether large scale precipitation originally forms in liquid or solid form. This can be done quite easily by replacing the L in (17.5) by an effective latent heat, L^* , given by:

$$L^* = \begin{cases} L & T_m \geq T_L \\ \left[\frac{(T_m - T_L')L + (T_L - T_m)L_i}{(T_L - T_L')} \right] & T_L > T_m > T_L' \\ L_i & T_m \leq T_L' \end{cases} \quad (28.1)$$

$$m = 850, 700, 500$$

where the numerical values of L , L_i , T_L , and T_L' are given in Table 26.

quantity	value	units
L	2.5×10^{10}	$\text{gm cm}^2 \text{ sec}^{-2}/(\text{gm H}_2\text{O})$
L_i	2.8×10^{10}	$\text{gm cm}^2 \text{ sec}^{-2}/(\text{gm H}_2\text{O})$
T_L	- 10	C deg
T_L'	- 20	C deg

Table 26 : Values of the constants used in the computation of the effective latent heat.

It is also easy to take into account the amount of latent heat absorbed due to the thawing, evaporation or sublimation of large scale precipitation as it falls through a dry layer from the layers above. The special heat function (A1.14) associated with this kind of process is defined to be H_2 , and is given by:

$$(H_2)_m = \begin{cases} \frac{R_g}{C_p P \Delta P} \left[L_a \{ (\tau_l)_m^{\leq 1} - (\tau_l)_m^e \} + L_b (\tau_l)_m^e \right] & m = 85, 70 \\ 0 & m = 500 \end{cases} \quad (28.2)$$

where

$$(\tau_l)_{70}^{\leq 1} = (\tau_l)_{50}$$

$$(\tau_l)_{70}^e = \hat{E}_{70}^{50} (\tau_l)_{50}^e$$

$$(\tau_l)_{85}^{\leq 1} = (\tau_l)_{70} + (\tau_l)_{50} - (\tau_l)_{70}^e$$

$$(\tau_l)_{85}^e = \hat{E}_{85}^{70} (\tau_l)_{70} + \hat{E}_{85}^{50} (\tau_l)_{50}^e$$

$$\hat{E}_{85}^{70} = \begin{cases} 1 & \text{if } E_{85}^{70} M_{85} \gg 1 \\ E_{85}^{70} M_{85} & \text{otherwise} \end{cases}$$

$$\hat{E}_{85}^{50} = \begin{cases} 1 & \text{if } E_{70}^{50} E_{85}^{50} M_{70} M_{85} \gg 1 \\ E_{70}^{50} E_{85}^{50} M_{70} M_{85} & \text{otherwise} \end{cases}$$

$$\hat{E}_{70}^{50} = \begin{cases} 1 & \text{if } E_{70}^{50} M_{70} \gg 1 \\ E_{70}^{50} M_{70} & \text{otherwise} \end{cases}$$

(28.3)

M_{70} and M_{85} are given by (21.3); E_{70}^{50} , E_{85}^{50} and E_{85}^{70} are given by (21.4); and L_a and L_b are appropriate latent heats obtained as indicated in Appendix H. The release of latent heat causes some technical difficulties in mountain areas; if one is not very

careful one finds lows developing inside mountains. Consequently, before actually being used, the quantities $(H_1 + H_2)_m$ are pre-multiplied by a mountain scaling factor, ϕ_m^h , whose values are given in Appendix H. For reference purposes, this process may be indicated symbolically by:

$$(H_1 + H_2)_m \rightarrow \phi_m^h (H_1 + H_2)_m \quad (28.4)$$

As will be explained later, latent heat effects are fed back into the baroclinic model by the method developed in the pilot project. There were a few misgivings about whether doing it in this way is 100% effective. Accordingly, it is appropriate to make some general remarks about the results of latent heat feedback. As in the pilot project, the presence of latent heat feedback generally leads to small improvements in the forecasts; the 850 mb lows are slightly deeper and move ahead slightly faster. These improvements were reduced to an even smaller significance when the change-over was made from the eddy diffusion techniques of the pilot model to the more sophisticated ones now in use. Presumably, most of this drop in significance is due to the inadvertent reduction in precipitation amounts which has also occurred; and so the interactions with the eddy diffusion terms are probably not of any great importance. What is important is that the effectiveness of latent heat feedback depends greatly on the temperature. From the values of $U_p(T)$ in Table 5 one would expect that, from the temperature variation alone, the latent heat feedback in low centres in really warm air would be about two or three times that in similar low centres in mid-continent in winter. But after running a few cases one gets the impression that the difference in sensitivity between warm air and cold air reflects a difference in the

effective amplification of the deepening rates by something more like an order of magnitude. Moderately intense low centres in cool air are only slightly affected by latent heat feedback, but quite weak low centres in warm air seem to deepen quite strikingly. This difference in behaviour could not hinge on the use of Petterssen's equation (23.5). In fact, as it stands (23.5) is not quite consistent with the static stability assumptions of the baroclinic model, namely that (σ/f) is constant at each pressure level. Equation (23.5) was derived assuming σ to be constant. The variant of (23.5) which assumes (σ/f) to be constant works out to be:

$$\nabla^2 \omega^{\text{II}} + \frac{f_0^2}{\sigma} \frac{\partial^2 \omega^{\text{II}}}{\partial p^2} = \frac{f_0}{\sigma} \nabla^2 \left(\frac{H_1}{f} \right) \quad (28.5)$$

Some of the first integrations were actually carried out with (28.5), but it was soon discovered that the $(1/f)$ factor on the R.H.S. merely enhances the differences between warm and cold air. Consequently, (23.5) was re-instated in the model. Another possibility was that the presence of the f_0 factor in (23.6) unduly favoured the warm air. Accordingly, some experiments were run with Q instead of f_0 . No real differences between the behaviour of warm and cold air were noted. However, some two gridlength waves made the charts look a bit noisy. As mentioned in Section 27, the same kind of phenomenon was encountered with the mountain term using the special P_9 field of Fig. 3 when Q was substituted for f in (27.2) and (27.3). Consequently, it was thought best to revert back to the use of f_0 . In retrospect, once again, it seems likely that \bar{Q} or even just f would have been a better choice. But, even so, it seems clear that the f_0 factor in (23.6) does not

explain the difference in sensitivity between cool air and warm air. One important physical factor which has been ignored so far is the formation of large scale clouds. Presumably, there is about as much latent heat released by the formation of clouds as there is by the production of precipitation. But this would still not explain the sensitivity difference unless the ratio of condensed water in large scale warm clouds to that in large scale cold clouds were much less than the corresponding ratios, i.e. 2 or 3, for the unit condensation rates, $U_p(T)$. This raises another important physical factor which has not been taken into account so far, namely the degree of organisation of the precipitating units. It could be that the low centres in cool air are deepened more efficiently by the release of latent heat than their warm air counterparts, simply because the precipitating units are larger and more highly organised. This hypothesis is confirmed by the unsuccessful experiments with latent heat feedback from small scale precipitation.

To summarise, the main conclusions of the latent heat feedback experiments are as follows:

- (i) Latent heat released from disorganised small scale precipitation does not directly affect the large scale flow patterns.
- (ii) Warm air low centres appear to be slightly over-sensitive to the release of latent heat from large scale precipitation, but similar cool air low centres appear to be moderately under-sensitive.
- (iii) This difference in sensitivity does not appear to have a numerical explanation.
- (iv) The only physical hypothesis which seems to account for this difference in sensitivity is as follows. First, latent heat released

220

by large scale cloud formation should be taken into account. Second, the efficiency with which the release of latent heat — both from large scale precipitation and from large scale clouds — drives the synoptic scale systems depends on the degree of organisation and the scale of the main cloud formations and precipitating units. Third, this efficiency appears to be greater for cool air than for warm air.

The physical hypothesis which has just been stated could have an important implication for future models. This is that the special heat functions for the release of latent heat from large scale precipitation, H_1 , should be multiplied by efficiency factors, e_H , before being used to compute the feedback. These efficiency factors would supposedly take large scale cloud formation and the scale and degree of organisation of the precipitating units into account. From experience gained so far, it looks as though e_H should vary from about 0.6 in very warm air to about 3 in a typical low centre in mid-continent in winter, and it also looks as if there should be some latitude dependence. So the first experiments could be done with:

$$e_H = (1.8 - 0.12 T_{70}) f/f_0 \quad (28.6)$$

Efficiency factors to take cloud into account were actually tried in one experiment, but a constant value of 1.33 was used everywhere for e_H . Unfortunately, this made the warm air lows more sensitive than ever without helping the cool air lows very much.

29. The Diabatic Effects: III Ocean Heating

The special heat function, H_3 , used to represent ocean heating effects is given by the following empirical formula:

$$(H_3)_m^t = \begin{cases} -A_\alpha \frac{R}{P_m} \left\{ \frac{[(T_{\alpha m}) - T_m^{t-1}]}{(h_\alpha)_m \gamma_\alpha} + \frac{[(T_{\alpha m}) + T_\beta - T_m^{t-1}]}{(h_\alpha)_m \gamma_\beta} \right\} & T_m^{t-1} < (T_{\alpha})_m \\ -A_\alpha \frac{R}{P_m} \left\{ \frac{[(T_{\alpha m}) + T_\beta - T_m^{t-1}]}{(h_\alpha)_m \gamma_\beta} \right\} & (T_{\alpha})_m \leq T_m^{t-1} \leq (T_{\alpha})_m + T_\beta \\ 0 & T_m^{t-1} \geq (T_{\alpha})_m + T_\beta \end{cases} \quad (29.1)$$

$m = 850, 700, 500$

where

$$(h_\alpha)_m = 1 + 10 \frac{(T_{\alpha 50} + 60)}{20} e^{-\frac{1}{2} \left\{ \frac{[(T_{\alpha})_m - T_m^{t-1}](c_\alpha)_m}{[(a_\alpha)_m + (b_\alpha)_m (T_{\alpha})_m]} \right\}^2} \quad (29.2)$$

and

$$m = 850, 700, 500$$

$\gamma_\alpha, \gamma_\beta, T_\beta, (a_\alpha)_m, (b_\alpha)_m,$ and $(c_\alpha)_m$ are given by Table 27.

For routine use, of course, formula (29.2) could be converted into tables, but there is no point in doing this while $(h_\alpha)_m$ is still in semi-experimental form. The $(T_{\alpha})_m$ are fields of effective ocean equilibrium temperature, i.e. fields of temperature at 850, 700 and 500 mb which are in moist adiabatic equilibrium with the ocean surface. They are determined by the method described in Appendix I. The A_α is a "climatological" field of effective ocean area which is assigned a value of 1 over open oceans, 0.1 over frozen oceans, and meteorologically appropriate values over land areas.

The first experiments with ocean heating were carried out without

the factor $(h_{\alpha})_m$, i.e. with $(h_{\alpha})_m$ effectively equal to unity. The principal effect was thus that temperatures were warmed up exponentially at constant pressure to the effective ocean equilibrium temperatures, and the time constant for this process was τ_{α} . The secondary effect was a similar but much smaller "counter-gradient" constant pressure warming with time constant τ_{β} .

Constant	Level (mb)			Units
	850	700	500	
τ_{α}	10	10	10	hours
τ_{β}	100	100	100	hours
T_{β}	10	10	10	C deg
a_{α}	5.5	13.5	29.0	C deg
b_{α}	0.091	0.22	0.41	-
c_{α}	3	3	3	-

Table 27 : Values of the constants used in the ocean heating term.

The A_{α} factor merely provided a means to allow quasi-ocean heating effects over vegetation and lakes in summer with the same formula. This meant, of course, that fictitious but not unreasonable "ocean temperatures", T_{ϕ} , had to be specified for the land areas. However, far too much warming took place in the tropics without the $(h_{\alpha})_m$ factor. This happened because the spread between the moist and dry adiabatic lapse rates becomes very large when the temperatures are very warm. In the tropics, in fact, the actual 500 mb temperature are

are normally much cooler than $(T_{\alpha})_{50}$. The expression (29.2) for $(h_{\alpha})_m$ was developed by trial and error, and has now evolved into a form that gives reasonable constant pressure warming rates over the ocean areas of interest. At least the performance of (29.1) under static conditions now seems acceptable. As will be discussed later, it is extremely difficult to pass judgement on its dynamic efficacy. One reason for this is that there is some difficulty in incorporating H_3 into the vertical motion computations. Similar problems occur with the radiation heat function, H_4 , and these are discussed in the next Section. Also, the ocean areas are at best regions of low data coverage. However, in spite of the peculiar things that sometimes happen in the no data areas, one is left with the impression that the weakness of the present formulation is that it does not permit the latent heat effects and ocean heating to reinforce one another in a grand enough manner off Cape Hatteras. Yet, if some kind of reinforcement were permitted everywhere, the no data areas would go completely wild. The pragmatic solution would therefore be to permit reinforcement only in the region just off the East Coast, and nowhere else.

The ocean heating and radiation terms were developed separately. It therefore came as something of a disappointment to discover that the two effects, when combined together, tended to cancel each other out to some degree. This occurred especially in northern latitudes where the constant pressure ocean heating rates had been chosen to give desirable net constant pressure warming rates. Consequently, as an interim measure, to avoid interactions during the first experiments, it was decided to multiply the radiation term by $(1 - A_{\alpha})$. This measure means that (29.1) has to be regarded as the net effect of ocean heating and radiation acting together.

The effective moisture source, Γ_S^{III} , assumed to be associated with the ocean heating effects of (29.1) is given by:

$$\Gamma_S^{\text{III}} = \begin{cases} \frac{A_\alpha S_m^{t-1}}{(h_\alpha)_m} \left\{ \frac{1}{\tau_\alpha} + \frac{1}{\tau_\beta} \right\} & \text{if } T_m^{t-1} < (T_\alpha)_m \\ \frac{A_\alpha S_m^{t-1}}{(h_\alpha)_m} \left\{ \frac{1}{\tau_\beta} \right\} & \text{if } (T_\alpha)_m \leq T_m^{t-1} \leq (T_\alpha)_m + T_\beta \\ 0 & \text{if } T_m^{t-1} > (T_\alpha)_m + T_\beta \end{cases} \quad (29.3)$$

where $(h_\alpha)_m$ is given by (29.2) and τ_α , τ_β , and T_β are given in Table 27. Γ_S^{III} may be regarded as a component of Γ_S for substitution into (19.3) additional to the Γ_S^{I} and Γ_S^{II} of (19.6).

30. The Diabatic Effects: IV Radiation

The special heat function, H_{L_r} , which is used to simulate net radiation effects, including those due to the cooling or heating of the underlying ground surface, is given by the empirical formula:

$$(H_{L_r})_m = -\frac{R}{P_m} \cdot \frac{1}{(T_{\delta})_m} \cdot \left\{ (1-X_N) \left[(T_{\delta})_m + (\Delta T_{\delta})_m - T_m^{*+1} \right] - X_N \left[\frac{T_m^{*+1} + 273.2}{0.8} \right] \right\} \quad (30.1)$$

$m = 850, 700, 500$

where

$$X_N = (1 - A_{\alpha}) X_N^* \quad (30.2)$$

$$X_N^* = \begin{cases} 1 & \text{if } \phi > \phi_s + \frac{\pi}{2} \\ \sin^2(\phi - \phi_s) & \text{if } \phi_s \leq \phi \leq \phi_s + \frac{\pi}{2} \\ 0 & \text{if } \phi < \phi_s \end{cases} \quad (30.3)$$

$$(\Delta T_{\delta})_m = -X_S (A_{\delta})_m \cos \frac{2\pi t_{\delta}}{24} B_{\delta}(P_g) \quad (30.4)$$

$$X_S = (1 - A_{\alpha})(1 - X_N^*) \quad (30.5)$$

$$B_{\delta}(P_g) = \begin{cases} 1 & \text{if } P_g \geq 1000 \\ 1 + \left[\frac{1000 - P_g}{300} \right] & \text{if } P_g < 1000 \end{cases} \quad (30.6)$$

$$(\tau_{\delta})_m = e_m + \sum_{n=1}^3 \delta_n (e_{mn} + e_{mnn} \delta_m) \quad (30.7)$$

$$\delta_m = \begin{cases} 1 & \text{if } S \leq S^* \text{ and } \omega \leq 0 \\ \frac{(S_{\delta} - S) + (S - S^*) a_s}{S_{\delta} - S^*} & \text{if } S^* < S \leq S_{\delta} \text{ and } \omega \leq 0 \\ \frac{(S_{\delta}^* - S) a_s}{S_{\delta}^*} & \text{if } S_{\delta} < S < S_{\delta}^* \text{ and } \omega \leq 0 \\ \frac{(S_{\delta}^* - S) a_s}{S_{\delta}^*} & \text{if } S \leq S_{\delta}^* \text{ and } \omega > 0 \\ 0 & \text{if } S \geq S_{\delta}^* \end{cases} \quad (30.8)$$

$$(S_{\delta}^*)_m = \begin{cases} (T_m^{t-1} - T_s^*) & \text{if } (T_m^{t-1} - T_s^*) \geq S_{\delta} \\ S_{\delta} & \text{if } (T_m^{t-1} - T_s^*) < S_{\delta} \end{cases} \quad (30.9)$$

A_{δ} , a_{δ} , a_s , S_{δ} and T_s^* are constants given in Table 29 ; the $(T_{\delta})_m$ are the climatological temperatures interpolated from the monthly mean charts; A_{α} is the effective ocean area field described in Section 29 ; t_{δ} is the local time-of-day in hours measured from midnight; ϕ is the latitude ; ϕ_s is the latitude at which the sun is overhead at mid-day, taking north of the equator as positive ; S^* is given by (15.8) or (15.9); the e_m , e_{mn} , and e_{mnn} are linearly interpolated from Table 28 according to the value of P_3 , except that 1000 mb values are used if $P_3 > 1000$; and in the summation of (30.7) the subscripts $n = 1, 2, 3$ correspond to 850, 700 and

m	e_m	e_{1m}	e_{11m}	e_{2m}	e_{22m}	e_{3m}	e_{33m}	P_3
1	48	0	0	12	0	0	0	1000
2	96	48	12	-24	0	-12	0	1000
3	168	60	24	48	48	-48	0	1000
1	39.36	0	0	8.16	0	0	0	925
2	78.72	32.64	8.16	-16.32	0	-8.16	0	925
3	137.76	40.8	16.32	32.64	32.64	-32.64	0	925
1	52.8	20.16	5.4	-10.8	0	-5.4	0	775
2	52.8	20.16	5.4	-10.8	0	-5.4	0	775
3	92.4	25.56	10.8	21.6	21.6	-21.6	0	775
1	47.88	14.1	5.64	11.28	11.28	-11.28	0	625
2	47.88	14.1	5.64	11.28	11.28	-11.28	0	625
3	47.88	14.1	5.64	11.28	11.28	-11.28	0	625

Table 28 : Values in hours of the e_m , e_{mn} , and e_{mmn} used in the computation of $(\gamma_{\gamma})_m$ when $P_3 = 1000, 925, 775$ and 625 mb. In the notation a subscript of 1 corresponds to 850 mb, 2 to 700 mb, and 3 to 500 mb.

Constant	Level (mb)			Units
	850	700	500	
A_{γ}	8	4	1.4	C deg
a_{γ}	17	17	17	-
a_s	0.1	0.1	0.1	-
S_{γ}	10	10	10	C deg
T_s^*	-40	-40	-40	C deg

Table 29 : Values of the constants, other than the e-factors, which are used in the computation of the radiation term.

500 mb respectively.

The main properties of the preceding formulation will now be discussed. The first thing to note is that over the oceans the temperatures are merely restored exponentially to their climatological values with a time constant τ_γ . This feature was built into the scheme as an interim measure to cope with the ocean heating interactions mentioned in the last Section. One extreme of (30.1) occurs in lowland areas during the polar night. At constant pressure the temperatures cool off exponentially to absolute zero with a time constant of $(\alpha_\gamma \tau_\gamma)$. Under dry and cloudless skies the typical constant pressure cooling rates arising from the values of the constants listed in Tables 28 and 29 are about 4.2, 2.1, and 1.1 C deg/ day at 850, 700, and 500 mb respectively. The corresponding constant pressure cooling rates for completely cloudy skies are about 1.1, 1.1, and 1.9 C deg / day, again at 850, 700 and 500 mb respectively. Conditions of partial cloudiness, or moisture presence without cloud, are deemed to occur when (30.8) gives fractional values for the δ_m . These lead to appropriate constant pressure cooling rates of the same order of magnitude as those for completely cloudy or completely dry skies; the actual values will always be intermediate ones at 850 and 500 mb, but can be as high as about 2.3 C deg/ day at 700 mb. At the other extreme of (30.1) are the hypothetical diurnal changes that would occur in tropical lowland deserts in summer, if there were such areas inside the grid. Under dry conditions and with climatological temperatures the noon-time constant pressure warming rates would be about 3, 0.75, and 0.1 C deg/ day at 850, 700 and 500 mb respectively, and the corresponding midnight constant pressure cooling rates would be of the same magnitude. Under completely

cloudy conditions these values become about 0.75, 0.2, and 0.2 deg C/ day respectively at 850, 700 and 500 mb. Similar magnitude diurnal changes would take place with non-climatological temperatures, but then either the warming or the cooling would be of larger magnitude so as to tend to restore the daily mean to the climatological value. To most regions of the chart, of course, formula (30.1) assigns appropriate values of H_4 interpolated between the extremes of polar night and tropical desert. The first radiation experiments were carried out with a rudimentary form of (30.1). The most irregular aspects of the results were strange little anomalies which occurred in the mountain areas. Consequently, a dependence on P_g had to be built into the formulation to overcome these difficulties. Another point worth mentioning is that the numerical values presently assigned to the various constants are not necessarily optimum ones. There are three reasons for this. First, and most important, the values of the constants depend on the use to be made of H_4 . The warming and cooling rates quoted are not realised in practice because radiation effects do not take place at constant pressure. For instance, consider what would happen with polar night cooling under zero horizontal flow conditions. The subsidence which would occur would tend to raise the air at a given pressure level, and would thus counteract radiational cooling. Unfortunately, as will be seen later, there are difficulties in predicting the right amount of subsidence for a given distribution of H_4 . So compromises have to be made which involve H_4 itself as well as the method for predicting the subsidence. The second reason for the current ambiguity of the H_4 constants is that the moisture dependence has deliberately been under-estimated. With a stronger moisture dependence the model became over-sensitive, so that moderately moist areas at 500 mb cooled off and became saturated much more rapidly

in the model than in the atmosphere. Presumably, this is further evidence that the radiation effects are not being taken into account properly by the vertical motion computations. The third reason is simply that not enough experiments have been carried out. For instance, it seems likely that the diurnal effects should be made stronger than they are now. In particular, the solar heating should have less dependence on the climatological temperature and more dependence on the solar constant, and some slight reformulation would be required to do this properly. However, as has been pointed out, the real problem with H_4 is not how to compute it; the problem is what to do with it once you have it. There is not much point in adjusting the constants or refining the formulation until a satisfactory solution has been found.

There is one obvious criticism of the whole empirical formula approach. Radiation effects could also be handled by the more direct methods of the type proposed by Danard (1969a). The following remarks constitute a rebuttal of this criticism. First, the most important radiation effects are the indirect ones arising from heating or cooling of the ground. In all probability these would have to be handled empirically in any case. Second, as already mentioned, there is not much point in computing H_4 by more elaborate methods until it can be used more effectively than at present. Third, experience has shown that scale considerations such as those encountered with radiation effects are often better dealt with by an empirical approach.

31. The Parallel Baroclinic Model

31.1 The final version

Each of the component parts of the parallel baroclinic model has now been described. All that remains is to piece them together so as to get an overall view of how the model works.

The equations of the model are still of the form (6.1), though the four main working levels at which stream function information is carried have become 850, 700, 500 and 200 mb. The time step equation has evolved to the form (26.16) to permit coupling between odd and even time steps. The control coefficients are given by (25.1); they have a seasonal variation. There have been two changes in the numerical procedures of the main integration cycle described in Appendix C. First, the three-dimensional relaxation of Appendix F has replaced the normalised two-dimensional relaxation of Appendix G. Second, at 200 mb the short wave advection speeds have been slowed down by substituting the standard Jacobian operator (B11.1) for the Shuman form (B12.1) in (C1.2) and (C1.4); at the other levels the Shuman Jacobian is retained. In (6.1) the primary constraints are evaluated as follows. The eddy diffusion constraint $\langle E_m \rangle$ is computed from (26.4), in which the coefficient of eddy diffusion of potential vorticity depends on the baroclinicity. The terrain constraint $\langle G_m \rangle$ is computed from formula (27.1), which reduces to lower boundary forcing in lowland areas, but to induced divergence forcing in mountains. The diabatic constraint $\langle B_m \rangle$ is computed by the Petterssen equation method embodied in (23.4), (23.5) and (23.6), except that

$$\left[(H_1 + H_2 + H_3 + H_4) + \int_D (x, y, P_m, t) K \nabla^2 (H_1 + H_2 + H_3 + H_4) \right] \quad (31.1.1)$$

replaces H_1 in (23.5); the values of $\chi_D(x, y, p_m, t)$ are given by (26.15). In the time step equation (26.16) the secondary eddy diffusion constraint is evaluated by (26.17). The model is integrated over the 1221-point grid of Fig. 1. The eddy diffusion and terrain constraints are evaluated over the whole of this grid, but the diabatic constraint is only applied over a 667-point sub-area, also shown in Fig. 1. That completes the picture of the final version of the parallel baroclinic model.

31.2 The unsuccessful experiments

The experiments that failed fell into three categories:

- (i) Experiments with the direct method of imposing the diabatic constraint.
- (ii) Experiments with the neglected terms of the vorticity equation.
- (iii) Experiments with variable static stability.

The pilot model experiments with (23.4), the direct method of incorporating diabatic effects, were repeated with the main parallel model. When all the diabatic effects were included the integrations were again unstable. This had been expected because of earlier suspicions that the latent heat term should be evaluated at the current hour in this approach, not at (hour - 1), because of its explicit dependence on ω . Next, some experiments were carried out with the radiation term alone. Obviously, the evaluation of $\frac{\partial H}{\partial p}$ at the outside levels led to some difficulties. Several reasonable methods were tried, but none of these made much difference to the results. The integrations were moderately unstable in spite of the comparative mildness of the radiation term. At this stage the numerical aspects of the problem, including of course the possibility of coding

errors, were re-examined very carefully. The conclusion was that the limitation was physical in nature. The explanation is as follows. Diabatic effects must normally involve expansions or contractions of the air, i.e. they must lead to flows which are predominantly divergent in nature. In particular, consider steady state conditions in which the isotherms are parallel to the stream function lines on a constant pressure surface. In this case thermodynamic equation (A1.13) reduces to:

$$-\frac{R}{p} \underline{V}^d \cdot \nabla T + \omega \sigma = H \quad (31.2.1)$$

Obviously, the $\underline{V}^d \cdot \nabla T$ term is an all-important one which cannot be neglected. This naturally leads to the supposition that the $\underline{V}^d \cdot \nabla T$ term is of vital importance for diabatic effects in general. Consequently, a direct method of computing the diabatic constraints, such as that of (23.4), cannot be expected to work unless the formulation properly accounts for the divergent advection components. On the other hand, the approach based on Petterssen's equation does not suffer from the same limitations. If the divergent advection terms, both from the thermodynamic equation and from the vorticity equation, are included in the derivation of Petterssen's equation (23.5) — see the discussion on page 203 — they automatically form part of the definition of ω^I . There is no way they can appear in (23.5), the definition of ω^{II} . This exposes as fallacious the customary designations of $(\omega^I + \omega^{II})$ and ω^I as being the vertical motions with and without diabatic effects. The ω^I , if completely defined, takes into account the all-important divergent advectons arising from the presence of diabatic effects, and so it is a misnomer to call it the vertical motion that would exist in the absence of diabatic effects.

Similarly, ω^{II} is more correctly designated as that portion of the vertical motion due to the combination of diabatic effects and their induced divergent circulations. To be completely rigorous, of course, one should also admit that there will be changes in the rotational advections due to the presence of diabatic effects; i.e. the stream function patterns associated with given height and temperature configurations will be slightly different according as to whether or not diabatic effects are present. But, unlike their divergent advection counterparts, these changes would be comparatively unimportant ones. The foregoing remarks also explain why the diabatic constraint (23.6), which is based on ω^{II} , is an appropriate formulation for a model in which divergent advections are neglected. However, whereas vertical boundary conditions of $\omega^{\text{II}} = 0$ at 1000 and 200 mb are quite reasonable for latent heat effects which are confined to the middle troposphere, they can scarcely be regarded as realistic for radiation and ocean heating. In lowland and ocean areas the real lower boundary condition is:

$$\omega^{\text{I}} + \omega^{\text{II}} = \omega_g \quad (31.2.2)$$

where ω_g is the terrain-induced vertical motion at the ground. If ω_g is zero, all that (31.2.2) says is that $\omega^{\text{II}} = -\omega^{\text{I}}$, a singularly unhelpful relationship which is something quite different from $\omega^{\text{II}} = 0$, the lower boundary condition which was actually used in the final series of test integrations.

Some attempts were made to incorporate the neglected terms of the vorticity equation into the baroclinic model. These experiments were undertaken because the author — see Campbell and Davies (1966) — had

earlier shown that the magnitudes of the neglected terms become important in the neighbourhood of baroclinic short waves. The main problem turned out to be the computation of the divergent part of the wind. In one approach the velocity potential function was computed from (hour - 1) information and used to provide divergent parts of the wind for the current hour. The forecasts produced in these experiments were not as good as those produced by the same model without the neglected terms, but on the whole they were surprisingly similar. In a second approach a complicated relaxation scheme was set up in which both $\frac{\partial \psi}{\partial t}$ and χ for the current hour were the unknowns. This relaxation appeared to converge satisfactorily, but by 12 hours two-gridlength divergence patterns had established themselves all over the map. Although both approaches were unsuccessful, they provided some experience in dealing with the divergent part of the wind. The most noteworthy feature of the velocity potential fields is that they tend to have sharp local peaks near baroclinic short waves and be quite flat elsewhere. Further, the physical structure of the divergent wind fields near a velocity potential maximum is quite different from that of rotational wind fields near a stream function minimum. The real divergent part of the wind presumably attains its maximum magnitude considerably closer than one grid-point away from the maximum in the velocity potential field, whereas the rotational part of the wind attains its maximum magnitude some distance away, usually two gridlengths or more, from the minimum in the stream function field. Consequently, scale considerations must be much more critical for the divergent winds than they are for rotational winds. In particular, finite difference truncation effects must be quite severe when one computes a divergent advection near a maximum of the velocity potential field. These

conclusions for the divergent advection terms probably also apply to the other neglected terms. Further, after studying a few cases, one is left with the impression that the eddy diffusion terms carry out at least part of the role of the neglected terms, and that they do it in a more efficient manner than explicit evaluations.

The experiments with variable static stability have already been discussed in Section 25. They apparently failed because of the correlation that exists between the magnitude of the static stability and the sign of the stream function tendency.

32. The Parallel Precipitation Scheme

32.1 The large scale precipitation amount

The large scale precipitation amount is computed by (15.1), i.e. by the same method as in the 1970 model. The S^* in this formula is still evaluated from (15.8) or (15.9), but ΔS^* has been reset to a value of 1 C deg instead of the 2.5 C deg used earlier. This means that the threshold dew point depression drops from 7.5 C deg to 6.5 C deg during a 48-hour forecast, instead of from 7.5 C deg to 5 C deg as in the 1970 model.

32.2 The "dry" vertical motion

At the general time step the 700 and 500 mb "dry" vertical motions are computed from:

$$w_d|_n^t = w_A|_n^t + w_B|_n^t + w_G|_n^t \quad n=700, 500 \quad (32.2.1)$$

where

$$w_A|_n^t = -\frac{gf}{\sigma f_0} \left\{ \left[\left\langle \frac{\partial \psi}{\partial p} \right\rangle \Big|_n^{t+1} - \left\langle \frac{\partial \psi}{\partial p} \right\rangle \Big|_n^{t-1} \right] \frac{1}{2\Delta t} + K \int_g^s (\psi_n^t, \left\langle \frac{\partial \psi}{\partial p} \right\rangle \Big|_n^t) \right\} \quad n=700, 500 \quad (32.2.2)$$

$$w_B|_n^t = \begin{cases} -w_A|_n^t & \text{if } (w_A + w_B^*)w_A < 0 \\ w_B^*|_n^t & \text{if } (w_A + w_B^*)w_A \geq 0 \end{cases} \quad n=700, 500 \quad (32.2.3)$$

$$w_B^*|_n^t = -\frac{gf}{\sigma f_0} K K_w \nabla^2 \left(\left\langle \frac{\partial \psi}{\partial p} \right\rangle \Big|_n^{t-1} \right) \quad n=700, 500 \quad (32.2.4)$$

$$w_G|_n^t = N_g w_g^*|_n^t \quad n=850, 700, 500 \quad (32.2.5)$$

$$K_w = K_D (1 - a_\eta \sin \alpha_c) + K_d (1 + a_\eta^* \sin \alpha_c) [1 + (t - t_0) a_t] \quad (32.2.6)$$

where Δt is as usual the time step of one hour; the superscripts $(t+1)$, t and $(t-1)$ refer to the next, current, and preceding hour values respectively; the factor (f/σ) is assumed to depend on pressure only, and is evaluated at latitude 45 N by taking the static stability to have the "dry" standard atmosphere values given in Table 2; the vertical finite difference operators are evaluated by the parabolic fit formula (E13.2); K is defined by (E1.3); J_g is the Shuman Jacobian (E12.1); N_g is taken to be 0.67; ω_g^* is given by (27.5); K_D , K_d , a_η , a_η^* and a_t are given in Table 25; α_c is given by (25.5); and $(t-t_0)$ is the time in hours which has elapsed since initial time.

Note that the preceding formulation differs from (16.3) in that:

- (i) The advection term is evaluated by the Shuman Jacobian instead of the standard one.
- (ii) The N_g has been reduced to 0.67 from unity.
- (iii) The eddy diffusion coefficient is taken outside the pressure derivative operator instead of being kept inside.
- (iv) The eddy diffusion term is not allowed to reverse the sign of the vertical motion given by the tendency and advection terms, whereas no such restriction was imposed before.

Note also that no allowance is made for the fact that the standard Jacobian is used at 200 mb in the baroclinic model. Unfortunately, it was not possible to use $0.5 \chi_D'(x, y, p, t)$ instead of $K_D (1 - a_\eta \sin \alpha_c)$ in the definition of K_w without some major reprogramming.

The desirability of the 0.5 factor had been established in earlier experiments with the parallel model. Consequently, it was included in the 1970 operational model, but it was omitted from the final parallel model due to an oversight. As will be seen from the results, the omission of the 0.5 factor and the lack of a variable eddy diffusion coefficient both contributed to under-estimates of the vertical motion. The consequent under-forecasting of large scale precipitation amount was particularly noticeable in the latter stages of the occlusion process.

At 850 mb, at the general time step, the "dry" vertical motion is computed from:

$$w_d|_{850}^t = w_d|_{700}^t + \Delta p \left\langle \frac{\partial w}{\partial p} \right\rangle \Big|_{775}^t - w_G|_{700}^t + w_G|_{850}^t \quad (32.2.7)$$

where

$$\begin{aligned} \left\langle \frac{\partial w}{\partial p} \right\rangle \Big|_{775}^t = & \frac{K}{2f_0} \left\{ \frac{4\Phi^2 (\psi_{850}^{t+1} + \psi_{700}^{t+1} - \psi_{850}^{t-1} - \psi_{700}^{t-1})}{2\Delta t} \right. \\ & + \mathcal{J}_g(\psi_{850}^t, [4K\Phi^2\psi_{850}^t + f]) \\ & + \mathcal{J}_g(\psi_{700}^t, [4K\Phi^2\psi_{700}^t + f]) \\ & \left. - K_w\Phi^2 [4K\Phi^2(\psi_{850}^{t-1} + \psi_{700}^{t-1}) + 2f] \right\} \quad (32.2.8) \end{aligned}$$

$w_d|_{700}^t$ is given by (32.2.1); $w_G|_{700}^t$ and $w_G|_{850}^t$ are given by (32.2.5); Δp is 150 mb; \mathcal{J}_g is the Shuman Jacobian (B12.1); K is defined by (C1.3); and K_w is given by (32.2.6). This method of computing $w_d|_{850}^t$ overcomes the phasing deficiencies of (16.4).

At initial time the $(t-1)$ superscripts are replaced by t , and the $2\Delta t$ factors are replaced by Δt .

32.3 The "wet" vertical motion

First, a preliminary "wet" vertical motion is computed from the "dry" vertical motion by an application of (17.1). For convenience, the values of ω so obtained are redefined as ω_{\pm} . The final "wet" vertical motions are then obtained from:

$$\omega|_n = \omega_{\pm}|_n + a_H|_n (H_3 + H_4)|_n \frac{f_n}{(\sigma_s)_n f^*} \quad (32.3.1)$$

$n = 850, 700, 500$

where

$$f^* = \begin{cases} f & \text{if } f \geq 0.2 \\ 0.2 & \text{if } f < 0.2 \end{cases} \quad (32.3.2)$$

H_3 is given by (29.1); H_4 is given by (30.1); σ_s is the "dry" standard atmosphere static stability given by Table 2; and a_H is an empirical correction factor given by:

$$a_H = \begin{cases} 1 & \text{if } n = 850 \\ 0.95 & \text{if } n = 700 \\ 0.9 & \text{if } n = 500 \end{cases} \quad (32.3.3)$$

The purpose of the a_H factors is to compensate for the lack of a divergent advection term in (32.2.2). In retrospect it seems likely that these a_H values are too high.

Note that this method of computing the final "wet" vertical motion does not permit a full interaction between ocean heating and the release of latent heat, since such a linkage is undesirable in no data areas.

32.4 The temperature forecasts

The temperature forecasts are produced from the following formula:

$$\begin{aligned}
T_n^{t+1} = & T_n^{t-1} + 2\Delta t \left\{ -K J_g(\psi_n^t, T_n^t) \right. \\
& + (\omega')_n^t \left[\frac{dT}{dp} \Big|_n^t - a_b \Big|_n \overline{\left\langle \frac{\partial T}{\partial p} \right\rangle}_{700}^t \right] \\
& + KK_D \nabla^2 T_n^{t-1} - \frac{P}{R} (H_3 + H_4) \Big|_n^{t-1} \\
& \left. - \frac{P}{R} KK_D \nabla^2 [(H_3 + H_4) \Big|_n^{t-1}] + h_s \Big|_n^t \right\} \quad (32.4.1)
\end{aligned}$$

$n = 850, 700, 500$

where Δt is one hour; the superscripts t and $(t-1)$ refer to current and previous hour values; J_g is the Shuman Jacobian (E12.1); $(\omega')_n^t$ is evaluated by means of the vertical motion damping formula (18.4), but with the values of w_c and b_c from Table 30; $\frac{dT}{dp} \Big|_n^t$ is computed from (18.5); $\overline{\left\langle \frac{\partial T}{\partial p} \right\rangle}_{700}^t$ is evaluated by the parabolic fit formula (E13.1); ∇^2 is the standard smoothing operator (B3.1); H_3 is given by (29.1); H_4 is given by (30.1); at all three levels K_D is set equal to a value of 5 dkm at initial time, corresponding to a K_D^* value of 4.29×10^7 dkm² hour⁻¹, and is augmented by 2% per hour thereafter; $h_s \Big|_n^t$ is computed from (18.3); and $a_b \Big|_n$ is given by values which reflect the standard atmosphere relationships, viz:

$$a_b \Big|_n = \begin{cases} 0.8235 & \text{if } n = 850 \\ 1 & \text{if } n = 700 \\ 1.4 & \text{if } n = 500 \end{cases} \quad (32.4.2)$$

Equation (32.4.1) is, of course, a somewhat modified form of (18.2). From early experiments with the parallel model it became apparent that

Level (mb)	Predicted Quantity	ω (mb hour ⁻¹)	ω_c (mb hour ⁻¹)	b_c
850	T	all	18	0.2
700	T	all	27	0.2
500	T	all	18	0.2
all	S	all	75	0.2

Table 30 : Values of the constants used in the vertical motion damping formula in the parallel model experiments. The constant b_c is dimensionless. The values given for ω_c are for initial time; these are augmented by 1% per hour. (c.f. Table 10)

the vertical motion damping had to be made less restrictive with the Shuman Jacobian. So it seems that in the 1970 model the success of the heavy vertical motion damping is due to the use of the standard Jacobian. Lighter damping meant that $\left\langle \frac{\partial T}{\partial p} \right\rangle$ had to be evaluated more realistically at the outer levels. Several methods utilising information from the horizontal temperature fields were tried, but most of these had systematic deficiencies. The best that could be done was to use smoothed 700 mb values of $\left\langle \frac{\partial T}{\partial p} \right\rangle$ at all levels, adjusted slightly to reflect the standard atmosphere relationships. The term representing the eddy diffusion of $(H_3 + H_4)$ was added to correct for a specific deficiency. This was a spurious cooling phenomenon which occurred at over-land grid points upwind from grid points where ocean heating was taking place; it is a finite difference effect which arises from the advection term. It was rather disappointing to find significantly better temperature forecasts were obtained by using approximately $0.5(H_3 + H_4)$ in (32.4.1), but discounting both H_3 and H_4 entirely in the baroclinic model and in the vertical motion computations (32.3.1). Most of the problems seem

to arise when $w_z|_n$ in (32.3.1) is small. For instance, if $w_z|_n$ is zero, and H_3 is zero, $w|_n$ becomes just $(a_H H_4 f_0 / c_s f^*)$. In the polar night the resultant subsidence can easily be large enough to negate the cooling produced by the $(-\frac{P}{R} H_4)$ term in (32.4.1). Of course, the same kind of effect goes on in the real atmosphere, but it is difficult to simulate this exactly without a divergent advection term, and without taking the real value of σ into account.

32.5 The dew point depression forecasts

The dew point depression forecasts are produced from the following formula:

$$S_n^{t+1} = S_n^{t-1} + 2\Delta t \left\{ -J_g(\psi_n^t, S_n^t) + (w')|_n^t \left[\frac{dS|_n^t}{dP|_n} - \Lambda|_n^t \right] + KK_D \nabla^2 S_n^{t-1} - \gamma_s|_n \frac{P}{R} \left[H_4|_n^{t-1} + KK_D \nabla^2 (H_4|_n^{t-1}) \right] - \Gamma|_n^t \right\} \quad (32.5.1)$$

$$n = 850, 700, 500$$

where

$$\Lambda|_n^t = \Lambda^*|_n^t \quad \text{if } n = 850, 700 \quad (32.5.2)$$

$$\Lambda|_{500}^t = \begin{cases} \Lambda^*|_{500}^t & \text{if } w_{500} < 0 \text{ or } T_{500} \geq -20 \\ \left(\frac{-20 - T_{500}}{10} \right) \Lambda^{**}|_{500}^t + \left(\frac{30 + T_{500}}{10} \right) \Lambda^*|_{500}^t & \text{if } w_{500} > 0 \text{ and } -20 > T_{500} > -30 \\ \Lambda^{**}|_{500}^t & \text{if } w_{500} > 0 \text{ and } -30 > T_{500} \end{cases} \quad (32.5.3)$$

$$A^*|_n^t = a_b|_n \left\langle \frac{\partial S}{\partial P} \right\rangle|_{700}^t \quad n=850, 700, 500 \quad (32.5.4)$$

$$A^{**}|_{500}^t = \frac{S_{700} - 30}{4.00} \quad (32.5.5)$$

$$\Gamma_S = \Gamma_S^I + \Gamma_S^{II} + \Gamma_S^{III} + \Gamma_S^{IV} + KK_D \nabla^2 (\Gamma_S^{III} + \Gamma_S^{IV}) \quad (32.5.6)$$

$$\Gamma_S^{IV} = \begin{cases} 0 & \text{if } n=850, 700 \\ \left(\frac{\sum_1 \tau_s}{3 \hat{\gamma} \tau_s} \right) S_{500}^{t-1} & \text{if } n=500 \end{cases} \quad (32.5.7)$$

where Δt is one hour; the superscripts t and $(t-1)$ correspond to current and previous hour values; K is given by (C1.3); J_s is the Shuman Jacobian (E12.1); $(w')_n^t$ is evaluated by means of the vertical motion damping formula (18.4), but with values of w_c and b_c from Table 30; $\left. \frac{dS}{dp} \right|_n^t$ is computed from (19.4); $\left\langle \frac{\partial S}{\partial P} \right\rangle|_{700}^t$ is evaluated by means of the parabolic fit formula (E13.1); ∇^2 is the standard smoothing operator (B3.1); H_4 is given by (30.1); at all three levels K_D is set equal to 5 dkm at initial time, corresponding to a K_D^* value of 4.29×10^7 dkm² hour⁻¹, and is augmented by 2% per hour; $a_b|_n$ is given by (32.4.2); Γ_S^I is given by (19.7); Γ_S^{II} is given by (19.8); Γ_S^{III} is given by (29.3); $\sum_1 \tau_s$ is the sum of the small scale precipitation contributions from all three layers, after corrections for mountains and evaporation; $\hat{\gamma}$ is the same as in Section 21, i.e. 0.05556 inches; τ is 12 hours; and the $\tau_s|_n$ are empirical correction factors given by:

$$\gamma_s|_n = \begin{cases} 1 & \text{if } n = 850 \\ 1.25 & \text{if } n = 700 \\ 1.5 & \text{if } n = 500 \end{cases} \quad (32.5.8)$$

Equation (32.5.1) is a modified form of (19.3) in much the same way that (32.4.1) is a modified form of (18.2). The remarks made about the Shuman Jacobian, the vertical motion, and the diabatic effects for (32.4.1) also apply to some degree to (32.5.1). In particular, the ambiguity introduced by the $\gamma_s|_n$ is again due to the neglect of the divergent advection term and the use of an artificial static stability. There are two other features of note. First, (32.5.3) accounts for the descent of very dry stratospheric air into the troposphere. Second, (32.5.8) accounts for the transport of moisture upwards by small scale shower activity.

32.6 The small scale precipitation amount

The small scale precipitation amount is computed exactly as in Section 20 except for one minor change. In Table 21 the value of K_f has been reduced from 4.762×10^{-4} to 4.0×10^{-4} , where the units are $C \text{ deg}^{-3} (2 \times \text{grid distance})^2$.

32.7 The total precipitation

The total precipitation is computed exactly as in Section 21. However, there has been a small change in the precipitation type criteria of page 161. If there is snow cover on the ground, then the lapse rate in the lowest layer of air is assumed to be isothermal, and 0 C deg replaces - 3 C deg as the 850 mb temperature which divides snow areas from rain areas. The daily snow cover charts are climatological ones obtained by interpolation from the monthly mean charts.

33. Other Features

33.1 Cloud Forecasts

The parallel model produces cloud forecasts for the same three layers of the atmosphere as it produces precipitation forecasts. Briefly, overcast stratiform cloud is assumed to exist under similar conditions as large scale precipitation, but with a slightly higher threshold value for the dew point depression. An even higher threshold value is assumed to mark the onset of stratiform cloud formation, and intermediate dew point depressions are assumed to give partly cloudy conditions. Similarly, overcast cumuliform clouds are predicted when the small scale precipitation formulae indicate the onset of showers. And all threshold values are assumed to be somewhat less restrictive for the onset of cumuliform cloud formation. Once again intermediate values are assumed to give partly cloudy conditions. When both stratiform and cumuliform clouds are predicted to be present, reasonable rules are employed to decide which type is dominant, or whether the whole conglomeration should just be regarded as mixed. No attempt is made to compute the latent heat released by cloud formation.

As far as can be judged, the cloud forecasts produced in this way are excellent. They are fully compatible with the baroclinic model forecasts, and are quite realistic in that partly cloudy conditions normally exist only in very narrow bands around the main low centres and frontal bands. From the practical point of view, there are two questions which still have to be answered:

- (i) What is the most useful method of displaying predicted cloud information for three layers?
- (ii) How should the cloud forecasts be objectively verified?

33.2 Terminal Forecasts

Terminal forecasts of upper cloud and precipitation are produced for selected Canadian stations by interpolation from the grid point forecasts. They actually consist of a series of coded statements of significant changes in weather conditions, and the times these changes will occur. It is interesting to note that the correct sequence of cloud and precipitation is predicted as a low centre passes near a station, though usually the timing is a bit off because the baroclinic model does not move things with quite the right speed. Overcast high cloud moves in first, then overcast middle cloud, then precipitation soon followed by low cloud; after the storm has gone by the low level cloud is often the last to break up. The outstanding technical problems are twofold:

- (i) Significant changes in weather conditions have to be redefined to reduce the amount of print-out.
- (ii) The terminal forecasts have to be converted from an internal computer code to a more standard format.

Ceiling, visibility, and surface wind predictions could be added to the terminal forecasts with very little extra effort, as statistical techniques for doing this have already been developed elsewhere.

33.3 Derived 1000 mb Height Forecasts

The parallel model produces derived 1000 mb height forecasts by applying the thermodynamic equation to the 1000-700 mb layer, and making use of the known vertical velocity at 850 mb. Theoretically, this approach should overcome the phasing deficiencies of the operational 1000 mb forecasts -- see Davies and Harlow (1967) for a discussion of this problem. In practice, several technical problems have arisen and it has not yet been possible to give them more than superficial attention. These all involve the primary constraints, i.e. the terrain, eddy diffusion and diabatic effects.

34. Results

Eleven cases were integrated to 48 hours both with the parallel model and with the 1968 model. The initial times of these cases were:

- (i) 12Z Jan 29 th 1969
- (ii) 00Z Jul 26 th 1969
- (iii) 12Z Sep 9 th 1969
- (iv) 00Z Nov 18 th 1969
- (v) 00Z Dec 21 st 1969
- (vi) 12Z Dec 25 th 1969
- (vii) 00Z Jan 25 th 1970
- (viii) 00Z Jan 27 th 1970
- (ix) 00Z Jan 28 th 1970
- (x) 00Z Mar 3 rd 1970
- (xi) 00Z Mar 26 th 1970

Figs. 33-76 display height and precipitation charts for nine of these cases in chronological order. The case of 00Z Jul 26 th 1969 was omitted because the seasonal variation of the control coefficients in the parallel model led to insufficient linkage between the levels in summer. The case of 12Z Sep 9 th 1969 was omitted because the only feature of interest in the analyses was a secondary low which developed off Cape Hatteras and became a major storm. Both models missed this development.

The height Figs. each display four charts for the same level. The initial time objective analysis is shown at the top left. The verifying objective analysis valid 48 hours later is shown at the top right. The 48-hour forecast produced by the 1968 model is shown at

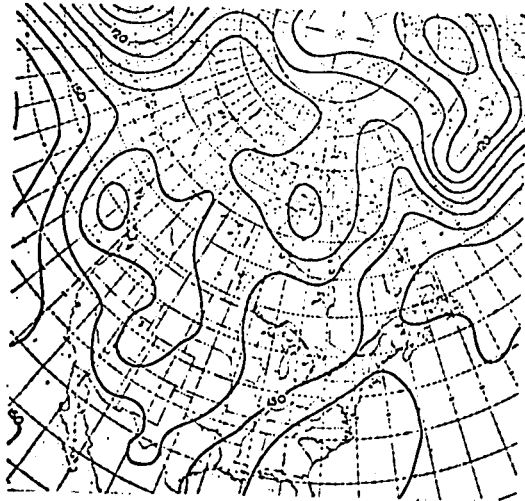
the bottom left. And the 48-hour forecast produced by the parallel model is shown at the bottom right. The Figs. include sets of charts for 850 and 500 mb for all nine cases, and those for 700 and 200 mb for four cases (12Z Jan 29 th 1969, 00Z Dec 21 st 1969, 12Z Dec 25 th 1969, and 00Z Jan 27 th 1970). The four sets of 700 mb charts were included to show that the parallel model forecasts at this level are fully consistent with those at 850 and 500 mb. The four sets of 200 mb charts were included to demonstrate the clear superiority of the parallel model forecasts at this level.

The precipitation Figs. each display four charts of 24-hour precipitation amount for the same time period. The subjective analysis of the observed reports is shown at the top left. The objective analysis of the same observed reports is shown at the top right. The forecast produced by the 1968 model is shown at the bottom left. And the forecast produced by the parallel model is shown at the bottom right. The Figs. include charts for 00-24 hours and 24-48 hours for all nine cases. In examining the precipitation analyses it should be borne in mind that no reports were available from Greenland, Mexico, or the ocean areas, so these must be regarded as unanalysed regions.

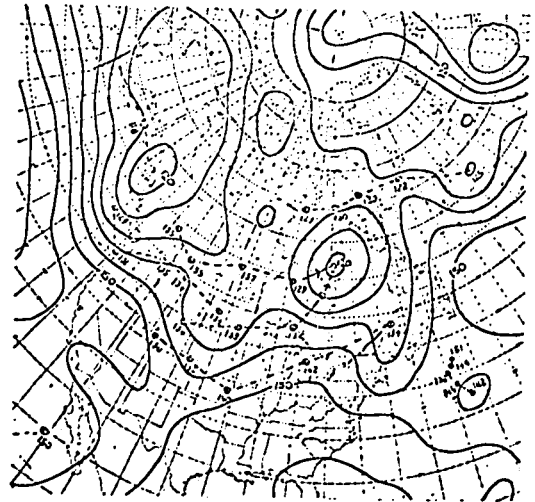
Tables 31-42 list the CRMSE verification scores for the 850, 700, 500 and 200 mb height forecasts for the 238-point grid, the 504-point grid, and the interior of the 1221-point grid. The 700 mb height forecasts are missing for three of the cases (12Z Sep 9 th 1969, 00Z Mar 3 rd 1970, and 00Z Mar 26 th 1970) because the reverse balance equation program failed to work at this level after some software changes had been made to the computer operating system. Tables 43-51 list the RMSE verification scores for the 850, 700 and 500 mb temperature forecasts for

the 238-point grid, the 504-point grid, and the interior of the 1015-point grid. Tables 52-60 list the RMSE verification scores for the 850, 700 and 500 mb dew point depression forecasts for the 238-point grid, the 504-point grid, and the interior of the 1015-point grid. Each of these Tables 31-60 lists results for the parallel model, the 1968 model, and persistence.

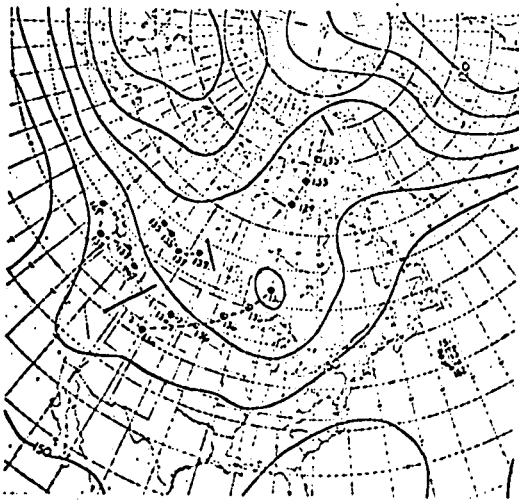
Tables 61-66 list Threat Score evaluations of the precipitation forecasts. Table 61 lists Threat Scores for 00-24 hours for a threshold of 0.01 inches, for both large scale and total precipitation, for all received Canadian stations, all received U.S. stations, and Canadian and U.S. stations combined. Tables 62 and 63 list the same information for 12-36 hours and 24-48 hours. Table 64 lists Threat Scores for 00-24 hours for thresholds of 0.25 inches, 0.50 inches, and 1.0 inch, for both large scale and total precipitation, for all received North American stations. Tables 65 and 66 list the same information for 12-36 hours and 24-48 hours. Tables 67-73 list Skill Factor evaluations of the precipitation forecasts. Table 67 lists Skill Factors for 06-12 hours, for both large scale and total precipitation, and for both Table I and Table II penalty tables, for Class A grid points in the 238-point grid. (See Appendix E for a description of the Skill Factor verification procedure.) Tables 68,69,70,71,72, and 73 list the same information for 18-24 hours, 30-36 hours, 42-48 hours, 00-24 hours, 12-36 hours, and 24-48 hours respectively. Each of the Tables 61-73 list the results for the parallel model and the 1968 model.



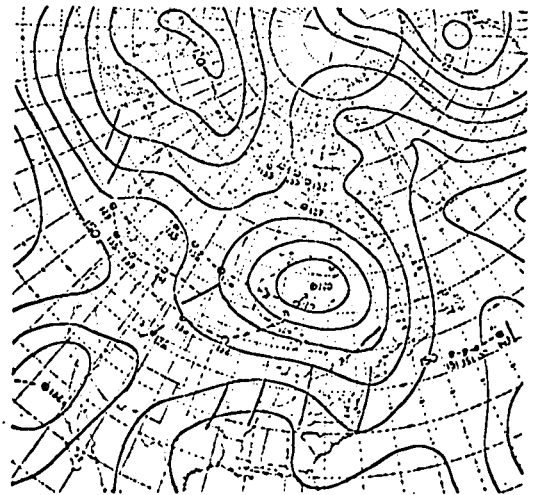
initial analysis



verifying analysis

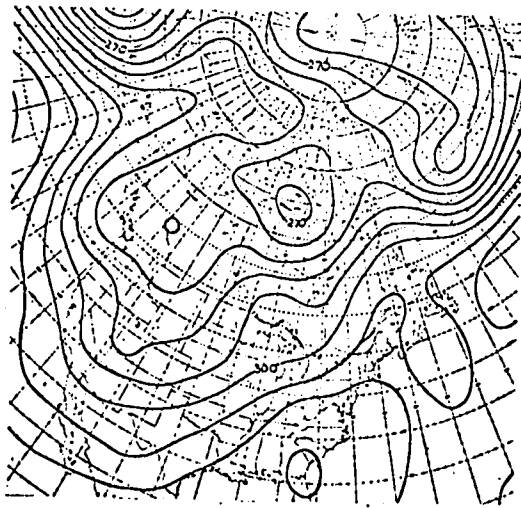


1968 model 48-hour forecast

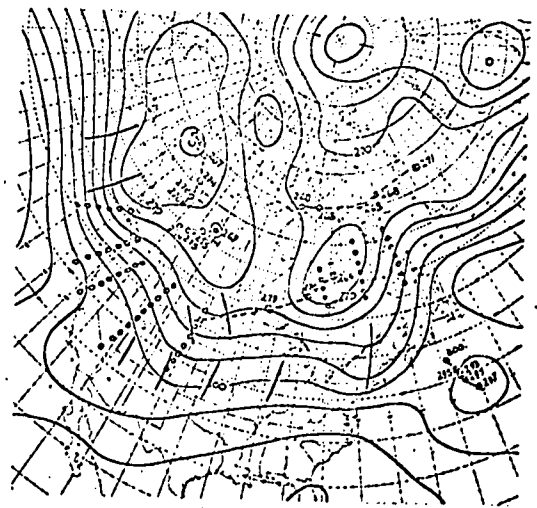


parallel model 48-hour forecast

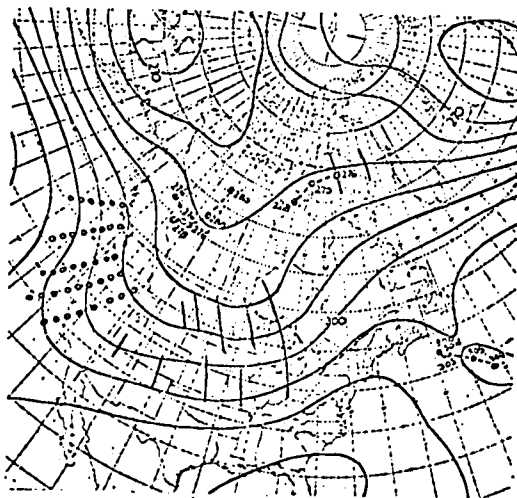
Fig. 33 : The set of 850 mb height charts for the case of 12Z Jan 29 th 1969.



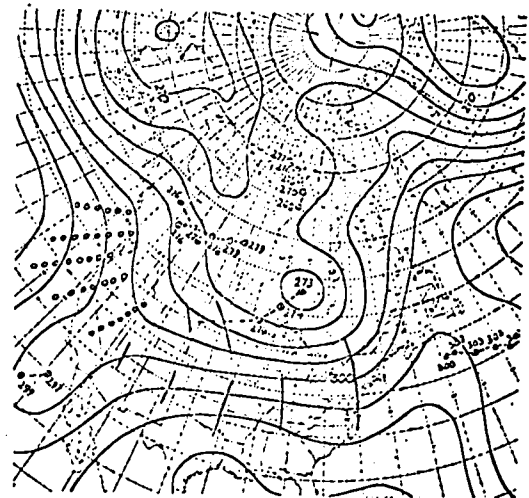
initial analysis



verifying analysis

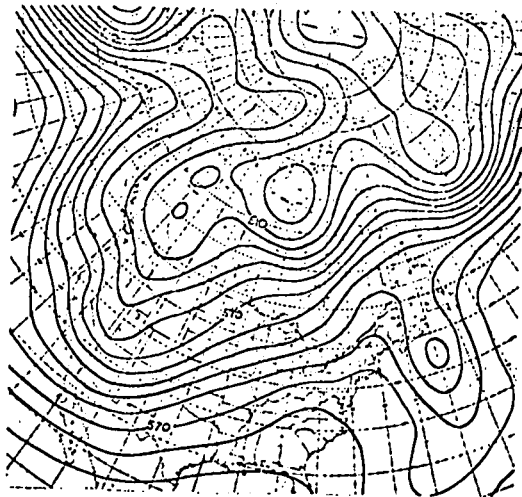


1968 model 48-hour forecast

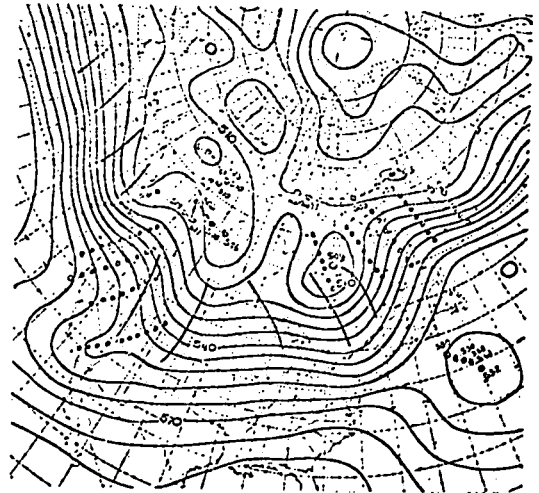


parallel model 48-hour forecast

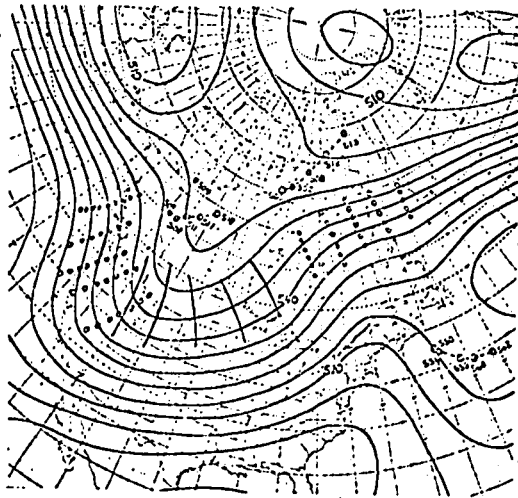
Fig. 34 : The set of 700 mb height charts for
the case of 12Z Jan 29 th 1969.



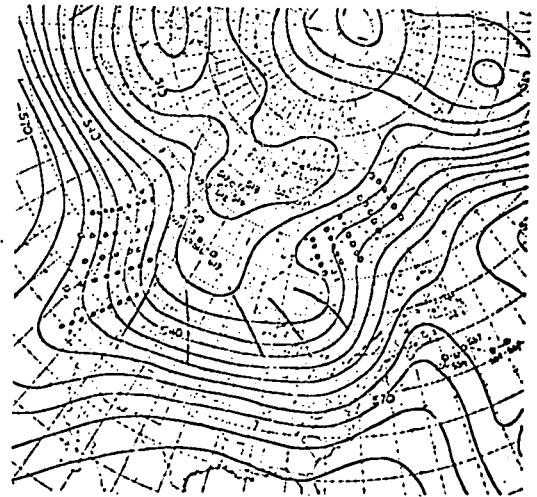
initial analysis



verifying analysis

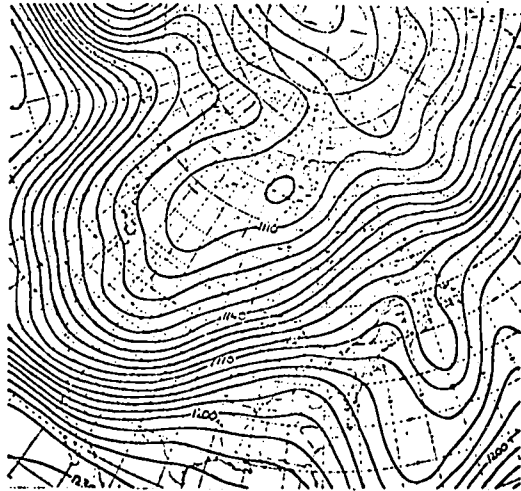


1968 model 48-hour forecast

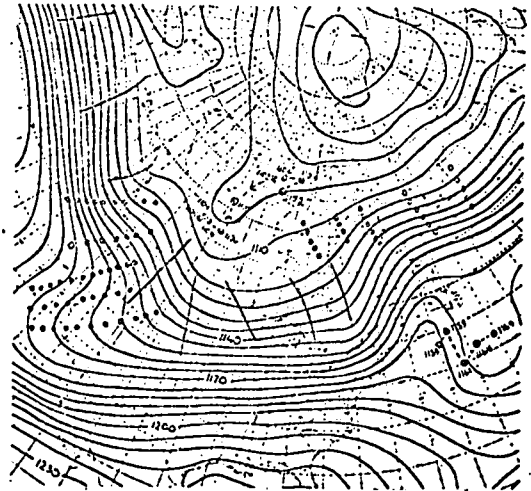


parallel model 48-hour forecast

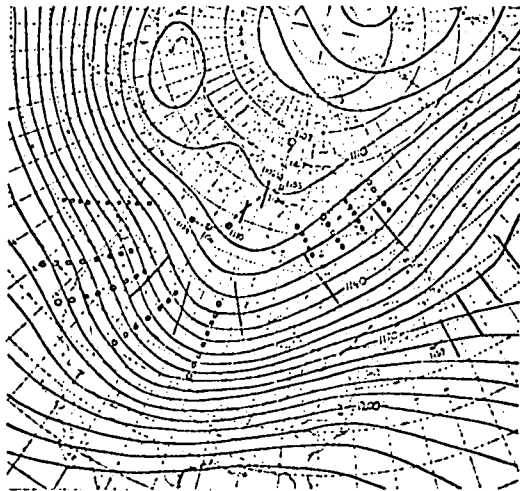
Fig. 35 : The set of 500 mb height charts for
the case of 12Z Jan 29 th 1969.



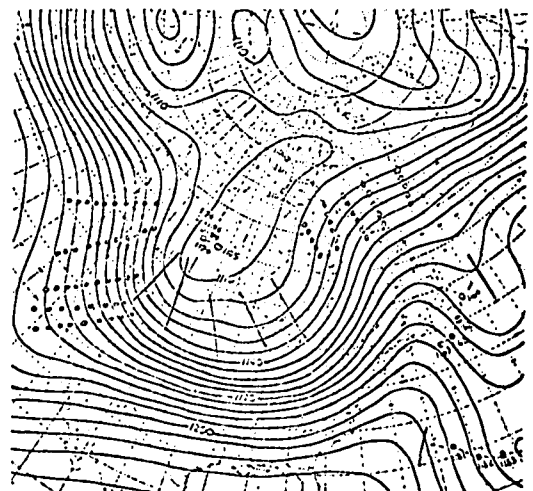
initial analysis



verifying analysis

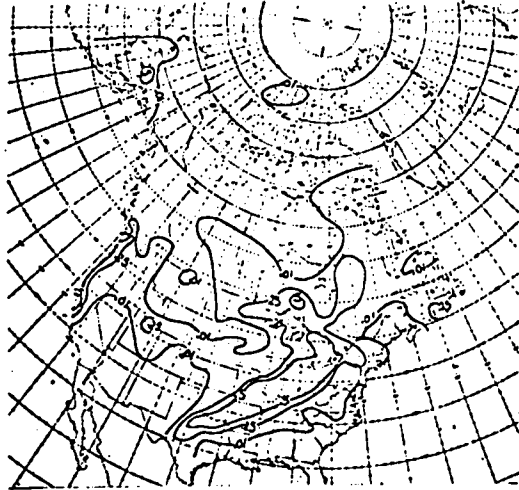


1968 model 48-hour forecast

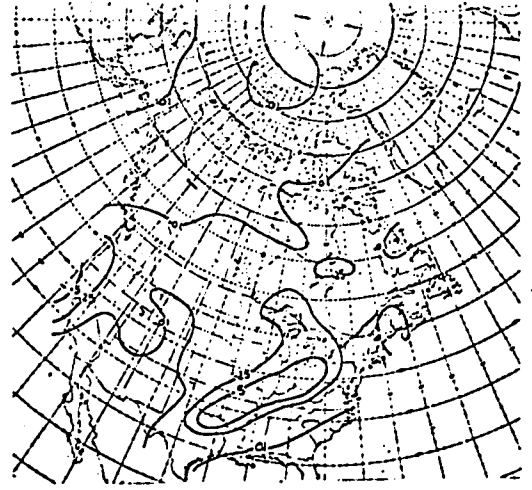


parallel model 48-hour forecast

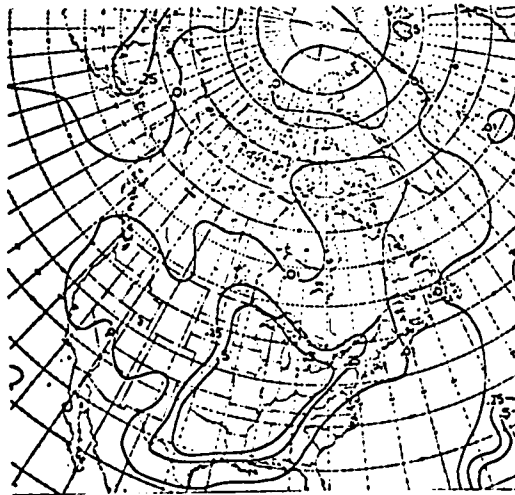
Fig. 36 : The set of 200 mb height charts for the case of 12Z Jan 29th 1969.



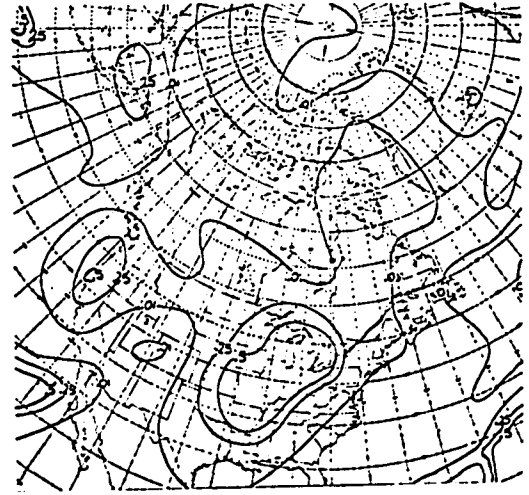
subjective analysis



objective analysis

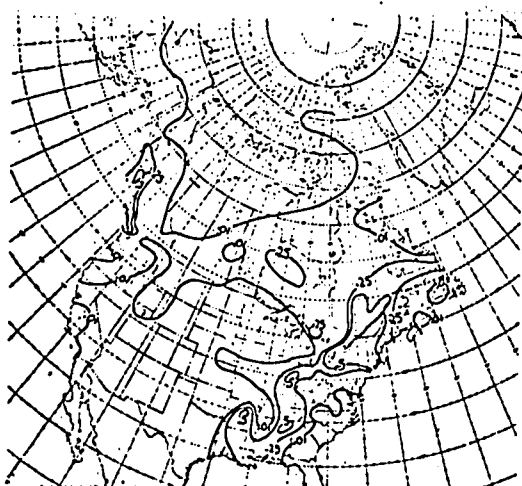


1968 model forecast

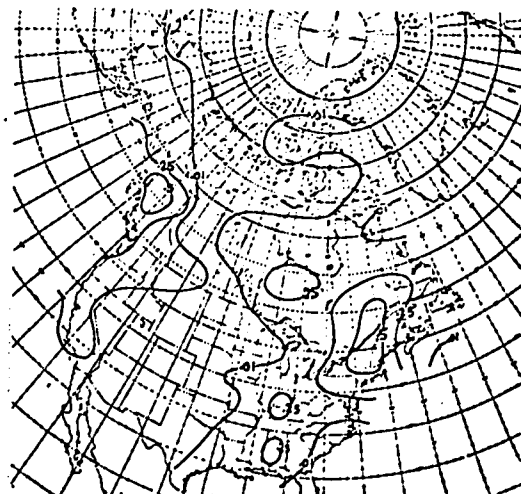


parallel model forecast

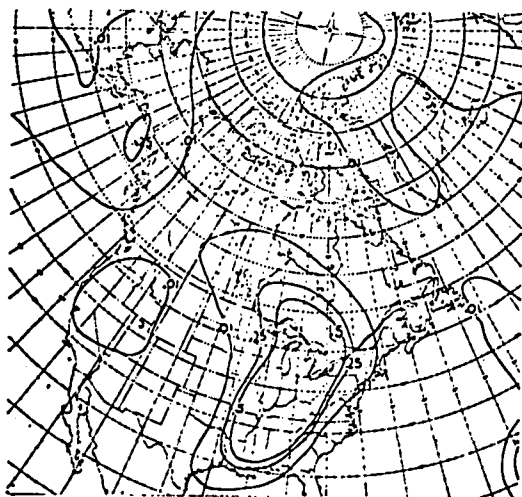
Fig. 37 : The set of 00-24 hour precipitation charts
for the case of 12Z Jan 29 th 1969.



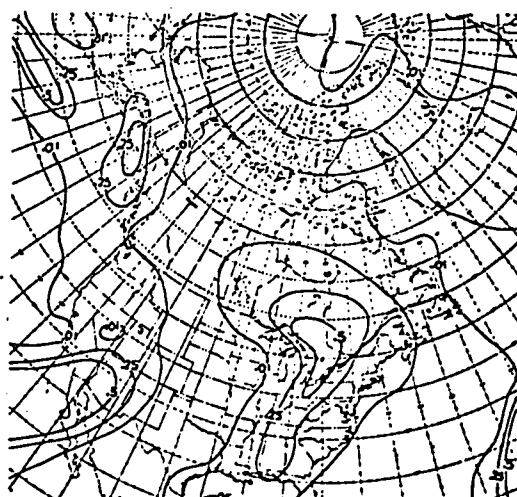
subjective analysis



objective analysis

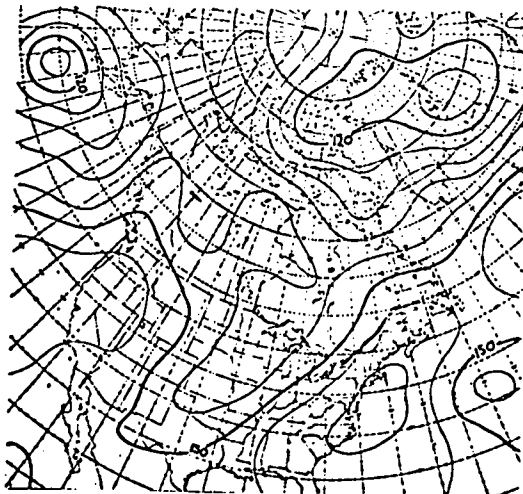


1968 model forecast

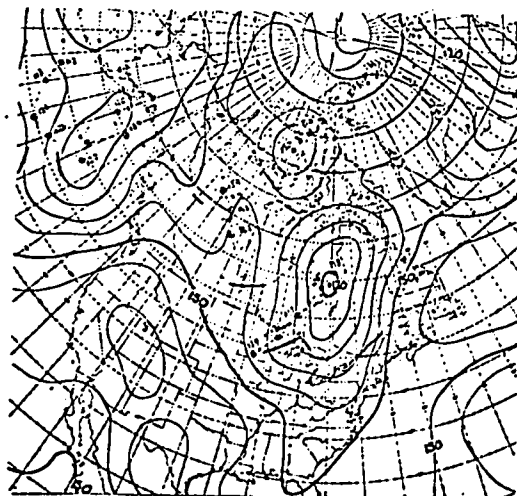


parallel model forecast

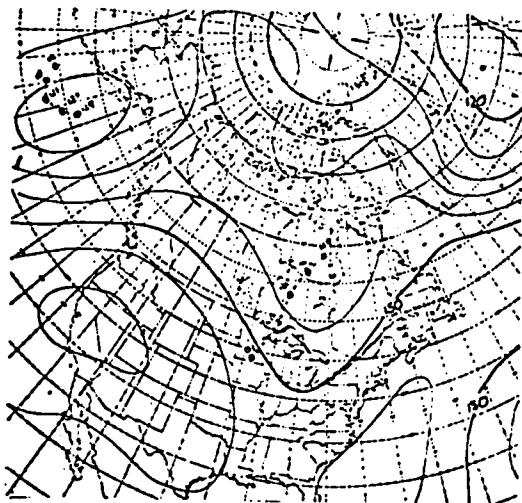
Fig. 38 : The set of 24-48 hour precipitation charts
for the case of 12Z Jan 29 th 1969.



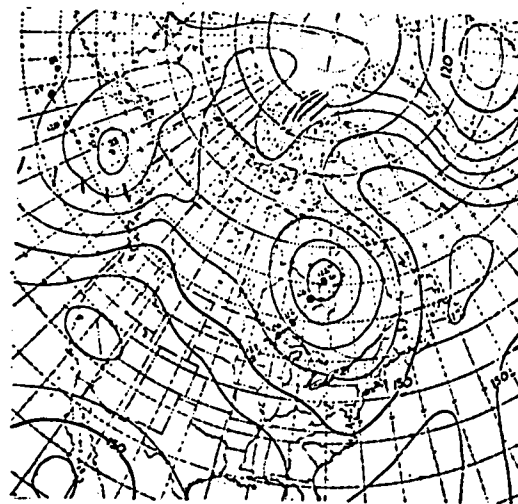
initial analysis



verifying analysis

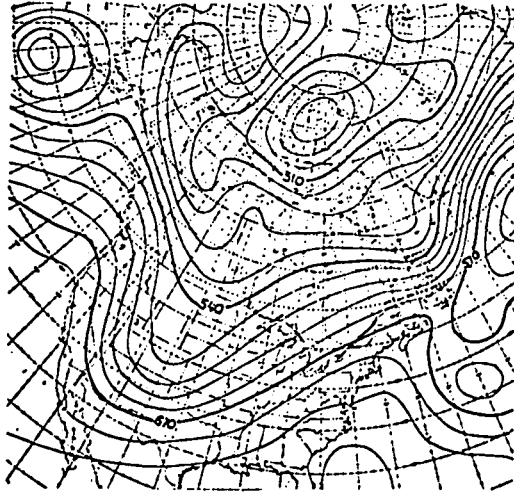


1968 model 48-hour forecast

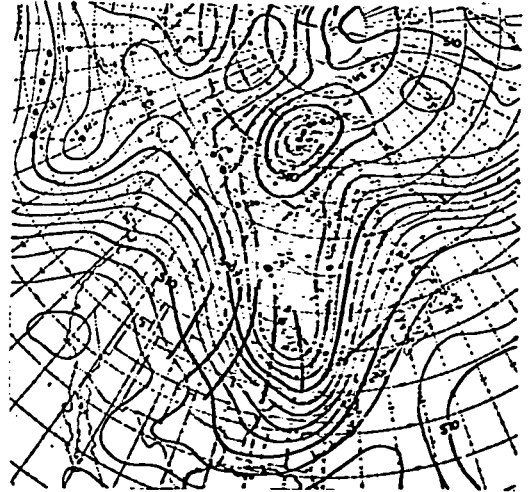


parallel model 48-hour forecast

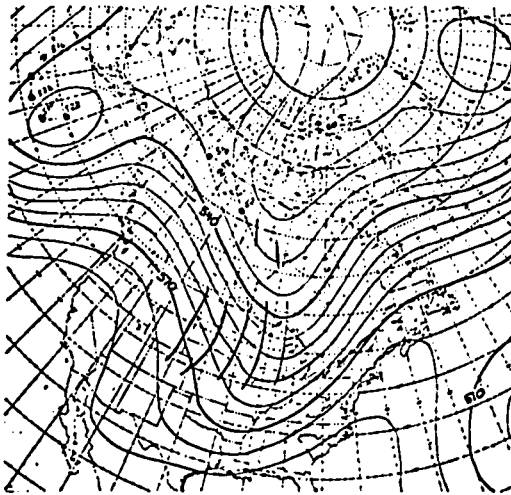
Fig. 39 : The set of 850 mb height charts for the case of 00Z Nov 18 th 1969.



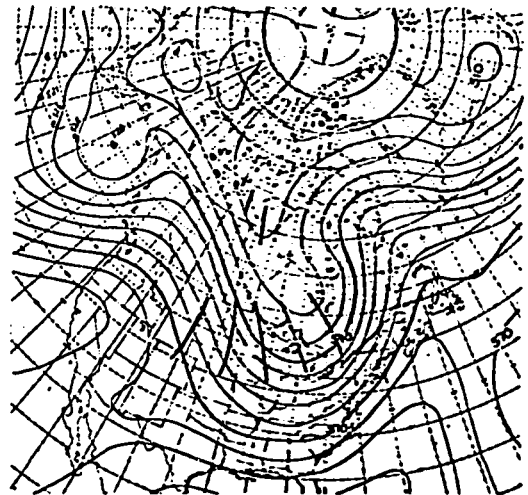
initial analysis



verifying analysis

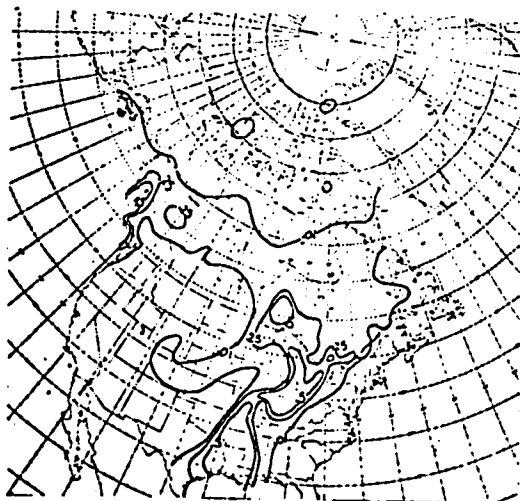


1968 model 48-hour forecast

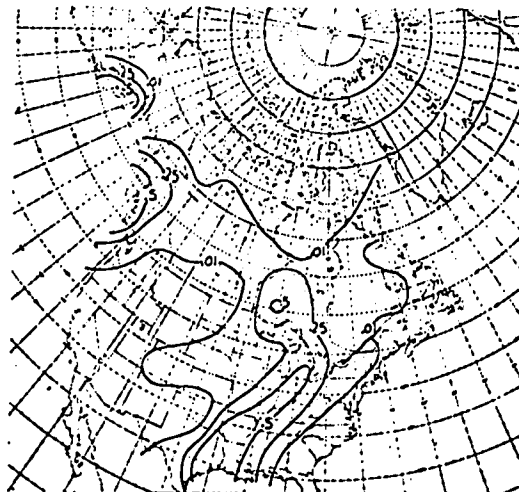


parallel model 48-hour forecast

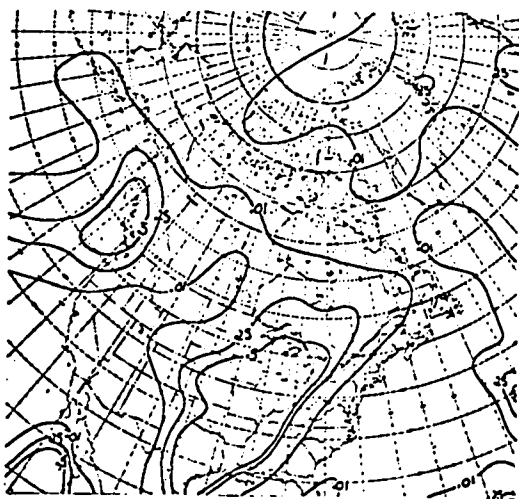
Fig. 40 : The set of 500 mb height charts for
the case of 00Z Nov 18 th 1969.



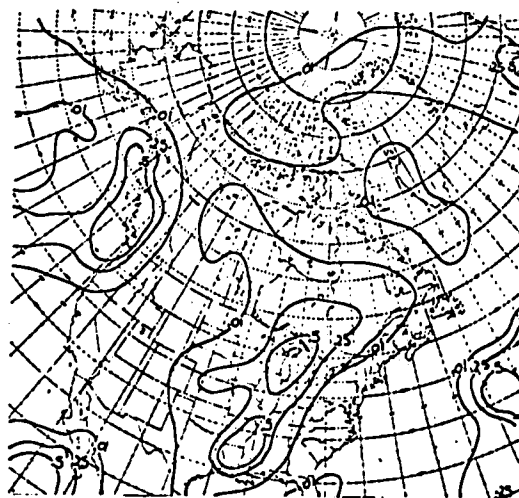
subjective analysis



objective analysis

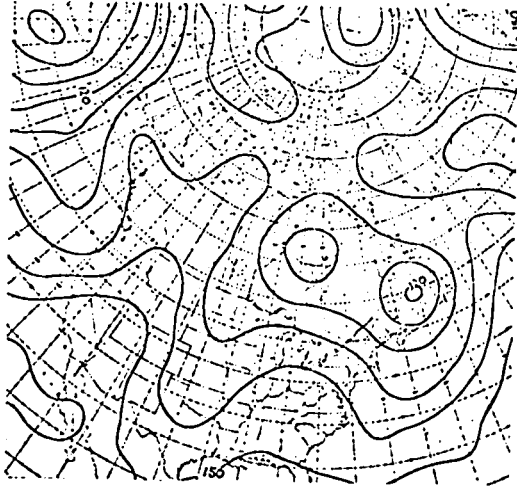


1968 model forecast

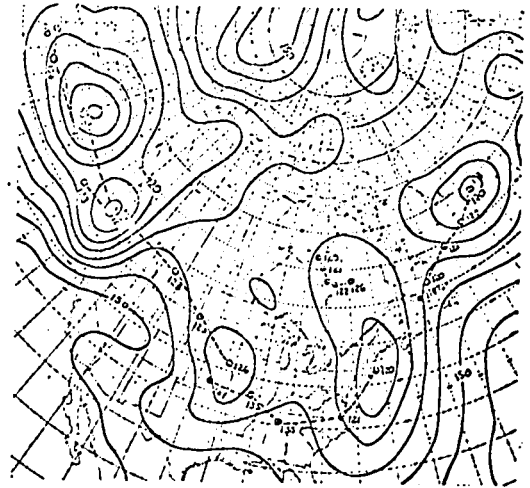


parallel model forecast

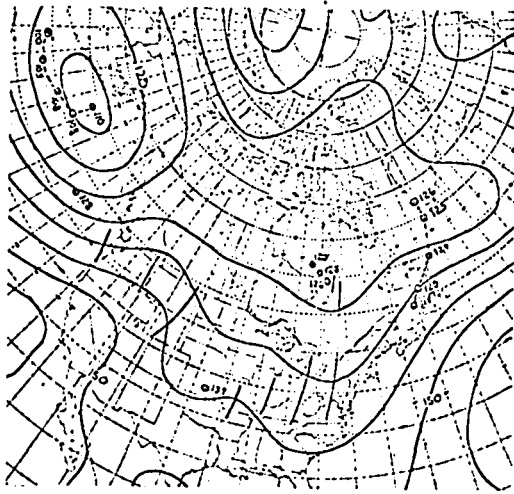
Fig. 41 : The set of 00-24 hour precipitation charts
for the case of 00Z Nov 18 th 1969.



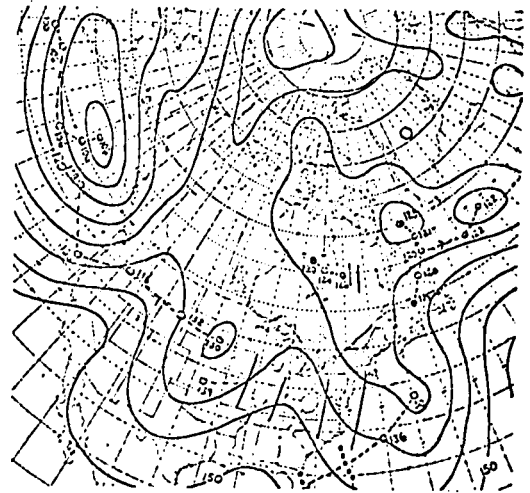
initial analysis



verifying analysis

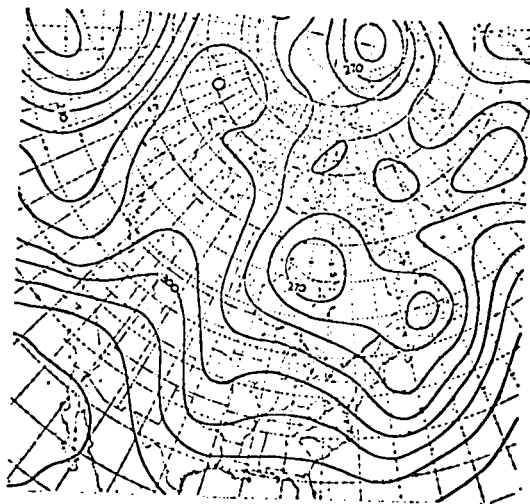


1968 model 48-hour forecast

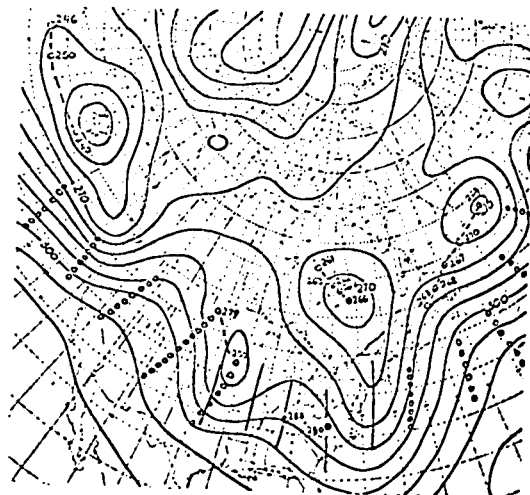


parallel model 48-hour forecast

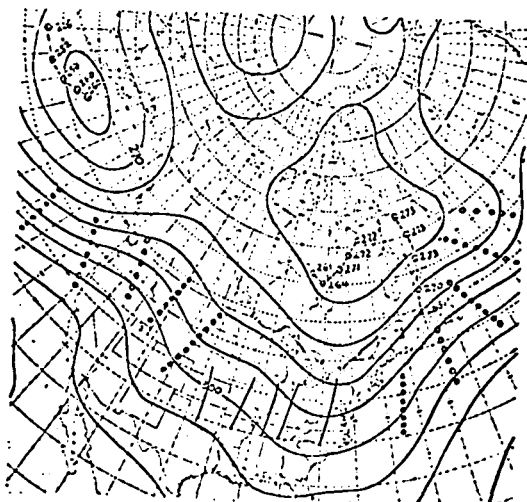
Fig. 43 : The set of 850 mb height charts for
the case of 00Z Dec 21 st 1969.



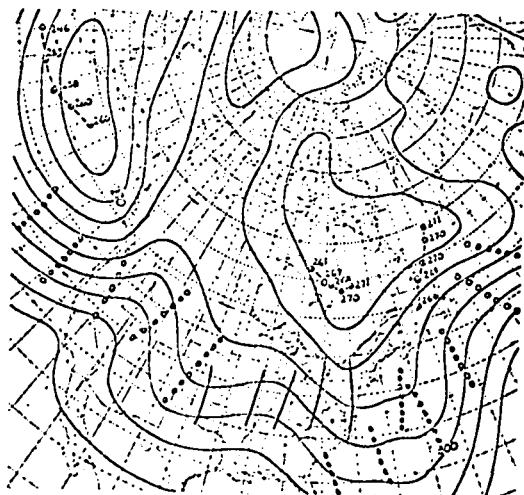
initial analysis



verifying analysis

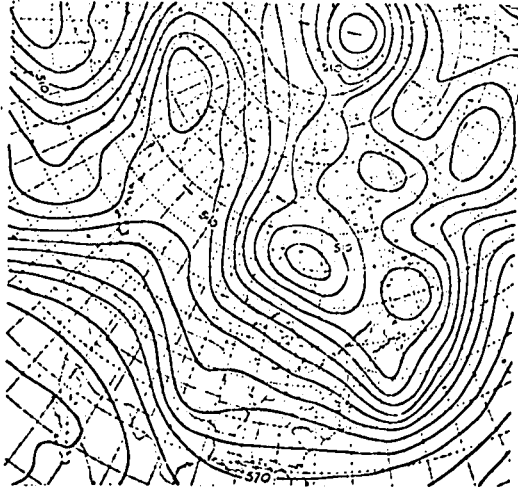


1968 model 48-hour forecast

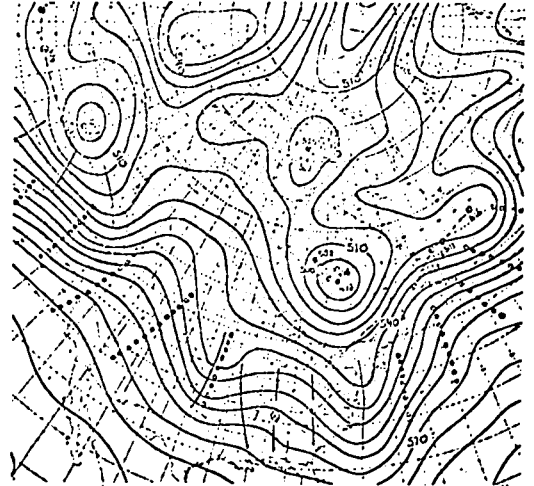


parallel model 48-hour forecast

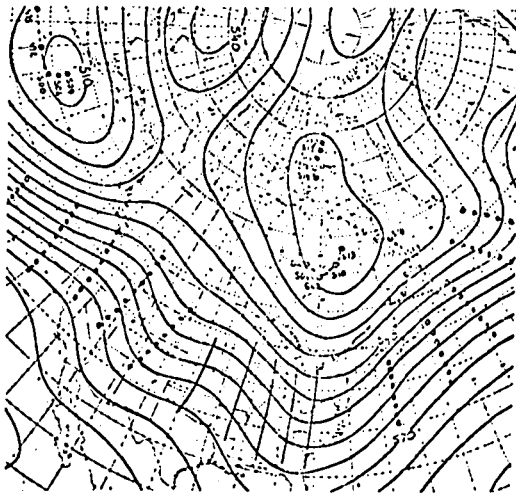
Fig. 44 : The set of 700 mb height charts for the case of 00Z Dec 21 st 1969.



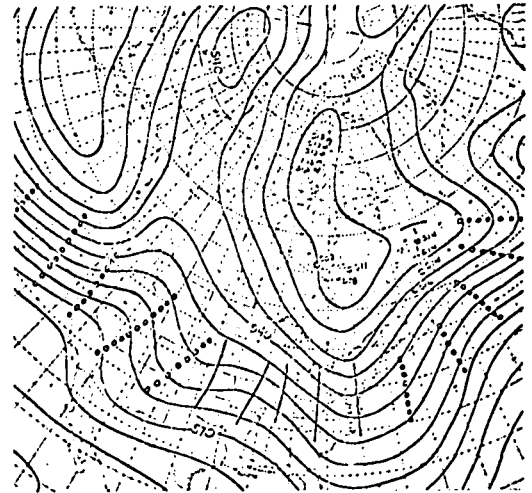
initial analysis



verifying analysis

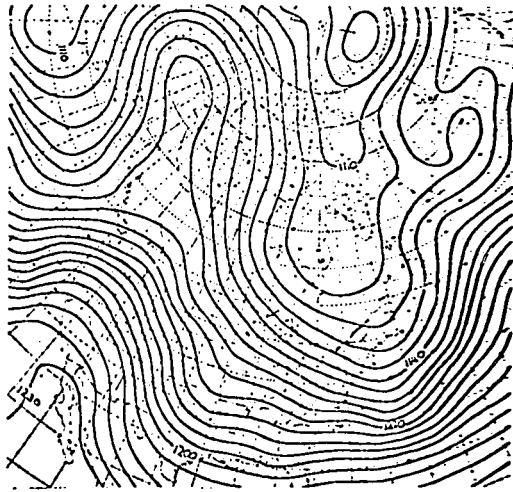


1968 model 48-hour forecast

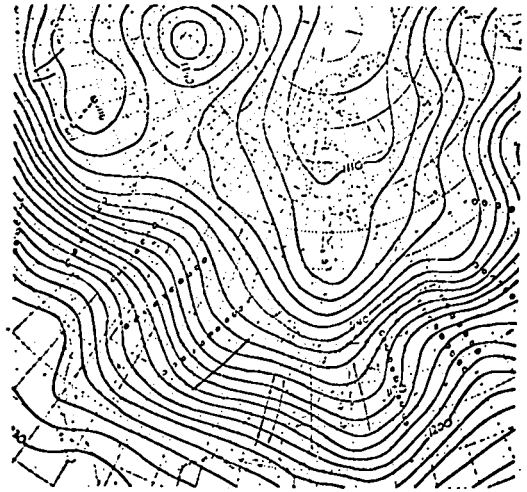


parallel model 48-hour forecast

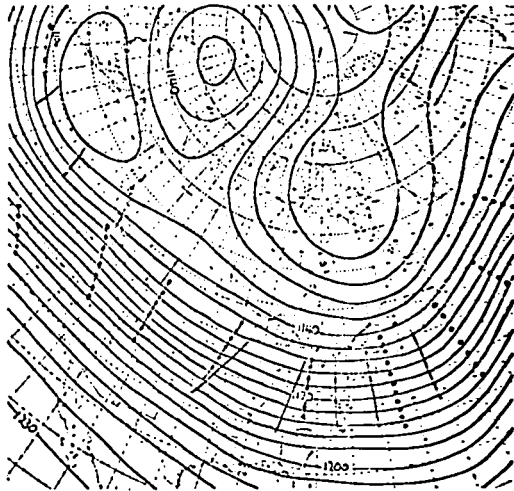
Fig. 45 : The set of 500 mb height charts for
the case of 00Z Dec 21 st 1969.



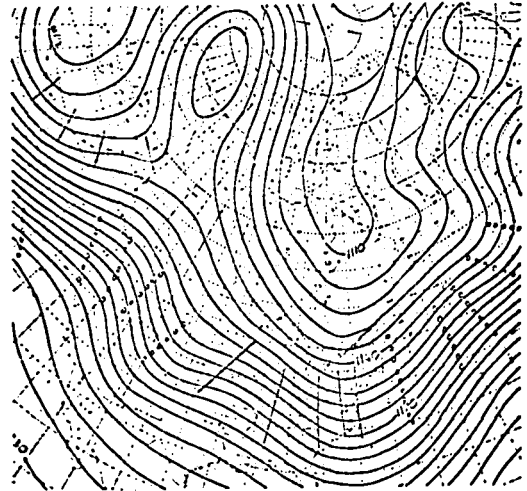
initial analysis



verifying analysis

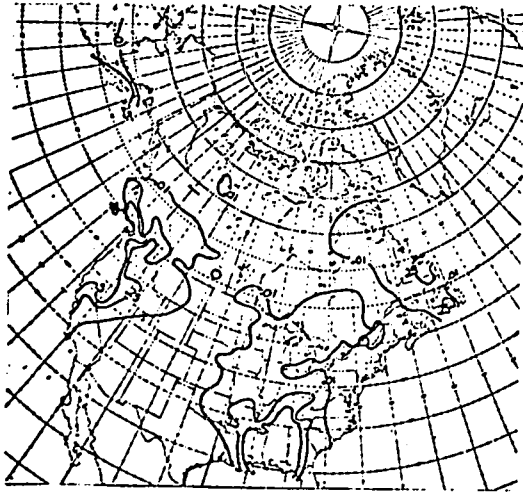


1968 model 48-hour forecast

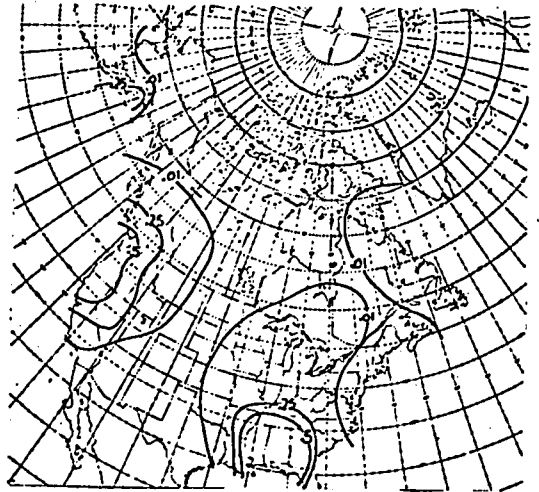


parallel model 48-hour forecast

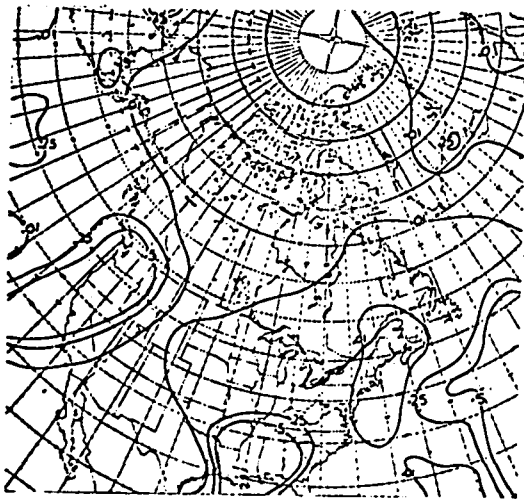
Fig. 46 : The set of 200 mb height charts for
the case of 00Z Dec 21 st 1969.



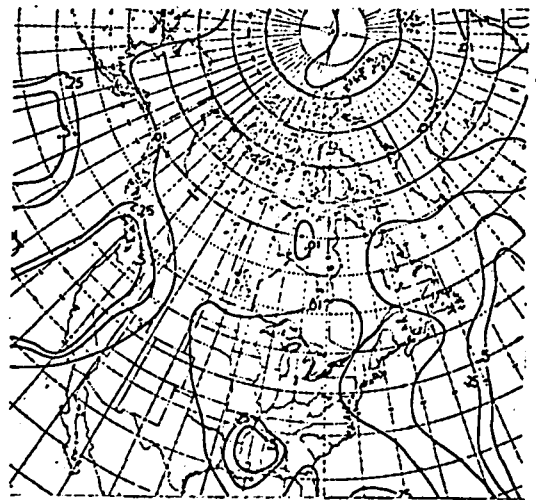
subjective analysis



objective analysis



1968 model forecast

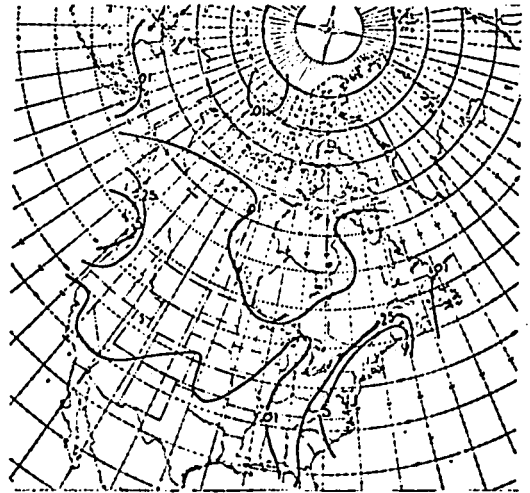


parallel model forecast

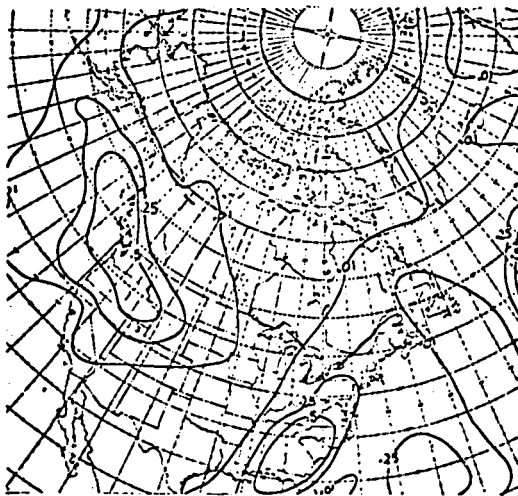
Fig. 47 : The set of 00-24 hour precipitation charts
for the case of 00Z Dec 21 st 1969.



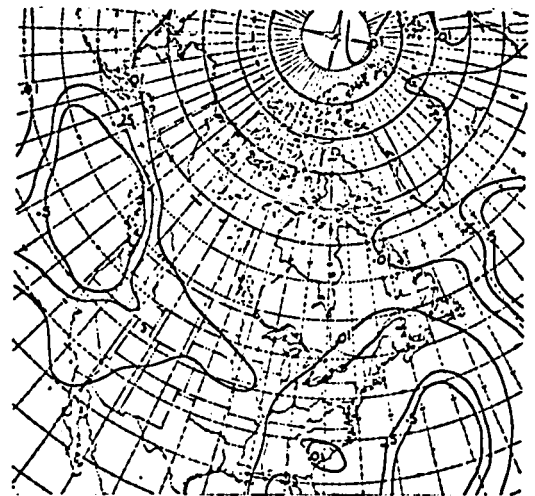
subjective analysis



objective analysis

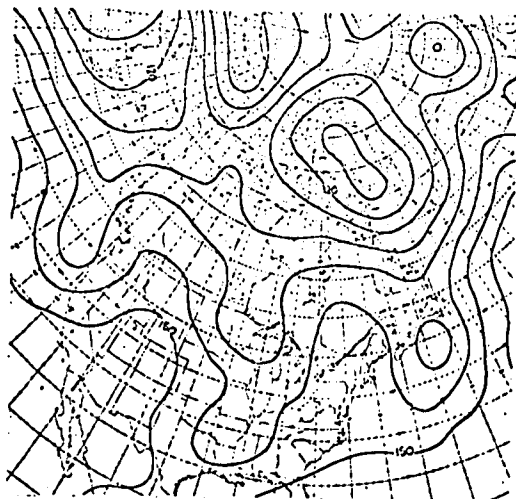


1968 model forecast



parallel model forecast

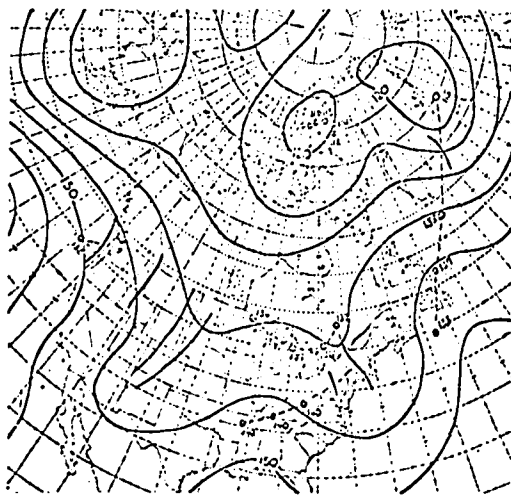
Fig. 48 : The set of 24-48 hour precipitation charts
for the case of 00Z Dec 21 st 1969.



initial analysis



verifying analysis

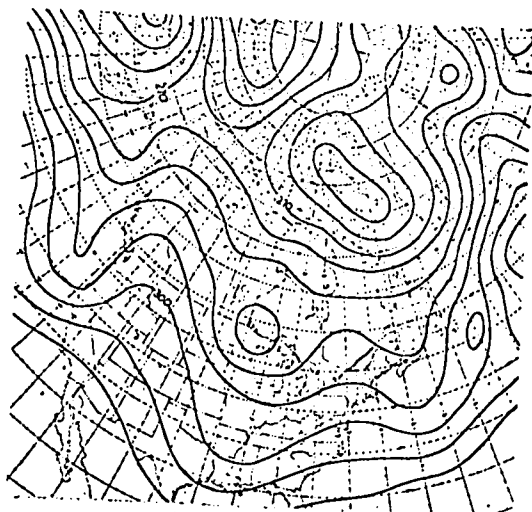


1968 model 48-hour forecast



parallel model 48-hour forecast

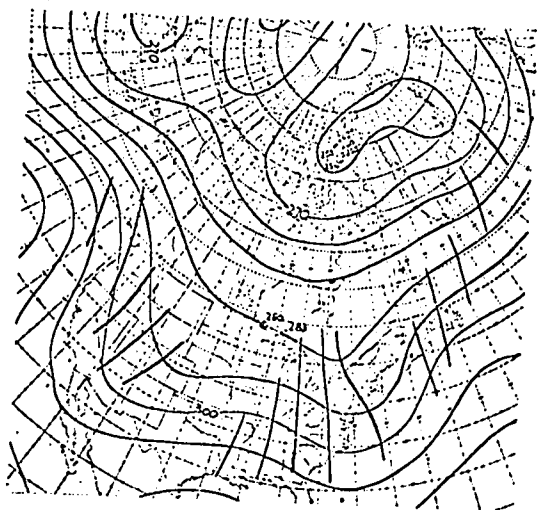
Fig. 49 : The set of 850 mb height charts for
the case of 12Z Dec 25 th 1969.



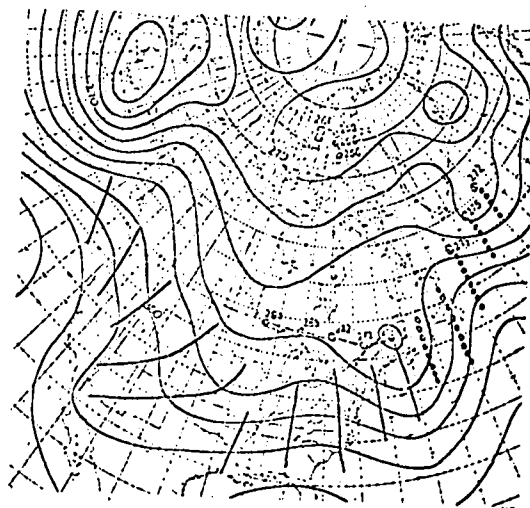
initial analysis



verifying analysis

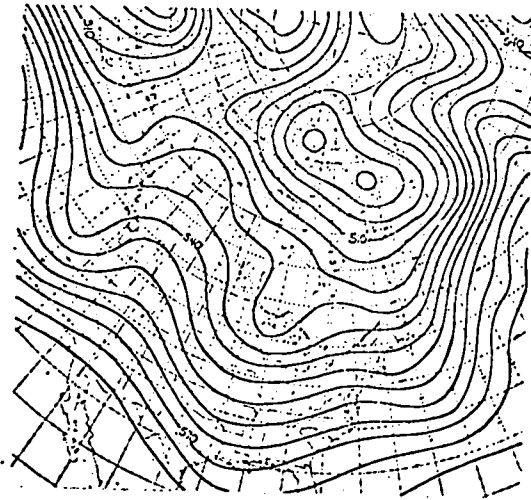


1968 model 48-hour forecast



parallel model 48-hour forecast

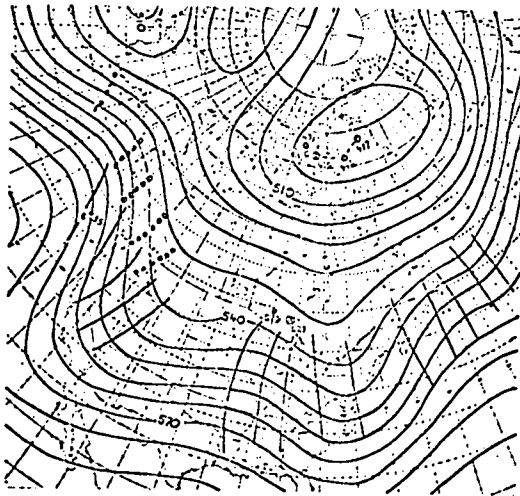
Fig. 50 : The set of 700 mb height charts for
the case of 12Z Dec 25 th 1969.



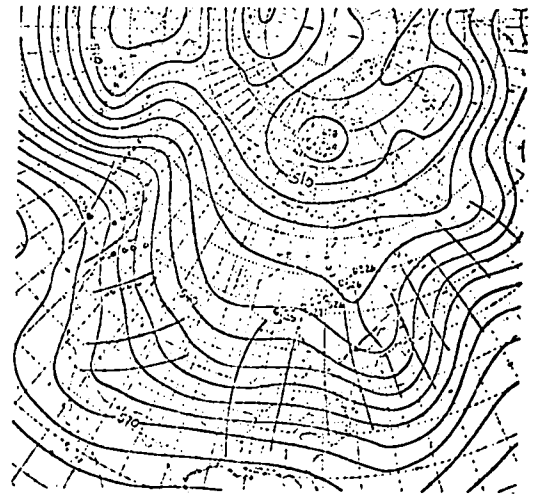
initial analysis



verifying analysis

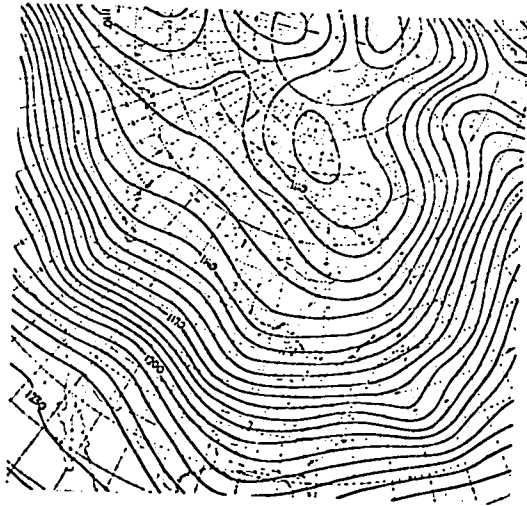


1968 model 48-hour forecast

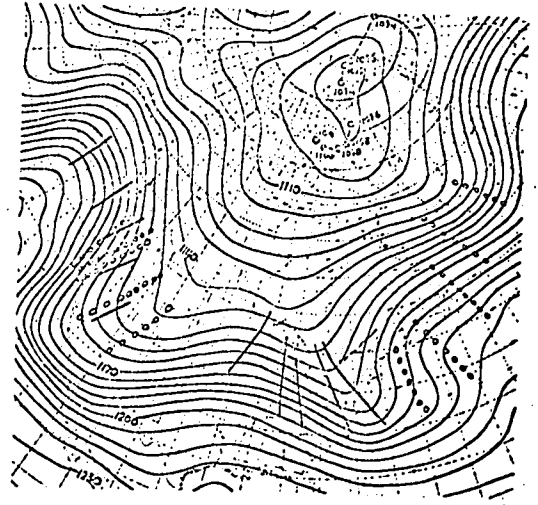


parallel model 48-hour forecast

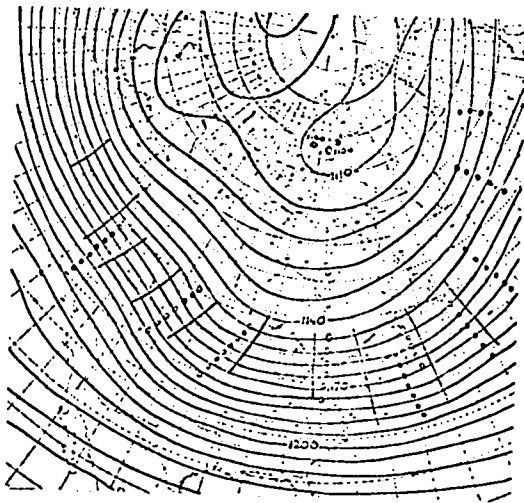
Fig. 51 : The set of 500 mb height charts for
the case of 12Z Dec 25 th 1969.



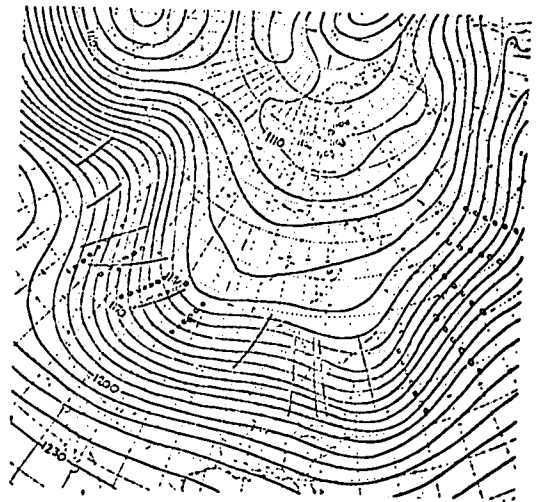
initial analysis



verifying analysis



1968 model 48-hour forecast

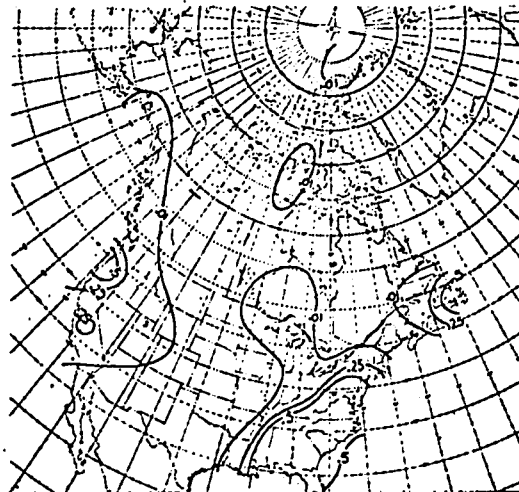


parallel model 48-hour forecast

Fig. 52 : The set of 200 mb height charts for
the case of 12Z Dec 25 th 1969.



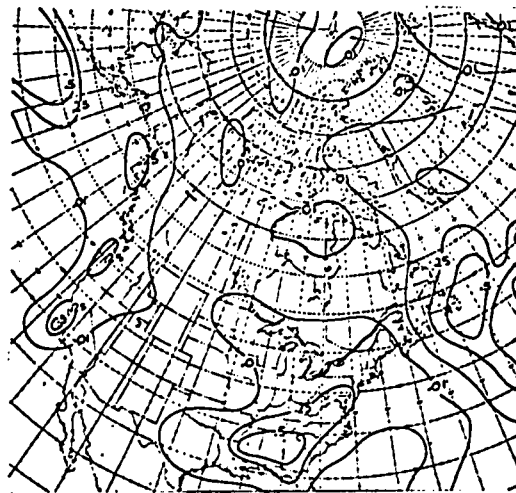
subjective analysis



objective analysis

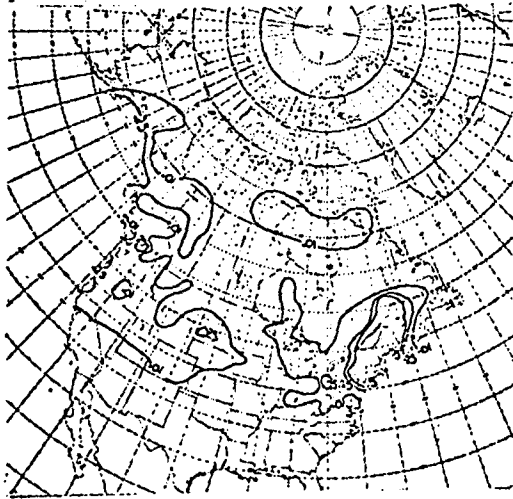


1968 model forecast

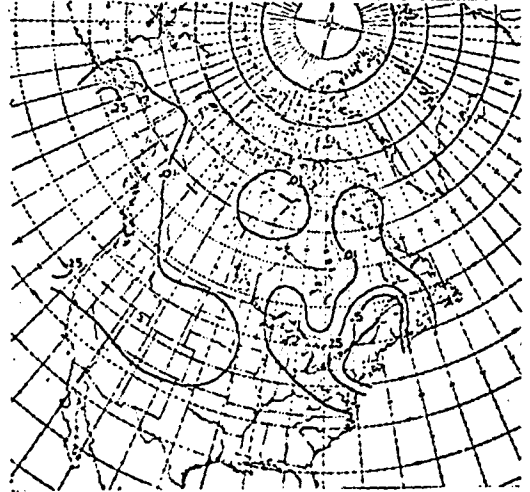


parallel model forecast

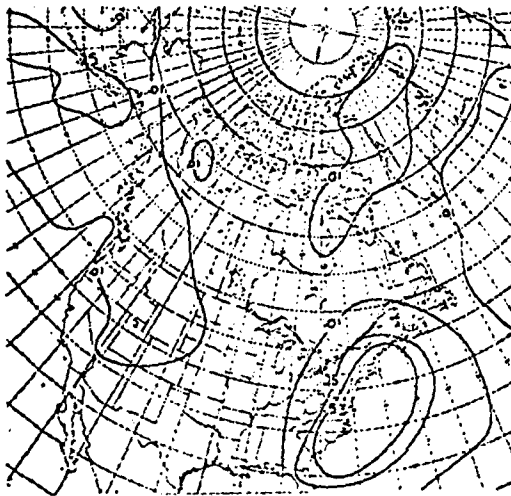
Fig. 53 : The set of 00-24 hour precipitation charts
for the case of 12Z Dec 25 th 1969.



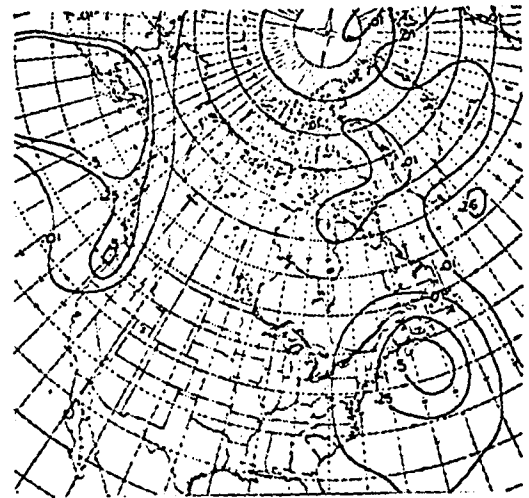
subjective analysis



objective analysis

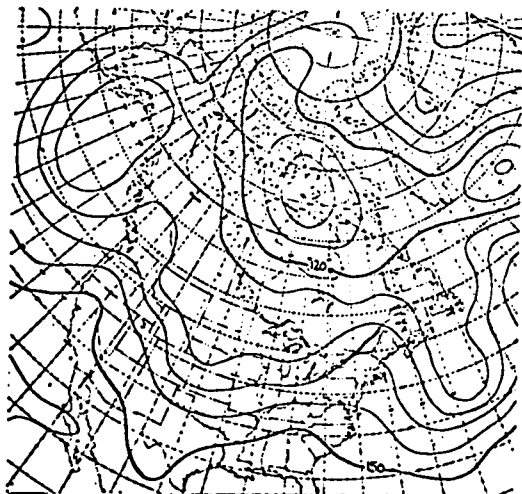


1968 model forecast

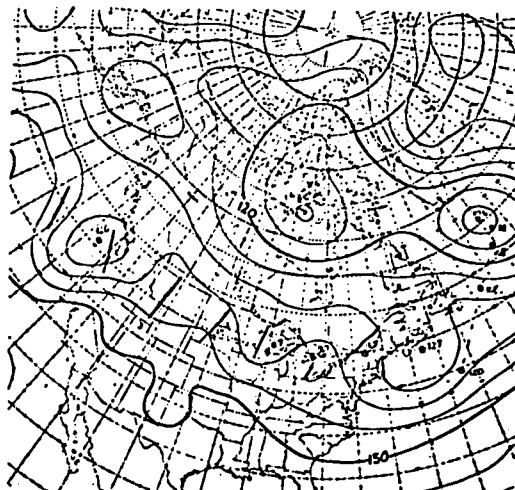


parallel model forecast

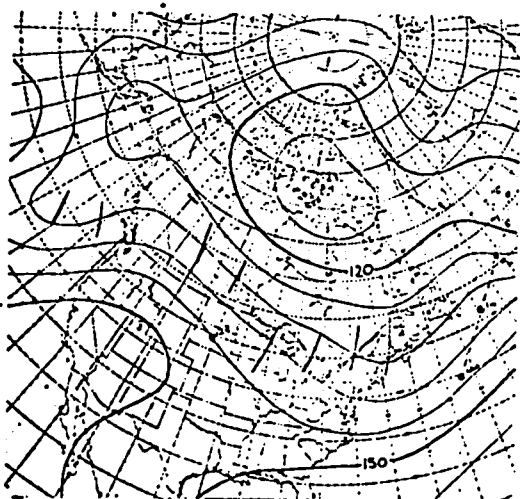
Fig. 54 : The set of 24-48 hour precipitation charts
for the case of 12Z Dec 25 th 1969.



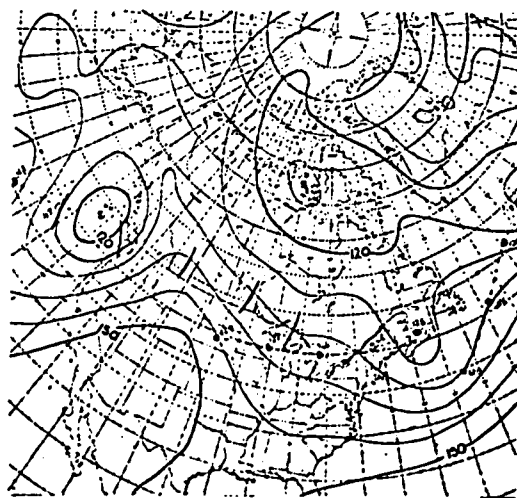
initial analysis



verifying analysis

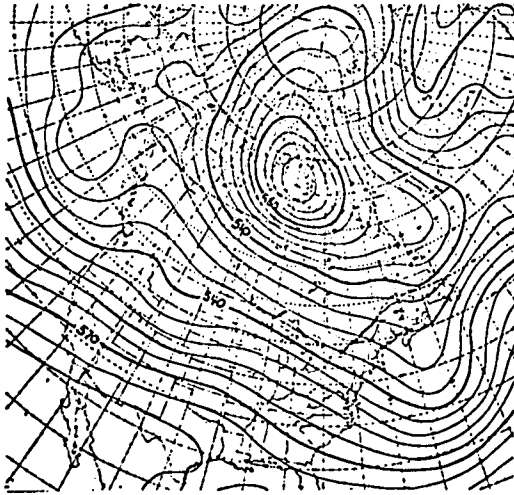


1968 model 48-hour forecast

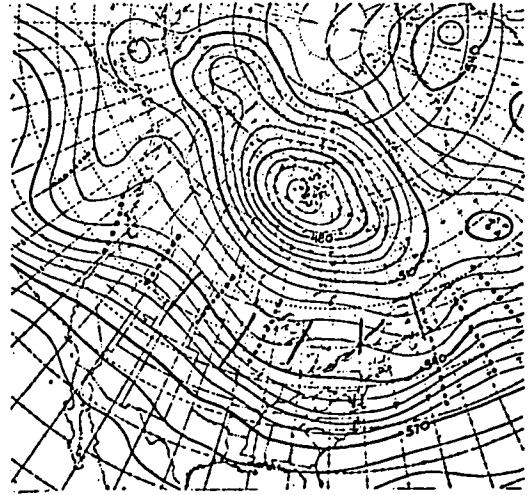


parallel model 48-hour forecast

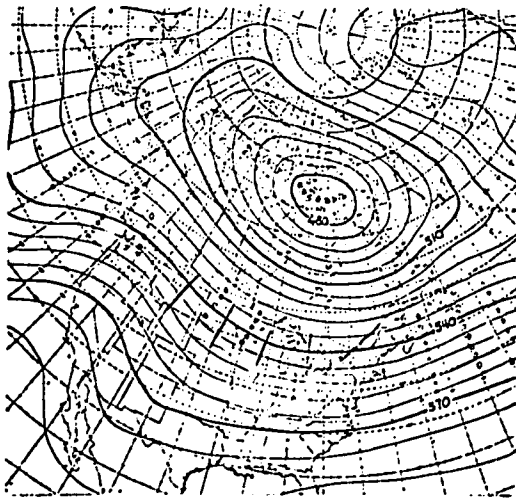
Fig. 55 : The set of 850 mb height charts for
the case of 00Z Jan 25 th 1970.



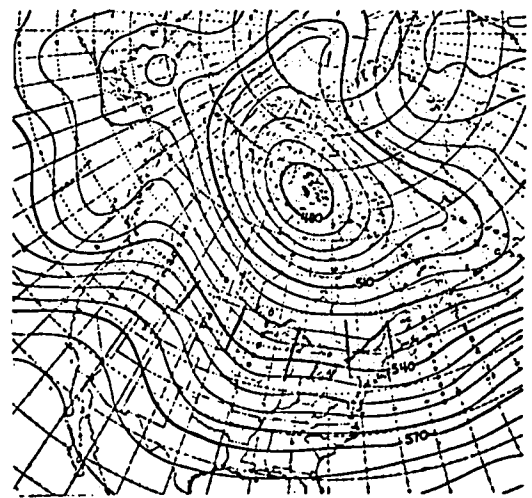
initial analysis



verifying analysis



1968 model 48-hour forecast

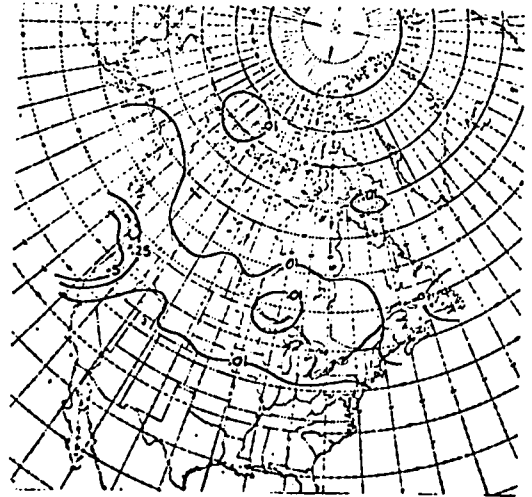


parallel model 48-hour forecast

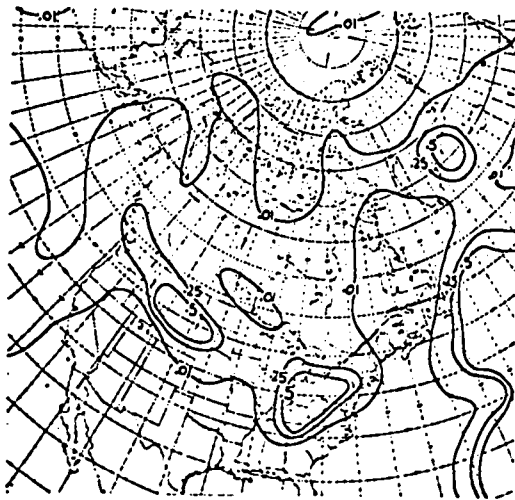
Fig. 56 : The set of 500 mb height charts for
the case of 00Z Jan 25 th 1970.



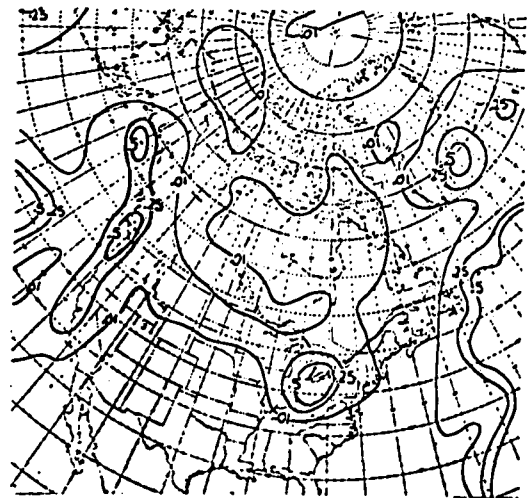
subjective analysis



objective analysis

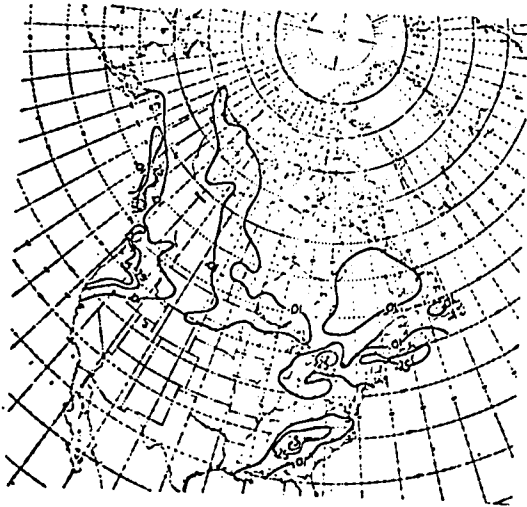


1968 model forecast

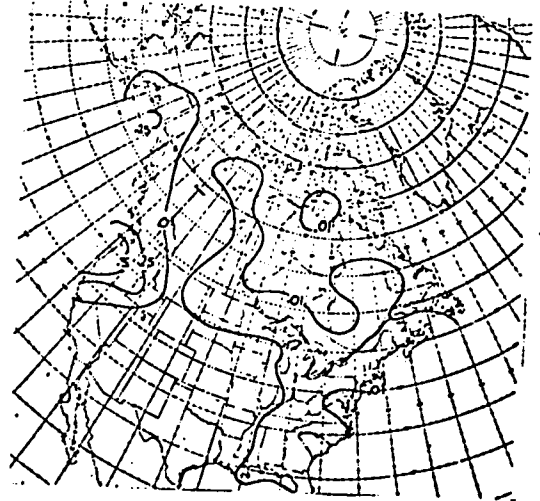


parallel model forecast

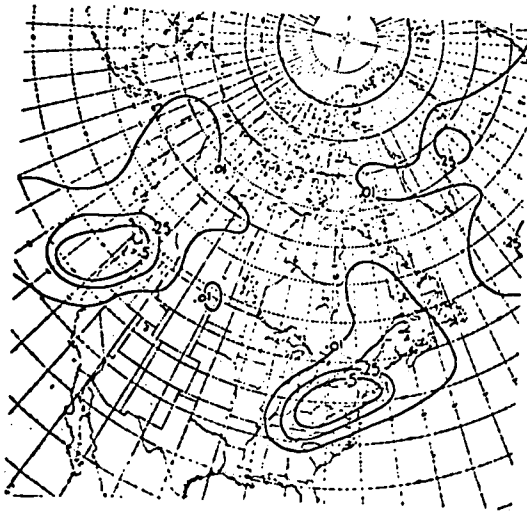
Fig. 57 : The set of 00-24 hour precipitation charts for the case of 00Z Jan 25 th 1970.



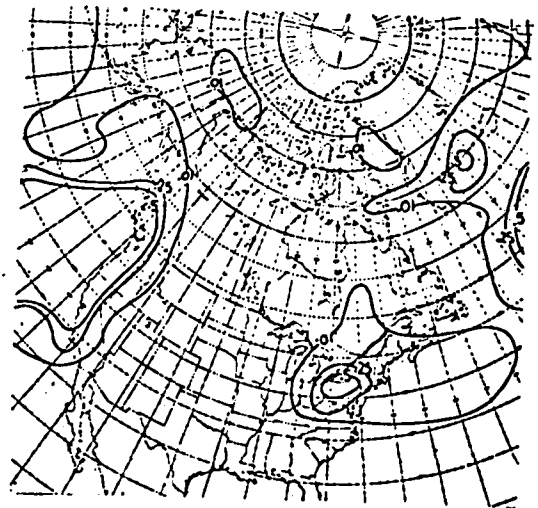
subjective analysis



objective analysis

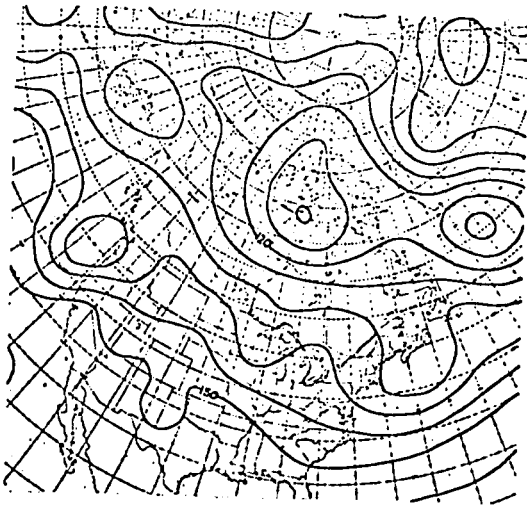


1968 model forecast

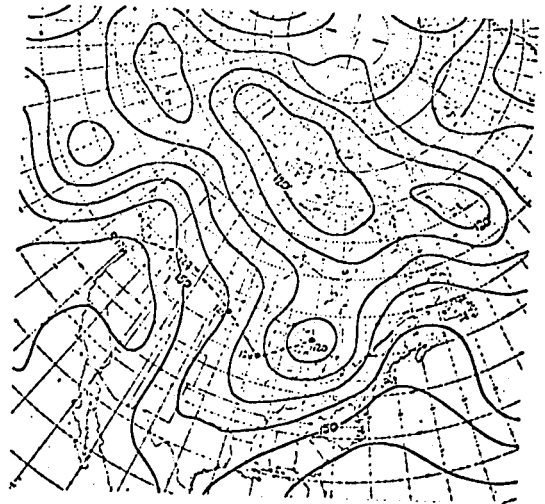


parallel model forecast

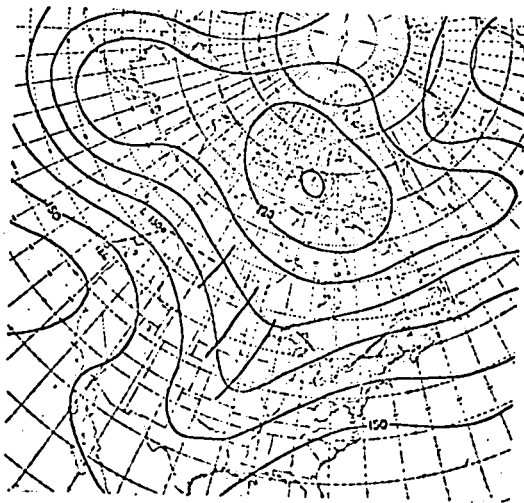
Fig. 58 : The set of 24-48 hour precipitation charts
for the case of 00Z Jan 25 th 1970.



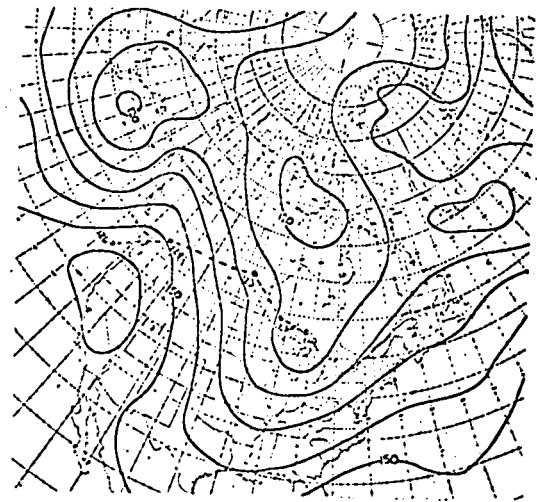
initial analysis



verifying analysis

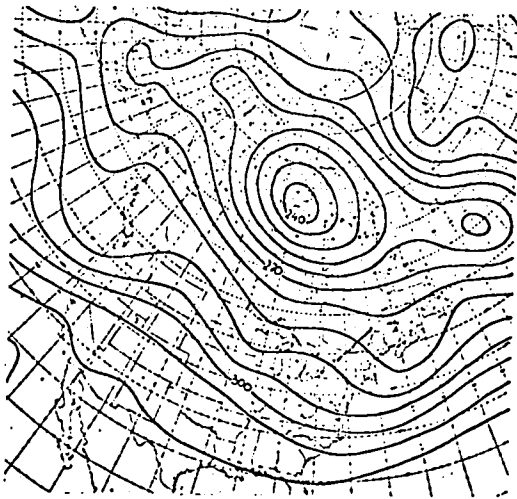


1968 model 48-hour forecast

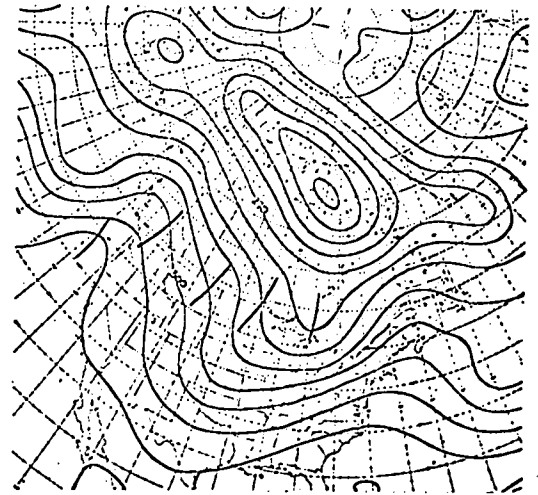


parallel model 48-hour forecast

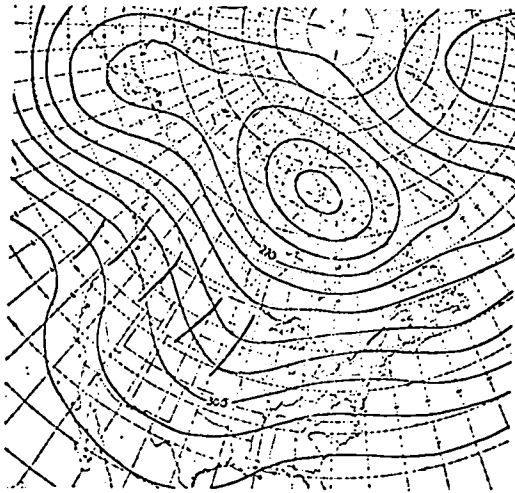
Fig. 59 : The set of 850 mb height charts for
the case of 00Z Jan 27 th 1970.



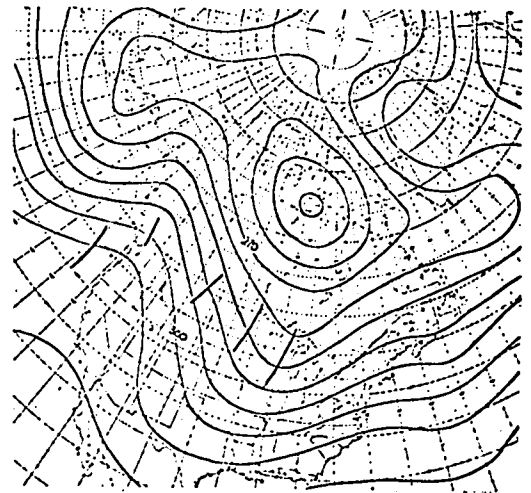
initial analysis



verifying analysis

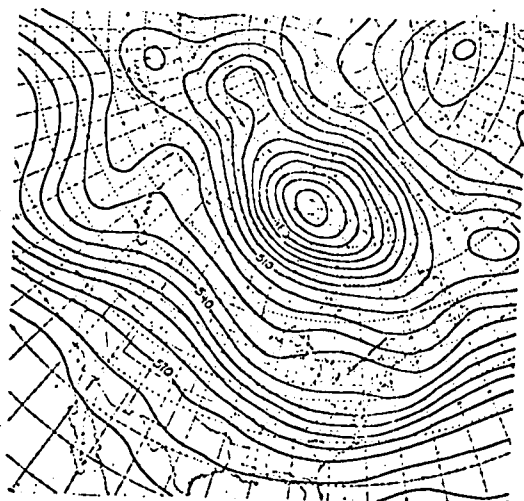


1968 model 48-hour forecast

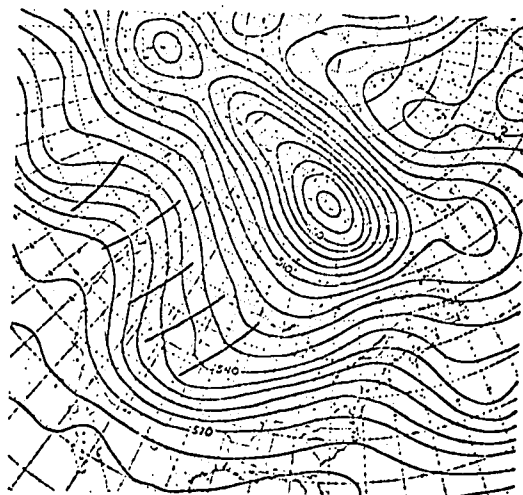


parallel model 48-hour forecast

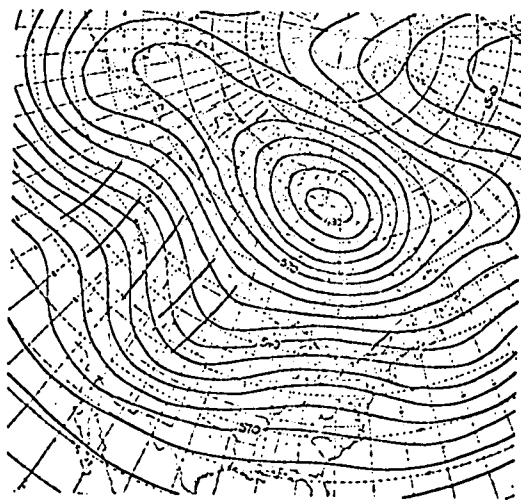
Fig. 60 : The set of 700 mb height charts for the case of 00Z Jan 27 th 1970.



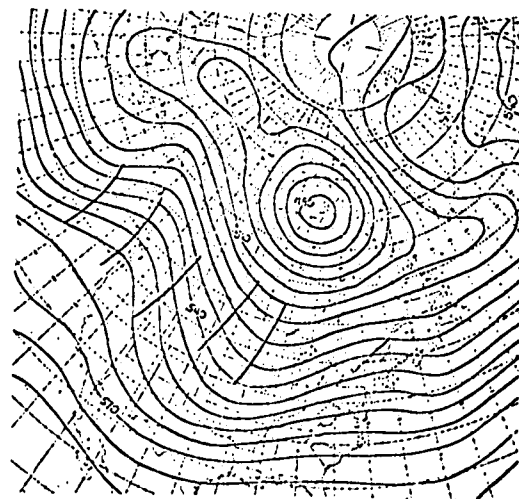
initial analysis



verifying analysis

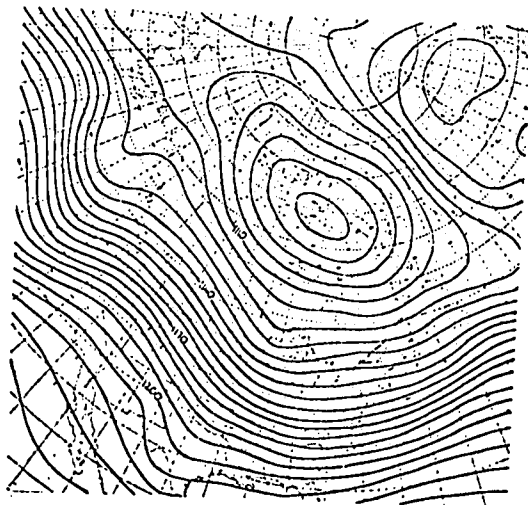


1968 model 48-hour forecast

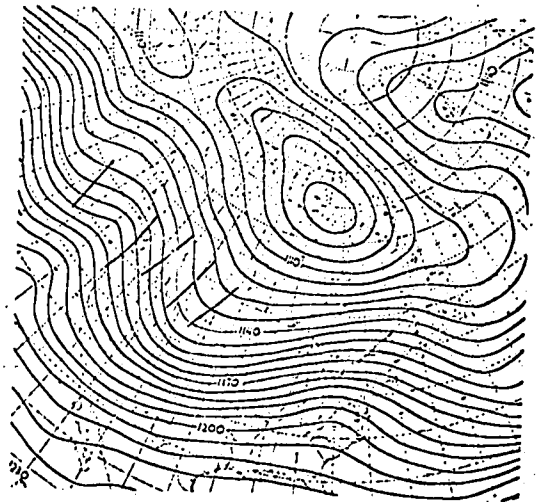


parallel model 48-hour forecast

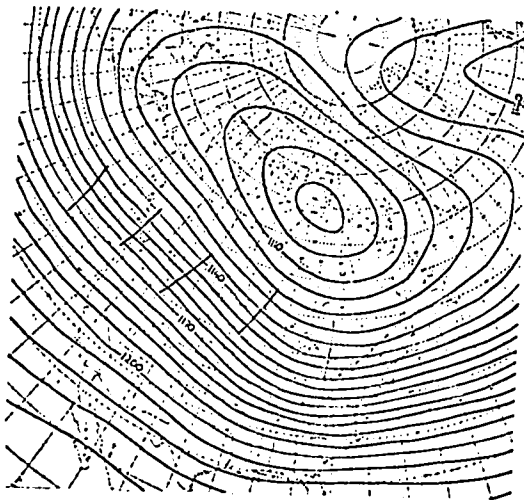
Fig. 61 : The set of 500 mb height charts for
the case of 00Z Jan 27 th 1970.



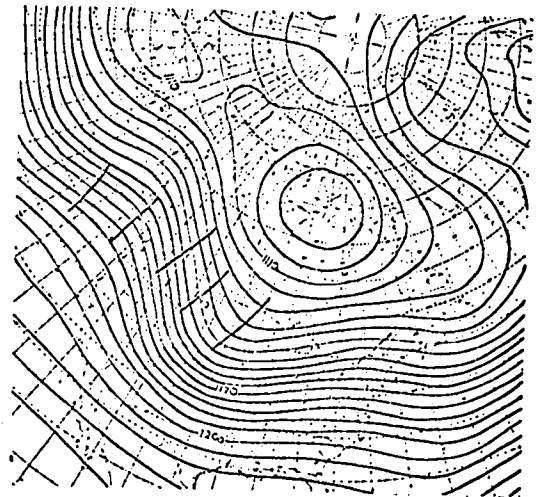
initial analysis



verifying analysis

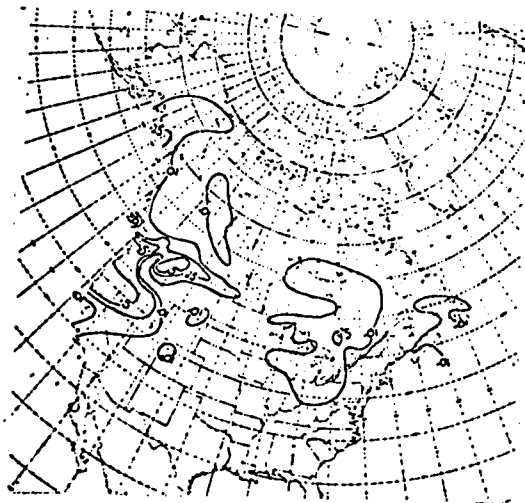


1968 model 48-hour forecast

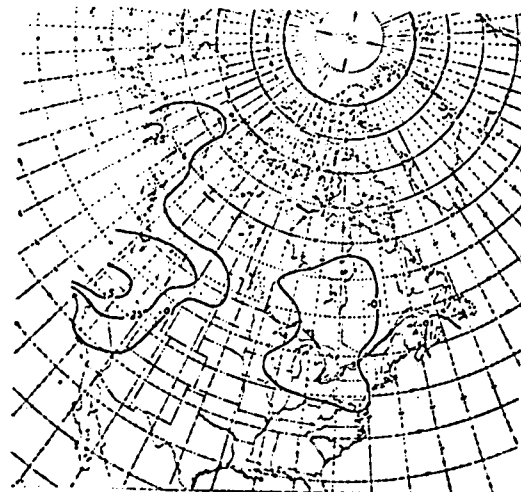


parallel model 48-hour forecast

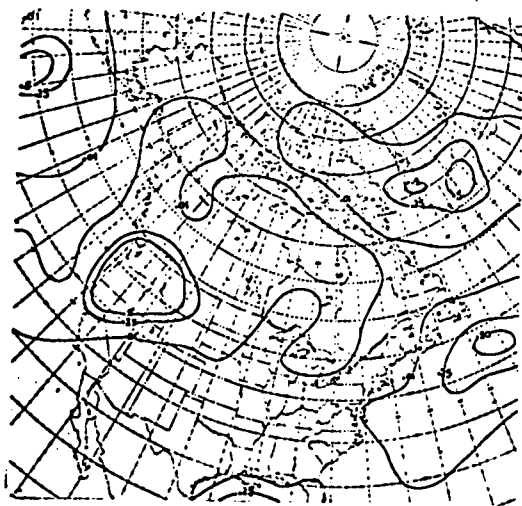
Fig. 62 : The set of 200 mb height charts for the case of 00Z Jan 27 th 1970.



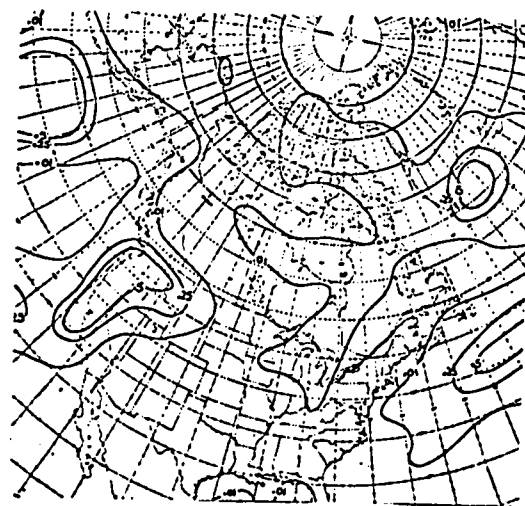
subjective analysis



objective analysis

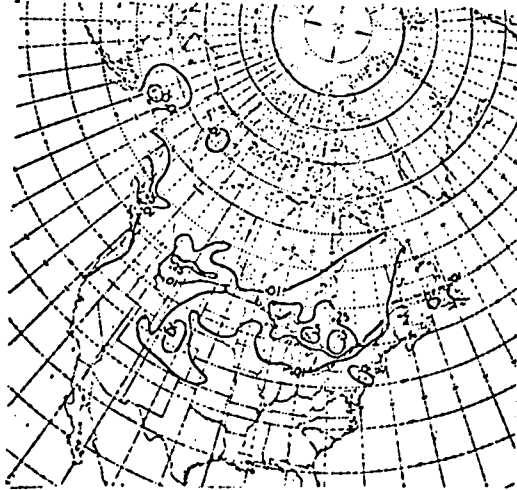


1968 model forecast

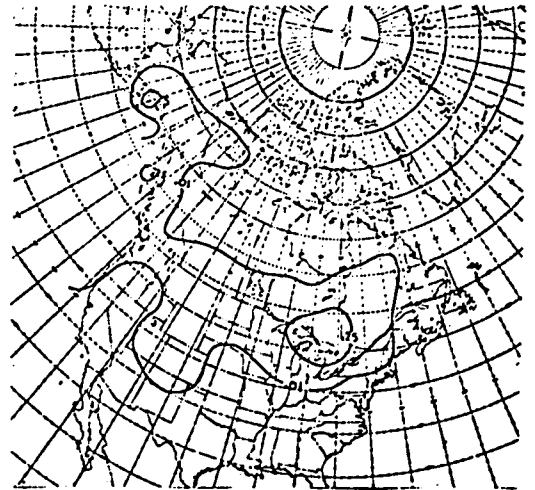


parallel model forecast

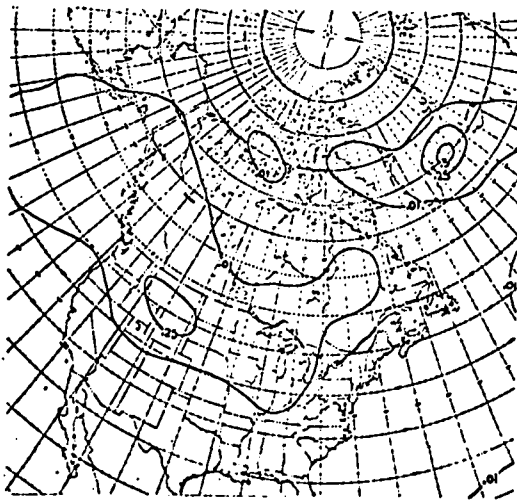
Fig. 63 : The set of 00-24 hour precipitation charts
for the case of 00Z Jan 27 th 1970.



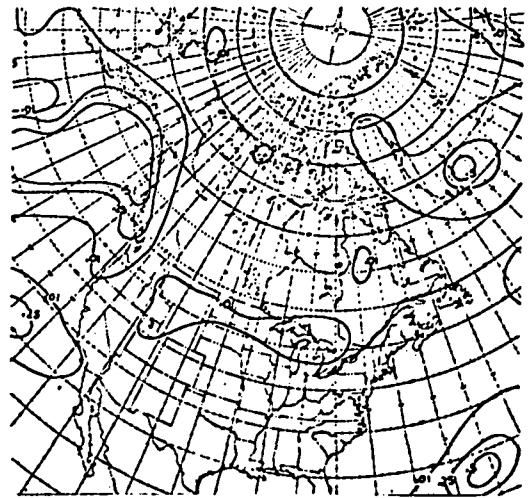
subjective analysis



objective analysis

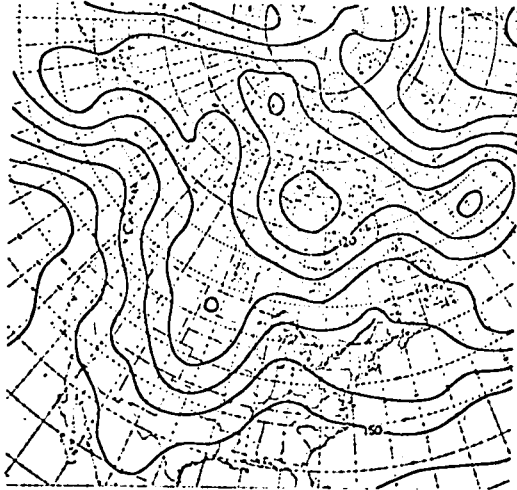


1968 model forecast



parallel model forecast

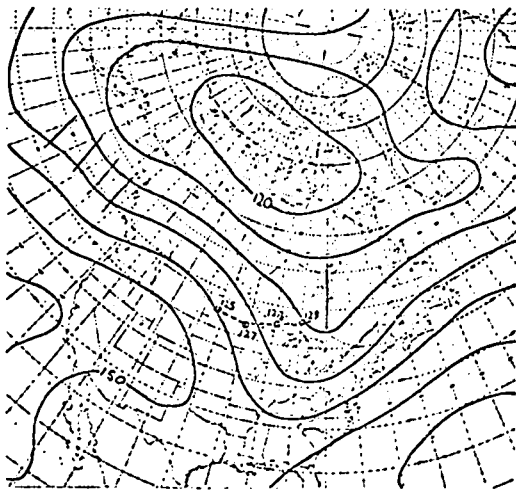
Fig. 64 : The set of 24-48 hour precipitation charts
for the case of 00Z Jan 27 th 1970.



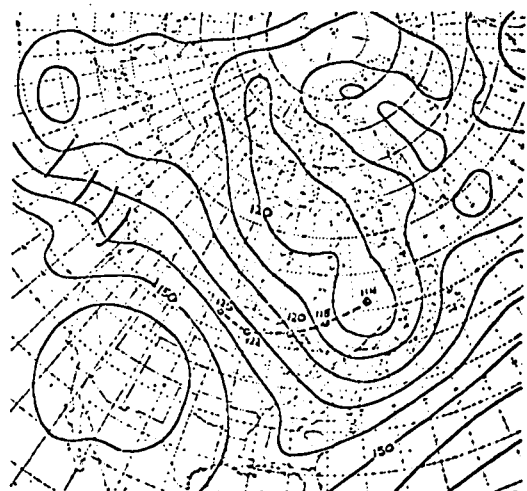
initial analysis



verifying analysis

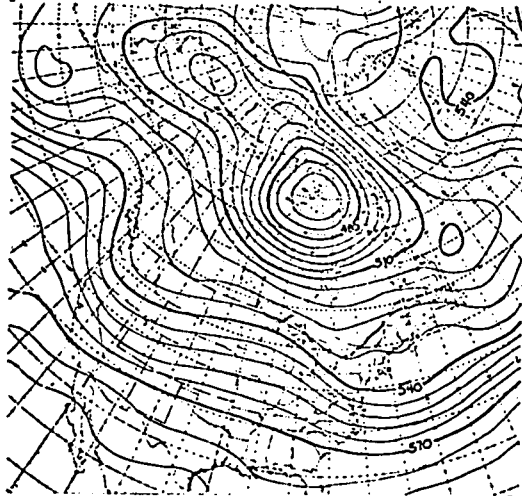


1968 model 48-hour forecast

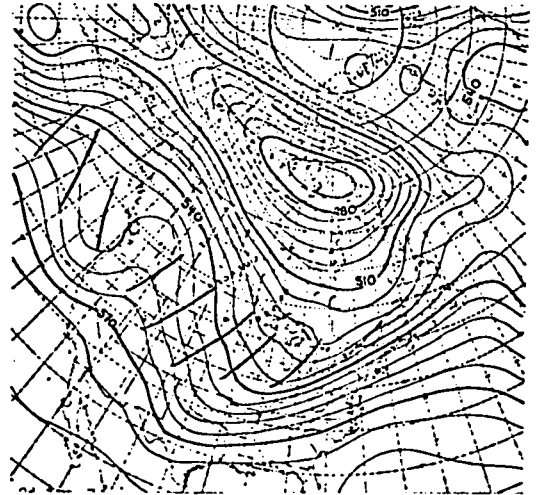


parallel model 48-hour forecast

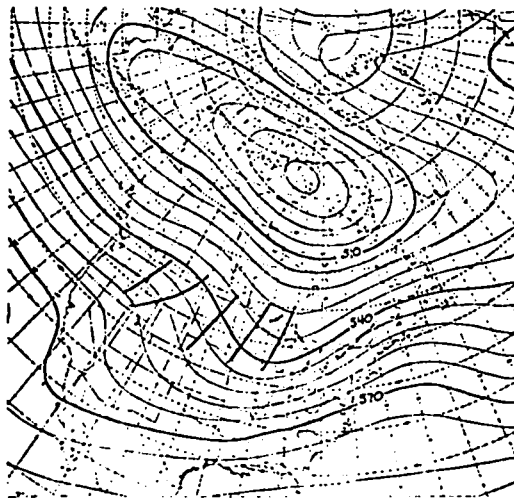
Fig. 65 : The set of 850 mb height charts for
the case of 00Z Jan 28 th 1970



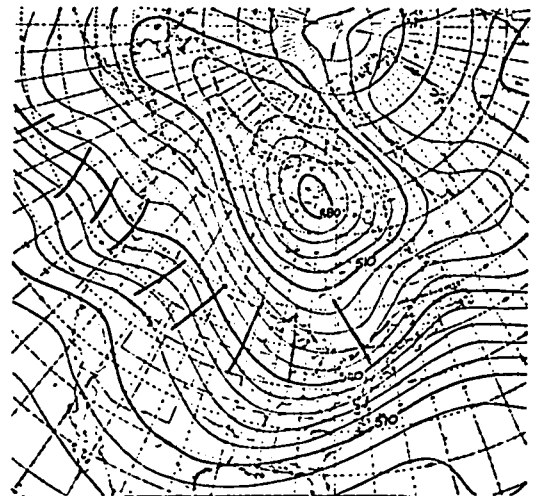
initial analysis



verifying analysis



1968 model 48-hour forecast

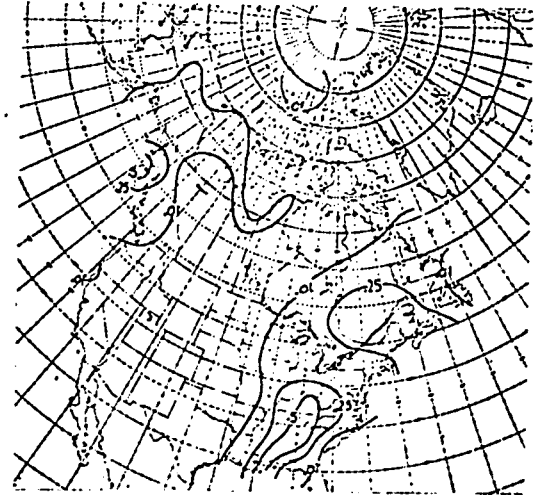


parallel model 48-hour forecast

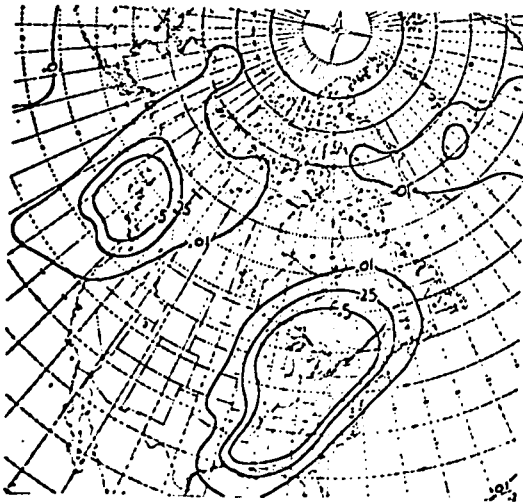
Fig. 66 : The set of 500 mb height charts for the case of 00Z Jan 28 th 1970.



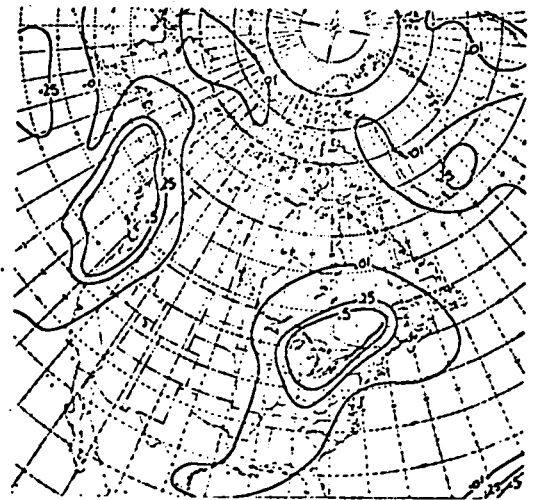
subjective analysis



objective analysis

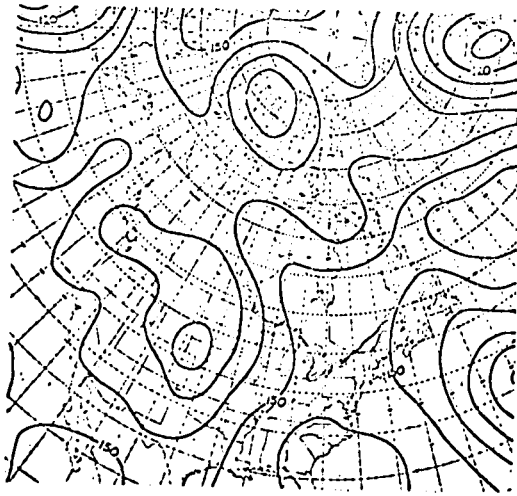


1968 model forecast



parallel model forecast

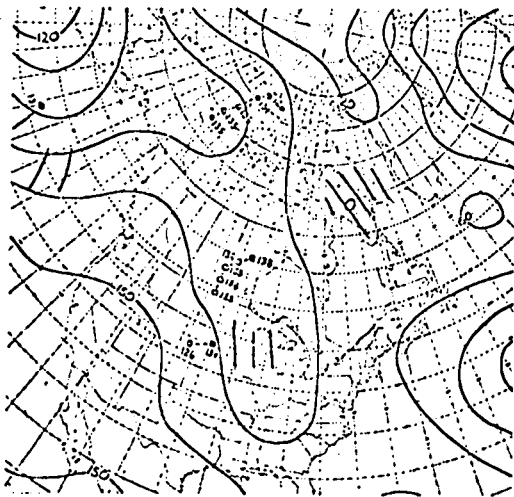
Fig. 68 : The set of 24-48 hour precipitation charts
for the case of 00Z Jan 28 th 1970.



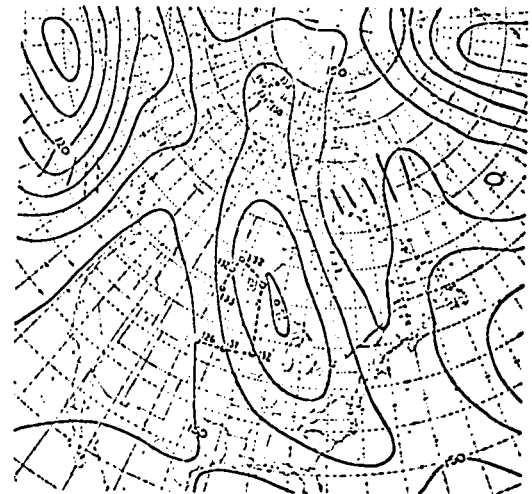
initial analysis



verifying analysis

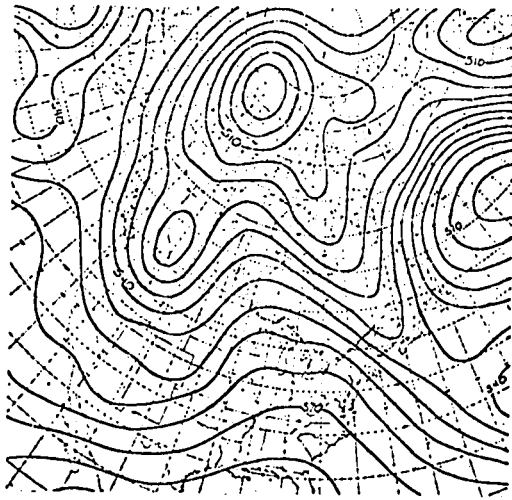


1968 model 48-hour forecast

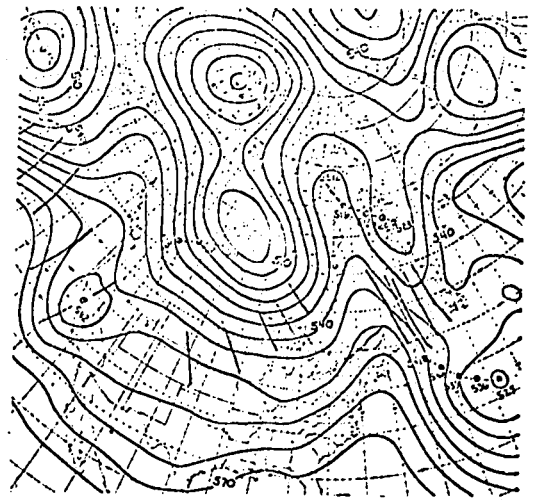


parallel model 48-hour forecast

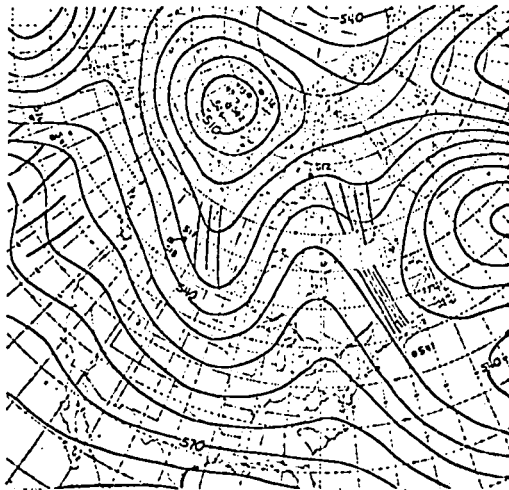
Fig. 69 : The set of 850 mb height charts for
the case of 00Z Mar 3 rd 1970.



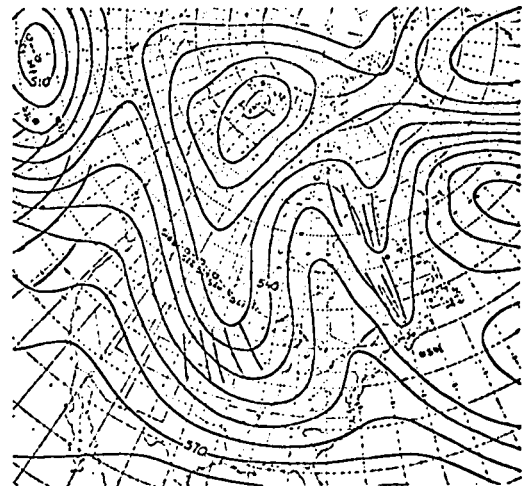
initial analysis



verifying analysis

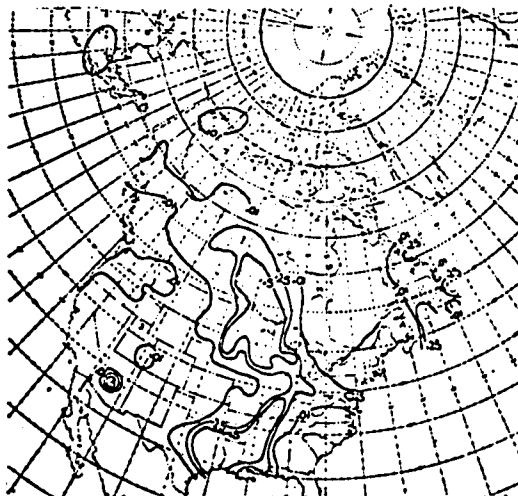


1968 model 48-hour forecast

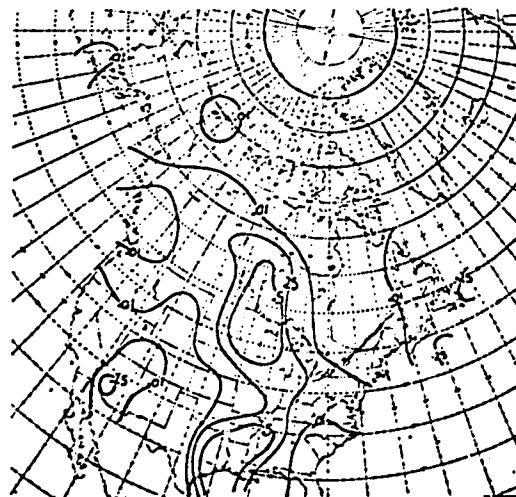


parallel model 48-hour forecast

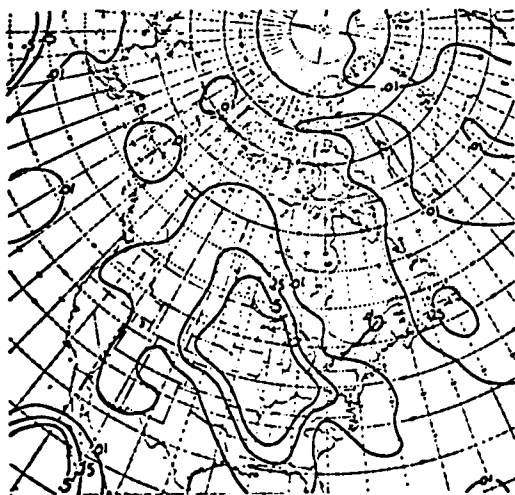
Fig. 70 : The set of 500 mb height charts for
the case of 00Z Mar 3 rd 1970.



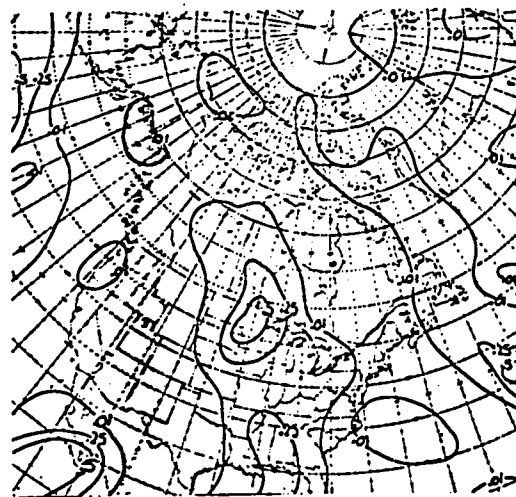
subjective analysis



objective analysis



1968 model forecast

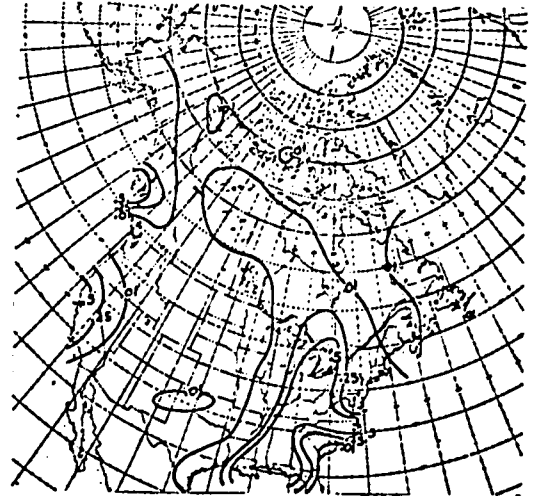


parallel model forecast

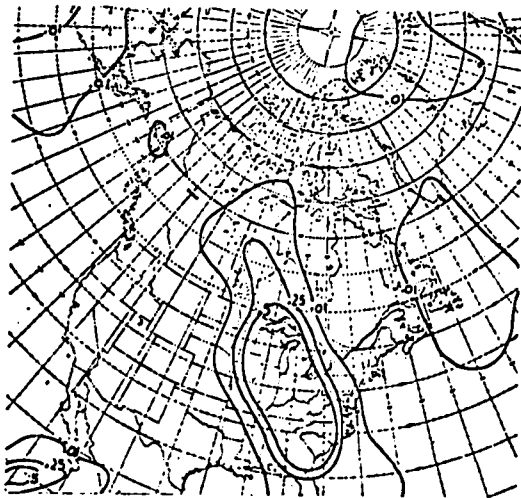
Fig. 71 : The set of 00-24 hour precipitation charts
for the case of 00Z Mar 3 rd 1970.



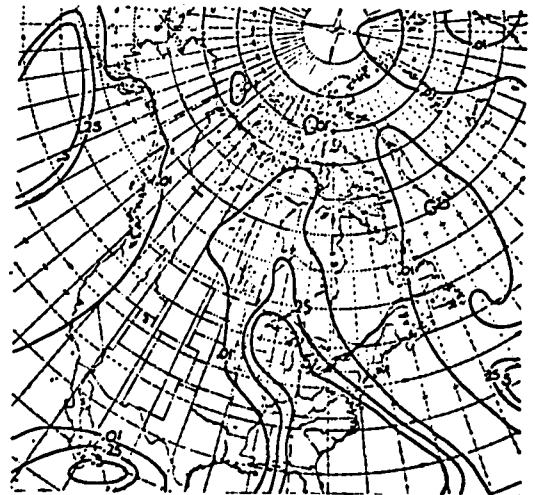
subjective analysis



objective analysis

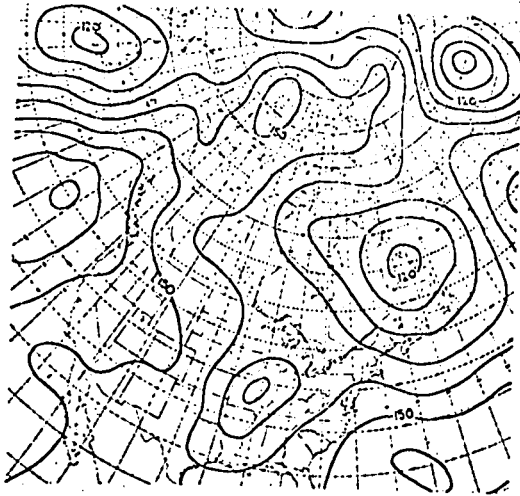


1968 model forecast

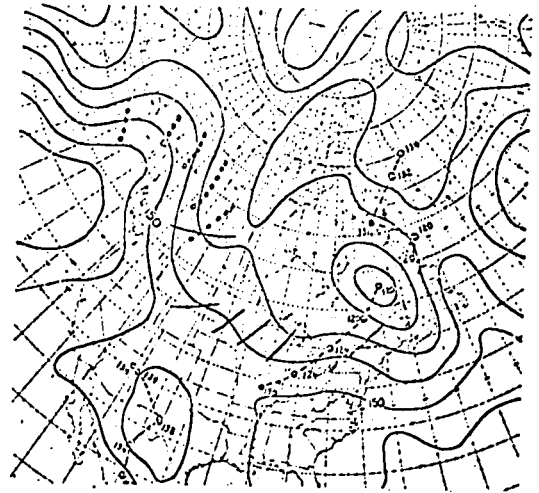


parallel model forecast

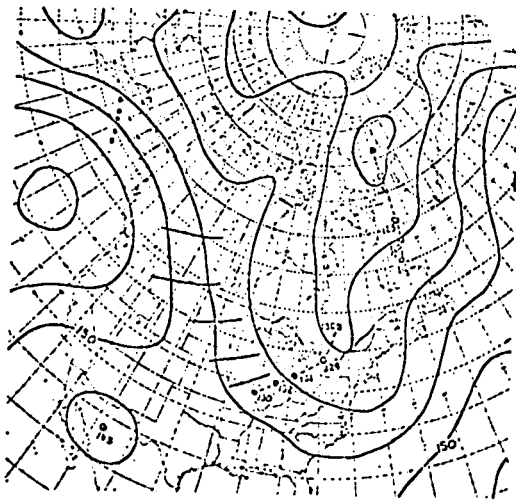
Fig. 72 : The set of 24-48 hour precipitation charts
for the case of 00Z Mar 3rd 1970.



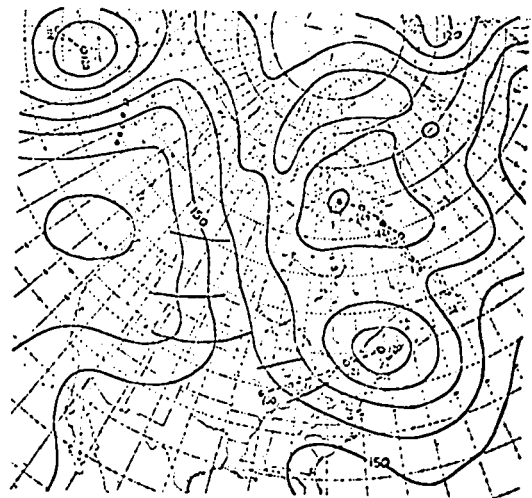
initial analysis



verifying analysis

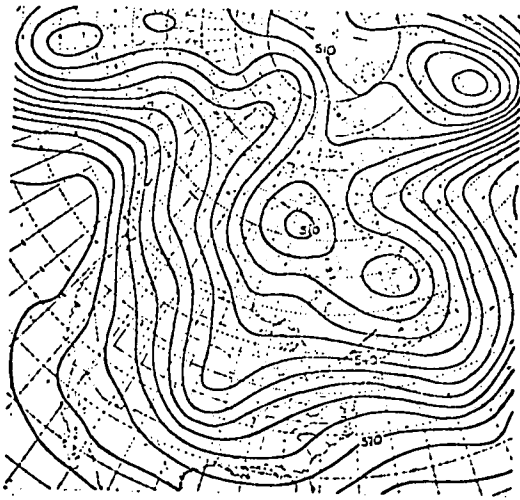


1968 model 48-hour forecast

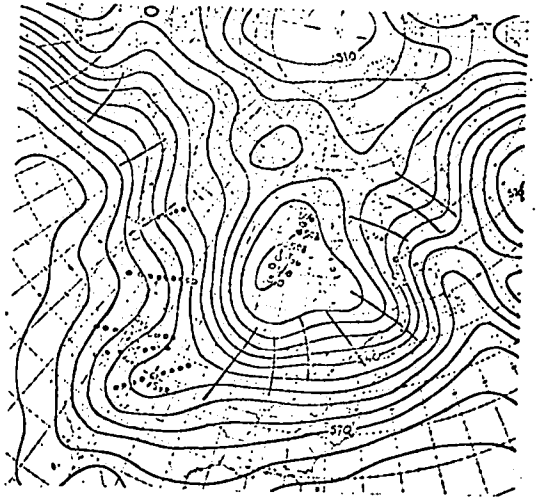


parallel model 48-hour forecast

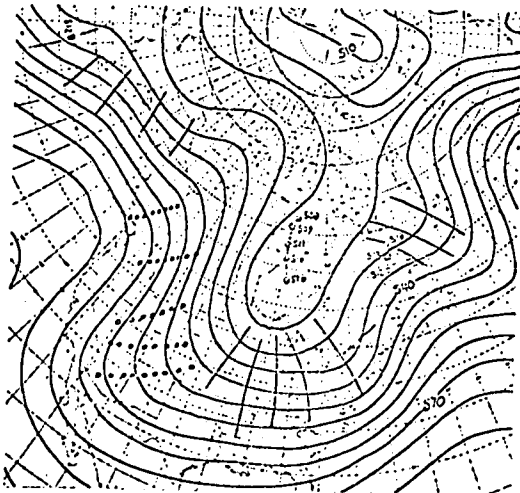
Fig. 73 : The set of 850 mb height charts for
the case of 00Z Mar 26 th 1970.



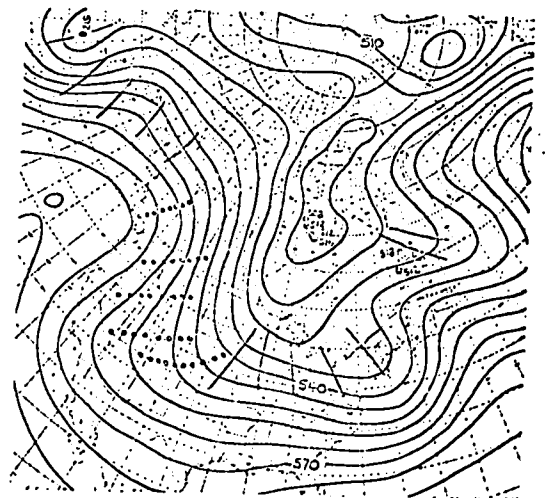
initial analysis



verifying analysis

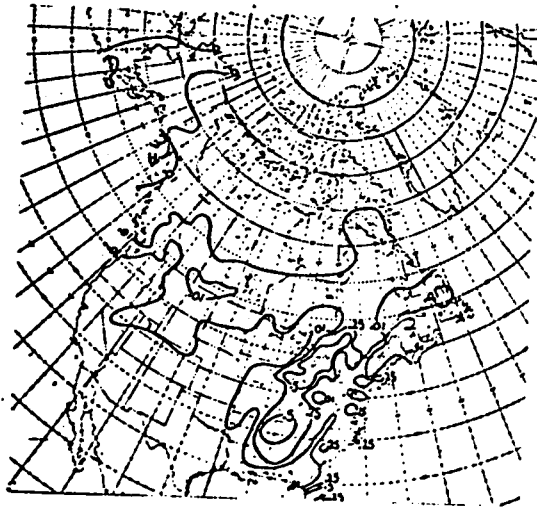


1968 model 48-hour forecast

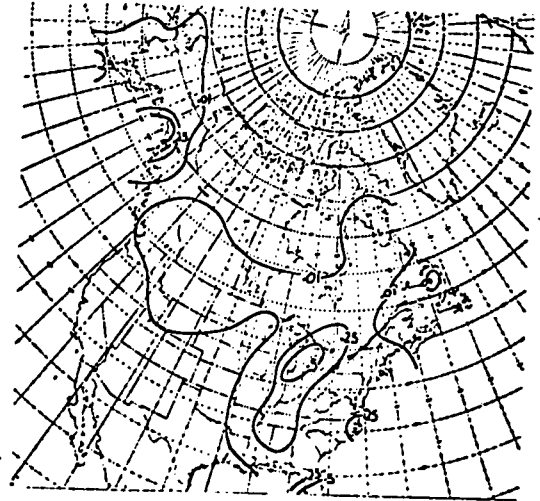


parallel model 48-hour forecast

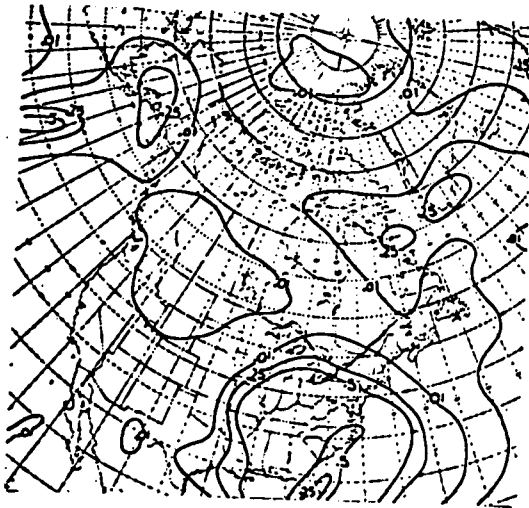
Fig. 74 : The set of 500 mb height charts for
the case of 00Z Mar 26 th 1970.



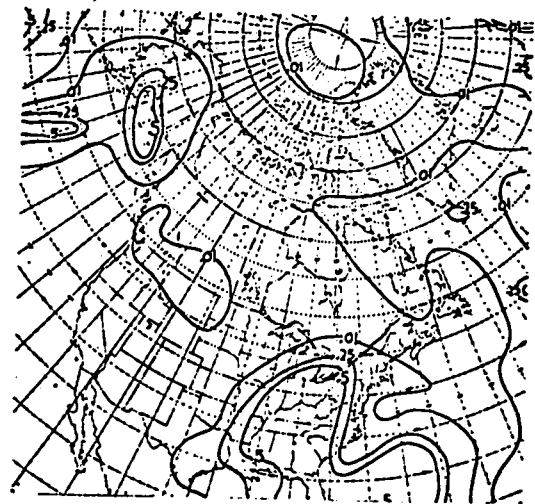
subjective analysis



objective analysis

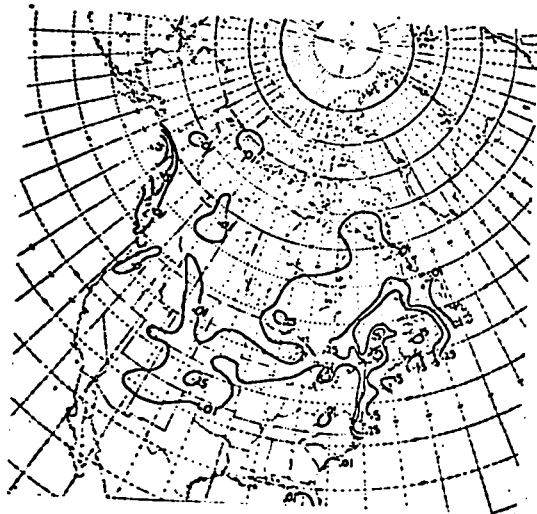


1968 model forecast

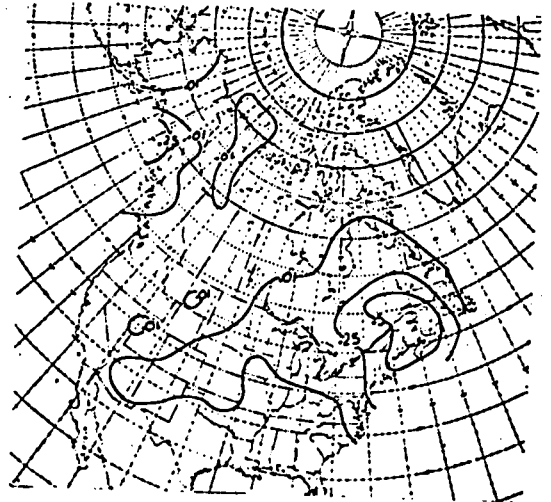


parallel model forecast

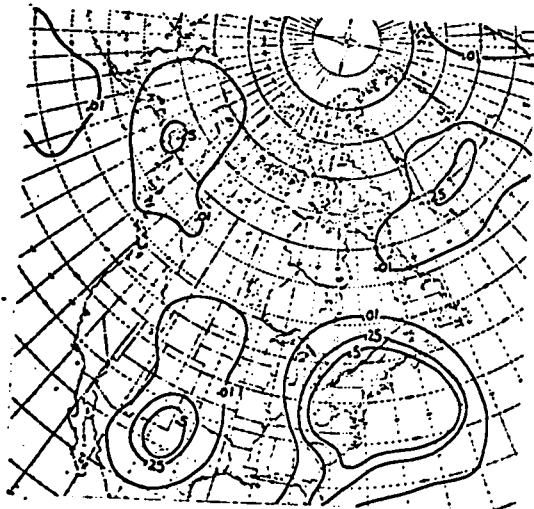
Fig. 75 : The set of 00-24 hour precipitation charts
for the case of 00Z Mar 26 th 1970.



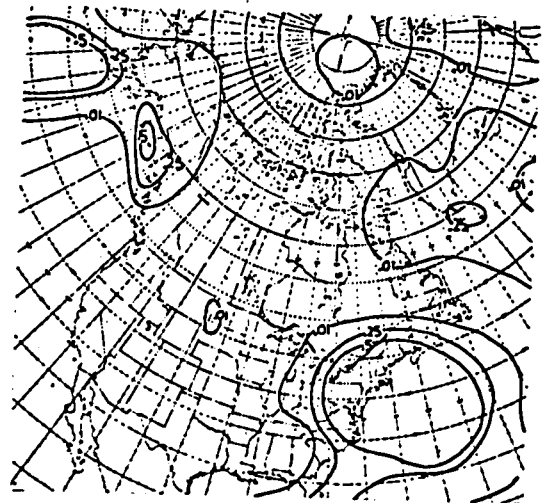
subjective analysis



objective analysis



1968 model forecast



parallel model forecast

Fig. 76 : The set of 24-48 hour precipitation charts
for the case of 00Z Mar 26 th 1970.

Case	PARALLEL MODEL				1968 MODEL				PERSISTENCE			
	12	24	36	48	12	24	36	48	12	24	36	48
12Z Jan 29th 1969	4.1	5.6	7.0	7.6	2.7	4.0	5.2	6.0	3.8	6.3	7.9	8.3
00Z Jul 26th 1969	2.2	3.3	4.1	4.1	2.1	2.3	2.7	2.9	2.5	3.5	4.3	4.5
12Z Sep 9th 1969	2.7	4.3	5.6	6.5	2.3	3.6	4.7	5.5	3.3	6.1	7.9	8.3
00Z Nov 18th 1969	2.8	3.9	3.9	4.5	2.3	3.8	4.9	5.7	3.2	6.1	8.1	9.4
00Z Dec 21st 1969	2.1	3.5	4.0	4.9	2.2	3.9	4.7	6.0	4.2	7.6	8.2	8.4
12Z Dec 25th 1969	2.2	3.4	5.5	7.9	2.1	3.6	5.5	6.9	4.2	6.8	8.8	10.5
00Z Jan 25th 1970	2.1	2.7	3.7	4.3	1.8	2.1	2.8	4.2	3.9	5.3	5.7	5.3
00Z Jan 27th 1970	2.3	3.1	4.2	4.3	2.4	3.7	4.2	4.0	3.9	6.5	7.7	7.8
00Z Jan 28th 1970	2.6	3.6	3.9	3.3	2.1	3.0	4.5	5.0	4.2	6.6	8.3	8.6
00Z Mar 3rd 1970	2.4	3.9	5.1	5.8	1.9	3.1	4.0	4.9	3.5	6.2	7.7	8.3
00Z Mar 26th 1970	3.1	5.5	6.6	6.7	2.9	4.7	5.2	5.1	4.4	7.4	8.0	6.7
Mean	2.6	3.9	4.9	5.4	2.3	3.4	4.4	5.1	3.7	6.2	7.5	7.8

Table 31 : CRMSE Verification Scores for the 238-point grid for the 850 mb height forecasts for the series of test cases integrated in the parallel model experiments.

Case	PARALLEL MODEL				1968 MODEL				PERSISTENCE			
	12	24	36	48	12	24	36	48	12	24	36	48
12Z Jan 29th 1969	3.3	4.9	6.4	7.3	2.5	4.0	5.8	6.9	3.8	6.3	8.3	8.9
00Z Jul 26th 1969	2.2	3.3	4.1	4.1	1.9	2.6	3.1	3.6	2.5	4.0	4.7	5.1
00Z Nov 18th 1969	2.5	3.7	3.7	4.7	2.3	4.2	5.1	6.3	3.3	6.3	8.4	10.3
00Z Dec 21st 1969	2.2	3.6	4.1	5.1	2.1	3.7	4.3	5.4	4.2	7.6	8.8	9.1
12Z Dec 25th 1969	2.2	3.4	5.2	7.7	2.0	3.4	5.1	6.7	4.0	6.6	8.8	11.1
00Z Jan 25th 1970	1.9	2.0	3.1	3.9	2.2	2.9	3.7	4.9	3.7	5.0	5.5	4.7
00Z Jan 27th 1970	2.0	2.5	3.8	4.2	2.4	3.2	4.2	4.5	3.6	5.5	7.2	7.6
00Z Jan 28th 1970	2.5	3.5	4.3	4.1	2.5	3.9	5.7	6.5	4.0	5.8	7.1	7.6
Mean	2.4	3.4	4.3	5.1	2.2	3.5	4.6	5.6	3.6	5.9	7.4	8.1

Table 32 : CRMSE Verification Scores for the 238-point grid for the 700 mb height forecasts for the series of test cases integrated in the parallel model experiments.

Case	PARALLEL MODEL				1968 MODEL				PERSISTENCE			
	12	24	36	48	12	24	36	48	12	24	36	48
12Z Jan 29th 1969	3.7	5.5	8.1	9.1	2.8	4.9	7.5	9.1	5.0	7.9	10.2	11.2
00Z Jul 26th 1969	2.4	3.7	4.7	5.3	1.7	2.6	3.4	4.7	3.4	5.2	6.1	6.5
12Z Sep 9th 1969	3.1	5.5	7.8	8.9	2.1	4.3	6.5	7.3	4.3	8.3	11.2	12.5
00Z Nov 18th 1969	3.0	3.9	4.9	6.4	2.7	4.3	6.0	7.6	5.6	9.7	13.1	16.3
00Z Dec 21st 1969	2.7	4.4	5.1	6.6	2.2	3.7	4.6	5.8	5.4	9.1	11.3	12.4
12Z Dec 25th 1969	2.8	4.3	6.6	9.5	2.5	3.8	5.6	7.4	5.5	8.7	12.1	15.4
00Z Jan 25th 1970	2.3	3.1	4.2	5.3	2.6	3.7	5.3	6.9	5.0	7.2	8.4	7.6
00Z Jan 27th 1970	2.5	3.5	5.1	5.7	2.8	4.0	5.3	6.0	4.7	7.3	9.5	10.5
00Z Jan 28th 1970	2.7	4.4	5.8	6.3	2.5	4.7	7.3	9.1	5.7	8.8	10.6	11.5
00Z Mar 3rd 1970	2.7	4.8	6.7	8.0	2.5	4.2	6.3	7.7	4.6	8.0	10.6	11.7
00Z Mar 26th 1970	3.9	6.2	8.4	8.8	3.2	5.1	6.6	7.4	6.9	10.7	11.8	10.2
Mean	2.9	4.5	6.1	7.3	2.5	4.1	5.9	7.2	5.1	8.3	10.4	11.4

Table 33 : CRMSE Verification Scores for the 238-point grid for the 500 mb height forecasts for the series of test cases integrated in the parallel model experiments.

Case	PARALLEL MODEL				1968 MODEL				PERSISTENCE			
	12	24	36	48	12	24	36	48	12	24	36	48
12Z Jan 29th 1969	4.7	5.8	8.7	10.4	5.2	6.6	6.8	6.8	4.9	7.8	12.0	13.0
00Z Jul 26th 1969	3.5	4.8	6.3	6.9	4.6	6.1	7.6	8.0	4.6	7.0	8.5	8.7
12Z Sep 9th 1969	4.2	6.5	9.2	10.3	5.7	9.4	12.0	12.9	6.0	10.2	13.9	15.2
00Z Nov 18th 1969	4.4	5.7	6.6	7.4	6.6	11.2	15.3	18.4	6.9	12.1	16.8	21.1
00Z Dec 21st 1969	3.7	5.1	6.5	8.2	4.5	7.1	8.2	8.4	5.7	9.3	12.1	13.0
12Z Dec 25th 1969	4.1	4.8	6.6	10.2	4.7	6.4	10.3	15.4	4.6	8.2	13.2	18.5
00Z Jan 25th 1970	3.0	3.9	5.0	5.4	3.3	5.6	8.1	10.0	5.7	9.6	12.3	11.6
00Z Jan 27th 1970	2.3	4.3	7.1	7.7	3.2	5.2	8.6	10.9	5.4	9.3	12.6	13.4
00Z Jan 28th 1970	3.2	4.6	5.5	6.0	4.5	7.6	9.5	10.8	7.6	12.0	14.5	14.6
00Z Mar 3rd 1970	3.6	5.9	7.3	8.6	4.7	8.2	11.0	12.3	5.8	10.0	12.8	14.5
00Z Mar 26th 1970	5.4	7.9	10.6	9.7	7.2	11.3	14.5	14.5	7.6	12.5	14.2	10.8
Mean	3.8	5.4	7.2	8.3	4.9	7.7	10.2	11.7	5.9	9.8	13.0	14.0

Table 34 : CRMSE Verification Scores for the 238-point grid for the 200 mb height forecasts for the series of test cases integrated in the parallel model experiments.

Case	PARALLEL MODEL				1968 MODEL				PERSISTENCE			
	12	24	36	48	12	24	36	48	12	24	36	48
12Z Jan 29th 1969	3.8	5.5	7.5	8.1	2.7	3.7	4.9	5.7	4.1	6.2	7.6	8.0
00Z Jul 26th 1969	2.2	3.1	4.5	5.3	1.9	2.2	2.9	3.4	2.4	3.4	4.2	5.0
12Z Sep 9th 1969	2.5	3.8	4.8	5.6	2.2	3.2	4.0	4.7	3.1	5.3	6.7	7.4
00Z Nov 18th 1969	2.7	4.1	4.3	5.2	2.2	3.9	4.6	5.7	3.8	6.7	8.1	9.2
00Z Dec 21th 1969	2.4	4.0	4.5	5.3	2.2	3.6	4.1	5.2	4.3	7.3	7.9	8.3
12Z Dec 25th 1969	2.9	4.2	6.8	8.4	2.6	3.8	5.7	6.8	4.6	6.7	8.6	9.5
00Z Jan 25th 1970	2.4	3.6	4.9	5.5	2.0	2.4	3.3	5.0	4.2	5.6	6.5	6.5
00Z Jan 27th 1970	2.2	3.2	4.2	5.0	2.1	3.1	3.7	4.5	3.8	5.8	6.7	7.0
00Z Jan 28th 1970	2.9	4.0	4.9	5.6	2.0	3.4	5.0	6.2	3.6	6.0	7.5	8.0
00Z Mar 3rd 1970	2.7	4.6	5.9	6.8	1.9	3.1	4.4	5.7	3.3	5.9	8.0	9.3
00Z Mar 26th 1970	3.0	4.8	5.8	6.1	2.6	4.1	4.6	5.1	4.7	6.9	7.7	6.8
Mean	2.7	4.1	5.3	6.1	2.2	3.3	4.3	5.3	3.8	6.0	7.2	7.7

Table 35 : CRMSE Verification Scores for the 504-point grid for the 350 mb height forecasts for the series of test cases integrated in the parallel model experiments.

Case	PARALLEL MODEL				1968 MODEL				PERSISTENCE			
	12	24	36	48	12	24	36	48	12	24	36	48
12Z Jan 29th 1969	3.2	5.0	6.8	7.9	2.4	3.6	5.2	6.4	4.3	6.6	8.2	8.6
00Z Jul 26th 1969	2.1	3.1	4.3	5.1	1.8	2.4	3.1	3.8	2.5	3.7	4.5	5.2
00Z Nov 18th 1969	2.5	4.0	4.2	5.2	2.3	4.1	4.8	6.0	3.9	7.3	8.8	10.0
00Z Dec 21st 1969	2.3	4.0	4.7	5.3	2.1	3.6	4.0	4.8	4.2	7.3	8.2	8.5
12Z Dec 25th 1969	3.2	4.5	6.5	8.2	2.7	3.8	5.8	6.9	4.5	6.9	9.3	10.0
00Z Jan 25th 1970	2.3	3.2	4.4	5.1	2.2	2.8	3.6	5.0	4.1	5.5	6.3	6.2
00Z Jan 27th 1970	2.0	2.8	3.9	4.9	2.1	3.0	3.6	4.7	3.6	5.5	6.4	6.8
00Z Jan 28th 1970	2.7	3.8	4.9	6.1	2.1	3.7	5.5	6.9	3.5	5.6	6.9	7.3
Mean	2.5	3.8	5.0	6.0	2.2	3.4	4.5	5.6	3.8	6.1	7.3	7.9

Table 36 : CRMSE Verification Scores for the 504-point grid for the 700 mb height forecasts for the series of test cases integrated in the parallel model experiments.

Case	PARALLEL MODEL				1968 MODEL				PERSISTENCE			
	12	24	36	48	12	24	36	48	12	24	36	48
12Z Jan 29th 1969	3.8	5.7	7.7	9.3	2.7	4.3	6.3	8.2	5.8	8.8	10.4	11.0
00Z Jul 26th 1969	2.3	3.5	5.0	6.0	1.6	2.5	3.5	4.7	3.2	4.9	6.1	6.6
12Z Sep 9th 1969	2.7	4.5	6.2	7.4	1.9	3.5	5.0	6.0	3.8	7.0	9.1	10.6
00Z Nov 18th 1969	3.2	4.5	5.5	6.5	2.7	4.2	5.4	7.1	5.8	10.0	12.7	14.7
00Z Dec 21st 1969	2.7	4.8	5.6	6.6	2.1	3.9	4.8	5.5	5.3	8.7	10.1	10.8
12Z Dec 25th 1969	3.4	5.1	7.2	9.5	2.7	5.1	6.1	8.0	5.7	9.4	11.9	14.6
00Z Jan 25th 1970	2.6	3.8	5.3	6.2	2.4	3.4	4.7	6.4	5.2	7.6	8.9	8.5
00Z Jan 27th 1970	2.5	3.5	5.0	6.3	2.8	3.8	4.8	6.0	5.3	7.5	8.6	9.2
00Z Jan 28th 1970	3.1	4.5	6.3	7.5	2.6	4.3	6.9	8.5	5.1	7.9	10.0	10.1
00Z Mar 3rd 1970	3.1	5.2	7.5	8.7	2.4	4.1	6.8	8.4	5.0	8.8	11.8	13.4
00Z Mar 26th 1970	3.6	5.5	7.1	7.8	3.1	4.6	5.7	6.7	6.7	10.3	11.4	10.5
Mean	3.0	4.6	6.2	7.4	2.5	4.0	5.5	6.9	5.2	8.3	10.1	10.9

Table 37 : CRMSE Verification Scores for the 504-point grid for the 500 mb height forecasts for the series of test cases integrated in the parallel model experiments.

Case	PARALLEL MODEL				1968 MODEL				PERSISTENCE			
	12	24	36	48	12	24	36	48	12	24	36	48
12Z Jan 29th 1969	5.2	6.7	8.7	10.0	5.8	8.1	8.7	9.5	6.2	9.3	12.7	13.7
00Z Jul 26th 1969	3.9	4.8	6.1	6.9	4.5	5.7	7.6	8.5	4.8	6.6	8.2	8.3
12Z Sep 9th 1969	3.8	5.5	7.7	9.4	5.0	7.7	10.0	11.4	5.0	8.0	11.2	13.3
00Z Nov 18th 1969	4.4	6.1	7.5	8.0	5.6	8.8	12.2	14.2	6.7	11.8	15.9	18.7
00Z Dec 21st 1969	3.7	5.2	6.7	7.7	4.8	6.7	8.7	8.8	6.2	8.9	10.9	11.5
12Z Dec 25th 1969	4.3	6.9	7.1	10.8	5.0	7.8	10.6	15.3	5.5	9.4	12.6	16.4
00Z Jan 25th 1970	3.5	3.6	5.4	6.0	3.5	5.4	8.6	10.2	5.4	8.2	11.1	10.6
00Z Jan 27th 1970	3.9	4.7	6.3	8.0	4.0	4.9	7.0	9.6	5.9	8.2	10.1	11.3
00Z Jan 28th 1970	3.5	5.3	6.8	8.0	3.9	6.5	9.1	10.9	6.2	10.3	12.2	12.2
00Z Mar 3rd 1970	3.8	5.7	7.5	8.9	5.1	7.2	10.0	11.0	5.4	9.4	12.6	14.2
00Z Mar 26th 1970	4.3	7.2	9.2	9.9	5.6	9.4	12.6	14.6	6.5	11.0	12.1	10.4
Mean	4.0	5.6	7.2	8.5	4.8	7.1	9.6	11.3	5.8	9.2	11.8	12.8

Table 38 : CRMSE Verification Scores for the 504-point grid for the 200 mb height forecasts for the series of test cases integrated in the parallel model experiments.

Case	PARALLEL MODEL				1968 MODEL				PERSISTENCE			
	12	24	36	48	12	24	36	48	12	24	36	48
12Z Jan 29th 1969	3.3	4.7	6.1	6.6	2.4	3.2	4.2	5.0	3.5	5.2	6.6	7.3
00Z Jul 26th 1969	1.8	2.7	3.8	4.5	1.6	2.1	2.7	3.3	2.0	3.1	3.8	4.5
12Z Sep 9th 1969	2.1	3.1	3.9	4.7	1.9	2.8	3.5	4.1	2.8	4.7	5.8	6.5
00Z Nov 18th 1969	2.3	3.7	4.6	5.7	2.0	3.5	4.7	5.7	3.1	5.3	6.7	7.7
00Z Dec 21st 1969	2.4	4.0	4.9	5.9	2.1	3.5	4.1	5.1	3.5	5.8	6.5	7.2
12Z Dec 25th 1969	2.5	4.0	6.4	7.9	2.4	3.8	5.7	6.9	3.6	5.6	7.3	7.6
00Z Jan 25th 1970	2.5	4.1	5.4	6.0	2.3	3.5	4.3	5.4	3.5	4.8	5.7	5.9
00Z Jan 27th 1970	2.4	3.3	4.4	5.2	2.4	3.3	4.3	5.3	3.4	4.9	6.0	6.6
00Z Jan 28th 1970	2.5	3.8	4.9	5.5	2.2	3.7	5.0	5.8	3.3	5.5	7.0	7.6
00Z Mar 3rd 1970	2.8	4.7	6.1	6.9	2.0	3.3	4.7	5.9	3.1	5.5	7.5	8.8
00Z Mar 26th 1970	2.4	4.3	5.6	6.2	2.3	4.4	5.1	5.7	3.7	5.9	6.6	6.6
Mean	2.5	3.9	5.1	5.9	2.1	3.4	4.4	5.3	3.2	5.1	6.3	6.9

Table 39 : CRMSE Verification Scores for the interior of the 1221-point grid for the 850 mb height forecasts for the series of test cases integrated in the parallel model experiments.

Case	PARALLEL MODEL				1968 MODEL				PERSISTENCE			
	12	24	36	48	12	24	36	48	12	24	36	48
12Z Jan 29th 1969	2.8	4.5	5.7	6.6	2.2	3.4	4.8	6.2	3.4	5.6	6.9	7.6
00Z Jul 26th 1969	1.9	2.7	3.6	4.4	1.7	2.3	2.9	3.6	2.1	3.2	3.9	4.7
00Z Nov 18th 1969	2.3	3.7	4.9	5.9	2.0	3.7	5.0	6.3	3.2	5.8	7.3	8.4
00Z Dec 21st 1969	2.3	4.0	4.8	5.6	2.2	3.7	4.3	4.9	3.5	6.0	6.9	7.3
12Z Dec 25th 1969	2.7	4.1	6.1	7.7	2.5	4.0	5.7	7.0	3.6	5.6	7.6	8.4
00Z Jan 25th 1970	2.4	3.9	5.4	6.2	2.2	3.2	4.4	5.5	3.5	4.8	5.7	5.9
00Z Jan 27th 1970	2.5	3.4	4.7	5.7	2.5	3.5	4.8	5.9	3.5	5.1	6.1	6.8
00Z Jan 28th 1970	2.5	3.8	5.0	6.2	2.3	3.9	5.5	6.8	3.3	5.4	6.7	7.6
Mean	2.4	3.8	5.0	6.0	2.2	3.5	4.7	5.8	3.3	5.2	6.4	7.1

Table 40 : CRMSE Verification Scores for the interior of the 1221-point grid for the 700 mb height forecasts for the series of test cases integrated in the parallel model experiments.

Case	PARALLEL MODEL				1968 MODEL				PERSISTENCE			
	12	24	36	48	12	24	36	48	12	24	36	48
12Z Jan 29th 1969	3.3	5.3	6.8	8.1	2.5	4.0	5.6	7.3	4.6	7.4	8.7	9.4
00Z Jul 26th 1969	2.1	3.1	4.4	5.3	1.7	2.4	3.4	4.3	2.7	4.1	5.1	5.8
12Z Sep 9th 1969	2.3	3.8	5.2	6.3	2.0	3.4	4.6	5.6	3.4	6.0	8.0	9.4
00Z Nov 18th 1969	3.0	4.7	6.7	8.1	2.8	4.6	6.7	8.3	4.9	8.3	10.9	12.5
00Z Dec 21st 1969	2.8	4.6	5.4	6.6	2.3	4.0	4.8	5.7	4.7	7.5	8.7	9.2
12Z Dec 25th 1969	3.1	4.8	6.9	8.8	2.8	5.3	6.4	8.1	4.8	8.3	10.0	11.7
00Z Jan 25th 1970	2.6	5.1	7.0	8.0	2.9	5.0	6.7	8.1	4.8	7.3	8.7	9.1
00Z Jan 27th 1970	3.4	4.7	6.4	7.6	3.6	5.0	6.5	7.8	5.3	7.4	8.2	9.0
00Z Jan 28th 1970	3.0	4.6	6.2	7.5	3.0	4.7	6.6	8.1	4.7	7.3	9.1	10.2
00Z Mar 3rd 1970	4.1	6.4	8.8	9.5	3.3	4.8	7.4	8.5	5.2	8.1	11.3	12.9
00Z Mar 26th 1970	3.1	5.3	7.3	8.6	2.8	5.5	7.0	8.2	5.1	8.4	9.7	9.8
Mean	3.0	4.8	6.5	7.7	2.7	4.4	6.0	7.3	4.6	7.3	8.9	9.9

Table 41 : CRMSE Verification Scores for the interior of the 1221-point grid for the 500 mb height forecasts for the series of test cases integrated in the parallel model experiments.

Case	PARALLEL MODEL				1968 MODEL				PERSISTENCE			
	12	24	36	48	12	24	36	48	12	24	36	48
12Z Jan 29th 1969	5.2	7.1	8.6	9.9	6.0	8.2	9.0	10.1	5.5	8.3	10.6	11.3
00Z Jul 26th 1969	3.8	4.8	6.0	7.2	4.0	4.9	6.6	7.8	4.1	5.6	6.9	7.6
12Z Sep 9th 1969	3.7	5.0	6.7	8.1	4.5	6.7	8.3	10.0	4.7	7.2	10.0	12.0
00Z Nov 18th 1969	4.7	6.8	9.2	10.8	5.7	8.9	12.4	14.4	6.7	11.0	14.6	16.8
00Z Dec 21st 1969	3.9	5.5	6.6	8.2	5.3	7.5	9.4	11.0	5.6	7.8	9.2	9.8
12Z Dec 25th 1969	4.4	7.6	8.3	10.6	5.7	9.6	11.8	14.9	6.0	9.7	11.8	14.2
00Z Jan 25th 1970	3.8	5.9	7.9	8.8	4.5	7.5	11.1	12.7	5.3	7.7	10.3	10.3
00Z Jan 27th 1970	4.8	6.1	8.6	9.7	5.6	7.6	10.7	12.3	6.2	8.4	9.8	10.6
00Z Jan 28th 1970	4.1	5.8	7.6	9.3	5.0	7.7	10.4	12.7	5.8	9.1	10.8	12.3
00Z Mar 3rd 1970	4.3	5.9	8.4	9.5	5.6	7.6	10.3	11.0	6.2	8.9	12.6	14.7
00Z Mar 26th 1970	4.3	8.9	10.5	12.0	5.9	11.3	13.7	15.5	5.8	9.9	10.6	10.1
Mean	4.3	6.3	8.0	9.5	5.3	8.0	10.3	12.0	5.6	8.5	10.7	11.8

Table 42: CRMSE Verification Scores for the interior of the 1221-point grid for the 200 mb height forecasts for the series of test cases integrated in the parallel model experiments.

Case	PARALLEL MODEL				1968 MODEL				PERSISTENCE			
	12	24	36	48	12	24	36	48	12	24	36	48
12Z Jan 29th 1969	3.8	4.0	5.3	5.6	3.3	3.9	5.5	6.3	3.3	4.9	5.0	5.7
00Z Jul 26th 1969	1.9	3.8	3.4	4.9	2.2	3.3	2.9	4.4	3.6	3.0	4.1	3.7
12Z Sep 9th 1969	3.4	3.5	5.6	5.3	3.1	2.9	4.7	4.5	3.2	4.1	5.3	5.2
00Z Nov 18th 1969	2.6	3.5	3.9	4.5	2.7	3.5	4.9	5.5	4.3	5.9	7.5	8.4
00Z Dec 21st 1969	2.7	4.0	3.6	4.9	2.6	4.0	5.0	6.6	3.1	4.1	5.3	6.1
12Z Dec 25th 1969	3.0	3.2	4.3	4.7	2.7	3.3	4.3	5.1	3.3	4.9	5.7	6.3
00Z Jan 25th 1970	3.3	5.4	5.6	6.7	2.8	4.0	4.8	5.9	4.5	6.2	7.1	6.1
00Z Jan 27th 1970	2.8	4.6	5.1	6.5	2.6	3.7	4.5	5.5	3.4	4.7	5.7	6.0
00Z Jan 28th 1970	2.9	5.2	5.7	6.2	2.9	4.3	6.0	7.4	4.1	5.9	8.6	8.8
00Z Mar 3rd 1970	2.8	4.1	3.9	5.8	3.0	3.8	4.4	5.7	3.8	4.2	5.6	5.4
00Z Mar 26th 1970	4.0	4.4	4.3	5.3	4.2	4.2	4.6	5.1	5.4	5.9	7.3	6.8
Mean	3.0	4.5	4.6	5.5	2.9	3.7	4.7	5.6	3.8	4.9	6.1	6.2

Table 43 : RMSE Verification Scores for the 238-point grid for the 850 mb temperature forecasts for the series of test cases integrated in the parallel model experiments.

Case	PARALLEL MODEL				1968 MODEL				PERSISTENCE			
	12	24	36	48	12	24	36	48	12	24	36	48
12Z Jan 29th 1969	2.5	2.9	3.2	3.9	2.1	2.6	3.4	4.4	3.0	3.8	4.2	4.6
00Z Jul 26th 1969	1.4	2.1	2.3	2.8	1.3	1.9	2.1	2.6	2.2	2.9	3.3	3.1
12Z Sep 9th 1969	1.7	2.4	3.6	4.0	1.5	1.9	3.2	3.6	2.1	3.3	4.2	4.7
00Z Nov 18th 1969	1.9	3.0	3.5	4.1	1.7	2.8	3.4	4.4	3.2	5.5	7.1	8.3
00Z Dec 21st 1969	1.9	2.5	3.3	4.0	2.0	2.4	3.3	4.2	2.5	3.5	4.3	5.6
12Z Dec 25th 1969	1.9	3.0	3.6	4.4	1.9	3.1	3.5	4.3	2.5	4.2	5.2	6.8
00Z Jan 25th 1970	1.9	3.1	4.2	5.4	1.9	2.6	3.7	5.0	3.4	4.8	5.2	5.5
00Z Jan 27th 1970	2.0	3.5	4.5	4.8	1.9	2.7	3.9	4.5	3.2	4.7	5.8	6.3
00Z Jan 28th 1970	2.2	3.2	4.1	4.4	2.0	2.8	4.4	5.4	3.5	5.8	7.4	8.1
00Z Mar 3rd 1970	1.9	2.5	2.9	3.6	2.1	2.9	3.6	4.3	2.8	4.1	5.3	5.8
00Z Mar 26th 1970	2.1	2.9	3.7	4.3	2.0	2.9	3.6	4.3	3.2	5.0	5.5	5.1
Mean	1.9	2.8	3.5	4.2	1.9	2.6	3.5	4.3	2.9	4.3	5.2	5.8

Table 44 : RMSE Verification Scores for the 238-point grid for the 700 mb temperature forecasts for the series of test cases integrated in the parallel model experiments.

Case	PARALLEL MODEL				1968 MODEL				PERSISTENCE			
	12	24	36	48	12	24	36	48	12	24	36	48
12Z Jan 29th 1969	2.0	2.6	3.4	4.0	1.8	2.5	3.5	4.3	2.9	3.9	4.6	4.8
00Z Jul 26th 1969	1.1	1.6	1.7	2.1	1.0	1.5	1.8	2.1	1.5	2.3	3.1	3.1
12Z Sep 9th 1969	1.6	2.3	3.3	3.6	1.3	1.8	2.7	2.9	2.2	3.3	4.0	4.4
00Z Nov 18th 1969	2.0	2.6	3.3	4.2	2.0	2.8	3.1	3.9	3.1	5.3	6.5	8.2
00Z Dec 21st 1969	2.0	2.4	2.7	3.3	2.0	2.6	3.2	3.3	2.5	3.6	4.4	5.4
12Z Dec 25th 1969	1.7	2.6	3.4	3.9	1.9	2.9	3.7	4.0	2.7	4.1	5.7	7.1
00Z Jan 25th 1970	1.8	2.4	3.1	3.8	1.7	2.2	3.2	4.1	2.6	4.1	4.9	4.7
00Z Jan 27th 1970	1.8	2.5	3.5	3.4	1.9	2.5	3.3	3.6	3.2	5.1	6.2	6.3
00Z Jan 28th 1970	1.9	2.4	2.8	3.1	1.7	2.2	3.2	3.8	3.7	6.0	7.1	7.3
00Z Mar 3rd 1970	1.8	2.9	3.3	3.6	2.0	2.7	3.3	3.8	2.9	4.5	5.9	6.4
00Z Mar 26th 1970	2.2	3.2	3.5	3.9	2.3	3.1	3.2	3.7	3.6	5.2	5.6	5.0
Mean	1.8	2.5	3.1	3.5	1.8	2.4	3.1	3.6	2.8	4.3	5.3	5.7

Table 45 : RMSE Verification Scores for the 238-point grid for the 500 mb temperature forecasts for the series of test cases integrated in the parallel model experiments.

Case	PARALLEL MODEL				1968 MODEL				PERSISTENCE			
	12	24	36	48	12	24	36	48	12	24	36	48
12Z Jan 29th 1969	3.1	3.4	4.3	4.6	3.0	3.5	4.5	5.1	3.1	4.3	4.4	5.1
00Z Jul 26th 1969	1.7	3.0	3.0	4.1	2.0	2.6	2.9	3.8	2.8	2.6	3.4	3.6
12Z Sep 9th 1969	2.7	2.9	4.2	4.5	2.4	2.4	3.5	3.9	2.5	3.4	4.2	4.6
00Z Nov 18th 1969	2.3	3.1	3.7	4.4	2.3	3.2	4.4	5.1	3.6	5.1	6.6	7.3
00Z Dec 21st 1969	2.8	3.5	3.2	4.4	2.7	3.6	4.2	5.5	3.5	4.6	5.1	5.9
12Z Dec 25th 1969	3.0	3.3	4.1	4.5	3.0	3.6	4.0	4.6	3.7	4.8	5.7	6.1
00Z Jan 25th 1970	3.1	5.1	5.4	6.0	2.7	3.9	3.9	5.0	4.2	5.9	6.6	5.9
00Z Jan 27th 1970	2.9	4.1	4.6	5.9	2.8	3.5	4.0	5.0	3.6	4.7	5.3	5.4
00Z Jan 28th 1970	2.7	4.6	5.3	5.9	2.6	3.7	5.0	6.0	3.5	5.1	7.0	7.0
00Z Mar 3rd 1970	2.7	3.5	3.9	4.8	2.8	3.5	4.3	5.1	3.6	4.5	5.5	5.5
00Z Mar 26th 1970	3.4	3.8	3.7	4.5	3.6	3.6	3.9	4.6	4.6	5.3	6.3	5.7
Mean	2.8	3.7	4.1	4.9	2.7	3.4	4.1	4.9	3.5	4.6	5.5	5.6

Table 46: RMSE Verification Scores for the 504-point grid for 850 mb temperature forecasts for the series of test cases integrated in the parallel model experiments.

Case	PARALLEL MODEL				1968 MODEL				PERSISTENCE			
	12	24	36	48	12	24	36	48	12	24	36	48
12Z Jan 29th 1969	2.4	2.7	2.9	3.4	2.2	2.7	2.9	3.7	3.0	3.9	4.2	4.7
00Z Jul 26th 1969	1.4	1.9	2.3	2.7	1.4	1.7	2.1	2.4	1.9	2.7	3.1	3.2
12Z Sep 9th 1969	1.5	2.0	2.8	3.5	1.4	1.7	2.6	3.3	1.9	2.8	3.5	4.5
00Z Nov 18th 1969	1.7	2.5	3.3	3.4	1.6	2.5	3.2	3.7	2.8	4.7	6.1	7.0
00Z Dec 21st 1969	1.8	2.3	2.9	3.6	1.8	2.3	3.0	3.6	3.0	3.9	4.2	5.1
12Z Dec 25th 1969	1.9	3.0	3.5	3.9	1.9	3.0	3.3	3.9	2.6	3.8	4.7	6.0
00Z Jan 25th 1970	1.8	3.1	5.6	4.5	1.7	2.6	3.4	4.1	3.2	4.8	5.3	5.2
00Z Jan 27th 1970	1.9	3.0	3.6	4.1	1.8	2.5	3.2	3.9	3.4	4.4	5.0	5.3
00Z Jan 28th 1970	1.9	2.7	3.6	3.9	1.8	2.4	3.6	4.3	2.9	4.8	5.8	6.3
00Z Mar 3rd 1970	1.9	2.5	3.2	3.9	1.9	2.7	3.4	4.2	2.7	4.0	4.9	5.6
00Z Mar 26th 1970	2.0	2.8	3.2	3.6	1.9	2.7	3.2	3.8	2.8	4.4	4.7	4.7
Mean	1.8	2.6	3.4	3.7	1.8	2.4	3.1	3.7	2.7	4.0	4.7	5.2

Table 47: RMSE Verification Scores for the 504-point grid for 700 mb temperature forecasts for the series of test cases integrated in the parallel model experiments.

Case	PARALLEL MODEL				1968 MODEL				PERSISTENCE			
	12	24	36	48	12	24	36	48	12	24	36	48
12Z Jan 29th 1969	2.1	2.6	3.0	3.6	2.2	2.6	3.1	3.8	3.2	4.3	4.7	4.9
00Z Jul 26th 1969	1.2	1.7	2.1	2.3	1.2	1.5	1.9	2.1	1.6	2.5	3.2	3.2
12Z Sep 9th 1969	1.6	2.0	2.7	3.4	1.3	1.7	2.4	2.9	2.0	2.8	3.5	4.3
00Z Nov 19th 1969	1.8	2.6	3.1	3.7	1.9	2.7	2.9	3.4	3.0	4.9	6.1	7.3
00Z Dec 21st 1969	1.8	2.2	2.6	3.1	1.9	2.4	3.0	3.1	3.0	3.7	4.0	4.8
12Z Dec 25th 1969	1.7	2.8	3.3	3.5	1.8	3.2	3.5	3.8	2.7	3.9	5.0	5.9
00Z Jan 25th 1970	1.7	2.4	3.1	3.4	1.7	2.3	2.9	3.5	2.8	4.2	4.9	4.5
00Z Jan 27th 1970	1.8	2.3	3.2	3.4	1.8	2.4	3.1	3.4	3.1	4.4	5.2	5.3
00Z Jan 28th 1970	1.8	2.3	2.8	2.8	1.8	2.1	2.9	3.3	3.2	4.8	5.8	5.9
00Z Mar 3rd 1970	1.7	2.6	3.1	3.7	1.8	2.6	3.2	4.0	2.6	4.2	5.1	5.8
00Z Mar 26th 1970	1.9	2.8	3.0	3.2	2.1	2.9	3.1	3.2	3.1	4.6	5.0	4.6
Mean	1.7	2.4	2.9	3.3	1.8	2.4	2.9	3.3	2.8	4.0	4.8	5.1

Table 48: RMSE

Verification Scores for the 504-point grid for 500 mb temperature forecasts for the series of test cases integrated in the parallel model experiments.

Case	PARALLEL MODEL				1968 MODEL				PERSISTENCE			
	12	24	36	48	12	24	36	48	12	24	36	48
12Z Jan 29th 1969	2.7	3.0	4.1	4.3	2.7	3.1	4.1	4.4	2.6	3.5	3.8	4.2
00Z Jul 26th 1969	1.6	2.5	2.7	3.4	1.7	2.2	2.6	3.2	2.5	2.4	3.1	3.2
12Z Sep 9th 1969	2.3	2.5	3.6	4.0	2.1	2.2	3.0	3.4	2.3	2.9	3.6	4.0
00Z Nov 19th 1969	2.0	2.6	3.2	3.8	2.1	2.7	3.7	4.4	3.2	4.4	5.5	6.0
00Z Dec 21st 1969	2.6	3.0	3.0	3.9	2.6	3.1	3.6	4.6	3.4	4.3	4.8	5.4
12Z Dec 25th 1969	2.7	2.9	3.6	3.9	2.7	3.2	3.5	4.0	3.3	4.4	5.3	5.1
00Z Jan 25th 1970	2.7	4.3	4.4	5.1	2.4	3.5	3.5	4.3	3.6	5.1	5.8	5.4
00Z Jan 27th 1970	2.6	3.5	3.8	5.0	2.5	3.2	3.6	4.5	3.2	4.1	4.6	4.9
00Z Jan 28th 1970	2.3	3.8	4.3	4.9	2.3	3.2	4.2	5.0	3.1	4.5	5.8	5.9
00Z Mar 3rd 1970	2.5	3.4	3.9	4.2	2.5	3.3	4.0	4.4	3.4	4.1	5.3	5.1
00Z Mar 26th 1970	2.9	3.4	3.3	3.8	3.0	3.2	3.4	3.8	3.9	4.7	5.3	4.8
Mean	2.4	3.2	3.6	4.2	2.4	3.0	3.6	4.2	3.1	4.0	4.8	4.9

Table 49: RMSE Verification Scores for the interior of the 1015-point grid for the 850 mb temperature forecasts for the series of test cases integrated in the parallel model experiments.

Case	PARALLEL MODEL				1968 MODEL				PERSISTENCE			
	12	24	36	48	12	24	36	48	12	24	36	48
12Z Jan 29th 1969	2.2	2.4	2.8	3.3	2.1	2.4	2.9	3.3	2.8	3.4	3.7	4.2
OOZ Jul 26th 1969	1.2	1.7	2.0	2.3	1.2	1.6	1.8	2.1	1.6	2.3	2.6	2.6
12Z Sep 9th 1969	1.3	1.7	2.5	3.1	1.2	1.5	2.2	2.9	1.7	2.4	3.2	3.9
OOZ Nov 18th 1969	1.5	2.3	3.0	3.3	1.4	2.3	2.9	3.5	2.5	4.1	5.2	6.0
OOZ Dec 21st 1969	1.7	2.1	2.5	3.1	1.7	2.2	2.6	3.2	2.7	3.7	4.0	4.7
12Z Dec 25th 1969	1.7	2.6	2.9	3.2	1.8	2.8	2.9	3.4	2.4	3.7	4.4	5.1
COZ Jan 25th 1970	1.7	2.7	3.5	4.0	1.7	2.4	3.1	3.7	2.8	4.2	4.8	4.7
OOZ Jan 27th 1970	1.8	2.5	3.1	3.4	1.7	2.3	2.8	3.5	2.9	3.9	4.3	4.7
OOZ Jan 28th 1970	1.7	2.4	3.1	3.4	1.7	2.2	3.1	3.7	2.4	4.0	4.8	5.4
OOZ Mar 3rd 1970	1.8	2.5	3.0	3.6	2.0	2.6	3.1	3.8	2.7	3.8	4.5	5.1
OOZ Mar 26th 1970	1.7	2.4	2.8	3.3	1.6	2.3	2.8	3.3	2.4	3.7	4.1	4.1
Mean	1.7	2.3	2.8	3.3	1.6	2.2	2.7	3.3	2.4	3.6	4.1	4.6

Table 50: RMSE Verification Scores for the interior of the 1015-point grid for the 700 mb temperature forecasts for the series of test cases integrated in the parallel model experiments.

Case	PARALLEL MODEL				1968 MODEL				PERSISTENCE			
	12	24	36	48	12	24	36	48	12	24	36	48
12Z Jan 29th 1969	1.9	2.3	2.8	3.2	1.9	2.3	2.8	3.2	2.7	3.6	3.9	4.1
00Z Jul 26th 1969	1.1	1.5	1.9	2.1	1.1	1.4	1.7	1.9	1.4	2.1	2.6	2.6
12Z Sep 9th 1969	1.5	1.8	2.3	3.0	1.3	1.6	2.1	2.7	1.8	2.4	3.0	3.9
00Z Nov 18th 1969	1.6	2.5	2.8	3.3	1.7	2.5	2.8	3.3	2.7	4.3	5.4	6.2
00Z Dec 21st 1969	1.7	2.1	2.4	2.7	1.8	2.4	2.9	2.8	2.6	3.4	3.8	4.3
12Z Dec 25th 1969	1.6	2.5	3.0	3.1	1.6	3.0	3.3	3.5	2.3	3.8	4.7	5.0
00Z Jan 25th 1970	1.6	2.2	2.9	3.2	1.8	2.2	2.7	3.2	2.5	3.9	4.6	4.3
00Z Jan 27th 1970	1.7	2.5	3.2	3.1	1.7	2.5	3.2	3.3	2.8	4.1	4.6	4.5
00Z Jan 28th 1970	1.7	2.0	2.4	2.5	1.7	1.9	2.6	2.9	2.7	4.0	4.8	4.9
00Z Mar 3rd 1970	1.7	2.5	2.9	3.4	1.9	2.6	3.1	3.7	2.7	3.9	4.6	5.2
00Z Mar 26th 1970	1.7	2.4	2.7	3.0	1.9	2.5	2.8	2.9	2.6	3.9	4.2	4.1
Mean	1.6	2.2	2.7	3.0	1.7	2.3	2.7	3.0	2.4	3.6	4.2	4.5

Table 51: RMSE Verification Scores for the interior of the 1015-point grid for the 500 mb temperature forecasts for the series of test cases integrated in the parallel model experiments.

Case	PARALLEL MODEL				1968 MODEL				PERSISTENCE			
	12	24	36	48	12	24	36	48	12	24	36	48
12Z Jan 29th 1969	4.4	4.9	5.2	5.5	4.2	4.3	4.9	4.6	5.8	6.2	7.5	7.0
00Z Jul 26th 1969	3.9	6.4	5.8	6.2	3.5	5.8	5.3	5.9	4.2	6.2	5.9	6.4
12Z Sep 9th 1969	4.7	4.3	5.7	5.4	4.7	4.0	5.6	5.3	5.5	5.9	6.9	6.1
00Z Nov 18th 1969	4.4	4.8	5.4	6.1	4.1	4.6	5.8	6.8	4.5	5.3	6.3	6.7
00Z Dec 21st 1969	4.4	4.7	4.0	6.0	4.0	4.1	3.6	5.3	5.5	6.7	6.4	6.5
12Z Dec 25th 1969	4.1	4.7	5.5	5.7	3.3	4.3	4.7	4.9	4.8	6.3	7.1	7.0
00Z Jan 25th 1970	4.5	5.4	4.5	5.1	4.6	4.9	4.7	5.1	5.8	6.8	6.6	6.3
00Z Jan 27th 1970	4.1	5.5	5.5	6.0	3.9	5.4	4.5	4.6	4.8	6.7	5.6	6.7
00Z Jan 28th 1970	5.1	5.7	5.3	6.4	4.8	4.7	4.7	5.8	6.5	6.8	6.5	7.0
00Z Mar 3rd 1970	3.9	4.2	4.3	5.4	3.7	3.8	4.7	5.6	4.7	5.7	6.7	7.2
00Z Mar 26th 1970	4.4	5.3	5.5	7.2	3.9	5.0	5.6	7.8	6.5	7.9	8.2	7.4
Mean	4.3	5.1	5.2	5.9	4.1	4.6	4.9	5.6	5.3	6.4	6.7	6.8

Table 52: RMSE Verification Scores for the 238-point grid for the 850 mb dew point depression forecasts for the series of test cases integrated in the parallel model experiments.

Case	PARALLEL MODEL				1968 MODEL				PERSISTENCE			
	12	24	36	48	12	24	36	48	12	24	36	48
12Z Jan 29th 1969	4.5	6.3	7.5	7.5	4.9	6.0	6.9	7.4	6.2	6.5	7.0	7.6
00Z Jul 26th 1969	4.4	5.3	5.5	5.9	4.6	4.9	5.5	5.5	4.5	5.9	6.1	6.9
12Z Sep 9th 1969	5.7	5.9	5.5	6.4	5.6	5.5	5.8	6.4	7.1	8.3	7.8	7.5
00Z Nov 18th 1969	4.5	5.2	5.8	7.3	4.4	4.4	6.8	7.3	5.3	5.9	6.8	7.3
00Z Dec 21st 1969	4.7	5.5	6.0	7.5	3.6	3.9	4.1	6.0	7.2	8.1	7.4	7.0
12Z Dec 25th 1969	3.9	6.1	7.4	7.1	3.6	5.0	5.7	6.2	5.3	7.0	7.6	7.5
00Z Jan 25th 1970	4.4	5.3	5.2	5.0	4.9	4.8	5.1	4.7	5.9	6.9	6.6	6.9
00Z Jan 27th 1970	4.0	5.5	6.7	5.7	3.8	4.1	4.8	5.4	5.1	6.1	5.6	6.2
00Z Jan 28th 1970	4.7	5.2	5.9	6.0	4.1	5.3	6.1	5.7	5.3	5.6	6.3	5.8
00Z Mar 3rd 1970	4.8	5.1	6.5	6.9	4.2	4.9	6.1	6.6	5.0	6.7	7.6	7.1
00Z Mar 26th 1970	4.6	4.8	6.8	8.2	4.6	4.9	7.2	8.2	5.7	6.7	6.6	6.3
Mean	4.6	5.5	6.3	6.7	4.4	4.9	5.8	6.3	5.7	6.7	6.9	6.9

Table 53: RMSE Verification Scores for the 238-point grid for the 700 mb dew point depression forecasts for the series of test cases integrated in the parallel model experiments.

Case	PARALLEL MODEL				1968 MODEL				PERSISTENCE			
	12	24	36	48	12	24	36	48	12	24	36	48
12Z Jan 29th 1969	5.2	6.3	6.2	6.7	5.8	6.4	7.1	7.2	5.0	5.8	5.8	6.6
00Z Jul 26th 1969	5.1	5.3	6.7	5.7	4.9	5.3	6.7	6.2	5.7	5.9	7.2	6.8
12Z Sep 9th 1969	4.1	5.7	5.7	6.9	4.3	5.9	5.8	7.2	5.1	7.0	7.3	7.2
00Z Nov 18th 1969	4.4	5.3	5.7	6.2	5.0	5.8	6.6	7.9	4.8	5.5	6.1	7.0
00Z Dec 21st 1969	4.0	4.8	6.2	5.8	4.1	4.6	5.9	6.6	4.6	4.9	5.4	4.8
12Z Dec 25th 1969	4.1	5.3	6.1	6.5	3.6	5.3	6.1	6.5	5.6	7.1	6.8	7.0
00Z Jan 25th 1970	4.8	4.4	5.0	6.0	4.6	4.0	4.8	5.5	4.9	5.1	6.0	5.9
00Z Jan 27th 1970	3.7	5.2	4.8	4.5	3.8	5.2	5.1	5.4	5.2	5.8	5.6	5.8
00Z Jan 28th 1970	3.9	4.2	5.3	5.5	4.5	5.4	6.4	5.2	5.1	5.3	5.8	6.0
00Z Mar 3rd 1970	4.2	5.0	5.5	5.8	3.8	4.6	5.6	6.2	4.8	5.6	5.4	6.1
00Z Mar 26th 1970	5.2	5.0	6.4	6.2	5.8	6.1	7.8	6.9	5.6	6.0	6.4	6.0
Mean	4.4	5.1	5.8	6.0	4.6	5.3	6.2	6.4	5.1	5.8	6.2	6.3

Table 54: RMSE Verification Scores for the 238-point grid for the 500 mb dew point depression forecasts for the series of test cases integrated in the parallel model experiments.

Case	PARALLEL MODEL				1968 MODEL				PERSISTENCE			
	12	24	36	48	12	24	36	48	12	24	36	48
12Z Jan 29th 1969	4.3	4.9	5.3	5.4	3.8	4.3	5.1	4.6	5.0	5.4	6.2	5.6
00Z Jul 26th 1969	4.0	5.5	5.3	5.8	3.9	5.2	5.2	5.6	4.2	5.8	5.6	6.0
12Z Sep 9th 1969	4.1	4.4	5.3	5.6	4.0	4.2	5.0	5.1	4.7	5.7	6.6	6.2
00Z Nov 18th 1969	4.2	5.1	5.7	4.0	4.0	4.6	6.2	6.9	5.0	6.2	6.7	7.4
00Z Dec 21st 1969	4.8	5.7	5.6	6.5	4.4	4.9	5.0	5.9	6.0	7.2	7.9	7.4
12Z Dec 25th 1969	4.8	5.1	6.2	6.3	4.5	4.7	5.8	5.7	5.6	6.8	7.9	8.4
00Z Jan 25th 1970	4.9	5.8	5.6	5.8	4.6	5.2	5.2	5.3	5.5	7.4	7.8	7.6
00Z Jan 27th 1970	4.7	5.8	6.1	6.6	4.2	5.3	4.9	5.5	5.4	7.2	7.1	7.3
00Z Jan 28th 1970	5.1	6.1	5.5	6.5	4.4	4.8	4.6	5.9	6.5	7.6	7.4	7.2
00Z Mar 3rd 1970	4.1	4.8	5.0	6.1	3.8	4.3	5.1	5.7	4.7	6.4	7.6	7.7
00Z Mar 26th 1970	5.5	6.7	6.1	7.1	4.9	6.0	5.6	7.2	7.1	9.1	8.8	8.1
Mean	4.6	5.4	5.6	6.1	4.2	4.9	5.2	5.8	5.4	6.8	7.2	7.2

337

Table 55: RMSE Verification Scores for the 504-point grid for the 850 mb dew point depression forecasts for the series of test cases integrated in the parallel model experiments.

Case	PARALLEL MODEL				1968 MODEL				PERSISTENCE			
	12	24	36	48	12	24	36	48	12	24	36	48
12Z Jan 29th 1969	4.5	6.3	7.0	7.1	4.4	5.9	6.2	6.6	4.9	5.6	6.1	6.6
00Z Jul 26th 1969	4.3	5.1	5.3	5.4	4.2	4.6	5.1	5.3	4.8	6.2	6.0	6.9
12Z Sep 9th 1969	5.1	5.8	5.8	6.9	4.9	5.2	5.5	6.1	6.0	7.5	7.0	7.3
00Z Nov 18th 1969	4.6	5.2	5.8	6.7	4.6	4.5	6.5	7.7	5.4	6.3	7.3	8.2
00Z Dec 21st 1969	5.1	6.4	6.8	7.2	3.8	4.8	5.0	5.8	6.7	8.5	8.2	7.5
12Z Dec 25th 1969	5.2	6.3	7.1	7.2	4.9	5.6	5.7	6.4	6.0	7.1	7.5	7.8
00Z Jan 25th 1970	4.8	5.7	6.1	5.6	4.8	5.0	5.7	5.2	5.8	7.5	7.6	8.0
00Z Jan 27th 1970	4.8	6.0	6.9	6.3	4.2	4.1	4.9	5.8	5.9	7.1	7.4	7.2
00Z Jan 28th 1970	4.7	5.2	6.3	6.7	3.8	4.9	5.8	6.3	5.5	7.1	7.3	7.2
00Z Mar 3rd 1970	4.8	5.4	6.9	8.0	3.9	4.7	5.7	7.0	5.2	7.1	7.6	7.7
00Z Mar 26th 1970	4.9	5.5	6.5	7.8	4.4	5.0	6.2	7.5	6.2	7.2	7.4	7.2
Mean	4.8	5.7	6.4	6.8	4.4	4.9	5.7	6.3	5.7	7.0	7.2	7.4

Table 56: RMSE Verification Scores for the 504-point grid for the 700 mb dew point depression forecasts for the series of test cases integrated in the parallel model experiments.

Case	PARALLEL MODEL				1968 MODEL				PERSISTENCE			
	12	24	36	48	12	24	36	48	12	24	36	48
12Z Jan 29th 1969	5.2	6.5	6.3	6.0	5.2	6.1	7.0	7.0	4.5	5.7	5.6	6.0
00Z Jul 26th 1969	4.7	5.2	6.4	6.1	4.6	4.8	5.9	6.3	5.5	5.9	7.3	7.2
12Z Sep 9th 1969	3.9	5.2	5.7	6.3	3.8	5.0	5.2	6.3	4.5	6.1	6.6	7.0
00Z Nov 18th 1969	4.2	5.1	5.6	6.2	4.6	5.7	6.3	7.9	5.0	6.0	6.5	7.2
00Z Dec 21st 1969	4.4	5.6	6.3	5.9	4.0	5.3	6.1	6.6	5.3	5.7	6.4	6.0
12Z Dec 25th 1969	4.6	5.5	6.2	6.4	4.4	5.6	6.3	7.1	5.2	6.8	6.8	7.3
00Z Jan 25th 1970	4.7	5.0	5.9	6.2	4.6	4.5	5.3	5.7	5.1	5.7	6.3	6.2
00Z Jan 27th 1970	4.0	5.1	5.1	5.1	3.5	4.8	5.1	5.3	5.4	7.2	6.8	6.5
00Z Jan 28th 1970	3.7	4.3	5.7	5.9	3.8	4.6	5.8	5.3	5.2	6.3	6.9	6.7
00Z Mar 3rd 1970	4.1	5.4	6.5	6.5	3.7	5.1	5.8	6.0	5.2	6.0	6.3	6.6
00Z Mar 26th 1970	5.1	5.7	5.9	6.3	5.3	5.9	6.8	6.9	6.4	6.9	7.2	6.8
Mean	4.4	5.3	6.0	6.1	4.3	5.2	6.0	6.4	5.2	6.2	6.6	6.7

Table 57: RMSE Verification Scores for the 504-point grid for the 500 mb dew point depression forecasts for the series of test cases integrated in the parallel model experiments.

Case	PARALLEL MODEL				1968 MODEL				PERSISTENCE			
	12	24	36	48	12	24	36	48	12	24	36	48
12Z Jan 29th 1969	3.6	4.2	4.7	4.8	3.1	3.6	4.4	4.2	4.0	4.4	5.0	4.7
00Z Jul 26th 1969	4.0	5.0	5.3	5.5	4.0	5.0	5.3	5.5	3.9	5.4	6.0	6.2
12Z Sep 9th 1969	4.0	4.7	5.4	6.0	4.0	4.5	5.0	5.5	4.6	5.8	6.4	6.8
00Z Nov 18th 1969	4.2	5.2	5.9	6.2	4.2	4.9	6.1	6.7	4.6	6.2	7.1	8.0
00Z Dec 21st 1969	4.7	5.4	5.6	6.4	4.5	5.1	5.1	5.9	5.9	7.2	7.8	7.6
12Z Dec 25th 1969	4.7	5.6	7.1	7.4	4.5	5.3	6.7	7.2	5.1	6.8	8.1	8.8
00Z Jan 25th 1970	5.1	6.1	6.1	6.4	4.8	5.5	5.6	5.9	5.3	6.9	7.6	7.7
00Z Jan 27th 1970	4.3	5.5	5.6	6.2	4.1	5.2	5.0	5.2	5.0	7.2	7.1	6.7
00Z Jan 28th 1970	4.5	5.8	5.9	6.3	4.0	5.0	5.5	6.0	6.0	7.6	7.8	7.3
00Z Mar 3rd 1970	4.6	5.3	6.1	6.8	4.3	4.8	5.7	6.2	5.4	7.0	8.1	7.9
00Z Mar 26th 1970	5.1	6.4	6.5	6.9	4.8	6.0	6.1	6.7	6.4	8.5	8.7	8.4
Mean	4.4	5.4	5.8	6.3	4.2	5.0	5.5	5.9	5.1	6.6	7.2	7.3

Table 58 : RMSE Verification Scores for the interior of the 1015-point grid for the 850 mb dew point depression forecasts for the series of test cases integrated in the parallel model experiments.

Case	PARALLEL MODEL				1968 MODEL				PERSISTENCE			
	12	24	36	48	12	24	36	48	12	24	36	48
12Z Jan 29th 1969	4.0	5.7	6.2	6.4	3.7	5.3	5.5	6.0	4.1	5.2	5.6	6.0
00Z Jul 26th 1969	4.0	4.7	5.1	5.2	3.9	4.6	5.1	5.3	4.5	6.0	6.1	6.8
12Z Sep 9th 1969	4.4	5.4	5.6	6.7	4.3	5.1	5.3	6.3	5.1	6.8	6.9	7.4
00Z Nov 18th 1969	4.5	5.4	6.2	6.7	4.4	4.9	6.4	7.1	5.0	6.5	7.9	8.7
00Z Dec 21st 1969	4.8	5.8	6.3	6.9	4.0	5.1	5.4	6.1	6.3	7.9	7.9	7.8
12Z Dec 25th 1969	4.9	6.3	7.5	7.7	4.6	5.9	6.7	7.4	5.4	7.3	8.1	8.4
00Z Jan 25th 1970	4.7	6.0	6.6	6.1	4.5	5.3	6.2	6.0	5.8	7.5	7.7	8.1
00Z Jan 27th 1970	4.6	5.8	6.3	6.4	4.2	4.9	5.4	5.9	5.5	7.4	7.5	7.5
00Z Jan 28th 1970	4.3	5.9	6.4	6.8	3.9	5.5	6.2	6.7	5.8	8.0	7.9	8.1
00Z Mar 3rd 1970	4.9	5.6	6.9	7.6	4.3	5.2	5.9	6.8	5.9	7.7	8.3	8.3
00Z Mar 26th 1970	4.6	5.4	6.4	7.9	4.5	5.1	6.0	7.2	6.0	7.2	7.6	8.2
Mean	4.5	5.6	6.3	6.8	4.2	5.2	5.8	6.4	5.4	7.0	7.4	7.8

Table 59: RMSE Verification Scores for the interior of the 1015-point grid for the 700 mb dew point depression forecasts for the series of test cases integrated in the parallel model experiments.

Case	PARALLEL MODEL				1968 MODEL				PERSISTENCE			
	12	24	36	48	12	24	36	48	12	24	36	48
12Z Jan 29th 1969	4.3	5.6	5.7	5.6	4.1	5.1	6.0	6.1	3.8	5.1	4.9	5.3
00Z Jul 26th 1969	4.3	4.7	5.9	5.9	4.2	4.4	5.5	6.0	4.9	5.5	6.6	7.1
12Z Sep 9th 1969	3.7	4.9	5.4	6.0	3.5	4.6	5.0	6.1	4.2	5.6	6.4	7.1
00Z Nov 18th 1969	4.1	5.1	5.8	5.9	4.2	5.4	6.3	7.2	5.0	6.2	7.1	7.5
00Z Dec 21st 1969	4.0	5.0	5.5	5.7	3.7	4.9	5.8	6.3	5.1	5.7	6.4	6.5
12Z Dec 25th 1969	4.4	5.6	6.0	6.2	4.2	5.8	6.2	6.9	4.9	6.6	6.9	7.4
00Z Jan 25th 1970	4.3	4.9	5.5	5.8	4.3	4.5	5.2	5.6	5.0	5.9	6.8	6.6
00Z Jan 27th 1970	3.9	4.8	4.9	5.2	3.7	4.8	5.1	5.3	5.1	6.8	6.5	6.5
00Z Jan 28th 1970	3.5	4.7	5.5	5.7	3.7	4.8	5.7	5.7	5.3	6.8	7.3	7.0
00Z Mar 3rd 1970	4.4	5.4	6.2	6.1	4.1	5.2	5.9	6.2	5.4	6.0	6.5	6.5
00Z Mar 26th 1970	4.5	5.2	5.5	6.1	4.9	5.6	6.3	6.4	6.2	7.0	7.4	7.0
Mean	4.1	5.1	5.6	5.8	4.1	5.0	5.7	6.2	5.0	6.1	6.6	6.8

Table 60 : RMSE Verification Scores for the interior of the 1015-point grid for the 500 mb dew point depression forecasts for the series of test cases integrated in the parallel model experiments.

Case	PARALLEL MODEL						1968 MODEL					
	CANADA		U.S.		N.A.		CANADA		U.S.		N.A.	
	Large	Total	Large	Total	Large	Total	Large	Total	Large	Total	Large	Total
12Z Jan 29th 1969	61.1	55.6	60.4	61.7	60.7	58.9	59.5	56.9	61.7	62.4	60.8	60.1
00Z Jul 26th 1969	50.9	57.0	15.1	28.1	39.3	47.4	59.8	60.8	27.5	37.7	48.2	51.4
12Z Sep 9th 1969	60.8	59.5	33.3	34.3	48.6	48.0	62.5	59.5	37.3	35.7	51.0	48.7
00Z Nov 18th 1969	57.6	58.9	71.8	69.2	64.0	63.6	60.7	62.3	65.0	65.8	62.8	64.0
00Z Dec 21st 1969	55.0	56.0	64.9	64.7	60.4	60.8	65.7	64.0	62.0	61.2	63.6	62.4
12Z Dec 25th 1969	31.3	30.4	71.2	67.4	53.3	51.1	34.7	33.0	72.4	71.9	55.1	54.0
00Z Jan 25th 1970	43.3	40.7	49.0	43.5	46.3	42.0	39.6	34.3	48.3	42.8	44.0	38.4
00Z Jan 27th 1970	39.8	39.8	45.3	46.8	42.3	42.7	51.0	44.2	46.8	45.6	49.2	44.7
00Z Jan 28th 1970	44.2	39.6	41.6	43.4	43.0	41.2	50.9	42.5	40.4	40.4	45.9	41.6
00Z Mar 3rd 1970	60.8	60.4	55.1	50.4	57.7	54.9	63.4	63.2	53.7	49.7	57.9	55.3
00Z Mar 26th 1970	17.8	17.3	34.8	36.4	27.0	27.4	32.2	31.5	38.9	38.2	35.9	35.1
Mean	47.5	46.8	49.3	49.6	49.3	48.9	52.7	50.2	50.4	50.1	52.2	50.5

Table 61 : Threat Scores for 00-24 hours for a threshold of 0.01 inches for the series of test cases integrated in the parallel model experiments. Separate results are given for all received Canadian stations, all received U.S. stations, and all received North American stations.

PARALLEL MODEL

1968 MODEL

Case	CANADA		U.S.		N.A.		CANADA		U.S.		N.A.	
	Large	Total	Large	Total	Large	Total	Large	Total	Large	Total	Large	Total
12Z Jan 29th 1969	55.3	53.5	58.3	58.1	56.8	55.9	54.2	55.0	59.1	61.7	56.7	58.5
00Z Jul 26th 1969	39.8	44.0	16.3	23.3	28.8	34.2	47.7	55.7	33.3	43.5	40.7	49.0
12Z Sep 9th 1969	52.0	49.0	22.0	23.1	42.0	40.1	53.9	53.9	25.5	26.3	44.0	44.0
00Z Nov 18th 1969	62.5	62.5	59.0	53.9	61.2	59.0	58.7	61.6	44.1	42.4	52.3	53.3
00Z Dec 21st 1969	46.7	47.2	76.4	77.0	63.9	64.6	69.4	68.8	81.3	81.3	76.3	76.0
12Z Dec 25th 1969	37.8	36.9	57.3	57.6	48.7	48.4	48.8	48.3	61.3	60.8	56.1	55.6
00Z Jan 25th 1970	31.1	31.5	41.1	43.8	36.2	37.6	36.7	34.1	54.7	57.9	44.9	44.3
00Z Jan 27th 1970	17.5	17.7	35.7	36.5	26.0	26.2	36.4	34.1	38.4	38.4	37.3	35.9
00Z Jan 28th 1970	42.9	41.1	54.4	52.2	48.2	46.1	48.2	45.8	43.0	42.7	45.5	44.2
00Z Mar 3rd 1970	48.9	45.0	46.6	44.4	47.6	44.7	65.4	62.2	47.1	47.5	54.5	53.5
00Z Mar 26th 1970	13.1	13.5	39.8	39.8	27.9	28.3	19.2	20.0	37.1	37.9	29.6	30.6
Mean	40.7	40.2	46.1	46.3	44.3	44.1	49.0	49.0	47.7	49.1	48.9	49.5

Table 62 : Threat Scores for 12-36 hours for a threshold of 0.01 inches for the series of test cases integrated in the parallel model experiments. Separate results are given for all received Canadian stations, all received U.S. stations, and all received North American stations.

Case	PARALLEL MODEL						1968 MODEL					
	CANADA		U.S.		N.A.		CANADA		U.S.		N.A.	
	Large	Total	Large	Total	Large	Total	Large	Total	Large	Total	Large	Total
12Z Jan 29th 1969	55.7	55.7	57.0	56.6	56.4	56.2	41.9	41.0	46.3	44.2	44.3	42.8
00Z Jul 26th 1969	21.2	27.0	13.9	28.7	17.5	27.9	40.4	53.5	26.6	47.6	33.0	50.0
12Z Sep 9th 1969	31.1	31.5	17.1	17.1	26.7	26.9	31.5	31.9	22.2	20.4	28.5	27.9
00Z Nov 18th 1969	57.4	57.4	57.9	59.0	57.6	58.1	59.3	61.1	57.3	55.9	58.2	58.4
00Z Dec 21st 1969	44.4	44.4	57.9	57.5	51.8	51.6	63.3	63.0	64.6	63.8	64.0	63.4
12Z Dec 25th 1969	34.7	34.7	31.2	31.5	33.0	33.2	44.0	44.0	42.6	42.7	43.3	43.3
00Z Jan 25th 1970	30.5	32.0	43.9	47.2	37.3	39.8	34.2	33.3	46.1	57.1	39.6	44.3
00Z Jan 27th 1970	28.4	27.8	42.6	42.6	34.2	33.8	41.1	39.8	43.2	43.2	42.0	41.2
00Z Jan 28th 1970	59.7	59.8	63.2	60.8	61.3	60.3	49.2	50.0	63.7	62.5	55.9	56.0
00Z Mar 3rd 1970	49.5	48.1	59.1	57.8	54.6	53.2	51.7	50.6	56.2	52.7	54.1	51.8
00Z Mar 26th 1970	24.0	23.1	57.6	56.5	39.8	38.8	25.2	23.6	46.1	50.0	36.6	38.0
Mean	39.7	40.1	45.6	46.8	42.7	43.6	43.8	44.7	46.8	49.0	45.4	47.0

Table 63 : Threat Scores for 24-48 hours for a threshold of 0.01 inches for the series of test cases integrated in the parallel model experiments. Separate results are given for all received Canadian stations, all received U.S. stations, and all received North American stations.

PARALLEL MODEL

1968 MODEL

Case	0.25		0.50		1.0		0.25		0.50		1.0	
	Large	Total										
12Z Jan 29th 1969	47.4	45.9	21.1	32.6	0.0	5.0	35.6	32.5	30.0	27.0	33.3	10.7
00Z Jul 26th 1969	6.5	18.2	6.7	12.1	0.0	0.0	6.8	23.5	0.0	11.6	0.0	6.7
12Z Sep 9th 1969	41.7	43.5	42.4	40.8	0.0	31.4	42.7	40.8	42.9	35.0	28.0	27.5
00Z Nov 18th 1969	37.9	41.0	19.6	25.5	0.0	11.1	47.6	40.9	32.1	27.8	14.3	22.5
00Z Dec 21st 1969	43.1	50.8	42.1	57.9	33.3	33.3	64.7	62.5	44.4	50.0	23.8	34.6
12Z Dec 25th 1969	42.9	51.7	0.0	29.7	0.0	6.3	59.7	58.1	42.1	58.7	0.0	9.7
00Z Jan 25th 1970	36.4	23.7	33.3	15.4	0.0	0.0	20.0	12.9	0.0	0.0	0.0	0.0
00Z Jan 27th 1970	51.3	51.3	20.0	20.0	0.0	0.0	58.1	55.6	40.7	41.4	0.0	0.0
00Z Jan 28th 1970	14.6	17.2	0.0	4.4	0.0	0.0	20.4	17.4	0.0	3.0	0.0	0.0
00Z Mar 3rd 1970	37.3	33.3	26.7	29.3	0.0	15.4	50.0	38.5	48.6	26.9	10.0	10.4
00Z Mar 26th 1970	11.1	12.6	2.2	5.3	0.0	0.0	11.4	14.4	4.0	6.1	0.0	3.2
Mean	33.7	35.4	19.5	24.8	3.0	9.3	37.9	36.1	25.9	26.1	9.9	11.4

Table 64 : Threat Scores for 00-24 hours for thresholds of 0.25 inches, 0.50 inches, and 1.00 inch for the series of test cases integrated in the parallel model experiments. These results are for all received North American stations.

PARALLEL MODEL

1968 MODEL

Case	0.25		0.50		1.0		0.25		0.50		1.0	
	Large	Total										
12Z Jan 29th 1969	50.0	46.3	22.0	30.8	0.0	8.3	39.5	34.7	24.6	27.9	15.4	10.0
00Z Jul 26th 1969	0.0	3.0	0.0	0.0	0.0	0.0	0.0	13.6	0.0	1.7	0.0	0.0
12Z Sep 9th 1969	34.0	33.9	16.7	25.6	0.0	16.7	35.1	30.4	25.0	26.1	0.0	10.0
00Z Nov 18th 1969	38.2	44.2	15.0	22.7	9.5	9.1	39.6	40.4	29.6	39.0	16.7	30.6
00Z Dec 21st 1969	22.1	24.7	14.0	19.2	0.0	0.0	48.0	48.1	28.3	32.9	0.0	6.1
12Z Dec 25th 1969	15.7	17.7	0.0	0.0	0.0	0.0	48.8	48.3	61.3	60.8	56.1	55.6
00Z Jan 25th 1970	30.0	23.1	25.0	12.1	0.0	0.0	15.1	17.5	0.0	2.0	0.0	0.0
00Z Jan 27th 1970	17.5	17.7	35.7	36.5	26.0	26.2	5.7	5.1	0.0	0.0	0.0	0.0
00Z Jan 28th 1970	36.4	34.5	15.6	25.8	0.0	4.9	34.4	26.0	23.0	19.1	0.0	3.0
00Z Mar 3rd 1970	30.8	30.3	7.4	21.0	0.0	3.3	46.3	43.8	30.0	30.9	0.0	1.9
00Z Mar 26th 1970	18.9	20.2	8.7	8.5	0.0	0.0	21.7	20.4	10.0	12.7	0.0	0.0
Mean	26.7	26.9	14.6	18.4	3.2	6.2	30.4	29.8	21.1	23.0	8.0	10.7

Table 65 : Threat Scores for 12-36 hours for thresholds of 0.25 inches, 0.50 inches, and 1.00 inch for the series of test cases integrated in the parallel model experiments. These results are for all received North American stations.

PARALLEL MODEL

1968 MODEL

Case	0.25		0.50		1.0		0.25		0.50		1.0	
	Large	Total										
12Z Jan 29th 1969	21.7	23.1	0.0	0.0	0.0	0.0	16.1	16.9	5.5	5.5	0.0	0.0
00Z Jul 26th 1969	0.0	0.0	0.0	0.0	0.0	0.0	0.0	10.8	0.0	0.0	0.0	0.0
12Z Sep 9th 1969	13.0	9.1	14.3	6.3	0.0	0.0	3.3	3.9	0.0	4.2	0.0	0.0
00Z Nov 18th 1969	19.6	21.2	8.7	8.7	9.1	8.8	47.6	45.4	23.1	24.7	9.1	20.5
00Z Dec 21st 1969	14.1	14.0	13.0	11.9	0.0	10.3	32.4	30.5	10.0	13.6	0.0	7.3
12Z Dec 25th 1969	22.8	22.4	0.0	0.0	0.0	0.0	28.3	27.3	23.1	16.7	0.0	0.0
00Z Jan 25th 1970	22.0	15.5	28.0	22.6	17.7	16.7	16.0	11.9	35.3	12.2	0.0	0.0
00Z Jan 27th 1970	13.2	13.2	0.0	0.0	0.0	0.0	0.0	0.0	0.0	0.0	0.0	0.0
00Z Jan 28th 1970	20.8	22.1	7.8	11.8	0.0	2.0	27.8	27.3	11.5	15.5	0.0	2.4
00Z Mar 3rd 1970	29.2	31.4	2.3	19.2	0.0	3.7	27.4	32.4	25.0	26.8	0.0	3.5
00Z Mar 26th 1970	21.4	24.5	6.2	14.6	0.0	0.0	26.9	29.1	16.2	25.0	0.0	0.0
Mean	18.0	17.9	7.3	8.6	2.4	3.8	20.5	21.4	13.6	13.1	0.8	3.1

Table 66 : Threat Scores for 24-48 hours for thresholds of 0.25 inches, 0.50 inches, and 1.0 inch for the series of test cases integrated in the parallel model experiments. These results are for all received North American stations.

	PARALLEL MODEL				TIME PERIOD = 06-12 1968 MODEL			
	TABLE I		TABLE II		TABLE I		TABLE II	
	LARGE	TOTAL	LARGE	TOTAL	LARGE	TOTAL	LARGE	TOTAL
12Z JAN 29TH 1969	33.32	30.21	29.23	23.59	31.91	42.92	26.11	29.95
00Z JUL 26TH 1969	89.00	89.17	83.89	83.20	68.73	69.04	61.81	57.80
12Z SEP 9TH 1969	29.96	27.93	28.73	26.21	32.79	35.22	27.45	28.64
00Z NOV 18TH 1969	49.59	54.79	43.74	46.29	42.99	47.66	32.69	32.95
00Z DEC 21ST 1969	31.63	32.94	29.41	29.50	34.07	35.93	26.33	26.96
12Z DEC 25TH 1969	46.91	50.00	36.44	34.76	46.91	49.78	30.80	30.91
00Z JAN 25TH 1970	99.14	92.09	76.62	67.85	106.42	104.36	75.01	66.93
00Z JAN 27TH 1970	75.02	106.23	71.90	84.36	56.26	111.98	46.85	68.52
00Z JAN 28TH 1970	95.75	115.39	76.12	84.00	91.21	146.70	52.31	79.23
00Z MAR 3RD 1970	48.81	56.92	42.77	46.47	44.84	53.09	37.38	37.08
00Z MAR 26TH 1970	69.50	69.87	61.37	61.55	64.97	57.76	53.42	45.93
MEAN	60.78	65.96	52.75	53.44	56.46	68.59	42.74	45.90

Table 67: Table I and Table II Skill Factors for 06-12 hours for the series of test cases integrated in the parallel model experiments. Separate Skill Factors are listed for the large scale and total precipitation forecasts.

	PARALLEL MODEL				TIME PERIOD = 18-24		1968 MODEL			
	TABLE I		TABLE II		TABLE I		TABLE II			
	LARGE	TOTAL	LARGE	TOTAL	LARGE	TOTAL	LARGE	TOTAL		
12Z JAN 29TH 1969	50.14	56.61	41.81	45.03	69.68	71.70	53.45	53.22		
00Z JUL 26TH 1969	81.28	86.65	78.06	79.79	68.88	65.10	63.28	53.93		
12Z SEP 9TH 1969	67.19	69.73	54.02	55.29	78.02	81.13	63.46	64.98		
00Z NOV 18TH 1969	51.95	52.74	43.13	43.57	56.95	58.87	42.90	41.87		
00Z DEC 21ST 1969	46.98	48.43	42.71	43.43	32.07	33.98	25.41	26.35		
12Z DEC 25TH 1969	62.85	57.76	59.05	54.01	47.27	48.33	37.61	38.16		
00Z JAN 25TH 1970	87.20	85.74	71.71	68.09	93.92	101.69	72.34	73.29		
00Z JAN 27TH 1970	62.86	68.57	60.00	62.86	70.23	78.80	55.14	58.00		
00Z JAN 28TH 1970	70.90	63.41	54.23	43.79	84.57	110.95	55.36	66.42		
00Z MAR 3RD 1970	62.37	74.34	47.67	52.20	63.34	78.39	43.71	50.79		
00Z MAR 26TH 1970	63.42	65.80	58.77	58.40	60.53	57.82	53.83	48.02		
MEAN	64.28	66.34	55.56	55.13	65.95	71.52	51.50	52.28		

Table 68: Table I and Table II Skill Factors for 18-24 hours for the series of test cases integrated in the parallel model experiments. Separate Skill Factors are listed for the large scale and total precipitation forecasts.

	PARALLEL MODEL		MODEL		TIME PERIOD = 30-36		MODEL	
	TABLE I		TABLE II		TABLE I		TABLE II	
	LARGE	TOTAL	LARGE	TOTAL	LARGE	TOTAL	LARGE	TOTAL
12Z JAN 29TH 1969	80.33	80.18	60.32	59.12	79.62	84.38	61.94	64.30
00Z JUL 26TH 1969	92.59	98.55	87.62	90.62	91.32	81.24	82.08	67.17
12Z SEP 9TH 1969	75.61	76.89	66.76	67.40	70.90	81.08	59.95	64.44
00Z NOV 18TH 1969	45.23	43.07	40.66	38.38	45.45	46.64	34.91	35.52
00Z DEC 21ST 1969	71.64	71.64	66.47	66.47	56.27	63.50	43.91	47.10
12Z DEC 25TH 1969	80.97	78.18	76.76	73.92	85.23	88.01	67.03	68.40
00Z JAN 25TH 1970	70.46	74.12	67.83	69.64	75.26	75.41	65.67	63.71
00Z JAN 27TH 1970	80.06	84.00	76.12	78.09	87.57	95.45	60.27	64.22
00Z JAN 28TH 1970	48.53	52.73	37.51	39.58	64.38	86.23	43.74	54.66
00Z MAR 3RD 1970	91.01	92.02	65.89	65.78	68.65	82.81	49.60	56.68
00Z MAR 26TH 1970	99.80	98.15	85.05	82.95	90.25	100.00	71.75	76.65
MEAN	76.02	77.23	66.45	66.54	74.08	80.43	58.26	60.26

Table 69: Table I and Table II Skill Factors for 30-36 hours for the series of test cases integrated in the parallel model experiments. Separate Skill Factors are listed for the large scale and total precipitation forecasts.

	PARALLEL MODEL				TIME PERIOD = 42-48 1968 MODEL			
	TABLE I		TABLE II		TABLE I		TABLE II	
	LARGE	TOTAL	LARGE	TOTAL	LARGE	TOTAL	LARGE	TOTAL
12Z JAN 29TH 1969	99.76	99.76	79.49	78.15	127.63	133.56	95.08	97.99
00Z JUL 26TH 1969	112.63	109.15	104.22	96.69	97.72	67.91	90.35	49.23
12Z SEP 9TH 1969	88.50	88.50	81.18	81.18	106.62	110.87	92.13	94.22
00Z NOV 18TH 1969	89.69	90.32	81.92	82.23	78.72	80.63	61.42	62.40
00Z DEC 21ST 1969	65.01	65.67	63.49	63.84	60.87	63.42	49.83	51.10
12Z DEC 25TH 1969	82.50	82.50	76.45	76.45	81.26	77.69	73.72	70.20
00Z JAN 25TH 1970	58.99	58.99	55.56	55.56	83.36	86.49	68.39	69.98
00Z JAN 27TH 1970	71.41	71.64	68.07	68.18	100.00	100.00	71.92	71.92
00Z JAN 28TH 1970	65.93	65.75	53.21	52.01	79.12	85.71	53.66	53.66
00Z MAR 3RD 1970	81.08	81.25	67.12	67.20	93.99	97.55	76.98	78.29
00Z MAR 26TH 1970	117.39	119.99	95.35	96.62	132.78	135.33	105.37	106.64
MEAN	84.81	84.87	75.10	74.37	94.73	94.47	76.26	73.24

Table 70: Table I and Table II Skill Factors for 42-48 hours for the series of test cases integrated in the parallel model experiments. Separate Skill Factors are listed for the large scale and total precipitation forecasts.

	PARALLEL MODEL				TIME PERIOD = 00-24 1968 MODEL			
	TABLE I		TABLE II		TABLE I		TABLE II	
	LARGE	TOTAL	LARGE	TOTAL	LARGE	TOTAL	LARGE	TOTAL
12Z JAN 29TH 1969	31.33	30.59	28.23	26.31	32.91	33.23	24.94	23.21
00Z JUL 26TH 1969	70.27	60.06	68.47	58.27	50.74	40.43	48.20	35.27
12Z SEP 9TH 1969	48.45	49.54	45.67	45.85	43.98	45.21	41.34	41.06
00Z NOV 18TH 1969	39.66	42.50	34.56	35.40	32.88	33.22	24.34	21.42
00Z DEC 21ST 1969	31.35	28.00	28.28	24.81	42.69	33.32	23.59	24.66
12Z DEC 25TH 1969	57.64	55.39	49.54	44.61	34.73	35.77	28.07	26.44
00Z JAN 25TH 1970	52.97	67.09	47.16	52.53	56.05	73.14	46.55	48.29
00Z JAN 27TH 1970	62.98	79.26	54.56	61.53	56.00	85.26	42.47	51.95
00Z JAN 28TH 1970	58.81	74.16	51.41	55.09	57.83	90.81	40.92	56.42
00Z MAR 3RD 1970	49.22	53.85	43.87	43.30	30.04	37.07	27.04	26.19
00Z MAR 26TH 1970	54.94	59.01	50.61	51.18	40.13	45.06	35.79	36.06
MEAN	50.69	54.50	45.67	45.35	43.45	50.23	34.84	35.54

Table 71: Table I and Table II Skill Factors for 00-24 hours for the series of test cases integrated in the parallel model experiments. Separate Skill Factors are listed for the large scale and total precipitation forecasts.

	PARALLEL MODEL				TIME PERIOD = 12-36 1968 MODEL			
	TABLE I		TABLE II		TABLE I		TABLE II	
	LARGE	TOTAL	LARGE	TOTAL	LARGE	TOTAL	LARGE	TOTAL
12Z JAN 29TH 1969	37.97	40.47	32.28	33.27	49.16	51.47	40.39	41.48
00Z JUL 26TH 1969	82.24	81.27	79.37	77.60	68.07	47.62	63.85	41.13
12Z SEP 9TH 1969	56.52	59.57	54.50	56.03	60.55	64.15	56.19	57.98
00Z NOV 18TH 1969	49.63	48.72	42.59	39.51	48.55	46.93	34.78	31.79
00Z DEC 21ST 1969	46.35	46.35	43.86	43.61	33.66	32.02	30.67	28.51
12Z DEC 25TH 1969	62.74	65.73	60.52	62.02	52.59	54.59	47.10	47.35
00Z JAN 25TH 1970	72.59	73.74	67.03	66.85	58.80	67.97	51.73	54.01
00Z JAN 27TH 1970	70.49	72.14	68.05	68.84	55.88	56.55	46.78	45.48
00Z JAN 28TH 1970	41.42	45.69	36.01	36.41	57.14	80.78	38.88	49.74
00Z MAR 3RD 1970	47.14	56.33	38.65	42.53	35.06	45.11	28.97	33.27
00Z MAR 26TH 1970	68.00	73.29	62.27	64.62	51.93	57.25	44.09	46.43
MEAN	57.74	60.30	53.19	53.75	51.94	54.95	43.95	43.38

Table 72: Table I and Table II Skill Factors for 12-36 hours for the series of test cases integrated in the parallel model experiments. Separate Skill Factors are listed for the large scale and total precipitation forecasts.

	PARALLEL MODEL		MODEL		TIME PERIOD = 24-48		MODEL	
	TABLE I		TABLE II		TABLE I		TABLE II	
	LARGE	TOTAL	LARGE	TOTAL	LARGE	TOTAL	LARGE	TOTAL
12Z JAN 29TH 1969	59.50	60.18	47.51	45.72	70.15	73.38	57.81	59.45
00Z JUL 26TH 1969	97.26	91.40	91.73	85.24	70.59	55.07	65.76	45.42
12Z SEP 9TH 1969	83.92	85.55	79.48	80.29	77.71	81.99	71.10	72.86
00Z NOV 18TH 1969	57.81	55.77	53.19	51.09	47.25	48.20	40.15	40.63
00Z DEC 21ST 1969	54.79	54.79	53.78	53.78	33.83	37.01	31.34	32.93
12Z DEC 25TH 1969	67.90	67.90	66.79	66.79	51.99	55.18	47.70	49.27
00Z JAN 25TH 1970	62.29	63.76	58.91	59.65	60.05	64.16	53.02	54.28
00Z JAN 27TH 1970	57.67	59.65	56.84	57.83	46.01	51.98	35.98	38.98
00Z JAN 28TH 1970	37.05	39.53	30.99	31.89	52.34	63.50	38.64	41.18
00Z MAR 3RD 1970	64.14	69.51	54.33	56.32	60.73	65.26	52.90	53.99
00Z MAR 26TH 1970	72.37	73.77	65.27	65.60	81.03	85.03	64.73	66.73
MEAN	64.97	65.62	59.89	59.47	59.24	61.89	50.83	50.52

Table 73: Table I and Table II Skill Factors for 24-48 hours for the series of test cases integrated in the parallel model experiments. Separate Skill Factors are listed for the large scale and total precipitation forecasts.

35. Discussion

35.1 The case of 12Z Jan 29th 1969

500 mb Analyses (Fig. 35): A major trough over Nevada at initial time moved rapidly across the continent to south-eastern Hudson Bay by 48 hours later. A second trough approaching the West Coast at initial time had moved to Utah by verifying time. A trough originally over Hudson Bay moved to the southern tip of Greenland. A cold low over Keewatin at initial time had moved to the Davis Straits by 12Z Jan 31st. There were two slow-moving cold lows over western Canada. The low in the Atlantic off Nova Scotia drifted south-eastwards during the period. The sock-like appendage protruding southwards from the Atlantic low is an unreal feature generated by the objective analysis scheme. The prognostic chart which formed the first guess field for the analysis moved the whole Atlantic trough too slowly, so that it lay significantly west of its true position. In the northern part there was sufficient data for the analysis to adjust the trough over to its correct position, but in the southern part where there was no data the trough retained its first guess position. The new trough over the West Coast at verifying time originated from the Aleutians, though the analysis did not really catch it till twelve hours after initial time.

200 mb Analyses (Fig. 36): The principal features are similar to those at 500 mb, except for slight phase displacements. Over the Atlantic, as at 500 mb, the initial time analysis still retains the first-guess field position in the southern no data areas, but catches the true position in the northern portion where there are some reports. Over the northern portions of the chart, where the 200 mb is deep in the stratosphere, it

is more difficult to relate the features to those at 500 mb.

850 mb Analyses (Fig. 33): The situation was more complex at 850 mb. Two lows could be resolved over Wyoming and Utah at initial time. The southernmost of these tracked across the Great Lakes to just west of the Gaspé peninsula by 48 hours. The low from northern Wyoming moved to south-eastern Hudson Bay by 48 hours, where it merged with a third low which originated in Alberta. The low off the West Coast at initial time moved to North Dakota by verifying time. The Atlantic low, like its 500 mb counterpart, drifted southeastwards during the period; it was scarcely discernible at initial time, but deepened by 13 dkm in the first 24 hours, presumably the result of ocean heating under the cold low at 500 mb. At verifying time a 150 dkm low centre shows up off the coast of Lower California.

700 mb Analyses (Fig. 34): The situation is intermediate between 850 mb and 500 mb.

500 mb Forecasts (Fig. 35): The parallel model caught the depth of the Hudson Bay low much more accurately than the 1968 model. It placed a 522 dkm low just west of James Bay, whereas the 1968 model merely carried a very weak trough slightly farther west; the actual low centre was 504 dkm over south-western Hudson Bay. The parallel model deepened the toe of the sock feature in the Atlantic and moved it out of display area; the 1968 model just smoothed it out with time. Neither model predicted anything off the West Coast at 48 hours, presumably because nothing was present in the initial analysis. In the south-western U.S. the parallel model did a better job of identifying the two currents evident on the verifying chart. The parallel model failed to predict the eastward

progression of the Keewatin low, but it handled the two slow moving lows in western Canada not too badly. The 1968 model moved the Keewatin low reasonably well, but lost one of the low centres in western Canada.

200 mb Forecasts (Fig. 36): The Hudson Bay trough was predicted to lie 450 nautical miles west of its actual position in the parallel model, but 600 nautical miles too far east in the 1968 model. The trough in the south-western U.S. was predicted dead on target by the parallel model, but 600 nautical miles too far east in the 1968 model. The northern part of the Atlantic trough was moved 150 nautical miles too far east by the parallel model, but 430 nautical miles too far east by the 1968 model.

850 mb Forecasts (Fig. 33): The parallel model predicted the merging of the Wyoming and Alberta lows, but 12 hours sooner than it actually happened; the final depth was 120 dkm, very close to the actual depth of 118 dkm, but the final position was 250 nautical miles too far south-west. The 1968 model did not catch the merger of these two lows, and predicted a final depth of 136 dkm and a final position 450 nautical miles too far southwest. The parallel model almost caught the position of the low that ended up in North Dakota, but failed to catch its amplitude. The 1968 model failed to catch either position or amplitude. In the Atlantic the circulation around the spurious development from the sock-like feature in the initial 500 mb analysis shows up at the edge of the parallel model chart; this development was greatly accentuated by latent heat effects. The parallel model caught the Pacific development with almost perfect positioning, but the 132 dkm low off Lower California is 18 dkm too deep. This is partly an analysis problem, but it is also another example of the over-effectiveness

of the release of latent heat in warm air. Both models failed to catch the West Coast low which originated in the Aleutians, again probably because of an analysis problem. However, the parallel model did catch a weak trough slightly out to sea, whereas the 1968 did not really show any such feature.

700 mb Forecasts (Fig. 34): The situation is intermediate between the 850 mb and 500 mb. In the parallel model there is some inconsistency between the depths of the Hudson Bay low at 850 and 700 mb.

Precipitation 00-24 hours (Fig. 37): The 0.25 and 0.50 inch precipitation areas in the central U.S. and on the West Coast look more realistic in the forecasts of the parallel model than those of the 1968 model. However, the 1968 model does a shade better with the 0.01 inch line on the map as a whole. Consequently, there is not much difference in the two sets of verification scores.

Precipitation 24-48 hours (Fig. 38): The forecasts of the parallel model are clearly much better than those of the 1968 model, except in the SW corner of the U.S. where too much rain moved in from the excessive development in the Pacific. This superiority reflects in the verification scores.

35.2 The case of 00Z Jul 26th 1970

No charts are shown for this case. An old low south of Hudson Bay at initial time moved to northern Quebec by 48 hours later. A baroclinic wave over western Canada at initial time swung down quite rapidly to the Great Lakes by verifying time. The parallel model handled this development quite poorly because the seasonal variations in the control coefficients

led to too weak a linkage between the levels in summer. The 1968 model did only slightly better. This was one of the few summer cases in which something interesting happened over the continent. So in a sense it was a mistake to pick it as a test case. On the other hand, it served to demonstrate that the control coefficients must be strong enough to allow developments to occur in summer. Note that this is the only case for which both the threat score and the skill factor evaluations indicate the total precipitation forecasts are much better than those of the large scale precipitation. So in this respect, at least, the test case was a typical summer one.

35.3 The case of 12Z Sep 9th 1969

No charts are shown for this case. At initial time the main 500 mb trough was over the Great Lakes, and a secondary low centre had just appeared at 850 mb off Cape Hatteras. The secondary low deepened strongly and moved up to Labrador by 48 hours. Neither model caught the secondary development and so both sets of forecasts were quite poor. Presumably, there was some critical linkage between ocean heating and latent heat effects near initial time, and the parallel model failed to simulate this linkage.

35.4 The case of 00Z Nov. 18th 1969

500 mb Analyses (Fig. 40): A major trough over Wyoming at initial time moved to Michigan by 48 hours later. Meanwhile a major cold low was drifting southwestwards over the Arctic islands and slowly filling. A second cold low over Great Bear Lake at initial time got caught up in the flow and plunged rapidly down to Lake Superior by verifying time. The low over the Pacific had an erratic history as it moved through the no data areas.

850 mb Analyses (Fig. 39): A 139 dkm low over Minnesota at initial time moved northeastwards and deepened rapidly to end up as a 118 dkm low over James Bay 48 hours later. The cold low over the Arctic islands drifted south-eastwards with its 500 mb counterpart and filled. The second cold was barely discernible over Great Bear Lake at initial time, but can be tracked on later charts to appear as a well-defined trough south of Lake Superior at verifying time. There appeared to be two lows in the Pacific and each had a separate history; however, there was no consistency about which was dominant.

500 mb Forecasts (Fig. 40): The parallel model moved the major Great Lakes trough too fast so that by 48 hours it was 250 nautical miles east of its actual position; the 1968 model moved the same feature too slow so that by 48 hours it was 150 nautical miles west of its actual position. Both models predicted the major cold low over the Arctic islands to drift slowly eastward, i. e. almost opposite to the true direction, and fill. Neither model handled the Great Bear Lake cold low very well, as neither caught the rapid plunge south-eastwards. However, the parallel model retained the feature as a separate entity, whereas the 1968 merged it with the Great Lakes trough. Both models handled the Pacific low more realistically than the analyses, but did not agree with each other too well. Coincidentally, the verifying position is mid-way between the two forecast positions.

850 mb Forecasts (Fig.39): The parallel model gave a very accurate prediction of both the position and depth of the James Bay low centre. The 1968 model only predicted a broad trough over Hudson Bay. As far as

the other features of interest are concerned, the inadequacies of the 500 mb forecast are reflected at 850 mb.

Precipitation 00-24 hours (Fig. 41): Both forecasts were quite good. The parallel model gave a better structure for the main precipitation area southward from the Great Lakes, but failed to link the two precipitation areas together over Alberta.

Precipitation 24-48 hours (Fig. 42): Both forecasts were reasonably good. However, in this case it was the 1968 model which gave a better structure to the main precipitation area, though this was marred slightly by the gross over-forecasting over Texas. The parallel model again failed over Alberta. Both models extended the precipitation area much too far south over the West Coast.

35.5 The case of 00Z Dec 21st 1969

500 mb Analyses (Fig. 45): A cold low drifted south-eastwards over James Bay during the period. A second cold low was quasi-stationary over northern Baffin Island. A series of short wave troughs were moving in the main flow across the continent. One moved in rapidly from the Pacific to end up over Kansas at verifying time. A second started out over Kansas and moved to the East Coast. A third originated off the East Coast and swung round to south of Greenland. A fourth from well out in the Pacific ended up off the West Coast; this appeared to be partially associated with a low with an erratic history.

200 mb Analyses (Fig. 46): A stationary trough over Ungava was well in the stratosphere. Further south, over the U.S., short wave troughs moved along in appropriate phase relationships with their counterparts at 500 mb.

550 mb Analyses (Fig. 43): The low off the West Coast at initial time tracked rapidly east-southeastwards to Kansas City by verifying time. The low over Oklahoma at initial time moved to Cape Cod by 48 hours, and deepened from 139 dkm to 120 dkm as it went. There was no evidence whatsoever of a secondary development. The low in the Gulf of the St. Lawrence at initial time moved to a position southeast of Greenland. There was no evidence of a splitting into two centres. By 48 hours a new low had arrived west of Vancouver Island, but its history was a complete mix-up which did not make any sense at all.

700 mb Analyses (Fig. 44): The situation is intermediate between 850 and 500 mb.

500 mb Forecasts (Fig. 45): Both models handled the cold lows in about the same way. The depths were predicted about 12 dkm too high, and the James Bay low was moved eastward rather than south-eastward. The trough which actually ended up over Kansas was predicted by the parallel model to be 300 nautical miles too far west, and by the 1968 model to be 400 nautical miles too far west. The trough which actually ended up over the East Coast was predicted by the parallel model to be 50 nautical miles too far west, and by the 1968 model to be 350 nautical miles too far west. The displacement of the Greenland trough was predicted better by the 1968 model, but the depth better by the parallel model. Neither model caught the second Pacific trough.

200mb Forecasts (Fig. 46): The stratospheric region around Ungava was handled slightly better by the parallel model. The Kansas trough was predicted 300 nautical miles west of its true position by the parallel model, and 1000 nautical miles too far east by the 1968 model. The East Coast trough was predicted 100 nautical miles west of its true position by the parallel model,

and 550 nautical miles too far east by the 1968 model. The Greenland trough was predicted 200 nautical miles west of its true position by the parallel model, but 800 nautical miles east by the 1968 model.

850 mb Forecasts (Fig. 43): The 1968 model did not do very well with this case. The Kansas City and Cape Cod lows were predicted to be weak broad troughs which had depths 15 to 20 dkm too high and locations 200 nautical miles too far west. The 1968 model is incapable of predicting a secondary development. The low from the Gulf of the St. Lawrence was predicted to track the wrong side of Greenland, though there was slight evidence of a splitting. The Vancouver Island low was missed altogether. The parallel model went sadly astray in different ways. The really devastating thing that happened was in association with the Cape Cod low. A secondary development took place south of Cape Hatteras at 24 hours and by 48 hours this new low had taken over as the main centre off the East Coast. This was precisely the type of thing which the author had previously tried to simulate in about half-a-dozen experiments with the Sept. 9th case, but without success. The reason for the secondary development was that a very weak trough in the initial analysis was amplified strongly by latent heat feedback. This is another good example of the over-sensitiveness of the parallel model to the release of latent heat in very warm air. The Kansas City low was handled quite well; the parallel model managed a 130 dkm centre, a mere 4 dkm too high, and placed it about 200 nautical miles northwest of Kansas City. The low from the Gulf of the St. Lawrence undeniably split into two as it approached the tip of Greenland at 36 hours, and one low went either side. Again this is the type of thing that sometimes happens in the real atmosphere but rarely in a model, so it was rather

disappointing to have it happen in the model but not in the atmosphere. The Vancouver Island low was also missed altogether by the parallel model.

700 mb Forecasts (Fig. 44): Again the situation is intermediate between 850 and 500 mb. The secondary development shows up at 700 mb as well as at 850 mb.

Precipitation 00-24 hours (Fig. 47): At first glance the main difference between the two forecasts is in the area centred on the state of Mississippi where the 1968 model produced a better forecast of the heavier precipitation areas. No precipitation was predicted for Florida, so the secondary development did not begin till the very weak trough over Florida at 12 hours had moved out to sea. The parallel model forecast fared slightly better with both kinds of verification scores.

Precipitation 24-48 hours (Fig. 48): Here the East Coast area is a disaster for the parallel model because of the secondary development. The excessive eddy diffusion coefficients in the vertical motion computations of the parallel model made the predicted precipitation area too small over Kansas, though the centre was nicely on target. The 1968 model correctly predicted very light precipitation for Alberta and Saskatchewan, but the parallel model failed to do so.

35.6 The case of 127 Dec 25th 1969

500 mb Analyses (Fig. 51): A low northwest of Lake Superior at initial time dipped down to New Jersey by verifying time. A low off the West Coast at initial time was just leaving Wyoming at 48 hours; it was closely followed by a secondary trough about 300 nautical miles upstream. A trough over the Gulf of St. Lawrence at initial time moved to the southeast of Greenland.

A cold low remained quasi-stationary over northern Baffin Island.

200 mb Analyses (Fig. 52): There are three troughs in the main flow which progress eastwards in step with their counterparts at 500 mb. The West Coast trough also has a double structure at 200 mb. The growth in amplitude of the main troughs over the continent makes a startling change from zonal to meridional flow during the period.

850 mb Analyses (Fig. 49): Lows from northwest of Lake Superior and Arkansas at initial time merged together at 36 hours to produce a deep low over Cape Cod at 48 hours. Or perhaps it would be more correct to say that a baroclinic development on the southern low swamped its northern companion, which was essentially in phase with the low at 500 mb and therefore a cold low. A low off the West Coast at initial time moved to North Dakota by 48 hours. And a new low had appeared during the period and ended up over northern Texas. A low south of Newfoundland at initial time moved to southeast of Greenland and deepened as it went.

700 mb Analyses (Fig. 50): The situation was intermediate between 850 and 500 mb.

500 mb Forecasts (Fig. 51): The parallel model moved the low from Lake Superior off in the wrong direction so that it ended up over northern Quebec instead on New Jersey. Nevertheless, it carried a well-defined trough to just off the East Coast. This would have been a reasonable forecast if it had been on position; unfortunately, it was not, it was 300 nautical miles too far east. The 1968 model lost the original low quite rapidly, but predicted the final trough position dead on target over New Jersey. Neither model performs too badly with the West Coast troughs, though both lose much of the detail. In the parallel model the stationary

low over Northern Baffin Island gets smoothed too heavily by the special low tropopause eddy diffusion. The parallel model fares best with the Greenland trough.

200 mb Forecasts (Fig. 52): The parallel model moves the New Jersey trough 150 miles too far east, and fails to catch the increase in amplitude. The 1968 model moves the same feature 1200 miles too far east. The parallel model retains the double structure of the West Coast trough throughout the forecast period, though it has almost disappeared by 48 hours, and predicts each of them to be about 100 miles too far east at verifying time. The 1968 model unaccountably separates the two West Coast troughs. The leading one is predicted nearly 2000 nautical miles too far east; and the following one is predicted 400 nautical miles too far east. The parallel model predicts the Greenland trough about 150 nautical miles west of its true position, the 1968 model predicts it 550 nautical miles too far east.

1000 mb Forecasts (Fig. 49): The parallel model pictured a reasonably accurate sequence of events over the eastern part of the continent. The low moved but 12 hours sooner than in the real atmosphere, and ended up as a respectable 126 dkm low over Nova Scotia. The trouble was that it was predicted 350 miles northeast of its real position, and the depth was predicted 12 dkm too high. The 1968 model only managed a broad flat trough, but it was predicted on the target. The parallel model also fared poorly with the West Coast low; it was only able to resolve a trough by 24 hours, and this was moved 400 nautical miles too far east by 48 hours. The 1968 model did a bit better with this feature. The parallel model predicted a better position for the Greenland low, but the 1968 model predicted a better depth.

700 mb Forecasts (Fig. 50): Again the situation was intermediate between 850 and 500 mb.

Precipitation 00-24 hours (Fig. 53): This was the beginning of the famous Christmas storm which dumped two feet of snow on Montreal before it had finished. The 1968 model does very well indeed because this is the extreme type of situation when consistent over-forecasting pays off handsomely, as it did during the original development work which dealt mostly with extreme cases. Nevertheless, the parallel model forecast is a pretty good one too. On the West Coast the parallel model catches the detailed patterns much better than the 1968 model, but loses out on the positioning of the 0.01 inch line.

Precipitation 24-48 hours (Fig. 54): Neither model predicted the northern penetration of the 0.5 inch line well into Quebec, and it is actually quite difficult to decide which forecast was the better. The parallel model failed especially with the light precipitation over the western U.S.; this was probably because of the excessive eddy diffusion coefficient in the vertical motion computations.

3500 The case of 00Z Jan 25th 1970

500 mb Lines (Fig. 56): A major cold low was drifting very slowly southwards just north of Hudson Bay. Two short wave troughs were moving rapidly across the continent during the period, a third was just moving out of the Maritimes at initial time, and a fourth was moving up on the West Coast at 48 hours.

850 mb Analyses (Fig. 55): The same cold low as at 500 mb showed up just north of Hudson Bay, but it did not appear as intense as at the upper level

because the air was extremely cold. The same four short wave troughs appeared at 850 mb as at 500 mb. The one which started out off the East Coast at initial time first deepened and moved rapidly north-eastwards, then the low centre occluded out and became more slow moving. The low off the West Coast at verifying time had an irregular history.

500 mb Forecasts (Fig. 56): The parallel model handled the major cold low and the four short wave troughs slightly better than the 1968 model. In particular, the amplitudes of the two short waves crossing the continent are still clearly evident in the 48-hour forecasts of the parallel model, whereas it takes a good deal of imagination to locate them on those of the 1968 model. This is one of the cases where the parallel model prediction of the cold low suffers from the extra eddy diffusion effects inserted with a low tropopause.

850 mb Forecasts (Fig. 55): The parallel model handled the low which ended up over Nova Scotia significantly better than the 1968 model. The parallel model was a shade too fast with the trough that ended up over Lake Superior, but the 1968 model had worse troubles with the same feature because it was outstripped by the 500 mb trough and just about lost its amplitude in the process. Surprisingly, the parallel model scores very well with the low off the West Coast at verifying time. This low had a well-defined history in the parallel model, but appeared almost out of nowhere in the objective analyses.

Precipitation 00-24 hours (Fig. 57): It is interesting to see that the Objective Analysis fails to resolve two separate lines of precipitation over the Prairies, except north of Lake Superior. Both models predicted very light snow south of the huge cold low which dominates the map, but

none appears to have been reported in this area. Both models predicted too much precipitation south of the Great Lakes, though a 0.23 value was reported. On the whole the parallel model forecast looks a bit more realistic than the one from the 1968 model, but there is not much to choose between them.

Precipitation 24-48 hours (Fig. 58): This was not a very successful case. Both models predicted a moderately intense maximum to the south-east of the Great Lakes, an area in which no precipitation was actually reported, although amounts in the vicinity of 0.50 were reported just to the north and just to the south. The actual precipitation over the southeastern U.S. was largely frontal and probably would have been caught by both models if it had occurred in the first 24-hour period. In spite of the vastly superior height forecast by the parallel model off the West Coast, the 1968 model produced a better precipitation forecast in that region.

35.8 The case of 00Z Jan 27th 1970

500 mb Analyses (Fig. 61): The flow was dominated by an intense cold vortex which drifted from west to east of Southampton Island during the period, filling from 456 to 466 dkm as it went. Of particular interest is the short wave off the West Coast at initial time. This moved to South Dakota by 00Z Jan 29th.

200 mb Analyses (Fig. 62): The Southampton Island vortex was much less intense because it was in the stratosphere. At initial time the West Coast trough was only 50 miles west of its 500 mb counterpart, but by 48 hours later the spacing was 280 miles. While the phasing of the initial time analyses might have been dubious, because the short wave

was over the ocean, the phasings of the later charts should be accurate enough and these confirm a gradual increase in the spacing.

850 mb Analyses (Fig. 59): The Southampton Island vortex was much less intense because the air was extremely cold. A well-defined low centre tracked from the West Coast at initial time to the Great Lakes by 48 hours later.

700 mb Analyses (Fig. 60): The situation was intermediate between 500 and 850 mb.

500 mb Forecasts (Fig. 61): Both models filled the cold vortex over Southampton Island to 476 dkm, but the 1968 model was dead on the target with the final position whereas the parallel model was slightly off. Once again with this intense cold low in the Arctic the low tropopause eddy diffusion hurts the parallel model forecast badly. However, the parallel model had the correct positioning for the trough leading off to Alaska, whereas the 1968 model moved it too far south. At 48 hours the parallel model predicted the short wave trough to be 150 miles east of its actual position, whereas the 1968 model had it 300 miles west. However, the 1968 model caught the angle of tilt a little better.

200 mb Forecasts (Fig. 62): At 48 hours the parallel model predicted the short wave trough to be 250 miles east of its actual position, whereas the 1968 model had it 1000 miles east.

850 mb Forecasts (Fig. 59): At 48 hours the parallel model predicted the correct depth, 120 dkm, and almost the correct position for the Great Lakes low. However, the intervening track did not match up quite so well with the objective analyses as the predicted low travelled on a more northerly trajectory. In the 1968 model the low centre loses its identity and

becomes a trough which ends up 300 miles too far west at 48 hours.

700 mb Forecasts (Fig. 60): The situation was intermediate between 850 and 500 mb.

Precipitation 00-24 hours (Fig. 63): The main deficiency of both models was that they predicted very light snow in the circulation around the intense vortex over Southampton Island, and none was actually reported in this region. Elsewhere the forecasts agree quite well with each other and with the analyses. However, the parallel model correctly predicted virtually no snow for the prairie Provinces, whereas the 1968 model covered this area with snow.

Precipitation 24-48 hours (Fig. 64): The two models differ considerably over the Great Lakes. The parallel model has the axis and centres of the precipitation area dead on target, but grossly underforecasts both the amounts and the areas. Once again this happened because of the excessive eddy diffusion coefficient used in the vertical motion computations. The 1968 model predicted the areas quite well, so the verification scores did not suffer too much from the under-advection of the 850 mb trough. The truly fantastic differences between the two forecasts are over the oceans.

35.9 The case of 00Z Jan 28th 1970

500 mb Analyses (Fig. 66): This is the day following the previous case. The situation is much the same, but with the main trough advancing to Michigan by verifying time. A secondary trough becomes resolved during the period and shows up just west of Lake Superior at 48 hours. A new trough appeared out of the Pacific and shows up just off the West Coast at verifying time.

850 mb Analyses (Fig. 65): The main low centre of interest in the previous case continued tracking east-northeastwards to eastern Quebec by verifying time.

500 mb Forecasts (Fig. 66): The parallel model moved the trough of chief interest to western Quebec. At first sight this does not agree that well with the verifying analysis, but a closer inspection shows more resemblance between the flow characteristics. The parallel model forecast places more emphasis on the northern part of the trough, and almost loses the southern part which bends back southwestward. In the analysis the southern part has prominence. The 1968 model moved the same trough to Wisconsin. Neither model caught the secondary trough, obviously because it was not present in the initial analysis. Both models had a slight trough off the West Coast by the end of the period, but that of the parallel model had the greater amplitude.

850 mb Forecasts (Fig. 65): The parallel model handled the Quebec low very well, though it actually deepened it 6 dkm too much. The 1968 model predicted a typical broad trough over James Bay.

Precipitation 00-24 hours (Fig. 67): Both models predicted the maximum precipitation to the south of the Great Lakes instead of to the north. Both models are still having trouble predicting light snow around the old cold low in the Arctic which is no longer active. The 1968 model predicts too much precipitation in the mountain States, and the parallel model predicts too little.

Precipitation 24-48 hours (Fig. 68): Both models predict a large area of precipitation for the eastern part of the continent, and an equally large area shows up in the analysis. Unfortunately, the internal structure

is wrong in both forecasts. Again, the parallel model forecast for the Quebec low suffers because of the excessive diffusion coefficient used in the vertical motion computations. Now a little bit of precipitation shows up in the circulation around the cold low, due to the low level flow intensifying slightly. But this is too late for the parallel model which has finally decided there is no snow in an old low. The 1968 model catches some of it.

35.10 The case of 00Z Mar 3rd 1970

500 mb Analyses (Fig. 70) : A 518 dkm low centre over southwestern Alberta at initial time moved to northern Saskatchewan by verifying time and deepened to 498 dkm. An associated trough over Colorado at initial time swung around to Northern Ontario by 48 hours. A cold low drifted southwestwards over the Beaufort Sea. A second, less intense cold low started out over the Melville Peninsula and moved southeastwards through the Hudson Strait. A Pacific low had moved over San Francisco Bay by the end of the period. There was a slow moving trough over the Gulf of St. Lawrence.

850 mb Analyses (Fig. 69) : At initial time there was a 133 dkm low centre over southern Saskatchewan, and a 126 dkm low centre over Nebraska. By verifying time these two lows had moved so as to become a 120 dkm centre over northern Saskatchewan and a 133 dkm centre south of James Bay.

500 mb Forecasts (Fig. 70) : The parallel model moved the Alberta low in the wrong direction, and it ended up as a 529 centre over southern Manitoba; the associated trough only swung over as far as Minnesota. The 1968 model moved the same low in the right direction, but could not resolve it after 12 hours; the associated trough could not be resolved as a separate entity. So the net result was that both models placed a long trough in the same

position, but the one of the parallel model was slightly deeper. The failure to catch the deepening of the low explains the slow motion of the associated trough. The Beaufort Sea low was filled too much by the low tropopause eddy diffusion in the parallel model. Both models had the linked troughs over Labrador about 100 nautical miles too far west. Neither model could pick up more than a hint of the Pacific low.

850 mb Forecasts (Fig. 69): In the parallel model the two lows in mid-continent merged at 36 hours and became a single 131 dkm centre north of Lake Superior by the end of the period. In the 1968 model both lows virtually disappeared and all that remained at 48 hours was a weak broad trough.

Precipitation 00-24 hours (Fig. 71): The internal structure of the main precipitation area over the middle of the continent was predicted much better by the parallel model. However, the 1968 model did a little better with the placing at the 0.01 inch line over most of the map. This was sufficient to give the 1968 model the edge in the skill factor verifications, though surprisingly not in the 0.01 inch threat scores.

Precipitation 24-48 hours (Fig. 72): Both forecasts are surprisingly good in view of the deficiencies at the height forecasts, but they reflect the under-forecasting of the displacements of the troughs over the Great Lakes. The small precipitation amounts reported over northern Saskatchewan indicate that the deepening of the 500 mb low in this region was not a true dynamic development, but instead simply a cold low passing from high land to low land.

35.11 The case of 00Z March 26th 1970

500 mb Analyses (Fig. 74) : A cold low over Hudson Bay at initial time moved slowly south-southwestwards. A trough over Minnesota at initial time moved to Quebec by 48 hours. A weak trough over British Columbia at initial time moved to New Mexico by verifying time. A low over Labrador at initial time moved northeastwards and filled. A Pacific trough ended up over British Columbia.

850 mb Analyses (Fig. 73) : The interesting feature was a low over Illinois at initial time which moved to central Quebec by 48 hours, deepening from 130 dkm to 120 dkm as it went. A weak trough over Saskatchewan at initial time moved to Wisconsin by verifying time.

500 mb Forecasts (Fig. 74) : The 1968 model caught the sinking of the Hudson Bay low, the parallel model did not. The parallel model had the Quebec trough 350 miles too far west; the 1968 model had it 450 miles too far west. Both models caught the position of the New Mexico trough quite well, but underestimated its amplitude.

850 mb Forecasts (Fig. 73) : The parallel model correctly predicted a low out of the Great Lakes development at 48 hours, but placed it 500 miles too far south. The 1968 model predicted a 130 dkm centre, but that was 400 miles too far southwest.

Precipitation 00-24 hours (Fig. 75) : Neither forecast verified too well because of missed areas of light precipitation, for instance over Ontario and Quebec. However, the 1968 model did a little better than the parallel model.

Precipitation 24-48 hours (Fig. 76) : Again both forecasts were relatively poor.

35.12 Summary

The Threat Scores and Skill Factors of Tables 61-73 are a fair reflection on the comparative merits of the two sets of precipitation scores. On the average the 1968 model forecasts were better, but in some individual cases the parallel forecasts came out on top.

The RMSE verification scores for the height forecasts for three different grids are given in Tables 31-42. These indicate very little difference between the two sets of forecasts at 850, 700 and 500 mb in spite of the much greater detail of the parallel model forecasts. Consequently, the parallel model will give better verification scores when the known weaknesses are eliminated. At 200 mb it is a different story. The parallel model forecasts verify much better than those of the 1968 model.

The RMSE verification scores for the temperature forecasts for three different grids are given in Tables 43-51. On the average they are roughly equal for the two models in spite of the extra detail in the parallel model forecasts. However, other experiments showed significant improvements in the parallel model forecasts if minor forms of the radiation and ocean mixing terms were introduced only in the temperature forecast equation, but not in the vertical motion computations or the baroclinic model. So this is a dilemma which still has to be resolved.

The RMSE verification scores for the dew point depression forecasts for three different grids are given in Tables 52-60. They show that on the average the parallel model forecasts beat their 1968 model counterparts by 0.3 to 0.4 deg C at 500 mb, but that the reverse holds true at 850 and 700 mb. This result probably reflects the changes in the eddy diffusion

coefficients as much as anything else. However, as in the case of the temperature forecasts, other experiments showed significant improvements in the parallel model forecasts if mild forms of the radiation and ocean heating terms were introduced in the forecast equation for dew point depression, but not in the vertical motion computations or the baroclinic model.

Most of the more important aspects of the results, such as the great temperature dependence of the effectiveness of latent heat feedback, are discussed elsewhere in this thesis so they will not be referred to again here. However, it is worth mentioning one or two small points not dealt with in other Sections. First, one gets the impression from these cases that the mountain correction to the threshold dew point depression, as given by (15.9), is too effective with the special mountain field of Fig. 3. In almost all cases a forecast somewhere intermediate between those of the two models would have been better in the inland mountain States. Second, none of the formulations of the terrain constraint manage to cope with the pseudo-deepening of a cold low at 500 mb as it moves off the mountains on to the plains. This is because no temperature dependence is built into the mountain term, and it really has nothing to do with the vertical motion at the ground. Third, one of the most difficult situations for a model to deal with appears to occur when there are two 500 mb cold lows a fair distance apart, but sharing a common circulation. If the dominant low is to the east or northeast, then the secondary low, after a period of slow movement, will suddenly get caught in the strong flow and plunge southwards with dramatic results. This happened in the Nov. 18th case and

the Dec 25th case, and also in some October cases integrated earlier. Fourth, just in case the point has not been emphasized enough already, the quality of the objective analysis leaves much to be desired in the ocean areas of no data; because of this the parallel model gets into difficulties in these regions.

Finally, a few remarks on varying the control coefficients. It was possible to get almost perfect forecasts for the Jan. 29th case by increasing the magnitudes of the control coefficients. The 48-hour CRMSE verification scores for the best integration of this case were 2 dkm lower than those quoted in Tables 313-315. But the values of the control coefficients were then too high for a sinusoidal seasonal variation, and even too high for other January cases. This point will be taken up in the concluding remarks.

PART VI : CONCLUSIONS36. Concluding Remarks

Sequential versions of the precipitation scheme and the baroclinic model have been integrated on a routine basis for the last 2½ years. The resulting precipitation forecasts have been judged highly successful in Canada, because they are the best objective guidance available at the Weather Centrals, and because they are transmitted over the facsimile circuits just over three hours after observation time.

However, the precipitation forecasts are not perfect and they suffer from three kinds of deficiencies. First, they are limited by the resolution of the standard grid. Second, they suffer from a few systematic deficiencies which have been revealed by the long term evaluation program. Third, they are limited, particularly on the second day, by the accuracy of the height forecasts produced by the baroclinic model. There are plans to alleviate the resolution problem by changing over to a finer grid mesh, but no precipitation experiments along these lines have yet been carried out. The systematic deficiencies have only just come to light; steps will be taken to correct them as soon as possible. The experiments on parallel operation were undertaken in an attempt to improve the height forecasts produced by the baroclinic model. Consequently, the main modifications were made to the baroclinic model, although some minor changes were also made in the precipitation scheme.

The parallel model experiments have met with partial success. The main innovations involved the formulation of eddy diffusion, terrain and diabatic constraints, the incorporation of the 700 mb stream function field as a full working level, and the introduction of a seasonal

variation in the control coefficients. The eddy diffusion constraints have worked out particularly well. Constant eddy diffusion coefficients lead to more detailed height forecasts without any deterioration in the CRMSE verification scores. Consequently, eddy diffusion constraints with constant coefficients were introduced into the 1970 operational model.

Eddy diffusion coefficients which depend on the baroclinicity lead to further improvements in the detail of the height forecasts. With this feature in the model, and with the 700 mb as a full working level, the depths of the predicted lows begin to match those of the actual lows. However, with such detailed forecast charts improvements in the verification scores can only come if the predicted displacements are reasonably accurate. The predicted displacements depend quite critically on the magnitudes of the control coefficients. It was discovered that the optimum values of the control coefficients in January were very different from those in the autumn. Consequently, sinusoidal seasonal variations were incorporated into the control coefficients in the final series of experiments. The results, especially for the summer case, demonstrated that this is not a particularly good way of coping with the month-to-month variations of the optimum values. However, the basic idea is probably a sound one. For it has been established that the optimum values of the control coefficients do depend on the case. It only remains to determine the best method of estimating these optimum values in advance. In view of the experience with seasonal variation, the obvious approach to try next is to compute the control coefficients from the initial time objective analyses of height and temperature. For instance, it seems likely that the optimum lower level linkages depend more on the frontal

activity than on the actual time-of-year, and for that matter probably more on the frontal activity than on the static stability. Similarly, it seems that the linkage between 500 mb and 200 mb depends more on the predominant position of the tropopause than on the time-of-year, but in a manner related more to the jet stream structure than to the static stability. It should not be a difficult matter to develop diagnostic techniques for computing the control coefficients before the start of each run. Provision could even be made for a monitoring meteorologist to apply corrections depending on how well the last 12-hour forecasts have worked out. For instance, he could provide the computer with the information that the last 12-hour forecasts of the 500 mb trough positions were 5% too slow, or 10% too fast, as the case may be, and this could be taken into account in arriving at the values of the set of control coefficients to be used in the new run. The importance of the frontal and jet stream structures in determining the control coefficients can be understood as follows. The values of the control coefficients are of greatest importance in the regions of baroclinic activity; they do not matter very much away from these regions. For instance, the values of the control coefficients are obviously irrelevant in barotropic situations. From the synoptic point of view, one interpretation of the function of fronts is that they appear to link the different levels of the atmosphere together. In practice, this happens because organised small scale circulations are established. A baroclinic model operating on the standard grid cannot hope to resolve these small scale circulations, but -- in conjunction with the eddy diffusion of potential vorticity -- it can simulate their large scale effects by control coefficients with increased magnitudes. This argument seems to suggest that it is not so important

to have the control coefficients vary from the cold air side to the warm air side of a particular baroclinic wave. But it still seems important to have different control coefficients for baroclinic waves in different air currents. So it would still be worthwhile to solve the problem of integrating the model with control coefficients which vary over the grid. One further conclusion can be drawn from the eddy diffusion experiments. The motion and development of single low centres can be predicted quite well on the standard grid by assigning appropriate values to the eddy diffusion coefficients and the control coefficients, even if there is some difficulty in deciding in advance what these appropriate values are. In principle, therefore, changing over to a finer grid cannot be expected to greatly improve the prediction of single low centres. For multiple-centred lows, on the other hand, the situation is quite different. The standard grid model resolves only one low, and grossly misforecasts the future behaviour of such systems because of this. A fine grid model should be able to produce much better forecasts by resolving the individual entities which constitute the multiple structures. This makes one wonder if fine grid integrations of the baroclinic model are really necessary over most of the map. Perhaps it would be possible to develop techniques for doing fine grid integrations only over those areas where they are really necessary, i.e. where there are low centres with multiple structures.

The innovations in the terrain constraint were small ones, but they appear to lead to significant improvements in dealing with West Coast ridging.

The diabatic constraints were in some ways a disappointment. Before the work was undertaken, it was assumed that any difficulties would lie in the evaluation of the actual amounts of heat involved in the diabatic effects. This was a misconception. Reasonable estimates of the amounts of heat were made in a straightforward manner. It is true that the problem of scale obtruded into the latent heat work, even with the large scale precipitation, but the solution evidently lies in some kind of efficiency factors dependent on temperature and latitude. It is also true that the estimates of radiation and ocean heating could be refined further. But the real problem appears to be that one cannot adequately formulate diabatic constraints without at the same time taking the induced divergence circulations into account. The approach based on Petterssen's equation circumvents this problem to some extent by eliminating the divergent advection terms, but it is unsatisfactory for radiation and ocean heating because of the upper and lower boundary conditions that have to be imposed. Nevertheless, some experience with diabatic effects has been gained, and this may be sufficient to lead to new ways of dealing with them. For instance, if the divergent motions induced by diabatic effects are as important as they seem to be, and if other kinds of divergent motion are accounted for adequately by the eddy diffusion constraints, then perhaps the solution would be to somehow compute a diabatic divergent wind, and include terms due to this in the diabatic constraint.

The precipitation forecasts produced in the parallel model experiments were definitely worse than their 1968 model counterparts. However, this is partly due to the excessive eddy diffusion coefficient used in the vertical motion computations, and partly due to the special deficiencies of the baroclinic height forecasts which have already been

discussed. Some aspects of the precipitation forecasts from the parallel model were very encouraging. In particular, the centres of the precipitation areas in the forecasts for 24-48 hours were often closer to the actual centres than in the 1968 model forecasts. In such cases the parallel model forecasts suffered because the predicted areas were too small. Another advantage of the parallel model forecasts was that the West Coast precipitation patterns were much more realistic than those of the 1968 model. In view of these redeeming features, and in view of the remarks made about the baroclinic model, there is every prospect of improving the precipitation forecasts with another round of experimentation.

This dissertation will conclude with a few brief remarks on two other topics. They are the place of probability in precipitation forecasts, and the implications of the parallel model experiments for primitive equations models.

Some kind of probability yardstick should be attached both to the height forecasts and to the precipitation forecasts. In other fields of physics it is customary to give an estimate of the error when a quantity is measured or predicted. The same kind of thing should be done in numerical weather prediction. In addition to predicting the depths and displacements of low centres, models should also estimate the probable errors of these depths and displacements. This could be done more meaningfully with a predictability approach rather than a purely statistical one. Once a probability yardstick has been attached to the height forecasts, it should be easy to carry over to the precipitation forecasts.

The obvious implications of the parallel model experiments for primitive equations models are as follows. The eddy diffusion coefficients

should depend on the baroclinicity. The latent heat computations should have efficiency factors associated with them to correct for scale effects. And the empirical methods for computing the radiation and eddy diffusion effects could be carried over directly. There could be other implications too. Briefly, if the eddy diffusion of potential vorticity is an important physical process in its own right, as it may well be when it comes to predictability computations, then it is most naturally treated by filtered equations models. Also, the rotational and divergent parts of the wind appear to have very different kinds of physical and numerical properties. They are naturally separated in filtered models, but no distinction is drawn between them in primitive equations models. So the future may not entirely lie with primitive equations models. Filtered equations models may be better suited for dealing with some physical processes. Who knows, perhaps the models of the 1980s will be hybrid ones, part primitive equations and part filtered equations. Only one thing is certain a decade hence. The computations of tomorrow's rain will still be based on the kind of techniques developed in this thesis.



References

- Asselin, R., 1966: "A technique for designing smoothing operators"
Canada Department of Transport, Meteorological Branch, CIR 4417,
TEC 615.
- Asselin, R., 1967: "The operational solution of the balance equation"
Tellus, 19, 24-32.
- Berkofsky, L. and Bertoni, E.A., 1955: "Mean topographic charts for the
entire Earth", Bull. Am. Met. Soc., 36, 350-354.
- Brooks, C.E.P. and Carruthers, N., 1953: "Handbook of statistical methods
in meteorology", London: Her Majesty's Stationery Office, pp 64-67
& 383.
- Bushby, F.H. and Timpson, M.S., 1967: "A 10-level atmospheric model and
frontal rain", Quart. J. Roy. Met. Soc., 93, 1-17.
- Campbell, J. and Davies, D., 1966: "Extreme values of the terms neglected
in the vorticity equation", Canada Department of Transport,
Meteorological Branch, CIR-4416, TEC-614.
- Charney, J.G., 1948: "On the scale of atmospheric motions", Geofys.
Publikasjoner, Oslo, 17, 17pp.
- Charney, J.G., Fjortoft, R., and Von Neumann, J., 1950: "Numerical
integration of the barotropic vorticity equation", Tellus, 2,
237-254.
- Collins, G.O., and Kuhn, P.M., 1954: "A generalised study of precipitation
forecasting, Part 3", Mon. Wea. Rev., 82, 173-182.
- Courant, R., Friedrichs, K., and Lewy, H., 1928: "Uber die partiellen
differenzgleichungen der mathematischen physik" Math. Ann., 100,
32-74.
- Cressman, G.P., 1958: "Barotropic divergence and very long atmospheric
waves", Mon. Wea. Rev. 86, 293-297.
- Cressman, G.P., 1960: "Improved terrain effects in barotropic forecasts",
Mon. Wea. Rev. 88, 327-342.
- Cressman, G.P., 1963: "A three-level model suitable for daily numerical
forecasting", Tech. Memo. No. 22, National Meteorological Center,
Weather Bureau, ESSA, U.S. Department of Commerce, 22p.
- Creswick, W.S. and Olson, M., (1970): "Time-dependent boundaries in a
baroclinic prediction model", unpublished manuscript, Central Analysis
Office, Canada Department of Transport, Meteorological Branch.
- Danard, M.B., 1963: "On the influence of released latent heat on cyclone
development", Sci. Rep. No. 10, Contract No. AF 19(604), Dept. of
the Geophys. Sci., Univ. of Chicago.

- Danard, M.B., 1964: "On the influence of released latent heat on cyclone development", *J. Appl. Met.*, 3, 27-37.
- Danard, M.B., 1966a: "A quasi-geostrophic numerical model incorporating effects of released latent heat", *J. Appl. Met.*, 5, 85-93.
- Danard, M.B., 1966b: "Further studies with a quasi-geostrophic numerical model incorporating effects of released latent heat", *J. Appl. Met.*, 5, 388-395.
- Danard, M.B., 1969a: "A simple method of including long wave radiation in a tropospheric numerical prediction model", *Mon. Wea. Rev.*, 97, 77-85.
- Danard, M.B., 1969b: "Numerical studies of effects of surface friction on large-scale atmospheric motions", *Mon. Wea. Rev.*, 97, 835-844.
- Davies, D., 1966: "The physics of macroscopic systems with non-unique futures", *Internat. J. Parapsych.*, 8, 417-443.
- (Davies, D. and Olson, M.) 1966: Report on activities in the Field of Numerical Weather Prediction in Canada, Third and Fourth Quarter, 1966. Canada Department of Transport, Meteorological Branch (For WMO distribution).
- Davies, D., 1967a: "Three-layer numerical forecasts of precipitation amount", Canada Department of Transport, Meteorological Branch, Canadian Meteorological Memoirs, 25.
- Davies, D., 1967b: "A perturbation analysis of the baroclinic model in use at the Central Analysis Office", Canada Department of Transport, Meteorological Branch TEC. 659.
- Davies, D. and Harlow, J.H., 1967: "A note on erratic phasing in numerical 1000 mb forecasts", Canada Department of Transport, Meteorological Branch TEC. 661.
- Davies, D. and Olson, M., 1968: "Operational Forecasts of 24-hour precipitation amount from the Central Analysis Office Computer", Canada Department of Transport, Meteorological Branch, TEC. 670.
- Davies, D., 1968: "Shock-wave effects arising from the earth's rotation", *Can. J. Physics*, 46, 935-937.
- Davies, D., 1970: "Numerical forecasts of precipitation amount", Eighth Stanstead Seminar, July 21-31 1969, Publication in Meteorology (in press), McGill University, Montreal.
- Davies, D. and Olson, M., (1971): Report on verification scores of baroclinic model and precipitation scheme, under preparation for publication.

- Eddy, A., McClellan, D.E., and Robert, A.J. (1961): "A report on the objective analysis of pressure height data on a medium-sized computer." Unpublished manuscript. Central Analysis Office. Canada Department of Transport, Meteorological Branch.
- Estoque, M.A., 1956: "An approach to quantitative precipitation forecasting", *J. Meteor.*, 13, 50-54.
- Fulks, J.R., 1935: "Rate of precipitation from adiabatically ascending air", *Mon. Wea. Rev.*, 63, 291-294.
- Godson, W.L., 1958a: "Atmospheric Thermodynamics", Canada Department of Transport, Meteorological Branch, special publication.
- Godson, W.L., 1958b: "Models for numerical prediction" Second Stanstead Seminar, July 29-Aug. 9, 1957. Publication in *Meteorology* No. 9, McGill University, Montreal.
- Glahn, H.R. and Lowry, D.A., 1967: "Short range, subsynoptic surface weather prediction", Techniques Development Laboratory, Silver Spring, Md., ESSA Technical Memorandum WBTM TDL-11, 10pp.
- Glahn, H.R. and Lowry, D.A., 1969: "An operational method for objectively forecasting probability of precipitation", Techniques Development Laboratory, Silver Spring, Md., ESSA Technical Memorandum WBTM TDL-27.
- Haltiner, G.J., Clarke, L.C., and Lawniczak, G.E., 1963: "Computation of the large scale vertical velocity", *J. Appl. Met.*, 2, 242-259.
- Harley, W.S., 1963: "An operational method of quantitative precipitation forecasting", Canada Department of Transport, Meteorological Branch, CIR-3852, TEC-471.
- Harley, W.S., 1965: "An operational method for quantitative precipitation forecasting", *J. Appl. Met.*, 4, 305-319.
- Harvey, R., 1969: "Some experiments with telescoping grids in a baroclinic model", M. Sc. Thesis, McGill University, Montreal.
- Henry, T.J.G., 1965a: "Studies in numerical weather prediction - Report No. 1. - Equations governing large-scale atmospheric motion", Canada Department of Transport, Meteorological Branch, Canadian Meteorological Memoirs, 20.
- Henry, T.J.G., 1965b: "Studies in numerical weather prediction - Report No. 2. - The use of atmospheric modelling equations", Canada Department of Transport, Meteorological Branch, Canadian Meteorological Memoirs, 21.
- Henry, T.J.G., 1965c: "Studies in numerical weather prediction - Report No. 3 - Studies of 12-hour changes and experimental numerical forecasts at 500 and 1000 mb", Canada Department of Transport, Meteorological Branch, Canadian Meteorological Memoirs, 22.

- Holyoke, D.L., 1965: "Verification of objective forecasts at the Central Analysis Office of the Meteorological Service of Canada", Canada Department of Transport, Meteorological Branch, CIR-4320, TEC-585.
- Kruger, H.B., 1965: "A statistical dynamical objective analysis scheme", Canada Department of Transport, Meteorological Branch, Canadian Meteorological Memoirs, 18,
- Kruger, H.B. and Asselin, R.J.M., 1968: "A statistical dynamical objective analysis scheme: Supplement No. 1.", Canada Department of Transport, Meteorological Branch, Canadian Meteorological Memoirs, 23.
- Kruger, H.B., 1969: "General and special approaches to the problem of objective analysis of meteorological variables" Quart. J. Roy. Met. Soc., 95, 21-39.
- Kruger, H.B., 1970: "A statistical dynamical objective analysis scheme: Supplement No. 2" Canada Department of Transport, Meteorological Branch, Canadian Meteorological Memoirs, 27 (in press).
- Kwizak, M., Leaver, J.M., Robert, A.J., and Strachan, R.A., 1960: "Application of electronic computers to provision of operational meteorological services in the Meteorological Branch, Department of Transport", Canada Department of Transport, Meteorological Branch, special publication.
- Kwizak, M., 1961: "A report on the solution of the barotropic model on a medium-sized computer", Canada Department of Transport, Meteorological Branch, Canadian Meteorological Memoirs, 9.
- Kwizak, M., and Robert, A.J., 1963: "An evaluation of simple non-geostrophic forecasts", Canada Department of Transport, Meteorological Branch, Canadian Meteorological Memoirs, 13.
- Kwizak, M., and Davies, D., 1969: "Numerical forecasts of 24-hour precipitation amount", Proceedings of the World Meteorological Organization International Union of Geodesy and Geophysics Symposium on Numerical Weather Prediction, Tokyo, 26 Nov. - 4 Dec. 1968, Meteorological Service of Japan.
- Kwizak, M., 1970: "Semi-implicit integration of a grid point model of the primitive equations" Ph.D. Thesis, McGill University, Montreal.
- Kuhn, P.M., 1953: "A generalised study of precipitation forecasting, Part 2", Mon. Wea. Rev., 81, 222-232.
- Lorenz, E.N., 1969: "Three approaches to atmospheric predictability", Bull. Amer. Met. Soc., 50, 345-349.
- McClellan, D.E., Page, D.E., Robinson, R.H. and Yacowar, N., 1966: "A numerical model for three-day thickness forecasts", Canada Department of Transport, Meteorological Branch, CIR-4381, TEC-600.

- (Paulin, G.), 1969: Report on numerical weather prediction activities in Canada, First half and second half 1969, Canada Department of Transport, Meteorological Branch (for WMO distribution).
- Pedersen, K., 1963: "On quantitative precipitation forecasting with a geostrophic model", *Geofys. Publ.*, 25, No.1, 25pp.
- Penner, C.M., 1963: "An operational method for the determination of vertical velocities", *J. Appl. Met.*, 2, 235-241.
- Petterssen, S., Bradbury, D.L., and Pedersen, K., 1962: "The Norwegian cyclone models in relation to heat and cold sources", *Geofys. Publ.*, 24, 243-280.
- Richtmyer, R.D., 1957: "Difference methods for initial-value problems" New York, Interscience, 238pp.
- Robert, A.J. and Laflamme, F. (1962): Unpublished report of a summer student project.
- Robert, A.J., 1963: "Baroclinic prediction experiments with a four-level statistical-dynamical model", Canada Department of Transport, Meteorological Branch, Canadian Meteorological Memoirs No. 15.
- (Robert, A.J. and Olson, M.), 1966: Report on activities in the field of numerical weather prediction in Canada, First and second quarters 1966, Canada Department of Transport, Meteorological Branch (For WMO distribution).
- (Robert, A.J. and Olson, M.), 1967: Report on activities in the field of numerical weather prediction in Canada, first and second quarters 1967, Canada Department of Transport, Meteorological Branch (For WMO distribution).
- Robert, A.J., Shuman, F.G., and Gerrity, J.P., 1970: "On partial differential equations in mathematical physics", *Mon. Wea. Rev.*, 98, 1-6.
- Shuman, F.G., 1957: "Numerical methods in numerical weather prediction: II Smoothing and filtering", *Mon. Wea. Rev.*, 85, 357-361.
- Shuman, F.G. and Vanderman, L.W., 1965: "Operational methods of truncation error control", National Meteorological Center, Weather Bureau, ESSA.
- Shuman, F.G. and Hovermale, J.B., 1968: "An operational six-layer primitive equations model", *J. Appl. Met.*, 7, 525-547.
- Simla, J., 1964: "Variations of vorticity in barotropic forecasts", Canada Department of Transport, Meteorological Branch, CIR-4417, TEC-615.
- Smagorinsky, J. and Collins, G.O., 1955: "On the numerical prediction of precipitation", *Mon. Wea. Rev.*, 83, 53-57.

- Smagorinsky, J., 1969: "Problems and promises of deterministic extended range forecasting", Bull. Amer. Met. Soc., 50, 286-311.
- Smebye, S.J., 1958: "Computation of precipitation from large scale motion", J. Meteor., 15, 547-560.
- Smithsonian Meteorological Tables, 1958: "Rate of precipitation from adiabatically ascending air", Smithsonian Institute, Washington, D.C., 325-326.
- Spar, J., 1963: "A suggested technique for quantitative precipitation forecasting", Mon. Wea. Rev., 81, 217-221.
- Strachan, R.A., 1962: "Integration of a three-level baroclinic model", Canada Department of Transport, Meteorological Branch, Canadian Meteorological Memoirs, 10.
- Strachan, R.A., 1965: "Automatic Data Processing", Canada Department of Transport, Meteorological Branch, CIR-4262, TEC-574.
- Swayne, W.W., 1956: "Quantitative analysis and forecasting of winter rainfall patterns", Mon. Wea. Rev., 84, 53-65.
- Thompson, J.C., and Collins, G.O., 1953: "A generalised study of precipitation forecasting, Part 1", Mon. Wea. Rev., 81, 91-100.
- Thompson, P.D., 1961: "Numerical weather analysis and prediction", New York, Macmillan.
- Vederman, J., 1961: "Forecasting precipitation with the aid of a high-speed electronic computer", Mon. Wea. Rev., 89, 243-250.
- Younkin, R.J., LaRue, J.A. and Saunders, F., 1965: "The objective prediction of clouds and precipitation using vertically integrated moisture and adiabatic vertical motions". J. Appl. Met., 4, 3-17.
- 1967a: "World weather watch - The plan and implementation program", WMO, Geneva.
- 1967b: "Report of the study conference held at Stockholm, 28 June - 11 July 1967, on the global atmospheric research program (GARP)", WMO.
- 1969: "A guide to GARP", Bull. Amer. Met. Soc., 50, 136-141.

APPENDIX A : A REVIEW OF SOME BASIC EQUATIONSA1. Equations governing a dry atmosphere

This Appendix consists of a brief review of those standard equations and relationships of dynamical meteorology which have some relevance to the main body of the thesis. The purpose of this review is to make the mathematical structure of the dissertation as coherent and complete as possible. For a fuller treatment of the material in this Section see textbooks on dynamic meteorology, such as Thompson (1961), or the Memoirs by Henry (1965a), (1965b), (1965c) which also provide a good introduction to numerical models of the atmosphere.

The dynamical behaviour of a dry atmosphere is governed by the classical principles of conservation of momentum, conservation of energy, and conservation of mass, supplemented by the equation of state for a gas. These principles may be written in mathematical form as a set of differential equations. The conservation of horizontal momentum is expressed by the equation of motion:

$$\frac{d\underline{V}}{dt} + \hat{k} \times f \underline{V} + g \nabla z = 0 \quad (\text{A1.1})$$

The conservation of vertical momentum is expressed by the hydrostatic equation:

$$\frac{\partial z}{\partial p} = - \frac{1}{g\rho} \quad (\text{A1.2})$$

The conservation of energy is expressed by the First Law of Thermodynamics:

$$C_v \frac{dT}{dt} + p \frac{d(1/e)}{dt} = \frac{dq}{dt} \quad (\text{A1.3})$$

The conservation of mass is expressed by the continuity equation:

$$\nabla \cdot \underline{V} + \frac{\partial \omega}{\partial p} = 0 \quad (\text{A1.4})$$

The equation of state for a dry atmosphere is given by the gas law:

$$p = \rho RT \quad (\text{A1.5})$$

Use of the gas law enables the thermodynamic equation (A1.3) to be rewritten in the form:

$$C_p \frac{dT}{dt} - \frac{RT}{p} \frac{dp}{dt} = \frac{dq}{dt} \quad (\text{A1.6})$$

In order to effect a further simplification of the thermodynamic equation, the potential temperature, θ , is defined by:

$$\theta = T (p_0/p)^{\kappa} \quad (\text{A1.7})$$

The thermodynamic equation (A1.6) then becomes:

$$\frac{C_p T}{\theta} \frac{d\theta}{dt} = \frac{dq}{dt} \quad (\text{A1.8})$$

Three explicit assumptions have been made in the derivation of these equations for a dry atmosphere. First, the effects of friction have been neglected. Second, the effects of the Earth's curvature have been neglected. Third, in the momentum equations any terms normally having a magnitude of less than 1% of the dominant terms have been dropped. This last assumption has two main consequences. The vertical component of the momentum equation reduces to the hydrostatic equation (A1.2). Use of the hydrostatic equation then enables the mass equation to be written in the simple form (A1.4). In addition to the assumptions which are explicit in the derivations, there

are two further assumptions which are usually implicit in the application of these equations. The first of these is that all variables are continuous and well-behaved in the mathematical sense. The second is that scale considerations do not have to be taken into account as a separate factor because they are looked after automatically by the equations. The first implicit assumption was mentioned in Section 3.1. An awareness of the second implicit assumption is one of the underlying themes of this thesis. It is shown that scale considerations are an important feature of the application of meteorological equations to numerical weather prediction. Although it is true that these two implicit assumptions and the explicit friction assumption are to some extent interdependent, they are given some prominence here because in the past their importance has usually been underemphasised.

The two most important derived equations are the vorticity equation and the divergence equation. The vorticity equation is obtained by operating on the horizontal momentum equation (A1.1) with $\hat{k} \cdot \nabla \times$, and then making use of the mass equation (A1.4):

$$\frac{dQ}{dt} + \hat{k} \cdot \nabla \omega \times \frac{\partial \underline{v}}{\partial p} = Q \frac{\partial \omega}{\partial p} \quad (\text{A1.9})$$

The divergence equation is obtained by operating on the horizontal momentum equation (A1.1) with $\nabla \cdot$:

$$\frac{d(\nabla \cdot \underline{v})}{dt} + (\nabla \cdot \underline{v})^2 - 2J(u, v) + \nabla \omega \cdot \frac{\partial \underline{v}}{\partial p} - \hat{k} \cdot \nabla f \times \underline{v} - f \hat{k} \cdot \nabla \times \underline{v} + g \nabla^2 \underline{z} = 0 \quad (\text{A1.10})$$

The so-called balance equation is a simplified form of the divergence equation. It is obtained by assuming that the divergent part of the wind

is identically zero, so that $\frac{d(\nabla \cdot \underline{V})}{dt} = 0$, $\nabla \cdot \underline{V} = 0$, and

$$\underline{V} = \underline{V}^r = \hat{k} \times (g/f_0) \nabla \psi, \text{ and also assuming } \nabla \omega \cdot \frac{\partial \underline{V}}{\partial p} = 0$$

$$f \nabla^2 \psi + \nabla f \cdot \nabla \psi - \frac{g}{f_0} J \left(\frac{\partial \psi}{\partial y}, \frac{\partial \psi}{\partial x} \right) = f_0 \nabla^2 z \quad (\text{A1.11})$$

Substituting the hydrostatic equation (A1.2) into the gas law (A1.5) yields a common expression for the temperature of a dry atmosphere:

$$T = - \frac{gP}{R} \frac{\partial z}{\partial p} \quad (\text{A1.12})$$

This enables the thermodynamic equation (A1.6) to be rewritten in an alternative form:

$$\frac{D^*}{Dt} \left(\frac{\partial z}{\partial p} \right) + \frac{\omega \sigma}{g} = \frac{H}{g} \quad (\text{A1.13})$$

where the special heat function, H , is defined by:

$$H = - \frac{R}{C_p P} \frac{dq}{dt} \quad (\text{A1.14})$$

The usual definition of the static stability is:

$$\sigma = - \frac{1}{\rho \theta} \frac{\partial \theta}{\partial p} \quad (\text{A1.15})$$

This can be written out in expanded form by substituting the definition of θ (A1.7) and making use of the gas law (A1.5):

$$\sigma = \frac{R}{P} \left(\frac{\kappa T}{P} - \frac{\partial T}{\partial p} \right) \quad (\text{A1.16})$$

Another useful form of the thermodynamic equation (A1.6) is:

$$C_p \left(\frac{dT}{dt} - \frac{dT}{dp} \Big|_{\omega} \right) = \frac{dq}{dt} \quad (\text{A1.17})$$

A2. Equations governing a moist unsaturated atmosphere

The dynamical behaviour of a moist but unsaturated atmosphere is governed by the same classical principles as a dry atmosphere. The set of differential equations corresponding to (A1.1), (A1.2), (A1.3), (A1.4), (A1.5) and (A1.6) will therefore retain the same form, but the specific heats and the gas constant will now refer to moist unsaturated air instead of dry air. Consequently, those equations which involve neither a specific heat nor the gas constant, namely equations (A1.1), (A1.2) and (A1.4), and the derived equations (A1.9) and (A1.10), are just as valid for moist unsaturated air as they are for dry air. The gas law (A1.5) will become:

$$p = \rho R' T \quad (A2.1)$$

And the thermodynamic equation (A1.6) will become:

$$C_p' \frac{dT}{dt} - \frac{R' T}{p} \frac{dp}{dt} = \frac{dq}{dt} \quad (A2.2)$$

The gas constant for pure water vapour, R_v , is related to the gas constant for dry air by:

$$R_v = R/\epsilon \quad (A2.3)$$

Hence, the gas constant for moist unsaturated air, R' , is given by:

$$R' = \frac{R(1 + r/\epsilon)}{(1 + r)} \quad (A2.4)$$

The specific heat at constant pressure for pure water vapour, C_{pV} , is approximately related to its dry air counterpart, e.g. see Godson (1958a), by:

$$C_{pV} \approx \frac{8C_p}{7\epsilon} \quad (A2.5)$$

Hence, the specific heat at constant pressure for moist unsaturated air, C_p' , is given by:

$$C_p' = \frac{C_p(1 + 8r/7\epsilon)}{(1+r)} \quad (\text{A2.6})$$

It follows that equations (A2.1) and (A2.2) may be rewritten respectively as:

$$p = \frac{\rho R(1+r/\epsilon)T}{(1+r)} \quad (\text{A2.7})$$

and

$$\frac{C_p(1+8r/7\epsilon)}{(1+r)} \frac{dT}{dt} - \frac{R(1+r/\epsilon)}{(1+r)} \frac{T}{p} \frac{dp}{dt} = \frac{dq}{dt} \quad (\text{A2.8})$$

From (A2.4) and (A2.6) it can be seen that the ratio R'/C_p' is given by:

$$\frac{R'}{C_p'} = \frac{(1+r/\epsilon)}{(1+8r/7\epsilon)} \frac{R}{C_p} \quad (\text{A2.9})$$

Now the saturation mixing ratios, even in warm air at low levels, will not normally exceed about 25 gm/kg, i.e. 0.025. And the actual mixing ratios over much of the Earth will be of the order of 2 or 3 gm/kg or less, i.e. of the order of 0.002 or 0.003 or less. Consequently, as $\epsilon \approx 0.62$, it is a very good approximation to assume:

$$\frac{R'}{C_p'} \approx \frac{R}{C_p} \quad (\text{A2.10})$$

Because (A2.10) is such a good approximation, it follows from equations (A1.6) and (A2.8) that adiabatic processes of ascent and descent in a moist unsaturated atmosphere are virtually identical to similar processes in a dry atmosphere. This means that, for most practical purposes, one

need not distinguish between a moist unsaturated atmosphere and a dry atmosphere when applying the thermodynamic equation to adiabatic situations.

In diabatic situations equation (A1.6) is not such a good approximation to equation (A2.8) as it is in the adiabatic case. This is because R' and C_p' now have to be considered separately instead of as a ratio. Estimates based on (A2.4) and (A2.6) indicate that R' and C_p' are normally about 0.3% greater than R and C_p , respectively, and even in extreme situations are only 3% greater. These percentage figures effectively translate into overestimates of the magnitude of $\frac{dq}{dt}$ if equation (A1.6) is used instead of equation (A2.8). However, in the work reported in this thesis all estimates of the heating term, $\frac{da}{dt}$, are made in a fairly crude manner. The objective of using these crude estimates in the model is to introduce some simulated heating effects which will have the same order of magnitude and the same sign as the actual heating effects. This is done in the expectation that the resulting forecasts will be an improvement on those obtained with no heating effects at all. The objective is not to simulate heating effects with great accuracy. On the average, in fact, it seems likely that the computed values of $\frac{da}{dt}$ will differ from the corresponding real values by at least 5% or 10%. This being the case, there does not seem to be much point in applying the 0.3% to 3% correction factors to $\frac{dq}{dt}$ in equation (A1.6) to take into account the presence of moisture. This is especially true as it will be seen in the next Section that larger but similar correction factors will be neglected in the theoretical version of the thermodynamic equation which is used when saturation occurs. Consequently, for the purposes of the work reported in this thesis, the various versions of the thermodynamic equation, (A1.6),

(A1.8), (A1.13) and (A1.17) are assumed to be valid for both dry air and moist unsaturated air. And this assumption is used in both adiabatic and diabatic situations.

A3. Equations governing a moist saturated atmosphere

The situation becomes much more complicated when the moist air is allowed to attain saturation. This is because condensation may lead to liquid water droplets, or sublimation to ice particles. In this Section all the equations will be written as they apply to the condensation of liquid water droplets. For the same equations apply equally well to the sublimation of ice particles. One merely has to substitute the latent heat of sublimation of ice, L_1 , for the latent heat of condensation of water, L ; substitute the specific heat of ice, C_1 , for the specific heat of water, C_L ; and substitute the ice mixing ratio, r_1 , for the liquid water mixing ratio, r_L .

When condensation into liquid water droplets occurs without supersaturation, Godson (1958a) has shown that the First Law of Thermodynamics takes the form:

$$\begin{aligned} \left\{ C_p + C_L(r_w + r_L) \right\} \frac{dT}{dt} - \frac{RT}{(p - e_w)} \frac{d(p - e_w)}{dt} + T \frac{d}{dt} \left(\frac{L r_w}{T} \right) \\ = (1 + r_w + r_L) \frac{dq}{dt} \end{aligned} \quad (\text{A3.1})$$

This equation, unlike equation (A1.6), does not have unique time-independent solutions under adiabatic conditions. This means it is not possible to construct unique reversible saturated adiabatic curves of ascent and descent on a thermodynamic diagram without assuming a specific pressure level at

which condensation occurs. However, if condensed products are removed (or added) as formed (or required) the r_L terms drop out and (A3.1) becomes:

$$\begin{aligned} (C_p + C_L r_w) \frac{dT}{dt} - \frac{RT}{(p - e_w)} \frac{d(p - e_w)}{dt} + T \frac{d}{dt} \left(\frac{L r_w}{T} \right) \\ = (1 + r_w) \frac{dq}{dt} \end{aligned} \quad (\text{A3.2})$$

There are two well-known thermodynamic relationships governing changes of phase. One is the Clausius-Clapeyron equation:

$$\left(\frac{1}{p_w} - \frac{1}{p_L} \right) \frac{de_w}{dT} = \frac{L}{T} \quad (\text{A3.3})$$

The other is:

$$\frac{dL}{dT} = (C_{pw} - C_L) - \left(\frac{p_w}{p_L - p_w} \right) \frac{L}{T} \quad (\text{A3.4})$$

Since $p_L \gg p_w$, equations (A3.3) and (A3.4), respectively, can be closely approximated by:

$$\frac{1}{e_w} \frac{de_w}{dT} = \frac{L}{RT^2} \quad (\text{A3.5})$$

and

$$\frac{dL}{dT} = C_{pw} - C_L \quad (\text{A3.6})$$

With the help of (A3.5) and (A3.6), and remembering that

$$p - e_w = \frac{\epsilon p}{(\epsilon + r_w)} \quad (\text{A3.7})$$

equation (A3.2) becomes:

$$\begin{aligned} C_p \left\{ 1 + \frac{r_w L}{RT} \cdot \frac{\epsilon L}{c_p T} + \frac{r_w}{\epsilon} \right\} \frac{dT}{dt} - \frac{RT}{p} \left\{ 1 + \frac{r_w L}{RT} \right\} \frac{dp}{dt} \\ = \frac{dq}{dt} \end{aligned} \quad (\text{A3.8})$$

The adiabatic form of (A3.8) is the differential equation defining the moist adiabats on the tephigram. They are curves of constant potential wet bulb temperature. For practical purposes the most useful form of equation (A3.8) is the counterpart of equation (A1.17), viz:

$$C_p'' \left(\frac{dT}{dz} - \frac{dT}{dp} \Big|_{e_w} w \right) = \frac{dq}{dz} \quad (\text{A3.9})$$

where

$$C_p'' = C_p \left(1 + \frac{r_w L}{R T} \cdot \frac{\epsilon L}{C_p T} + \frac{r_w}{7\epsilon} \right) \quad (\text{A3.10})$$

and both $\frac{dT}{dp} \Big|_{e_w}$ and C_p'' are expressed in tabular form.

The rate at which condensed products are formed between heights z_1 and z_2 in a column of saturated air undergoing moist adiabatic ascent is given by:

$$\gamma' = \int_{z_1}^{z_2} \frac{dr_w}{dz} \cdot \frac{\rho}{(1+r_w)} dz \quad (\text{A3.11})$$

The moist adiabatic assumption, it should be remembered, is that these condensed products are removed from the column at the same rate as they are formed. Actual numerical values for condensation rates per unit vertical motion per unit mass of air can be computed as a corollary to the derivation of the moist adiabatic curves on the tephigram. Fulks (1935) showed that these numerical values could be most conveniently expressed in tabular form, and they are now included in the Smithsonian Meteorological Tables (1958).

The preceding review of the principal thermodynamic consequences of saturation may be summarised as follows. Manageable mathematical relationships can only be derived if moist adiabatic conditions are assumed, i.e.

if it is assumed that condensed products are removed from saturated air in adiabatic ascent at the same rate as they are formed. This assumption leads to the definition of moist adiabatic curves on the tephigram, and their associated unique values of $\left(\frac{dT}{dp}\right)_{\theta_w}$ for given T and p . It also leads to uniquely defined condensation rates $\gamma'(T, p)$ for a unit mass of saturated air with unit ascending vertical motion.

The principal dynamic consequences of saturation may be summarised even more succinctly. Manageable mathematical relationships only exist if it is assumed that any condensed products are retained in suspension in the air. For with this assumption it is obvious that the original forms of equations (A1.1), (A1.2) and (A1.4) remain perfectly valid expressions of conservation of momentum and mass. And, consequently, it follows that with this same assumption the original forms of the vorticity equation, (A1.9), and the divergence equation (A1.10), are also valid as they stand for a moist saturated atmosphere.

Unfortunately, the required dynamic assumption is the antithesis of the thermodynamic one. The moist adiabatic assumption calls for the condensed products to be removed as they are formed. This is a contradiction that will have to be left unresolved. However, the situation is not as bad as it appears. There are more serious sources of forecast error in contemporary models of the atmosphere. The thesis demonstrates this by showing that there are at least some more serious sources of error which can be remedied.

Finally, of course, the gas law for the mixture of air and water vapour breaks down when condensation occurs. However, it still holds for the dry air component, so that:

$$(p - e_w) = (p - p_w) RT \quad (A3.12)$$

The breakdown of the gas law for the water vapour component means that:

$$e \neq p_v \frac{R}{\varepsilon} T \quad (A3.13)$$

insofar as, for instance, small increases in e under isothermal conditions will not produce gas law decreases of p_v . However, it is true, instantaneously at least, that:

$$e_w = p_w \frac{R}{\varepsilon} T \quad (A3.14)$$

insofar as this is the limiting case of the valid gas law for unsaturated water vapour. But the use of the w-subscript to indicate saturated values is equivalent to explicitly stating that only the instantaneous value of the mass of water present in the vapour phase is to be considered. The inequality relationship (A3.13), on the other hand, implicitly applies to 1 gm of water substance which may be either in the saturated vapour phase or the liquid phase.

APPENDIX B : A CATALOGUE OF NUMERICAL PROCEDURESB1. Introduction

Most of the finite difference and other numerical procedures used in the precipitation project are standard ones. Some are described by Asselin (1966), Haltiner, Clarke and Lawniczak (1963), Shuman (1957), Shuman and Vanderman (1965), and Thompson (1961). But there is no single reference sources which describes all of them. It is therefore appropriate to provide some documentation of such standard numerical procedures as part of the thesis. All material of this type has been collected together here in the form of an appendix in order to avoid unnecessary technical digressions in the main text. In addition it is convenient to include the details of a few of the more elaborate non-standard procedures.

One small point that should be mentioned in passing is that much of the early development work was done using an octagonal grid. Because of this certain precautions had to be employed in the corner regions. However, these difficulties will not be discussed here because all current and projected work is based on a rectangular grid.

B2. The definition of a stencil operator

Many procedures involving a field of grid-point values can be described most graphically by the use of stencil operators. An array of elements of the type

$$A = \frac{1}{A} \begin{array}{|c|c|c|} \hline a_{11} & a_{12} & a_{13} \\ \hline a_{21} & a_{22} & a_{23} \\ \hline a_{31} & a_{32} & a_{33} \\ \hline \end{array} \quad (\text{B2.1})$$

is defined to be a stencil operator if it acts on a given rectangular field of grid-point values, F_{ij} , so as to produce a resultant field,

$$AF_{ij}, \text{ whose values at the interior grid points are given by:}$$

$$AF_{ij} = \frac{1}{A} \left[a_{11} F_{i-1j+1} + a_{12} F_{ij+1} + a_{13} F_{i+1j+1} + a_{21} F_{i-1j} \right. \\ \left. + a_{22} F_{ij} + a_{23} F_{i+1j} + a_{31} F_{i-1j-1} + a_{32} F_{ij-1} + a_{33} F_{i+1j-1} \right] \quad (\text{B2.2})$$

Special procedures may or may not be stipulated in the boundary regions. If no special procedure is stipulated the boundary of the resultant field will be undefined.

B3. The standard smoother

The standard smoothing operator, denoted by the symbol \square , has the stencil form:

$$\square = \frac{1}{16} \begin{array}{|c|c|c|} \hline 1 & 2 & 1 \\ \hline 2 & 4 & 2 \\ \hline 1 & 2 & 1 \\ \hline \end{array} \quad (\text{B3.1})$$

Normally, the original boundaries are retained on the smoothed field.

The standard smoothing operator eliminates two-gridlength noise, but it also severely attenuates all short-wave patterns.

B4. The five-point smoother

The five-point smoother is an early form of smoother, denoted by the

symbol $\overline{\quad}$, which has the stencil form:

$$\overline{\quad} = \frac{1}{8} \begin{array}{|c|c|c|} \hline 0 & 1 & 0 \\ \hline 1 & 4 & 1 \\ \hline 0 & 1 & 0 \\ \hline \end{array} \quad (\text{B4.1})$$

B5. The standard unsmoother

The standard unsmoothing operator, denoted by the symbol \mathcal{Z} , has the following stencil form:

$$\mathcal{Z} = \frac{1}{16} \begin{array}{|c|c|c|} \hline 1 & -6 & 1 \\ \hline -6 & 36 & -6 \\ \hline 1 & -6 & 1 \\ \hline \end{array} \quad (\text{B5.1})$$

The standard unsmoother must not be allowed to act on points adjoining the boundary because boundary irregularities should not be drawn into the interior of the grid. Normally, therefore, the original rows and columns adjoining the boundaries and the original boundaries themselves are retained in the unsmoothed field.

When the standard unsmoother is used it is applied in series with the standard smoother. The combined effect of the two operators is to eliminate two-gridlength noise while retaining the amplitudes of other short waves as close as possible to their original values. The combined operators do not amplify any wavelength.

B6. The special unsmoother

In addition to the standard unsmoother, which has just been defined, there exists a special unsmoother which is encountered as part of the Shuman Jacobian computations. This special unsmoothing operator, defined by the symbol \mathcal{S} , has the stencil form:

$$\mathcal{S} = \frac{1}{36} \begin{bmatrix} 1 & -8 & 1 \\ -8 & 64 & -8 \\ 1 & -8 & 1 \end{bmatrix} \quad (\text{B6.1})$$

The special unsmoother, like the standard unsmoother, must not be allowed to act on points adjoining the boundary. Once again, therefore, the original rows and columns adjoining the boundaries and the original boundaries themselves are retained in the unsmoothed field.

The use of the special unsmoother will be discussed in Section B12 dealing with the Shuman Jacobian.

B7. Horizontal first derivatives: I standard finite difference formulae

It is convenient to define operators $[]_x$ and $[]_y$ given by:

$$[]_x = \begin{bmatrix} 0 & 0 & 0 \\ -1 & 0 & 1 \\ 0 & 0 & 0 \end{bmatrix} \quad (\text{B7.1})$$

and

$$\left[\right]_y = \begin{array}{|c|c|c|} \hline 0 & 1 & 0 \\ \hline 0 & 0 & 0 \\ \hline 0 & -1 & 0 \\ \hline \end{array} \quad (\text{B7.2})$$

Note that $\left[\right]_x$ is defined on the boundaries parallel to the x-direction, but not on the boundaries parallel to the y-direction. The reverse holds true for $\left[\right]_y$.

These operators are related to the first order finite difference approximations for $\frac{\partial}{\partial x}$ and $\frac{\partial}{\partial y}$ by the following formulae:

$$\left\langle \frac{\partial F}{\partial x} \right\rangle = \frac{m}{2d} \left[F \right]_x \quad (\text{B7.3})$$

$$\text{and } \left\langle \frac{\partial F}{\partial y} \right\rangle = \frac{m}{2d} \left[F \right]_y \quad (\text{B7.4})$$

The standard finite difference gradient operator, ∇ , is defined by

$$\nabla = \hat{i} \left[\right]_x + \hat{j} \left[\right]_y \quad (\text{B7.5})$$

B8. Horizontal first derivatives: II special finite difference formulae

The standard finite difference formulae for first order first derivatives in the horizontal have just been defined. In addition to these there exists some special finite difference formula for first

derivatives which are encountered in the definition of the Shuman Jacobian.

It is convenient to define operators $[\]_x$ and $[\]_y$

given by:

$$[\]_x = \frac{1}{6} \begin{bmatrix} -1 & 0 & 1 \\ -4 & 0 & 4 \\ -1 & 0 & 1 \end{bmatrix} \quad (\text{B8.1})$$

$$[\]_y = \frac{1}{6} \begin{bmatrix} 1 & 4 & 1 \\ 0 & 0 & 0 \\ -1 & -4 & 1 \end{bmatrix} \quad (\text{B8.2})$$

Neither $[\]_x$ nor $[\]_y$ is defined on the boundary.

These operators may be related to $\frac{\partial}{\partial x}$ and $\frac{\partial}{\partial y}$ by the following formulae:

$$\left\langle \frac{\partial F}{\partial x} \right\rangle = \frac{m}{2d} [F]_x \quad (\text{B8.3})$$

and $\left\langle \frac{\partial F}{\partial y} \right\rangle = \frac{m}{2d} [F]_y \quad (\text{B8.4})$

However, see Section B12 for an explanation of how they are used in conjunction with the special unsmoother of Section B6.

B9. Horizontal second derivatives: standard finite difference formulae

It is convenient to define operators $\left[\right]_{xx}$, $\left[\right]_{yy}$
 and $\left[\right]_{xy}$ given by:

$$\left[\right]_{xx} = \begin{array}{|c|c|c|} \hline 0 & 0 & 0 \\ \hline 1 & -2 & 1 \\ \hline 0 & 0 & 0 \\ \hline \end{array} \quad (\text{B9.1})$$

$$\left[\right]_{yy} = \begin{array}{|c|c|c|} \hline 0 & 1 & 0 \\ \hline 0 & -2 & 0 \\ \hline 0 & 1 & 0 \\ \hline \end{array} \quad (\text{B9.2})$$

$$\left[\right]_{xy} = \begin{array}{|c|c|c|} \hline -1 & 0 & 1 \\ \hline 0 & 0 & 0 \\ \hline 1 & 0 & -1 \\ \hline \end{array} \quad (\text{B9.3})$$

Note that $\left[\right]_{xx}$ is defined on the boundaries parallel to the x-direction, but not on the boundaries parallel to the y-direction. The reverse holds true for $\left[\right]_{yy}$. However, $\left[\right]_{xy}$ is not

defined on any boundary.

Neglecting the variation in the map scale factor, these operators are related to the first order finite difference approximations for

$$\frac{\partial^2}{\partial x^2} \quad \cdot \quad \frac{\partial^2}{\partial y^2} \quad \text{and} \quad \frac{\partial^2}{\partial x \partial y} \quad \text{by the following formulae:}$$

$$\left\langle \frac{\partial^2 F}{\partial x^2} \right\rangle = \frac{m^2}{d^2} [F]_{xx} \quad (\text{B9.4})$$

$$\left\langle \frac{\partial^2 F}{\partial y^2} \right\rangle = \frac{m^2}{d^2} [F]_{yy} \quad (\text{B9.5})$$

and

$$\left\langle \frac{\partial^2 F}{\partial x \partial y} \right\rangle = \frac{m^2}{4d^2} [F]_{xy} \quad (\text{B9.6})$$

B10. The Laplacian finite difference operator

Just as the analytical Laplacian is defined as the sum of the second derivatives with respect to x and y, the Laplacian finite difference

operator, ∇^2 , is defined as the sum of $[]_{xx}$ and $[]_{yy}$.

It may be written down as a single stencil operator:

$$\nabla^2 \quad \begin{array}{|c|c|c|} \hline 0 & 1 & 0 \\ \hline 1 & -4 & 1 \\ \hline 0 & 1 & 0 \\ \hline \end{array} \quad (\text{B10.1})$$

Note that ∇^2 is not defined along the boundary.

It is related to the analytical Laplacian by:

$$\langle \nabla^2 F \rangle = \frac{m^2}{d^2} \nabla^2 F \quad (\text{B10.2})$$

Here again the variation in map scale factor has been neglected.

B11. The standard first order Jacobian operator

The standard first order finite difference Jacobian operator may be defined as a combination of standard first order finite difference derivatives by analogy to its analytical counterpart. However, unlike the Laplacian, it cannot itself be expressed as a single stencil operator because it involves two fields. It is defined by :

$$\mathcal{J}(F_1, F_2) = \left\{ [F_1]_x [F_2]_y - [F_1]_y [F_2]_x \right\} \quad (\text{B11.1})$$

except along the boundaries where it is undefined.

It is related to the analytical Jacobian by:

$$\langle \mathcal{J}(F_1, F_2) \rangle = \frac{m^2}{4d^2} \mathcal{J}(F_1, F_2) \quad (\text{B11.2})$$

Jacobians arise in connection with the evaluation of the advection terms in the integrations of the meteorological equations. Unfortunately, rather severe truncation effects are associated with the standard first order Jacobian operator because it involves evaluating a difference of products. This results in short wave features being systematically under-advected in the forecast charts. Consequently, a second order finite difference Jacobian should be used wherever feasible.

B12. The Shuman Jacobian

The second order Jacobian operator in most common use is one due to Shuman and Vanderman (1965).

It is defined by:

$$\mathcal{J}_J(F_1, F_2) = \left\{ \begin{bmatrix} \bar{F}_1 \\ F_1 \end{bmatrix}_x \begin{bmatrix} \bar{F}_2 \\ F_2 \end{bmatrix}_y - \begin{bmatrix} \bar{F}_1 \\ F_1 \end{bmatrix}_y \begin{bmatrix} \bar{F}_2 \\ F_2 \end{bmatrix}_x \right\} \quad (\text{B12.1})$$

except along the boundaries where it is undefined.

It is related to the analytical Jacobian by:

$$\langle \mathcal{J}(F_1, F_2) \rangle = \frac{m^2}{4d^2} \mathcal{J}_J(F_1, F_2) \quad (\text{B12.2})$$

The truncation control inherent in the Shuman Jacobian greatly reduces the systematic underadvection of short waves.

One disadvantage that arises from the use of the Shuman Jacobian to evaluate advection terms is that the Courant-Friedrichs-Lewy criterion is slightly modified. Consequently, waves travelling slightly less than one gridlength in one time step can give rise to computational instability.

B13. First derivatives of pressure: Finite difference formulae

Haltiner, Clarke and Lawniczak (1963) used a parabolic fit formula for first derivatives of pressure; it is given by:

$$\left\langle \frac{\partial F}{\partial p} \right\rangle_c = \frac{1}{(\Delta P_U + \Delta P_L)} \left\{ \frac{\Delta P_U}{\Delta P_L} F_L - \left(\frac{\Delta P_U}{\Delta P_L} - \frac{\Delta P_L}{\Delta P_U} \right) F_c - \frac{\Delta P_L}{\Delta P_U} F_U \right\} \quad (\text{B13.1})$$

where the subscripts C, L, and U refer to centre, lower, and upper respectively; and Δp_L is the separation between the lower and centre pressure levels, and Δp_U is the separation between the centre and upper pressure levels.

In practice, of course, formula (B13.1) is applied in the precipitation project in the form:

$$\left\langle \frac{\partial F}{\partial p} \right\rangle_c = a'_L F_L + a'_C F_C + a'_U F_U \quad (\text{B13.2})$$

where a'_L , a'_C and a'_U have the numerical values given in Table 74 .

There are occasions when it is necessary to employ simple non-centred formulae at 850 and 500 mb. These may be regarded as special cases of (B13.2) in which either a'_L or a'_U is zero, and are accordingly also listed in Table 74 .

pressure levels (mb)			constant (10^{-2}mb^{-1})		
L	C	U	a'_L	a'_C	a'_U
1000	850	700	0.333333	0	- 0.333333
850	700	500	0.380952	- 0.166667	- 0.214285
700	500	200	0.3	- 0.166667	- 0.133333
850	500	200	0.131868	0.047619	- 0.179487
-	850	700	-	0.666667	- 0.666667
700	500	-	0.5	- 0.5	-

Table 74 : Numerical values of the constants in the formula for a first derivative of pressure (B13.2)

B14. Second derivatives of pressures: Finite difference formulae

Haltiner et al (1963) also used a parabolic fit formula for second derivatives of pressure; it is given by:

$$\left\langle \frac{\partial^2 F}{\partial p^2} \right\rangle_c = \frac{1}{\Delta P_L \Delta P_U} \left\{ \frac{2 \Delta P_U F_L}{(\Delta P_L + \Delta P_U)} - 2 F_C + \frac{2 \Delta P_L F_U}{(\Delta P_L + \Delta P_U)} \right\} \quad (B14.1)$$

where the notation is the same as that used in Section B13.

In the precipitation project formula (B14.1) is applied in the form:

$$\left\langle \frac{\partial^2 F}{\partial p^2} \right\rangle_c = a_L^2 F_L + a_C^2 F_C + a_U^2 F_U \quad (B14.2)$$

where a_L^2 , a_C^2 and a_U^2 have the numerical values given in Table 75 .

pressure levels (mb)			constant (10^{-4} mb^{-2})		
L	C	U	a_L^2	a_C^2	a_U^2
1000	850	700	0.444444	- 0.888889	0.444444
850	700	500	0.380952	- 0.666667	0.285714
700	500	200	0.2	- 0.333333	0.133333
850	500	200	0.087912	- 0.190476	0.102564

Table 75 : Numerical values of the constants in Haltiner's parabolic fit formula for a second derivative of pressure (B14.2)

B15. Special non-centred first derivative of pressure at 200 mb

By experiment it was found that non-centred formulae based on polynomial curve-fitting, including a parabolic fit, can lead to

physically unrealistic values for first derivatives. Their worst feature is that they can give the wrong sign in some cases. Although a simple non-centred linear formula gives the correct sign for a first derivative, it too exhibits certain systematic deviations from physical realism. Consequently, the following special formula was developed by the author; see Campbell and Davies (1966). It is essentially a corrected form of a non-centred linear formula which takes into account, in a physically realistic fashion, the information available from a third point.

Define:

$$a = (F_{500} - F_{200}) / 300 \quad (\text{B15.1})$$

$$b = (F_{700} - F_{200})(F_{500} - F_{200}) \quad (\text{B15.2})$$

$$c = (F_{700} - F_{200}) / (F_{500} - F_{200}) \quad (\text{B15.3})$$

then,

$$\left\langle \frac{\partial F}{\partial p} \right\rangle_{200} = \begin{cases} a & \text{if } a \leq \varepsilon(F) \\ 3a/2 & \text{if } b < 0 \text{ and } a > \varepsilon(F) \\ a/2 & \text{if } a > \varepsilon(F), b \geq 0 \text{ and } c \geq 10/3 \\ 3(5-c)a/10 & \text{if } a > \varepsilon(F), b \geq 0 \text{ and } c < 10/3 \end{cases} \quad (\text{B15.4})$$

where $\varepsilon(F)$ is chosen to be 10^{-10} times an average value of F .

B16. First derivatives of time: Finite difference formulae

Time derivatives are evaluated in two different ways. The centred time step formula is defined by:

$$\left\langle \frac{\partial F}{\partial t} \right\rangle_t = \frac{F(t + \Delta t) - F(t - \Delta t)}{2 \Delta t} \quad (\text{B16.1})$$

The forward time step formula is defined by:

$$\left\langle \frac{\partial F}{\partial t} \right\rangle_t = \frac{F(t + \Delta t) - F(t)}{\Delta t} \quad (\text{B16.2})$$

It can easily be shown, e.g. Thompson (1961), that time derivatives relating to advection processes lead to computationally stable integrations with a centred time step, but not with a forward time step. It can also be shown, e.g. Richtmeyer (1957), that the reverse holds true for time derivatives relating to dissipative processes. Consequently, a centred time step is used in conjunction with an advection term. But a forward time step is used in conjunction with a dissipation term. The only exception is at initial time when a forward time step has to be used even with advection terms in order to begin the leap-frog marching process.

In practice, forward and centred time steps can be used in the same equation. For instance, consider a predictive equation containing just an advection term and an eddy diffusion term as follows:

$$\frac{\partial F}{\partial t} = -\underline{v}(t) \cdot \nabla F(t) + K_d \nabla^2 F(t) \quad (\text{B16.3})$$

The finite difference form of (B16.3) is:

$$F(t + \Delta t) = F(t - \Delta t) + 2 \Delta t \left\{ \left\langle -\underline{v}(t) \cdot \nabla F(t) \right\rangle \Big|_t^{\dagger} + \left\langle K_d \nabla^2 F(t - \Delta t) \right\rangle \Big|_t^{\dagger - \Delta t} \right\} \quad (\text{B16.4})$$

A centred time step is used for the advection term by evaluating it at time t . But a forward time step is used for the eddy diffusion term by evaluating it at time $(t - \Delta t)$.

B17. Formulae for computing RMSE verification scores

Suppose that a forecast field, F_1 , and a verifying field, F_2 , are given for the same N grid-points. Then the root-mean-square error (RMSE) verification score, R_{12} , is defined as:

$$R_{12} = \sqrt{\left[\sum_{i=1}^N (F_{1i} - F_{2i})^2 \right] / N} \quad (\text{B17.1})$$

The RMSE verification score is a good measure of the accuracy of a predicted field when the errors are normally distributed. In the case of height fields, however, it has become fashionable to correct for the difference between the mean of the forecast field and the mean of the verifying field. This is done by defining the corrected root-mean-square error (CRMSE) verification score, R_{12}^* , to be:

$$R_{12}^* = \sqrt{\left\{ \sum_{i=1}^N [(F_{1i} - \bar{F}_1) - (F_{2i} - \bar{F}_2)]^2 \right\} / N} \quad (\text{B17.2})$$

$$\left. \begin{array}{l} \text{where} \quad \bar{F}_1 = \left(\sum_{i=1}^N F_{1i} \right) / N \\ \text{and} \quad \bar{F}_2 = \left(\sum_{i=1}^N F_{2i} \right) / N \end{array} \right\} \quad (\text{B17.3})$$

Formula (B17.2) may be rewritten as:

$$R_{12}^* = \sqrt{R_{12}^2 - (\bar{F}_1 - \bar{F}_2)^2 / N} \quad (\text{B17.4})$$

B18. Second derivatives parallel and normal to the flow

The finite difference second derivative parallel to the stream function flow, $\left[\frac{\partial^2 \psi}{\partial s^2} \right]_{pp}$, is given by:

$$\left[\frac{\partial^2 \psi}{\partial s^2} \right]_{pp} = \left[\frac{\partial^2 \psi}{\partial x^2} \right] (\cos \alpha_x)^2 + \left[\frac{\partial^2 \psi}{\partial y^2} \right] (\cos \alpha_y)^2 + \left[\frac{\partial^2 \psi}{\partial xy} \right] \frac{\cos \alpha_x \cos \alpha_y}{4} \quad (\text{B18.1})$$

where

$$\cos \alpha_x = - \left[\frac{\partial \psi}{\partial y} \right] / \left\{ \left(\left[\frac{\partial \psi}{\partial x} \right] \right)^2 + \left(\left[\frac{\partial \psi}{\partial y} \right] \right)^2 \right\}^{1/2} \quad (\text{B18.2})$$

and

$$\cos \alpha_y = \left[\frac{\partial \psi}{\partial x} \right] / \left\{ \left(\left[\frac{\partial \psi}{\partial x} \right] \right)^2 + \left(\left[\frac{\partial \psi}{\partial y} \right] \right)^2 \right\}^{1/2} \quad (\text{B18.3})$$

Similarly, the finite difference second derivative normal to the stream function flow, $\left[\frac{\partial^2 \psi}{\partial n^2} \right]_{NN}$, is given by:

$$\left[\frac{\partial^2 \psi}{\partial n^2} \right]_{NN} = \left[\frac{\partial^2 \psi}{\partial x^2} \right] (\cos \alpha_y)^2 + \left[\frac{\partial^2 \psi}{\partial y^2} \right] (\cos \alpha_x)^2 - \left[\frac{\partial^2 \psi}{\partial xy} \right] \frac{(\cos \alpha_x)(\cos \alpha_y)}{4} \quad (\text{B18.4})$$

$\left[\frac{\partial^2 \psi}{\partial s^2} \right]_{pp}$ and $\left[\frac{\partial^2 \psi}{\partial n^2} \right]_{NN}$ are related to their analytical

counterparts in the same way that $\left[\frac{\partial^2 \psi}{\partial x^2} \right]$ and $\left[\frac{\partial^2 \psi}{\partial y^2} \right]$ are related to $\frac{\partial^2}{\partial x^2}$ and $\frac{\partial^2}{\partial y^2}$.

APPENDIX C: THE MAIN INTEGRATION CYCLE OF THE SEQUENTIAL BAROCLINIC MODELC1. Details of the main integration cycle

The objective of this Appendix is to explain, as clearly as possible, how the stream function tendencies at some particular time step are obtained from a knowledge of the current stream function fields at that same time step. The primary constraint terms, which are discussed individually in Appendix D and Section 9, are assumed to have specified values. Much of the material that follows may also be found in Robert (1963). It is repeated here partly for the sake of completeness, and partly to provide up-to-date documentation of some of the details.

When equation (6.1) is written out in expanded form it becomes:

$$\begin{aligned} & \left\langle \frac{\partial}{\partial t} \left(\frac{g}{f_0} \nabla^2 \psi_m + f + \frac{1}{4} \sum_{n=1}^4 C_{mn} \psi_n \right) \right\rangle \\ & = - \left\langle J \left(\psi_m, \left[\frac{g}{f_0} \nabla^2 \psi_m + f + \frac{1}{4} \sum_{n=1}^4 C_{mn} \psi_n \right] \right) \right\rangle \quad (C1.1) \\ & \quad + \langle G_m \rangle + \langle E_m \rangle + \langle B_m \rangle \quad m=1, 2, 3, 4 \end{aligned}$$

Substituting the finite difference form of the Laplacian (which neglects the variation of the map scale factor) from (B10.1) and the second order finite difference form of the Jacobian - the Shuman Jacobian - from

(B12.1), and then dividing through by 4, yields:

$$\begin{aligned} & \frac{g m^2}{4 f_0 d^2} \nabla^2 \left\langle \frac{\partial \psi_m}{\partial t} \right\rangle + \sum_{n=1}^4 C_{mn} \left\langle \frac{\partial \psi_n}{\partial t} \right\rangle \\ & = - \frac{g m^2}{4 f_0 d^2} J \left(\psi_m, \left[\frac{g m^2}{4 f_0 d^2} \nabla^2 \psi_m + \frac{f}{4} + \sum_{n=1}^4 C_{mn} \psi_n \right] \right) \quad (C1.2) \\ & \quad + \frac{1}{4} \left\{ \langle G_m \rangle + \langle E_m \rangle + \langle B_m \rangle \right\} \\ & \quad \quad \quad m=1, 2, 3, 4 \end{aligned}$$

Define:

$$K = K(x, y) = \frac{gm^2}{4f_0d^2} \quad (C1.3)$$

and

$$J_m = -J_2 \left(\psi_m, \left[K \nabla^2 \psi_m + \frac{f}{4} + \sum_{n=1}^4 C_{mn} \psi_n \right] \right) + \frac{1}{4K} \left\{ \langle G_m \rangle + \langle E_m \rangle + \langle B_m \rangle \right\} \quad m=1,2,3,4 \quad (C1.4)$$

Values of J_m can be computed in a straightforward manner if the ψ_m are known and the values of the primary constraints $\langle G_m \rangle$, $\langle E_m \rangle$ and $\langle B_m \rangle$ are specified. After making use of these newly defined quantities, K and J_m , (C1.2) reduces to:

$$\nabla^2 \left\langle \frac{\partial \psi_m}{\partial t} \right\rangle + \frac{1}{K} \sum_{n=1}^4 C_{mn} \left\langle \frac{\partial \psi_n}{\partial t} \right\rangle = J_m \quad m=1,2,3,4 \quad (C1.5)$$

Once the J_m have been computed, equation (C1.5) has to be solved for $\left\langle \frac{\partial \psi_m}{\partial t} \right\rangle$. In the sequential version of the baroclinic model the next

step is to apply the normalization procedure developed by Strachan (1962) and Robert (1963). Define a new variable:

$$Y_\ell = \sum_{m=1}^4 A_{\ell m} \left\langle \frac{\partial \psi_m}{\partial t} \right\rangle, \quad \ell=1,2,3,4 \quad (C1.6)$$

For convenience, also define

$$J_\ell^* = \sum_{m=1}^4 A_{\ell m} J_m, \quad \ell=1,2,3,4 \quad (C1.7)$$

With the aid of (C1.6) and (C1.7) equation (C1.5) can be transformed into:

$$\nabla^2 Y_\ell + \frac{\lambda_\ell}{K} Y_\ell = J_\ell^*, \quad \ell=1,2,3,4 \quad (C1.8)$$

provided that

$$\sum_{m=1}^L A_{lm} C_{mn} = \lambda_l \delta_{ln} \quad (Cl.9)$$

where δ_{ln} is the Kronecker delta; i.e. provided that the A_{lm} and λ_l are the eigenvectors and eigenvalues of the control coefficient matrix $[C_{mn}]$. The important feature possessed by equations (Cl.8) is that each unknown Y_l appears in the l 'th equation only and not in any other; i.e. equations (Cl.8) are in normalised form. Consequently, each of the four equations (Cl.8) may be solved independently for one of the Y_l . In effect, then, the transformation (Cl.6) has converted the three-dimensional problem of simultaneously solving all the constituent equations of (Cl.5) for $\left(\frac{\partial \psi_m}{\partial t}\right)$ into four separate two-dimensional problems of solving each constituent equation of (Cl.8) separately for a Y_l .

Equations (Cl.8), which are Helmholtz equations of a standard form, are solved by an iterative procedure in which the N th guess, Y_l^N , is related to the $(N-1)$ th guess, Y_l^{N-1} , by the relaxation formula:

$$(Y_l^N)_{ij} = \frac{\alpha}{[4 - \lambda_l / (K)_{ij}]} \left\{ (Y_l^{N-1})_{i+1j} + (Y_l^{N-1})_{ij+1} + (Y_l^N)_{i-1j} + (Y_l^N)_{ij-1} + [4 - \lambda_l / (K)_{ij}] \left[\frac{1}{\alpha} - 1 \right] (Y_l^{N-1})_{ij} - (J_l^*)_{ij} \right\} \quad (Cl.10)$$

where α is the relaxation coefficient. At each time step, except the first, the Y_l fields of the previous hour are used as first guess fields and the relaxation is terminated after five scans with $\alpha = 1.28$. At the first time step zero first guess fields are used and the relaxation is extended out to ten scans. Prior to the advent of the 1970 model the stream function tendencies and $\nabla^2 \psi$ were taken to be zero along the

lateral boundaries, and so the Y_ℓ were also taken to be zero. In the 1970 model, as mentioned in (5.6), lateral boundary values of $\left\langle \frac{\partial \psi_m}{\partial t} \right\rangle$ and $\nabla^2 \psi_m$, and hence of Y_ℓ , are obtained for the 1221-point grid by integrating the same model over a hemispheric grid, starting from an initial time twelve hours earlier, and simply extracting the required values in a straightforward manner. Once the values of Y_ℓ have been determined, the stream function tendencies are obtained by the reverse transformation to (Cl.6), namely:

$$\left\langle \frac{\partial \psi_m}{\partial t} \right\rangle = \sum_{\ell=1}^4 A_{m\ell}^{-1} Y_\ell, \quad m=1,2,3,4 \quad (\text{Cl.11})$$

where the A^{-1} matrix is the inverse of the A matrix.

The normalization procedure reduces the amount of computer core storage required for the relaxation. However, it has the slight disadvantage that two extra steps have to be added to the integration cycle. The first of these is that, prior to the relaxation, the R.H.S.s of equation (Cl.5), the J_m , have to be multiplied by the A -matrix; this gives the R.H.S.s of equation (Cl.8), the J_ℓ^* . The other extra step is, of course, that after the relaxation the Y_ℓ have to be multiplied by the A^{-1} matrix to reconstitute the $\left\langle \frac{\partial \psi_m}{\partial t} \right\rangle$ via (Cl.11). Note, however, that the eigenvalue problem represented by equation (Cl.9) has only to be solved once. As far as the baroclinic model is concerned the $[A_{mn}]$ and $[A_{mn}^{-1}]$ matrices, and also the λ_ℓ , are just pre-computed numbers which are provided along with the values of the control coefficients, $[C_{mn}]$.

There are certain limitations on the main integration cycle procedure which has just been described. These will be discussed in the second part of this Appendix.

C2. Limitations on the main integration cycle.

The author has commented on a few theoretical aspects of normalization and relaxation elsewhere; see Davies (1967b). Some of the more important points raised in this earlier work are summarised here.

There are three limitations on the choice of control coefficients. These arise from the fact that there are certain theoretical requirements which have to be satisfied before the normalisation and relaxation procedures can be usefully employed. First, the control coefficient matrix should have real eigenvalues. The reason for this is simply that complex eigenvalues lead to so many complications that normalised two-dimensional relaxations no longer have any practical advantages over a standard three-dimensional relaxation. Second, the control coefficient matrix should not have two or more eigenvalues equal to one another.

This is because degeneracy occurs with equal eigenvalues and the results of normalization become indeterminate. In practice, to steer well clear of any numerical problems, no two eigenvalues should be allowed to become nearly equal to one another. Third, the control coefficient matrix must have negative eigenvalues. This is because it can be shown that convergence is impossible for the simultaneous relaxation corresponding to (C1.10) if:

$$0 < \frac{\lambda_e}{K_{\max}} \leq 8 \quad (\text{C2.1})$$

where K_{\max} is the maximum value of K .

In effect (C2.1) rules out positive eigenvalues altogether because one would need to assign physically unrealistic values to the control coefficients to make $\lambda_e > 8K_{\max}$. The same conclusion can be

expected to hold for sequential relaxation.

As is well known, there are also limitations on the choice of relaxation coefficient. Strachan (1962) has shown that, provided that the eigenvalues are all real and negative, the sequential relaxation (C1.10) converges if:

$$0 < \alpha < 2$$

(C2.2)

APPENDIX D: TERRAIN EFFECTSD1. Primary constraints due to terrain

In the 1970 operational model the primary constraints due to terrain,

G_m , which appear in equations (6.1) are given by:

$$\begin{aligned} G_1 &= G_3 = G_4 = 0 \\ G_2 &= \frac{[(g/f_0)\nabla^2\psi_2 + f](1000-200)}{(1000-775)(P_g - 200)} \omega_g \end{aligned} \quad (D1.1)$$

Here P_g is the pressure height of the mountains, i.e. the pressure of the standard atmosphere at the top of the mountains. And ω_g is the vertical motion at the ground due to the presence of mountains and effects of surface friction as given by the formula due to Cressman (1960):

$$\omega_g = \underline{V}_g \cdot \nabla P_g + \rho_g \frac{g}{f} \left[\frac{\partial}{\partial y} (C_d u_g |\underline{V}_g|) - \frac{\partial}{\partial x} (C_d v_g |\underline{V}_g|) \right] \quad (D1.2)$$

where \underline{V}_g is the wind at ground level, with x- and y-components u_g and v_g respectively, C_d is the surface drag coefficient, and ρ_g is the standard atmosphere density corresponding to P_g .

The simulation of terrain effects in the baroclinic model involves two distinct problems. First, there is the problem of computing the terrain-induced vertical motion at the ground, ω_g . Second, there is the problem of how the model should actually make use of the ω_g values, once these have been computed.

In the sequential version of the baroclinic model formula (D1.2) is taken as the theoretical basis for the computations of ω_g . Physically, it expresses the total terrain-induced large scale vertical motion at the ground as a sum of two components. The first component, given by the

$\underline{V}_g \cdot \nabla P_g$ term in (D1.2), is simply the upslope and downslope vertical motion induced by the mountains. The second component, given by the second term on the R.H.S. of (D1.2), is the effective vertical motion induced by the friction between the atmosphere and the Earth's surface. Whereas the method for computing the mountain component was already a standard one in 1960, the method for computing the friction component was not. Cressman (1960) finally arrived at the friction formula given in (D1.2) only after a careful examination of the various alternative ways that were proposed for handling the friction component.

Before (D1.2) can be applied in practice, one requires fields of the two terrain-dependent quantities, P_g and C_d . The grid-point values of the P_g field which are used are essentially the same as those extracted by Cressman (1960) from the smoothed field of mountain pressure heights published by Berkofsky and Bertoni (1955) for a 5 deg latitude-longitude grid mesh. However, Simla (1964) made a few minor adjustments in the Arctic regions to eliminate certain small anomalies which occasionally occurred in integrations of the CAO barotropic model. The North American portion of the adjusted P_g field is shown in contoured form in Fig. 2. The C_d field used by the sequential baroclinic model is taken directly from Cressman (1960). C_d is a dimensionless quantity which consists of an invariant component, C_{d1} , and a terrain-dependent component, C_{d2} . According to Cressman (1960), who took into account experimentally-determined values reported by several workers, $C_{d1} = 0.12 \times 10^{-2}$ and C_{d2} varies from zero over calm seas to 0.9×10^{-2} over the Himalayas.

The wind at ground level, \underline{V}_g , is obtained from the stream function winds given by the model. This is done either by simple interpolation

between levels if $P_g < 1000$, or by taking over the 1000 mb wind directly if $P_g \geq 1000$; i.e.:

$$\underline{V}_g = \frac{gm}{f_0 d} \left\{ \underline{U}_g \hat{i} + \underline{V}_g \hat{j} \right\} \quad (D1.3)$$

where, making use of the standard first derivative finite difference

operators $\left[\begin{array}{c} \\ \end{array} \right]_x$ and $\left[\begin{array}{c} \\ \end{array} \right]_y$ defined by (B7.1) and (B7.2)

$$\underline{U}_g = \begin{cases} - \left[\begin{array}{c} \psi_{1000} \\ \end{array} \right]_y & \text{if } P_g \geq 1000 \\ -b_{g1} \left[\begin{array}{c} \psi_{1000} \\ \end{array} \right]_y - (1-b_{g1}) \left[\begin{array}{c} \psi_{850} \\ \end{array} \right]_y & \text{if } 1000 > P_g \geq 850 \\ -b_{g2} \left[\begin{array}{c} \psi_{850} \\ \end{array} \right]_y - (1-b_{g2}) \left[\begin{array}{c} \psi_{500} \\ \end{array} \right]_y & \text{if } 850 > P_g \geq 500 \end{cases} \quad (D1.4)$$

and

$$\underline{V}_g = \begin{cases} \left[\begin{array}{c} \psi_{1000} \\ \end{array} \right]_x & \text{if } P_g \geq 1000 \\ b_{g1} \left[\begin{array}{c} \psi_{1000} \\ \end{array} \right]_x + (1-b_{g1}) \left[\begin{array}{c} \psi_{850} \\ \end{array} \right]_x & \text{if } 1000 > P_g \geq 850 \\ b_{g2} \left[\begin{array}{c} \psi_{850} \\ \end{array} \right]_x + (1-b_{g2}) \left[\begin{array}{c} \psi_{500} \\ \end{array} \right]_x & \text{if } 850 > P_g \geq 500 \end{cases} \quad (D1.5)$$

The coefficients b_{g1} and b_{g2} in (D1.4) and (D1.5) are given by:

$$b_{g1} = (P_g - 850) / (1000 - 850) \quad (D1.6)$$

and

$$b_{g2} = (P_g - 500) / (850 - 500) \quad (D1.7)$$

For convenience, define

$$V_g = \sqrt{U_g^2 + V_g^2} \quad (D1.8)$$

In the 1968 model, and also earlier in the advanced stages of the work on the octagon model, the following finite difference version of (D1.2) was found to be perfectly satisfactory:

$$\begin{aligned} \omega_g^t = & K \left\{ U_g^t [P_g]_x + V_g^t [P_g]_y \right\} \\ & + W_\alpha \left\{ [W_\beta U_g^t V_g^t]_y - [W_\beta V_g^t V_g^t]_x \right\} \end{aligned} \quad (D1.9)$$

where again the standard first derivative finite difference operators

$$[]_x \text{ and } []_y \text{ are defined by (B7.1) and (B7.2),}$$

$$W_\alpha = (p_g g m) / (2 f d) \quad (D1.10)$$

$$W_\beta = (c_d g^2 m^2) / (l_f f_0 d^2) \quad (D1.11)$$

K is defined by (C1.3), and the superscript t indicates values are computed at time t . Note that the mountain term cannot be expressed as a Jacobian because there is no such thing as a mountain-height stream function field.

In the 1970 model Creswick and Olson (1970) took the finite difference version of (D1.2) to be:

$$\begin{aligned} \omega_g^t = & K \left\{ U_g^t [P_g]_x + V_g^t [P_g]_y \right\} \\ & + W_\alpha \left\{ [W_\beta U_g^{t-1} V_g^{t-1}]_y - [W_\beta V_g^{t-1} V_g^{t-1}]_x \right\} \end{aligned} \quad (D1.12)$$

where now the special first derivative finite difference operators

$\left[\frac{\partial}{\partial x} \right]$ and $\left[\frac{\partial}{\partial y} \right]$ of (B8.1) and (B8.2) are used to evaluate the gradients of P_g and $C_d V_g / |V_g|$, instead of the standard ones of (B7.1) and (B7.2), and further the terrain winds in the friction term are evaluated at the previous time step, denoted by $(t-1)$, instead of the current time step t . Note, however, that the terrain wind in the mountain term is still evaluated at the current time step, and also that all terrain winds are still derived from the stream function fields using standard first derivative finite difference operators as indicated by (D1.4) and (D1.5). Creswick and Olson (1970) made the change-over from (D1.9) to (D1.12) because the introduction of eddy diffusion terms led to some uncoupling of the stream function fields at odd and even time steps over the Himalayas, and these difficulties were tracked down to the terrain term. They decided that, as surface friction is a dissipative effect, it would be more correct to use a forward time step rather than a centred one to evaluate the friction term of (D1.2). This seemed to cure the uncoupling in time, but left the forecast stream function charts a little noisy in space over the Himalayas. Consequently, the special first derivative finite difference operators (B8.1) and (B8.2) were substituted for the standard ones (B7.1) and (B7.2) in the evaluation of those terms containing the terrain-dependent quantities P_g and C_d , in order to make the terrain forcing a little smoother. This stratagem was completely successful and so (D1.12) was adopted as feature of the 1970 model. As is reported elsewhere in this thesis, the author quite independently reached rather similar conclusions about the inadequacy of (D1.9) when

eddy diffusion terms are incorporated into the baroclinic model.

Once W_g has been obtained, the next step is to compute the values of the primary constraints, G_m , to be used in the model equations (6.1). When a mountains and friction term was first introduced into the octagon model, Davies and Olson (1966) adopted the following approach. The primary constraints were assumed to be forced components of the divergence term on the R.H.S. of the complete vorticity equation (A1.9):

$$G_m = \left[(g/f_0) \nabla^2 \psi_m + f \right] \frac{\partial w_g^*}{\partial p} \Big|_m \quad (\text{D1.13})$$

where W_g^* is defined to be the terrain induced vertical motion through the troposphere, so that $W_g^* = W_g$ at the ground. In order to apply (D1.13) one has to specify the vertical profile of W_g^* . Assuming a linear fall off with decreasing pressure from ground level to 200 mb, but zero terrain induced divergence at 200 mb, the external constraints become:

$$\begin{aligned} G_1 &= 0 \\ G_2 &= \left[(g/f_0) \nabla^2 \psi_2 + f \right] W_g / (P_g - 200) \\ G_3 &= \left[(g/f_0) \nabla^2 \psi_3 + f \right] W_g / (P_g - 200) \\ G_k &= 0 \end{aligned} \quad (\text{D1.14})$$

where G_1 is taken to be zero because the 1000 mb stream function field is not a full working level of the model. One advantage of this method is that there is no inconsistency in using the absolute vorticity, $\left(\frac{g}{f_0} \nabla^2 \psi_m + f \right)$, as a pre-multiplier of the terrain induced divergence in (D1.13), as is done in the divergence term in the complete vorticity equation (A1.9),

instead of the f_0 which is used in the corresponding term of the simplified vorticity equation (7.2).

A different approach was adopted by Robert and Olson (1967) in later work on the octagon model. The W_g field was merely used to provide a lower boundary condition on W in the vertical finite difference form of (7.2). In other words it was assumed that when the control coefficients of (8.4) are derived one should insert $W = W_g(1000-200)/(p_0-200)$ instead of $W = 0$, as the lower boundary condition. However, at the cost of some inconsistency, the $\left(\frac{g}{f_0} \nabla^2 \psi_m + f^2\right)$ of the complete vorticity equation was retained as the pre-multiplier of W_g , instead of reverting to the f_0 of (7.2). And the Δp in the finite difference evaluation of $\frac{\partial W}{\partial p}$ was somewhat arbitrarily specified as (1000 - 775). The revised terrain constraints thus became those given by (D1.1), as with this approach G_3 is taken to be zero. As before, G_1 is zero because the 1000 mb stream function field is not a full working level of the model.

The comparative merits of the lower boundary forcing of (D1.1) and the terrain induced divergence forcing of (D1.14) were evaluated by Robert and Olson (1967). They carried out a series of octagon model integrations in duplicate. They found that the constraints of (D1.1) gave slightly better verification scores than those of (D1.14) for 12-hour and 24-hour forecasts, but slightly worse scores for 48-hour forecasts. The 36-hour scores were about the same. There were no plans for the operational integrations to go beyond 36 hours. Consequently, it was decided to use the constraints (D1.1), the lower boundary forcing, to simulate terrain effects in the 1968 model. The same feature was subsequently carried over to the 1970 model; except that, as already mentioned, the finite difference formula used to evaluate W_g was changed from (D1.9) to (D1.12).

APPENDIX E : SKILL FACTOR VERIFICATIONS OF PRECIPITATION AMOUNT FORECASTSE1. The grid-point approach to objective verification

The penalty table "skill factor" is an objective indicator of the usefulness of precipitation forecasts. It was specially designed by the author - Davies (1967a) - to do verifications of grid-point forecasts by grid-point analyses, and to take the amount of precipitation into account. The skill factor is therefore slightly more meaningful than the threat score, but it has the disadvantage of being unknown.

E2. The objective analysis of observed precipitation

The first step in the computation of the skill factor is to produce an objective analysis of the station reports of precipitation amount, i.e. to convert observed station data into grid-point data. This is done as follows. The grid-points are analysed in turn. The same station report may therefore feature in the computations at several different grid-points. In the computation of a grid-point value all stations within an influence area of radius 1.25 grid-lengths are assigned weights according to the curve of Fig. 77. Stations within 0.3 grid-lengths are assigned a weight 1; stations between 0.3 and 1 grid-length are assigned weights linearly decreasing from 1 to 0.1; and stations between 1 and 1.25 gridlengths are assigned a weight 0.1. If at a grid-point there are N_1 , N_2 , N_3 and N_4 stations in the 1st, 2nd, 3rd and 4th quadrants respectively; and if the i 'th station in the j 'th quadrant reports an observed amount A_i^j and is assigned a weight W_i^j , then define:

$$\bar{S}^j = \sum_{i=1}^{N_j} A_i^j W_i^j \quad j = 1, 2, 3, 4 \quad (E2.1)$$

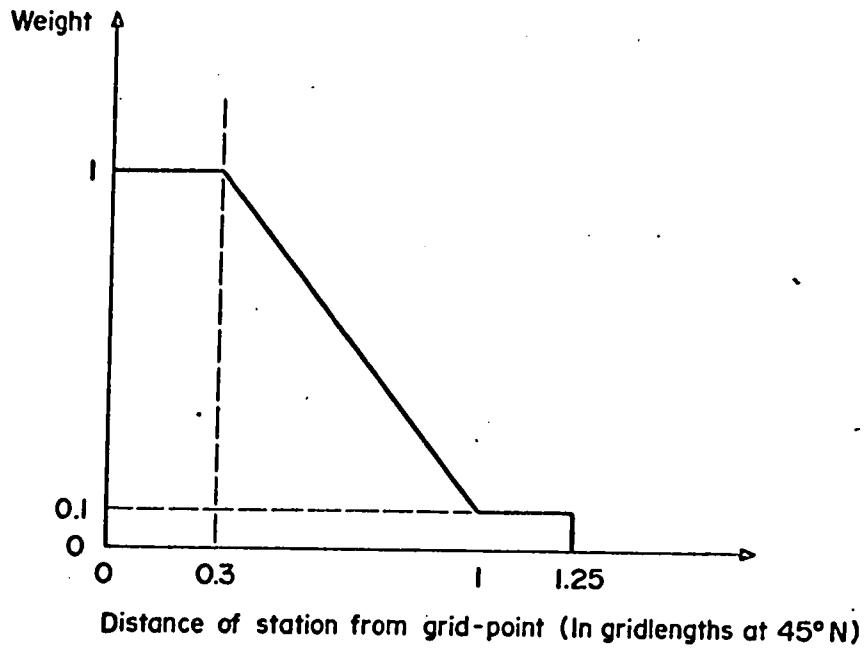


Fig. 77: Weight curve for objective analysis of observed reports of 6-hour & 24-hour precipitation amount.

$$\bar{W}^j = \frac{1}{N_j} \sum_i W_i^j \quad j = 1, 2, 3, 4 \quad (\text{E2.2})$$

$$\bar{A}^j = \bar{S}^j / (N_j \bar{W}^j) \quad j = 1, 2, 3, 4 \quad (\text{E2.3})$$

$$\bar{A}^T = \sum_j \bar{S}^j / (\sum_j N_j \bar{W}^j) \quad j = 1, 2, 3, 4 \quad (\text{E2.4})$$

The final analysed value, \bar{A}^F , at this grid point is given by:

$$\bar{A}^F = \frac{1}{2} \left\{ \bar{A}^T + \left[\frac{(\sum_j \bar{W}^j \bar{A}^j)}{(\sum_j \bar{W}^j)} \right] \right\} \quad (\text{E2.5})$$

This is merely a simple average, with equal weights, of: (i) a weighted mean by stations; and (ii) a weighted mean by quadrants. If there are no reporting stations at all within 1.25 grid-lengths of a grid-point, then that point is not analysed. Each grid point that is analysed is assigned a reliability indicator which reflect the data coverage in its neighbourhood. A grid-point is assigned to Class A if it satisfies either of the following two conditions:

- (a) There is at least one reporting station in each quadrant.
- (b) There is at least one reporting station within a distance of 0.3 grid-lengths.

A grid-point is assigned to Class B if it is not in Class A and it satisfies either one of the following two conditions:

- (a) There is at least one reporting station in each of three quadrants.

- (b) There is at least one reporting station within a distance of 0.5 grid-lengths.

A grid-point is assigned to Class C if it is not in Class A or Class B but there is at least one reporting station within the radius of influence. Most grid-points over continental North America are in a Class A data coverage region; but coastal grid-points are usually Class B or C. During the development of the analysis scheme those stations reporting trace amounts gave rise to some slight difficulty. Consequently, it was decided to arbitrarily classify trace reports as 0.003 inches.

E3. The penalty table verification score

The second step in the computation of a skill factor is to compute the penalty table verification scores of the forecasts as follows. The grid-point values of both forecasts and analyses are classified into four categories - "none", "light", "medium", or "heavy" - according to Table 76. This procedure may be carried out for both 6-hour and 24-hour precipitation amounts. At any given grid-point where the category of precipitation is incorrectly forecast, penalty marks are assigned according to the "usefulness" assessments of a penalty table carefully designed so as to reflect the interests of prospective users. For hypothetical "standard users" who mainly want to know whether it is going to rain or not, and who only have a secondary interest in the intensity of precipitation, the Penalty Tables I and II of Table 77 are appropriate. Penalty Table I should be used if equal inconvenience is caused by under-forecasting as by over-forecasting; e.g. if it is just as harmful to predict "none" and have "light" occur as it is to predict "light" and have "none" occur. Penalty Table II should be used if twice

as much inconvenience is caused by under-forecasting as by over-forecasting; e.g. if it is twice as harmful to predict "none" and have "light" occur as it is to predict "light" and have "none" occur. For a given penalty table, and for a given time period, three final verification scores are obtained by averaging the grid-point penalties over the verification area for the three different data-reliability classes.

E4. The penalty table skill factors

First, penalty table verification scores for null-forecasts, i.e. forecasts of zero precipitation everywhere, are computed exactly as in Section E3. The skill factors for each data-reliability class are then obtained by dividing the penalty table verification scores of the forecasts by the corresponding penalty table verification scores of the null-forecasts. The result is expressed as a percentage. Except in the absence or near absence of observed precipitation, these skill factors can be regarded as absolute measures of the usefulness of precipitation forecasts. In practice, over North America only the Class C scores occasionally run into trouble because of too little observed precipitation. Note that a perfect forecast would have a skill factor of 0%, whereas very poor forecasts would have skill factors of 200%, or even worse in the case of gross over-forecasting. It is fair to regard the 100% mark, i.e. the skill factor of a null-forecast, as the borderline between skill and lack of skill. This is a much more clearcut dividing line than exists for threat scores.

Category	6-hour amount in inches		24-hour amount in inches	
None	0	- 0.005	0	- 0.02
Light	0.005	- 0.1	0.02	- 0.4
Medium	0.1	- 0.5	0.4	- 2.0
Heavy		0.5		2.0

Table 76 : Definitions of the precipitation amount categories

		Forecast			
		None	Light	Medium	Heavy
Observed	None	0	60	90	100
	Light	60	0	25	35
	Medium	90	25	0	5
	Heavy	100	35	5	0

Penalty Table I : For use when under-forecasting and over-forecasting are equally harmful.

		Forecast			
		None	Light	Medium	Heavy
Observed	None	0	30	45	50
	Light	60	0	12.5	17.5
	Medium	90	25	0	2.5
	Heavy	100	35	5	0

Penalty Table II : For use when under-forecasting is twice as harmful as over-forecasting.

Table 77 : Penalty tables reflecting the interests of prospective users mainly concerned about whether precipitation will or will not occur. The numbers are penalty marks to be assigned to incorrect forecasts of the category of precipitation amount.

APPENDIX F : THE THREE-DIMENSIONAL RELAXATIONSF1. . Petterssen's Equation

The finite difference form of (23.5) may be written:

$$\nabla^2 \omega_m^{\text{II}} + A_m^* \left\{ (a_L^2)_{m-1} \omega_{m-1}^{\text{II}} + (a_c^2)_m \omega_m^{\text{II}} + (a_U^2)_{m+1} \omega_{m+1}^{\text{II}} \right\} = B_m^* , m = 2, 3, 4 \quad (\text{Fl.1})$$

where

$$A_m^* = gf / [4K (\sigma_s)_m] \quad (\text{Fl.2})$$

$$B_m^* = (\nabla^2 H) / (\sigma_s)_m \quad (\text{Fl.3})$$

$m = 1, 2, 3, 4, 5$ correspond to 1000, 850, 700, 500 and 200 mb respectively; $(a_L^2)_{m-1}$, $(a_c^2)_m$, and $(a_U^2)_{m+1}$ are given by (El4.2); K is defined by (Cl.3); $(\sigma_s)_m$ are the standard atmosphere static stabilities given in Table 2 ; the vertical boundary conditions are $\omega_1^{\text{II}} = 0$ and $\omega_5^{\text{II}} = 0$; and the lateral boundary conditions are $\omega_m^{\text{II}} = 0$. Equation (Fl.1)

may be solved by the following straightforward three-dimensional relaxation formula relating the N 'th guess, $(\omega_m^{\text{II}})^N$, to the $(N - 1)$ 'th, $(\omega_m^{\text{I}})^{N-1}$:

$$\begin{aligned} (\omega_m^{\text{II}})_{ij}^N &= \frac{\alpha}{[4 - (a_c^2)_m A_m^*]} \left\{ (\omega_m^{\text{II}})_{i-j}^N + (\omega_m^{\text{II}})_{i+j-1}^N + (\omega_m^{\text{II}})_{i+j}^{N-1} + (\omega_m^{\text{II}})_{i+j+1}^{N-1} \right. \\ &\quad \left. + A_m^* \left[(a_L^2)_{m-1} (\omega_{m-1})_{ij}^N + (a_U^2)_{m+1} (\omega_{m+1})_{ij}^{N-1} \right] - B_m^* \right. \\ &\quad \left. + [4 - (a_c^2)_m A_m^*] \left[\frac{1}{\alpha} - 1 \right] (\omega_m^{\text{I}})_{ij}^{N-1} \right\} \quad (\text{Fl.4}) \end{aligned}$$

where the relaxation coefficient, α , is taken to be 1.4114. At initial time the relaxation starts with a zero first guess field and is terminated after 20 scans. At subsequent hours the relaxation starts with the previous hour's ω_m^{II} values as first guess fields and terminates after 7 scans.

F2. The baroclinic model

In the main integration cycle of the baroclinic model equation (C1.5) may be rewritten as:

$$\nabla^2 X_m^* + \frac{1}{K} \sum_{n=1}^4 C_{mn} X_n^* = J_m, \quad m = 1, 2, 3, 4 \quad (\text{F2.1})$$

where

$$X_m^* = \left\langle \frac{\partial \psi_m}{\partial t} \right\rangle \quad (\text{F2.2})$$

Equation (F2.1) may be solved directly by the following straightforward three-dimensional relaxation formula relating the N 'th guess, $(X_m^*)^N$, to the $(N-1)$ 'th, $(X_m^*)^{N-1}$:

$$\begin{aligned} (X_m^*)_{ij}^N &= \frac{\alpha_m}{(4 - C_{mm}/K)} \left\{ (X_m^*)_{i-1j}^N + (X_m^*)_{ij-1}^N + (X_m^*)_{i+1j}^{N-1} \right. \\ &\quad \left. + (X_m^*)_{ij+1}^{N-1} + \left[\sum_{\substack{n=1 \\ n \neq m}}^4 C_{mn} (X_n^*)_{ij}^M \right] / K - J_m \right. \\ &\quad \left. + (4 - C_{mm}/K) \left[\frac{1}{\alpha_m} - 1 \right] (X_m^*)_{ij}^{N-1} \right\} \quad (\text{F2.3}) \end{aligned}$$

where

$$M = \begin{cases} N & \text{if } m > n \\ N-1 & \text{if } m < n \end{cases} \quad (\text{F2.4})$$

and for a model with four full working levels $\alpha_2 = \alpha_3 = 1.414$ and $\alpha_1 = \alpha_4 = 1.28$. The lateral boundary conditions could be specified from earlier integrations over a larger grid, but in the three-dimensional relaxations carried out so far the boundary stream function tendencies have been specified as zero. At initial time the relaxation starts with a zero first guess field and is terminated after 20 scans. At subsequent hours the relaxation starts with the previous hour's stream function tendency values as first guess fields and terminates after 7 scans.

APPENDIX G : THE LOW TROPOPAUSE MARKERG1. The definition of N_{ϵ}

The low tropopause marker, N_{ϵ} , which appears in equation (26.20) is defined by:

$$N_{\epsilon} = \begin{cases} 0 & \text{if } \delta_1 > 0 \text{ or } \delta_2 > 0 \text{ or } \delta_3 > 0 \\ 1 & \text{otherwise} \end{cases} \quad (\text{G1.1})$$

where

$$\delta_1 = \nabla^2(\psi_{20} - \psi_{50}) \quad (\text{G1.2})$$

$$\delta_2 = [\nabla(\psi_{20} - \psi_{50})], [\nabla\psi_{20}] \quad (\text{G1.3})$$

$$\delta_3 = [\nabla(\psi_{20} - \psi_{50})], [\nabla(|\nabla\psi_{20}|^2)] \quad (\text{G1.4})$$

∇ is the finite difference gradient operator (B7.5), and ∇^2 is the finite difference Laplacian operator (B10.1).

APPENDIX H : FORMULAE FOR SECONDARY LATENT HEAT EFFECTSHL. Liquefaction or freezing of falling precipitation

The appropriate value of L_a in (28.2) is obtained as follows:

Case (i) : $T_m \geq T_L$, $m = 1, 2$

$$(L_a)_m = \begin{cases} 0 & \text{if } T_{m+1} \geq T_L \\ \left(\frac{T_L - T_{m+1}}{T_L - T_L'} \right) (L_i - L) & \text{if } T_L > T_{m+1} > T_L' \\ (L_i - L) & \text{if } T_L' \geq T_{m+1} \end{cases} \quad (\text{HL.1})$$

Case (ii) : $T_L > T_m > T_L'$, $m = 1, 2$

$$(L_a)_m = \begin{cases} - \left(\frac{T_L - T_m}{T_L - T_L'} \right) (L_i - L) & \text{if } T_{m+1} \geq T_L \\ \left(\frac{T_m - T_{m+1}}{T_L - T_L'} \right) (L_i - L) & \text{if } T_L > T_{m+1} > T_L' \\ \left(\frac{T_m - T_L'}{T_L - T_L'} \right) (L_i - L) & \text{if } T_L' \geq T_{m+1} \end{cases} \quad (\text{HL.2})$$

Case (iii) : $T_L' \geq T_m$, $m = 1, 2$

$$(L_a)_m = \begin{cases} - (L_i - L) & \text{if } T_{m+1} \geq T_L \\ - \left(\frac{T_{m+1} - T_L'}{T_L - T_L'} \right) (L_i - L) & \text{if } T_L > T_{m+1} > T_L' \\ 0 & \text{if } T_L' \geq T_{m+1} \end{cases} \quad (\text{HL.3})$$

where the subscripts $m = 1, 2, 3$ correspond to 850, 700 and 500 mb respectively, and L_i , L , T_L and T_L' are given in Table 26.

H2. Evaporation of falling precipitation

The appropriate value of L_b in (28.2) is given by:

$$(L_b)_m = \begin{cases} L & \text{if } T_{m+1} \geq T_L \\ \left(\frac{T_L - T_{m+1}}{T_L - T_L'} \right) L_i + \left(\frac{T_{m+1} - T_L}{T_L - T_L'} \right) L & \text{if } T_L > T_{m+1} > T_L' \\ L_i & \text{if } T_L' \geq T_{m+1} \end{cases} \quad \text{(H2.1)} \quad m = 1, 2$$

where once again the subscripts $m = 1, 2, 3$ correspond to 850, 700, and 500 mb respectively, and L_i , L , T_L and T_L' are given in Table 26.

APPENDIX I : THE EFFECTIVE OCEAN EQUILIBRIUM TEMPERATURESII. At the 1000 mb level

The effective ocean equilibrium temperature at 1000 mb, $(T_\alpha)_{1000}$, is the temperature a parcel of air would have at this level if it had ascended or, hypothetically, descended moist adiabatically from the ocean surface, and had started out with the temperature, T_0 , and pressure of the ocean surface. However, $(T_\alpha)_{1000}$ is only computed at initial time, not at every time step. Consequently, the computations are based on a triple-smoothed version of the 1000 mb height chart, \bar{z}_{1000} , which is obtained by applying the standard smoothing operator (B3.1) three times in succession to the initial time 1000 mb height chart. An iterative procedure is employed. Let $(T_\alpha)_{1000}^N$ be the N th guess at $(T_\alpha)_{1000}$, $(\rho_{1000})^N$ the N th guess at the corresponding density, $(\Delta p_{1000})^N$ and $(\Delta \rho_{1000})^N$ the N th guesses at the pressure and density increments, respectively, of the ocean surface over 1000 mb — so that the pressure at the ocean surface is $(1000 + \Delta p_{1000})$, and the density is $(\rho_{1000} + \Delta \rho_{1000})$. The N th guesses of these quantities are related to the $(N-1)$ th guesses as follows:

$$(\rho_{1000})^N = a_1^* [(T_\alpha)_{1000}^{N-1}]^2 + a_2^* (T_\alpha)_{1000}^{N-1} + a_3^* \quad (\text{II.1})$$

$$(\Delta \rho_{1000})^N = [a_4^* (T_\alpha)_{1000}^{N-1} + a_5^*] (\Delta p_{1000})^{N-1} \quad (\text{II.2})$$

$$(\Delta p_{1000})^N = a_6^* \left(\rho_{1000}^N + \frac{1}{2} \Delta \rho_{1000}^N \right) \bar{z}_{1000} \quad (\text{II.3})$$

Constant	Condition	Value	Units
Q_1^*	-	0.175×10^{-5}	$\text{Kg m}^{-3} (\text{C deg})^{-2}$
Q_2^*	-	-0.465×10^{-3}	$\text{Kg m}^{-3} (\text{C deg})^{-1}$
Q_3^*	-	1.276	Kg m^{-3}
Q_4^*	-	-0.5×10^{-5}	$\text{Kg m}^{-3} (\text{C deg})^{-1} \text{mb}^{-1}$
Q_5^*	-	0.1285×10^{-2}	$\text{Kg m}^{-3} \text{mb}^{-1}$
Q_6^*	-	-0.981	dkm sec^{-2}
Q_7^*	$30 > (T_\alpha)_{1000}^{N-1} \geq 10$	-0.7×10^{-3}	mb^{-1}
Q_7^*	$10 > (T_\alpha)_{1000}^{N-1} \geq 0$	-0.9×10^{-3}	mb^{-1}
Q_7^*	$0 > (T_\alpha)_{1000}^{N-1} \geq -20$	-0.5×10^{-3}	mb^{-1}
Q_7^*	$-20 > (T_\alpha)_{1000}^{N-1}$	-0.5×10^{-4}	mb^{-1}
Q_8^*	$30 > (T_\alpha)_{1000}^{N-1} \geq 10$	5.1×10^{-2}	C deg mb^{-1}
Q_8^*	$10 > (T_\alpha)_{1000}^{N-1} \geq 0$	5.2×10^{-2}	C deg mb^{-1}
Q_8^*	$0 > (T_\alpha)_{1000}^{N-1} \geq -20$	5.3×10^{-2}	C deg mb^{-1}
Q_8^*	$-20 > (T_\alpha)_{1000}^{N-1}$	6.2×10^{-2}	C deg mb^{-1}

Table 78 : Values of the constants used in the iteration to determine the effective ocean equilibrium temperature at 1000 mb, $(T_\alpha)_{1000}$.

$$\left(\frac{dT}{dP}\right)_{\theta_w} \Big|_{1000}^N = a_7^* (T_\alpha)_{1000}^{N-1} + a_8^* \quad (\text{II.4})$$

$$(T_\alpha^N)_{1000} = (T_\alpha^{N-1})_{1000} - \left(\frac{dT}{dP}\right)_{\theta_w} \Big|_{1000}^N (\Delta P_{1000})^N \quad (\text{II.5})$$

where the values of the constants a_1^* , a_2^* , a_3^* , a_4^* , a_5^* , a_6^* , a_7^* , and a_8^* are given in Table 78. The climatological ocean surface temperature, T_ϕ , is used as a first guess field for $(T_\alpha)_{1000}$ and the iteration is terminated after five scans. T_ϕ is obtained by interpolation from the corresponding monthly mean charts.

12. At the levels aloft

The empirical ocean heating term (29.1) requires the specification of effective ocean equilibrium temperatures at 850, 700 and 500 mb, $(T_\alpha)_{850}$, $(T_\alpha)_{700}$, and $(T_\alpha)_{500}$, i.e. the temperatures that parcels of air would have at these levels if they had ascended moist adiabatically from the ocean surface, and had started out with the temperature, T_ϕ , and pressure of the ocean surface. These are obtained directly from $(T_\alpha)_{1000}$ by the following formula:

$$(T_\alpha)_m = a_9^* (T_\alpha)_{1000}^2 + a_{10}^* (T_\alpha)_{1000} - a_{11}^* + \frac{w_{850} T_e}{w_\alpha (p_0 w_{850})} \quad (\text{12.1})$$

where

$$W_{\alpha}(P_9, W_{850}) = \begin{cases} \infty & \text{if } \hat{P}_9 < \hat{P}_9^* \\ \hat{W}_{\alpha} & \text{if } |W_{850}| \leq \hat{W}_{\alpha} \text{ and } \hat{P}_9 \geq \hat{P}_9^* \\ |W_{850}| & \text{if } |W_{850}| > \hat{W}_{\alpha} \text{ and } \hat{P}_9 \geq \hat{P}_9^* \end{cases} \quad (\text{I2.2})$$

where \hat{P}_9^* is the minimum value of P_9 in the square nine-point stencil area centred on the point for which W_{α} is being evaluated,

$\hat{W}_{\alpha} = 20$ mb/hour, $\hat{P}_9^* = 900$ mb, $T_E = -1.5$ C deg, and a_q^* , a_{10}^* , and a_{11}^* are given in Table 79.

Constant	Level (mb)	$(T_{\alpha}) < -20$ <small>1000</small>	$-20 < (T_{\alpha}) \leq 0$ <small>1000</small>	$0 < (T_{\alpha}) \leq 20$ <small>1000</small>	$(T_{\alpha}) > 20$ <small>1000</small>	Units
a_q^*	850	0	0	0	0	(C deg) ⁻¹
a_{10}^*	850	1.0	1.11	1.11	1.11	-
a_{11}^*	850	8.5	8.3	8.3	8.3	C deg
a_q^*	700	0	0.5×10^{-2}	0.15×10^{-2}	0	(C deg) ⁻¹
a_{10}^*	700	0.95	1.25	1.285	1.23	-
a_{11}^*	700	24.0	20.0	20.0	18.3	C deg
a_q^*	500	0.5×10^{-2}	0.5×10^{-2}	0.1×10^{-1}	0	(C deg) ⁻¹
a_{10}^*	500	1.25	1.25	1.42	1.6	-
a_{11}^*	500	41.0	41.0	41.0	40.6	C deg

Table 79 : Values of the constants used in the determination of the effective ocean equilibrium temperatures aloft.